

DE GRUYTER



REVIEWS in MINERALOGY

Volume 24

MODERN METHODS OF IGNEOUS PETROLOGY: Understanding Magmatic Processes

J. Nicholls & J. K. Russell, editors

- PRINCIPLES OF THERMODYNAMIC MODELING
OF IGNEOUS PROCESSES *J. NICHOLLS*
- THERMODYNAMIC PROPERTIES OF SILICATE LIQUIDS
WITH EMPHASIS ON DENSITY, THERMAL EXPANSION
AND COMPRESSIBILITY *R.L. LANGE & I.S.E. CARMICHAEL*
- SIMULATION OF IGNEOUS DIFFERENTIATION
PROCESSES *R.L. NIELSEN*
- THE MATHEMATICS OF FLUID FLOW AND A SIMPLE
APPLICATION TO PROBLEMS OF MAGMA TRANSPORT *J. NICHOLLS*
- PHYSICAL PROCESSES IN THE EVOLUTION OF
MAGMAS *S. TAIT & C. JAUPART*
- MAGMA MIXING PROCESSES: INSIGHTS AND CONSTRAINTS
FROM THERMODYNAMIC CALCULATIONS *J.K. RUSSELL*
- CONTROLS ON OXIDATION-REDUCTION RELATIONS
IN MAGMAS *I.S.E. CARMICHAEL & M.S. GHIORSO*
- DYNAMICS OF ERUPTIVE PHENOMENA *C. JAUPART & S. TAIT*
- MELT FRACTION DIAGRAMS: THE LINK BETWEEN
CHEMICAL AND TRANSPORT MODELS *G. BERGANTZ*
- TEXTURAL CONSTRAINTS ON THE KINETICS OF
CRYSTALLIZATION OF IGNEOUS ROCKS *K.V. CASHMAN*

Series Editor: Paul H. Ribbe

MINERALOGICAL SOCIETY OF AMERICA

REVIEWS IN MINERALOGY

VOLUME 24

**MODERN METHODS OF IGNEOUS
PETROLOGY: UNDERSTANDING
MAGMATIC PROCESSES**

J. NICHOLLS & J. K. RUSSELL, editors

Authors:

GEORGE BERGANTZ
MARK S. GHIORSO
Dept. of Geological Sciences
University of Washington
Seattle, Washington 98195

IAN S. E. CARMICHAEL
Dept. of Geology & Geophysics
University of California
Berkeley, California 94720

KATHARINE V. CASHMAN
REBECCA L. LANGE
Dept. of Geological &
Geophysical Sciences
Princeton University
Princeton, New Jersey 08544

CLAUDE JAUPART
Department of Geology
University of Bristol,
Wills Memorial Building
Queens Road
Bristol B58 1RJ, England

JAMES NICHOLLS
Dept. of Geology & Geophysics
University of Calgary
Calgary, Alberta T2N 1N4
Canada

ROGER L. NIELSEN
College of Oceanography
Oregon State University at
Corvallis
Corvallis, Oregon 97331

KELLY RUSSELL
Dept. of Geological Sciences
University of British Columbia
Vancouver, British Columbia
V6T 2B4 Canada

STEPHEN TAIT
Laboratoire de Dynamic des
Systèmes Géologiques
Université de Paris 7
Institut de Physique du Globe
4 Place Jussieu, Tour 14-15
75252 Paris Cédex 05, France

Series Editor:

PAUL H. RIBBE
Department of Geological Sciences
Virginia Polytechnic Institute and State University
Blacksburg, Virginia 24061

PUBLISHED BY THE MINERALOGICAL SOCIETY OF AMERICA

1130 SEVENTEENTH STREET, N.W., SUITE 330, WASHINGTON, D.C. 20036

COPYRIGHT: 1990

MINERALOGICAL SOCIETY of AMERICA

Printed by BookCrafters, Inc., Chelsea, Michigan 48118

REVIEWS in MINERALOGY
(Formerly: *SHORT COURSE NOTES*)

ISSN 0275-0279

Volume 24

**MODERN METHODS OF IGNEOUS PETROLOGY:
UNDERSTANDING MAGMATIC PROCESSES**

ISBN 0-939950-29-4

ADDITIONAL COPIES of this volume as well as those listed below
may be obtained from the MINERALOGICAL SOCIETY OF AMERICA,
1130 Seventeenth Street, N.W., Suite 330, Washington, D.C. 20036 U.S.A.

| <u>Vol.</u> | <u>Year</u> | <u>Pages</u> | <u>Editor(s)</u> | <u>Title</u> |
|-------------|-----------------|--------------|---|--|
| 1 | 1974 | 284 | P. H. Ribbe | SULFIDE MINERALOGY |
| 2 | 1983 | 362 | P. H. Ribbe | FELDSPAR MINERALOGY (2nd edition) |
| 3 | out of print | | | OXIDE MINERALS |
| 4 | 1977 | 232 | F. A. Mumpton | MINERALOGY AND GEOLOGY OF NATURAL ZEOLITES |
| 5 | 1982 | 450 | P. H. Ribbe | ORTHOSILICATES (2nd edition) |
| 6 | 1979 | 380 | R. G. Burns | MARINE MINERALS |
| 7 | 1980 | 525 | C. T. Prewitt | PYROXENES |
| 8 | 1981 | 398 | A. C. Lasaga R. J. Kirkpatrick | KINETICS OF GEOCHEMICAL PROCESSES |
| 9A | 1981 | 372 | D. R. Veblen | AMPHIBOLES AND OTHER HYDROUS PYRIBOLES— MINERALOGY |
| 9B | 1982 | 390 | D. R. Veblen P. H. Ribbe | AMPHIBOLES: PETROLOGY AND EXPERIMENTAL PHASE RELATIONS |
| 10 | 1982 | 397 | J. M. Ferry | CHARACTERIZATION OF METAMORPHISM THROUGH MINERAL EQUILIBRIA |
| 11 | 1983 | 394 | R. J. Reeder | CARBONATES: MINERALOGY AND CHEMISTRY |
| 12 | 1983 | 644 | E. Roedder | FLUID INCLUSIONS (Monograph) |
| 13 | 1984 | 584 | S. W. Bailey | MICAS |
| 14 | 1985 | 428 | S. W. Kieffer A. Navrotsky | MICROSCOPIC TO MACROSCOPIC: ATOMIC ENVIRONMENTS TO MINERAL THERMODYNAMICS |
| 15 | 1990 | 406 | M. B. Boisen, Jr. G. V. Gibbs | MATHEMATICAL CRYSTALLOGRAPHY (Revised) |
| 16 | 1986 | 570 | J. W. Valley H. P. Taylor, Jr. J. R. O'Neil | STABLE ISOTOPES IN HIGH TEMPERATURE GEOLOGICAL PROCESSES |
| 17 | 1987 | 500 | H. P. Eugster I. S. E. Carmichael | THERMODYNAMIC MODELLING OF GEOLOGICAL MATERIALS: MINERALS, FLUIDS, MELTS |
| 18 | 1988 | 698 | F. C. Hawthorne | SPECTROSCOPIC METHODS IN MINERALOGY AND GEOLOGY |
| 19 | 1988 | 698 | S. W. Bailey | HYDROUS PHYLLOSILICATES (EXCLUSIVE OF MICAS) |
| 20 | 1989 | 369 | D. L. Bish J. E. Post | MODERN POWDER DIFFRACTION |
| 21 | 1989 | 348 | B. R. Lipin G. A. McKay | GEOCHEMISTRY AND MINERALOGY OF RARE EARTH ELEMENTS |
| 22 | 1990 | 406 | D. M. Kerrick | THE Al_2SiO_5 POLYMORPHS (Monograph) |
| 23 | 1990 | 603 | M. F. Hochella, Jr. A. F. White | MINERAL-WATER INTERFACE GEOCHEMISTRY |
| 24 | 1990 | | J. Nicholls J. K. Russell | MODERN METHODS OF IGNEOUS PETROLOGY— UNDERSTANDING MAGMATIC PROCESSES |

MODERN METHODS OF IGNEOUS PETROLOGY: UNDERSTANDING MAGMATIC PROCESSES

FOREWORD

The Mineralogical Society of America (MSA) sponsored a short course by this title December 1990 at the Cathedral Hill Hotel in San Francisco, California. It was organized by the editors, Jim Nicholls and Kelly Russell, and presented by the authors of this volume to about 80 participants in conjunction with the Fall Meeting of the American Geophysical Union.

As with other volumes in the *Reviews in Mineralogy* series, this one was prepared camera-ready by the authors and *RiM*'s editorial assistant, Marianne Stern. Margie Sentelle is gratefully acknowledged for her contributions to formatting and typing.

Paul H. Ribbe
Blacksburg, VA
23 October 1990

PREFACE

Igneous petrology, in its broadest applications, treats the transfer of matter and energy from planetary interiors to their exteriors. Over the past several decades igneous petrology has gained sophistication in three areas that deal with such transfers: the properties of silicate melts and solids can be estimated as functions of pressure, temperature and composition; some results of experimental and theoretical studies of the physics of multiphase flow are available; and many of the algorithms for realistically modeling magmatic processes are in place. Each of these fields of study, to some extent, have to be pursued independently. In our opinion, now is an ideal time to collect some features of these studies as preparation for more integrated future work and to show some consequences of applying current ideas to the study of igneous processes. We have attempted to bring together the basic data and fundamental theoretical constraints on magmatic processes with applications to specific problems in igneous petrology.

This book is the result of the dedication, cooperation, and understanding of every author, the series editor, Paul Ribbe, and the MSA staff. We very much appreciate their efforts. Many of the ideas and studies herein originated with the work, guidance, and inspiration of Ian Carmichael. In the year of his 60th birthday, we dedicate this volume to him in appreciation.

J. Nicholls
Calgary, Canada

J. K. Russell
Vancouver, Canada

October 1990

TABLE OF CONTENTS

Page

- ii Copyright; Additional Copies
- iii Foreword; Preface

Chapter 1

J. Nicholls

PRINCIPLES OF THERMODYNAMIC MODELING OF IGNEOUS PROCESSES

- 1 INTRODUCTION
- 1 DUEHM'S THEOREM AND THE PHASE RULE
- 3 Example of the application of Duhem's theorem
- 6 CALCULATION OF CRYSTALLIZATION PATHS
- 8 Perfect equilibrium paths
- 10 Isobaric perfect fractionation paths
- 13 Polybaric fractionation curves
- 15 Multiphase fractionation paths
- 16 TESTING THERMODYNAMIC MODELS
- 19 ACKNOWLEDGMENTS
- 19 REFERENCES
- 20 APPENDIX: DERIVATION OF FRACTIONATION EQUATION AT CONSTANT H_{melt}

Chapter 2

R.L. Lange & I.S.E. Carmichael

THERMODYNAMIC PROPERTIES OF SILICATE LIQUIDS WITH EMPHASIS ON DENSITY, THERMAL EXPANSION AND COMPRESSIBILITY

- 25 INTRODUCTION
- 27 THE STANDARD STATE FREE ENERGY OF NATURAL LIQUIDS
- 28 VOLUMETRIC PROPERTIES OF SILICATE LIQUIDS
- 29 The compositional dependence of liquid volumes at 1 bar
- 30 *TiO₂-bearing liquids*
- 31 *Iron-bearing liquids*
- 35 Thermal expansion of silicate liquids
- 39 Volumes of fusion at 1 bar
- 41 Compressibility of silicate liquids
- 41 *Compositional dependence of $(dV/dP)_T$*
- 44 *Compressibility of the ferric component*
- 45 *The pressure dependence of compressibility*
- 48 The effect of volatiles on silicate liquid densities
- 49 *The partial molar volume of H₂O*
- 54 *The partial molar volume of CO₂*
- 56 SUMMARY
- 57 APPENDIX: CALORIMETRIC DATA
- 57 Enthalpies and entropies of fusion
- 57 Heat capacities of silicate liquids and glasses
- 59 ACKNOWLEDGMENTS
- 59 REFERENCES

Chapter 3

R.L. Nielsen

SIMULATION OF IGNEOUS DIFFERENTIATION PROCESSES

| | |
|-----|--|
| 65 | INTRODUCTION |
| 65 | THEORETICAL BACKGROUND |
| 65 | Major element phase equilibria |
| 66 | Trace element partitioning |
| 69 | Assumptions and options of the program |
| 70 | MODELING OPEN SYSTEM PROCESSES |
| 70 | Paired recharge and fractionation |
| 71 | Recharge rate and fractionating mineral proportions |
| 74 | Phase equilibria constraints on bulk partition coefficient |
| 76 | Variable oxygen fugacity |
| 76 | Periodic mixing |
| 78 | In situ fractionation |
| 84 | TESTING PETROLOGIC TOOLS WITH MODELED RESULTS |
| 84 | Calculation of parental magma compositions |
| 85 | Least-squares-mass balance fractionation models |
| 88 | Derivation of D from log-log plots |
| 88 | Pearce element ratio analysis |
| 95 | PROBLEM SOLVING IN NATURAL SYSTEMS |
| 95 | Uwekehuna Bluff |
| 99 | Galapagos spreading center |
| 100 | Kilauea Iki – olivine resorption |
| 102 | CONCLUSIONS |
| 103 | ACKNOWLEDGMENTS |
| 103 | REFERENCES |

Chapter 4

J. Nicholls

THE MATHEMATICS OF FLUID FLOW AND A SIMPLE APPLICATION TO PROBLEMS OF MAGMA TRANSPORT

| | |
|-----|---|
| 107 | INTRODUCTION |
| 107 | MATHEMATICAL OPERATORS |
| 109 | DIFFERENTIAL EQUATIONS OF FLUID MECHANICS |
| 109 | The equation of continuity |
| 110 | The Navier-Stokes equations |
| 110 | Conservation of energy |
| 111 | UNIDIRECTIONAL FLOWS |
| 111 | Application to a simple problem |
| 117 | Interpretation |
| 122 | Conclusions |
| 123 | REFERENCES CITED |

Chapter 5

S. Tait & C. Jaupart

PHYSICAL PROCESSES IN THE EVOLUTION OF MAGMAS

| | |
|-----|-------------------------------|
| 125 | FOREWORD |
| 125 | INTRODUCTION |
| 125 | Physical properties of magmas |

| | |
|-----|---|
| 127 | Evidence from fossil magma chambers |
| 128 | Chemical aspects |
| 130 | THERMAL CONVECTION |
| 130 | Temperature of contact between magma and country rock |
| 131 | Structure of the thermal boundary layers |
| 132 | Structure of the convecting interior |
| 135 | Thermal flux balance at the roof |
| 137 | Further complexities of upper boundary layer structure |
| 137 | FREEZING OF A BINARY ALLOY AND COMPOSITIONAL CONVECTION |
| 137 | Solidification and constitutional supercooling |
| 139 | Structure of a "mushy" crystallization boundary layer |
| 141 | Onset of compositional convection |
| 143 | Convective transport of solute |
| 144 | Vertical walls |
| 146 | Conclusion |
| 146 | SUMMARY OF OTHER PHENOMENA |
| 147 | Crystal settling |
| 147 | The kinetics of crystal nucleation and growth |
| 148 | Magma chamber replenishment |
| 151 | REFERENCES |

Chapter 6

J.K. Russell

MAGMA MIXING PROCESSES: INSIGHTS AND CONSTRAINTS FROM THERMODYNAMIC CALCULATIONS

| | |
|-----|--|
| 153 | INTRODUCTION |
| 154 | HISTORY OF TREATMENT |
| 155 | TESTABILITY OF THE MAGMA MIXING HYPOTHESIS |
| 157 | ELEMENTARY PRINCIPLES OF MAGMA MIXING |
| 159 | Melt mixing |
| 164 | Solid phase saturation |
| 166 | Oxidation potential and H ₂ O solubility |
| 171 | MODELLING THE MAGMA MIXING PROCESS |
| 171 | Magmatic paths: fractional mixing vs. equilibrium mixing |
| 172 | Thermodynamic paths of magma mixing |
| 174 | COMPUTATIONAL ALGORITHM |
| 174 | Temperature as the independent variable |
| 176 | Temperature of as a dependent variable |
| 177 | Adiabatic and non-adiabatic paths |
| 178 | MODEL SIMULATIONS |
| 186 | CONCLUSIONS |
| 187 | ACKNOWLEDGMENTS |
| 187 | REFERENCES |

Chapter 7

I.S.E. Carmichael & M.S. Ghiorso

THE EFFECT OF OXYGEN FUGACITY ON THE REDOX STATE OF NATURAL LIQUIDS AND THEIR CRYSTALLIZING PHASES

| | |
|-----|---|
| 191 | INTRODUCTION |
| 192 | REDOX STATE AND OXYGEN FUGACITY IN NATURAL SILICATE LIQUIDS |
| 197 | METALS OF VARIABLE VALENCE AND OXYGEN FUGACITY |

| | |
|-----|---|
| 200 | THE EFFECT OF REDOX STATE ON OLIVINE-LIQUID EQUILIBRIUM |
| 205 | THE EFFECT OF REDOX STATE OF PYROXENE-LIQUID EQUILIBRIA |
| 207 | HYDROUS MINERALS AND THEIR RELATIONSHIPS TO LIQUIDS |
| 208 | IRON-TITANIUM OXIDES AND SULFIDES AND THE REDOX STATE OF THE LIQUID |
| 209 | CONCLUSIONS |
| 210 | A PETROLOGICAL CONCERN |
| 210 | REFERENCES |

Chapter 8

C. Jaupart & S. Tait

DYNAMICS OF ERUPTIVE PHENOMENA

| | |
|-----|---|
| 213 | FOREWORD |
| 213 | INTRODUCTION |
| 213 | BASIC PRINCIPLES AND OBSERVATIONS |
| 213 | Dimensions of volcanic systems |
| 214 | Velocity and mass flux of eruptions |
| 215 | Eruption triggering |
| 216 | Effect of eruptions on the magma chamber |
| 217 | THE PROPERTIES OF VOLCANIC LIQUIDS |
| 217 | Physical properties of lava |
| 217 | <i>The viscosity of silicate melts</i> |
| 218 | <i>The viscosity of bubbly liquids</i> |
| 219 | <i>The temperature dependence of viscosity</i> |
| 219 | The solubility of gas species of silicate melts |
| 219 | The density of magmatic gases |
| 220 | The fragmentation process |
| 221 | Conclusions |
| 222 | FLOW EQUATIONS |
| 222 | Basic principles and equations |
| 223 | The mass flux of an eruption |
| 224 | <i>Constant conduit radius</i> |
| 225 | <i>Variable conduit radius</i> |
| 227 | <i>Conclusion</i> |
| 227 | COMPRESSIBLE FLOW |
| 227 | Laminar regime and variable properties |
| 228 | Choking conditions |
| 231 | Conduit flow in explosive eruption regimes |
| 231 | Generalized momentum balance |
| 232 | Conclusion |
| 232 | OTHER EFFECTS ON FLOW CONDITIONS |
| 232 | Separated flow |
| 233 | The physics of bubble growth |
| 234 | <i>Bubble nucleation</i> |
| 234 | <i>Bubble expansion</i> |
| 235 | <i>Chemical diffusion</i> |
| 235 | <i>Conclusion</i> |
| 235 | GENERAL CONCLUSION |
| 236 | REFERENCES |

Chapter 9

G.W. Bergantz

MELT FRACTION DIAGRAMS: THE LINK BETWEEN CHEMICAL AND TRANSPORT MODELS

| | |
|-----|---|
| 239 | INTRODUCTION |
| 241 | MELT FRACTION DISTRIBUTIONS |
| 241 | A general energy conservation expression |
| 245 | Generic elements of melt fraction curves |
| 248 | GEOLOGICAL IMPLICATIONS |
| 243 | The MASH hypothesis and a baseline physical state |
| 254 | REFERENCES |

Chapter 10

K.V. Cashman

TEXTURAL CONSTRAINTS ON THE KINETICS OF CRYSTALLIZATION OF IGNEOUS ROCKS

| | |
|-----|--|
| 259 | INTRODUCTION |
| 260 | NUCLEATION |
| 260 | Theory |
| 260 | Homogeneous nucleation |
| 263 | Heterogeneous nucleation |
| 264 | Experimental constraints |
| 266 | CRYSTAL GROWTH |
| 266 | Theory |
| 266 | <i>Crystallization without a change in composition</i> |
| 268 | <i>Crystallization in multicomponent systems</i> |
| 268 | Experimental constraints |
| 274 | COUPLED NUCLEATION AND GROWTH (AVRAMI EQUATION) |
| 282 | CRYSTALLIZATION IN NATURAL SYSTEMS |
| 283 | Crystallization of dikes |
| 287 | Crystal size distributions |
| 287 | Theory |
| 291 | <i>Isobaric cooling</i> |
| 295 | <i>Isothermal depressurization</i> |
| 297 | <i>Crystallization caused by change in supersaturation</i> |
| 297 | <i>Residence times</i> |
| 299 | <i>Effect of physical processes</i> |
| 300 | <i>Further potential applications of CSDs</i> |
| 300 | CONCLUSIONS |
| 303 | APPENDIX: STEREOLOGY AND IMAGE ANALYSIS |
| 309 | ACKNOWLEDGMENTS |
| 309 | REFERENCES |

PRINCIPLES OF THERMODYNAMIC MODELING OF IGNEOUS PROCESSES

INTRODUCTION

This chapter is an outline of the thermodynamic basis for modeling crystal-melt equilibria. Because the purpose of the chapter is illustrative, rather than rigorous applications to specific problems, numerical analysis can be kept to a minimum by treating solutions as ideal, thus eliminating the effects of activity coefficients. In addition, the standard state Gibbs energies of crystallization are assumed to be linear functions of temperature and pressure. This eliminates the numerical problems that arise from thermal expansion, compressibility and heat capacity changes. Once the features of ideal systems are mastered, the principles involved in modeling real systems are easily followed.

DUHEM'S THEOREM AND THE PHASE RULE

The first question to sort out is how much information must be available before modeling can be applied? The answer is surprisingly simple: if we know the composition of the system, then we need only two other pieces of information. Duhem's theorem (Duhem, 1898a, 1898b), a little known form of a phase rule, can be stated:

Given the composition of a chemical system, then two and only two independent variables need be fixed to determine the equilibrium state of the system.

The more commonly known phase rule, the Gibbs phase rule, can be written:

$$F = c - \phi + 2 \quad (1)$$

where F is the degrees of freedom or number of variables that must be fixed in order to define the equilibrium state of the system, c is the number of components in the system and ϕ is the number of phases in the system. The import of Duhem's theorem is that the degrees of freedom are equal to two if we know the composition of the system.

In chemical systems of interest to petrologists, the intensive variables include P , T and the compositions of all the phases present. In addition to P , T and phase compositions, igneous petrologists have traditionally been preoccupied with the modal abundances of the phases in the system (e.g., Johannsen, 1931). Modal amounts are not considered intensive variables in derivations of the Gibbs phase rule (e.g., Prigogine and Defay, 1954, p. 174-175). They are, however, intensive variables because they are measured in relative units (e.g., volume percent, weight percent, etc.). The intensive variables describing the phase compositions are related to properties of the phases, such as volumes, by partial molar quantities:

$$v^\alpha = \sum_i v_i^\alpha x_i^\alpha \quad (2)$$

where v^α is the molar volume of phase α , v_i^α is the partial molar volume of component i in phase α , and x_i^α is the mole fraction of component i in phase α . The summation is over index $i = 1..N$, N being the number of components in phase α .

Whereas phase properties are related to partial molar quantities and compositions, properties of the chemical system itself are related to the phase properties and the modal amounts:

$$v = \sum_{\alpha} v^{\alpha} z^{\alpha} \quad (3)$$

where v is the molar volume of the chemical system, z^α is the molar concentration of phase α in the system and v^α is the molar volume of phase α . In Equation (3), the sum is over index $\alpha = 1..\phi$, ϕ being the number of phases in the system. Consequently, we see that the molar volumes of the phases stand in relation to the molar volume of the system like the partial molar volumes stand relative to the molar volumes of the phases. Both the molar system properties, such as v , and the molar phase properties, for example v^α , are intensive variables.

A typical statement of Duhem's theorem is (Prigogine and Defay, 1954, p. 188):

"Whatever the number of phases, of components or of chemical reactions, the equilibrium state of a closed system, for which we know the initial masses [of the constituents] is completely determined by two independent variables."

Compared to the statement given earlier, this is a much more restrictive version of Duhem's theorem in two ways. First, the initial masses of a chemical system can be more difficult to estimate than the composition of the system. For example, part of a rock body may not be exposed. Second, the system need not remain closed after we calculate its equilibrium state; all that is required by Duhem's theorem is the composition of the system in an equilibrium state, even if instantaneous.

The two different statements of Duhem's theorem can be reconciled (mass vs concentration) by realizing that when calculating the properties of the phases or of the system, the size of an equilibrium system can be arbitrarily set: Two systems differing in size but with the same composition and in the same equilibrium state will differ neither in P , T , phase compositions, nor in modal concentration of the phases. The difference in size can be accounted for by extensive variables that are related by a single scalar multiple (see Duhem, 1898b).

The equilibrium state of an igneous system is defined when numerical values for P , T , the phase compositions and the mode are available. Consequently, the variables are P , T , ϕ values of z^α , and $(\phi \times N)$ values of x_i^α . The total number of variables in a system of known composition is $2 + \phi(1 + N)$. With this many variables, only two of which can be arbitrarily changed, there must be some equations relating them.

Given the composition of the system, we can always write down N mass balance constraints. Generally, the mass balance constraints are written in terms of extensive amounts of the phases and constituents:

$$\begin{aligned}
 \Sigma_{\alpha} m^{\alpha} x_1^{\alpha} &= n_1^{\circ} \\
 \Sigma_{\alpha} m^{\alpha} x_2^{\alpha} &= n_2^{\circ} \\
 &\vdots \\
 \Sigma_{\alpha} m^{\alpha} x_N^{\alpha} &= n_N^{\circ}
 \end{aligned} \tag{4}$$

for $\alpha = 1.. \phi$. The m^{α} and n_i° are moles of phases and moles of components or constituents in the system and the latter are derived from the initial masses of the system. These extensive variables can be converted to intensive ones by dividing by the size of the system, represented by:

$$S_n = \Sigma_i n_i^{\circ} \tag{5}$$

After the division, the mass balance equations are:

$$\begin{aligned}
 \Sigma_{\alpha} z^{\alpha} x_1^{\alpha} &= y_1^{\circ} \\
 \Sigma_{\alpha} z^{\alpha} x_2^{\alpha} &= y_2^{\circ} \\
 &\vdots \\
 \Sigma_{\alpha} z^{\alpha} x_N^{\alpha} &= y_N^{\circ}
 \end{aligned} \tag{6}$$

where the $z^{\alpha} = m^{\alpha}/S_n$ and $y_i^{\circ} = n_i^{\circ}/S_n$ are the mole fractions of the phases in the system and the mole fractions of the components or constituents in the system, respectively.

Subtracting the number of mass balance equations, N , from the number of variables leaves $2 + \phi + N(\phi - 1)$ as the number by which the variables exceed the equations. Duhem's theorem says only two of these can be independently varied. Consequently, there must be an additional $\phi + N(\phi - 1)$ equations we can write down. The additional equations are thermodynamic ones, describing the equilibrium conditions. The most familiar are equations relating chemical potentials:

$$\mu_i^{\alpha}(P, T, x_i^{\alpha}) = \mu_i^{\beta}(P, T, x_i^{\beta}) \tag{7}$$

Generally, petrologic modeling has been done with P and T fixed arbitrarily; the set of nonlinear equations are then solved for the remaining variables.

Example of the application of Duhem's Theorem

As a simple example of the application of Duhem's theorem, consider a ternary chemical system consisting of a binary solid solution and a melt (Fig. 1). The composition of the system is known and is expressed as the mole fractions of two components, C and B . The concentration of the third component, A , in the system is given by:

$$y_A^{\circ} = 1 - y_B^{\circ} - y_C^{\circ} \tag{8}$$

The variables describing the equilibrium state of the system are T , P , the composition of the solid, x , the composition of the melt, y_B and y_C , and the fractions of each phase, solid and melt, in the system, z^S and z^L , a total of seven.

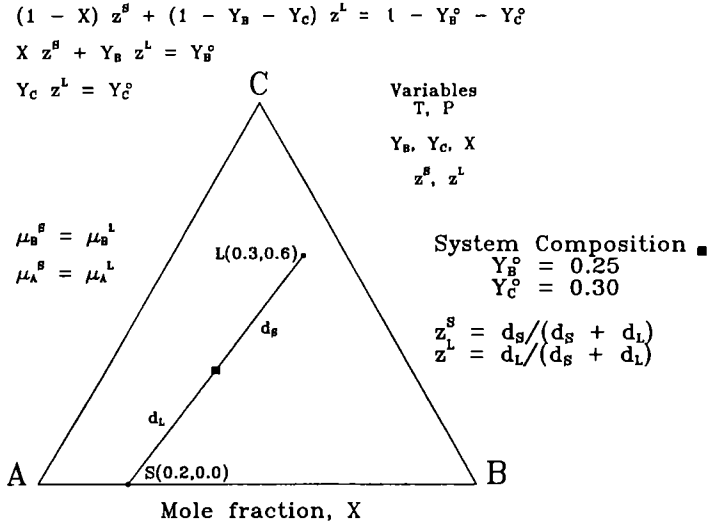


Figure 1. Example of the application of Duhem's theorem. Given the initial composition of the chemical system, y_B^o and y_C^o , and the values of two other variables, T and P , there are five equations to be solved for the remaining variables; three mass balance equations and two thermodynamic ones. The remaining variables are the composition of the melt (y_B, y_C), the composition of the solid ($x, 0$) and the fractions of each phase, z^S and z^L .

Relating these variables are three mass or materials balance equations:

$$(1 - x) z^S + (1 - y_B - y_C) z^L = 1 - y_B^o - y_C^o \quad (9)$$

$$x z^S + Y_B z^L = y_B^o \quad (10)$$

$$Y_C z^L = y_C^o \quad (11)$$

and two thermodynamic ones:

$$\mu_A^S(P, T, x) = \mu_A^L(P, T, y_B, y_C) \quad (12)$$

$$\mu_B^S(P, T, x) = \mu_B^L(P, T, y_B, y_C) \quad (13)$$

for a total of five equations in seven variables. As Duhem's theorem states, we must fix two variables in order to calculate the others.

As stated, P and T are the two variables most commonly fixed in thermodynamic modeling of igneous processes. However, any two of the seven listed variables could be fixed and the remaining ones calculated. Alternatively, any variable that is a function of the seven listed could be fixed instead. For example, the molar volume of the system is given by the appropriate modification of Equation (3):

$$v = v^S z^S + v^L z^L \quad (14)$$

If the molar volume of the system, v , is known, this last equation provides a relationship

between P , T and the compositional variables because v^S and v^L are functions of P , T and phase compositions. Consequently, with v fixed, either P or T , but not both, could be calculated, along with the compositional variables, from the sets of Equations (9)-(11), (12)-(13) and (14).

The simplest and crudest approximation to the thermodynamic equations [Eqns. (12) and (13)] is to use distribution coefficients and assume they are approximately constant:

$$x/y_B = K_{d1} \quad (15)$$

$$(1 - x)/(1 - y_B - y_C) = K_{d2} \quad (16)$$

The distribution coefficients are experimentally determined (e.g., Roeder and Emslie, 1970) or can be derived from thermodynamic data sets that are, in turn, constructed from experimental data (Ghiorso et al., 1983; Nielsen and Dungan, 1983; Berman, 1988). Distribution coefficients are seldom, if ever, constants and to make reasonably accurate models one must use a thermodynamic data set to evaluate the thermodynamic equations. To illustrate the nature of the calculation however, suppose at a known P and T , we have:

$$K_{d1} = 2/3 \quad (17)$$

$$K_{d2} = 8 \quad (18)$$

Then, with some algebra, one can calculate:

$$x = 0.2 \quad (19)$$

$$y_B = 0.3 \quad (20)$$

$$y_C = 0.6 \quad (21)$$

$$z_S = 0.5 \quad (22)$$

$$z_L = 0.5 \quad (23)$$

The sets of equations that must be solved for the remaining variables after fixing two are nonlinear. Nonlinear equations always create numerical and calculational problems. Consequently, there is a considerable literature on how to solve the equilibrium problem. The most efficient way is not to solve the set of nonlinear equations; rather, the preferred method is to minimize the Gibbs energy, G , or some other thermodynamic potential for the system (see, for example, Ghiorso, 1987). The numerical consequences of the different approaches to this problem are significant (Press et al., 1986, p. 269-272).

The selection of the two independent variables to fix, as required by Duhem's theorem, can usually be phase variables (e.g., x_i^α) or the physical conditions T and P . Occasionally, however, the variance as defined by the Gibbs phase rule [Eqn. (1)] will be less than two (0 or 1), precluding selection of only phase compositions, P or T as the ones to fix. Under such circumstances, the independent variables fixed must be system variables. If F , as defined by the Gibbs phase rule, is one, then one independent variable must be a system variable. If F is equal to zero (i.e., the system is at an invariant point according to the Gibbs phase rule), then both fixed variables must be system variables, such as V .

CALCULATION OF CRYSTALLIZATION PATHS.

A thermodynamic model of an igneous process should provide the compositional variations expected in the chemical system during the process and the P-T conditions at which the system and the included phases attained specific compositions during the process. Essential processes which need modeling, even if they serve only as a standard of comparison, are crystallization paths. A crystallization path consists of a set of melt compositions in equilibrium with crystallizing solids and the P-T coordinates of the equilibria. This is true whether the path is one of perfect fractional crystallization or perfect equilibrium crystallization.

The first step in constructing a crystallization path is to find the saturation temperature and pressure of the crystallizing assemblage. These coordinates, combined with the melt composition mark the initial point on the crystallization path. In most instances, the composition of the system we want to model will have the composition of the rock body being studied. From this composition we can calculate the mole fractions of the components in the initial melt. However, the composition of the saturating solid and the temperature and pressure of saturation are both unknown. If the saturating solid is binary, then there are two equilibrium relations, [for example, Eqns. (12) and (13)]. There is only one compositional variable in a binary solution, however, because the mole fractions of the two components must sum to one. Consequently, we can use the two equilibrium relations to calculate temperature and the composition of the solid solution.

We cannot, however, calculate the temperature, pressure and composition of saturation for any given solid, a consequence of Duhem's theorem. If the system is just saturated, then the mode will consist of melt and an infinitesimal amount of solid. In the mass balance equations [e.g., Eqns. (9)-(11) or the set of Eqns. (6)], the mole fractions of the solids, z^α , in the system are set to zero. There must still be another variable fixed before we can calculate the remaining variables defining the equilibrium state. Usually pressure is set to some value which is based on hunch, experience or guess as to where in the earth the process took place.

The assumption of a binary solid does not restrict the generality of this discussion. It is easy to demonstrate that for any solid solution of N components we can write equilibrium relations for each component. But the number of independent compositional variables in the solid solution is $N - 1$ because the sum of the mole fractions must equal one. This means there is one more equation than independently variable components (IV components, Thompson, 1982) in the phase. Consequently, we can always calculate the saturation temperature and composition of a phase, given the melt composition and pressure.

Given an initial composition for the system, there will be a set of phases that could saturate the melt. For example, given a basaltic composition, olivine, plagioclase and augite are three phases that could be on the liquidus of the initial composition. The discussion above provides us with a means for determining which possible solid phase will be the liquidus phase and saturate the melt because it will have the highest liquidus temperature at a fixed pressure:

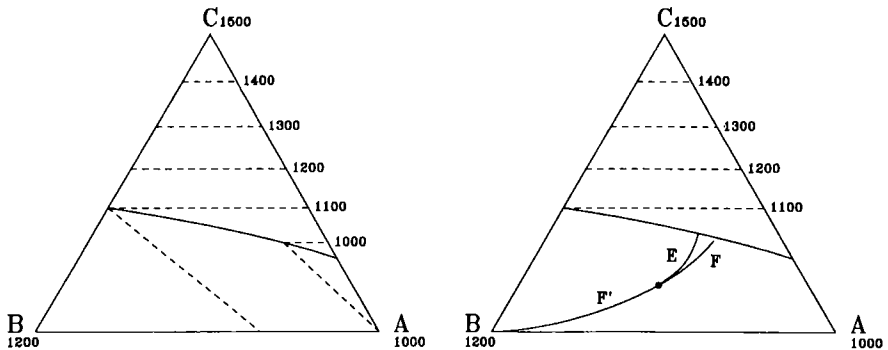


Figure 2. Phase diagram calculated from the data in Table 1. Shown are the isotherms on the liquidus surface (dashed lines) and crystallization paths (right diagram). The initial composition on the crystallization paths is marked with a dot, curve E is the perfect equilibrium path at constant pressure. The curve labelled F and F' are parts of the perfect fractionation path at constant pressure through the initial composition.

Table 1: Compositional and thermodynamic data for calculating saturation temperatures and crystallization paths.

| Component, i | $\Delta\mu_i^\circ$ crystallization | Fusion Temperature | Initial Melt Composition |
|--------------|-------------------------------------|----------------------------|--------------------------|
| A: | $-45000 + 45 \text{ T J/mol};$ | $T_{A,f} = 1000 \text{ K}$ | 40% |
| B: | $-60000 + 50 \text{ T J/mol};$ | $T_{B,f} = 1200 \text{ K}$ | 45% |
| C: | $-30000 + 20 \text{ T J/mol};$ | $T_{C,f} = 1500 \text{ K}$ | 15% |

Calculate the saturation temperature for all possible phases. The primary phase field belongs to the solid with the highest saturation temperature.

An example, a phase diagram, is illustrated on Figure 2; the relevant thermodynamic and compositional data required to construct the phase diagram are listed in Table 1. The equilibrium between pure C and melt with $y_C = 0.15$ is given by:

$$\ln y_C = -\Delta\mu_C^\circ/RT \quad (24)$$

where $\Delta\mu_C^\circ$ is the standard state Gibbs energy change for the crystallization reaction of component C, R is the gas constant ($R = 8.3143 \text{ J/K-mol}$). By substituting the expression for $\Delta\mu_C^\circ$ from Table 1 you can show that the initial composition with 15% C saturates with pure C at approximately 839 K.

In our example, the equilibrium relations for components A and B can be written:

$$x = y_A \exp(-\Delta\mu_A^\circ/RT) \quad (25)$$

$$x = 1 - y_B \exp(-\Delta\mu_B^\circ/RT) \quad (26)$$

where x is the mole fraction of component A in the solid solution, y_A and y_B are mole fractions in the melt.

These two equations can be solved for the saturation composition, x , and the saturation temperature of the solid solution in the initial melt. Unfortunately, the equations are nonlinear and their solution is not trivial (see Ghiorso, 1985, p. 113-115). One method is to plot both equations on the same graph and find the temperature at which they are equal. This will be the saturation temperature. The saturation temperature can then be substituted into either equation and the saturation composition calculated.

In this example, the solid solution saturates at approximately 1104 K, a higher temperature than the saturation temperature of phase C. Consequently, the AB-solid solution is the liquidus phase for this initial melt. You can determine from the isotherms (Fig. 2) that this temperature is approximately correct. The composition of the solid solution that would saturate the initial melt is approximately 24% A.

An example for a basaltic composition for a lava from Diamond Craters, Oregon (Russell and Nicholls, 1987) is shown on Figure 3. Olivine has the highest saturation temperature, compared to plagioclase and augite, at all pressures between zero and one GPa. The saturation curves were calculated from the thermodynamic data base constructed by Ghiorso et al. (1983).

Perfect equilibrium paths

The calculation of perfect equilibrium crystallization paths can be efficiently organized by invoking Duhem's theorem. For the example illustrated on Figure 2 (see also Table 1), the mass or material balance equations for the system are the same at each point on the crystallization path until another phase saturates the melt:

$$x z^S + y_A z^L = y_A^o \quad (27)$$

$$(1 - x) z^S + y_B z^L = y_B^o \quad (28)$$

$$y_C z^L = y_C^o \quad (29)$$

In addition to the equations representing conservation of matter, there are the equilibrium relations between components of the melt and solid solution, Equations (25) and (26). In addition, we require that the sum of the mole fractions of the melt components equal 1:

$$y_A + y_B + y_C = 1 \quad (30)$$

At a known pressure and temperature, Equations (25)-(30) constitute a system of six equations in six unknowns, z^S , z^L , x , y_A , y_B and y_C .

The procedure for calculating the perfect equilibrium path for this chemical system is to solve this set of equations at successive P-T points on the curve. If the desired curve is at constant pressure, then successive points will be at successively lower temperatures. In this example, the procedure is continued until the melt saturates with both an AB solid solution and pure C. Notice that in calculating the perfect equilibrium path, the right hand sides of Equations (27)-(29) remain constant from step to step. The composition of the system does not change.

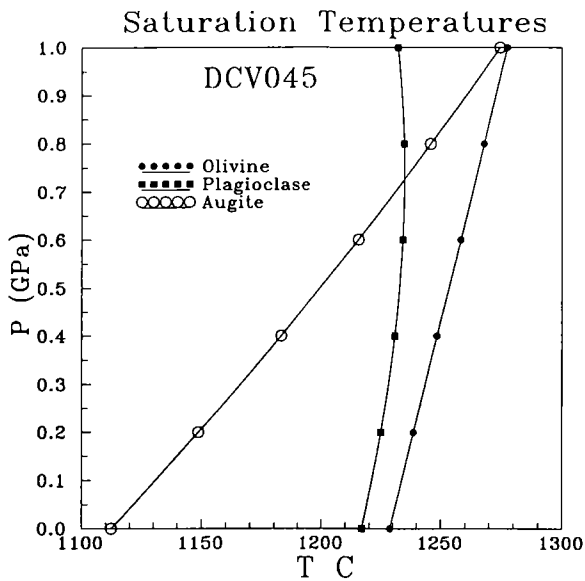


Figure 3. Calculated saturation curves for a basaltic composition from Diamond Craters, Oregon (Russell and Nicholls, 1987). The plagioclase and augite saturation curves are metastable in the pressure range of the crust (0-1 Gpa) whereas the olivine saturation curve is stable as olivine has the highest saturation temperature.

Table 2: Coordinates of the perfect equilibrium path, E (Fig. 2), at constant pressure, for the composition listed in Table 1.

| T K | x | y _A | y _C |
|------|-------|----------------|----------------|
| 1100 | 0.249 | 0.408 | 0.158 |
| 1080 | 0.292 | 0.436 | 0.201 |
| 1070 | 0.312 | 0.444 | 0.225 |
| 1060 | 0.329 | 0.447 | 0.250 |
| 1050 | 0.345 | 0.446 | 0.276 |
| 1040 | 0.359 | 0.442 | 0.304 |
| 1030 | 0.371 | 0.435 | 0.332 |

Generally, the solution of the material balance and thermodynamic equations requires numerical analysis techniques. In this instance, however, some algebra can be used to eliminate all the unknown compositional variables except x to give:

$$x^2 (f_2 - f_1) - x (y_A^\circ + y_C^\circ)[f_1(f_2 - 2) + f_2] + y_A^\circ f_1(f_2 - 1) = 0 \tag{31}$$

where:

$$f_i = \exp(-\Delta\mu_i^\circ/RT) \tag{32}$$

Equation (31) is a quadratic equation in x which will provide two values on

solution. Examination of the phase diagram (Fig. 2) will show that the smaller value is correct. It is then a straight forward matter to back substitute into Equations (27)-(30) to calculate the remaining variables. The perfect equilibrium crystallization path for the composition listed in Table 1 is plotted on Figure 2, curve E. Some results are listed in Table 2.

Isobaric perfect fractionation paths

Perfect fractionation paths can be conveniently approximated in two different ways:

1. They can be calculated as a series of perfect equilibrium crystallization steps, with the system composition changing with each step. The melt from the n th step becomes the system composition for the $(n + 1)$ th step. Between each step, the P-T conditions are changed by a small amount (say 5° or 0-10 MPa or both). At each stage the calculations proceed in the same way as calculating a point on a perfect equilibrium path. The only difference is that the right hand sides of Equations (27)-(29) change from step to step along the fractionation path whereas they are constant along the equilibrium path. Details of the calculations are found in (Russell and Nicholls, 1985; Ghiorso, 1985; Ghiorso, 1987; Ghiorso and Carmichael, 1987)
2. They can be calculated by invoking the compositional constraint of perfect fractionation; the composition of the material leaving (or entering the melt) has the composition of the instantaneously crystallizing solid:

$$x = dn_i / (dn_i + dn_j) \quad (33)$$

where x is the mole fraction of component i in the solid and n_i and n_j are the moles of components i and j in the melt. This constraint can be used to derive a relationship between the changes in melt mole fractions (Nicholls et al., 1986):

$$dy_j/dy_i = (1 - x - y_j)/(x - y_i) \quad (34)$$

Equation (34) is the fundamental equation for modeling perfect fractionation paths using this second method. It describes the effect of perfect fractionation of a binary solid solution on the composition of a melt. The expression is completely general; it does not depend upon the solutions being ideal and is independent of the mole fractions of all components except those that enter the solid solution (i.e., the expression is independent of y_k , $k \neq i, j$).

Integration of Equation (34) will provide y_j as a function of y_i with the constant of integration fixed by the initial melt composition. Consequently, if we know the initial composition of the fractionating system, we can calculate the fractionation curve through the initial composition at all other values of y_i . The integration cannot be carried out, however, until the relationship between x and y_i is specified. This relationship is necessarily a thermodynamic one [e.g., Eqns. (25) and (26)] and its exact nature will depend on the degree of nonideality of the solid and liquid solutions.

A second equation describing the mass balance and constraining the state of a system during a perfect fractionation process is one from which we can calculate the amount of uncrystallized melt. As in most petrological calculations, we are not after the absolute amount of melt but rather the fraction of the original melt that has not crystallized. This fraction, F , is defined by:

$$F = S_n/S_n^\circ \quad (35)$$

where S_n° is the sum of the number of moles of each component originally present in the magma before fractionation and is equal to the size, in moles, of the initial system. S_n is the size of the system, in moles, at the current stage of fractionation. The system is the melt phase at each stage of fractionation.

Equation (35) is a definition rather than a practical recipe for calculating F ; an equation for calculation is (Nicholls et al., 1986):

$$F = (1 - y_i^\circ - y_j^\circ)/(1 - y_i - y_j) \quad (36)$$

The concentrations of melt components excluded from the fractionating phases are related by:

$$F = y_k^\circ/y_k, \quad k \neq i, j \quad (37)$$

The starting point in calculating a perfect fractionation curve has the coordinates of the saturation conditions of the initial composition (See Table 1). Equations similar to Equations (25) and (26) are used to calculate x and T , at a known pressure. The next step is to calculate the composition of a melt slightly displaced in composition from the original. To do this, slightly change the value of y_i and call this increment dy_i . Next calculate the increment in y_j , dy_j , with Equation (34). The mole fractions of y_i' and y_j' in the new melt are then given by:

$$y_i' = y_i + dy_i \quad (38)$$

$$y_j' = y_j + dy_j \quad (39)$$

The fractionation stage is calculated with Equation (36). The remaining mole fractions in the new melt are then calculated with Equation (37).

One then begins the process anew: first, calculate a solid composition and equilibrium temperature for the new melt with the thermodynamic equations, then find another melt composition on the fractionation curve by incrementally increasing y_i and calculating y_j . The process is repeated until the calculated composition of the melt either saturates with another phase or until the melt is exhausted in some component.

Comparison of the two procedures shows that at constant pressure, the second fixed variable required by Duhem's theorem is T in the first method and the saturation condition, $z^\alpha = 0$, $\alpha \neq L$, in the second. The amount of change in the system, which is open because of solid removal, is dictated by a temperature change in the first method and a compositional change in the second.

Table 3: Fractionation curve coordinates for curve FF' on Figure 2. The coordinates for the initial composition (y_A^0 , y_B^0) are at a temperature of 1103.9 K.

| T | y_A | y_B | X | dy_B/dy_A |
|--------|--------|--------|--------|-------------|
| 1200.0 | 0.0000 | 1.0000 | 0.0000 | |
| 1194.1 | 0.0450 | 0.9524 | 0.0187 | -1.0993 |
| 1184.0 | 0.1091 | 0.8788 | 0.0470 | -1.1951 |
| 1174.0 | 0.1638 | 0.8112 | 0.0734 | -1.2766 |
| 1164.0 | 0.2116 | 0.7484 | 0.0987 | -1.3547 |
| 1154.0 | 0.2535 | 0.6900 | 0.1231 | -1.4335 |
| 1144.0 | 0.2905 | 0.6354 | 0.1470 | -1.5161 |
| 1134.0 | 0.3232 | 0.5844 | 0.1705 | -1.6048 |
| 1123.9 | 0.3522 | 0.5366 | 0.1939 | -1.7027 |
| 1113.9 | 0.3777 | 0.4918 | 0.2172 | -1.8130 |
| 1103.9 | 0.4000 | 0.4500 | 0.2404 | -1.9396 |
| 1093.9 | 0.4195 | 0.4108 | 0.2637 | -2.0890 |
| 1083.8 | 0.4363 | 0.3742 | 0.2871 | -2.2694 |
| 1073.8 | 0.4508 | 0.3400 | 0.3107 | -2.4943 |
| 1063.8 | 0.4629 | 0.3080 | 0.3347 | -2.7860 |
| 1053.7 | 0.4730 | 0.2782 | 0.3589 | -3.1815 |
| 1043.7 | 0.4811 | 0.2504 | 0.3836 | -3.7548 |
| 1033.6 | 0.4873 | 0.2246 | 0.4087 | -4.6636 |
| 1023.5 | 0.4918 | 0.2006 | 0.4342 | -6.3464 |

If an explicit integral of Equation (34) could be obtained, the second method of finding the perfect fractionation path would provide an exact answer whereas the first method cannot provide more than an approximation. An explicit integral of Equation (34) cannot be obtained unless the solutions are ideal and unless the standard state Gibbs energies of the crystallization reactions (Table 1) that appear in Equations (25) and (26) are constants independent of P and T. Magmatic solutions are not ideal and standard state Gibbs energies of crystallization depend on P and T. Consequently, both methods can give only approximate solutions to the fractionation path because calculations can only be made with numbers of finite precision. Given a computer with the ability to calculate exactly and infinite time, both methods could calculate paths indistinguishable from the exact path.

The first method provides a direct accounting of the fractionated solids. Their amounts and compositions must be calculated in order to obtain the composition of the remaining melt. The second method requires more bookkeeping to account for the compositions and fractions of the solid phases. The first procedure does not provide a means for extrapolating to precursors of the initial melt composition, assuming it was derived by perfect fractionation, whereas the second method does. The use of fractionation curves for determining more primitive melt compositions was described several years ago (Irvine, 1977; Pearce, 1978). At the time, the lack of knowledge of the temperature and compositional dependence of the distribution coefficients of components between crystal and melt precluded accurate calculations.

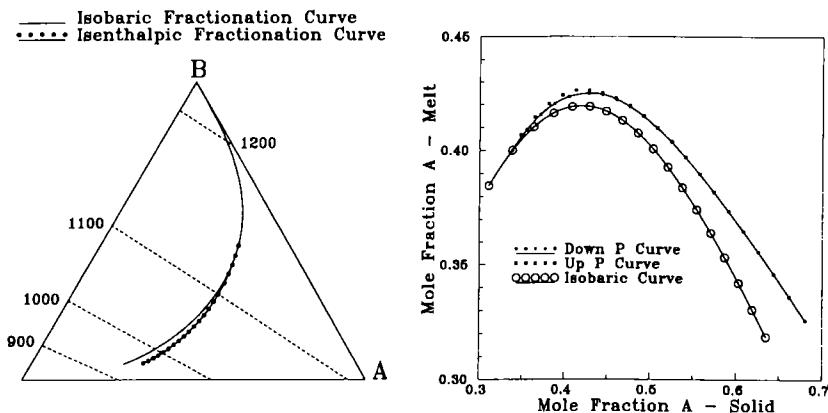


Figure 4. Comparison of an isobaric perfect fractionation path and an isenthalpic fractionation path. Both are equilibrium paths in the sense that $\mu_i^\alpha = \mu_i^L$ holds for all components. The isenthalpic path, however, is not a reversible path whereas the isobaric path is.

To apply this discussion to the example listed in Table 1, we first make a small change in notation to Equation (34):

$$dy_B/dy_A = (1 - x - y_B)/(x - y_A) \quad (40)$$

The first step of the calculations has already been done. From the calculation of the saturation temperature and composition of the solid solution we know x . The original composition of the system provides y_A and y_B . Substitution into Equation (40) gives us the slope of the fractionation curve at the composition of the original melt ($dy_B/dy_A = -1.94$).

Next pick a fractionation step by choosing a value for dy_A . This is possibly the most critical step. Choose too large a step and the fractionation path will be imprecisely located; if the step is too small, at best a lot of time and effort will be spent calculating the path. In addition, if the calculation is part of a computer program, round off error may cause the calculations to be wrong. The calculated fractionation path is shown on Figure 2 (Curve FF'). The coordinates of the curve are listed in Table 3, along with the slopes calculated with Equation (34).

Polybaric fractionation curves

If another thermodynamic property of the melt can be set, then the pressure need not be fixed and a polybaric fractionation path can be calculated. A tractable path to calculate is one in which there is no heat lost from the melt; the only heat extracted from the magma would be that carried by the fractionating solids. The relevant equation for a single fractionating binary solid is derived in the appendix:

$$-(x - y_A) [v (1 - \alpha T) dP/dT + C_p] = [x h_A + (1 - x) h_B] dy_A/dT \quad (41)$$

where h_i is the partial molar enthalpy of component i in the melt, x is the mole fraction of component A in the solid, v and C_p are the molar volume and heat capacity of the melt and are usually functions of P , T , and melt composition. α is the coefficient of thermal expansion of the melt and, in general, is a function of P , T , and melt composition.

To minimize numerical problems, α and C_p will be set to zero in the following illustration. Generally, α is of the order 1×10^{-6} and T of the order 1000. Consequently, αT is considerably less than one and the assumption of α equal to zero is a reasonable one. C_p , however, is not zero and would need to be included in a real calculation. With these stipulations, Equation (41) becomes:

$$dP = - [x h_A^\circ + (1 - x) h_B^\circ] dy_A / [v (x - y_A)] \quad (42)$$

where h_i° is the standard state enthalpy of component i . The standard state molar enthalpy can be used in place of the partial molar enthalpy because of the assumption of ideal melt solutions.

Given an initial melt composition and an initial pressure, the calculation of the fractionation path begins with solving Equations (25) and (26):

$$x = y_A \exp(-\Delta\mu_A^\circ/RT) \quad (25)$$

$$x = 1 - y_B \exp(-\Delta\mu_B^\circ/RT) \quad (26)$$

for x and T . A value for dy_A is selected and the change in concentration of component B is calculated with Equation (34):

$$dy_B = (1 - x - y_B) dy_A / (x - y_A) \quad (34)$$

The pressure change is calculated from Equation (42) and the cycle of calculations repeated.

An example is shown on Figure 4. As expected, the polybaric, isenthalpic path diverges from the isobaric path. As a result, the solid compositions fractionating from derivative melts will be different along the two paths, even though the initial melt composition and conditions were identical. The isobaric perfect fractionation path is reversible. By changing the sign of dy_A at any stage of fractionation one reproduces points on the path above the fractionation stage where the sign change was made. In contrast, the polybaric, isenthalpic path is not reversible. The isenthalpic path shown on Figure 4 was calculated from high pressure to low starting with a composition where the two paths, isobaric and isenthalpic, diverge on the left-hand diagram (40% A, 45% B). Again, change the sign of dy_A and starting at the low pressure end of the original isenthalpic path (32.6% A, 5.5% B) calculate a path under isenthalpic conditions; it does not exactly coincide with the original. This is more apparent on the plot of melt mole fraction A vs solid mole fraction A (Fig. 4, right) where the compositions near the maximum on the fractionation paths are distinct. Isenthalpic paths are not reversible paths (see, for example, Waldbaum, 1971; Lewis and Randall, 1961, p. 46-51), whereas isentropic paths are.

Multiphase fractionation paths

Multiphase isobaric fractionation paths are much easier to compute using the first method listed above than the second. If the object is to calculate a fractionation path by constraining some variable, such as heat content, rather than fixing P , then the second method may be the only course to take. This second method, using derivatives [e.g., Eqn. (34)], usually requires considerable computational bookkeeping and a detailed discussion is more than can be done here. A short discussion of the degrees of freedom along a general fractionation curve will at least outline the number of constraints that have to be supplied.

Starting with the definition of the mole fraction of a component in the melt:

$$y_i = n_i/Sn \quad (5)$$

we find its total differential:

$$dy_i = (dn_i/Sn) - y_i dSn/Sn \quad (43)$$

From the definition of the fraction stage, F [Eqn. (35)] one obtains:

$$dF/F = dSn/Sn \quad (44)$$

From these last two equations one gets:

$$(F dy_i + y_i dF)/F = dn_i/Sn \quad (45)$$

An equation like Equation (45) can obviously be written for every component in the melt. What we are after are expressions relating the concentrations of components i and j that are leaving the melt and going into the fractionating solids. The kind of expression we get will depend on whether i and j are leaving to the same solid solution or to different solid solutions. In what follows, we will assume the solid solutions are binary in order to keep the equations within reason. This is not required however, and the conclusions remain the same whether the solid solutions are binary or higher order.

If both components enter the same binary solid solution then:

$$x_i^\alpha = dn_i/(dn_i + dn_j) \quad (46)$$

Combining Equation (46) with two equations like Equation (45) for components i and j gives:

$$x_i^\alpha dy_j = (1 - x_i^\alpha) dy_i + [(1 - x_i^\alpha) y_i - x_i^\alpha y_j] dF/F \quad (47)$$

There is an equation like (47) for every solid solution that is on the liquidus of the melt. If the melt is saturated with ϕ solid solutions, there are ϕ such equations.

If the two melt components, i and k , enter separate solid solutions, there will be two solid phase mole fractions:

$$x_i^\alpha = dn_i / (dn_i + dn_j) \quad (48)$$

$$x_k^\beta = dn_k / (dn_k + dn_i) \quad (49)$$

In order to combine Equations (48) and (49) with two like Equation (45) for components i and k we have to fix the number of saturating phases. If there are two solid solutions, then:

$$dSn = (dn_i + dn_j) + (dn_k + dn_i) \quad (50)$$

and the combined equation is:

$$dy_k = - (x_k^\beta / x_i^\alpha) dy_i + [x_k^\beta - y_k - (x_k^\beta / x_i^\alpha) y_i] dF/F \quad (51)$$

One equation like Equation (50) can be written at any stage on a fractionation path. It is derived from the specification of dSn , the change in the size of the system [Eqn. (50)] and, consequently, there can be only one such independent equation.

The remaining equations have already been discussed. They are the equilibrium relations between the components in the melt and the solid solutions:

$$\mu_i^\alpha(P, T, x_i^\alpha) = \mu_i^L(P, T, y_i, y_j, y_k \dots) \quad (12)$$

$$\mu_j^\alpha(P, T, x_i^\alpha) = \mu_j^L(P, T, y_i, y_j, y_k \dots) \quad (13)$$

There will be two such equations for each binary solid solution.

The variables in the model are T , P and the change in fraction stage, dF . In addition, there is an independent mole fraction in each solid solution, x_i^α , and two changes in the mole fractions of components in the melt for each solid solution, dy_i and dy_j , making a total of ϕ solid compositional variables and 2ϕ changes in the melt concentrations. The degrees of freedom in the model remains:

$$3\phi + 3 - (\phi + 1 + 2\phi) = 2 \quad (52)$$

Duhem's theorem still holds when calculating fractionation curves of any kind. Fractionation requires the melt to always be just at saturation. The number of phases at saturation is always sufficient to ensure that two and only two variables need be fixed to calculate the rest of the properties of the melt.

TESTING THERMODYNAMIC MODELS

"We should reserve the word 'model' for well-constrained, logical propositions, not necessarily mathematical, that have necessary and testable consequences."

H.J. Greenwood, (1989).

If Greenwood's definition applies to thermodynamic models of igneous processes then they must be testable against observable features in rocks. Temperatures, pressures and flow velocities are not observable quantities in any but the most recent volcanic events. In old rocks all that can be observed are phase assemblages, phase compositions and spatial distributions of the phases. From these observable features must come the

Figure 5. Fractionation paths, x-y plots, and T-x, y plots for binary AB solid solutions. Curves calculated with the thermodynamic data listed on Table 1. The fractionation paths are metastable in the primary phase field of C.

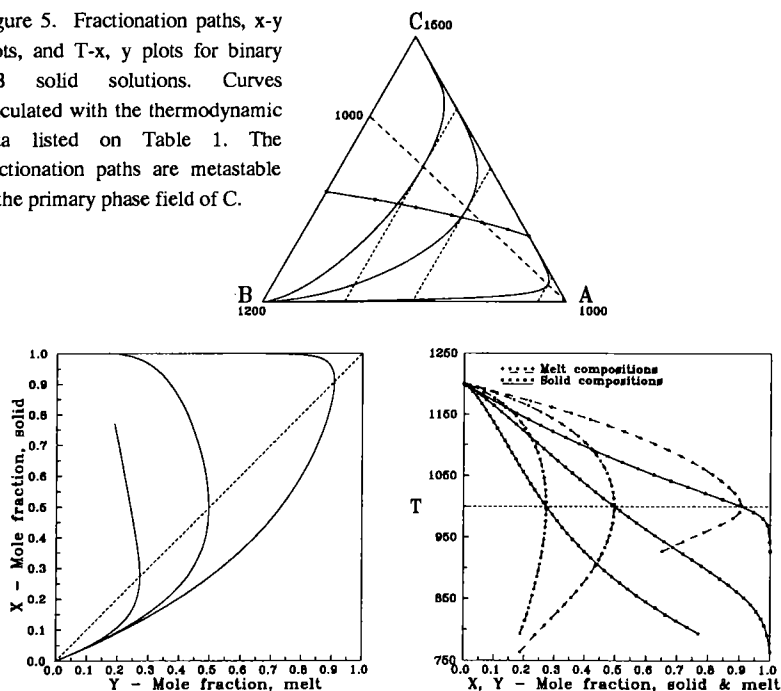
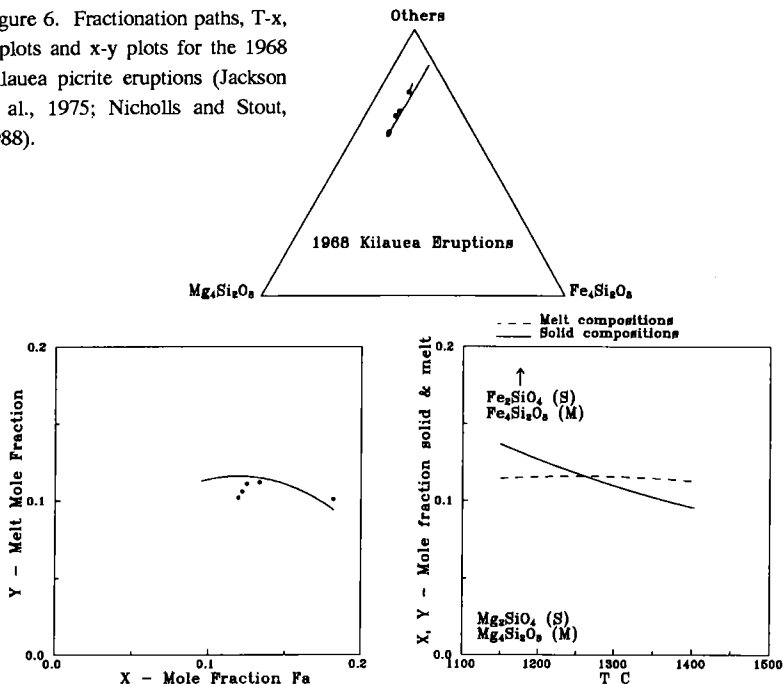


Figure 6. Fractionation paths, T-x, y plots and x-y plots for the 1968 Kilauea picrite eruptions (Jackson et al., 1975; Nicholls and Stout, 1988).



data that can be compared to predictions of the model. Temperatures and pressures can be calculated from a thermodynamic model but they are inferences from the model and their reliability as estimates of the conditions under which a rock formed depends on whether the model itself has been tested against observation. An example is shown on Figure 5. The top diagram shows three fractionation curves. Those portions of the paths shown crossing the primary phase field of C are metastable with respect to the liquidus surface of phase C. These metastable extensions can have an influence on crystal-liquid equilibria in more complex systems because the extent of the fractionation curve accessible to a process depends on the nature of the other components. For example, if the crystallization temperature of C, a function of C's standard state properties, were lower, the cotectic curve would lie at larger mole fractions of C. In natural systems, the analogous circumstances could apply. In one system, a single solid fractionation curve could be stable and extend to lower temperatures and different compositions than in another.

The top diagram in Figure 5 shows predicted changes in melt composition with fractionation and even a diagram as simple as this one can be used in real situations. Figure 6, an analogous diagram for the 1968 Kilauea eruptions, was drawn using the thermodynamic data base constructed by Ghiorso et al., (1983). The lavas erupted along the East Rift zone in 1968 are picrites containing phenocrysts of olivine and oxides (Jackson et al., 1975; Nicholls and Stout, 1988). Assuming changes in melt composition are dominated by crystal sorting, the chemical system is effectively ternary with the melt components $\text{Mg}_4\text{Si}_2\text{O}_8$, $\text{Fe}_4\text{Si}_2\text{O}_8$, and others.

Also shown on the diagram are coordinates of the picrites and the least differentiated basalt from the lavas thought to belong to the same magma batch (Nicholls and Russell, in press). The rock compositions fall slightly off the predicted trend through the most Mg-rich picrite composition. Also, the fractionation curve through the least differentiated basalt has a slightly different slope than the fractionation curve through the picrite composition. Consequently, we conclude that the thermodynamic model is not perfectly consistent with data and that the postulated process is either more complex than olivine fractionation alone, the process occurred under different conditions than entered the model (i.e., the pressure was significantly different than 0), or the thermodynamic data base is not accurate.

On any fractionation curve there will be a point where the mole fraction of a component in the melt and in the solid will be equal (or to some combination of melt components if the solid component is a combination of melt components, see Ghiorso et al., 1983). At this point, the tangent to the fractionation curve will be parallel to the y_C axis (Fig. 5). The tangents are shown as short dashed lines on the top diagram, Figure 5. In an ideal system, the point of tangency falls on the isotherm corresponding to the fusion temperature of the low-melting component of the solid solution. Notice that on Figure 5, the maximum on the fractionation curve does not correspond to the point of maximum curvature on the plot of melt component vs solid component. In nonideal solutions, such need not be the case. At temperatures higher than the temperature of tangency, the solid solution is richer in the component with the higher fusion temperature than the melt. At temperatures lower than the temperature of tangency, the reverse is true. It is difficult to detect on Figure 6 whether the Kilauea lavas reached such a fractionation stage but the

melts in Thingmuli Volcano in Iceland (Carmichael, 1964, 1967) presumably did reach such a stage with respect to total iron.

A more complete test of the thermodynamic model would involve the compositions of more than one phase. Such diagrams are shown on the lower left of Figure 5 and Figure 6. The composition of the solid solution is plotted against the concentration of an appropriate component in the melt. The analogous diagram for the Kilauea lavas (Fig. 6) shows the rock data falling off the curve, especially at the higher temperature fractionation stages, suggesting processes other than or in addition to fractionation have operated in the formation of these rocks. The lack of correspondence between predicted and solid olivine compositions suggested that diffusion at high temperature homogenized the olivine phenocrysts (Nicholls and Stout, 1988).

The third diagram on Figure 5 and Figure 6 cannot test the thermodynamic model because T is almost never an observable variable. Rather it is a prediction from the model and its reliability is a function of the degree of testing of the thermodynamic model and the agreement with observed parameters. If the tests have not or cannot be made, then a prediction from the model has no reliability. With respect to the Kilauea lavas, the higher temperatures predicted by the model have little or no reliability because the model is, for one reason or another, inconsistent with the data. The lower temperatures predicted by the model are more reliable because the model is consistent with the compositional data in the less magnesian rocks. The lower predicted temperatures are also consistent with measured basaltic eruption temperatures at Kilauea.

ACKNOWLEDGMENTS

Support was provided by NSERC operating grant A7372 and by The University of Calgary. Reviews by M.Z. Stout and J.K. Russell improved the paper.

REFERENCES

- Berman, R.G. (1988) Internally-consistent thermodynamic data for minerals in the system $\text{Na}_2\text{O}-\text{K}_2\text{O}-\text{CaO}-\text{MgO}-\text{FeO}-\text{Fe}_2\text{O}_3-\text{Al}_2\text{O}_3-\text{SiO}_2-\text{TiO}_2-\text{H}_2\text{O}-\text{CO}_2$. *J. Petrol.*, 29, 445-522.
- Carmichael, I.S.E. (1964) The petrology of Thingmuli, a Tertiary volcano in Eastern Iceland. *J. Petrol.*, 5, 435-460.
- Carmichael, I.S.E. (1967) The mineralogy of Thingmuli, a volcano in eastern Iceland. *Am. Mineral.*, 52, 1815-1841.
- Denbigh, K.G. (1981) *The Principles of Chemical Equilibrium*. Cambridge University Press, Cambridge, 494 pp.
- Duhem, P. (1898a) On the general problem of chemical statics. *J. Phys. Chem.*, 2, 1-42.
- Duhem, P. (1898b) On the general problem of chemical statics. *J. Phys. Chem.*, 2, 91-115.
- Ghiorso, M.S. (1985) Chemical mass transfer in magmatic processes. I. Thermodynamic relations and numerical algorithms. *Contrib. Mineral. Petrol.*, 90, 107-120.
- Ghiorso, M.S. (1987) Modeling magmatic systems: Thermodynamic relations. In: I. S.E. Carmichael, and H.P. Eugster, Eds., *Thermodynamic Modeling of Geological Materials: Minerals, Fluids and Melts*, *Rev. Mineral.* 17, 443-465.

- Ghiorso, M.S., and Carmichael, I.S.E. (1987) Modeling magmatic systems: Petrologic applications. In: I.S.E. Carmichael, and H.P. Eugster, Eds., *Thermodynamic Modeling of Geological Materials: Minerals, Fluids and Melts*, Rev. Mineral. 17, 467-499.
- Ghiorso, M.S., Carmichael, I.S.E., Rivers, M.L., and Sack, R.O. (1983) The Gibbs free energy of mixing of natural silicate liquids; an expanded regular solution approximation for the calculation of magmatic intensive variables. *Contrib. Mineral. Petrol.*, 84, 107-145.
- Greenwood, H.J. (1989) On models and modeling. *Can. Mineral.*, 27, 1-14.
- Irvine, T.N. (1977) Definition of primitive liquids for basic magmas. *Carnegie Inst. Wash. Yearb.*, 76, 454-461.
- Jackson, D.B., Swanson, D.A., Koyanagi, R.Y., and Wright, T.L. (1975) The August and October 1968 East Rift eruptions of Kilauea Volcano, Hawaii. *U. S. Geol. Surv. Prof. Paper*, 890, 1-33.
- Johannsen, A. (1931) *A Descriptive Petrography of the Igneous Rocks. I. Introduction, Textures, Classifications, and Glossary*. The University of Chicago Press, Chicago, 318 p.
- Lewis, G.N., and Randall, M. (1961) *Thermodynamics*. McGraw-Hill Book Co., New York, 723 pp.
- Nicholls, J., and Stout, M.Z. (1988) Picritic melts in Kilauea - Evidence from the 1967-1968 Halemaumau and Hiiaka eruptions. *J. Petrol.*, 29, 1031-1057.
- Nicholls, J., Russell, J.K., and Stout, M.Z. (1986) Testing magmatic hypotheses with thermodynamic modelling. In: C.M. Scarfe, Ed., *Short Course in Silicate Melts*, vol. 12, Mineralogical Assoc. of Canada, Toronto, 210-235.
- Nielsen, R.L., and Dungan, M.A. (1983) Low pressure mineral-melt equilibria in natural anhydrous mafic systems. *Contrib. Mineral. Petrol.*, 84, 310-326.
- Pearce, T.H. (1978) Olivine fractionation curves for basaltic and ultrabasic liquids. *Nature*, 276, 771-774.
- Press, W.H., Flannery, B.P., Teukolsky, S.A., and Vetterling, W.T. (1986) *Numerical Recipes, The Art of Scientific Computing*. Cambridge University Press, New York, 818 pp.
- Prigogine, I., and Defay, R. (1954) *Chemical Thermodynamics*. Longmans, Green and Co., Ltd., London, 543 pp.
- Roeder, P.L., and Emslie, R.F. (1970) Olivine-liquid equilibrium. *Contrib. Mineral. Petrol.*, 29, 275-289.
- Russell, J.K., and Nicholls, J. (1985) Application of Duhem's theorem to the estimation of extensive and intensive properties of basaltic magmas. *Can. Mineral.*, 23, 479-488.
- Russell, J.K., and Nicholls, J. (1987) Early crystallization history of alkali olivine basalts, Diamond Craters, Oregon. *Geochim. Cosmochim. Acta*, 51, 143-154.
- Thompson, J.B. (1982) Composition space: An algebraic and geometric approach. In: J.M. Ferry, Ed., *Characterization of Metamorphism through Mineral Equilibria*, Rev. Mineral. 10, 1-32.
- Waldbaum, D.R. (1971) Temperature changes associated with adiabatic decompression in geological processes. *Nature*, 232, 545-547.

APPENDIX: DERIVATION OF FRACTIONATION EQUATION AT CONSTANT H^{melt}

This appendix provides detailed derivation of an equation describing the relationships between melt components, P and T along an isenthalpic P-T path in a system fractionating a binary solid solution. It is assumed that only the melt is on the isenthalpic path; fractionated solids are removed from the system on crystallization.

The differentials of H and S as functions of P, T, V, S and number of moles in the melt are given by:

$$dH = V dP + T dS + \sum_{i,N} \mu_i dn_i \quad (A1)$$

and:

$$dS = (C_p/T) dT + (\partial S/\partial P)_{T,n} dP + \sum_{i,N} (\partial S/\partial n_i)_{T,P} dn_i \quad (A2)$$

In order to find dH as a function of P and T , we need to substitute for dS (as a function of P , T and the n_i) in Equation (A1). In order to do this, we need to find an expression for the coefficient of dP in Equation (A2) in terms of melt properties (V , C_p , etc.). The differential of the Gibbs function is given by:

$$dG = V dP - S dT + \sum_{i,N} \mu_i dn_i \quad (A3)$$

Applying Maxwell's relations (Denbigh, 1981, p. 90-92) gives:

$$(\partial S/\partial P)_{T,n} = -(\partial V/\partial T)_{P,n} \quad (A4)$$

The coefficient of thermal expansion, α , is related to the partial derivative of the volume with respect to temperature by:

$$(\partial V/\partial T)_{P,n} = \alpha V \quad (A5)$$

Substituting into Equation (A2) gives:

$$dS = (C_p/T) dT - \alpha V dP + \sum_{i,N} (\partial S/\partial n_i)_{T,P} dn_i \quad (A6)$$

A further substitution of this last equation into Equation (A1) gives:

$$dH = V(1 - \alpha T) dP + C_p dT + T \sum_{i,N} (\partial S/\partial n_i)_{T,P} dn_i + \sum_{i,N} \mu_i dn_i \quad (A7)$$

The coefficients of dn_i can be combined by noting that the partial derivatives of S with respect to n_i are partial molar entropies and are related to the partial molar enthalpies, h_i , by:

$$\mu_i + T (\partial S/\partial n_i)_{T,P} = h_i \quad (A8)$$

The general equation for changes in H due to changes in P , T and n_i is given by the following equation:

$$dH = V(1 - \alpha T) dP + C_p dT + \sum_{i,N} h_i dn_i \quad (A9)$$

The next step is to introduce the constraints generated by a single, fractionating, binary solid. The mole fraction of component 1 in the solid will be represented by x and the corresponding mole fraction in the melt will be represented by y_1 . The mole fraction of component 2 in the solid is $(1 - x)$ and is y_2 in the melt. The size of the system is the sum of the moles of each component and is given by:

$$S_n = \sum_{i,N} n_i \quad (A10)$$

Divide Equation (A9) by S_n :

$$dH/S_n = (V/S_n)(1 - \alpha T) dP + (C_p/S_n) dT + \sum_{i,N} h_i dn_i/S_n \quad (A11)$$

Introduce molar quantities:

$$v = V/S_n; c_p = C_p/S_n \quad (A12)$$

to get:

$$dH/S_n = v(1 - \alpha T) dP + c_p dT + \sum_{i,N} h_i dn_i/S_n \quad (A13)$$

If only components 1 and 2 are crystallizing as a solid solution then Equation (A13) becomes:

$$dH/S_n = v(1 - \alpha T) dP + c_p dT + h_1 dn_1/S_n + h_2 dn_2/S_n \quad (A14)$$

The composition of the fractionating solid is given by:

$$x = dn_1/(dn_1 + dn_2) \quad (A15)$$

Substituting this last equation into the penultimate gives:

$$dH/S_n = v(1 - \alpha T) dP + c_p dT + [x h_1 + (1 - x) h_2](dn_1 + dn_2)/S_n \quad (A16)$$

If only a binary solid composed of components 1 and 2 is fractionating, then the change in the size of the system is given by:

$$dS_n = dn_1 + dn_2 \quad (A17)$$

The mole fraction of component 1 in the melt is given by:

$$y_1 = n_1/S_n \quad (A18)$$

Its differential is given by:

$$dy_1 = dn_1/S_n - y_1 dS_n/S_n \quad (A19)$$

An analogous expression can be written for y_2 :

$$dy_2 = dn_2/S_n - y_2 dS_n/S_n \quad (A20)$$

Adding Equations (A19) and (A20) gives:

$$(dn_1 + dn_2)/S_n = (dy_1 + dy_2)/(1 - y_1 - y_2) \quad (A21)$$

Substituting the result into Equation (A16) gives:

$$dH/S_n = v(1 - \alpha T) dP + c_p dT + [x h_1 + (1 - x) h_2](dy_1 + dy_2)/(1 - y_1 - y_2) \quad (A22)$$

Under conditions of constant H, Equation (A18) can be written:

$$-(1 - y_1 - y_2)[v(1 - \alpha T) dP/dT + c_p] = [x h_1 + (1 - x) h_2](dy_1/dT + dy_2/dT) \quad (A23)$$

In a fractionating system, the derivatives of the mole fractions in the melt are not independent, but are related by (Nicholls et al., 1986):

$$dy_2/dT = [(1 - x - y_2)/(x - y_1)] dy_1/dT \quad (\text{A24})$$

Combining these last two equations gives:

$$-(x - y_1)[v(1 - \alpha T) dP + c_p dT] = [x h_1 + (1 - x) h_2] dy_1 \quad (\text{A25})$$

Given a melt composition and a pressure, one can calculate the liquidus temperature and solid composition at the initial point on the fractionation curve from the equilibrium relations:

$$F_1 = \mu_1^s(T, P, x) - \mu_1^m(P, T, y_1) = 0 \quad (\text{A26})$$

$$F_2 = \mu_2^s(T, P, x) - \mu_2^m(P, T, y_1) = 0 \quad (\text{A27})$$

where the superscripts indicate solid (s) and melt (m). To find the second point on the fractionation curve, differentiate Equations (A25) and (A26):

$$(\partial F_1/\partial x)_{P,T} dx + (\partial F_1/\partial T)_{x,P} dT + (\partial F_1/\partial P)_{x,T} dP - \sum_{i \neq 1} \mu_{1i} dy_i = 0 \quad (\text{A28})$$

$$(\partial F_2/\partial x)_{P,T} dx + (\partial F_2/\partial T)_{x,P} dT + (\partial F_2/\partial P)_{x,T} dP - \sum_{i \neq 2} \mu_{2i} dy_i = 0 \quad (\text{A29})$$

where μ_{ij} is the derivative of the chemical potential of component i with respect to n_j :

$$\mu_{ij} = \partial^2 G / \partial n_i \partial n_j \quad (\text{A30})$$

Equations (A24), (A25), (A27) and (A28) are four equations in the differentials, dy_1 , dx , dT and dP . Additional equations can be constructed between the mole fractions of the fractionating components and the mole fractions of the components remaining in the melt of the form:

$$dy_k = y_k[x dy_2 - (1 - x) dy_1] / [x y_2 - (1 - x)y_1] \quad (\text{A31})$$

In theory at least, these equations can be integrated to produce an equation expressing y_1 , say, as a function of P , T , x and y_2 . Practically, however, numerical techniques are used with small finite changes, Δx , ΔT , ΔP , Δy_1 and Δy_2 , approximating the differentials. One differential is fixed and the others are calculated from the equations. The fractionation path is derived by a sequence of such calculations.

THERMODYNAMIC PROPERTIES OF SILICATE LIQUIDS WITH EMPHASIS ON DENSITY, THERMAL EXPANSION AND COMPRESSIBILITY

INTRODUCTION

A brief survey of the igneous petrology literature in recent years indicates a general consensus that it is the physical aspects of a magma's history that control its chemistry. Segregation dynamics, crystal fractionation, magma mixing, assimilation and convection are all mechanisms that are proposed to explain the chemical diversity of lavas observed on the Earth's surface. Although the dynamic path that a magma follows undoubtedly controls the composition of erupted lava, the inverse statement is equally true; namely, the driving force behind many physical processes is the response of the magmatic system to chemical disequilibria. Trace element and isotope concentrations can be used to infer the relative importance and influence of various dynamic mechanisms. However, their trace quantities preclude their control of the physical processes, and it is the major-element chemistry that dictates the position of thermodynamic equilibria: the temperature at which melting begins, the order and abundance of crystallizing phases, and the density of a crystal-melt assemblage. As a consequence, in order to understand what controls the dynamic evolution of a magma body, attention must also turn to the thermodynamic state properties that determine both the composition and percentage of melts generated in a source region and their subsequent crystallization paths.

The role that thermodynamic properties play in controlling melting and crystallization in magmatic systems can be visualized most simply by considering the change in the Gibbs free energy function with temperature and pressure during fusion of a congruently melting mineral:

$$\Delta G(T,P) = G^{\text{liq}}(T,P) - G^{\text{sol}}(T,P) \quad (1)$$

At equilibrium, for one component:

$$\begin{aligned} \Delta G(T,P) = 0 = & \Delta H(T_{\text{ref}}) + \int_{T_{\text{ref}}}^T \Delta C_p(T) dT - T[\Delta S(T_{\text{ref}}) \\ & + \int_{T_{\text{ref}}}^T (\Delta C_p(T)/T) dT] + \int_1^P \Delta V_T(P) dP, \end{aligned} \quad (2)$$

where $\Delta H(T_{\text{ref}})$ and $\Delta S(T_{\text{ref}})$ are the enthalpy and entropy of fusion of the mineral at a reference temperature (typically the melting temperature at 1 bar), $\Delta C_p(T)$ is the difference in heat capacity between the liquid and solid, and $\Delta V_T(P)$ is the volume of fusion at temperature T . Enthalpy, entropy, and heat capacity are thermodynamic state properties through which temperature affects crystal-melt equilibria. Similarly, the volume function, and its temperature and pressure derivatives, are the properties through which pressure affects the equilibria.

The role that these properties play in a variety of dynamic processes can also be readily appreciated. For example, the latent heat of crystallization produced by a cooling magma body is one of the principal factors that influences its thermal evolution, its imprint on surrounding country rocks, and the time required to solidify. Assimilation of country rock is often used to explain anomalous isotope and trace element concentrations, but rarely is there a rigorous evaluation of the heat required to fuse the proposed mass of material. The segregation of newly generated melt from its residual matrix is driven by the buoyancy

differential between the melt and solid; thus a description of the volume of the melt phase as a function of composition, temperature and pressure is required. Convection within magma chambers is a hotly debated issue (e.g., Sparks, 1990; Marsh, 1990) for which the driving force is a density instability postulated to develop within ponded magma bodies. Thermally-induced and compositionally-induced density instabilities are distinguished (Martin et al., 1989); modelling the former requires accurate knowledge of the thermal expansion of silicate melts, whereas the latter relies on information on how melt densities change with crystallization. As a consequence, in addition to requiring a description of melt densities as a function of composition, it is also necessary to know what phases are crystallizing from a magma and in what proportion. In virtually all cases the magma bodies are at depth, and hence the effect of pressure on melt densities must also be known.

The primary vehicle by which measurements of enthalpy, heat capacity, and volume can be quantitatively exploited to fully describe the chemical and physical changes in a cooling magma body, is a thermodynamic model that accurately predicts crystal-melt equilibria. In the last ten years, there has been remarkable growth in the sophistication and success of such models (Ghiorso et al., 1983; Ghiorso, 1985, 1987; Ghiorso and Carmichael, 1985, 1987; Berman and Brown, 1984, 1987). However, the success of any model in accurately predicting phase equilibria is critically dependent on the quality of the thermodynamic data that is used for calibration of the standard state properties and activities of chosen components. Before a thermodynamic model can be used, for example, to calculate how much heat is available to a basaltic liquid to assimilate a proposed mass of country rock (Ghiorso and Keleman, 1987), the model must first be calibrated on accurate enthalpy of fusion, enthalpy of mixing and heat capacity data.

In general, the calorimetric and volumetric data available for the various mineral phases found in igneous rocks are far more abundant, accurate and precise than those available for the liquid phase. The reason for this disparity stems primarily from the difficulty of making measurements of thermodynamic properties at the high temperatures where silicates are molten. Moreover, in order to be relevant to magmatic systems, thermodynamic descriptions of silicate liquids must extend to compositions that include iron and volatiles. However, these components present a host of additional experimental difficulties because (1) the ferric-ferrous ratio in silicate liquids (at constant f_{O_2}) is strongly dependent on temperature, requiring accurate characterization of ferric and ferrous concentrations in liquids *during* measurements of thermodynamic properties, and (2) volatiles have low solubilities in silicate melts at 1 bar, requiring measurements of thermodynamic properties to be made at high pressure. Unfortunately, neither of these requirements is easily achieved.

Despite these difficulties, there has been a marked increase in both the quality and quantity of thermodynamic data on silicate liquids in recent years. The volume, thermal expansion, compressibility and heat capacity of both the ferric and ferrous components in silicate liquids are now well constrained (Lange and Carmichael, 1987, 1989; Dingwell and Brearley, 1988; Dingwell et al., 1988; Kress and Carmichael, 1989, 1991; Lange and Navrotsky, 1990). This allows an evaluation of the effect of oxidation state on silicate liquid volumes and enthalpies. The partial molar thermodynamic properties of volatile components in multicomponent silicate liquids remain elusive, although through analysis of solubility curves (Spera and Bergman, 1980; Silver et al., 1990), their values can be estimated. The purpose of this chapter is to review these data with an emphasis on their practical application to petrologic problems. We focus attention primarily on the volumetric properties of silicate liquids because the calorimetric properties (enthalpy, entropy and heat capacity) have been thoroughly reviewed in several recent papers (Stebbins et al., 1984; Navrotsky, 1986; Richet and Bottinga, 1986). In our opinion, there has not been enough new data reported in the literature in the last five years to warrant yet another comprehensive discussion of these properties. In contrast, although there are reviews in the literature on the density of silicate liquids (Kushiro, 1980; Scarfe, 1986), there has been a significant amount of new data reported subsequent to those reviews, particularly on the compressibility of silicate liquids (Manghnani et al., 1986; Rivers and Carmichael, 1987;

Kress et al., 1988; Kress and Carmichael, 1991; Rigden et al., 1984, 1988, 1989; Agee and Walker, 1988). As a consequence, we believe it is appropriate at this time to present a discussion of these new thermodynamic data. Before turning attention to the volumetric properties, however, we first outline the most fundamental application of thermodynamic data on silicate liquids to magmas.

THE STANDARD STATE FREE ENERGY OF NATURAL LIQUIDS

The most obvious and direct application of thermodynamic data on silicate liquids is the calculation of crystal-melt phase equilibria in a magma. Following Ghiorso et al. (1983), in order to define the *minimum* total Gibbs free energy of a magmatic system (condition of equilibrium), it is necessary to first describe the Gibbs free energy of the liquid phase as a function of temperature, pressure and composition. The free energy of a natural liquid solution per gram formula weight (g.f.w.)¹ can be expressed as:

$$G_{T,P,X_i}^{\text{liquid}} = \sum X_i [\mu_{i,T,P}^\circ + RT \ln a_i] \quad (3)$$

where R is the gas constant, T is temperature in Kelvins, X_i is the mole fraction and a_i is the activity of component i in the liquid solution, and $\mu_{i,T,P}^\circ$ is the *standard state* chemical potential of pure component i in the liquid state at temperature T and pressure P . The necessary thermodynamic properties required for the definition of $\mu_{i,T,P}^\circ$ can be seen in the following equation:

$$\mu_{i,T,P}^\circ = H_{T_r,P_r} + \int_{T_r}^T C_p(T) dT - T[S_{T_r,P_r} + \int_{T_r}^T (C_p(T)/T) dT] + \int_1^P V_T(P) dP \quad (4)$$

It is essential, therefore, to know the enthalpy (H_{T_r,P_r}) and entropy (S_{T_r,P_r}) of the pure liquid components at a reference temperature and pressure, as well as the heat capacity (C_p) and volume (V) functions in order to calculate the standard state chemical potentials at elevated temperatures and pressures. If these data are available for all chosen components, then the only unknowns are the activities of the components (a_i) which can be calibrated from experimental phase equilibria data (see Ghiorso, 1985, 1987 and Berman and Brown, 1987 for a detailed discussion and examples), or in some cases, can be measured directly (Fraser et al., 1983; Fraser and Bottinga, 1985).

The amount, type and quality of available data with which to define the standard state chemical potentials places an important constraint on the choice of components. In general, two approaches can be taken: (1) components can be chosen that represent actual species in the liquid. This allows the Gibbs free energy of the liquid solution to be expressed primarily by mechanical and ideal (configurational) mixing terms. Unfortunately, there is little information on what species are actually present in liquids of natural compositions, nor are there thermodynamic data available for such components. Alternatively, (2) simple oxide or stoichiometric mineral components can be chosen for which thermodynamic data are available. The problem with this choice is that complex non-ideal mixing terms are necessary in order to fully describe the free energy of the multicomponent liquid solution.

The most pragmatic approach for magmatic liquids is the latter option, namely components that mimic mineral formulae (Ghiorso et al., 1983). The primary motivation for this choice stems from the fact that any thermodynamic description of the liquid phase that is to be applied to magmas must be internally consistent with the thermodynamic properties of the solid phases that crystallize out of magmas. The only way of making an internally

¹ Gram formula weight of a multicomponent liquid = $\sum X_i (M.W.)_i$ where X_i is the mole fraction of oxide component i and $(M.W.)_i$ is the molecular weight of oxide component i .

consistent transition from the solid to liquid state is with accurate enthalpy of fusion data for the chosen components. This can be seen in the following equation:

$$H^{\circ}_{\text{liq}}(T_r) = \Delta_f H^{\circ}_{\text{sol}}(298) + \int_{298}^{T_{\text{fus}}} C_p^{\circ}_{\text{sol}} dT + \Delta H^{\circ}_{\text{fus}}(T_{\text{fus}}) + \int_{T_{\text{fus}}}^T C_p^{\circ}_{\text{liq}} dT, \quad (5)$$

where $H^{\circ}_{\text{liq}}(T_r)$ is the standard state liquid enthalpy at temperature T_r , $\Delta_f H^{\circ}_{\text{sol}}(298)$ is the heat of formation of the pure solid component at 298 K, $C_p^{\circ}_{\text{sol}}$ is the heat capacity function for the solid, $\Delta H^{\circ}_{\text{fus}}(T_{\text{fus}})$ is the heat of fusion, and $C_p^{\circ}_{\text{liq}}$ is the liquid heat capacity function. Similarly, in order to calculate an accurate value of the standard state entropy of a pure liquid component, $S^{\circ}_{\text{liq}}(T_r)$, the following calculation must be made:

$$S^{\circ}_{\text{liq}}(T_r) = S^{\circ}_{\text{Third Law}}(298) + \int_{298}^{T_{\text{fus}}} (C_p^{\circ}_{\text{sol}}/T) dT + \Delta S^{\circ}_{\text{fus}}(T_{\text{fus}}) + \int_{T_{\text{fus}}}^T (C_p^{\circ}_{\text{liq}}/T) dT. \quad (6)$$

The requisite data are the third law entropy of the solid component at 298.15, the heat capacity and entropy of fusion of the pure solid, and the heat capacity of the pure liquid. From the relation,

$$\Delta G(T_{\text{fus}}) = 0 = \Delta H(T_{\text{fus}}) - T_{\text{fus}} \Delta S_{\text{fus}}, \quad (7)$$

entropies of fusion (ΔS_{fus}) can be derived from enthalpy of fusion (ΔH_{fus}) data. Unlike the case for enthalpy and entropy, the liquid volume of component i does not need to be referenced to the solid state; it has an absolute value rather than a relative one. Its integrated function over the pressure interval, P to 1 bar, allows the standard state chemical potential of component i to be calculated at any elevated pressure P .

Examination of Equations (4), (5) and (6) indicate those thermodynamic parameters that are required to describe the standard state free energy of natural liquids as a function of temperature, pressure and bulk composition. For a thorough analysis and compilation of thermodynamic data for a wide variety of stoichiometric *mineral* phases, the reader is referred to Berman (1988). As mentioned earlier, both Stebbins et al. (1984) and Richet and Bottinga (1986) provide thorough reviews of the enthalpy, entropy and heat capacity of silicate liquids as a function of temperature and composition (see Appendix). Detailed discussions of how these thermodynamic state properties are incorporated into theoretical models that describe crystal-melt equilibria in multicomponent systems are found in both Berman and Brown (1987) and Ghiorso (1987). Given the focus of this chapter, the data that will be discussed and applied to magmatic systems are the density, thermal expansion and compressibility of silicate liquids.

VOLUMETRIC PROPERTIES OF SILICATE LIQUIDS

An equation of state, or pressure-temperature-density relation, for multicomponent silicate liquids is essential for calculations of magmatic phase relations at pressure and for determining the direction and velocity of magma transport in the Earth. Thus, the experimental goal is to obtain a sufficient data base that allows a model equation to be formulated for silicate liquid volumes as a function of temperature, pressure and composition. Although model equations describing the volume of silicate liquids as a function of composition and temperature (at 1 bar) have been available in the literature for twenty years (Bottinga and Weill, 1970), the precision of such models has increased by almost an order of magnitude in recent years (Lange and Carmichael, 1987), reflecting an increase in the quality and quantity of density data since 1970. Moreover, as recently as five years ago, insufficient data were available to incorporate the effect of pressure into any general model

describing the volume of natural liquids. Yet, virtually all magmas originate and evolve at pressure, making information on the densities of natural liquids as a function of pressure imperative. The derivative function of volume with respect to pressure can be extracted from measurements of sound speed and from shock-wave experiments (Rivers and Carmichael, 1987; Kress et al., 1988; Rigden et al., 1988, 1989). But in all cases, compressibility data cannot be derived without precise volume and thermal expansion data at 1 bar. This section begins, therefore, with a discussion of 1 bar density measurements on silicate liquids.

The compositional dependence of liquid volumes at 1 bar

Only one decade ago, the primary source of 1 bar density data on silicate liquids was the metallurgy literature and, as a consequence, the data were confined to simple binary and ternary compositions. Bottinga and Weill (1970) were the first to tap this resource for geologists and to suggest that density data on two- and three-component melts can be used to calibrate a model equation for silicate liquid volumes that is applicable to natural liquids. To test this hypothesis, they postulated a simple model equation:

$$V_{\text{liq}}(T) = \sum X_i \bar{V}_i(T) \quad , \quad (8)$$

where $V_{\text{liq}}(T)$ is the measured liquid molar volume, X_i is the analyzed mole fraction and \bar{V}_i is the fitted partial molar volume of oxide component i in the melt. Implicit in this equation is the assumption that the partial molar volumes of the liquid oxide components are *independent* of composition. If this assumption is valid within the uncertainty of the measurements, then a limited number of volume measurements on binary and ternary silicate melts, thus covering a wide compositional range, can be used to calibrate a model equation applicable to natural, multicomponent liquids.

Because the original model equation of Bottinga and Weill (1970) was calibrated on data obtained primarily by metallurgists, components important to natural liquids, such as TiO_2 and Fe_2O_3 , were missing. As geologists began to make density measurements themselves, liquids containing these components were added to the available data (Nelson and Carmichael, 1979; Mo et al., 1982). In the meantime, new density data on silicate liquids were also reported in the literature by both glass scientists and metallurgists, significantly expanding the data set. All the model equations of liquid volume presented thus far in the literature had a standard error of 1-2% and had partial molar oxide volumes that were independent of composition. Bottinga et al. (1982) recognized that the standard error on these model equations often *exceeded* the reported precision and accuracy of the actual volume measurements (typically $\leq 0.5\%$) and that such large errors in the model may reflect its over-simplicity. As a consequence, they proposed a more complex model equation for liquid volumes that included a linear compositional dependence to the partial molar volume of Al_2O_3 , postulated to reflect structural changes in the melt associated with aluminum. Ghiorso and Carmichael (1984) questioned the validity of the Bottinga et al. model; at the heart of the controversy was the fact that there are *two* possibilities that can explain the inadequacy of Equation (8) in predicting liquid volumes within the reported uncertainty of the measurements. The first (proposed by Bottinga et al., 1982), is that the assumption of *constant* partial molar volumes implicit in Equation (8) is too simple and that excess volume terms reflecting *measurable* structural changes in the melt are required. The second possibility is that the large errors associated with Equation (8) are due primarily to interlaboratory errors in the data set used to calibrate the model. Such errors could arise because different techniques were employed to measure the liquid densities reported in the literature (maximum bubble pressure method, double-bob Archimedean method, sphere densitometry, and X-radiographic imaging), all of which have a different precision and accuracy.

The most precise technique is the double-bob Archimedean method developed by Bockris et al. (1956) which has been the primary source of 1 bar silicate liquid density data

obtained in the last five years (Stein et al., 1986; Lange and Carmichael, 1987; Johnson and Carmichael, 1987; Dingwell et al., 1988; Dingwell and Brearley, 1989; Taniguchi, 1989). This method is based on measurements of the buoyancy of a submerged Pt bob of known volume in a silicate melt over a range of temperatures. Lange and Carmichael (1987) showed that by including data obtained only by the double-bob method, volumes of iron-free multicomponent silicate liquids could be described as a linear function of composition, with the exception of the TiO_2 component, to a high precision (0.2%). It was thus demonstrated that Al_2O_3 has a constant partial molar volume at 1 bar over a wide range of metaluminous and peralkaline compositions.

TiO₂-bearing liquids. Although the controversy over the postulate of constant partial molar volumes was initially focused on the Al_2O_3 component (Ghiorso and Carmichael, 1984; Bottinga et al., 1984), the density measurements of Lange and Carmichael (1987) indicate a strong compositional dependence to the partial molar volume of TiO_2 . Specifically, the densities of two calcium-bearing and two sodium-bearing titanium silicate liquids were measured. It was observed that the partial molar volume of TiO_2 in the sodic melts has a regressed value of 28.02 cc/mole at 1673 K whereas in the calcic melts, the fitted value at 1673 K is only 23.16 cc/mole. This latter value is strikingly similar to the volume of anatase at 1673 K (21.61 cc/mole) and suggests that titanium is primarily in octahedral coordination in the calcic melts. Likewise, the much larger partial molar volume of TiO_2 in the sodic melts implies that Ti^{4+} is present in lower coordination environments. It should be noted that one of the two calcium-bearing titanium liquids contains alumina while the other does not, and the same is true for the two sodium-titanium-silicate liquids. Therefore, the difference in \bar{V}_{TiO_2} between the sodic and calcic melts is not a reflection of effects caused by alumina. Nor are the derived values of \bar{V}_{TiO_2} likely to be affected by the presence of Ti^{3+} in the sample liquids as Schreiber (1987) demonstrated that $\text{Ti}^{3+}/\text{Ti}^{4+}$ ratios in silicate liquids are less than 0.01 at oxygen fugacities $\geq 10^{-6}$. Since the density measurements in question were performed in air, it is unlikely that any significant concentrations of Ti^{3+} were present in the experimental melts. Although density measurements are not the most direct probe of melt structure, these results are suggestive regarding the coordination of titanium. Ti^{4+} is known to be four, five and six-fold coordinated by oxygen atoms in various crystal structures. A number of recent spectroscopic, X-ray emission and phase equilibria investigations (Yarker et al., 1986; Dickinson and Hess, 1985; Hanada and Soga, 1980; Gregor et al., 1983) indicate that similar Ti^{4+} coordinations exist in liquids and glasses. The conclusions drawn by these studies are not, however, always in agreement and the factors controlling the coordination of titanium are not unambiguously established.

The problem for petrologists is how to express the partial molar volume of TiO_2 in natural liquids. To address this issue, Johnson and Carmichael (1987) and Johnson (1990) report density measurements on a wide variety of titanium-bearing liquids, including natural compositions doped with excess TiO_2 . The goal was to examine the effect of MgO and K_2O on derived values of the partial molar volume of TiO_2 , the effect of mixed cations (i.e., $\text{K}_2\text{O}-\text{CaO}-\text{TiO}_2-\text{SiO}_2$; $\text{Na}_2\text{O}-\text{CaO}-\text{TiO}_2-\text{SiO}_2$; $\text{MgO}-\text{CaO}-\text{TiO}_2-\text{SiO}_2$; etc.) as well as the effect of both ferric and ferrous iron. The results indicate that the partial molar volume of TiO_2 in both calcic and magnesian silicate liquids is a constant with a fitted value of $23.61 \pm .35$ cc/mole at 1673 K (Johnson, 1990). Likewise, the partial molar volume of TiO_2 in the alkaline silicate liquids can also be fitted, but with values of 29.59 ± 0.57 and 34.14 ± 0.90 cc/mole at 1673 K for the sodic and potassic liquids respectively. These results indicate that the partial molar volume of TiO_2 increases as the polarizing power of the network modifying cation decreases. The compositional dependence of the partial molar volume of TiO_2 in the alkaline liquids may reflect the presence of more than one coordination environment for Ti^{4+} in these melts. In contrast, Ti^{4+} appears to reside almost exclusively in an octahedral coordination in alkaline earth silicate liquids. Liquids with mixed alkali and alkaline earth cations have \bar{V}_{TiO_2} values that indicate a strong and complex compositional dependence (Ghiorso, personal comm.) and suggest the presence of more than one coordination geometry for Ti^{4+} in these liquids.

Determining a value for \bar{V}_{TiO_2} that is best applied to natural liquids is an important consideration since a difference between 23 and 34 cc/mole at 1673 K will greatly affect the calculated molar volumes of various natural liquid compositions. For an andesite with less than 0.5 wt % TiO_2 , the effect is negligible, but for a ugardite lava that contains over 5 wt % TiO_2 , the uncertainty in volume is approximately 1.4%—well outside the uncertainty of the volume measurements. Fortunately, the complications apparent in these simple systems do not appear to be present in liquids of natural compositions, although the data are limited. For example, an andesite doped with 8.36 mol % TiO_2 (Johnson, 1990) has a measured density that reflects a value for \bar{V}_{TiO_2} of 24.29 cc/mole at 1673 K (calculated from the volume equation of Lange and Carmichael (1987): $\bar{V}_{\text{TiO}_2} = [V_{\text{meas}} - \sum X_i \bar{V}_i] / X_{\text{TiO}_2}$). Likewise, a Kilauea tholeiite with 2.75 mol % TiO_2 has a measured density (Mo et al., 1982; sample 004) that is consistent with a value for \bar{V}_{TiO_2} of 23.02 cc/mole at 1673 K, whereas a ugardite lava with 3.46 mol % TiO_2 , and both a low alumina and a high alkali content (sample 28; Lange and Carmichael, 1987) has a measured density consistent with a value for \bar{V}_{TiO_2} of 19.97 cc/mole at 1673 K. Considering that *all* the errors in the density measurements, the compositional analyses and the volume equation of Lange and Carmichael (1987) are effectively being placed on these derived values of \bar{V}_{TiO_2} , and that these lavas contain relatively low concentrations of titanium, the results are remarkably uniform. They are suggestive that Ti^{4+} is predominantly in an octahedral coordination in natural liquids with a partial molar volume that is best constrained by the alkaline earth silicate liquids. Moreover, it is anticipated that the effect of pressure will be to favor an octahedral coordination geometry for Ti^{4+} in natural liquids, since the volume difference between tetrahedral and octahedral Ti^{4+} appears to be significant.

Iron-bearing liquids. Fe_2O_3 is another component of natural liquids that is postulated to have a partial molar volume that is dependent on composition (Dingwell and Brearley, 1988), possibly reflecting the amphoteric behavior of Fe^{3+} to occupy both tetrahedral and octahedral coordination geometries. Such a dual coordination environment for Fe^{3+} has been deduced from Mössbauer spectroscopic results on a wide variety of silicate glasses (Bowker et al., 1981; Levy et al., 1976; Pargamin et al., 1972; Iwamoto et al., 1978). Again, the question for petrologists is what value for $\bar{V}_{\text{Fe}_2\text{O}_3}$ should be applied to natural liquids, and whether or not it is dependent on composition over the range spanned by magmas. These are extremely important issues to resolve as magmatic Fe_2O_3 concentrations can reach significant levels in various lava types erupted in both subduction and rift zone environments (Carmichael, 1991). As a consequence, any uncertainty in $\bar{V}_{\text{Fe}_2\text{O}_3}$ can lead to large errors in natural melt densities that are well outside the experimental precision. Moreover, precise information on both the ferric and ferrous partial molar volumes is required in order to evaluate the effect of oxidation state on natural melt densities.

To address this issue concerning $\bar{V}_{\text{Fe}_2\text{O}_3}$, several studies in recent years have reported double-bob density measurements on iron-bearing silicate liquids in both simple 4-component systems (Mo et al., 1982; Dingwell et al., 1988; Dingwell and Brearley, 1988) and in the natural 9-component system (Mo et al., 1982; Lange and Carmichael, 1987). However, despite this expanding body of density data, large uncertainties remain associated with the partial molar volume of Fe_2O_3 (Dingwell et al., 1988; Dingwell and Brearley, 1988). This may be attributed in part, perhaps, to the amphoteric behavior of Fe^{3+} , although the inherent difficulty of accurately characterizing ferric and ferrous concentrations in sample liquids during measurements of density can also add uncertainty. This can be seen by examination of the following equation:

$$V_{\text{liq}}(T) = \sum [X_i(T) (M.W.)_i] / \rho_{\text{liq}}(T) \quad (9)$$

where $V_{\text{liq}}(T)$ is the molar volume of the liquid at temperature T , $X_i(T)$ is the mole fraction of oxide component i in the liquid at temperature T , $(M.W.)_i$ is the molecular weight of oxide component i , and $\rho_{\text{liq}}(T)$ is the density of the liquid at temperature T . Clearly, any

uncertainty in the compositional analysis of the liquid (and hence, X_i) can lead to significant uncertainty in volume, even if density is precisely known. Moreover, in order to extract precise partial molar volumes of the oxide components, precise determination of the mole fractions of each oxide component are also required, as seen in Equation (8).

The difficulty with iron-bearing silicate liquids resides in the strong temperature dependence of the ferric-ferrous ratio; thus X_i is a function of temperature in Equation (9). This requires that the redox state of the experimental liquids be determined at each temperature of measurement. Unfortunately, this is not always easily achieved because it is difficult to sample and rapidly quench the liquid during the course of an experiment. However, if the liquid samples are in thermal equilibrium during the density measurements, independent determinations of equilibrium ferric-ferrous ratios as a function of temperature (via Pt-loop drop quench experiments) can be applied. Clearly, before the postulate of a compositionally-dependent partial molar volume of Fe_2O_3 can be fully explored, accurate characterization of ferric-ferrous concentrations in the sample liquids must be assured.

As an example, Dingwell et al. (1988) and Dingwell and Brearly (1988) report density measurements on liquids in the $\text{Na}_2\text{O-FeO-Fe}_2\text{O}_3\text{-SiO}_2$ and $\text{CaO-FeO-Fe}_2\text{O}_3\text{-SiO}_2$ systems, respectively. They used Mössbauer spectra to analyze the ferric-ferrous ratio of their samples quenched to glasses from Pt-loop equilibrations in air at the temperatures of the density measurements. Unfortunately, Mössbauer spectroscopy has been shown to be a poor technique applied to iron-rich glasses ($> 14 \text{ wt } \% \text{ Fe}_2\text{O}_3$) if the spectra are taken at 298 K since the absorption efficiencies of Fe^{3+} and Fe^{2+} are not equivalent (Sawatzky et al., 1969; Bowker, 1979), leading to an under-estimation of the ferrous component (see Mysen et al., 1985: Table 1 and Lange and Carmichael, 1989: Table 2). Lange and Carmichael (1989) and Kress and Carmichael (1989) experimentally calibrated by wet chemical methods appropriate model equations that allow calculation of equilibrium ferric-ferrous ratios for liquids in the systems $\text{Na}_2\text{O-FeO-Fe}_2\text{O}_3\text{-SiO}_2$ and $\text{CaO-FeO-Fe}_2\text{O}_3\text{-SiO}_2$, respectively. These models were used to re-interpret the density data of Dingwell et al. (1988) on liquids in the sodium-iron-silica system and the data of Dingwell and Brearly (1988) on liquids in the lime-iron-silica system. Lange and Carmichael (1989) were able to demonstrate that the linear volume equation of Equation (8) could fit the density measurements of Dingwell et al. (1988) on $\text{Na}_2\text{O-FeO-Fe}_2\text{O}_3\text{-SiO}_2$ liquids within the quoted experimental errors, and perhaps more significantly, were able to show that the partial molar volumes derived from Dingwell et al.'s (1988) data set are equivalent (within error) to those reported by Lange and Carmichael (1987) as seen in Table 1. This is a significant result as it implies that the partial molar volume of Fe_2O_3 is essentially a constant over a wide range of compositions that include those in the sodium-iron-silica system as well as those represented by both the simple 4-component and natural 9-component liquids that were used in the calibration of Lange and Carmichael's (1987) volume equation². In addition, it establishes that the density measurements of Dingwell et al. (1988) are consistent with those of Stein et al. (1986), Brockris et al. (1956), Mo et al. (1982) and Lange and Carmichael (1987), all of which are based upon the Pt double-bob Archimedean technique.

In contrast to the sodic system, however, a re-interpretation of the density data in the calcium-iron-silica system leads to conclusions that support the original suggestion of Dingwell and Brearly (1988), namely that the partial molar volume of Fe_2O_3 is dependent on composition in this simple system. Kress and Carmichael (1989) were able to fit the

² It should be noted that of the 11 Fe_2O_3 -bearing compositions included in the regression of Lange and Carmichael (1987), four samples did not have their ferric-ferrous ratios determined by Pt-loop equilibrations. However, subsequent equilibrations led to ferric-ferrous ratios that did not differ significantly from those originally published for three of the four samples. A re-calibration of the volume equation of Lange and Carmichael (1987) based upon the revised ferric-ferrous data for all four samples did *not* change the fitted partial molar volume parameters for the oxide components within their reported 1σ errors.

Table 1. Fitted oxide partial molar volumes.

| | V_i (DBD) ¹ (cc/mole $\pm 1\sigma$) | V_i (LC) ² (cc/mole $\pm 1\sigma$) |
|--------------------------------|--|---|
| 1573 K | | |
| SiO ₂ | 26.60 \pm 0.15 | 26.92 \pm 0.06 |
| Fe ₂ O ₃ | 41.39 \pm 0.37 | 41.44 \pm 0.31 |
| FeO | 13.61 \pm 0.33 | 13.35 \pm 0.18 |
| Na ₂ O | 28.48 \pm 0.23 | 28.02 \pm 0.12 |
| 1673 K | | |
| SiO ₂ | 26.68 \pm 0.16 | 26.90 \pm 0.06 |
| Fe ₂ O ₃ | 41.78 \pm 0.41 | 42.13 \pm 0.28 |
| FeO | 13.85 \pm 0.34 | 13.65 \pm 0.15 |
| Na ₂ O | 29.14 \pm 0.25 | 28.78 \pm 0.10 |
| 1773 K | | |
| SiO ₂ | 26.74 \pm 0.17 | 26.91 \pm 0.06 |
| Fe ₂ O ₃ | 42.46 \pm 0.49 | 42.97 \pm 0.29 |
| FeO | 14.12 \pm 0.37 | 13.97 \pm 0.14 |
| Na ₂ O | 29.80 \pm 0.26 | 29.51 \pm 0.10 |

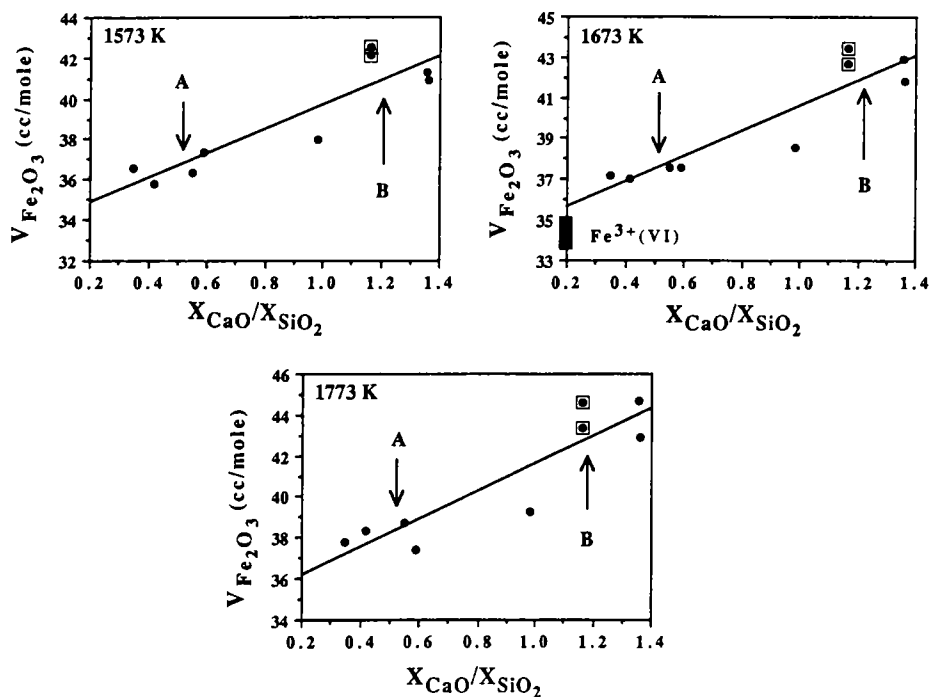
¹Calibrated on density data of Dingwell et al. (1988).²From Lange and Carmichael (1987).

Figure 1. Calculated values of the effective partial molar volume of Fe₂O₃ in CaO-FeO-Fe₂O₃-SiO₂ liquids plotted as a function of the molar CaO:SiO₂ ratio in the melts (see text for discussion). Solid circles represent data based on the density measurements of Dingwell and Brearley (1988), whereas solid circles enclosed in open squares are based on the measurements of Mo et al. (1982). The partial molar volume of Fe₂O₃ in which Fe³⁺ is entirely in octahedral coordination is estimated to be between 33.6-35.2 cc/mole at 1673 K; this range is denoted by the solid rectangle on the vertical axis denoting $V_{Fe_2O_3}$ at 1673 K.

measured liquid volumes of Dingwell and Brearley (1988) in the CaO-FeO-Fe₂O₃-SiO₂ system well within experimental error with a linear model equation (Eqn. 8) that invoked no excess volume mixing terms. However, their derived partial molar volumes for the oxide components are quite different from those presented by Lange and Carmichael (1987). This is due, in part, to the fact that their fit is calibrated on only seven CaO-FeO-Fe₂O₃-SiO₂ liquid compositions (from Dingwell and Brearley, 1988). In contrast, the fit of Lange and Carmichael (1987) is based upon 64 liquid compositions, all of which contain silica and 23 of which contain CaO, thus providing tight constraints on the partial molar volumes of these two oxide components. It is, therefore, an interesting exercise to use the volume equation of Lange and Carmichael (1987) to calculate the effective partial molar volume of Fe₂O₃ in each of the experimental CaO-FeO-Fe₂O₃-SiO₂ liquids, where $\bar{V}_{\text{Fe}_2\text{O}_3} = [V_{\text{meas}} - \sum X_i \bar{V}_i] / X_{\text{Fe}_2\text{O}_3}$. These values are plotted as a function of the mole fraction ratio of CaO over SiO₂ at 1573, 1673 and 1773 K in Figure 1. The motivation for choosing $X_{\text{CaO}}/X_{\text{SiO}_2}$ as a parameter by which to plot $\bar{V}_{\text{Fe}_2\text{O}_3}$ stems from the Mössbauer studies of Moringa et al. (1976) and Iwamoto et al. (1978) - both report an increase in the proportion of tetrahedral to octahedral Fe³⁺ with increasing basicity (CaO:SiO₂ ratio) of the calcium-iron-silica glasses.

The results plotted in Figure 1 demonstrate a strong, positive correlation between the partial molar volume of Fe₂O₃ and the CaO:SiO₂ ratio in the liquid. This is especially significant in light of the observation of Kress and Carmichael (1989) that the iron redox ratio in CaO-FeO-Fe₂O₃-SiO₂ liquids is also a strong function of the lime to silica molar ratio which is in marked contrast to the redox equilibria trends in the Na₂O-FeO-Fe₂O₃-SiO₂ system (Lange and Carmichael, 1989). These results suggest that by stabilizing an increasing proportion of tetrahedral Fe³⁺, the ferric-ferrous ratio is also increased in calcic liquids. It is also of interest to note that the two CaO-FeO-Fe₂O₃-SiO₂ samples of Mo et al. (1982; 003b and 010, indicated by squares enclosing solid circles in Fig. 1) have derived values of $\bar{V}_{\text{Fe}_2\text{O}_3}$ that are consistent with those derived for similar bulk compositions measured by Dingwell and Brearley (1988). Again, this confirms that the density measurements of Mo et al. (1982) are consistent with those of Dingwell and Brearley (1988). Moreover, the fact that the two calcium-iron-silica compositions measured by Mo et al. (1982) have high CaO:SiO₂ ratios, and thus large values of $\bar{V}_{\text{Fe}_2\text{O}_3}$ (similar to those derived in the sodic system), explains why Lange and Carmichael (1987) did not see any compositional dependence to the partial molar volume of Fe₂O₃ in the lime-iron-silica liquids of Mo et al. (1982) that were included in their calibration.

As stated earlier, the issue at hand for petrologists is to determine what value for $\bar{V}_{\text{Fe}_2\text{O}_3}$ is best applied to natural liquids. The results in the CaO-FeO-Fe₂O₃-SiO₂ system indicate a possible range for $\bar{V}_{\text{Fe}_2\text{O}_3}$ at 1673 K of 37 to 43 cc/mole. Such a variation in $\bar{V}_{\text{Fe}_2\text{O}_3}$ can lead to significant differences in calculated densities of various natural liquid compositions, especially at low temperatures and at high oxygen fugacities where the ferric component is favored. Fortunately, however, as in the situation with Ti⁴⁺, the complications apparent in the CaO-FeO-Fe₂O₃-SiO₂ system do not appear to be present in liquids of natural compositions, although again, the data are limited. For example, a Kilauea lava doped with iron and thus containing 13.32 mol % Fe₂O₃ (Mo et al., 1982; sample 006) has a measured density that reflects a value for $\bar{V}_{\text{Fe}_2\text{O}_3}$ of 41.32 cc/mole at 1673 K (calculated from the volume equation of Lange and Carmichael (1987): $\bar{V}_{\text{Fe}_2\text{O}_3} = [V_{\text{meas}} - \sum X_i \bar{V}_i] / X_{\text{Fe}_2\text{O}_3}$). Similarly, a pristine Kilauea lava with 4.45 mol % Fe₂O₃ (Mo et al., 1982; sample 004), an andesite with 3.04 mol % Fe₂O₃ (Lange and Carmichael, 1987; sample 26) and a ugandite lava spiked with iron and containing 7.46 mol % Fe₂O₃ (Lange and Carmichael, 1987; sample 28) all have measured densities that reflect values for $\bar{V}_{\text{Fe}_2\text{O}_3}$ at 1673 K of 42.04, 40.87 and 40.65 cc/mole, respectively. Once again, considering that *all* the errors in the density measurements, the compositional analyses and the volume equation of Lange and Carmichael (1987) are effectively being placed on these derived values of $\bar{V}_{\text{Fe}_2\text{O}_3}$, and that these lavas contain relatively low concentrations of Fe₂O₃, the results are in remarkable agreement. The practical point to be made is that the partial molar volume of Fe₂O₃ reported by Lange and Carmichael (1987) remains our best estimate for magmatic liquids. Recommended values for the partial molar volume of all the oxide components significant to natural liquids are tabulated in Table 3.

It is informative to compare the liquid partial molar volumes of the oxide components with their crystalline molar volumes (Table 2). Both Al_2O_3 and Fe_2O_3 each show a large increase in their liquid partial molar volume values compared to the molar volumes of corundum and hematite in which the respective cations are in octahedral coordination. The implication is that the regressed values of $V_{\text{Al}_2\text{O}_3}$ and $V_{\text{Fe}_2\text{O}_3}$ presented in Table 3 are representative of each cation in tetrahedral coordination. Numerous spectroscopic studies of aluminosilicate glasses (i.e., McKeown et al., 1984; White and Minser, 1984) support the evidence for tetrahedral aluminum in non-peraluminous liquids. We can, in addition, examine the crystalline volumes of KAlSi_3O_8 and KFeSi_3O_8 at 298 K (Table 2), in which Al^{3+} and Fe^{3+} are both in *tetrahedral* coordination, and compare them to their liquid volumes at 1673 K (calculated from the data in Table 3). The ratio of the crystalline volumes of KAlSi_3O_8 and KFeSi_3O_8 is 0.97, whereas the ratio of their liquid volumes is 0.98. This similarity suggests that if the partial molar volume of Al_2O_3 presented in Table 3 is representative of Al^{3+} in tetrahedral coordination, then the partial molar volume of Fe_2O_3 in Table 3 represents Fe^{3+} primarily in tetrahedral coordination as well. In addition, if we take the crystalline volume of hematite at 1673 K (Table 2) and assume an increase in volume associated with fusion of ~5-10%, we can estimate a partial molar volume for Fe_2O_3 , in which Fe^{3+} is entirely in an octahedral coordination, of ~33.6-35.2 cc/mole at 1673 K. These values are plotted in Figure 1 and illustrate the the range of $V_{\text{Fe}_2\text{O}_3}$ values calculated for the $\text{CaO-FeO-Fe}_2\text{O}_3\text{-SiO}_2$ liquid falls between the two estimated end members where Fe^{3+} is entirely four- and six-coordinated.

Thermal expansion of silicate liquids

The precise estimation of the thermal expansion of magmatic liquids has a variety of important applications. Not only does it allow the change in volume of a natural liquid to be calculated over a range of magmatic temperatures, but it is also an essential parameter by which measurements of sound velocities in silicate liquids are converted to values of liquid compressibilities (Rivers and Carmichael, 1987). In fact, 60% of the uncertainty in derived values of dV/dP from sound velocity data stems from the uncertainty in liquid thermal expansion (Lange and Carmichael, 1987). Although the thermal expansion of various solids can be measured to a high precision by high-temperature X-ray diffraction for crystalline materials, and by dilatometry and interferometry for glassy materials (Touloukian et

Table 2. Volumes of crystalline and liquid oxides (cc/mole).

| Oxide | V_{sol} (298 K) | V_{sol} (1673 K) | V_{liq} (1673 K) | V_{liq} (cc/O ²⁻ atom) | $V_{\text{liq}}/V_{\text{sol}}$ (1673 K) |
|------------------------------------|-----------------------------|------------------------------|------------------------------|---|---|
| SiO_2 (glass) | 27.27 | 27.32 | 26.90 | 13.45 | 0.99 |
| SiO_2 (cristobalite) | 25.79 | 27.44 | 26.90 | 13.45 | 0.98 |
| SiO_2 (quartz) | 22.69 | 23.49 | 26.90 | 13.45 | 1.15 |
| TiO_2 (anatase) | 20.53 | 21.61 | 23.16 | 11.58 | 1.07 |
| Al_2O_3 (corundum) | 25.57 | 26.57 | 37.11 | 12.37 | 1.40 |
| Fe_2O_3 (hematite) | 30.31 | 31.98 | 42.13 | 14.04 | 1.32 |
| KAlSi_3O_8 | 109.05 | - | 122.18 | 15.27 | - |
| KFeSi_3O_8 | 112.81 | - | 124.69 | 15.59 | - |
| FeO | 11.98 | 12.67 | 13.65 | 13.65 | 1.08 |
| MgO | 11.25 | 11.95 | 11.45 | 11.45 | 0.96 |
| CaO | 16.78 | 17.76 | 16.57 | 16.57 | 0.93 |
| Na_2O | 25.88 | - | 28.78 | 28.78 | - |
| K_2O | 40.38 | - | 45.84 | 45.84 | - |
| H_2O (ice, 273 K) | 19.64 | - | 20 | 20 | - |
| CO_2 (solid, 194 K) | 28.21 | - | 33 | 17 | - |

Crystalline volume data from Taylor (1984a, b, c, 1985) and Robie et al. (1967).

al., 1978), none of these methods can be applied to silicate liquids. Liquids have neither the long-range order and periodic structure required for X-ray diffraction, nor are they rigid and able to maintain their shape outside a container, as required by both dilatometry and interferometry. As a consequence, all information on the thermal expansion of silicate liquids comes from measurements of the integral property, volume, as a function of temperature. In general, the precision of volume measurements obtained by the double-bob method is on the order of 0.2-0.3% (Lange and Carmichael, 1987) and typically taken over a range of 200-300 K for a single liquid composition. A simple propagation of errors indicates that dV/dT can be derived from such measurements with an estimated uncertainty of 25-30%. This uncertainty may, however, be an over-estimation as Lange and Carmichael (1987) found that the average deviation between their measured and calculated values of dV/dT is only 13%. The fitted values for dV_i/dT from Lange and Carmichael (1987) that allow the thermal expansion of natural silicate liquids to be calculated are given in Table 3.

As the determination of dV/dT is not direct but derived from measurements of the integral property as a function of temperature, the errors are large. It is important, therefore, to examine the derived dV_i/dT values and consider whether or not these parameters represent reasonable estimates. In general, thermal expansion of liquids results from an increase in the average amplitude of thermal molecular vibrations. However, covalent bonds such as Si-O undergo little, if any, expansion and the principal mode of expansion in silica-rich melts involves changes in the Si-O-Si bridging angle. As silica-rich melts are expanded structures with regard to Si-O-Si bond angles, we anticipate limited expansion through this mechanism. This is consistent with the derived value for dV_{SiO_2}/dT which is essentially zero (Table 3). In contrast, the Al-O-Si bond angle is apparently more responsive to thermal effects as indicated by the derived value for $dV_{Al_2O_3}/dT$ of 2.62×10^{-3} cc/mol-K. For the alkali and alkaline earth cations, we can compare their respective oxide values of dV_i/dT as a function of cation field strength (Fig. 3), defined as $z/(1.35 + r)^2$ where z is the cation charge, r is the cation radius for octahedral coordination and 1.35 Å is the radius of the O^{2-} anion (Shannon and Prewitt, 1969). The trend in Figure 3 indicates a pronounced correlation between decreasing thermal expansion and increasing field strength which is analogous to that found for the constant volume partial molar heat capacities (Stebbins et al., 1984).

An obvious application of these thermal expansion data is to calculate liquid densities over the range of temperature spanned by the liquidus-solidus interval of a magma, typically 300-400 K. From Table 3, it can be anticipated that liquids that are low in silica and rich in alkalis and ferric iron will exhibit a large thermal expansion. This effect can be

Table 3. Partial molar volumes, thermal expansions and compressibilities of oxide components.

$$V_{liq}(T,P,X_i) = \sum X_i [V_{i,1673K} + dV_i/dT (T-1673\text{ K}) + dV_i/dP (P - 1\text{ bar})]$$

| | $V_{i,1673K}$ (cc/mole) | $(dV_i/dT)_{1bar}$ (10^{-3} cc/mole-K) | $(dV_i/dP)_{1673K}$ (10^{-4} cc/mole-bar) | $[(dV_i/dP)]/dT$ (10^{-7} cc/mole-bar-K) |
|--|----------------------------|--|---|--|
| SiO ₂ | 26.90 ± .06 | 0.00 ± 0.50 | -1.89 ± .02 | 1.3 ± 0.1 |
| TiO ₂ | 23.16 ± .26 | 7.24 ± 0.46 | -2.31 ± .06 | ----- |
| Al ₂ O ₃ | 37.11 ± .18 | 2.62 ± 0.17 | -2.26 ± .09 | 2.7 ± 0.5 |
| Fe ₂ O ₃ | 42.13 ± .28 | 9.09 ± 3.49 | -2.53 ± .09 | 3.1 ± 0.5 |
| FeO | 13.65 ± .15 | 2.92 ± 1.62 | -0.45 ± .03 | -1.8 ± 0.3 |
| MgO | 11.45 ± .13 | 2.62 ± 0.61 | 0.27 ± 0.7* | -1.3 ± 0.4 |
| CaO | 16.57 ± .09 | 2.92 ± 0.58 | 0.34 ± .05* | -2.9 ± 0.3 |
| Na ₂ O | 28.78 ± .10 | 7.41 ± 0.58 | -2.40 ± .05 | -6.6 ± 0.4 |
| K ₂ O | 45.84 ± .17 | 11.91 ± 0.89 | -6.75 ± .14 | -14.5 ± 1.5 |
| Li ₂ O | 16.85 ± .15 | 5.25 ± 0.81 | -1.02 ± .06 | -4.6 ± 0.4 |
| Na ₂ O-Al ₂ O ₃ | ----- | ----- | 10.18 ± .50 | ---- |

Volume and thermal expansion data from Lange and Carmichael (1987).
Compressibility data from Kress and Carmichael (1991); * see text.

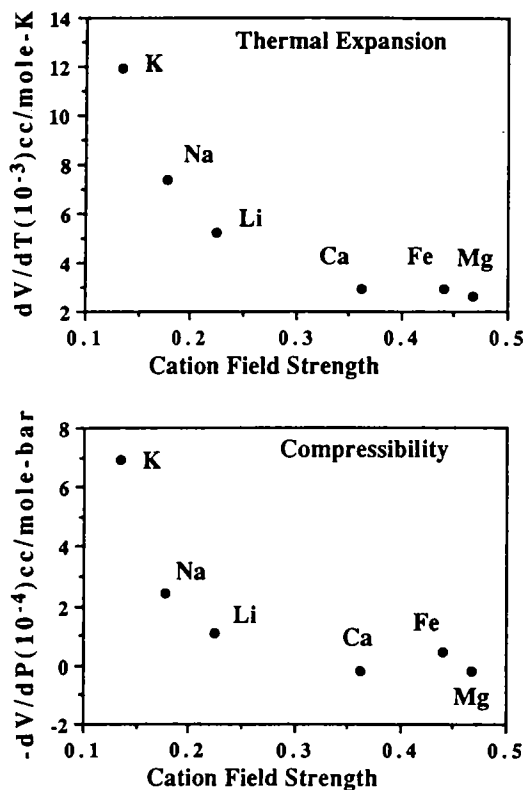


Figure 3. Fitted values of dV/dT and dV/dP plotted as a function of cation field strength defined as $z/(r + 1.35)^2$ where z is the cation charge, r is the cation radius for octahedral coordination and 1.35 Å is the radius of the O^{2-} anion (from Shannon and Prewitt, 1969).

seen in Figure 4 where the liquid densities of four different lava types (ugandite, tholeiite, andesite, peralkaline rhyolite) have been plotted as a function of temperature at three different oxidation states relative to the Ni-NiO buffer.³ The ugandite lava with only 39.23 wt % SiO_2 (Table 4) has the strongest temperature dependence whereas the andesite (58.34 wt % SiO_2) and peralkaline rhyolite (71.02 wt % SiO_2) have the least. Note that the effect of increasing silica content between the peralkaline rhyolite and the andesite on liquid thermal expansion has been offset by the rhyolite's extremely high alkali content (Table 4; Fig. 4). Also clear from Figure 4 is that the effect of oxidation state on liquid density is most pronounced for lavas with high iron contents. For example, a variation of 3 log units in fO_2 at constant temperature results in a density variation of 0.33 and 0.27% respectively for the ugandite and tholeiite lavas. For comparison, such a variation in density is equivalent to the effect caused by changing the temperature 40 K for the ugandite and 51 K for the tholeiite. In contrast, for the andesite and peralkaline rhyolite, a similar difference in oxidation state leads to only a 0.14 and 0.16% variation in density, which is equivalent to changing the temperature of the andesite and rhyolite lavas by 29 K and 42 K respectively.

³ The parameter ΔNNO in Figures 4, 6 and 8 is defined as: $\log fO_2$ (sample) - $\log fO_2$ (Ni-NiO buffer) at the temperature indicated.

Table 4. Compositions of Lavas Used in Examples (wt %)

| Sample: | Peralkaline Rhyolite | Andesite | Basaltic Andesite | Kilauea Tholeiite | Olivine Minette | Ugandite | Melilite Nephelinite |
|--------------------------------|----------------------|----------|-------------------|-------------------|-----------------|----------|----------------------|
| SiO ₂ | 71.03 | 57.07 | 52.48 | 50.29 | 49.86 | 39.51 | 36.03 |
| TiO ₂ | 0.28 | 0.74 | 0.80 | 1.82 | 1.82 | 5.64 | 1.13 |
| Al ₂ O ₃ | 8.03 | 16.91 | 16.53 | 13.91 | 12.87 | 9.89 | 15.19 |
| Fe ₂ O ₃ | 7.29 | 4.94 | 1.26 | 9.17 | 4.45 | 11.66 | 5.94 |
| FeO | 1.58 | 2.11 | 5.27 | 3.45 | 2.91 | 2.63 | 9.55 |
| MgO | 0.18 | 5.87 | 7.96 | 6.01 | 8.63 | 6.69 | 8.60 |
| CaO | 0.52 | 7.42 | 8.31 | 9.78 | 7.44 | 14.82 | 15.52 |
| Na ₂ O | 6.08 | 3.63 | 4.03 | 2.34 | 2.71 | 2.27 | 4.23 |
| K ₂ O | 3.81 | 0.95 | 1.02 | 0.54 | 5.72 | 4.23 | 1.85 |

Compositions are normalized and ferric-ferrous ratios are calculated with the parameters in Table 6 for the various examples in the text.

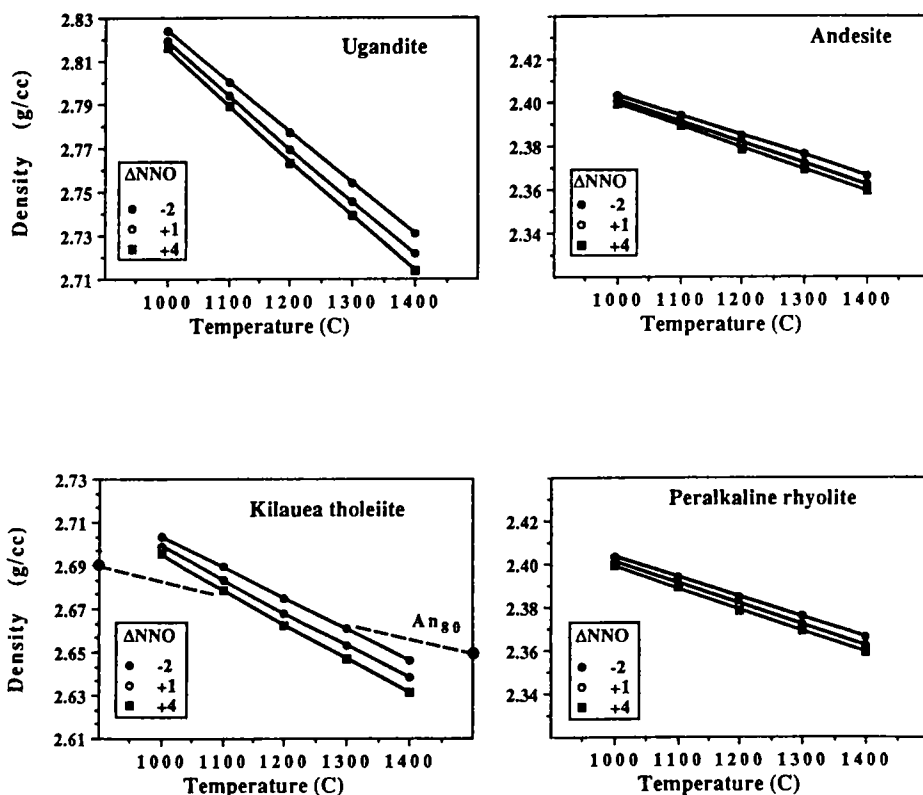


Figure 4. The densities of four natural liquids: ugandite, tholeiitic basalt, andesite, and peralkaline rhyolite, as a function of temperature. Densities are plotted at three different oxidation states relative to the Ni-NiO oxygen buffer. The density of crystalline An_{80} is shown relative to the density of the liquid tholeiite.

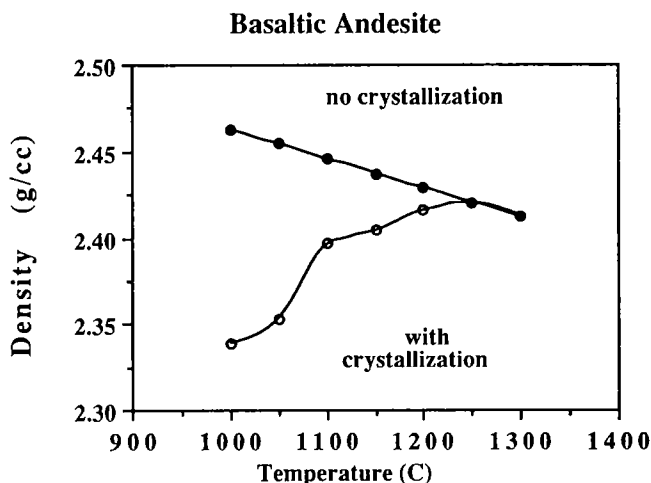


Figure 5. The density of a basaltic andesite liquid plotted as a function of temperature (1) assuming constant composition, and (2) as a function of changing composition due to the effects of fractional crystallization. The crystallization path was calculated using the thermodynamic solution model (SILMIN) of Ghiorso et al. (1983).

Clearly, in examining the change in *liquid* density across the liquidus-solidus interval of a magma, consideration must be given to the effect of changing composition due to crystallization. This effect is explored in Figure 5 where the density of a basaltic andesite is plotted as a function of temperature at constant composition and also plotted as a function of both temperature and changing composition due to effects of crystallization. The composition of the residual liquid of the basaltic andesite during crystallization was calculated under dry, 1 bar conditions along the Ni-NiO buffer with the thermodynamic solution model (SILMIN) of Ghiorso et al. (1983). Two points are made clear in this example: (1) the effect of changing composition during crystallization is to lower the liquid density of a basaltic andesite magma by 3.0%, despite the concomitant decrease in temperature of 300 K. In addition, (2) realistic evaluations of a magma's *liquid* density during crystallization cannot be made without knowledge of what phases are crystallizing out of a magma and in what proportion. Such predictions are feasible with a comprehensive thermodynamic model applicable to magmas such as SILMIN (Ghiorso et al., 1983; Ghiorso and Carmichael, 1985, 1987).

In considering silicic lavas such as andesite and rhyolite, as well as more mafic lavas such as minette and ugandite, realistic liquid densities cannot be calculated without incorporating the effect of volatiles. Water concentrations in silicic ash-flow tuffs have been estimated to reach up to 5 wt % based on experimental phase equilibria data (Johnson and Rutherford, 1990), whereas in minette lavas, typically characterized by abundant phlogopite phenocrysts, water contents may reach comparable levels (Esperanca and Holloway, 1987). However, since water has a negligible solubility in silicate liquids at 1 bar, we postpone consideration of its effect on liquid densities until after the effect of pressure on liquid volumes has been discussed.

Volumes of fusion at 1 bar

A fundamental application of the volume and thermal expansion data is to calculate liquid volumes and volumes of fusion (ΔV_{fus}) for a variety of minerals for which the crystalline volumes are known as a function of temperature (Berman, 1988). Table 5 lists calculated volumes of fusion for 12 mineral compositions. Several interesting trends can

Table 5. Volumes of fusion.

| Mineral | Temperature (K) | V_{liq} (cc/mol) | V_{sol} (cc/mol) | V_{liq}/V_{sol} | V_{fusion} (cc/mol) |
|--|-----------------|--------------------|--------------------|-------------------|-----------------------|
| SiO ₂ (cristobalite) | 1999 | 26.91 | 27.44 | 0.98 | -0.53 |
| SiO ₂ (cristobalite) | 1999 | 28.15 ¹ | 27.44 | 1.03 | 0.71 |
| NaAlSi ₃ O ₈ | 1393 | 112.83 | 104.13 | 1.08 | 8.64 |
| KAlSi ₃ O ₈ | 1473 | 121.24 | 111.72 | 1.09 | 9.75 |
| CaAl ₂ Si ₂ O ₈ | 1830 | 108.41 | 103.42 | 1.05 | 5.48 |
| CaSiO ₃ | 1817 | 43.89 | 41.87 | 1.05 | 2.31 |
| MgSiO ₃ | 1830 | 38.85 | 33.07 | 1.18 | 5.99 |
| CaMgSi ₂ O ₆ | 1665 | 81.80 | 69.74 | 1.18 | 12.62 |
| Ca ₂ MgSi ₂ O ₇ | 1727 | 99.70 | 97.10 | 1.03 | 2.60 |
| Ca ₃ MgSi ₂ O ₈ | 1848 | 118.09 | 105.02 | 1.12 | 13.07 |
| Fe ₂ SiO ₄ | 1490 | 53.15 | 48.29 | 1.11 | 5.49 |
| Mg ₂ SiO ₄ | 2163 | 52.37 | 47.41 | 1.12 | 5.53 |
| CaTiSiO ₅ | 1670 | 67.61 | 57.57 | 1.17 | 10.04 |

¹Liquid volume extrapolated from measurements of Bacon (1960).
Crystalline volume data from Berman (1988).

be found in this compilation. For example, the volume of fusion for pseudowollastonite (CaSiO₃) is quite small relative to the two pyroxenes, diopside (CaMgSi₂O₆) and enstatite (MgSiO₃). This result is primarily an effect caused by the large volume of pseudowollastonite relative to the two pyroxenes and not to an abnormally small volume of liquid CaSiO₃ relative to liquid MgSiO₃ and CaMgSi₂O₆. In support of this observation, the ²⁹Si NMR spectra of crystalline and glassy CaSiO₃, MgSiO₃ and CaMgSi₂O₆ samples (Murdoch et al., 1985) suggest that crystalline CaSiO₃, with its silicate chain repeat length of three tetrahedral units, relaxes in a glass to a chain structure more like that of the pyroxenes CaMgSi₂O₆ and MgSiO₃. Our calculation of liquid and solid volumes for these metasilicate minerals is in agreement with this interpretation.

The volume of fusion for anorthite is also significantly smaller than that for either albite or sanidine, although the crystalline molar volume of anorthite and albite are close at their respective fusion temperatures. This is consistent with Taylor and Brown's (1979) interpretation of X-ray radial distribution functions (RDF) derived from diffraction data on NaAlSi₃O₈, KAlSi₃O₈ and CaAl₂Si₂O₈ glasses. Their experimental RDFs indicate that the alkali feldspar glasses have a tridymite-like structure based on six-membered rings of tetrahedra, whereas the RDF for the calcic feldspar glass indicates a four-membered ring structure of the type found in crystalline feldspars. The lower volume of anorthite liquid is, therefore, a reflection of the tighter T-O-T bond angles and the small ΔV_{fus} reflects the similarity in structure between crystalline and molten anorthite. In contrast, alkali feldspars with four-membered rings of tetrahedra undergo a significant volume change during fusion to a tridymite-like structure.

An important application of these calculations relates to volumetric changes within crystallizing magmas. Ubiquitous quartz and aplite/pegmatite veins within granitic intrusions exemplify the contraction of silicic magmas during solidification. Approximate calculations, based upon the liquid volume and thermal expansion data in Table 3, combined with data for quartz, albite and orthoclase (Berman, 1988) indicate that a typical anhydrous granitic melt will contract by 8.2% during crystallization between 1173 K and 873 K. Hydrous silicic melts, on the other hand, with 1-3 wt % H₂O (assumed to completely exsolve during crystallization), undergo a more significant decrease in volume of 9.9-11.7% over the same temperature range. (The value for V_{H_2O} is estimated to be 20 cc/mole for reasons discussed in the section on the partial molar volume of water.) A similar calculation can be made for more mafic magmas. As noted in Table 5, the olivine and pyroxene endmembers (forsterite, fayalite, enstatite, and diopside) are all characterized by larger volumes of fusion than either quartz or the feldspars. Thus an intrusive tholeiitic liquid is

expected to undergo significant contraction during crystallization relative to a silicic melt. Based upon the calculated phase proportions crystallizing from a Thingmuli olivine tholeiite (Ghiorso and Carmichael, 1985), the volume data in Tables 3 and 5 indicate that such a magma's volume will decrease by 10.6% during cooling from 1473 to 1073 K.

Compressibility of silicate liquids

In recent years, considerable attention has been focused on measuring the compression properties of silicate liquids (Murase and McBirney, 1973; Murase, 1982; Rivers and Carmichael, 1987; Manghnani et al., 1986; Kress et al., 1988; Kress and Carmichael, 1991), particularly at elevated pressures (Fujii and Kushiro, 1977; Kushiro, 1982; Ridgen et al., 1984, 1988, 1989; Agee and Walker, 1988). Interest is sparked by the observation that silicate liquids are more than an order of magnitude more compressible than most silicate minerals, leading Stolper et al. (1981) to postulate that the density contrast between melts and upper mantle rocks must diminish rapidly at depths approaching 150-200 km. Such a density cross-over at high pressure will have a profound effect on the depths from which magmas ascend from their source regions and hence, on the distribution of chemical components in the crust and mantle (Agee and Walker, 1988). The density contrast between crystals and melts is of interest over a wide range of shallow pressures as well, since the rate of melt segregation from both mantle and crustal source regions is determined, in part, by the buoyancy differential between liquids and solids. This contrast in density between crystals and liquid is extremely important for postulated mechanisms of magmatic differentiation that include composition-induced convection and crystal settling. It also plays a role in establishing regions of neutral buoyancy between magmatic fluids and surrounding country rock (Ryan, 1987).

As a consequence of the petrologic and geophysical importance of silicate liquid densities over a range of pressures, a model equation for liquid volumes that incorporates the effect of pressure is imperative. The functional dependence of volume on pressure can be anticipated to decrease more rapidly at low pressures than at high pressures. Generally speaking, the first derivative function of volume with respect to pressure, dV/dP , is sufficient to describe the volume of natural liquids to 20-30 kbar. At higher pressures, however, the second derivative function, d^2V/dP^2 , is required. Before addressing measurements and applications of the second derivative function of volume with pressure, this section begins with a discussion of the first derivative function and its compositional dependence.

Compositional dependence of $(dV/dP)_T$. Only five years ago, insufficient data were available on silicate liquid compressibilities as a *systematic* function of composition to be incorporated into any general volume equation applicable to natural liquids. As an example, a simplified model is shown below:

$$V_{\text{liq}}(X_i, T, P) = \sum [\bar{V}_i(T_{\text{ref}}, 1 \text{ bar}) + \frac{d\bar{V}_i}{dT} (T - T_{\text{ref}}) + \frac{d\bar{V}_i}{dP} (P - 1 \text{ bar})] X_i, \quad (10)$$

where $\bar{V}_i(T_{\text{ref}}, 1 \text{ bar})$ is the partial molar volume of component i in the liquid at a reference temperature, T_{ref} , and 1 bar, $d\bar{V}_i/dT$ and $d\bar{V}_i/dP$ are the temperature and pressure derivatives of the partial molar volume of component i , and X_i is the mole fraction of component i in the liquid. Although measurements of silicate liquid densities up to 30 kbar by the falling sphere method were available (Kushiro, 1978, 1982; Fujii and Kushiro, 1977; Scarfe et al., 1979), these data were limited to only a few compositions (one calcium-magnesium-silicate, two sodium-silicate, and seven basaltic liquids), and extrapolation of information on silicate liquid compressibilities to all compositions found in nature was not possible.

Recent measurements of silicate liquid compressibilities as a systematic function of composition are derived primarily from measurements of ultrasonic acoustic velocity

(Rivers and Carmichael, 1987; Manghnani et al., 1986; Kress et al., 1988; Kress and Carmichael, 1991). The first comprehensive model equation describing silicate liquid compressibilities as a function of composition was presented by Rivers and Carmichael (1987). They measured ultrasonic sound velocities in 22 synthetic and three natural liquids to derive isothermal compressibilities (β_T) using the relation:

$$\beta_T = V_T/c^2 + (TV_T\alpha^2)/C_p, \quad (11)$$

$$\text{where} \quad V_T\beta_T = -(dV/dP)_T. \quad (12)$$

In order to calculate accurate values of liquid isothermal compressibilities (β_T) from measurements of ultrasonic velocity (c), accurate 1 bar volume (V), thermal expansion (α) and heat capacity (C_p) data are required. From calculated values of $(dV/dP)_T$ and β_T for each experimental liquid, combined with their analyzed compositions, a model equation can be developed to describe liquid compressibilities as a function of composition. It was shown earlier in this text that silicate liquids mix ideally with respect to volume at 1 bar over the range of composition spanned by magmas. If volume mixes ideally at pressures greater than 1 bar, then the following equation can be applied:

$$V(T,P) = \sum X_i(T)\bar{V}_i(T,P). \quad (13)$$

Differentiation of Equation (13) with respect to pressure at constant T yields:

$$(dV/dP)_T = \sum X_{i,T} (d\bar{V}_i/dP)_T. \quad (14)$$

Here $(dV/dP)_T$ is a partial molar quantity that is assumed to mix linearly with mole fraction as in an ideal solution.

Rivers and Carmichael (1987) combined their data on 25 liquids with compressibility data on 40 additional binary and ternary silicate liquid compositions, for which acoustic velocities were reported by Bockris and Kojonen (1960), Baidov and Kunin (1968) and Sokolov et al. (1971). These data were combined to calibrate the regression model of Equation (14) and to derive fitted values of $d\bar{V}_i/dP$ for the major oxide components found in natural liquids. The single component important to natural liquids that was not represented in their data set was Fe_2O_3 . The reason for its absence is that virtually all high-temperature ultrasonic studies on silicate melts prior to 1990 were performed in a highly reducing atmosphere because the ultrasonic apparatus contained metallic parts (such as a Mo rod) that quickly oxidize at oxygen fugacities above the iron-wüstite oxygen buffer at high temperatures. As a consequence, virtually all the iron in the sample liquids was present as ferrous iron. We also note that the only sample containing significant quantities of TiO_2 has the composition of sphene (CaTiSiO_5). As a consequence, the derived value of $d\bar{V}_{\text{TiO}_2}/dP$ is probably representative of Ti^{4+} in an octahedral coordination and, from the 1 bar volume data discussed earlier, is an appropriate value for natural liquids.

When the results of Rivers and Carmichael (1987) were published, the best model equations of silicate liquid volumes at 1 bar were those of Bottinga et al. (1982) and Stebbins et al. (1984) with standard errors of 1% on V and 28% on dV/dT . However, as pointed out earlier, 60% of the uncertainty in derived values of dV/dP arise from errors in the coefficient of thermal expansion. Lange and Carmichael (1987) were able to demonstrate that by using their volume and thermal expansion data to calculate compressibilities from the sound velocity data of Rivers and Carmichael (1987), the relative standard error on the fit of Equation (14) was reduced from 13.4 to 5.3%. This reduction in error was due to entirely to the increased precision of the volume and thermal expansion data.

The error on the fit to Equation (14) has been further reduced in the more recent study of Kress and Carmichael (1991). In that study, data used to calibrate their regression

model only included the relaxed acoustic velocity measurements of Rivers and Carmichael (1987), Kress et al. (1988) and Kress and Carmichael (1991). Sound speed measurements from Bockris and Kojonen (1960), Baidov and Kunin (1968) and Sokolov et al. (1971), which were included in the fits of Rivers and Carmichael (1987) and Lange and Carmichael (1987), were omitted from the fit of Kress and Carmichael (1991) because it is not possible to establish conclusively whether or not the acoustic velocities in these studies were relaxed or not. The importance of only considering relaxed acoustic velocity data (where the timescale of the response, or relaxation, of the silicate melt to the sound wave is less than the timescale of the measurement) has been recently emphasized by Kress et al. (1989) and Dingwell and Webb (1989). In addition, the regression of Kress and Carmichael (1991) includes acoustic velocity data on seven new Fe_2O_3 -rich liquid compositions, as well as liquid velocity data on eight compositions in the Na_2O - NaAlO_2 - SiO_2 system from the study of Kress et al. (1988). The relative standard error on their fit is only 2.7% which represents a substantial improvement over the model equations presented by Rivers and Carmichael (1987) and Lange and Carmichael (1987). The regression equation of Kress and Carmichael (1991) and their fitted parameters of $d\bar{V}_i/dP$ are presented in Table 3; these values are recommended for calculating liquid volumes at elevated pressures. The reader is referred to Kress and Carmichael (1991) for a detailed discussion of these results. For the purpose of this review, a few salient points brought up in their discussion will be summarized.

The derived values of $d\bar{V}_i/dP$ for each oxide component can be evaluated in a similar manner as those of $d\bar{V}_i/dT$. Again, the covalent nature of the Si-O bond is such that its principal mode of low-pressure compression does not involve shortening of the bond but rather changes in the Si-O-Si bond angle. It can be anticipated, therefore, that (at low pressures) silica-rich liquids can accommodate a substantial degree of compression through this mechanism. Thus, we expect a value for $d\bar{V}_{\text{SiO}_2}/dP$ derived from 1 bar sound velocities that is large relative to those for the other oxide components. This is observed in Table 3 with $d\bar{V}_{\text{SiO}_2}/dP$ more negative than derived values for FeO, MgO and CaO. Like values of $d\bar{V}_i/dT$, those of $d\bar{V}_i/dP$ (for the alkali and alkaline earth cations) are correlated to cation field strength (Fig. 3) with $d\bar{V}_i/dP$, in general, becoming more negative with decreasing field strength. This can be attributed to an increase in non-bridging oxygens and a breakdown of the open three-dimensional silicate framework that accompanies substitution of high field strength cations for low field strength cations in silicate liquids and glasses (Murdoch et al., 1985). Note that the positive values for $d\bar{V}_{\text{MgO}}/dP$ and $d\bar{V}_{\text{CaO}}/dP$ would violate thermodynamic stability criteria if extrapolated to the respective end members, as emphasized by Kress and Carmichael (1991). As a consequence, the parameters listed in Table 3 should not be applied to liquids that contain a mole fraction of any component (except SiO_2) that is greater than 0.5. It should also be noted that for some values of $d\bar{V}_i/dP$, a temperature dependence has been resolved. From the thermodynamic identity,

$$-d\beta/dT = d\alpha/dP, \quad (15)$$

it follows that the pressure dependence to thermal expansion can also be calculated from these data.

A notable feature of the regression model of Kress and Carmichael (1991) is that it includes an excess-mixing term between the Na_2O and Al_2O_3 liquid components. The data that support this deviation from the ideality implicit in Equation (14) are the relaxed ultrasonic velocities of Kress et al. (1988) on liquids in the Na_2O - NaAlO_2 - SiO_2 system. The large, positive fitted value of $d\bar{V}_{\text{Na}_2\text{O}-\text{Al}_2\text{O}_3}/dP$ is consistent with the conclusion of Navrotsky et al. (1985) that bridging oxygen bonds associated with alkali-aluminate units are more narrow and less flexible than those bridging silicate units. As a consequence, if the dominant mode of low-pressure compression in a sodium aluminosilicate liquid is due to bending of T-O-T bonds, it follows that the decreased flexibility of the T-O-T angle induced by substitution of $(\text{NaAl})^{4+}$ for Si^{4+} should decrease the compressibility of the

liquid. It is probable, therefore, that similar large, positive excess mixing terms between Li_2O and Al_2O_3 as well as K_2O and Al_2O_3 would be resolved if compressibility data on Li- and K-aluminosilicate liquids were available. The fact that excess mixing is observed in the derivative property, dV/dP , and not in the integral property, V , brings up an important point bearing on the distinction between integral and derivative properties. It is anticipated that derivative properties such as thermal expansion (dV/dT), compressibility (dV/dP), and heat capacity (dH/dT) will be much more sensitive to structural changes in a liquid (or solid) than integral properties such as volume (V) and enthalpy (H). It is of interest, therefore, that no compositional dependence to $d\bar{V}_{\text{Fe}_2\text{O}_3}/dP$ was resolved from the experiments of Kress and Carmichael (1991).

Compressibility of the ferric component. Kress and Carmichael (1991) measured acoustic velocities in seven Fe_2O_3 -rich compositions: two $\text{CaO-FeO-Fe}_2\text{O}_3\text{-SiO}_2$ liquids, three $\text{Na}_2\text{O-FeO-Fe}_2\text{O}_3\text{-SiO}_2$ liquids, a Kilauea tholeiite doped with 5 wt % Fe_2O_3 , and an iron-rich basalt from Labrador. From our earlier discussion of the partial molar volume of Fe_2O_3 , it is expected that the coordination environment of Fe^{3+} is similar in the two natural liquids as well as in the three sodic compositions. In contrast, the coordination environment of Fe^{3+} in the calcic liquids appears to be variable and related to the molar CaO:SiO_2 ratio. As a consequence, consider where the two $\text{CaO-FeO-Fe}_2\text{O}_3\text{-SiO}_2$ liquids, whose sound speeds were measured by Kress and Carmichael (1991), fall on the $\bar{V}_{\text{Fe}_2\text{O}_3}$ vs. $X_{\text{CaO}}/X_{\text{SiO}_2}$ diagram of Figure 1. The composition labelled A has a low CaO:SiO_2 molar ratio and is anticipated to contain a higher proportion of octahedral Fe^{3+} than natural liquids at ambient pressure. In contrast, the composition labelled B has a high CaO:SiO_2 molar ratio, similar to those values observed for the two $\text{CaO-FeO-Fe}_2\text{O}_3\text{-SiO}_2$ compositions of Mo et al. (1982), and is expected to contain Fe^{3+} in a similar coordination environment as that found in natural liquids. As a consequence, only one of the seven iron-bearing compositions considered by Kress and Carmichael (1991) is expected to reflect a value for $d\bar{V}_{\text{Fe}_2\text{O}_3}/dP$ that is different from the others. The lack of any observable compositional dependence suggests that any difference in the compressibility of ferric iron in octahedral vs. tetrahedral coordination cannot be resolved within the precision of the measurements. It should be emphasized, however, that the derived value of $d\bar{V}_{\text{Fe}_2\text{O}_3}/dP$ presented by Kress and Carmichael (1991) is calibrated primarily on Fe_2O_3 -bearing liquids that contain ferric iron in a coordination environment that is similar to that in natural liquids.

Measurement of the partial molar compressibility of the ferric component in silicate liquids is an extremely important contribution as it is an essential parameter in any compressibility model for silicate liquids that can be applied to magmas. Perhaps more important, however, information on the respective compressibilities of the ferric and ferrous components allows estimation of how the ferric-ferrous ratio in a natural silicate liquid changes as a function of pressure. The dependence of the iron redox state on T , $f\text{O}_2$ and composition has been well calibrated at 1 bar over a wide range of melt compositions found in nature (Sack et al., 1980; Kilinc et al., 1983; Kress and Carmichael, 1989). However, the pressure dependence of the ferric-ferrous ratio has been poorly constrained, despite the fact that its value bears directly on the issue of whether or not the oxidation states of erupted lavas reflect the oxidation states of their source regions (Carmichael, 1991). The pressure dependence of the ferric-ferrous ratio in a magma is controlled by the magnitude and sign of the volume change accompanying the following homogeneous reaction:



from which the following relationship can be obtained:

$$\ln [X_{\text{Fe}_2\text{O}_3}/X_{\text{FeO}^2}]_P = \ln [X_{\text{Fe}_2\text{O}_3}/X_{\text{FeO}^2}]_{1 \text{ bar}} + \int_{1 \text{ bar}}^P \frac{\Delta V_T(P)}{RT} dP, \quad (17)$$

where $\Delta V_T(P) = V_{\text{Fe}_2\text{O}_3}(P) - 2V_{\text{FeO}}(P)$ at temperature T . Kress and Carmichael used their compressibility data on the ferric and ferrous components to derive a model equation that allows the ferric-ferrous ratio of any natural liquid to be calculated as a function of T , P , $f\text{O}_2$ and composition. Their model equation and fitted parameters are presented in Table 6.

The compressibility data on the ferric and ferrous components allow natural liquid densities to be calculated over a range of pressures at different oxidation states. In performing this calculation, the mole fraction of ferric and ferrous iron in the liquid should first be determined at the specified $f\text{O}_2$, temperature and pressure from the parameters in Table 6, before applying the compressibility data presented in Table 3. Examination of the different values of dV_i/dP for each of the oxide components leads one to anticipate that crustal melts that are rich in silica, alumina and alkalis will be more compressible than basic liquids that contain little silica and high concentrations of calcium and magnesium. This point is emphasized in Figure 6 where the anhydrous liquid density of a peralkaline rhyolite as a function of pressure is compared to that of a ugandite. Due to the fact that the ferric-ferrous ratio in natural liquids decreases with pressure (since ferric iron has a larger volume than ferrous iron), the effect of varying the oxygen fugacity of the liquid by 3 log units (at 1400°C) leads to a variation in density that either increases or decreases with pressure. For example, for the peralkaline rhyolite liquid, the variation in density is only 0.06% at 1 bar (because most of the iron is ferric, even at low oxygen fugacities) and 0.26% at 20 kbar; similarly, for the ugandite liquid, the variation is 0.31% at 1 bar and 0.26% at 20 kbar. The effect of varying the oxidation state is negligible, however, compared to the change in density induced by increasing pressure. For the peralkaline rhyolite, density varies 15.5% between 1 bar and 20 kbar, whereas for the ugandite, the variation is 11.6%. Clearly, the effect of pressure on liquid density is dominant relative to the effect of temperature: increasing pressure one kbar is equivalent to decreasing temperature 129 K for the peralkaline rhyolite and 68 K for the ugandite.

The pressure dependence of compressibility. Magmatic processes are by no means restricted to pressures ≤ 20 kbar, and it is essential, therefore, to obtain information on how the compressibility function itself, for natural liquids, changes with pressure. The functional dependence of compressibility on pressure, $d\beta_T/dP$, could be determined from measurements of acoustic velocity through silicate liquids at pressures greater than 1 bar. These experiments are, however, technically difficult and have yet to be done. In lieu of experimental results, we can predict that the compressibility function will generally decrease with increasing pressure (assuming a single compression mechanism), such that a simple polynomial of the form

$$\beta(T,P) = \beta(T)[1 - bP - cP^2] \quad , \quad (18)$$

could be used to fit the behavior of β over an experimental range of pressure. Volume, which is a thermodynamic state function, could then be expressed as

$$V(T,P) = V(T) \exp(-\beta(T)[1 - bP - cP^2]dP) \quad , \quad (19)$$

derived from the relation in Equation (13); b and c are fit parameters corresponding to the second and third derivative functions of volume with respect to pressure. The advantage of this formulation for volume is that it ensures exact differentials, a thermodynamic requirement for any state function (Lewis and Randall, 1961). However, the form most commonly used to relate pressure-density relations is the third-order Birch-Murnaghan equation of state:

$$P = 3/2 K (R^{7/3} - R^{5/3})[1 - 3/4 (4 - K')(R^{2/3} - 1)] \quad , \quad (21)$$

where $R = V_{T,0}/V_{T,P}$ and K is the zero pressure (1 bar) bulk modulus ($K_T = 1/\beta_T$), and K' is the derivative of K_T with pressure (dK_T/dP). The equation is a truncated series expan-

Table 6. Best fit parameters from Kress and Carmichael (1991) to calculate ferric-ferrous ratio in natural liquids.

$$\ln[X_{\text{Fe2O3}}/X_{\text{FeO}}] = a \ln f\text{O}_2 + b/T + c + \sum X_i d_i + e [1 - T_0/T - \ln(T/T_0)] + (P/T)[f + g(T - T_0) + hP]$$

| Parameter | Value | Units |
|-------------------------|---------------------------|---------------------|
| a | 0.196 | |
| b | 11,492 | K |
| c | -6.675 | |
| d _{Al2O3} | -2.243 | |
| d _{FeO(total)} | -1.828 | |
| d _{CaO} | 3.201 | |
| d _{Na2O} | 5.854 | |
| d _{K2O} | 6.215 | |
| e | -3.364 | |
| f | -70.06 | K/kbar |
| g | -1.535 x 10 ⁻² | kbar ⁻¹ |
| h | 4.147 x 10 ⁻⁹ | K/kbar ² |

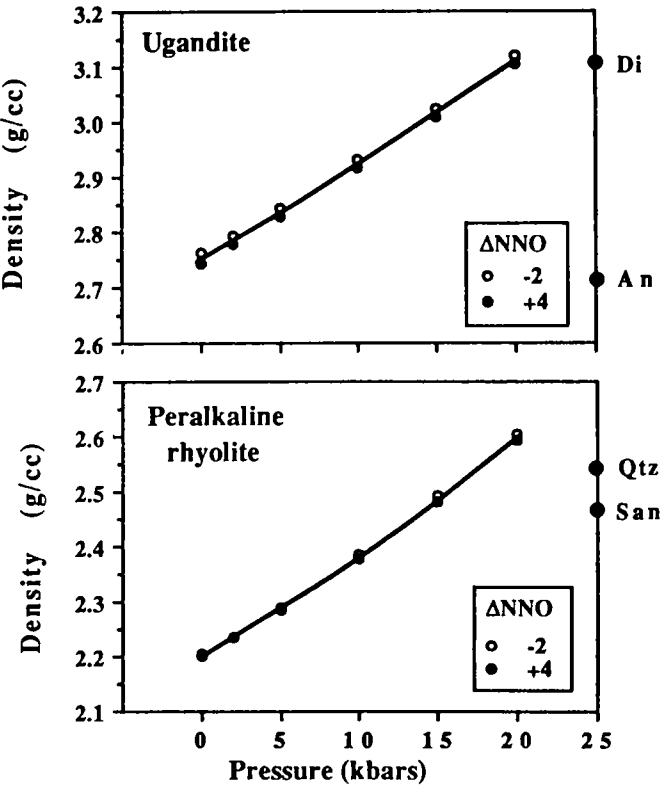


Figure 6. The density of a ugandite (rich in CaO and MgO) relative to a peralkaline rhyolite (rich in silica and the alkalis) as a function of pressure. The density of the ugandite varies by 11.6% over 20 kbar, whereas the density of the peralkaline rhyolite varies by 15.5%. The effect of varying the oxygen fugacity by three log units is negligible ($\leq 0.3\%$) relative to the effect of pressure. The crystalline densities of diopside, anorthite, quartz and sanidine are shown at 25 kbar for scale; their densities change by less than 0.02 g/cc between 1 bar and 25 kbar.

sion derived from finite strain theory and models the compressions of solids under hydrostatic pressure extremely well. It has the advantage of expressing volume ($V_{T,P}$) over an extensive range of pressure with only three parameters: $V_{T,0}$ (volume at 1 bar), K_T and K_T' , unlike Equation (19) which requires four: $V_{T,0}$, β_T , b and c .

Measurements of silicate liquid densities to high pressures are extremely limited, and prior to 1984 were confined to the falling sphere method of Fujii and Kushiro (1978) to 30 kbar. The first direct measurements of molten silicate densities to extremely high pressures in excess of 250 kbar were performed by Ridgen et al. (1984, 1988, 1989) with shock-wave techniques. Ridgen et al. (1984, 1988) measured the density of a model basalt (36 mol % $\text{CaAl}_2\text{Si}_2\text{O}_8$ and 64 mol % $\text{CaMgSi}_2\text{O}_6$) initially at ~ 2000 K and observed that from atmospheric pressure up to 250 kbar, there is a substantial ($\sim 50\%$), yet gradual increase in density. Above 250 kbar, the trend of gradual compression ceases, and the material becomes considerably stiffer, leading to little increase in density with increasing pressure. Ridgen et al. (1988) proposed that the abrupt stiffening of the $\text{An}_{36}\text{Di}_{64}$ composition above 250 kbar indicates that the gradual structural changes characteristic of the lower pressure regime (0-250 kbar) are essentially complete by ~ 250 kbar. They postulated that these gradual changes reflect the continuous conversion of Al^{3+} and Si^{4+} from a dominantly tetrahedral coordination by oxygen to a dominantly octahedral coordination. These results are consistent with the in-situ infrared spectra of Williams and Jeanloz (1988) on SiO_2 , $\text{CaMgSi}_2\text{O}_6$ and $\text{CaAlSi}_2\text{O}_8$ composition glasses to 400 kbar in a diamond anvil cell, but at the much lower temperature of 300 K. Williams and Jeanloz (1988) observed that at pressures above 200 kbar the regular tetrahedral coordination of oxygen around both silicon and aluminum ions is severely disrupted and that a variety of coordination environments, from sixfold to fourfold, appears to be present at pressures as high as 400 kbar. The fact that Ridgen et al. (1988) measured the density of a silicate *liquid* rather than a glass may explain their evidence for complete conversion of silicon to octahedral coordination at the much lower pressure of 250 kbar.

Ridgen et al. (1988) fitted their liquid density data on the model basalt ($\text{An}_{36}\text{Di}_{64}$) over the lower pressure regime (0-250 kbar) to a Birch-Murnaghan equation of state and derived a 1 atm isentropic bulk modulus (K_S) of 242 kbar and a pressure derivative (K_S') of 4.8. In general, values for isentropic bulk moduli (K_S) are slightly larger but well within the experimental error of values for isothermal bulk moduli (K_T). Therefore, for first order comparison purposes, the difference between isentropic and isothermal bulk moduli can be neglected. From the relationship, $K_T = V_T / (dV/dP)_T$, the data in Tables 3 and 5 can be used to calculate a value of K_T that is based upon acoustic velocity data. For the composition $\text{An}_{36}\text{Di}_{64}$, a value of 230 kbar is obtained, which is in close agreement with the shock-wave results. Ridgen et al. (1989) extended their experiments to include the two end-member compositions of their model basalt and derived values of K_S and K_S' of 224 kbar and 6.9 for diopside and 179 kbar and 5.3 for anorthite. Again, the values of the bulk moduli derived for diopside and anorthite are in good agreement with those calculated from the data in Table 3 (251 and 194 kbar respectively). Ridgen et al. (1989) combined their data on anorthite and diopside with results on the model basalt to examine the degree to which silicate liquids mix ideally with respect to volume at high pressure: for the eutectic composition ($\text{An}_{36}\text{Di}_{64}$) at 1673 K, the volumes of anorthite and diopside appear to mix ideally to 250 kbar.

The shock-wave results of Ridgen et al. (1989) on diopside, anorthite and $\text{An}_{36}\text{Di}_{64}$ liquids indicate that values of K_T' are more sensitive to liquid composition than values of K_T and that the magnitude of K_T' in silicate melts varies inversely with the concentration of network forming, initially tetrahedrally coordinated cations (e.g., Al^{3+} , Si^{4+}). Ridgen et al. (1989) estimate that values of K_T' vary from greater than ~ 7 for molten anorthite, enstatite, and diopside, to ~ 8 for molten ferrosillite, to ~ 10 for molten forsterite, and to ~ 11 for molten fayalite. It is important to realize that these values of K_T' derived from the shock wave results reflect the second derivative function of volume integrated over an enormous range of pressure. This is a critical point as Williams and Jeanloz (1988) note that the

compression of silicate glasses between 0 and 300 kbar appears to be accommodated by three distinct processes: (1) below 100 kbar, compression is achieved by decreasing Si-O-Si and Al-O-Si bond angles between tetrahedra; (2) between 100-200 kbar, it is anticipated that tetrahedra begin to distort and that O-Si-O bond angles may deviate from the ideal tetrahedral value of 109.5°; (3) at pressures in excess of 200 kbar, the data of Williams and Jeanloz (1988) on glasses indicate that silicon coordination increases toward sixfold with distorted tetrahedra converted to octahedra. Thus, as emphasized by Rigden et al. (1989), the values of K_T' derived from shock wave experiments probably represent the integrated effect of all three of these compression mechanisms.

The compressibility of silicate liquids at elevated pressures can also be measured under static conditions as demonstrated by the novel "sink/float" experiments of Agee and Walker (1988). They measured the compression of komatiite and peridotite liquids by bracketing sinking and floating of olivine crystals of known density at pressures between 10-60 kbar. The pressure interval explored by Agee and Walker (1988) extends up to the range where the second derivative function of volume with pressure is probably required to accurately describe the volumes of silicate liquids. However, the 10-60 kbar interval is well below the pressure range where silicon is anticipated to begin to transform from a fourfold to sixfold coordination. As a consequence, values of K_T' derived from the experimental results of Agee and Walker (1988) using a Birch-Murnaghan equation of state will represent an integration over a pressure interval where compression is achieved primarily by changes in tetrahedral bond angles rather than cation coordination number. It is of interest, therefore, to compare values of K_T' derived by Agee and Walker (1988) for ultrabasic liquids between 10-60 kbar with those inferred from shock wave experiments to 250 kbar.

Agee and Walker (1988) observed that the komatiite and peridotite liquids (\pm molten fayalite) all showed constant density changes with pressure of ~ 0.7 g/cc/kbar along their liquid. These compression curves are less steep than would be the case for isothermal or isentropic conditions, as thermal expansion along the liquidus retards compression. Agee and Walker (1988) converted their compression results on the komatiite liquid to an isothermal curve at 1673 K to facilitate comparison with the shock wave measurements on the basalt analog of Ridgen et al. (1984). Based on the initial results of Ridgen et al. (1984), Agee and Walker (1988) assumed a value of $K_T' = 4$ for komatiite liquid and fit their compression data on komatiite liquid to a Birch-Murnaghan equation of state to obtain an isothermal bulk modulus of 267 kbar. Again, from the relation, $K_T = V_T / (dV/dP)_T$, the data in Table 3 can be used to calculate a value for the 1 atm bulk modulus (K_T) of the komatiite liquid that is based upon acoustic velocity data. The calculated value is 262 kbar which is in excellent agreement with the compression data of Agee and Walker (1988) and reflects less than a 2% difference in $(dV/dP)_T$ between the direct measurements and the model equation in Table 3. Agee and Walker (1988) note that the distribution of their compression data points implies a relatively small pressure derivative of the bulk modulus (K_T'), but that its value is not constrained rigorously, which is why an assumption of $K_T' = 4$ was made. Although this value is much lower than estimates of $K_T' = 9-10$ that are inferred from shock-wave results for such ultrabasic liquid compositions, this may be explained by the fact that over the 10-60 kbar pressure interval of Agee and Walker's (1988) experiments, compression of the ultrabasic liquid is achieved primarily by decreasing Si-O-Si bond angles and not by changing cation coordination number. Alternately, it may reflect the difficulty in resolving K_T' over the smaller pressure interval explored by Agee and Walker (1988).

The effect of volatiles on silicate liquid densities

We have postponed discussion of the effect of volatiles on silicate liquid densities until after the effect of pressure was considered. The reason, of course, is that the solubility of volatile components such as H₂O and CO₂ in silicate liquids is extremely limited at 1 bar.

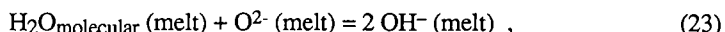
As a consequence, neither 1 bar density measurements obtained by the double-bob Archimedeian method nor 1 bar acoustic velocity measurements can be applied to volatile-bearing silicate liquids. Direct density and compressibility measurements must be made at elevated pressures where sufficiently high concentrations of H₂O and CO₂ can dissolve in the melts in order to place tight constraints on their partial molar volumetric properties. Such experiments are extremely important as most workers agree that H₂O (35 to 90 mol %) and CO₂ (5 to 50 mol %) are the two most abundant volatile components in basaltic and andesitic magmas (Anderson, 1975; Basaltic Volcanism Study Project, 1981; Gerlach, 1981). Although these two components typically make up less than 5 wt % of most magmatic liquids, their extremely low molecular weights translate their concentrations into high mole fractions. For example, the molecular weight of H₂O is only 18.015 g/mole, whereas that of SiO₂ is 60.085 g/mole. As a consequence, the mole percent of water is about 50 in an albitic liquid that contains only 6.4 wt % H₂O (Burnham, 1975, 1979). Due to the fact that the *mole fractions* of H₂O and CO₂ can reach significant levels in magmas, any model equation describing the densities of natural liquids must incorporate information on the partial molar volumes of both these volatile components. Despite the paucity of direct density measurements, information on the partial molar volume of CO₂ and H₂O in silicate melts can be obtained by indirect methods that are outlined below.

The partial molar volume of H₂O. Unfortunately, very few direct measurements are available on the density of hydrous silicate liquids. These are primarily confined to the P-V-T determinations made by Burnham and Davis (1971) on H₂O-NaAlSi₃O₈ liquids and to the falling sphere measurements of Kushiro (1978) on a hydrous calc-alkaline andesite. Burnham and Davis (1971) fitted their data on the densities of hydrous albitic melts (with 8.25 and 10.9 wt % dissolved water) to a third-order polynomial in P and T. Calculated values of the partial molar volume of water vary from 15-17 cc/mole between 1023-1223 K and 3.5-8.5 kbar. A similar value of 16.55 cc/mole for $\bar{V}_{\text{H}_2\text{O}}$ was calculated by Hodges (1974) from the presence of an inflection point in the water-saturated melting curve of diopside near 20 kbar. At the inflection point, dP/dT approaches infinity and from the Clapeyron relation:

$$dP/dT = \Delta S/\Delta V, \quad (22)$$

it can be inferred that the volume change during fusion approaches zero at 20 kbar. Since the partial molar volume of the diopside component in the silicate melt is well known (Lange and Carmichael, 1987), as well as the volume of crystalline diopside (Berman, 1988) and water vapor (Holloway, 1977, 1987), the only unknown is the partial molar volume of water. The derived value based upon the more recent data referenced above is 17.12 cc/mole and applies to water in diopside melt at 20 kbar and 1513 K.

While these measured values of the partial molar volume of bulk water in silicate melts provide no distinction between molecular water and hydroxyl groups, it is well established from spectroscopic investigations that water dissolves in silicate glasses in these two forms (Orlova, 1962; Ostrovskiy et al., 1964; Persikov, 1972; Bartholomew and Schreurs, 1980; Bartholomew et al., 1980; Stolper, 1982a,b; McMillan et al., 1983; Eckert et al., 1987, 1988; Silver and Stolper, 1985, 1989). The two hydrous species are postulated to interact through the following homogeneous equilibrium:



where O²⁻ = an oxygen atom, OH⁻ = a hydroxyl group and H₂O_{molecular} = a water molecule in the melt (Stolper, 1982b; Silver and Stolper, 1985). If the partial molar volume of molecular water is different from the partial molar volume of an hydroxyl group, then we can anticipate a pressure dependence to the equilibrium reaction in Equation (23). Nogami and Tomozawa (1984) infer from their study on the effect of stress on water diffusion in silica glass that ΔV for the reaction in Equation (23) is negative. However, the pressure dependence of the speciation of water in silicate liquids appears to be weak

(Stolper, 1989), so that the partial molar volume of molecular water in a silicate melt may be similar to that of an hydroxyl group. If this assumption is valid, then determinations of the partial molar volume of *molecular* water may be incorporated into a general model equation describing the volumes of hydrous silicate liquids.

The partial molar volume of molecular water in silicate liquids can be derived from water solubility data obtained over a wide range of pressures, combined with spectroscopic measurements of the concentration of molecular water in the quenched glasses (Silver and Stolper, 1985; Silver et al., 1990). Constraints can be placed on $\bar{V}_{\text{H}_2\text{O},\text{molecular}}$ from water solubility curves because activity-composition relations for molecular water dissolved in silicate liquids can be well characterized due to the observed Henrian behavior (Silver et al., 1990). For example, the measured mole fractions of molecular water in silicate glasses quenched from water-saturated melts at low pressures are proportional to the water fugacity and hence, the activity of molecular water in the liquid. At elevated pressures, the levelling off of water solubility curves is due to the non-zero partial molar volume of water. As a consequence, Silver et al. (1990) were able to use their activity-composition relations determined for molecular water in silicate liquids at low pressures, combined with water solubility data obtained over a wide range of pressures, to estimate the partial molar volume of molecular water in four experimental liquids: albite, orthoclase, a calcium aluminosilicate, and a rhyolite.

Silver et al. (1990) combined their data on the speciation of water in undersaturated glasses quenched from albitic melts with the water solubility data of Hamilton and Oxtoby (1986) up to 8 kbar and at temperatures between 1023-1648 K to constrain the value of $\bar{V}_{\text{H}_2\text{O},\text{molecular}}$ in albitic liquids. They assumed that the partial molar volume of molecular water is independent of pressure up to 8 kbar, but allowed a linear dependence on temperature. At 1273 K, their best fit to $\bar{V}_{\text{H}_2\text{O},\text{molecular}}$ is ~ 22 cc/mole and the derived coefficient of thermal expansion is about $4.5 (10^{-4}) \text{ K}^{-1}$. These values compare favorably with those determined from the volume measurements of Burnham and Davis (1971). Over the 3-8 kbar pressure range at 1273 K, the model of Burnham and Davis (1971) predicts that the partial molar volume of (bulk) water varies from 22-17 cc/mole, whereas the coefficient of thermal expansion is $\sim 7\text{-}8 (10^{-4}) \text{ K}^{-1}$.

Silver et al. (1990) also combined their speciation data on water in orthoclastic glasses with the water solubility data of Oxtoby and Hamilton (1978) from 1-7 kbar and 1173-1613 K. The solubility data level off at high pressure in such a fashion that, assuming Henry's Law holds for the dissolution of molecular water in orthoclastic liquids, a relatively high value for $\bar{V}_{\text{H}_2\text{O},\text{molecular}}$ of ~ 25 cc/mole is derived. Silver et al. (1990) also determined the solubility and speciation of water in a number of calcium aluminosilicate glasses quenched from melts (single anhydrous composition) equilibrated with water vapor at pressures up to 5.1 kbar at ~ 1453 K. The best fit value of $\bar{V}_{\text{H}_2\text{O},\text{molecular}}$ in the calcium aluminosilicate liquid is ~ 16 cc/mole. Silver et al. (1990) note that this value is highly sensitive to the single solubility data point at ~ 5 kbar (the next data point is at a pressure < 2 kbar). This sensitivity of derived values of $\bar{V}_{\text{H}_2\text{O},\text{molecular}}$ to high-pressure solubility data is important to the analysis of the data for the rhyolite liquid. Silver et al. (1990) measured the solubility and speciation of water in hydrous rhyolitic glasses quenched from water-saturated melts held at pressures only up to 1.5 kbar at 1123 K. From their data, the best fit values of $\bar{V}_{\text{H}_2\text{O},\text{molecular}}$ is approximately zero (-3.3 ± 2.8 cc/mole). This value is much lower than those derived from the solubility and speciation data on the synthetic liquids, as well as those determined from the volume measurements of Burnham and Davis (1971) on hydrous albitic liquids. However, Silver et al. (1990) point out that a low partial molar volume for water is consistent with results of McMillan and Chlebik (1980), who found that density increases as hydroxyl is added (at the several hundreds ppm level) to a sodium silicate glass. Silver et al. (1990) further note that a small partial molar volume would result if molecular water enters the melt by filling holes. On the other hand, Silver et al. (1990) point out the need for further work in order to determine

Table 7. Estimates of the partial molar volume of H₂O in silicate liquids.

| Composition | V _{H2O} (cc/mole) | P range (kbars) | T range (°C) | Reference |
|------------------------------------|-------------------------------|--------------------|-----------------|------------------------|
| NaAlSi ₃ O ₈ | 17-22 | 3-8 | 1000 | Burnham & Davis (1971) |
| NaAlSi ₃ O ₈ | ~22 | 1-8 | 1000 | Silver et al. (1990) |
| KAlSi ₃ O ₈ | ~25 | 1-7 | 900-1340 | Silver et al. (1990) |
| Ca-Al-silicate | ~16 | 1-5 | 1180 | Silver et al. (1990) |
| CaMgSi ₂ O ₆ | ~17 | 20 | 1240 | Hodges (1974) |
| Rhyolite | ~0 | ≤ 1.5 | 850 | Silver et al. (1990) |

if the partial molar volume of molecular water in rhyolitic liquids is really so low or if it reflects the difficulty of resolving values for $\bar{V}_{\text{H}_2\text{O},\text{molecular}}$ over such a small pressure interval (see Table 7).

Although the information on $\bar{V}_{\text{H}_2\text{O},\text{molecular}}$ provided by this approach is potentially very useful, considerable uncertainty still surrounds the value of $\bar{V}_{\text{H}_2\text{O}}$ that should be applied to natural liquids. It is difficult, for example, to assess whether the different estimated values of $\bar{V}_{\text{H}_2\text{O},\text{molecular}}$ in orthoclastic vs. calcium aluminosilicate liquids (~25 vs. ~16 cc/mole) is due to compositional effects or uncertainties inherent to the thermodynamic analysis. The data compiled in Table 7 suggest that the partial molar volume of water in silicate melts may be a function of melt composition, although the data are extremely limited. Unfortunately, this uncertainty in $\bar{V}_{\text{H}_2\text{O}}$ translates into significant uncertainties in the densities of natural liquids containing substantial amounts of water. For example, the density of an andesite liquid with 2 wt % dissolved water is plotted in Figure 7 as a function of temperature (along the Ni-NiO buffer and at 5 kbar) assuming three different values for $\bar{V}_{\text{H}_2\text{O}}$: 15, 20 and 25 cc/mole. The data in Figure 7 illustrate the sensitivity of hydrous liquid densities to the value chosen for the partial molar volume of water. An uncertainty in $\bar{V}_{\text{H}_2\text{O}}$ of ± 5 cc/mole propagates into an uncertainty in the density of the hydrous andesite liquid of $\pm 1.3\%$. Clearly, this error will be magnified for liquids containing higher concentrations of water, such as hydrous crustal melts or basic minette liquids.

Although the precise value of $\bar{V}_{\text{H}_2\text{O}}$ in silicate melts remains uncertain, we can still explore the relative effect water will have on the liquid densities of different lavas types

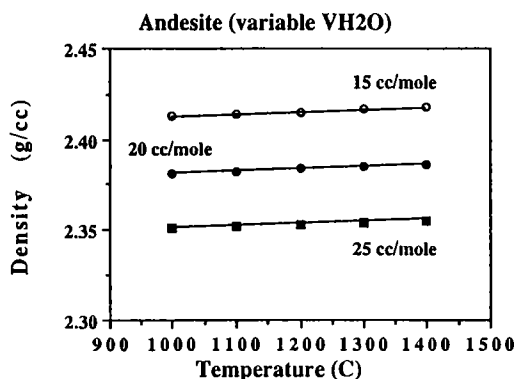


Figure 7. The density of an andesite liquid containing 2 wt % H₂O as a function of temperature assuming three different values for the partial molar volume of H₂O: 15, 20, and 25 cc/mole. Calculations of density were made for conditions along the Ni-NiO oxygen buffer and 2 kbar pressure. An uncertainty in $\bar{V}_{\text{H}_2\text{O}}$ of ± 5 cc/mole translates into an uncertainty in the density of the hydrous andesite of $\pm 1.3\%$.

containing variable amounts of water. Two examples are presented in Figure 8, where the liquid densities of a minette and peralkaline rhyolite containing 0, 1, 3 and 5 wt % H_2O are plotted as a function of pressure. To mimic conditions above the liquidus for these two lavas, temperatures of 1400° and 1200°C were chosen for the minette and peralkaline rhyolite respectively. For all calculations, the partial molar volume was assumed to be 20 cc/mole. In addition, a bulk modulus of 200 kbar was chosen for dissolved water as it represents a typical value for oxygens in silicate melts (Stolper et al., 1981). This translates into a value for $d\bar{V}_{\text{H}_2\text{O}}/dP$ of ~ 0.1 cc/mole/kbar. From the data plotted in Figure 8, it can be seen that the concentration of water has a marked effect on the densities of these two natural liquids. For the minette liquid, the effect of adding 3 wt % H_2O (10 mol %) is to decrease its liquid density by 3.4%. Similarly, for the peralkaline rhyolite the addition of 3 wt % H_2O (10 mol %) decreases its liquid density by 2.5%. Clearly (assuming $\bar{V}_{\text{H}_2\text{O}} = 20$ cc/mole is appropriate), the effect of dissolved water on a magma's liquid density is significant and comparable in magnitude to the effect caused by decreasing pressure: adding 1 wt % H_2O is equivalent to decreasing pressure by 1.4 kbar for the minette and 1.3 kbar for the peralkaline rhyolite. For comparison, this effect is equivalent to raising the temperature 129 K for the minette and 161 K for the rhyolite.

A far more practical application of estimates of $\bar{V}_{\text{H}_2\text{O}}$ in silicate liquids is to examine how the density of a *residual* liquid changes during crystallization of a hydrous

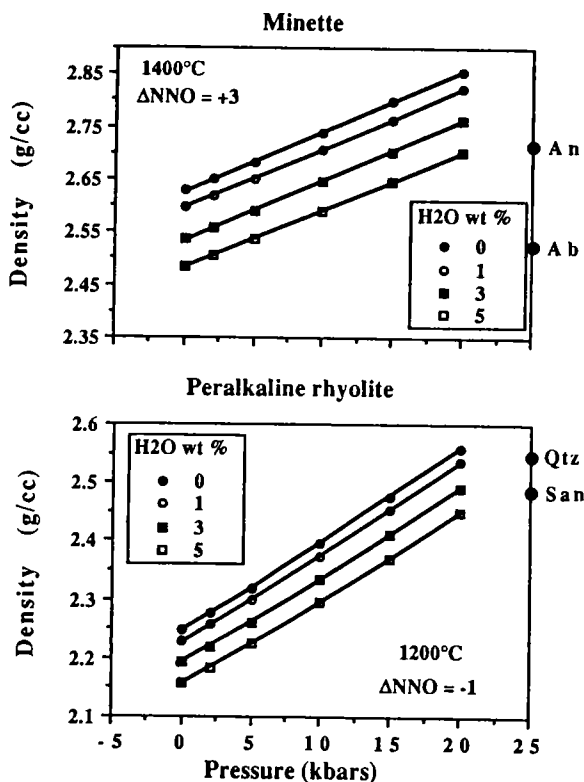


Figure 8. The liquid densities of two hydrous lava types, a minette and a peralkaline rhyolite, as a function of pressure assuming concentrations of 0, 1, 3, and 5 wt % H_2O . The partial molar volume and compressibility of H_2O is assumed to be 20 cc/mole and 0.1 cc/mole/kbar respectively (see text). The effect of adding 3 wt % H_2O is to decrease the liquid density of the minette and the peralkaline rhyolite by 3.4 and 2.5% respectively. The crystalline densities of anorthite, albite, quartz and sanidine are shown at 25 kbar for scale; their densities change by less than 0.02 g/cc between 1 bar and 25 kbar.

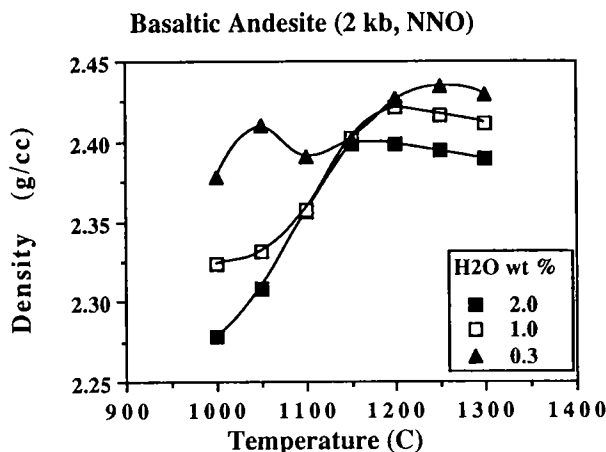


Figure 9. The density of a basaltic andesite's residual liquid as a function of temperature for three initial water contents: 0.3, 1.0 and 2.0 wt %. The fractional crystallization paths for these three liquids were calculated with the thermodynamic solution model (SILMIN) of Ghiorso et al. (1983) at a pressure of 2 kbar and along the Ni-NiO oxygen buffer. The difference in liquid density between the driest and most hydrous basaltic andesite is 1.7 % prior to crystallization at 1300°C, whereas after 300 degrees of fractional crystallization, the difference in density between their respective residual liquids has grown to 4.2%.

magma. Two dominant effects will control the density of the residual liquid: (1) the build-up of water in the melt due to crystallization of anhydrous phases; and (2) the effect of water on the liquidus phase relations and hence, the bulk composition of the residual liquid. This example is presented in Figure 9 where the density of a basaltic andesite's residual liquid is plotted as a function of temperature for three different initial water contents: 0.3, 1.0, and 2.0 wt %. The water concentrations considered in this example are well within the range estimated for basaltic andesites erupted in subduction zone environments (Eggler, 1972). Again, as in the example above, the partial molar volume of water is assumed to be 20 cc/mole. The compositions of the basaltic andesite residual liquids were calculated under fractional crystallization conditions along the Ni-NiO oxygen buffer at a pressure of 2 kbar with the thermodynamic solution model (SILMIN) of Ghiorso et al. (1983).

One of the interesting features of the diagram in Figure 9 is that the density minimum observed for the residual liquid under the driest initial condition (0.3 wt % H₂O) disappears with increasing water contents. This minimum is caused by initial crystallization of dense olivine causing the liquid to become less dense followed by crystallization of relatively buoyant plagioclase causing the residual liquid to become more dense. Both Stolper and Walker (1980) and Sparks et al. (1980) suggested that this minimum in the liquid density vs. fractionation trend of anhydrous, basic magmas may lead to a preferred average composition of erupted basalts since the lower density will favor eruption of lavas at this stage of differentiation relative to more or less fractionated liquids. The disappearance of the density minimum under more hydrous conditions is due to the dominant effect water has on decreasing the density of the residual liquid. This result was anticipated by Mahood and Baker (1986) in their study of the iron-rich alkalic lavas of Pantelleria, Sicily. Note that all three density curves intersect at ~1150°C; this merely corresponds to the liquidus temperature, and hence density maximum, of the most hydrous basaltic andesite liquid. Perhaps the most important observation to be made in Figure 9 is the contrast in density between the three basaltic andesite liquids at 1300° and at 1000°C. The difference in liquid density between the driest and most hydrous basaltic andesite is 1.7% prior to crystallization at 1300°C, whereas after 300 degrees of fractional crystallization, the difference in density between their respective residual liquids has grown to 4.2%. This illustrates the necessity of considering not only the effect of V_{H_2O} on the density of a magmatic liquid, but also the

effect water has on the crystallization sequence and hence, the bulk composition of the residual liquid. Clearly, realistic evaluations of a magma's liquid density during crystallization cannot be made without knowledge of how much water is in a magma and how it will affect the compositions, proportions and crystallization temperatures of the various phenocryst phases. Equally important, however, are direct measurements on the densities of hydrous liquids over a wide range of composition in order to further constrain values of V_{H_2O} applicable to magmas.

The partial molar volume of CO_2 . We are not aware that any direct density measurements on CO_2 -bearing silicate liquids have been made, unlike the case for hydrous liquids. Yet the presence of CO_2 in the upper mantle and its enhanced solubility in undersaturated (silica-poor and alkali-rich) magmas have been well documented (Mysen et al., 1975; Brey and Green, 1975; Eggler, 1978; Wendlandt and Mysen, 1978). In fact, the intimate association of carbon dioxide with the alkaline and kimberlitic rock clan has been long recognized (Heinrich, 1966; Tuttle and Gittins, 1966; Wyllie, 1967). As a consequence, information on the partial molar volume of CO_2 in these magmatic liquids is central to understanding both their transport to the Earth's surface as well as their equilibrium phase relationships at elevated pressures.

Table 8. Estimates of the partial molar volume of CO_2 in silicate liquids.

| Composition | V_{CO_2} (cc/mole) | P range (kbars) | T range (°C) | Reference |
|------------------------------------|-------------------------|--------------------|-----------------|-----------------------------|
| NaAlSi ₃ O ₈ | 34.4 | 10-30 | 1460-1620 | Spera and Bergman (1980) |
| NaAlSi ₂ O ₆ | 33.8 | 10-30 | 1460-1620 | Spera and Bergman (1980) |
| NaAlSiO ₄ | 32.9 | 10-30 | 1460-1620 | Spera and Bergman (1980) |
| Andesite | 33.9 | 15-30 | 1450-1650 | Spera and Bergman (1980) |
| Tholeiite | 32.7 | 15-30 | 1450-1650 | Spera and Bergman (1980) |
| Tholeiite | 33.0 | 15-30 | 1450-1650 | Stolper and Holloway (1986) |
| Olivine Melilitite | 29.3 | 15-30 | 1450-1650 | Spera and Bergman (1980) |

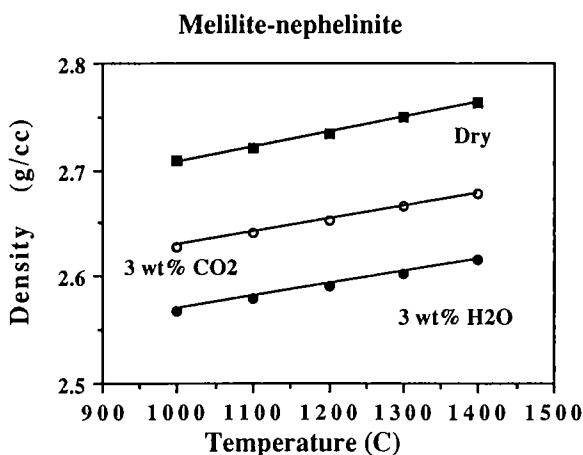
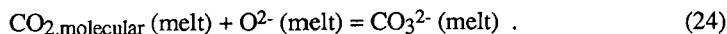


Figure 10. The liquid density of a melilite nephelinite as a function of temperature under dry, $CO_2 = 3$ wt %, and $H_2O = 3$ wt % conditions. Values of $V_{H_2O} = 20$ cc/mole and $V_{CO_2} = 33$ cc/mole were assumed (see text). The effect of adding 3 wt % CO_2 (4.32 mol %) is to decrease the liquid density by 3.0%, whereas the effect of 3 wt % H_2O (9.93 mol %) is to decrease density by 5.3%.

Despite the lack of any direct volume measurements of CO₂-bearing liquids, the partial molar volume of dissolved CO₂ in silicate melts can be extracted from CO₂ solubility curves in an analogous approach to that of Silver et al. (1990) for molecular water outlined above. Spera and Bergman (1980) were the first to analyze the available data on the pressure and temperature dependence of CO₂ solubility in silicate melts in order to derive a value for \bar{V}_{CO_2} . They constructed a thermodynamic model in which the activity of CO₂ dissolved in the melt was assumed to be proportional to the mole fraction of total dissolved CO₂. They were able to determine a value for the partial molar volume of CO₂ in a wide range of melt compositions (albite, jadeite, and nepheline as well as andesite, tholeiite and olivine melilitite) for which CO₂ solubility data were available. The average of their derived values for \bar{V}_{CO_2} of 33.4 ± 0.4 cc/mole is remarkably well constrained considering the wide range of compositions explored (see Table 8).

This essentially constant value for \bar{V}_{CO_2} is especially significant in light of the spectroscopic measurements of Fine and Stolper (1985a, 1985b) that demonstrate that CO₂ can dissolve in silicate liquids as both carbonate (CO₃²⁻) and molecular CO₂. The two species are postulated by Fine and Stolper (1985a) to interact through the following homogenous equilibrium:



Fine and Stolper (1985a) also observed that the proportion of dissolved molecular CO₂ relative to carbonate is strongly dependent on the activity of silica in the melt, with molecular CO₂ contents highest in the most silicic liquids. For example, most of the dissolved CO₂ in albitic liquid is molecular CO₂, whereas most in nepheline is expected to be carbonate (Fine and Stolper, 1985a). The fact that Spera and Bergman (1980) found \bar{V}_{CO_2} to be essentially identical in both these melt compositions, despite the difference in their speciation of CO₂, suggests that the volume change associated with the reaction in Equation (24) is essentially zero. This is consistent with the observations of Fine and Stolper (1985a) that CO₂ speciation is only weakly dependent on pressure.

Stolper and Holloway (1988) were able to derive values for the partial molar volume of CO₂ in basaltic liquid from solubility data with an approach analogous to that of Spera and Bergman (1980). However, Stolper and Holloway's (1988) activity-composition relations for dissolved CO₂ are based on spectroscopic determinations of the mole fraction of carbonate dissolved in the basaltic glasses. Their results, as well as those of Fine and Stolper (1985a) on sodium aluminosilicate liquids, suggest that the relationship between activity and composition in CO₂-bearing melts can be approximated as linear. This explains why Spera and Bergman's (1980) ideal model for the relationship between the activity of CO₂ and its mole fraction is so successful at explaining phase equilibria data. Moreover, the derived value for \bar{V}_{CO_2} derived by Stolper and Holloway (1988) in basaltic liquids of 33.0 ± 0.5 cc/mole is in excellent agreement with the values presented by Spera and Bergman (1980). It appears, therefore, that despite the absence of any direct density measurements on CO₂-bearing melts, the partial molar volume of dissolved CO₂ in silicate liquids is, in fact, well constrained.

The value of 33 cc/mole for \bar{V}_{CO_2} can be used to examine how the liquid density of a melilitite-bearing nephelinitite will vary as a function of CO₂ content. In Figure 10, the density of this lava type (composition in Table 4) is plotted as a function of temperature under both dry and CO₂ = 3 wt % conditions at a pressure of 10 kbar. In order to directly compare the effect of carbon dioxide relative to water on liquid densities, the density of the melilitite nephelinitite liquid containing 3 wt % H₂O is also shown. Again, a value for $V_{\text{H}_2\text{O}} = 20$ cc/mole is assumed. The data indicate that the effect of adding 3 wt % CO₂ (4.32 mol %) is to decrease the liquid density by 3.0%. In contrast, the effect of adding 3 wt % H₂O (9.93 mol %) is to decrease the density by 5.3%. Although the effect of water on decreasing the density of the liquid is more pronounced, the effect of carbon dioxide at a concen-

tration of only 3 wt % is still quite significant. Its high solubility in extremely undersaturated magmas may thus play an important role in the rapid transport of CO₂-bearing alkalic lavas to the Earth's surface.

SUMMARY

In the last five years, there has been a significant influx of new data in the literature on all aspects of the volumetric properties of silicate liquids. Several studies report 1 bar density measurements on a variety of multicomponent silicate liquids (Lange and Carmichael, 1987; Johnson and Carmichael, 1987; Dingwell and Brearley, 1988; Dingwell et al., 1988; Taniguchi, 1989). As a consequence of these recent data, the controversy surrounding the partial molar volume of Al₂O₃ in multicomponent silicate liquids (Ghiorso and Carmichael, 1984; Bottinga et al., 1984) has been resolved, and the partial molar volumes of Fe₂O₃ and TiO₂ in *natural* silicate liquids are now well constrained (although they both exhibit a strong compositional dependence in simple three- and four-component liquids). Perhaps most important, the precision of model equations describing the volume and thermal expansion of natural silicate liquids (Lange and Carmichael, 1987) has increased substantially since the original model of Bottinga and Weill (1970). This has extremely important consequences for the precision of model equations describing the compressibility of natural silicate liquids, since the derivation of compressibility data from both acoustic velocity and shock-wave experiments is critically dependent on accurate 1 bar volume and thermal expansion data.

The compressibility of natural silicate liquids can now be readily calculated for any anhydrous composition because of the recent measurements of acoustic velocity in silicate liquids as a *systematic* function of composition (Rivers and Carmichael, 1987; Kress et al., 1988). These sound speed data have been extended to include Fe₂O₃-bearing silicate liquids (Kress and Carmichael, 1991) and allow the ferric component to be incorporated into a general model equation describing the volumes of natural liquids as a function of pressure. Perhaps more important, measurements of the compressibilities of both the ferric and ferrous components in silicate melts provide information on how the ferric-ferrous ratio in a natural liquid changes as a function of pressure. Thus the question of whether or not the redox states of erupted lavas reflect the redox states of their source regions (Carmichael, 1991) can be quantitatively addressed.

Both the dynamic shock-wave experiments of Rigden et al. (1984, 1988, 1989) to 250 kbar and the static compression measurements of Agee and Walker (1988) between 10-60 kbar provide information on how the compressibility function itself, for silicate liquids, changes with pressure. These experiments allow direct evaluation of the postulate of Stolper et al. (1981) that olivine will float and coexisting melts will sink at sufficiently high pressures in the Earth's interior. More data obtained by these methods will allow further constraints to be placed on how the pressure derivative of the bulk modulus (K_T') changes as a function of composition. Preliminary results indicate that values of K_T' are more sensitive to composition than values of K_T and that K_T' increases (compressibility decreases) as the proportion of initially tetrahedrally coordinated cations (e.g., Al³⁺ and Si⁴⁺) decreases in the liquid (Rigden et al., 1989).

The volumetric properties of volatile-bearing silicate liquids have a limited experimental basis. Despite the paucity of direct density measurements of H₂O- and CO₂-bearing silicate liquids, thermodynamic analysis of solubility curves for both water and carbon dioxide allows estimation of their partial molar volumes in silicate liquids (Spera and Bergman, 1980; Stolper and Holloway, 1980; Silver et al., 1990). Current estimates are $\bar{V}_{H_2O} = 20 \pm 5$ cc/mole and $\bar{V}_{CO_2} = 33 \pm 1$ cc/mole. Further constraints on the temperature, pressure and compositional dependence of these values are highly desirable. The importance of considering the effect of water and carbon dioxide is easily recognized since both components have a dramatic effect on reducing silicate melt densities. Postulated mechanisms of

magmatic differentiation, such as compositionally-induced convection or crystal settling in magma chambers, must consider the effect of water on the density of residual liquids. Not only will the concentration of water in the residual liquid steadily increase as crystallization (of anhydrous phases) proceeds, but small amounts of water can significantly alter the composition, proportion and crystallization temperatures of the phenocryst phases and hence, the bulk composition of the residual liquid. This illustrates the necessity of a thermodynamic model (calibrated on accurate thermodynamic data) that can predict crystal-melt equilibria over a wide range of magmatic conditions in order to quantitatively model the physical aspects of a magma's evolution.

APPENDIX: CALORIMETRIC DATA

Thermodynamic modelling of crystal-melt equilibria in magmas requires information on both the volumetric and calorimetric properties (enthalpy, entropy and heat capacity) of silicate liquids. These latter properties play a fundamental role in the *thermal* evolution of magma bodies. In this appendix, the most recent data available on the enthalpies and entropies of fusion of various mineral phases and models for the heat capacity of silicate liquids and glasses. For a thorough discussion of these properties and methods of their measurement, see Stebbins et al. (1984) and Richet and Bottinga (1986).

Enthalpies and entropies of fusion

Richet and Bottinga (1986) tabulated available ΔH_{fus} and ΔS_{fus} values for a wide variety of mineral phases. Their tabulation, combined with data obtained subsequent to 1986, is presented in Table A1.

Heat capacities of silicate liquids and glasses

Heat capacities of silicate liquids are required in order to calculate enthalpies of fusion over a wide range of temperatures. For example, although forsterite melts at ~2163 K and fayalite melts at 1490 K, the temperature range over which olivine crystallizes in a basaltic melt is much lower, typically 1373-1573 K. Thus, extrapolation of high temperature ΔH_{fus} data to magmatic temperatures is required. This can be done using the following relation:

$$\Delta H_{\text{fus}}(T) = \Delta H_{\text{fus}}(T_{\text{fus}}) + \left[\int_{T_{\text{fus}}}^T C_{\text{pliq}}(T) dT - \int_{T_{\text{fus}}}^T C_{\text{pcryst}}(T) dT \right] \quad (\text{A1})$$

In this calculation, the heat capacity of the liquid is extrapolated into the supercooled (metastable) liquid region between T_{fus} and T . In some cases, a component may go through its glass transition temperature (T_g ; the temperature at which a rapidly cooled liquid becomes a glass) between T_{fus} and T . An example is quartz which has a fusion temperature of 1700 K, a glass transition temperature of ~1400-1500 K (dependent on the cooling rate; Richet et al., 1982), and typically crystallizes in magmas between 973-1273 K. In this case, the following calculation is required:

$$\Delta H_{\text{fus}}(T) = \Delta H_{\text{fus}}(T_{\text{fus}}) + \left[\int_{T_{\text{fus}}}^{T_g} C_{\text{pliq}}(T) dT + \int_{T_g}^T C_{\text{pglass}}(T) dT - \int_{T_{\text{fus}}}^T C_{\text{pcryst}}(T) dT \right] \quad (\text{A2})$$

As a consequence, data on both liquid and glass heat capacities are required. The models of Stebbins et al. (1984) for liquid and glass heat capacities of multicomponent silicates are presented in Tables A2 and A3.

Table A1. Enthalpies and entropies of fusion.

| Formula | Temperature (K) | ΔH_{fus} (kJ/mole) | ΔS_{fus} (J/mole-K) | Reference |
|--|-------------------|-----------------------------------|------------------------------------|--------------------------------|
| Fe _{0.947} O | 1652 | 31.3 ± 0.2 | 19.0 ± 0.1 | Coughlin et al. (1951) |
| FeTiO ₃ | 1640 | 21.7 ± 0.1 | 13.2 ± 0.1 | Naylor and Cook (1946) |
| SiO ₂ (quartz) ^a | 1700 | 94.0 ± 1.0 | 5.53 ± 0.56 | Richet et al. (1982) |
| SiO ₂ (cristobalite) | 1999 | 8.92 ± 1.0 | 4.46 ± 0.50 | Richet et al. (1982) |
| MgSiO ₃ ^a | 1834 | 77.4 | 42.2 | Stebbins et al. (1984) |
| MgSiO ₃ ^a | 1834 | 73.2 ± 6.0 | 39.9 ± 3.3 | Richet and Bottinga (1986) |
| CaSiO ₃ (wollastonite) ^a | 1770 | 61.7 ± 4.0 | 34.9 ± 2.3 | Richet and Bottinga (1984b) |
| CaSiO ₃ (pseudowoll) | 1817 | 57.3 ± 2.9 | 31.5 ± 1.6 | Adamkovicova et al. (1980) |
| CaMgSi ₂ O ₆ | 1665 ^b | 138.1 ± 2.1 | 82.9 ± 1.3 | Stebbins et al. (1984) |
| CaMgSi ₂ O ₆ | 1670 ^a | 137.7 ± 2.0 | 82.5 ± 1.2 | Richet and Bottinga (1984b) |
| CaMgSi ₂ O ₆ | 1665 ^b | 138.5 ± 3.2 | 83.2 ± 1.9 | Ziegler and Navrotsky (1986) |
| CaMgSi ₂ O ₆ | 1665 ^b | 137.7 ± 2.4 | 82.7 ± 1.4 | Lange et al. (1990) |
| Ca ₂ MgSi ₂ O ₇ | 1727 | 123.9 ± 3.2 | 71.7 ± 1.9 | Proks et al. (1977) |
| Ca ₃ MgSi ₃ O ₈ ^b | 1848 | 125 ± 15 | 67.5 ± 8.1 | Kosa et al. (1981) |
| Fe ₂ SiO ₄ | 1490 ^b | 92.2 ± 0.3 | 61.9 ± 0.2 | Orr (1953) |
| Fe ₂ SiO ₄ | 1490 ^a | 89.3 ± 1.1 | 59.9 ± 0.7 | Stebbins and Carmichael (1984) |
| Mn ₂ SiO ₄ | 1620 | 89. ± 0.5 | 55.2 ± 0.3 | Mah (1960) |
| Mg ₂ SiO ₄ | 2163 | 114 ± 20 | 53 ± 9 | Navrotsky et al. (1989) |
| CaTiSiO ₅ | 1670 | 123.8 ± 0.4 | 74.1 ± 0.2 | King et al. (1954) |
| NaAlSi ₃ O ₈ | 1373 | 62.8± 2.1 | 45.7 ± 1.5 | Stebbins et al. (1983) |
| NaAlSi ₃ O ₈ | 1373 | 64.3 ± 3.0 | 46.2 ± 2.2 | Richet and Bottinga (1984a) |
| NaAlSi ₃ O ₈ | 1393 | 64.5 ± 3.0 | 46.3 ± 2.2 | Richet and Bottinga (1984a) |
| NaAlSi ₂ O ₆ ^a | 1100 | 59.3 ± 3.0 | 53.9 ± 2.7 | Richet and Bottinga (1984a) |
| NaAlSi ₂ O ₆ ^a | 1750 | 49.0 ± 2.1 | 28.0 ± 1.2 | Stebbins et al. (1984) |
| NaAlSiO ₄ | 1720 | 46.3 ± 2.0 | 26.9 ± 1.2 | Richet and Bottinga (1984a) |
| KAlSi ₃ O ₈ ^a | 1473 | 57.7 ± 4.2 | 39.2 ± 2.8 | Stebbins et al. (1984) |
| KAlSi ₃ O ₈ ^a | 1500 | 54.0 ± 4.0 | 36.0 ± 2.7 | Richet and Bottinga (1984a) |
| CaAlSi ₂ O ₈ | 1830 | 135.6 ± 8.8 | 74.1 ± 4.8 | Weill et al. (1980) |
| CaAlSi ₂ O ₈ | 1830 | 133.0 ± 4.0 | 72.7 ± 2.2 | Richet and Bottinga (1984b) |
| Mg ₃ Al ₂ Si ₃ O ₁₂ ^a | 1500 | 243 ± 8 | 162 ± 5 | Richet and Bottinga (1984b) |
| Mg ₂ Al ₄ Si ₅ O ₁₈ ^a | 1740 | 346 ± 10 | 199 ± 6 | Richet and Bottinga (1984b) |
| KMg ₃ AlSi ₃ O ₁₀ F ₂ | 1670 | 308.8 ± 1.3 | 185 ± 1 | Kelley et al. (1959) |

^aMetastable congruent melting

^bIncongruent melting

Table A2. Fit parameters for silicate liquid heat capacities from Stebbins et al. (1984).

| $C_p = \sum C_{p_i} X_i \text{ (J K}^{-1} \text{ gfw}^{-1}\text{)}$ | | |
|---|-----------|------|
| C_{p_i} | 1σ | |
| SiO ₂ | 80.0 ± | 0.9 |
| TiO ₂ | 111.8 ± | 5.1 |
| Al ₂ O ₃ | 157.6 ± | 3.4 |
| Fe ₂ O ₃ | 229.0 ± | 18.4 |
| FeO | 78.9 ± | 4.9 |
| MgO | 99.7 ± | 7.3 |
| CaO | 99.9 ± | 7.2 |
| BaO | 83.4 ± | 6.0 |
| Li ₂ O | 104.8 ± | 3.2 |
| Na ₂ O | 102.3 ± | 1.9 |
| K ₂ O | 97.0 ± | 5.1 |
| Rb ₂ O | 97.9 ± | 3.6 |

Table A3. Coefficients for the heat capacity of silicate glasses (400-1000 K) from Stebbins et al. (1984).

| $C_p(T) = \sum a_i X_i + \sum b_i X_i T + \sum c_i X_i T^{-2} \text{ (J K}^{-1} \text{ gfw}^{-1}\text{)}$ | | | |
|---|---------|-------------------|----------------------|
| | a_i | $b_i \times 10^2$ | $c_i \times 10^{-5}$ |
| SiO ₂ | 66.354 | 0.7797 | -28.003 |
| TiO ₂ | 33.851 | 6.4572 | 4.470 |
| Al ₂ O ₃ | 91.404 | 4.4940 | -21.465 |
| Fe ₂ O ₃ | 58.714 | 11.3841 | 19.915 |
| FeO | 40.949 | 2.9349 | -7.6986 |
| MgO | 32.244 | 2.7288 | 1.7549 |
| CaO | 46.677 | 0.3565 | -1.9322 |
| Na ₂ O | 69.067 | 1.8603 | 2.9101 |
| K ₂ O | 107.194 | -3.2194 | -28.929 |

ACKNOWLEDGMENTS

The support of NSF grants EAR88-04641 and EAR88-03215 are acknowledged. This manuscript was improved by comments from Drs. K. Cashman, M. Ghiorso, V. Kress and J. Nicholls.

REFERENCES

- Agee, C.B. and Walker, D. (1988) Static compression and olivine floatation in ultrabasic silicate liquids. *J. Geophys. Res.*, 93, 3437-3449.
- Anderson, A.T. (1975) Some basaltic and andesitic gases. *Rev. Geophys. Space Physics*, 13, 37-55.
- Bacon, J.F., Hasapis, A.A. and Wholley, J.W., Jr. (1960) Viscosity and density of molten silica and high silica content glasses. *Phys. Chem. Glasses*, 1, 90-98.
- Baidov, V.V. and Kunin, L.L. (1968) Speed of ultrasound and compressibility of molten silica. *Sov. Phys. Dok.*, 13, 64-65.
- Bartholomew, R.F. and Schreurs, I.W.H. (1980) Wide-line NMR study of the protons in hydrosilicate glasses of different water content. *J. Non-Cryst. Solids*, 38/39, 679-684.
- Bartholomew, R.F., Butler, B.L., Hoover, H.L. and Wu, C.K. (1980) Infrared spectra of a water-containing glass. *J. Am. Ceram. Soc.*, 63, 481-485.
- Basaltic Volcanism Study Project (1981) Basaltic volcanism on terrestrial planets. Pergamon Press, New York, 1-1286.
- Berman, R.G. (1988) Internally-consistent thermodynamic data for minerals in the system $K_2O-Na_2O-CaO-MgO-FeO-Fe_2O_3-Al_2O_3-SiO_2-TiO_2-H_2O-CO_2$. *J. Petrol.*, 29, 445-522.
- Berman, R.G. and Brown, T.H. (1984) A thermodynamic model for multicomponent melts, with application to the system $CaO-Al_2O_3-SiO_2$. *Geochim. Cosmochim. Acta*, 48, 661-678.
- Berman, R.G. and Brown, T.H. (1987) Development of models for multicomponent melts: analysis of synthetic systems. In: Carmichael and Eugster, Eds., *Thermodynamic modeling of geological materials: Minerals, fluids, and melts. Reviews in Mineralogy*, 17, 405-442.
- Bockris, J.O'M., and Kojonen, E. (1960) The compressibilities of certain molten silicates and borates. *J. Am. Ceram. Soc.*, 82, 4493-4497.
- Bockris, J.O'M., Tomlinson, J.W. and White, J.L. (1956) The structure of the liquid silicates: partial molar volumes and expansivities. *Faraday Soc. Trans.*, 52, 299-310.
- Bottinga, Y. and Weill, D. (1970) Densities of liquid silicate systems calculated from partial molar volumes of oxide components. *Am. J. Sci.*, 269, 169-182.
- Bottinga, Y., Weill, D. and Richet, P. (1982) Density calculations for silicate liquids. I. Revised method for aluminosilicate compositions. *Geochim. Cosmochim. Acta*, 46, 909-919.
- Bottinga, Y., Weill, D. and Richet, P. (1984) Density calculations for silicate liquids: Reply to a critical comment by Ghiorso and Carmichael. *Geochim. Cosmochim. Acta*, 48, 409-414.
- Bowker, J.C. (1979) Statistical models and Mössbauer spectroscopy of slags. Ph.D. dissertation, Carnegie-Mellon University, Pittsburgh, PA.
- Bowker, J.C., Lupis, C.H.P. and Flinn, P.A. (1981) Structural studies of slags by Mössbauer spectroscopy. *Canadian Metall. Quat.*, 20, 69-78.
- Brey, G. and Green, D.H. (1975) The role of CO_2 in the genesis of olivine melilitite. *Contrib. Mineral. Petrol.*, 49, 93-103.
- Burnham, C.W. (1975) Water and magmas: a mixing model. *Geochim. Cosmochim. Acta*, 39, 1077-1084.
- Burnham, C.W. (1979) The importance of volatile constituents. In: Yoder, Ed., *The evolution of the igneous rocks*. Princeton Univ. Press, Princeton, 439-482.
- Burnham, C.W. and Davis, N.F. (1971) The role of H_2O in silicate melts: I. P-V-T relations in the system $NaAlSi_3O_8-H_2O$ to 1 kilobars and $1000^\circ C$. *Am. J. Sci.*, 270, 54-79.
- Carmichael, I.S.E. (1991) The redox state of basic and silicic magmas: a reflection of their source regions? *Contrib. Mineral. Petrol.* (in press)
- Coughlin, J.P., King E.G., and Bonnickson, K.R. (1951) High temperature heat content of ferrous oxide, magnetite and ferric oxide. *J. Am. Ceram. Soc.*, 73, 3891-2893.
- Dickinson, J.E. and Hess, P.C. (1985) Rutile solubility and titanium coordination in silicate melts. *Geochim. Cosmochim. Acta*, 49, 2289-2296.
- Dingwell, D.B. and Brearley, M. (1988) Melt densities in the $CaO-FeO-Fe_2O_3-SiO_2$ system and the compositional dependence of the partial molar volume of ferric iron in silicate melts. *Geochim. Cosmochim. Acta*, 52, 2815-2825.
- Dingwell, D.B., Brearley, M. and Dickinson, J.E., Jr. (1988) Melt densities in the $Na_2O-FeO-Fe_2O_3-SiO_2$ system and the partial molar volume of tetrahedrally-coordinated ferric iron in silicate melts. *Geochim. Cosmochim. Acta*, 52, 2467-2475.

- Dingwell, D.B. and Webb, S.L. (1989) Structural relaxation in silicate melts and non-Newtonian melt rheology in geological processes. *Phys. Chem. Mineral.*, 16, 508-516.
- Eckert, H., Yesinowski, J.P., Stolper, E.M., Stanton, T.R. and Holloway, J. (1987) The state of water in rhyolitic glasses: a deuterium NMR study. *J. Non-Cryst. Solids*, 93, 93-114.
- Eckert, H., Yesinowski, J.P., Silver, L.A. and Stolper, E.M. (1988) Water in silicate glasses: quantitation and structural studies by ^1H solid echo and MAS-NMR methods. *J. Chem. Phys.*, 92, 2055-2064.
- Eggler, D.H. (1972) Water-saturated and undersaturated melting relations in a Parícutin andesite and an estimate of water content in the natural magma. *Contrib. Mineral. Petrol.*, 34, 261-271.
- Eggler, D.H. (1978) The effect of CO_2 upon partial melting of peridotite in the system $\text{Na}_2\text{O}-\text{CaO}-\text{Al}_2\text{O}_3-\text{MgO}-\text{SiO}_2-\text{CO}_2$ to 35 kb, with an analysis of melting in a peridotite- $\text{H}_2\text{O}-\text{CO}_2$ system. *Am. J. Sci.*, 278, 305-343.
- Esperanca, S. and Holloway, J.R. (1987) On the origin of some mica-lamprophyres: experimental evidence from a mafic minette. *Contrib. Mineral. Petrol.*, 95, 207-216.
- Fine, G. and Stolper, E. (1985) The speciation of carbon dioxide in sodium aluminosilicate glasses. *Contrib. Mineral. Petrol.*, 91, 105-121.
- Fine, G. and Stolper, E. (1985/86) Dissolved carbon dioxide in basaltic glasses: concentrations and speciation. *Earth Planet. Sci. Lett.*, 76, 263-278.
- Fraser, D.G. and Bottinga, Y. (1985) The properties of melts and glasses in the system $\text{NaAlSi}_3\text{O}_8-\text{KAlSi}_3\text{O}_8$: comparison of experimental data obtained by Knudsen-cell mass spectroscopy and solution calorimetry. *Geochim. Cosmochim. Acta*, 49, 1377-1381.
- Fraser, D.G., Rammensee, W. and Jones, R.H. (1983) The mixing properties of melts in the system $\text{NaAlSi}_2\text{O}_6-\text{KAlSi}_2\text{O}_6$ determined by Knudsen cell mass spectrometry. *Bull. Mineral.*, 106, 111-117.
- Fujii, T. and Kushiro, I. (1977) Density, viscosity, and compressibility of basaltic liquid at high pressure. *Carnegie Inst. Wash. Yearb.*, 76, 419-424.
- Gerlach, T.M. (1981) Restoration of new volcanic gas analyses from basalts of the Afar region: further evidence of CO_2 -degassing trends.
- Ghiorso, M.S. (1985) Chemical mass transfer in magmatic processes: I. Thermodynamic relations and numerical algorithms. *Contrib. Mineral. Petrol.*, 90, 107-120.
- Ghiorso, M.S. (1987) Modeling magmatic systems: thermodynamic relations. In: Carmichael and Eugster, Eds., *Thermodynamic modeling of geological materials: Minerals, fluids, and melts. Reviews in Mineralogy*, 17, 443-465.
- Ghiorso, M.S. and Carmichael, I.S.E. (1984) Comment on "Density calculations for silicate liquids. I. Revised method for aluminosilicate compositions" by Bottinga, Weill and Richet. *Geochim. Cosmochim. Acta*, 48, 401-408.
- Ghiorso, M.S. and Carmichael, I.S.E. (1985) Chemical mass transfer in magmatic processes. II. Applications in equilibrium crystallization, fractionation and assimilation. *Contrib. Mineral. Petrol.*, 90, 121-141.
- Ghiorso, M.S. and Carmichael, I.S.E. (1987) Modeling magmatic systems: petrologic applications. In: Carmichael and Eugster, Eds., *Thermodynamic modeling of geological materials: Minerals, fluids, and melts. Reviews in Mineralogy*, 17, 467-499.
- Ghiorso, M.S., Carmichael, I.S.E., Rivers, M.L. and Sack, R.O. (1983) The Gibbs Free Energy of mixing of natural silicate liquids: an expanded regular solution approximation for the calculation of magmatic intensive variables. *Contrib. Mineral. Petrol.*, 84, 107-145.
- Ghiorso, M.S. and Kelemen, P.B. (1987) Evaluating reaction stoichiometry in magmatic systems evolving under generalized thermodynamic constraints: examples comparing isothermal and isenthalpic assimilation. In: B.O. Mysen, Ed., *Magmatic processes: Physicochemical principles. Geochemical Soc. Spec. Pub.*, 1, 319-336.
- Hamilton, D.L. and Oxtoby, S. (1986) Solubility of water in albite-melt determined by the weight-loss method. *J. Geol.* 94, 626-630.
- Hanada, T. and Soga, N. (1980) Coordination of titanium in sodium titanium silicate glasses. *J. Non-Cryst. Solids*, 38-39, 105-110.
- Heinrich, E.W. (1966) *The Geology of Carbonatites*. Rand McNally, New York, 608 pp.
- Hodges, F.W. (1974) The solubility of H_2O in silicate melts. *Carnegie Inst. Wash. Year Book*, 73, 251-255.
- Iwamoto, N., Tsunawaki, Y., Nakagawa, H., Yoshimura, T. and Wakabayashi, N. (1978) Investigation of calcium-iron-silicate glasses by the Mössbauer method. *J. Non-Cryst. Solids*, 29, 347-356.
- Johnson, M.C. and Rutherford, M. J. (1989) Experimentally determined conditions in the Fish Canyon Tuff, Colorado, Magma Chamber. *J. Petrol.*, 30, 711-737.
- Johnson, T. (1990) The partial molar volume of TiO_2 in multicomponent silicate melts. M.S. Thesis, University of California, Berkeley.
- Johnson, T. and Carmichael, I.S.E. (1987) The partial molar volume of TiO_2 in multicomponent silicate melts (abstr.). *Geol. Soc. Am. Abstr. Prog.*, 19, 719.

- Kelley, K.K., Barany, R., King, E.G. and Christensen, A.U. (1959) Some thermodynamic properties of fluorophlogopite mica. U.S. Bur. Mines Rep. Invest., 5436, 16 p.
- King, E.G., Orr, R.L. and Bonnickson, K.R. (1954) Low-temperature heat capacity, entropy at 298.16 K and high-temperature heat content of sphene (CaTiSiO_5). J. Am. Chem. Soc., 70, 4320-4321.
- Kosa, L., Adamkovicova, K. and Proks, I. (1981) Determining the heat of incongruent decomposition of merwinite, Silikaty Prague, 25, 199-206.
- Kress, V.C. and Carmichael, I.S.E. (1988) Stoichiometry of the iron oxidation reaction in silicate melts. Am. Mineral., 73, 1267-1274.
- Kress, V.C. and Carmichael, I.S.E. (1989) The lime-iron-silicate melt system: redox and volume systematics. Geochim. Cosmochim. Acta, 53, 2883-2892.
- Kress, V.C. and Carmichael, I.S.E. (1990) The iron redox state in silicate liquids: the effect of pressure, temperature, oxygen fugacity and composition, with application to the genesis of basic magma. Contrib. Mineral. Petrol. (submitted)
- Kress, V.C., Williams, Q. and Carmichael, I.S.E. (1988) Ultrasonic investigation of melts in the system $\text{Na}_2\text{O}-\text{Al}_2\text{O}_3-\text{SiO}_2$. Geochim. Cosmochim. Acta, 52, 283-293.
- Kress, V.C., Williams, Q. and Carmichael, I.S.E. (1989) When is a silicate melt not a liquid? Geochim. Cosmochim. Acta, 53, 1687-1692.
- Kushiro, I. (1978) Density and viscosity of hydrous calc-alkaline andesite magma at high pressures. Carnegie Inst. Wash. Year Book, 77, 675-677.
- Kushiro, I. (1980) Viscosity, density, and structure of silicate melts at high pressures, and their petrological applications. In: R.B. Hargraves, Ed., Physics of magmatic processes. Princeton University Press, Princeton, NJ, 93-120.
- Kushiro, I. (1982) Density of tholeiite and alkali basalt magmas at high pressures. Carnegie Inst. Wash. Year Book, 81, 305-309.
- Lange, R. and Carmichael, I.S.E. (1987) Densities of $\text{Na}_2\text{O}-\text{K}_2\text{O}-\text{CaO}-\text{MgO}-\text{FeO}-\text{Fe}_2\text{O}_3-\text{TiO}_2-\text{SiO}_2$ liquids: new measurements and derived partial molar properties. Geochim. Cosmochim. Acta, 51, 2931-2946.
- Lange, R.A. and Carmichael, I.S.E. (1989) Ferric-ferrous equilibria in $\text{Na}_2\text{O}-\text{FeO}-\text{Fe}_2\text{O}_3-\text{SiO}_2$ melts: effects of analytical techniques on derived partial molar volumes. Geochim. Cosmochim. Acta, 53, 2195-2204.
- Lange, R.A., DeYoreo, J.J. and Navrotsky, A. (1990) Scanning calorimetric measurement of heat capacity during incongruent melting of diopside. Am. Mineral. (in press).
- Lange, R.A. and Navrotsky, A. (1990) Direct measurements of liquid heat capacities in the $\text{Na}_2\text{O}-\text{FeO}-\text{Fe}_2\text{O}_3-\text{SiO}_2$ and $\text{CaO}-\text{FeO}-\text{Fe}_2\text{O}_3-\text{SiO}_2$ systems (abstr.). Geol. Soc. Am. Abstr. Prog. (in press)
- Lewis, G.N. and Randall, M. (1961) Thermodynamics. Revised by K.S. Pitzer and L. Brewer, McGraw-Hill, New York, 723 p.
- Levy, R.A., Lupis, C.H.P., Flinn, P.A. (1976) Mössbauer analysis of the valence and coordination of iron cations in $\text{SiO}_2-\text{Na}_2\text{O}-\text{CaO}$ -glasses. Phys. Chem. Glasses, 17, 94-103.
- Mah, A.D. (1960) Thermodynamic properties of manganese and its compounds. U.S. Bur. Mines Rep. Invest., 5600, 34 p.
- Mahood, G. and Baker, D.R. (1986) Experimental constraints on depths of fractionation of mildly alkalic basalts and associated felsic rocks: Pantelleria, Strait of Sicily. Contrib. Mineral. Petrol., 93, 251-264.
- Manghnani, M.H., Sato, H., Rai, C.S. (1986) Ultrasonic velocity and attenuation measurements on basalt melts to 1500°C: role of composition and structure in the viscoelastic properties. J. Geophys. Res., 91, 9333-9342.
- Marsh, B. (1990) Crystal capture, sorting, and retention in convecting magma: Reply. Geol. Soc. Am. Bull., 102, 849-850.
- Martin, D., Griffiths, R.W. and Campbell, I.A. (1987) Compositional and thermal convection in magma chambers. Contrib. Mineral. Petrol., 96, 465-475.
- McKeown, D.A., Galeener, F.L. and Brown, G.E., Jr. (1984) Raman studies of Al coordination in silica-rich sodium aluminosilicate glasses and some related minerals. J. Non-Cryst. Solids, 68, 361-378.
- McMillan, P.W. and Chlebik, A. (1980) The effect of hydroxyl ion content on the mechanical and other properties of soda-lime-silica glass. J. Non-Cryst. Solids, 38/39, 509-514.
- McMillan, P.W., Jakobsson, S., Holloway, J.R. and Silver, L.A. (1983) A note on the Raman spectra of water-bearing albite glass. Geochim. Cosmochim. Acta, 47, 1937-1943.
- Mo, X., Carmichael, I.S.E., Rivers, M. and Stebbins, J. (1982) The partial molar volume of Fe_2O_3 in multicomponent silicate liquids and the pressure dependence of oxygen fugacity in magmas. Mineral. Mag., 45, 237-245.
- Moringa, K., Sugihara, Y. and Yanagase, T. (1976) J. Jap. Inst. of Metals, 40, 480.
- Murase, T. (1982) Density and compressional wave velocity of basaltic and andesitic liquids. Carnegie Inst. Wash. Year Book, 81, 303-305.

- Murase, T. and McBirney, A.R. (1973) Properties of some common igneous rocks and their melts at high temperatures. *Geol. Soc. Am. Bull.*, 84, 3563-3592.
- Murdoch, J.B., Stebbins, J.F. and Carmichael, I.S.E. (1985) High-resolution ^{29}Si NMR study of silicate and aluminosilicate glasses: the effect of network-modifying cations. *Am. Mineral.*, 70, 332-343.
- Mysen, B.O., Arculus, R. J. and Eggler, D.H. (1975) Solubility of carbon dioxide in natural nephelinite, tholeiite and andesite melts to 30 kbar pressure.
- Mysen, B.O., Carmichael, I.S.E. and Virgo, D. (1985) A comparison of iron redox ratios in silicate glasses determined by wet-chemical and ^{57}Fe Mössbauer resonant absorption methods. *Contrib. Mineral. Petrol.*, 90, 101-106.
- Naylor, B.F. and Cook, O.A. (1946) High-temperature heat contents of the metatitanates of calcium, iron and magnesium. *J. Am. Chem. Soc.*, 68, 1003-1005.
- Navrotsky, A. (1986) Thermodynamics of silicate melts and glasses. In: C.M. Scarfe, Ed., *Short Course in Silicate Melts*, Mineral. Assoc. Canada, v.12, 130-153.
- Navrotsky, A., Geisenger, K.L., McMillan, P. and Gibbs, G.V. (1985) The tetrahedral framework in glasses and melts: inference from molecular orbital calculations and implications for structure, thermodynamics and physical properties. *Phys. Chem. Minerals*, 11, 284-298.
- Navrotsky, A., Zeigler, D., Oestrike, R. and Manier, P. (1989) Calorimetry of silicate melts at 1773 K: measurement of enthalpies of fusion and of mixing in the systems diopside-anorthite-albite and anorthite-forsterite. *Contrib. Mineral. Petrol.*, 101, 1 22-130.
- Nekvasil, H. (1988) Calculation of equilibrium crystallization paths of compositionally simple hydrous felsic melts. *Am. Mineral.*, 73, 956-965.
- Nelson, S.A. and Carmichael, I.S.E. (1979) Partial molar volumes of oxide components in silicate liquids. *Contrib. Mineral. Petrol.*, 71, 117-124.
- Nogami, M. and Tomozawa, M. (1984) Effect of stress on water diffusion in silica glass. *J. Am. Ceram. Soc.*, 67, 151-154.
- Orlova, G.P. (1962) The solubility of water in albite melts. *Int. Geol. Rev.*, 6, 254-258.
- Orr, R.L. (1953) High temperature heat contents of magnesium orthosilicate and ferrous orthosilicate. *J. Am. Chem. Soc.*, 75, 528-529.
- Ostrovskiy, I.A., Orlova, G.P. and Rudnitskaya, Y.S. (1964) Stoichiometry in the solution of water in alkali-aluminosilicate melts. *Doklady Akad. Nauk. SSR*, 157, 149-151.
- Oxtoby, S. and Hamilton, D.L. (1978) Solubility of water in melts of the $\text{Na}_2\text{O}-\text{Al}_2\text{O}_3-\text{SiO}_2$ and $\text{K}_2\text{O}-\text{Al}_2\text{O}_3-\text{SiO}_2$ systems. In: Mackenzie, Ed., *Progress in Experimental Petrology*. Natl. Environ. Res. Council Pub. Ser. D, 11, Dept. Geology, Manchester Univ.
- Pargamin, L., Lupis, C.H.P. and Flinn, P.A. (1972) Mössbauer analysis of the distribution of iron cations in silicate slags. *Metall. Trans.*, 3, 2093-2105.
- Proks, I., Eliasova, M. and Kosa, L. (1977) The heat of fusion of akermanite, *Silikaty Prague*, 21, 3-11.
- Richet, P. and Bottinga, Y. (1984a) Heat capacity of silicate liquids: new measurements on $\text{NaAlSi}_3\text{O}_8$ and KAlSi_3O_8 . *Geochim. Cosmochim. Acta*, 48, 453-470.
- Richet, P. and Bottinga, Y. (1984b) Anorthite, andesine, wollastonite, diopside, cordierite and pyrope: thermodynamics of melting, glass transitions and properties of the amorphous phases. *Earth Planet. Sci. Lett.*, 67, 415-432.
- Richet, P. and Bottinga, Y. (1986) Thermochemical properties of silicate glasses and liquids: a review. *Rev. Geophys.*, 24, 1-25.
- Rigden, S.M., Ahrens, T.J. and Stolper, E.M. (1984) Density of liquid silicates at high pressures. *Science*, 226, 1071-1074.
- Rigden, S.M., Ahrens, T.J. and Stolper, E.M. (1988) Shock compression of molten silicate: results for a model basaltic composition. *J. Geophys. Res.*, 93, 367-382.
- Rigden, S.M., Ahrens, T.J. and Stolper, E.M. (1989) High pressure equation of state of molten anorthite and diopside. *J. Geophys. Res.*, 94, 9508-9522.
- Rivers, M.L. and Carmichael, I.S.E. (1987) Ultrasonic studies of silicate melts. *J. Geophys. Res.*, 92, 9247-9270.
- Robie, R.A., Bethke, P.M. and Beardsley, K.M. (1967) Selected X-ray Crystallographic Data, Molar Volumes, and Densities of Minerals and Related Substances. *U.S. Geol. Surv. Bull.* 1248.
- Ryan, M.P. (1987) Neutral buoyancy and the mechanical evolution of magmatic systems. In: B.O. Mysen, Ed., *Magmatic Processes: Physicochemical Principles*. *Geochem. Soc. Special Pub.*, 1, 259-287.
- Sawatzky, G.A., Van Der Woude, F. and Morrish, A.H. (1969) Recoilless-fraction ratios for ^{57}Fe in octahedral and tetrahedral sites of a spinel and a garnet. *Phys. Rev.*, 183, 383-386.
- Scarfe, C.M. (1986) Viscosity and density of silicate melts. In: C.M. Scarfe, Ed., *Short Course in Silicate Melts*. Mineral. Assoc. Canada, 12, 36-56.
- Scarfe, C.M., Mysen, B.O. and Virgo, D. (1979) Changes in viscosity and density of melts of sodium disilicate, sodium metasilicate, and diopside composition with pressure. *Carnegie Inst. Wash. Year Book*, 78, 547-551.

- Schreiber, H.D. (1987) An electrochemical series of redox couples in silicate melts: a review and applications to geochemistry. *J. Geophys. Res.*, 92, 9225-9232.
- Shannon, R.D. and Prewitt, C.T. (1969) Effective ionic radii in oxides and fluorides. *Acta Crystallogr.*, B25, 925-946.
- Silver, L. and Stolper, E. (1985) A thermodynamic model for hydrous silicate melts. *J. Geol.*, 93, 161-178.
- Silver, L. and Stolper, E. (1989) Water in albitic glasses. *J. Petrol.*, 30, 667-709.
- Silver, L., Ihinger, P.D. and Stolper, E. (1990) The influence of bulk composition on the speciation of water in silicate glasses. *Contrib. Mineral. Petrol.*, 104, 142-162.
- Sokolov, L.N., Baidov, V.V., Kunin, L.L. and Dymov, V.V. (1971) Surface and volume characteristics of melted slags of the calcium oxide-alumina-silica system. *Sb. Tr. Tsent. Nauchno-Issled. Inst. Chern. Metall.*, 75, 53-61.
- Sparks, R.S.J. (1990) Crystal capture, sorting and retention in convecting magma: Discussion and reply. *Geol. Soc. Am. Bull.*, 102, 847-848.
- Sparks, R.S.J., Meyer, P. and Sigurdson, H. (1980) Density variation amongst mid-ocean ridge basalts: implications for magma mixing and the scarcity of primitive lavas. *Earth Planet. Sci. Lett.*, 46, 419-430.
- Spera, F.J. and Bergman, S.C. (1980) Carbon dioxide in igneous petrogenesis: I. Aspects of the dissolution of CO₂ in silicate liquids. *Contrib. Mineral. Petrol.*, 74, 55-66.
- Stebbins, J.F., Carmichael, I.S.E. (1983) The heat of fusion of fayalite. *Am. Mineral.*, 69, 292-297.
- Stebbins, J.F., Carmichael, I.S.E. and Moret, L.K. (1984) Heat capacities and entropies of silicate liquids and glasses. *Contrib. Mineral. Petrol.*, 86, 131-148.
- Stebbins, J.F., Carmichael, I.S.E. and Weill, D. (1983) The high temperature liquid and glass heat contents and the heats of fusion of diopside, albite, sanidine, and nepheline. *Am. Mineral.*, 68, 717-730.
- Stein, D.J., Stebbins, J.F. and Carmichael, I.S.E. (1986) Density of molten sodium aluminosilicates. *J. Am. Cer. Soc.*, 69, 396-399.
- Stolper, E.M. (1982a) Water in silicate glasses: an infrared spectroscopic study. *Contrib. Mineral. Petrol.*, 94, 178-182.
- Stolper, E.M. (1982b) The speciation of water in silicate melts. *Geochim. Cosmochim. Acta*, 46, 2609-2620.
- Stolper, E. (1989) Temperature dependence of the speciation of water in rhyolitic melts and glasses. *Am. Mineral.*, 74, 1247-1257.
- Stolper, E. and Holloway, J.R. (1988) Experimental determination of the solubility of carbon dioxide in molten basalt at low pressure. *Earth Planet. Sci. Lett.*, 87, 397-408.
- Stolper, E. and Walker, D. (1980) Melt density and the average composition of basalt. *Contrib. Mineral. Petrol.*, 74, 7-12.
- Stolper, E., Walker, D., Hager, B.H. and Hays, J.F. (1981) Melt segregation from partially molten source regions: the importance of melt density and source region size. *J. Geophys. Res.*, 86, 6261-6271.
- Taniguchi, H. (1989) Densities of melts in the system CaMgSi₂O₆-CaAlSi₂O₈ at low and high pressures and their structural significance. *Contrib. Mineral. Petrol.*, 103, 325-334.
- Taylor, D. (1984a) Thermal expansion data: I. Binary oxides with the sodium chloride and wurtzite structures. *MO. Brit. Ceram. Trans. J.*, 83, 5-9.
- Taylor, D. (1984b) Thermal expansion data: II. Sesquioxides, M₂O₃, with the corundum and the A-, B-, and C-M₂O₃ structures. *Brit. Ceram. Trans. J.*, 83, 92-98.
- Taylor, D. (1984c) Thermal expansion data: IV. Binary oxides with the silica structures. *Brit. Ceram. Trans. J.*, 83, 129-134.
- Taylor, D. (1985) Thermal expansion data: V. Miscellaneous binary oxides. *Brit. Ceram. Trans. J.*, 84, 9-14.
- Touloukian, Y.S., Kirby, R.K., Taylor, R.E. and Lee, R.K. (1978) Methods for the measurement of the thermal expansion of solids. In: Touloukian et al., Eds. *Thermophysical Properties of Matter*, vol. 13, 17a-26a.
- Tuttle, O.F. and Gittens, J. (eds) (1966) *Carbonatites*. Interscience, 591 pp.
- Weill, D.F., Stebbins, J.F., Hon, R. and Carmichael, I.S.E. (1980) The enthalpy of fusion of anorthite. *Contrib. Mineral. Petrol.*, 74, 95-102.
- Wendlandt, R.F. and Mysen, B.O. (1978) Melting phase relations of natural peridotite and CO₂ as a function of degree of partial melting at 15 and 30 kbar. *Carnegie Inst. Wash. Year Book*, 77, 756-761.
- White, W.B. and Minser, D.G. (1984) Raman spectra and structure of natural glasses. *J. Non-Cryst. Solids*, 67, 45-49.
- Williams, Q. and Jeanloz, R. (1988) Spectroscopic evidence for pressure-induced coordination changes in silicate glasses and melts. *Science*, 239, 902-905.
- Wu, C.K. (1980) Nature of incorporated water in hydrated silicate glasses. *J. Am. Ceram. Soc.*, 63, 453-457.

- Wyllie, P.J. (1967) *Ultramafic and Related Rocks*. Wiley, New York.
- Yarker, C.A., Johnson, P.A.V., Wright, A.C., Wong, J., Gregor, R.B., Lytle, F.W. and Sinclair, R.N. (1986) Neutron diffraction and EXAFS evidence for TiO_5 units in vitreous $\text{K}_2\text{O-TiO}_2\text{-2SiO}_2$. *J. Non-Cryst. Solids*, 79, 117-136.
- Zeigler, D. and Navrotsky, A. (1986) Direct measurement of the enthalpy of fusion of diopside. *Geochim. Cosmochim. Acta*, 50, 2461-2466.

SIMULATION OF IGNEOUS DIFFERENTIATION PROCESSES

INTRODUCTION

One of the primary goals of igneous petrology is the definition and evaluation of the roles of the processes responsible for chemical differentiation. Quantitative simulation of these processes not only requires an understanding of the systematics of mineral-liquid equilibria in natural systems but also some understanding of how different processes interact.

The programs presented here consist of empirically calibrated expressions of mineral-melt equilibria that are built around a thermodynamic framework. The framework of the programs (which are designed to model phase equilibria based igneous differentiation) have been published in earlier works (Nielsen and Dungan, 1983; Nielsen, 1985; Nielsen, 1988a,b; Nielsen et al., 1988). This presentation is to show how modeling can be used to gain otherwise unobtainable insights into the mechanics of igneous differentiation, in particular, for processes that are difficult to simulate in the laboratory.

In this chapter we will simulate the major differentiation processes that are characteristic of shallow igneous magma chambers. These processes include crystallization, recharge, assimilation and eruption. In each example, we will examine how observations of natural systems can be converted into the mathematical constraints necessary for the construction of computer based models. Since our primary goal is to model natural igneous systems, the examples show how phase equilibria modeling can be used to help solve problems related to interpretation of the chemical and mineralogic diversity of suites of natural lavas.

THEORETICAL BACKGROUND

Major element phase equilibria

The most basic constraint required in order to simulate igneous differentiation, is a method to express the chemical equilibria between minerals and melt numerically. This can be achieved by conducting experiments to determine what minerals will crystallize from a melt under a given set of conditions. We can then use the results of these experiments to derive a set of expressions that describe the thermodynamics of crystallization. From these expressions and a melt composition, we can calculate what phase has the lowest free energy and the equilibrium temperature and composition of that phase.

One of the problems modelers of igneous systems have encountered in deriving the necessary thermodynamic expressions, is the inadequacy of our understanding of the thermodynamics of silicate melts. Past approaches to model the activities of silicate melt components have been complicated by the fact that we are not sure of the identity of those components. This has, until recently, been the missing link in our ability to model the phase equilibria natural magmas.

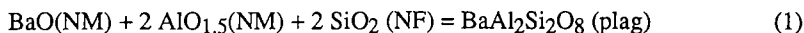
Approaches taken over the past decade have had varying amounts of success. In general, existing models fall into two class, models that only work for synthetic systems with a restricted number of components (e.g., Berman and Brown, 1984), and those that are calibrated against experiments on natural composition lavas, and work only for natural systems. The models useful for simulating natural systems include regular solution models using standard state thermodynamic constraints, and fictive melt components (Ghiorso and Carmichael, 1985; Nekvasil, 1986), simple oxide melt components and multiple regression

(Nathan and Van Kirk, 1979), and melt components based upon hypothetical melt complexes (Nielsen, 1985, 1988). It is not the purpose of this study to compare the attributes of these various approaches. Each of them is designed to solve a different problem and each is useful in dealing with the intended system and its constraints. All programs designed to model natural igneous phase equilibria are dependent on essentially the same experimental data base. All are empirical to the degree that the accuracy of the calculated models are dependent on the quality of the data with which they are calibrated.

Trace element partitioning

The problems associated with the compositional and temperature dependence of trace element partitioning are also related to our lack of understanding of melt component activity. However, we can show that by applying a melt component activity model, and by calculating mineral component reactions, we can account for the compositional dependence to the extent that we can calculate expressions describing them as a function of temperature alone.

Ba partitioning between plagioclase and melt is one example. By calculating the equilibrium constant for a mineral component crystallization reaction in the form,



where BaO(NM) is the mole fraction of Ba in the network modifier quasi-lattice, we can describe the partitioning behavior of Ba over a wide range of temperatures and melt compositions (Fig. 1) in terms of a linear regression of the experimental data.

Recent work on the partitioning of Sc, Y and REE between augite and natural mafic to intermediate magmas has provided additional information regarding the relative importance of the temperature and compositional dependence of trace element partitioning (Gallahan and Nielsen, 1989). These experimental results indicate that in the temperature range 1050-1200°C, there is a strong melt composition effect on the partitioning of both Sc, Y and the REE between pyroxene and melt which is most closely related to the Al content of the melt (Fig. 2). Much of the compositional dependence can be removed by calculating a REE-Al pyroxene component reaction and applying a melt component activity model. The crystallization reaction can be expressed in the form:



where FMO(NM) is the activity of a ferromagnesian component in the melt. We have constructed the equilibrium constant for this reaction assuming that the Fe/Mg ratio, and the distribution of Fe and Mg on the M sites has no effect on the partitioning of the REE. This can also be expressed as the assumption that the ratio of the activity of the ferromagnesian component in the pyroxene over the activity of the ferromagnesian component in the melt is constant at a given temperature. Expressions based on these assumptions have allowed us to predict the REE composition of the equilibrium pyroxene to within 15% (Fig. 3).

Table 1 is a compilation of the partition coefficients calculated to date. In the case of a series of similar elements, temperature dependence was assumed to be constant if information did not exist for all the elements. For example, for rare earth element (REE) partitioning in clinopyroxene, only La, Sm, Gd, Ho and Lu have sufficient experimental data for temperature dependence to be determined. In order to best approximate the coefficients for the other elements, the temperature dependence for the known elements are interpolated to predict the behavior of the other REE. There are many elements, however, where the temperature dependence can be determined neither from experimental data nor by analogy. If values do not exist for an element of interest, an approximation can be made using literature derived single value partition coefficients if that element behaves as a

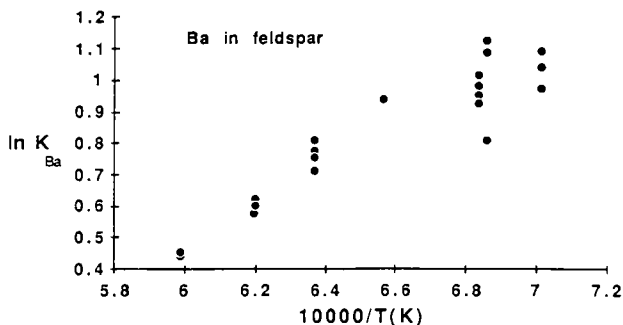


Figure 1. Correlation of $\ln K$ for Ba-feldspar with reciprocal temperature. Data are the 1 atm experimental results of Drake(1972). Melt component activities are calculated using the two-lattice melt model of Nielsen (1985).

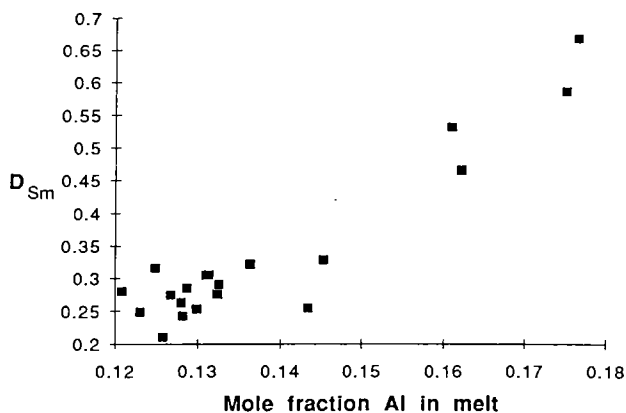


Figure 2. Correlation of the augite-melt partition coefficients for Sm and the mole fraction of Al in the melt. The range of temperature is 1135-1070°C. Partition coefficients are expressed in terms of the mole fraction of the element in the mineral over the mole fraction of the element in the liquid (each point is an average of at least 3 analyses).

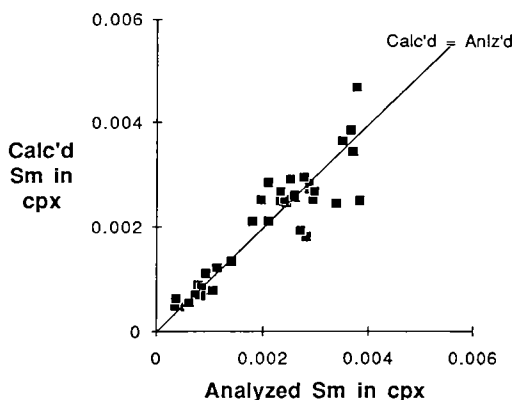


Figure 3. Comparison of the mole fraction of Sm in augite as determined by microprobe analysis of the experimental charges with the mole fraction of Sm in the augite as calculated using the experimental liquids as unknowns and the expression derived from the experimental results.

Table 1. Compositionally compensated partitioning expressions in the form $\ln d^* = a/T(K) + b$. In cases where a and b are 0.0, d^* is assumed to be 0.0. Expressions where only a is 0.0 assume that partitioning is independent of temperature.

| | | OL | OPX | CPX | PLAG | SP | ILMEN | PIG |
|------|---|--------|-------|----------|----------|-------|-------|-------|
| Co | a | .00 | .00 | .00 | .00 | .00 | .00 | .00 |
| | b | -.71 | -.51 | -.38 | .00 | 1.16 | -.50 | -.50 |
| Sc | a | .00 | .00 | 11956.00 | .00 | .00 | .00 | .00 |
| | b | -1.91 | -.88 | -5.23 | -2.80 | -.51 | -.51 | -.58 |
| V | a | .00 | .00 | .00 | .00 | .00 | .00 | .00 |
| | b | -4.13 | -2.31 | -1.90 | -4.00 | 2.40 | 1.60 | -1.80 |
| Sr | a | .00 | .00 | 26282.00 | 2779.00 | .00 | .00 | .00 |
| | b | -7.80 | -5.50 | -20.90 | -2.46 | .00 | .00 | -4.80 |
| Y | a | .00 | .00 | 12084.00 | .00 | .00 | .00 | .00 |
| | b | -5.50 | -3.52 | -8.81 | -4.40 | -3.22 | .00 | -2.50 |
| Zr | a | .00 | .00 | .00 | .00 | .00 | .00 | .00 |
| | b | -5.50 | -4.42 | -3.04 | -5.50 | -3.22 | .00 | -4.10 |
| Nb | a | .00 | .00 | .00 | .00 | .00 | .00 | .00 |
| | b | -5.50 | -4.80 | -3.10 | -5.50 | -1.83 | -1.13 | -3.80 |
| Ba | a | .00 | .00 | .00 | .00 | .00 | .00 | .00 |
| | b | -6.03 | .00 | -4.00 | -2.39 | .00 | .00 | -5.43 |
| La | a | .00 | .00 | 119.00 | -2400.00 | .00 | .00 | .00 |
| | b | -10.10 | -5.88 | -1.95 | -1.44 | .00 | -6.21 | -5.88 |
| Ce | a | .00 | .00 | 2369.00 | -4150.00 | .00 | .00 | .00 |
| | b | -9.90 | -5.75 | -3.28 | -.73 | .00 | -6.03 | -5.75 |
| Nd | a | .00 | .00 | 6870.00 | -4150.00 | .00 | .00 | .00 |
| | b | -9.57 | -5.11 | -5.94 | -.70 | .00 | -5.88 | -5.11 |
| Sm | a | .00 | .00 | 11371.00 | -5000.00 | .00 | .00 | .00 |
| | b | -7.45 | -4.61 | -8.60 | -.70 | .00 | -5.52 | -4.61 |
| Eu+2 | a | .00 | .00 | 26282.00 | 2779.00 | .00 | .00 | .00 |
| | b | -7.10 | -5.26 | -20.04 | -2.46 | .00 | -6.21 | -5.26 |
| Eu+3 | a | .00 | .00 | 10165.00 | -5400.00 | .00 | .00 | .00 |
| | b | -7.10 | -4.83 | -7.61 | -.36 | .00 | -5.11 | -4.83 |
| Gd | a | .00 | .00 | 8959.00 | -6100.00 | .00 | .00 | .00 |
| | b | -6.89 | -4.13 | -6.62 | -.29 | .00 | -4.83 | -4.13 |
| Dy | a | .00 | .00 | 6393.00 | -4000.00 | .00 | .00 | .00 |
| | b | -6.50 | -3.72 | -4.64 | -1.65 | .00 | -4.80 | -3.72 |
| Ho | a | .00 | .00 | 5110.00 | -4000.00 | .00 | .00 | .00 |
| | b | -6.10 | -3.44 | -3.65 | -1.70 | .00 | -4.49 | -3.44 |
| Er | a | .00 | .00 | 8759.00 | -4000.00 | .00 | .00 | .00 |
| | b | -5.85 | -3.21 | -6.31 | -1.75 | .00 | -4.13 | -3.21 |
| Yb | a | .00 | .00 | 16056.00 | -4000.00 | .00 | .00 | .00 |
| | b | -3.94 | -2.63 | -11.6 | -1.85 | .00 | -3.57 | -2.63 |
| Lu | a | .00 | .00 | 1704.00 | -3370.00 | .00 | .00 | .00 |
| | b | -3.40 | -2.48 | -14.30 | -2.35 | .00 | -3.40 | -2.48 |
| Hf | a | .00 | .00 | .00 | .00 | .00 | .00 | .00 |
| | b | .00 | .00 | .00 | .00 | -2.53 | .00 | .00 |
| Ta | a | .00 | .00 | .00 | .00 | .00 | .00 | .00 |
| | b | .00 | .00 | .00 | .00 | -1.09 | .00 | .00 |
| Th | a | .00 | .00 | .00 | .00 | .00 | .00 | .00 |
| | b | .00 | .00 | -5.00 | .00 | -3.44 | .00 | .00 |

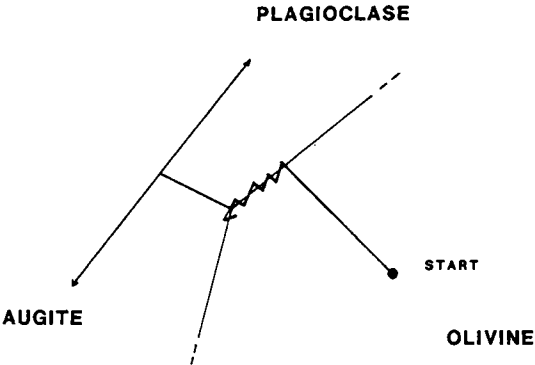


Figure 4. Expanded section of a hypothetical augite-plagioclase-olivine phase diagram showing a schematic liquid line of descent.

network modifier. The slope is assumed to be 0.0 because the assumption of temperature independence must be made (in spite of the fact that we have just shown that it is not a good assumption). The compositional dependence can be reduced by multiplying the literature single value partition coefficient by the sum of the mole fractions of the network modifiers in the system (Nielsen, 1988b). The natural log of that value can then be entered into the input file.

Assumptions and options of the program

The phase equilibria constraints described above allow us to calculate the equilibrium mineralogy and temperature of a crystallizing magma. This however, does not simulate fractionation. In order to do that, we must construct a numerical mechanism for how we crystallize the melt. We generally think of crystallization as something that occurs as a factor of time or temperature, but the relationship between % crystallization and time is poorly constrained. To be a useful modeling parameter, it must be related to temperature or % crystallization in some fashion. Those are the characteristics of the system that change as it evolves. Thus, we have two choices, temperature and % crystallization as the variable that we track. We can lower the temperature and calculate the amount of crystals we need to remove to re-equilibrate the system, or we can remove an increment of the liquidus phase and recalculate the temperature of the system. Both are valid approaches, the one used depends upon the information desired.

The advantage of the crystallization increment approach for models involving mixing, lies in the fact that we can tie the amount of recharge, assimilation, etc. to the crystallization rate, therefore relating mass to mass. In addition, this reduces the problems caused by the fact that the amount of crystals formed per degree of cooling varies depending on if it is multiply saturated or not. The amount of crystals formed is closely related to the amount of heat lost from the system. That in turn is related to time. The relationship of temperature vs time or heat loss on the other hand, is non-linear.

I will describe two basic methods for the simulation of crystallization, homogeneous crystallization, where crystallization is assumed to take place homogeneously throughout the magma chamber, and In situ fractionation, where crystallization only takes place along the walls of the cooling magma chamber. To simulate homogeneous crystallization, the program calculates the identity and composition of the liquidus phase, then removes an increment of that phase. The program then loops back and calculates the liquidus phase of the residual liquid and removes an increment of that phase. The method of simulating the crystallization of a multiply saturated system can best be described by referring to a schematic phase diagram (Fig. 4). Roeder (1974) developed a technique where the cotectic is modeled in terms of the removal of a large number of small increments of the liquidus phase. As the fractionation calculations proceed, the program will remove increments of the liquidus phase (olivine in Fig. 4) until the iteration where another phase is the calculated liquidus phase (plagioclase in Fig. 4). Removal of that phase will cause the free energy of that phase to drop, and the free energy of the original liquidus phase to rise. The amount that the free energy will rise is dependent on the composition of the phases, the temperature and the size of the crystallization increment. This controls the proportion of each phase that is removed. Continuing the procedure, the system will oscillate down the cotectic. The fractionating mineral proportions can be calculated from the number of times each phase is removed. The smaller the crystallization increment, the more accurate the approximation of the cotectic, and the proportion of phases fractionating from the system.

In addition to crystallization, the program also provides options which permit the calculation of liquid lines of descent during fractionation paired with magma mixing and magma chamber tapping. These basic options are:

1. Magma chamber recharge — magma added to the chamber is the same composition as the starting composition.

2. Assimilation — magma added is not related to the starting composition. For example, a crustal contaminant.
3. Eruption — a fraction of the magma chamber is removed from the system, as if it were being erupted to the surface. This option can also be used to model the trapping of intercumulus liquid.

In order to regulate the amount of recharged or assimilated material added to the system, I have assumed that the rate of input (or output in the case of eruption) can be expressed in terms of the amount of crystallization of the system. As each increment of liquidus phase is removed by the model, an increment of the parental magma or assimilated magma composition is added. In addition, an increment of the system is removed by eruption, reducing the size of the system. The relative sizes of the input vs output is a program variable. For example, a recharge constant of 1 represents the case where, for each fraction of mineral removed, an equal amount of the primitive magma (starting composition) is added to the system. The assimilation rate and eruption rate are treated similarly. Perfect fractional crystallization with no mixing is a 0-0-0 model. A model with no assimilation, but with a recharge rate twice the crystallization rate, and a rate of eruption equal to crystallization is a 2-0-1 model. This model is a steady-state model, meaning that the sum of the input (recharge + assimilation) is equal to the output (eruption + crystallization).

In addition to the mixing and fractionation parameters in the program, we must also decide how to sample the calculations. Liquid compositions are calculated at intervals of ~0.1%. It is not logistically reasonable to save all of those calculations. In addition, that is not how the information from natural systems is presented to us. We see only those compositions that are occasionally erupted to the surface. We have chosen to model two endmember cases. First, we have the option (program CHAOS) of sampling the calculation at some fixed interval, for example, every 5% crystallization. This simulates the case where we dip into the evolving magma chamber at even intervals. The second case (program ERUPT) assumes that the system erupts only following mixing events, and we only see the magma that is erupted. The relative bias of this approach is toward the more evolved compositions produced in the calculations.

MODELING OPEN SYSTEM PROCESSES

Paired recharge and fractionation

In our first example, we begin with the simplest mixing scenario, self mixing, or magma chamber recharge, paired with fractionation and eruption. This case is designed to simulate the geochemical behavior of a system such as a mid-ocean ridge segment, or an oceanic island where there is a long-lived fractionating magma chamber simultaneously undergoing mixing and fractionation. The composition used in this example is a Kilauean olivine tholeiite (Table 2). This liquid has olivine as the liquidus phase followed by augite, plagioclase and oxides. The results of several scenarios at different flux rates (Fig. 5) illustrate several of the characteristics that have been attributed to self-mixed, recharge magma chambers (Langmuir, 1980; O'Hara and Mathews, 1981; Nielsen, 1988, 1989), including the generation of a steady state liquid composition, and elevated compatible element contents. The points at which new phases reach the liquidus are reflected in the inflection points along the calculated liquid lines of descent. Increase in flux rate has the effect of increasing the compatible element concentration and decreasing the incompatible element concentration of the steady state liquid. The more compatible or incompatible the element, the stronger the effect. Most major elements are relatively insensitive to changes in flux rate because they are constrained by the cotectic. Consequently, the liquid line of descent for the major element pairs follow paths similar to those produced by fractional crystallization (0-0-0). This effect is accentuated at low recharge rates because of the relatively larger role of fractionation (Defant and Nielsen, 1990).

Table 2. Starting compositions and assimilants for calculations in text.

| | Colima | Uwek Parent | Silicic Assim | Luzon Parent | Tonalite | Reunion | Kilauea Iki | Galapagos Spreading Center |
|--------------------------------|--------|----------------|------------------|-----------------|----------|---------|----------------|----------------------------------|
| Reference: | 1 | 2 | 3 | 4 | 5 | -- | 6 | 7 |
| Na ₂ O | 3.47 | 2.01 | 3.94 | 1.30 | 5.47 | 2.03 | 2.33 | 2.34 |
| MgO | 9.29 | 12.35 | 0.35 | 10.87 | 0.43 | 15.08 | 10.03 | 6.24 |
| Al ₂ O ₃ | 16.44 | 11.82 | 15.03 | 13.80 | 15.80 | 11.92 | 12.10 | 13.10 |
| SiO ₂ | 52.10 | 48.93 | 73.23 | 47.54 | 73.50 | 47.00 | 49.18 | 51.30 |
| P ₂ O ₅ | 0.14 | 0.23 | 0.10 | 0.22 | 0.05 | 0.64 | 0.22 | 0.12 |
| K ₂ O | 0.74 | 0.38 | 3.08 | 0.41 | 1.69 | 0.35 | 0.52 | 0.10 |
| CaO | 8.46 | 10.01 | 1.32 | 12.62 | 2.28 | 9.48 | 11.17 | 10.30 |
| TiO ₂ | 0.81 | 2.11 | 0.20 | 0.62 | 0.20 | 2.00 | 2.49 | 2.00 |
| MnO | 0.14 | 0.18 | 0.10 | 0.21 | 0.01 | 0.17 | 0.13 | 0.20 |
| FeO | 6.55 | 10.59 | 1.70 | 9.70 | 1.00 | 10.02 | 9.90 | 11.20 |
| Fe ₂ O ₃ | 1.00 | 1.25 | 0.60 | 1.13 | 0.22 | 1.13 | 1.37 | 1.80 |
| Trace elements (ppm) | | | | | | | | |
| Ni | 261 | 537 | 0 | 88 | 5 | 500 | 300 | - |
| Co | 43 | 49 | 6 | - | - | 59 | - | - |
| Sc | 28 | 30 | 9 | 38 | 5 | 31 | 30 | - |
| V | 186 | 163 | 20 | - | - | 254 | - | - |
| Zn | 100 | 97 | 20 | - | - | 97 | - | - |
| Rb | 20 | 13 | 50 | - | - | 13 | - | - |
| Sr | 397 | 347 | 200 | 185 | 807 | 305 | 320 | - |
| Y | 20 | 18 | 9 | - | - | 24 | - | - |
| Zr | 100 | 114 | 200 | 37 | 33 | 167 | 200 | - |
| Nb | 5 | 4.4 | 9 | - | - | 20 | - | - |
| Cs | 3 | 10 | 5 | - | - | - | - | - |
| Ba | 200 | 100 | 200 | - | - | - | - | - |
| La | 7.9 | 9.62 | 40 | - | - | - | - | - |
| Ce | 18.3 | 22.84 | 91 | - | - | - | - | - |
| Nd | - | 15.73 | 46 | - | - | - | - | - |
| Sm | 2.6 | 4.61 | 8 | - | - | - | - | - |
| Eu | 0.9 | 1.5 | 2.6 | - | - | - | - | - |
| Yb | 1.96 | 1.8 | 1.46 | - | - | - | - | - |
| Lu | 0.26 | 0.2 | 0.16 | - | - | - | - | - |
| Hf | 3 | 3.15 | 12 | - | - | - | - | - |
| Ta | 0.81 | 0.81 | 13 | - | - | - | - | - |
| Pb | 20 | 10 | 50 | - | - | - | - | - |
| Th | 0.75 | 0.75 | 5 | - | - | - | - | - |
| U | 0.25 | 0.20 | 10 | - | - | - | - | - |

References: (1) Luhr et al. (1988); (2) calculated from data from Casaduvall and Dzurisen (1987); (3) Defant and Nielsen (1990); (4) Defant et al. (1988); (5) Dean (1981) tonalite used as assimilant in Luzon calculations; (6) Helz (1987a); (7) Juster et al. (1989) Galapagos Spreading Center basalt.

Recharge rate and fractionating mineral proportions

In a closed system undergoing homogeneous fractionation, the fractionating mineral proportions removed from a liquid are determined by the position of the cotectic in compositional space. In an open system, the addition of magma whose composition is not on the cotectic will perturb the system so that the fractionating mineral proportions will change as a function of the amount of magma being added. The distance from the cotectic that the system will be perturbed depends on the composition and relative amount of each of the mixed magmas. As the system continues to fractionate, it is continuously driven back to the cotectic. Therefore, if the increments of input are small relative to the size of the magma chamber and to the amount of crystallization, the magma composition will remain near the cotectic. The magmas generated by the open system will evolve along a cotectic, but the composition of the cumulates will be significantly different than those characteristic of a closed system.

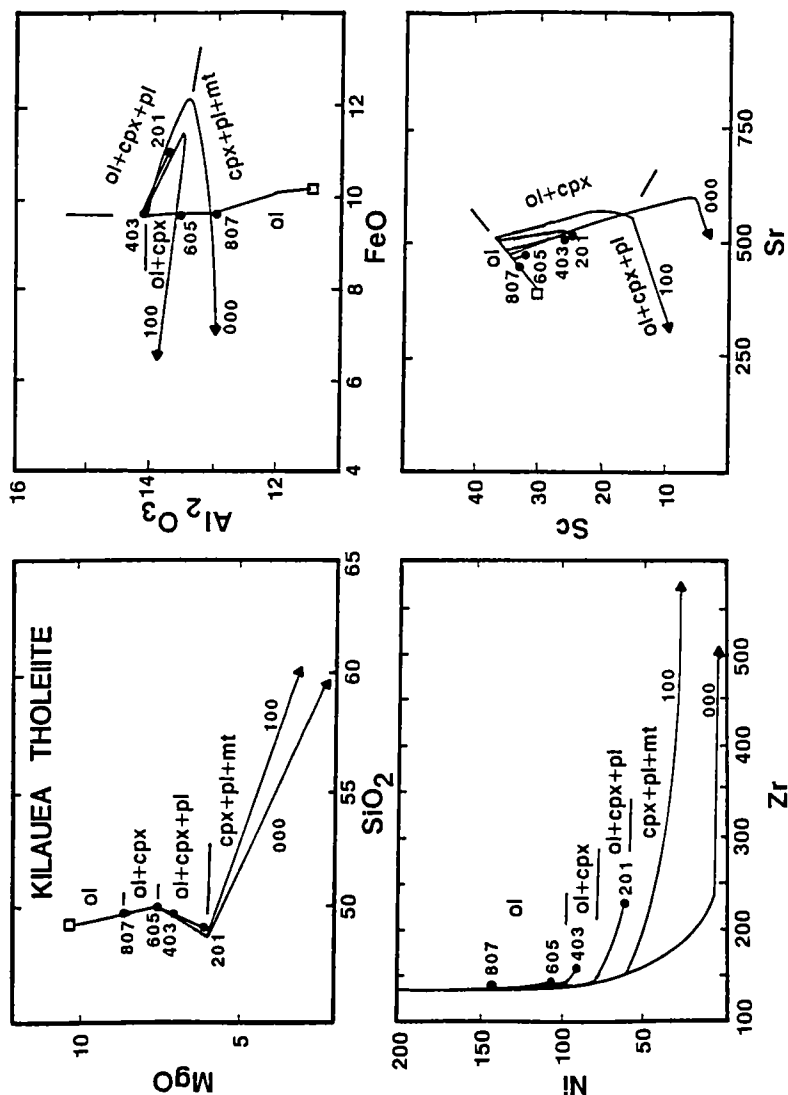


Figure 5. Results of calculated liquid lines of descent (LLD) for several scenarios at different magma chamber flux rates using ERUPT. Parent magma (open square) is an olivine tholeiite from Kilauea (Table 1). The model parameters (e.g., 605) represent the amount of recharge, assimilation, and eruption relative to the amount of crystallization. Solid dots represent steady state liquids. The initial values used are hypothetical but approximate realistic concentrations taken from Casa devall and Dzurisen (1987): Ni = 300, Sr = 320, Sc = 25 and Zr = 230.

The potential consequences of this can be tested by calculation of the fractionating mineral proportions for different systems. The two examples used here are a Kilauea tholeiite (Helz, 1987a) and an alkali basalt from Molokai (Beeson, 1976). Both are high Mg basalts differing primarily in their alkalis and Ca/Al ratios and resultantly in the order of crystallization. The tholeiite crystallizes in the order olivine, augite, plagioclase, and the basalt from Molokai crystallizes in the order olivine, plagioclase, augite. The effect of mixing rate will be tested with the case of magma chamber recharge. As each of the systems evolve, they are continuously replenished with magma of the same composition as the parental magma. Figure 6 illustrates the results of the calculations in terms of the fractionating mineral proportions for the system after it has reached the point where the composition has reached a steady state. An exception to this are the calculations at recharge rates of 0 and 1. In those cases the fractionating mineral proportions were taken from the results at the olivine + augite + plagioclase cotectic. These results indicate that as the rate of recharge increases, the proportion of the liquidus phase increases. For both of these systems the proportion of olivine increases as the magma is continuously pulled back toward olivine saturation. For the Kilauea tholeiite, the proportion of augite increases up to a recharge rate of 5. Above that rate, the system is never saturated with plagioclase, and the steady state liquid is perched on the olivine-augite cotectic. The steady state magma composition for the Molokai basalt on the other hand, is multiply saturated with olivine, augite and plagioclase up to a recharge rate of 5, but the relative proportions are completely different than for the Kilauean tholeiite. At higher recharge rates, the magma is perched on the olivine-plagioclase cotectic, and finally at a recharge rate of 7, the system fractionates only olivine.

There are no mineralogical criteria for the identification of recharge rate for most natural systems because, for example, all liquids produced by recharge rates less than 5 for these two examples are on the olivine-augite-plagioclase cotectic. If they were erupted and crystallized, both would appear mineralogically similar. Variations in mineral proportions would nevertheless have a strong effect on the compositions of derived liquids and cumulates. Both major and trace elements are affected. The major elements are constrained to the position of the cotectic, but that cotectic can move in n-component space.

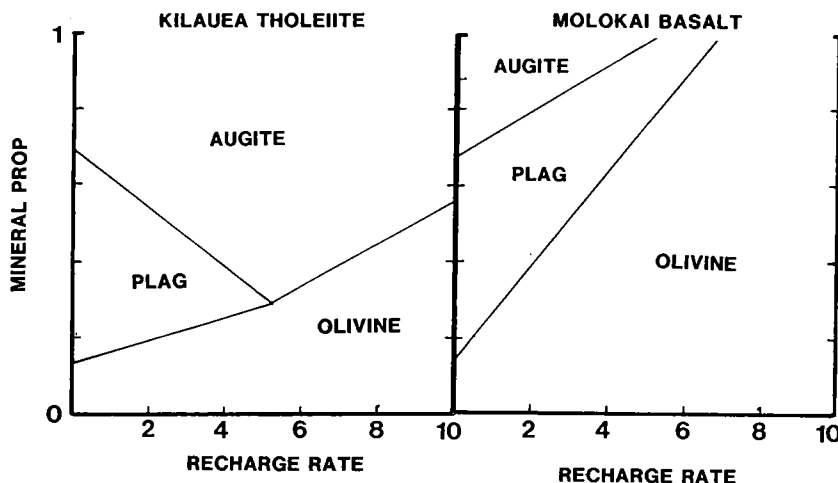


Figure 6. Fractionating mineral proportions for a Kilauean tholeiite (Helz, 1987) and an olivine basalt from Molokai (Beeson, 1976) as a function of recharge rate. All models assume constant magma chamber size. Therefore, recharge is balanced by fractionation, set at 1, and eruption, which is equal to recharge minus 1. Thus, recharge of 5 is calculated as a 5-0-4 simulation.

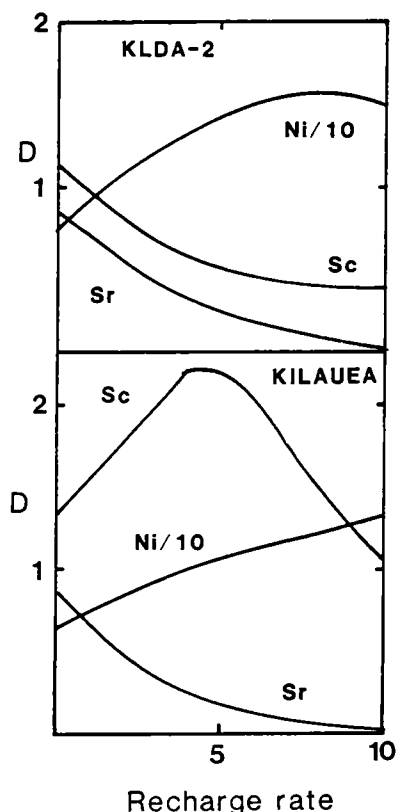


Figure 7. Bulk partition coefficients calculated on the basis of fractionating mineral proportions as given in Figure 6. The curvature of the lines is due to temperature and compositional dependence.

Phase equilibria constraints on bulk partition coefficient.

Variation in fractionating mineral proportions will also have a significant effect on the calculated values of bulk D 's. The bulk D of the fractionating assemblage is the value used for modeling open systems by most trace element models (DePaolo, 1981; O'Hara and Mathews, 1981). To date, bulk D has generally been calculated using mineral proportions appropriate to closed system crystallization. If one calculates bulk D based upon the open system fractionating mineral proportions (Fig. 7) the results indicate that bulk D can vary by as much as a factor of 5 as functions of recharge rate. In addition, the variation in bulk D with recharge rate and liquid composition can be large, even within the range of basaltic compositional space. Differences in bulk D are propagated through the calculations, resulting in equivalent differences in the calculated magma compositions.

This can be seen by comparing the calculated results for the Kilauea tholeiite using the assumptions of O'Hara and Mathews (1981) versus the results calculated using ERUPT. For the O'Hara and Mathews type calculations I used the fractionating mineral proportions and bulk D 's calculated by ERUPT for the case of perfect fractional crystallization in a closed system. In addition, I used those same closed system results as my guide as to the position of the inflection points representing where the system encounters each cotectic. The primary difference between the approaches involves the difference in the calculated fractionating mineral proportions.

Perhaps the most striking difference between the two sets of results (Figs. 5 and 8) is that Ni increases in the later stages of recharge and fractionation in the calculations assuming fixed fractionating mineral proportions (Fig. 8). The Ni content in the magma of

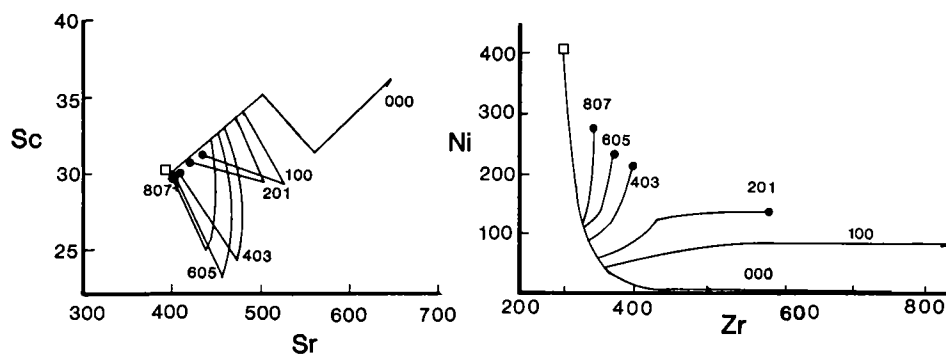


Figure 8. LLD calculated assuming fixed bulk distribution coefficients. Model parameters are the same as described in Figure 5. Mineral partition coefficients are taken from calculations for the Kilauea tholeiite. Mineral proportions are assumed to be fixed as a function of recharge rate. The parent compositions are given as open squares.

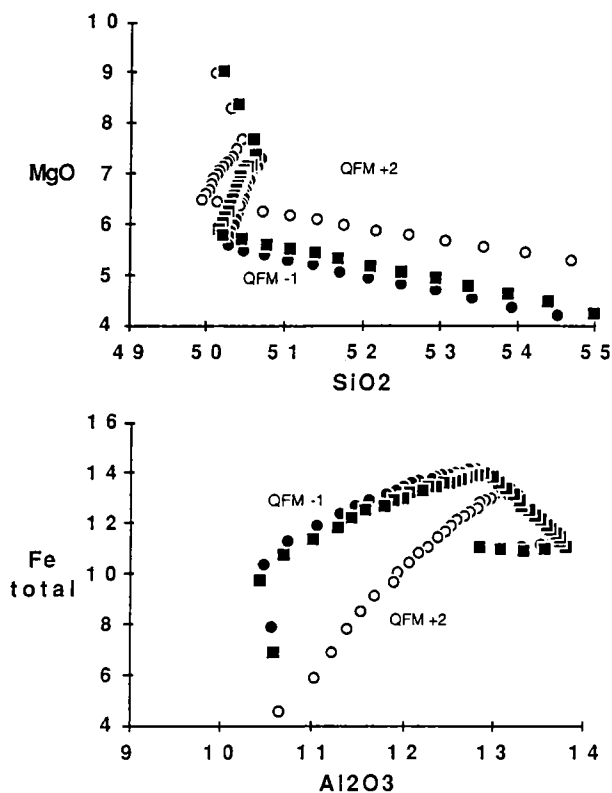


Figure 9. The effect of fO_2 on calculated LLD.

an evolving open system is a balance between the Ni added to the system by recharge, and the Ni being removed by fractionation, as determined by the bulk D for Ni. The Ni content of the evolving liquid in this example begins to rise after it becomes multiply saturated with olivine, plagioclase and augite. The change from olivine to olivine + augite + plagioclase saturation causes the bulk D for Ni to drop due to the relatively low D for Ni and plagioclase. Thus, fractionation is less effective at removing Ni, and recharge will cause the Ni content to rise to a level in balance with that new bulk D. This does not happen in the ERUPT simulation because the fractionating mineral proportions are related to the recharge rate. As recharge rate increases, increasing the amount of Ni input into the system, the fractionating mineral proportions of olivine increase, increasing the bulk D and balancing the system's Ni content. This has the additional effect of generating much lower values of Ni in the steady state liquid at a given recharge rate. The factor of two difference in the steady state composition will result in an equivalent error in the estimated recharge rate.

Variable oxygen fugacity

ERUPT has two options for the control of the oxidation state of iron. The first is to assume that the oxygen fugacity is controlled externally. One way to simulate this is to assume that the fugacity will remain constant relative to the QFM buffer. The $\text{Fe}^{+2}/\text{Fe}^{+3}$ can be calculated from the relationship between melt composition and temperature (Kilinc et al., 1983). The other option assumes the system is closed to oxygen. This is simulated by assuming that Fe^{+2} and Fe^{+3} act as separate components. The $\text{Fe}^{+2}/\text{Fe}^{+3}$ ratio is set by the proportion of the fractionating phases.

A simple test of the effects of varying the fugacity, and the mechanism for fugacity control, liquid lines of descent for several scenarios were calculated beginning with a parent magma taken from the lavas erupted from the Pu'u O'o eruption of Kilauea (Wolff et al., 1987). The three sets of results are shown in Figure 9. In the first case (filled circles) the system was fixed at one log unit below the QFM buffer. The second case was for a fugacity two log units above QFM (open circles). In the third case, $\text{Fe}^{+2}/\text{Fe}^{+3}$ was set by the fractionating mineralogy (filled squares). For this last calculation I set the initial $\text{Fe}^{+2}/\text{Fe}^{+3}$ ratio to the value calculated for the liquidus temperature and at the QFM buffer. Therefore, this third calculation started at a oxidation between the first two sets of calculations. For all calculations, the distance between the points represents 2% fractional crystallization.

There are several differences between the results at 1 log unit below the QFM buffer and those at 2 log units above QFM. The most obvious is relatively rapid depletion in Fe and enrichment in Si under more oxidizing conditions. In addition, higher fO_2 also causes augite to crystallize earlier, causing an initial depletion in Si relative to the more reduced conditions. Only after titanomagnetite begins to crystallize does the Si content begin to increase.

The results from the closed system calculations suggests that for this system, the internal buffer determined by the equilibria between augite, plagioclase, basaltic liquid and titanomagnetite is between QFM and one log unit below QFM. The accuracy of this prediction is dependent upon the accuracy of our predictions of the phase equilibria for the major phases, particularly the oxide phases.

Periodic mixing

Stratigraphically correlated compositional information from many natural systems suggests mixing episodes are separated by quiescent periods of fractional crystallization (Reagan and Gill, 1987; Wolff et al., 1988). We can model this periodicity by allowing the system fractionate for a interval measured in terms of % crystallization between mixing

events. How and when mixing occurs is another question. In many natural suites, the most evolved magma is erupted first, suggesting that during a recharge event, evolved magma resident in the chamber is pushed out prior to any mixing with the primitive magma. If the magma flux is large, all the evolved magma will be pushed out before mixing can occur. In that case, each fractionation path would be the same, beginning at the parent magma composition.

Another related point is the regularity, or lack thereof, of the periodicity and mixing parameters. Given the information evident from records of active systems, the periodicity is almost certainly not regular. A regular sampling or mixing interval has the unfortunate consequence of producing artifacts within the modeled results. For example (Fig. 10a), results calculated from a Hawaiian basaltic parent with the model parameters 2-0-1 and recharge at intervals of 20% crystallization, creates a cluster of data at 9% MgO, 11.4% CaO. This cluster exists only because of the regularity of the model parameters.

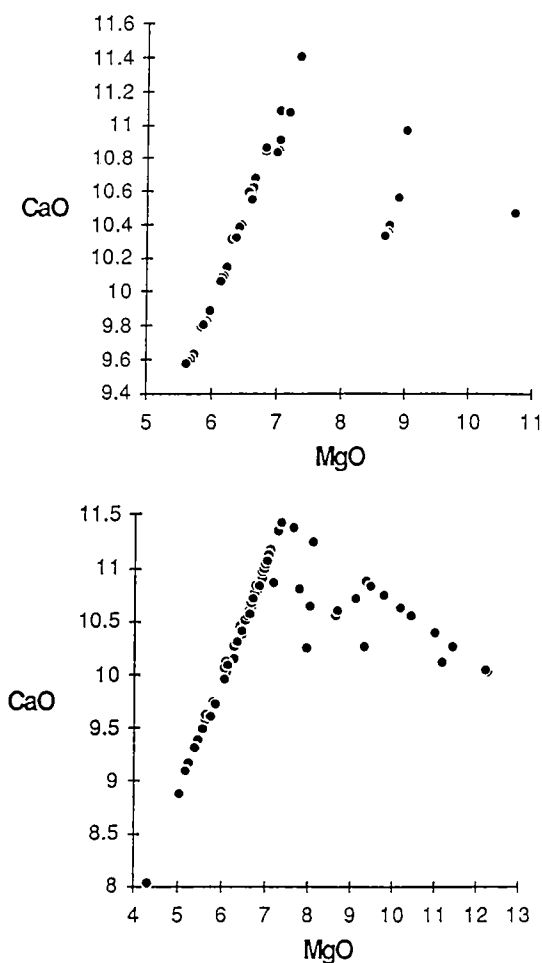


Figure 10. Calculated data sets for (a) fixed mixing parameters and (b) randomized mixing parameters. Note that the regular distribution of points in (a) is disrupted in (b).

The next question is, if not regular, how is mixing irregular. At least partly due to a lack of any evidence to the contrary, the periodicity of the model parameters was assumed to have a normal distribution. This was simulated in the program by multiplying the model parameter by a random number each time the parameter was applied. The random number is selected from a file of 10^4 random numbers that have a mean of 1 and a standard deviation of 0.33. The program then multiplies the input model parameter by it. Therefore, the long term average model parameters remain fixed, but on the short term they are irregular. We can have some confidence then that any regular patterns generated in the data are due to the phase equilibria constraints. The pattern evident in the results of a model using randomized mixing parameters (Fig. 10b) illustrates the tight distribution near the olivine, plagioclase, augite cotectic at $\text{MgO} < 7\%$. In addition, the artificial clusters at high MgO are gone.

The program ERUPT has the ability to vary the periodicity, make it bimodal, or randomize the parameters. This results in an large number of possible variants. Figure 11 shows the frequency distribution for two cases where the periodicity has been randomized. In the first case the calculations were for a bimodal distribution of periodicity at 5 and 10%. This results in a single, asymmetric distribution. The second case is for a bimodal distribution at 5 and 30% periodic. Here we can see the frequency of the short periods separated from the long periodicities. The program assumes that the number of short periods in a bimodal distribution will be an average of five times as common as the long periods.

In spite of the irregularity of many of the parameters involved in the petrogenesis of natural systems, there are some basic rules that all systems must follow. First, is that the any distribution of magma compositions must be constrained by the phase equilibria. An example of this can be seen in the simulated data set illustrated in Figure 12. These results were generated assuming fractional crystallization alone, bounds the data set generated assuming a recharge rate of 2 and an eruption rate of 1 (2-0-1). Mixing was assumed to be periodic at an interval of 35% with all mixing parameters randomized. Note that even though periodic mixing generated scatter, all the compositions generated are inside the curve representing the case of perfect fractional crystallization (open circles). This illustrates another point, the shape of the fractionation curve determines the aspect ratio of the synthetic data distribution. This is in turn dependent on the periodicity of the system, the size of the mixing events and parent magma composition, and most importantly, the phase equilibria of the system. The curvature in the Ca-Mg fractionation trend in Figure 12 is due to the beginning of augite and plagioclase crystallization at 7.5% MgO and 11.5% CaO. If the fractionation curve is straight or only slightly curved, mixing will simply drive the composition back up the fractionation curve, resulting in little scatter, and an apparently simple pattern. In general, when the fractionation and mixing vectors are in the same or opposite directions, there will be relatively little scatter. If these vectors are at a high angle to one another and/or the magnitude of each is large, there will be greater scatter. In addition, the vector length will change as the magma composition evolves. Unless the vectors caused by each of the active processes are individually recognizable and can be evaluated separately, it is difficult to interpret information from mixed systems.

In situ fractionation

Up to this point, our modeling has assumed that crystallization takes place homogeneously throughout the magma chamber. The crystals formed are then either assumed to be immediately removed from the system, or to reside in the magma and to remain, at least to some degree in chemical communication with the evolving magma. In either case, the crystals being formed are exclusively the liquidus phase(s), and the liquid path is therefore determined by the removal of those components.

The assumption of homogeneous crystallization has been made in spite of field evidence and numerical modeling of cooling bodies suggesting that heat loss and therefore

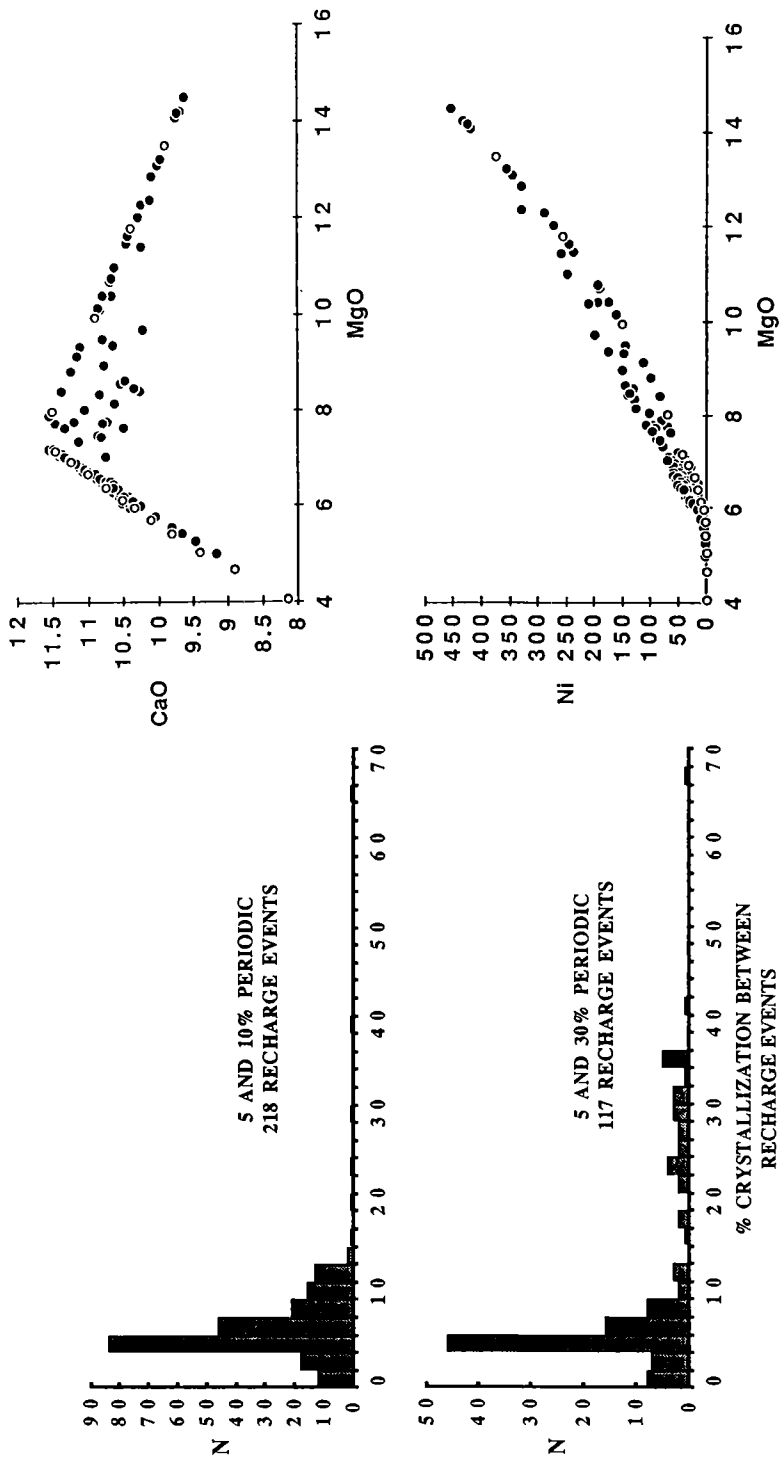


Figure 11. Frequency diagram for randomized periodicities.

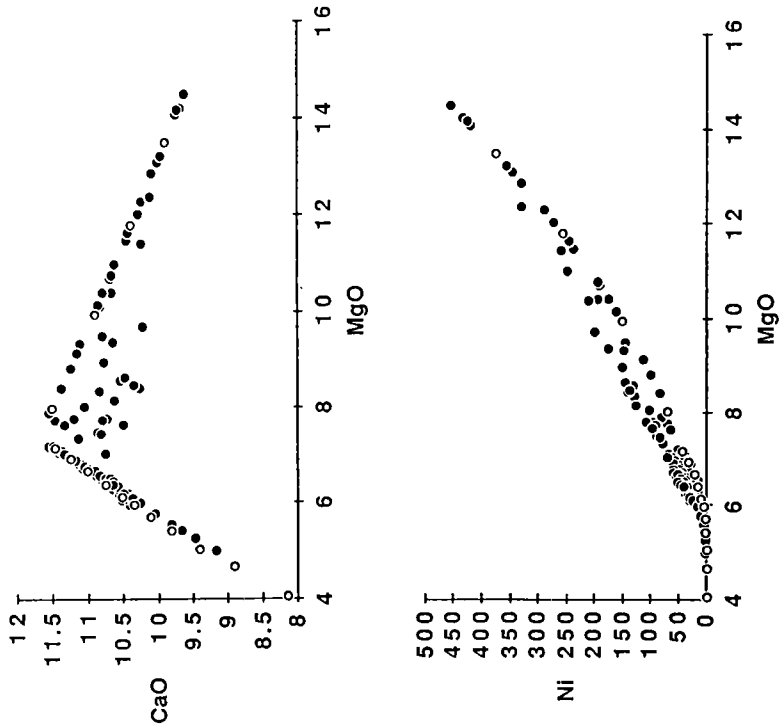


Figure 12. Comparison of synthetic data sets generated by simple fractional crystallization (open circles) and a data set generated by periodic recharge and fractionation (closed circles). The model parameters are 2-0-1 and 35% periodic. Sampling interval, recharge and eruption rates, and periodicity were randomized.

crystallization should occur primarily near or on the magma chamber walls (Jackson, 1961; Campbell, 1978; McBirney and Noyes, 1979). In an analytical approach to this problem, Langmuir (1989) proposed a model for in situ crystallization that occurs in a solidification zone at the boundaries of the evolving magma chamber. The evolved melt generated in the solidification zone is assumed to migrate back into the main magma body. Thus, the system evolves by the fractionation of the mineral assemblage in the solidification zone. That mineral assemblage, and the liquid composition that migrates out of the solidification zone is dependent upon the degree of crystallization that occurs in the solidification zone prior to the point where the cumulates are no longer permeable.

Even though in situ fractionation is essentially a magma mixing process, there is a critical difference between it and recharge. In recharged systems, the magma chamber fractionates only the liquidus phase(s), and the liquid is constrained to the cotectics as the magma evolves. In addition, recharge will always drive the magma composition back towards a fixed composition, that of the parent magma. For in situ crystallization, the magma composition is not constrained to the cotectic. As the system evolves, the magma trapped in the solidification zone will also evolve. Therefore, there is no fixed reference point, any effects of fractionation are positively reinforced. For paired homogeneous fractionation and recharge, the magma chamber composition is relatively evolved, remaining near the cotectic. For in situ fractionation, the magma chamber is relatively primitive compared to the magmas entering it from the solidification zone.

In order to simulate in situ crystallization, an increment of the magma chamber is segregated and allowed to crystallize to a given amount, then the residual magma is mixed into the magma chamber. The process is repeated, driving the magma towards the composition of the trapped liquid. If the size of the segregated solidification zone magmas is sufficiently small, the result will be the same as if the trapped liquids were removed continuously. The dynamics of the process can be seen by considering the results shown in Figure 13 for the Uwekehuna parent given in Table 2. The magma is assumed to crystallize 70% in the solidification zone prior to extraction. A homogeneous fractionation LLD is added for reference.

In the first iteration, 5% of the magma chamber is segregated into the solidification zone and allowed to crystallize 70%. That magma, equivalent to 1.5% of the magma chamber, is then added to the remaining 95% of the magma chamber. Another 5% of the mixed magma is then segregated and allowed to crystallize 70%. The residual liquid produced by 70% crystallization of the mixed liquid will be different from the first increment of evolved magma produced in the solidification zone, because the starting point, the composition of the magma chamber, is more evolved. As the process continues, the composition of both the solidification zone liquids, and the magma chamber evolves, positively reinforcing the effects of fractionation. The model assumes that the % liquid in the solidification zone never increases. As the process continues, the composition of both the solidification zone liquids, and the magma chamber evolves toward the moving target represented by the solidification zone liquids. This can be illustrated in another way by a comparison of projections of calculated in situ and homogeneous fractionation liquid lines of descent (Fig. 14). The homogeneous fractionation path moves from olivine saturation directly to the olivine-augite-plagioclase cotectic, then towards low Ca pyroxene and the quartz apex. In situ fractionation drives the liquids directly toward the quartz apex while remaining saturated with olivine alone.

One important aspect of in situ fractionation is the saturation of the solidification zone with respect to phases that normally appear late in the crystallization sequence. Specifically, mafic magmas can be expected to saturate with oxides and apatite when the % crystallization in the solidification zone is high. These phases are commonly found in gabbros, but are relatively rare in lavas. In order to better simulate fractionation in the solidification zone, apatite was added to the fractionating mineralogy by adding the expressions of Harrison and Watson (1984). It is quite possible that magmas can be pro-

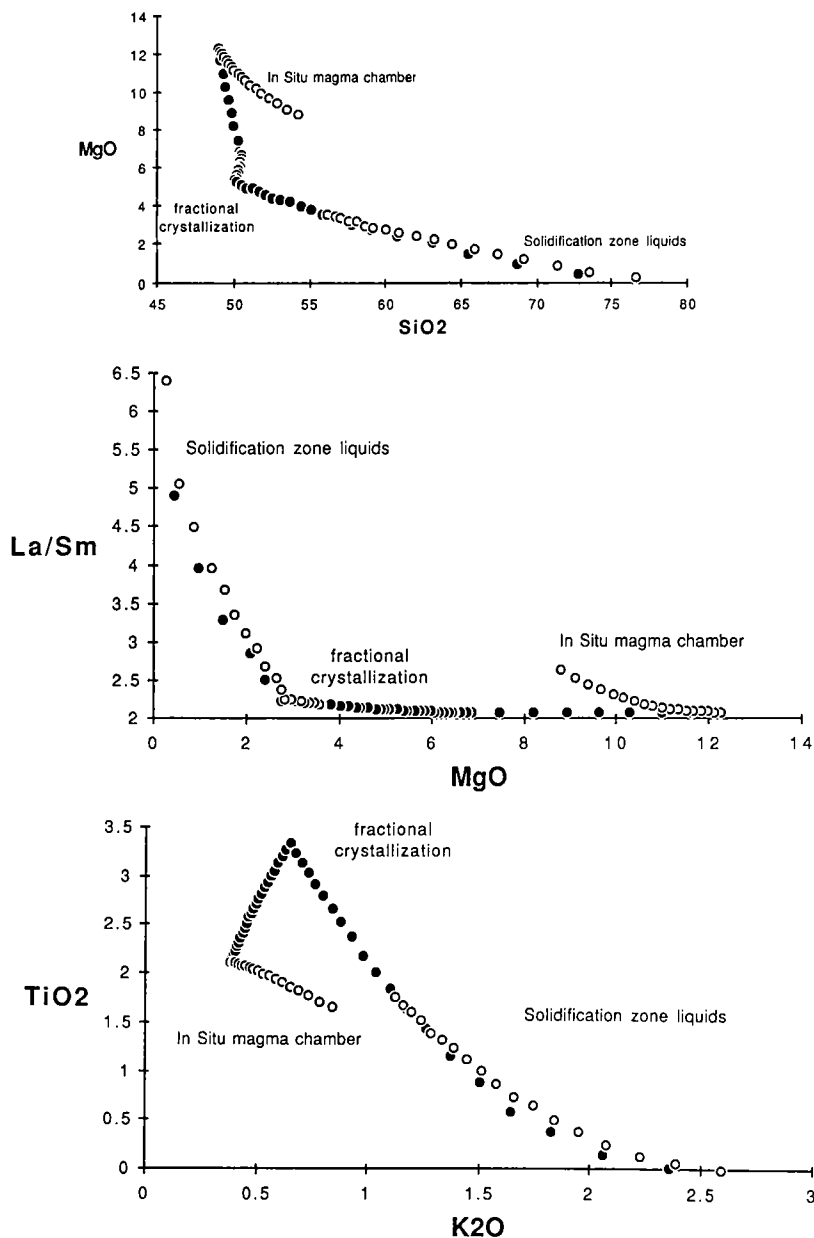


Figure 13. Comparison of results of uniform fractional crystallization (filled circles) and in situ fractionation (open circles). Solidification zone liquids are the product of 70% fractionation of the magma segregated into the solidification zone. These magmas are then added to the evolving magma chamber.

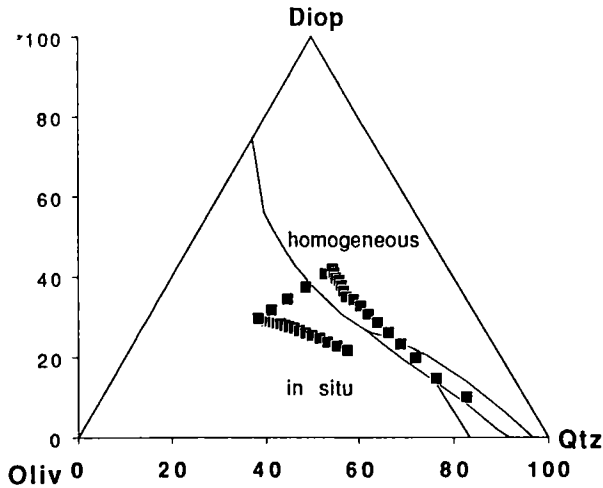


Figure 14. In-situ and homogeneous crystallization liquid lines of descent projected onto pseudo-ternary as calculated by Grove et al. (1982). Note that the multiply-saturated liquids are richer in diopside components than the liquids used by Grove et al. to derive the diagram. This is consistent with the composition of the Kilauean lavas.

duced by in situ fractionation, including fractionation of minor phases, yet if liquid extraction is efficient, those phases would not be evident in the erupted lavas. The chemistry of the lavas would nevertheless be influenced by the fractionation of those phases. This can be seen in plots of the calculated liquids (Fig. 15) calculated assuming different amounts of crystallization in the solidification zone. As the % crystallization in the solidification zone increases, the Ca, Ti and P enrichments characteristic of homogeneous fractionation disappear. The composition of the calculated liquids for the simulation assuming 70% crystallization in the solidification zone do not show the Ti enrichment evident in the fractionation trend because titanomagnetite is being removed in the solidification zone. Yet if erupted, the magma chamber liquids would be saturated with olivine alone. This characteristic will be evident for any component that is being withdrawn in the solidification zone. For example, if augite is crystallizing in the solidification zone, the magma removed from that zone will have been influenced by augite and consequently when it mixes with the magma chamber will cause the suppressed Ca trend seen in Figure 15. Likewise, if apatite is crystallizing in the solidification zone, the P enrichment in the differentiating liquids will be suppressed. The pattern of which elements are effected is dependent not only on the % crystallization in the solidification zone, but also on the phase equilibria of the system.

The ability to produce magmas with a variety of incompatible element ratios in relatively primitive, high Mg lavas has generally been attributed to processes active in the mantle. One important exception is the hypothesis of O'hara and Mathews (1981) who stated that in open magma systems, where the magma chamber is continuously being recharged as it fractionated, it was possible to generate magmas characterized by a wide range of incompatible element contents. We can test this hypothesis by simulating paired fractionation and recharge using ERUPT. In this first example, it was assumed that the recharge rate was double the crystallization rate, and magma was erupted at a rate equal to the crystallization rate. A comparison of the results of these calculations (Fig.16) with simulations of homogeneous fractionation alone, and in situ fractionation show how it is possible with in situ fractionation to increase the La/Sm ratio of the system by 20-30%, and still be saturated with olivine alone ($MgO > 7.1\%$). Paired recharge and homogeneous fractionation can produce increases in incompatible element ratios where there is a significant difference in the element's partitioning behavior, such as La/Sm., but it can not produce increases in La/Sm and remain primitive in composition (high MgO). The reason

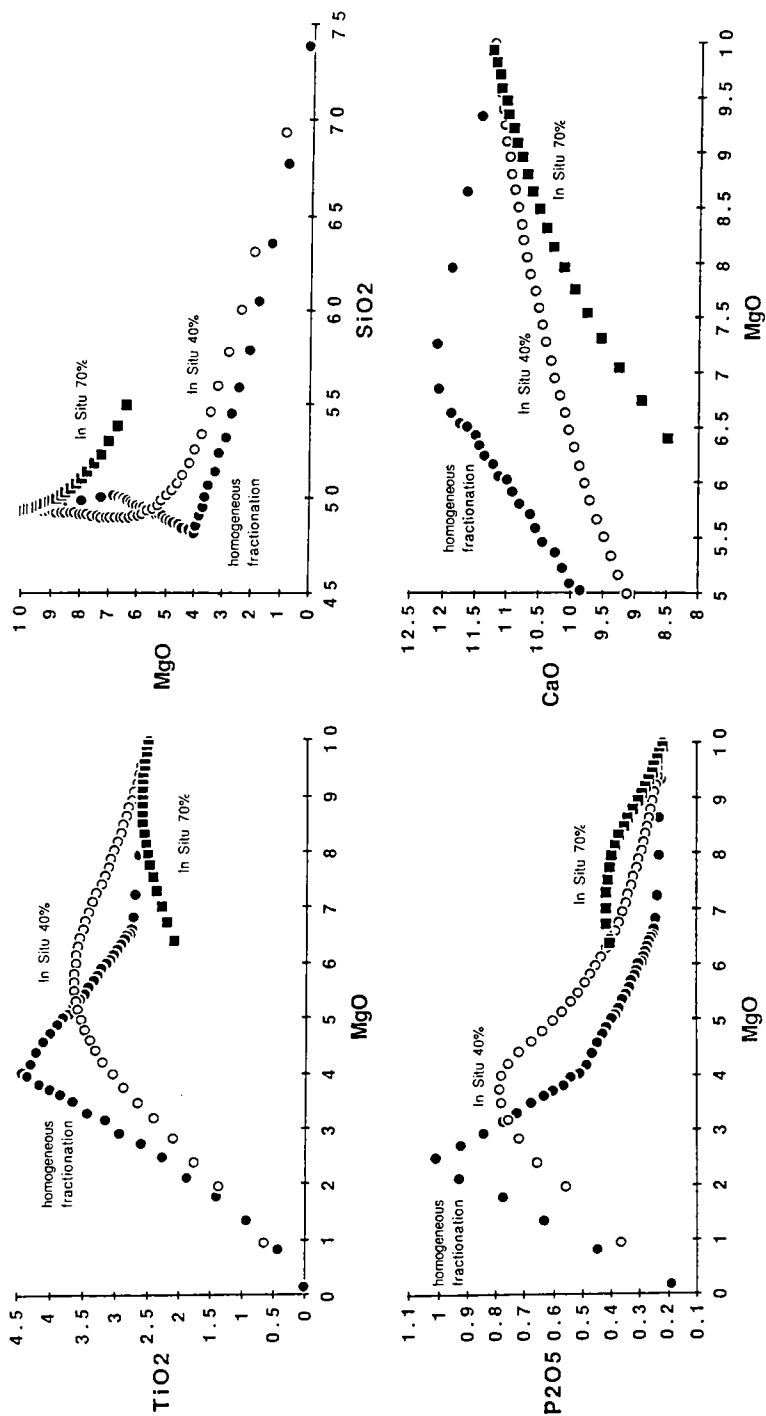


Figure 15. Simulated LLD for homogeneous fractionation, and two in-situ fractionation scenarios, one at 40% fractionation and the other at 70% fractionation in the solidification zone.

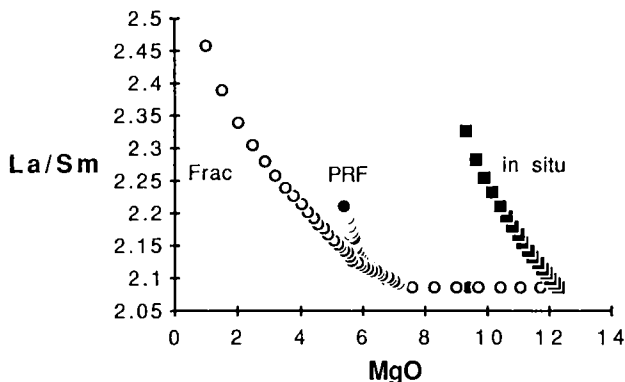


Figure 16. Simulated LLD comparing the results of paired fractionation and recharge, fractional crystallization alone, and in-situ fractionation.

for this is the difference in the basic mechanism for mixing in the two cases. In paired homogeneous fractionation, recharge and eruption, the entire magma chamber is fractionating while a relatively minor amount of primitive material is added. With in situ fractionation, the system evolves by mixing in a small amount of magma with an extreme composition, particularly with respect to its trace element character. Addition of this material will have a much larger effect on the trace element patterns of the mixture than on the major element characteristics.

TESTING PETROLOGIC TOOLS WITH MODELED RESULTS

The use of the results of modeled results as synthetic data sets to test modeling tools is a well established technique in other fields of geology such as geophysics. Their use in petrology has not been common, partly because of a lack of a reliable means of accurately simulating igneous processes. The advantage of using a set of simulated compositions as if it were a real data set, is that you have control over the processes involved in the generation of the trends. Therefore, you know what information is in the "data", and thus can determine how effective a given technique is at extracting information in a coherent form.

Calculation of parental magma compositions

In order to calculate any realistic scenario, one first needs a starting point. If our current hypotheses regarding the degree to which natural magma systems are open to recharge and eruption, it is probably rare that the magma composition representing the parental magma is actually erupted to the surface. However, to estimate such parameters as recharge rate and periodicity, the parental magma composition must be known. For systems where we believe the parent is olivine saturated, one approach is to select a composition near, but slightly above the point where the magma becomes multiply saturated with augite or plagioclase. These magmas have seen the least augite or plagioclase fractionation. We can then run the composition through the program to see how close the magma is to multiple saturation. Compared with the rest of the suite, the chosen composition should be low in incompatibles and high in elements such as Sc and Sr at a given MgO content.

We then run the composition through the program backwards, adding olivine incrementally until the liquid was in equilibrium with Fo₉₀ olivine. The actual point at which one stops the calculation depends on the discretion of the modeler. The end product of this set of calculations is a parent magma composition that is consistent with at least part of the data set that is to be modeled. This is not to say that it is necessarily consistent with the entire data set. That depends on the extent to which the parental magma varied in the

natural system. Given this starting point, we can then generate synthetic data sets that can be used for a variety of purposes, including the evaluation of the currently available petrogenetic modeling tools.

Least-squares-mass balance fractionation models

If, as we have stated above, recharge causes a change in the fractionating mineral proportions, this should be evident from the calculated liquid lines of descent. Mass balance calculations are a commonly used method for the estimation of modal proportions of fractionated assemblages from natural systems (e.g., Bryan et al., 1968; Wright and Doherty, 1971; Stormer and Nicholls, 1978). To assess the validity of mass balance calculations, we have applied the calculations to our simulations. Our analysis uses the Bryan et al (1968) mass balance model, but any methodology will yield similar results. As an initial test, we used the results of the homogeneous fractional crystallization simulation (000) calculated for the olivine tholeiite parent (Table 2) calculated from the Uwekehuna Bluff sequence in Hawaii (Casadevall and Dzurisen, 1987). Calculated liquid lines of descent (Fig. 5) show the inflection points caused by the change in fractionating mineralogy as the magma evolved. The starting composition for the mass balance calculation was taken from the point where the olivine-augite-plagioclase cotectic was reached, and the derived liquid composition was taken from the point where the magma began to crystallize oxides. The composition of the fractionating phases was chosen from the calculated results at the midpoint between the two liquid compositions. The mass balance model results (Table 3) reproduced the phase equilibria generated results, with a small sum of the squares of the residuals, and the same proportions of the fractionating phases as those generated by ERUPT.

The same test was applied to the results for the recharged simulation (201) calculated by ERUPT, again assuming homogeneous crystallization. The application of mass balance calculations to the calculated results in this case is similar to the case where a petrologist might apply mass balance calculations to a suite of rocks they believe to be related by fractional crystallization alone, but where the system actually underwent recharge. The starting liquid for the mass balance calculations was selected at the point where the system first encountered the olivine-augite-plagioclase cotectic, the final liquid was the steady state composition which was, in this case, perched on the olivine-plagioclase cotectic. Again, the mineral compositions were chosen from the calculated compositions. The mass balance model results indicate the liquids are related by 25% fractional crystallization of olivine, plagioclase and augite, with the mineral proportions virtually identical to those calculated for the (000) simulation. These bear no resemblance, however, to the actual mineral proportions or % fractionation calculated by ERUPT. At this recharge rate, however, fractionation is still powerful enough to drive the magma continuously back to the olivine-augite-plagioclase cotectic. All the compositions generated lie near that cotectic and thus, can be related to one another by the fractionation of the cotectic mineral proportions. From the major element results, it is clear that mass balance models cannot be used to detect magma mixing in natural systems, and if used, can imply that simple fractional crystallization was the only process taking place.

The trace element liquid lines of descent are not constrained by this process because they are not buffered by the cotectic. As stated above, major element liquid lines of descent follow the same cotectic generated by the 0-0-0 simulation, regardless of the recharge rate. Many of the trace elements, however, follow divergent paths. If the percent fractionation from the 2-0-1 results are calculated using the simple Rayleigh-distillation equation, the results are a function of the bulk D for that element (Table 3). Elements with high D, have a small calculated % fractionation, whereas the incompatible elements are relatively enriched and generate high % fractionation, in this case by approximately 50% compared to the mass balance results. These are characteristic of compositional patterns reported for many large basaltic systems.

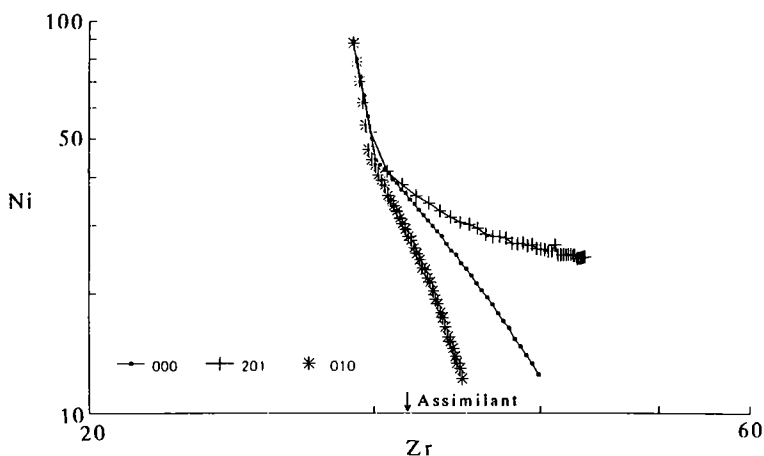


Figure 17. Log-log plot of Ni versus Zr for a variety of simulations. Tangents to the LLD have been used to calculate bulk partition coefficients (Table 4). The assimilant is a tonalite-trondhjemite (Table 1).

Table 5. Bulk distribution coefficients calculated from three synthetic data sets (ERUPT), and slopes of tangents (tangent) to points along the curves in Figure 17 based on the assumption that the slope = $(1 - D_{Ni})$ for any log-log diagram.

| | D_{Ni} tangent | D_{Ni} ERUPT | Ni(ppm) | Zr(ppm) |
|--------------|---------------------|-------------------|---------|---------|
| 0-0-0 | | | | |
| point 1 | 15.29 | 14.99 | 52 | 39 |
| point 2 | 3.83 | 3.87 | 31 | 45 |
| point 3 | 5.07 | 4.02 | 24 | 49 |
| point 4 | 4.16 | 4.17 | 20 | 59 |
| point 5 | 5.16 | 4.82 | 13 | 59 |
| 2-0-1 | | | | |
| point 1 | 3.16 | 7.00 | 40 | 42 |
| point 2 | 2.45 | 5.65 | 32 | 47 |
| point 3 | 2.92 | 6.07 | 29 | 52 |
| point 4 | 2.46 | 6.09 | 27 | 58 |
| point 5 | 1.00 | 6.40 | 25 | 63 |
| 0-1-0 | | | | |
| point 1 | 17.51 | 13.97 | 66 | 39 |
| point 2 | 4.71 | 5.14 | 44 | 40 |
| point 3 | 9.28 | 5.46 | 37 | 41 |
| point 4 | 5.92 | 4.79 | 26 | 44 |
| point 5 | 5.34 | 4.76 | 18 | 47 |

Table 6. Pearce element ratios used to make mole mineral indices. Compositions are in terms of cation-normalized mole fractions.

| Mineral | Indices |
|-------------------|---|
| Molar olivine | $0.25 \text{ Al} + 0.5(\text{Mg} + \text{Fe}) - 0.5 \text{ Ca} - 0.25 \text{ Na}$ |
| Molar plagioclase | $0.5 \text{ Na} + 0.5 \text{ Al}$ |
| Molar augite | $\text{Ca} + 0.5 \text{ Na} - 0.5 \text{ Al}$ |

Derivation of D from log-log plots

Allegre et al. (1977) showed that log-log diagrams may be effective in the analysis of fractional crystallization. If the bulk D for an element remained constant, then any magma undergoing fractional crystallization will be represented by a straight line on a log-log diagram. The slope of the line will be $(D_y - 1)/(D_x - 1)$ where D_x and D_y represent the bulk distribution coefficients for the elements plotted on the x and y axes. Several authors have attempted to use this approach in examining petrogenetic processes (e.g., Masuda, 1965; McCarthy and Hasty, 1976; Clague et al., 1981; Villemant et al., 1981; Gill, 1981; Wyers and Barton, 1987).

Mineral partition coefficients vary as a function of the extent and nature of differentiation. Furthermore, because magmatic processes other than simple fractional crystallization occur simultaneously with evolving magmas, the sense of curvature of liquid lines of descent will not be unique for any one process or combination of processes (Fig. 17). In that case therefore, log-log diagrams could not be used to discriminate between magmatic processes. In addition, bulk partition coefficients will vary as a function of temperature, melt composition and fractionating mineral proportions, all of which are variable as a system evolves.

Recently, Wyers and Barton (1987) have documented fairly continuous curves on log-log diagrams from Patmos (Greece) data. They state that distribution coefficients necessary to explain variations in Sc, V, Ni, Cr and Ba (vs Th) in terms of fractional crystallization may be derived from the slopes of tangents to the curved trends on log-log diagrams, even though they believe that more complex petrogenetic processes have taken place. To test the possibility of approximating D from log-log diagrams by taking tangents to the liquid lines of descent curves, we used a compatible element, Ni on the abscissa and Zr, an incompatible element on the ordinate. Three curves were generated (000,010,201) using ERUPT and an arc basalt from Luzon, the Philippines (Table 2) as a starting composition (Fig. 16). The results are presented in Table 5. D_{Ni} (listed "as from tangent" in Table 5) were determined from the slopes of tangents to points along the curves based on the relationship that the slope is equal to $(D_{Ni} - 1)/(D_{Zr} - 1)$. Because Zr behaves incompatibly, D_{Zr} can be assumed to be 0.0 and the slope becomes $(1 - D_{Ni})$. The D_{Ni} from the simulation using ERUPT are also reported in Table 5 (reported as "from ERUPT" in the table) along with the Zr and Ni ppm values at the points chosen along the curves.

Partition coefficients determined from the slopes of tangents and from the ERUPT simulation are quite similar for the liquid lines of descent generated by fractional crystallization alone (000) (Table 5). The predictions for more complex processes are considerably more dissimilar. Striking variations exist between the D's from the simulation as opposed to those calculated from the slopes of the log-log plots. Clearly, partition coefficients cannot be predicted under these circumstances. In addition, log-log graphs result in the loss of information by compressing the observed variations and the inflection points where the fractionating mineralogy changes are more difficult to see on these plots.

Pearce element ratio analysis

The basic assumption of Pearce element ratio analysis is that petrologic processes can be measured by normalizing system components (molar mineral indices – Table 6) to excluded components (Pearce, 1968). Potentially this technique can be powerful for the determination of many petrologic parameters. However, the technique is inherently sensitive to the validity of a number of its basic assumptions. In particular, it is sensitive to the assumption that a given excluded element is actually effectively excluded ($D \sim 0$) during the entire crystallization sequence, and to contamination involving that element. The extent to which a given element is excluded can be tested by comparison of different Pearce element

ratio diagrams for a given data set. The results calculated by ERUPT affords us an opportunity to check the sensitivity of the technique against a known data set.

The first example uses a starting composition calculated from the data of Casadevall and Dzurisen (1988) from the Uwekehuna Bluff at the edge of the summit crater of Kilauea on the island of Hawaii. I used a technique described above to calculate a potential parental magma from the distribution of the natural data. This model parent is calculated to be in equilibrium with Fogg olivine (Table 2).

The first case we will examine is that of simple fractional crystallization (Fig. 18). The molar mineral components of the simulated data were calculated after the method of Russell and Nicholls (1988) and Stanley and Russell (1988). From the mineral PER plots we can see that the liquidus phase was olivine, followed by augite then plagioclase in quick

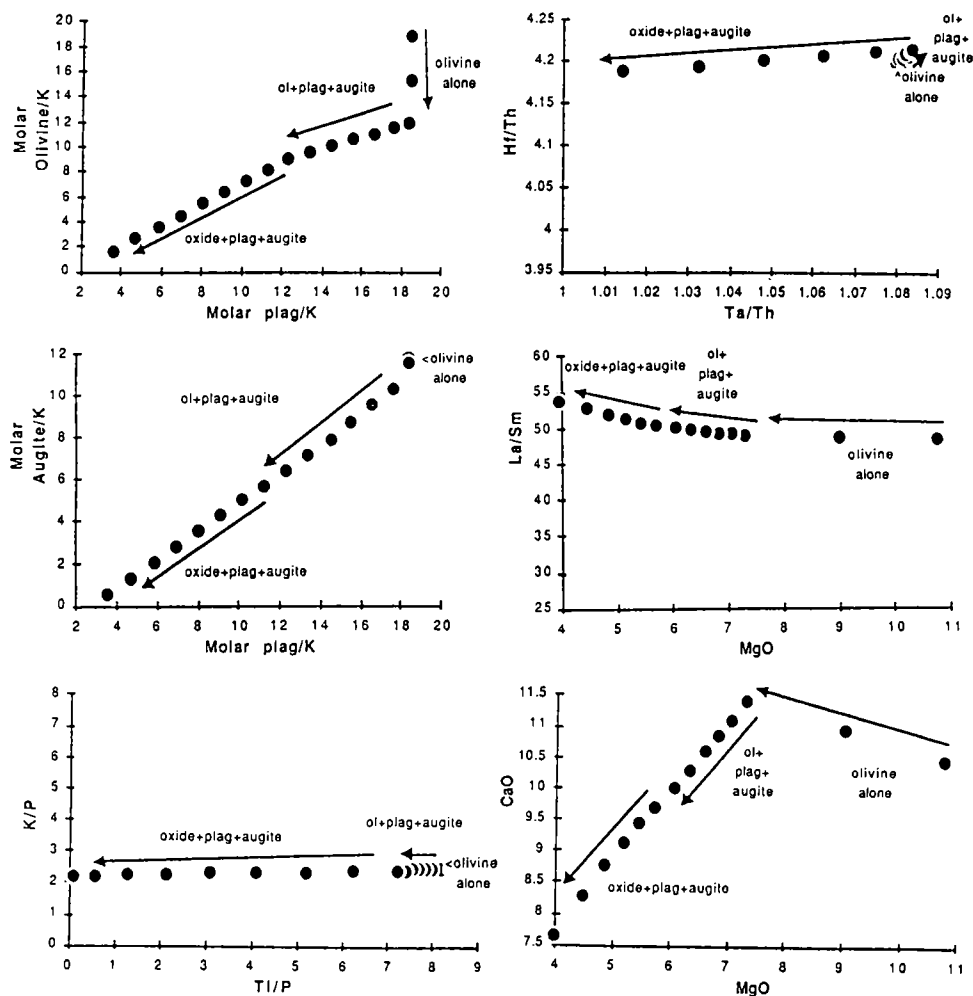


Figure 18. Simulated data set calculated by ERUPT assuming perfect fractional crystallization. Parent magma was calculated from the Uwekehuna Bluff suite using the procedure of Defant and Nielsen, 1989. Mineral components were calculated by the method of Stanley and Russell (1988). Points are separated by intervals of 5% fractional crystallization.

succession. This can also be seen in the CaO vs MgO plot. Because the molar mineral components are referenced to the same excluded element, the slope of a regression through the data is equivalent to the relative fractionating mineral proportions of those minerals, assuming those are the only phases crystallizing. The results in this case indicate that the fractionating mineral proportions on the olivine + augite + plagioclase cotectic were 13:33:54. This is consistent with other determinations of this cotectic at low pressure (Grove and Baker, 1984), with the ERUPT-generated calculations, and with the petrography and experimental work done on similar Kilauean tholeiites (Helz and Thornbur, 1987). The inflection points in the trends at lower molar plg/K are due to the beginning of oxide crystallization. This is better documented in the rapid drop in the Ti/P ratio beginning at that point. Incompatible element ratios such as Hf/Th and Ta/Th, where there is only a small contrast in partition coefficient, are essentially unchanged. As with the calculations documented earlier, La/Lu, an element pair with a slightly greater partition coefficient contrast, shows a significant increase, but only at compositions below 4% MgO.

For the next example, the model parameters used in ERUPT were chosen to simulate the case of homogeneous fractionation paired with recharge and eruption (PRF). The mixing parameters were set at 2-0-1, or recharge rate of 2, and eruption rate of 1 relative to the crystallization rate. Mixing was assumed to occur at an interval of 20% crystallization. The periodicity of mixing, sampling interval, recharge and eruption rate were all independently randomized.

The PER molar mineral plots show that the results (Fig. 19) are heavily influenced by the effect of augite fractionation. This can also be seen in the plots of Ca vs Mg, and to a lesser extent in the La/Lu and Ti/P plots. The effect of recharge is more subtle, but can be determined from examination of the slopes of the molar mineral component plots. Calculation of the slopes on those diagrams, over the interval where olivine, augite and plagioclase are fractionating, again using the method of Stanley and Russell (1988), yields fractionating mineral proportions of olivine (21%), augite (37%), plagioclase (42%). These values are significantly different from those for closed system fractionation (13/33/54), and are consistent with the predicted values for a recharged system with this crystallization sequence at this recharge rate (Nielsen, 1988a, Defant and Nielsen, 1989).

This change in the fractionating mineral proportions can best be described in terms of the relationship of the evolving system to the cotectic. For systems whose parent has the crystallization sequence olivine-augite-plagioclase, as magma is recharged into an evolving multiply saturated magma chamber, the liquid will be pulled into the olivine field. Further crystallization will produce olivine, then olivine + augite, then olivine + augite + plagioclase, as the liquid evolves from one cotectic to another. Thus the long term amount of olivine and augite removed from the system will be greater than the proportions crystallizing along the olivine + augite + plagioclase cotectic in a closed system (Nielsen, 1988a). This variation of fractionating mineral proportions will propagate through to the calculation of the bulk distribution coefficients. Thus the mixing parameters (recharge and assimilation rates) and trace element partitioning are interdependent.

One other important observation regarding these results relates to the relatively little scatter exhibited. This is the case even though the mixing periodicity, sampling interval, recharge rate and eruption rates were all randomized. In fact, very few points lie off the trend representing the cotectic. This tells us that in natural suites, we need to look at a large number of samples before we will find evidence of magma mixing in the glass compositions. In large part, this is due to the small amount of olivine required to push the liquid composition back to the cotectic after each mixing event.

The model calculates titanomagnetite to begin crystallizing at 5.5% MgO. The influence of this is not self evident in plots of the molar mineral components shown here. However, it is clear in the Ti/P and Ta/Th plots. The variation in Ti/P is only partly due to magnetite fractionation. Much of the variation in the range $Ti/P > 7$ is due to the influence

of augite, whose partition coefficient for Ti is ~ 0.5 -1.0. Interpretation of this simulated data suggests that for this set of conditions we can expect a variation by up to 20% due to augite alone. This will be dependent on such parameters as recharge rate, temperature, melt composition and crystallization sequence.

In contrast to the conclusions of O'Hara and Mathews (1981), these results indicate that incompatible element ratios do not change in PRF generated systems. In this example, for magma with $>5\%$ MgO, La/Lu varies by only 4-5%. Only in the more evolved magmas does the variation increase. Thus, for this set of conditions, REE ratios will not vary significantly within the range of basaltic compositions. The small increase that is observed is almost entirely due to the role of augite fractionation. The ratio of elements that have smaller contrasts in their bulk distribution coefficients (e.g., Hf/Th) do not vary enough to be seen above analytical error. For the purposes of petrogenetic modeling,

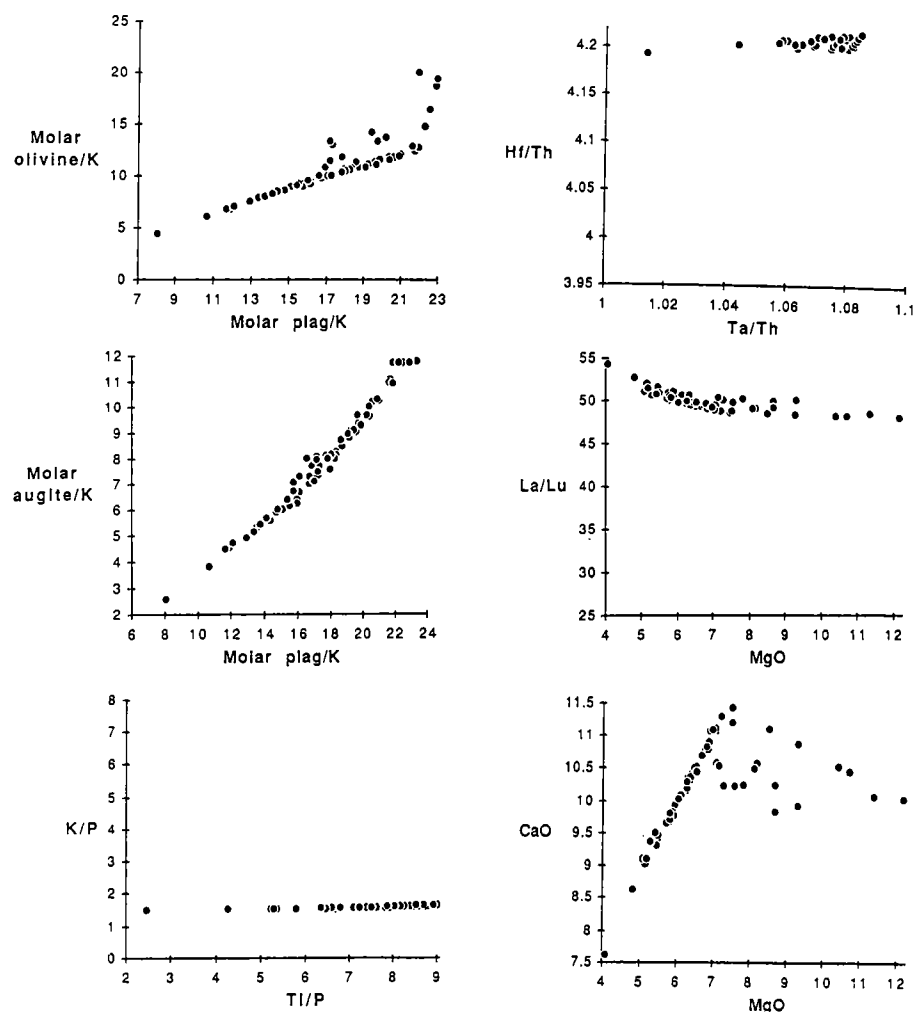


Figure 19. Simulated data set calculated by ERUPT on Uwekchuna parent magma. The model parameters were set to a recharge rate of 2, an assimilation rate of 1, fractional crystallization, parallel to the QFM buffer, 20% fractionation between recharge episodes. Sampling interval, periodicity, recharge rate, and eruption rate are randomized.

variation in those elements can thus be ascribed to other processes (mantle heterogeneity, assimilation, fractionation of high field strength element-rich phases).

Our second example uses a parent (Table 2) taken from Luhr et al. (1988). This is a calc-alkaline basalt with a crystallization sequence, olivine-plagioclase-augite. The model parameters for this simulation were recharge/eruption/crystallization in a ratio of 3/2/1 (3-0-2 simulation). As with the first example, the periodicity of mixing was assumed to be 20%. Periodicity, sampling interval, recharge and eruption rates were all independently randomized.

For comparison, the results for this case are plotted on the same scale as the calculations above (Fig. 20). The fractionating mineral proportions calculated from the slopes on the molar mineral plots are olivine (43), plagioclase (58), augite (-1). Within

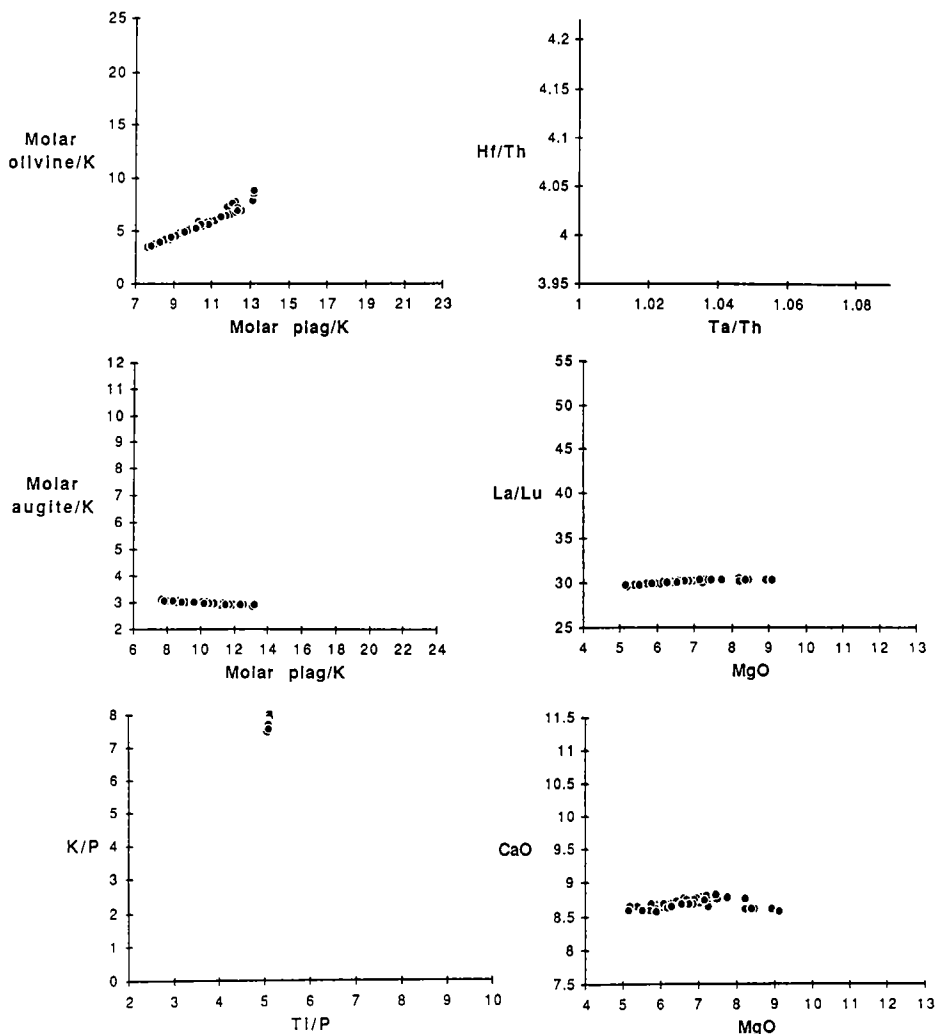


Figure 20. Simulated data set for a calc-alkaline basalt parent from the Colima graben (Luhr et al., 1988). Model parameters are 3-0-2, 20% periodic. Sampling interval, recharge rate, periodicity and eruption rate are randomized. The scales of the plots are the same as Figure 1 for purposes of comparison.

limits, this is consistent with what one expects with recharge with a parent with olivine and plagioclase near the liquidus (Nielsen, 1988a). The negative augite/K value is due to two factors, K is not a perfectly incompatible element (Ernst et al., 1988), and the difference between the stoichiometric mineral components assumed by Stanley and Russell (1988) and the compositions removed by the ERUPT model. No augite was removed by the ERUPT model calculation. The high recharge rate kept the system saturated with olivine and plagioclase alone.

The low partition coefficient for most trace elements between olivine or plagioclase and basaltic liquids results in very small variation in the incompatible element ratios for this system. Due to the smaller role of augite, the partition coefficient contrast for most element pairs is less for this example compared with the Kilauea calculations. The small variation in K/P is due to the effect of K partitioning into plagioclase. Hf/Th, Ta, Th, Ti/P and La/Lu are almost invariant. With any case where olivine and plagioclase are the dominant fractionating phases, there will be little variation in most incompatible element ratios.

The phase equilibria of the parent magma has a large effect on the predicted incompatible element ratio variation. Systems where augite (or amphibole) is on or near the liquidus of the parent, or at least crystallizes before plagioclase, will show more variation in their incompatible element ratios. This could be an important point when considering high pressure fractionation where augite is more stable. The extent of this variation is dependent on the phase equilibria of the parent, temperature, pressure, element of interest, recharge and eruption rates and the periodicity of mixing. Because of the complexity of the interdependence of these variables, each case must be evaluated individually.

Our next comparison is between two models using the Colima basin calc-alkaline basalt parent. The first is the simulated data set described above (3-0-2, PRF). The second is the case where, in addition to a recharge rate of 3 and an eruption rate of 2, we are assimilating a small amount of silicic material (Table 2). The assumed assimilation rate was 0.1, or 1/30 the recharge rate. The periodicity of mixing was assumed to be 20% for both cases. The sampling interval, periodicity, recharge, assimilation, and eruption rates were all independently randomized.

A comparison of the data plotted on the molar mineral component diagrams (Fig. 21) shows that the slope, and thus the proportion of olivine and plagioclase seem largely unaffected. The molar augite/K however, exhibits a wide range of scatter for the 3-0.1-2 case. A linear regression through the augite-plagioclase data would suggest ~10% augite fractionation. No augite was removed by the calculations. The observed pattern is due to a combination of olivine and plagioclase fractionation, paired with mixing between the evolving basalt and a silicic contaminant with a low augite/K ratio.

The role of mixing can be seen in most of the incompatible element ratio diagrams. The larger the chemical contrast between assimilant and basalt, the larger the effect. Considerable variation can be generated in REE ratios even at these low assimilation rates. Although each modeled system will be different, the direction and approximate magnitude of the variation evident in these results should be within the range of typical values.

In contrast, compatible element contents are not very sensitive to small amounts of assimilation. For example, in this comparison, the Ni vs Zr patterns are virtually identical. Thus, in general, compatible elements are more strongly influenced by recharge and fractionation, and incompatible elements are more sensitive to assimilation.

The difference in the calculated mineral proportions calculated by least squares mass balance models and those calculated by PER analysis lies in the fact that in PER the molar mineral components are normalized to a conserved element. As an open, recharged system evolves, the conserved components will remain in the system, their concentrations rising with respect to the more compatible components (O'Hara and Mathews, 1981, Nielsen,

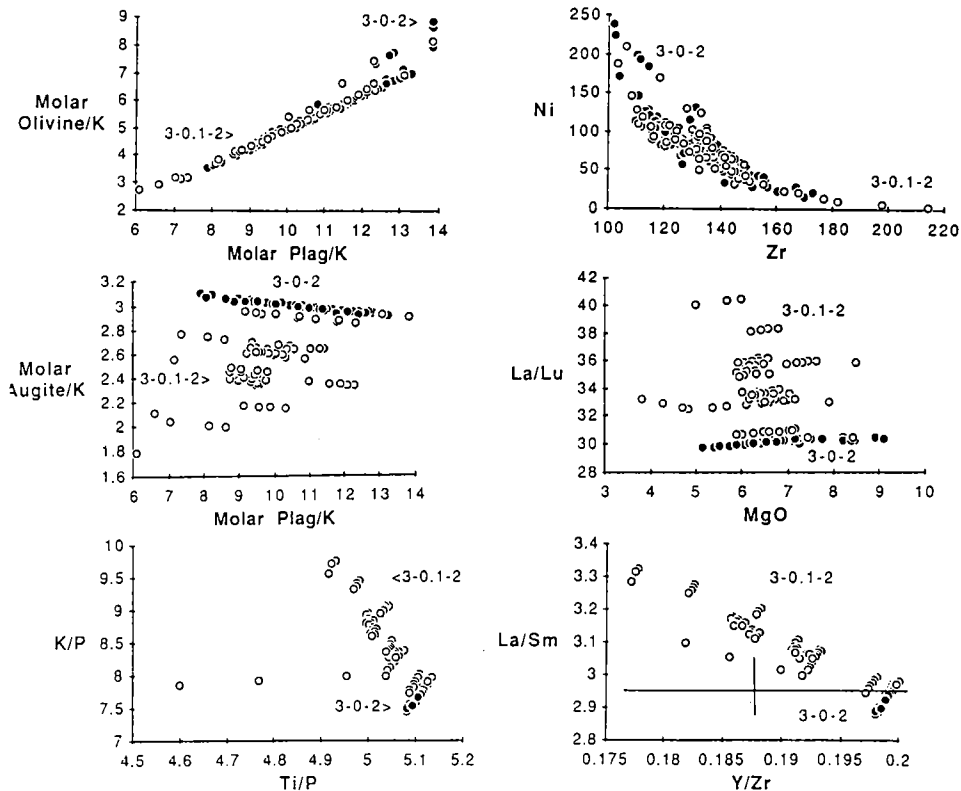


Figure 21. Comparison of simulated liquids generated by PRF (3-0-2 – filled circles) versus FEAR (3-0.1-2 – open circles). Cross on La/Sm versus Y/Zr plot represents typical propagated analytical error.

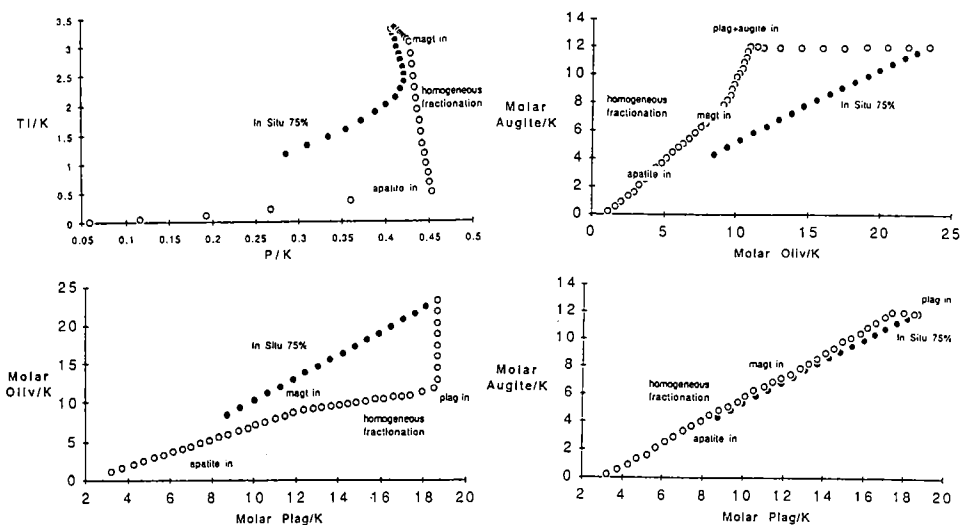


Figure 22. Comparison of the characteristics of homogeneous and in situ fractionation as seen with PER ratio analysis.

1988a). Thus they provide the necessary reference for the PER. Since mass balance models do not take this into account, the results are heavily weighted upon the major element results.

PER analysis of the results of In situ fractionation involve several complications. First, In situ fractionation often involves the fractionation of phases that are not on the liquidus of the main magma chamber, such as oxides or apatite. This can be addressed by PER by constructing diagrams with appropriate axis. PER analysis itself makes no claims involving crystal-liquid equilibria, nevertheless, we as petrologists applying PER generally do. However, rather than toss out PER in cases where in situ crystallization may be an important processes, we can simulate the effect of that process and examine its fingerprint when examined in terms of PER analysis. Figure 22 illustrates the calculated LLD for both homogeneous and in situ fraction for the Uwekehuna parental composition. If we first consider the homogeneous fractionation LLD, the value of normalized molar mineral components reflects the calculated crystallization sequence as described above. Olivine is on the liquidus, followed by augite, then almost immediately, plagioclase. Therefore the path followed by the liquid indicates a drop in olivine/K with constant plagioclase/K and augite/K. When those phases begin to crystallize, those ratios begin to drop, reflected in an inflection point in the curve.

Prior to oxide and apatite fractionation, the Ti/K and P/K ratios vary very little. Ti/K drops due to the partitioning of Ti in augite. P/K actually increases, because K is accepted to a minor degree in feldspar. After titanomagnetite begins to crystallize, Ti/K drops rapidly, followed by apatite crystallization and a drop in P/K. The crystallization of these phases does not show up in the plots of the major mineral PER components. The beginning of oxide fractionation causes a slight inflection in the path related to olivine/K, but it is not large enough to be seen in natural suites due to the contribution of analytical error to the scatter in the data.

The path followed by the in situ fractionation curve is significantly different. All the liquids in this trend are saturated with olivine alone and have MgO contents greater than 8.5%. As with the mass balance model, the implication of the molar mineral plots is that the in situ trend can be produced by fractionation of olivine, augite, plagioclase and titanomagnetite. This is true in the sense that those phases have been removed in the solidification zone, but the liquids in the main magma chamber are not in equilibrium with those phases. If interpreted assuming homogeneous fractionation, one would have to develop a scenario that would allow these liquids to be in equilibrium with all those phases. This is only possible at high pressure. Therefore, similar trends in natural suites have been interpreted as related by high pressure fractionation (Furman et al., 1990). This may be the case, but it is not necessarily so. The alternative process of in situ fractionation should certainly be taken into account when interpreting suites that seem to require high pressure clinopyroxene fractionation, or in cases where parental magma types have been designated on the basis of their incompatible element ratios.

PROBLEM SOLVING IN NATURAL SYSTEMS

Uwekehuna Bluff

Two of the primary questions associated with volcanism in Hawaii are the variability of parental magma types with time and the extent to which low pressure open system processes are responsible for the variety of magma composition observed. The lavas exposed on the Uwekehuna bluff in the rim of Kilauea Crater offer an excellent opportunity for obtaining information regarding the time dependence of the compositional variability of Kilauea. Over 50 flows are exposed in the bluff. Analyses of these flows (Casadevall and Dzurisen, 1987) show that the lavas can be divided into two groups on the basis of both stratigraphy and composition (Fig. 23). From the distribution of the data one

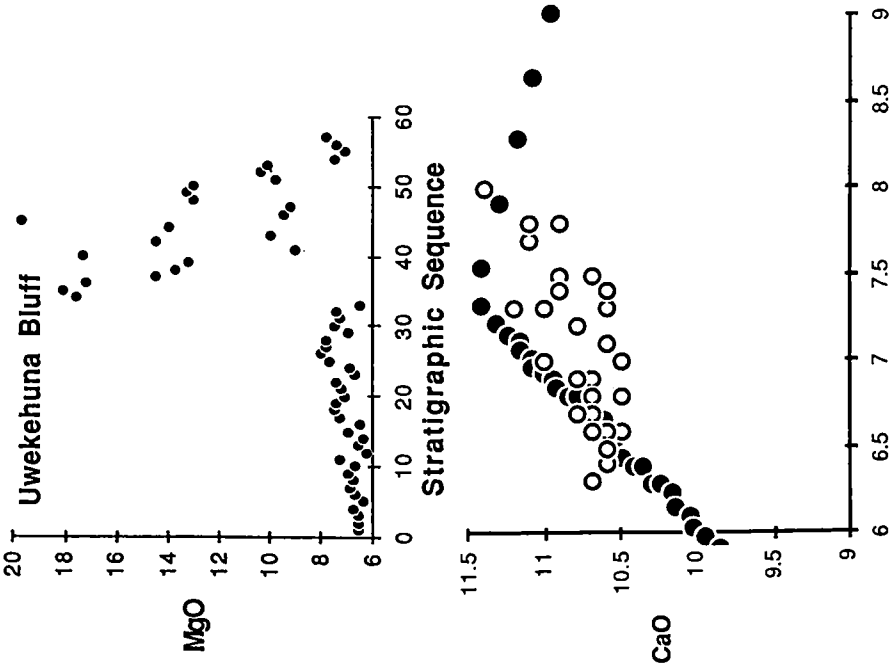
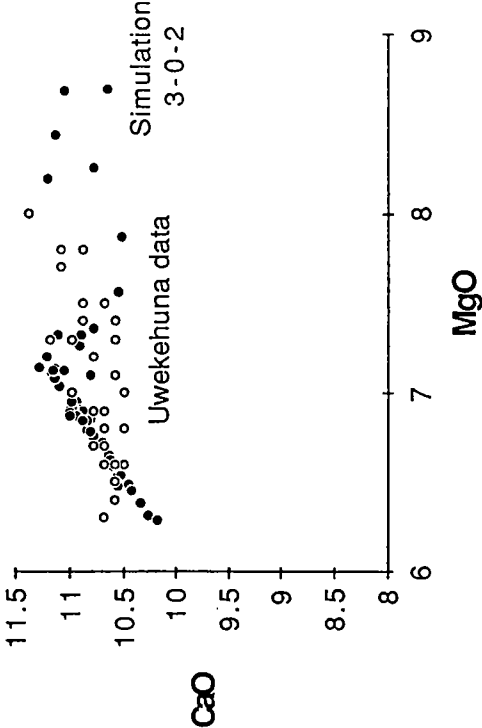


Figure 23 (above, left). Relationship of MgO with stratigraphic position for lavas from the Uwekehuna Bluff (Casedevall and Dzurißen, 1987). Flow 56 is the oldest.

Figure 24 (left). Ca-Mg of Uwekehuna Bluff flows 1-31 (open circles), and calculated fractional crystallization path (closed circles).

Figure 25 (above, right). Comparison of natural bulk composition of flows 1-31 from the Uwekehuna bluff with two synthetic data sets (closed circles) (a) data set generated with model parameters 2-0-1, 20% periodic, (b) data set generated with model parameters 3-0-2, 5 and 10% bimodal periodic.



can see that there is a natural break at flow 32. The early lavas (flows 32+) contain abundant evidence for cumulate olivine. The younger lavas are largely aphyric. Therefore, we will use only the upper 32 flows in these calculations.

The natural data (open circles, Fig. 24) were used to calculate a parental magma composition according to the procedure described above. A homogeneous fractional crystallization liquid line of descent was calculated from that parent (Fig. 24). The modeled data points are separated by 1% fractional crystallization. Note that the natural data fall within the inflection of the calculated trend. Therefore all of our assumptions are internally consistent, but this tells us very little about the dynamics of the system.

In Hawaii, we know that the volcanic system is dynamic and influenced by magma chamber recharge, eruption and fractionation. Therefore we need to model those parameters and to randomize the mixing parameters to avoid artifacts due to regular mixing intervals in order for the simulations to be a realistic reproduction of the active processes.

The first attempt is shown in Figure 25a. The synthetic data were generated at a recharge rate of 2 and an eruption rate of 1. Periodicity was set at an interval of 20%, crystallization was assumed to be homogeneous and all the mixing parameters were randomized. The synthetic data do not covers the correct area, and the range of composition is too large.

The scenario that was found to match the major element distribution of the natural data (Fig. 25b) was a recharge rate of 3 and an eruption rate of 2. Periodicity was bimodal at 5 and 10%. This would mean that ~1/3 of the magma entering the Kilauean magma chamber remained in the edifice as cumulates. One must remember however that these conclusions depend on many of the model assumptions, not least the parental magma composition. If the parent has a lower MgO content, the result would be shorter periodicity and higher flux rate and hence lower % cumulates left behind in the edifice.

Our next test involves the trace element data from this system (Fig. 26). The evidence suggests that there is a systematic change in many incompatible element ratios with time (e.g., La/Sm), yet other ratios are unaffected (e.g., Ta/Th). As noted above, it has been suggested that open system processes can significantly alter incompatible element ratios (O'Hara and Mathews, 1981) if there is a finite difference in the partitioning behavior of the elements.

There are several hypotheses to be considered regarding the origin of the distribution of magma compositions. These include open system processes that are active in the crust, including both in situ and homogeneous fractionation, different degrees of partial melting of a homogeneous mantle, and finally, sampling partial melts of a heterogeneous mantle. We can test the first hypothesis by looking at the calculated variation of incompatible element ratios. The results (Fig. 27) for an open PRF system assuming homogeneous fractionation indicate that the variation of the calculated La/Sm ratio is too small. There is some small increase at low MgO contents, but not within the range of composition represented by the natural data (open circles).

In situ fractionation paired with recharge, however (Fig. 28), can produce the appropriate range of La/Sm values in magmas that are saturated with olivine alone, without a significant increase in the overall concentration of REE, and with a much smaller recharge rate (1.2-0-0.2). The simulated data set does not precisely correspond the the distribution of the natural data, however, fractionation of the liquidus phases in a shallow dike system by homogeneous fractionation will drive those magmas horizontally to lower MgO at a constant La/Sm (arrows).

The La/Sm ratio is more sensitive to differentiation than the Ta/Th ratio because of the greater difference in the partition coefficients for La and Sm. Therefore, any change in

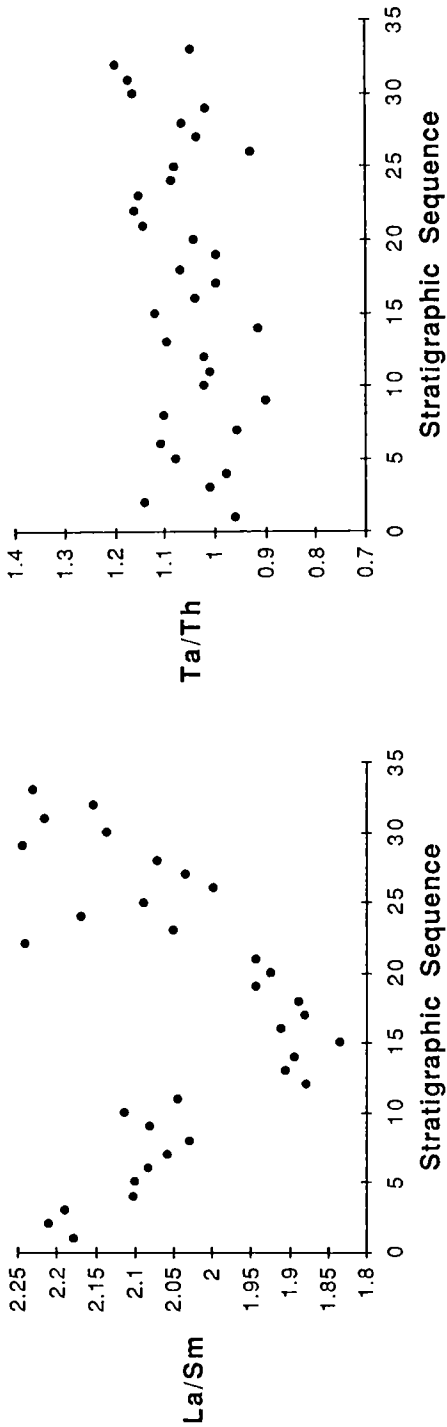


Figure 26 (top, left and right). Correlation of the incompatible element ratios La/Sm and Hf/Th with stratigraphic position.

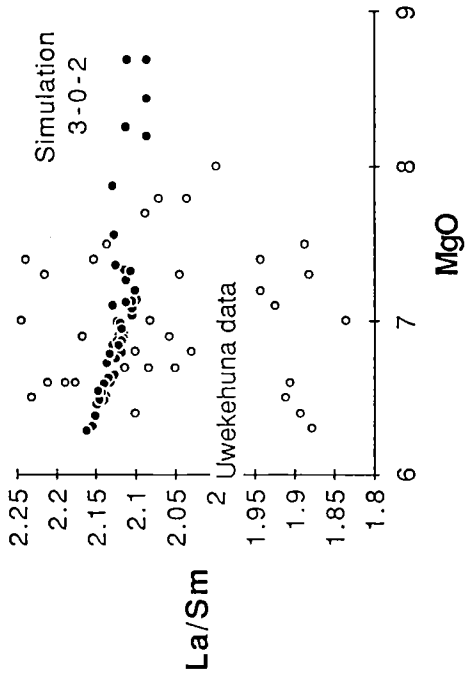


Figure 27 (left). Comparison of natural distribution of La/Sm and MgO (open circles) versus a synthetic data set (3-0-2) (closed circles).

Ta/Th or any equivalent ratio where the partition coefficients are small and similar, is indicative of a heterogeneous mantle. Examination of the natural data indicates no variation in Ta/Th outside of that which can be attributed to analytical error.

In conclusion, the major element composition of the Kilauean lavas are controlled by low pressure fractionation and magma mixing. The crystallization mechanism is a mixture of in situ and homogeneous fractionation. The evidence for in situ crystallization is found most clearly in the trace element signature. Some part of this trace element pattern could be attributed to different degrees of partial melting of the mantle, but there is no evidence for significant heterogeneity in the source region.

Galapagos spreading center

The Galapagos spreading center extends from the East Pacific Rise to the Panama fracture zone. The ridge bisects a magnetic anomaly zone that is characterized by Fe-Ti basalts, andesites and dacites. The anomaly terminates on the west at 95°W longitude and on the east at 85°W longitude. Each of the terminations is characterized by different evolved basalts. At 85°W, the magma trend has a strong Fe, P and Ti enrichment as a function of decreasing MgO. At 95°W these strong enrichments are not present. The maximum TiO₂ is ~2.5% and the maximum P₂O₅ is ~0.22 %. In addition, the 95°W trend is characterized by a lower Fe enrichment, accompanied by slight SiO₂ enrichment. Juster et al. (1989) conducted a series of experiments on the Galapagos basalts to determine the effect of fractionation, olivine addition and increased fO₂ on the LLD. On the basis of their results, they explained the difference in the trends by ascribing the 85°W pattern to low pressure fractional crystallization in a crystal-rich magma chamber where fO₂ was near the QFM buffer. The trends at 95°W were explained by higher pressure crystallization (1-2

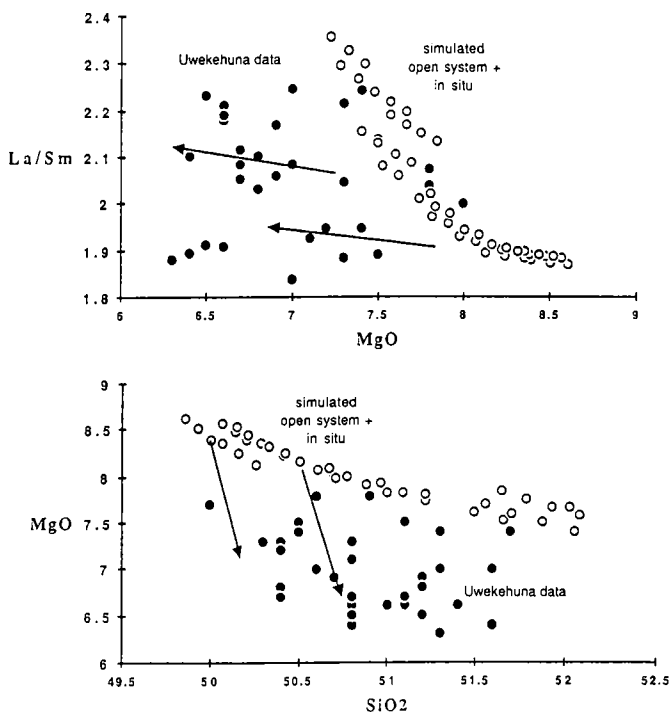


Figure 28. Comparison of natural distribution of La/Sm and MgO (closed circles) versus a synthetic data set involving paired recharge and fractionation (open circles). Arrows represent the path the liquids would follow by homogeneous fractionation.

kbar) in a relatively crystal poor magma chamber. The composition of low P_2O_5 andesites at 95°W were explained by mixing between the rhyodacites and evolved basaltic magmas. The relatively low Ti and Fe enrichment trajectories in the 95°W lavas was attributed to fractionation at higher fO_2 , due either to a lack of olivine re-equilibration or reaction with oxidized wallrocks. In addition, the 95°W have a more rapid drop in CaO (relative to MgO) than the 85°W lavas. This point was not addressed by Juster et al. (1989), but presumably could be ascribed to higher pressure fractionation where clinopyroxene fractionation would have a greater influence. Thus, a variety of processes were required by Juster et al. (1989) to explain the differences in the trends at the Galapagos Spreading Center.

The experimental reproduction of the trends characteristic of the lavas at 85°W by Juster et al. (1989) can be confirmed by simulating differentiation under the same conditions (Fig. 29). The effects of homogeneous fractionation of the parent magma used by Juster et al. (1989) were calculated assuming incremental addition of Fo₉₀ olivine and fO_2 set at QFM. In addition, a homogeneous fractionation LLD was calculated assuming no olivine addition. Olivine addition produces a Ti trajectory that is enhanced, and an Fe trajectory that is suppressed compared to homogeneous fractionation alone. The natural data from 85°W are close to both simulations and are consistent with fractionation paired with olivine re-equilibration.

As predicted by Juster et al. (1989) the 95°W lavas do not match either trend. Nor do they match a fractionation trend calculated at NiNiO + 2. To evaluate the applicability of in situ fractionation to this problem, an in situ fractional crystallization scenario was calculated assuming 50% crystallization in the solidification zone, and fO_2 set at the QFM buffer. The results show many of the characteristics associated with the trends at 95°W, including suppression of Ti, Fe, Ca and P enrichment trends at MgO = 4-7%. As with the example above, in situ fractionation will drive the evolving magma directly toward the composition of the solidification zone magmas, not along any specific cotectic. Inflections in the LLD are caused by the beginning of crystallization of a new phase in the solidification zone. This simulation does not explain all the information, such as mixing textures in the 95°W andesites, but it does suggest that most of the geochemical data can be explained by a single low pressure fractionation process. In addition, the use of this process to explain the differences between 85° and 95°W does not preclude other processes such as differentiation at high pressure, mixing or assimilation, all of which may have occurred simultaneously.

Kilauea Iki – olivine resorption

In her treatment of the liquids generated during the evolution of the Kilauea Iki lava lake, Helz (1987b) noted a correlation between the Fe/Al ratio of the liquids and the amount of olivine present. In environments with abundant olivine, the liquid had a relatively low Fe/Al ratio. She inferred that this was related to olivine resorption. In order to test this hypothesis we must decide on several model parameters. If xenocrystic olivine is being resorbed, it is effectively behaving as an assimilate. The composition of this assimilated olivine was assumed to be Fo₉₀ with 2000 ppm Ni. The parent magma composition was taken from a glass analysis from the same eruption (Table 2). The results show that the homogeneous fractional crystallization liquid line of descent traces a path high in Fe and low in Al compared to the range of the natural data (Fig. 30). Increased olivine re-equilibration decreases the Fe/Al ratio of the liquid. The actual reactions taking place in the calculations vary as the system evolves. From 10-8% MgO, the reaction is Fo₉₀ olivine reacting to form a more Fe rich olivine. At ~7.5% MgO, augite begins to crystallize, and below 7% MgO, plagioclase begins to crystallize. Below 5.5% MgO, the reaction is olivine to augite, plagioclase and Fe-Ti oxides. The results indicate that for every 1% crystallization, the liquid dissolved 0-0.15% forsteritic olivine.

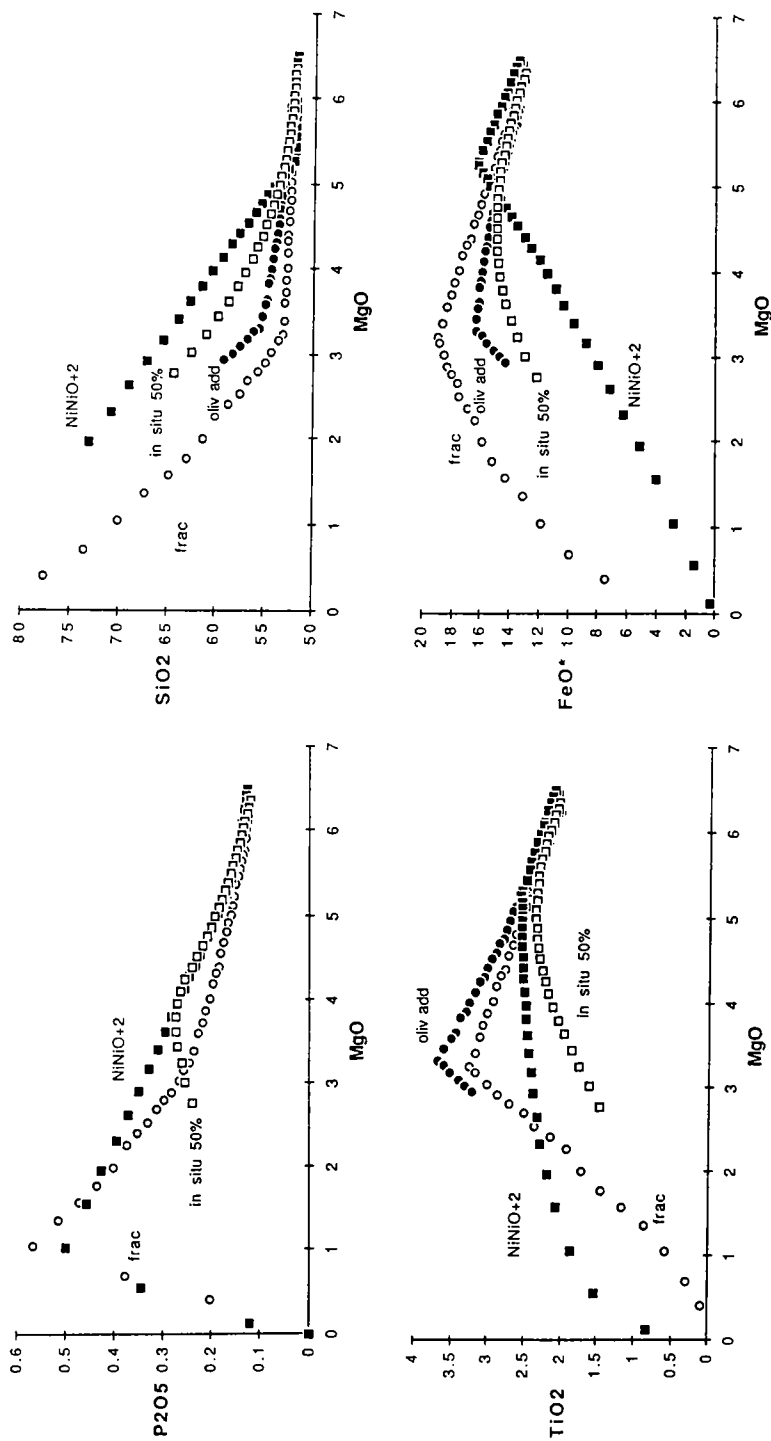


Figure 29. Calculated LLF using starting composition of Juster et al.(1989) for homogeneous fractionation at QFM (frac-open circles), olivine addition (closed circles); homogeneous fractionation at NINiO+2 (filled squares); and in situ fractionation at QFM assuming 50% crystallization in the solidification zone (open squares).

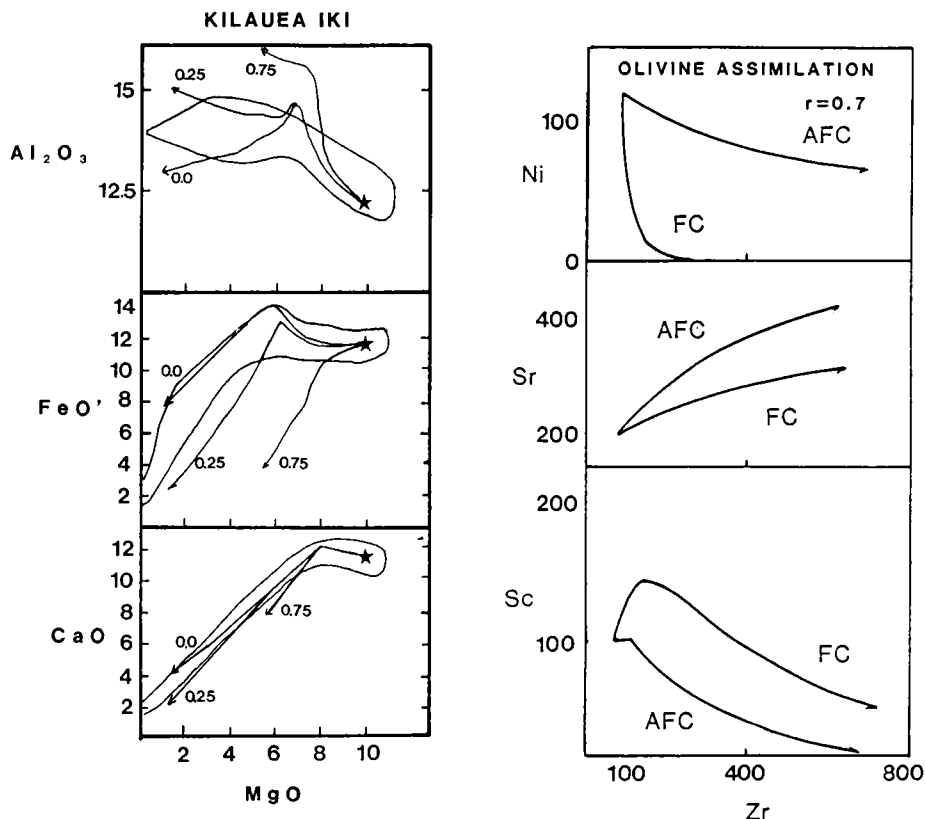


Figure 30. Comparison of calculated liquid lines of descent with data from Kilauea Iki whole rock and glass analyses (envelopes – Helz, 1987). The three simulations represent different levels of olivine re-equilibration, paired with fractional crystallization. They represent fractional crystallization alone, 0.25% olivine resorption/1% crystallization, and 0.75% olivine resorption/1% crystallization. Parent magma for these calculations is a glass from a Kilauea Iki flow (Helz, 1987). Calculated crystallization sequence: olivine at the liquidus, augite at 7.9% MgO, plagioclase at 7% MgO, titanomagnetite at 5.5-6% MgO. The experimental results (Helz, 1987) on a similar rock were olivine on the liquidus, augite at 1172, plagioclase at 1163, ilmenite at 1106 and magnetite at 1090.

The trace element consequences of olivine resorption are equally significant. In addition to suppressing the Fe-enrichment and Al depletion characteristic of low pressure fractionation of basalt, the assimilation of olivine generates liquid lines of descent with elevated Ni. However because of an increase in the augite/plagioclase ratio in the fractionating mineral proportions, the Sc liquid lines of descent is lower and Sr liquid lines of descent is higher for the assimilation calculations (Fig. 30). Therefore, we not only can confirm the inference of Helz (1987b), but we can quantify the amount of olivine resorption, and we can predict the trace element trends.

CONCLUSIONS

The real power of phase-equilibria based differentiation calculations is the ability to simulate differentiation processes that can not be adequately investigated in an experimental apparatus. This not only provides us the ability to describe the magnitude of such open

system parameters such as recharge rate, periodicity, and fractionation mechanism, but also allows us to calculate results that can be used as synthetic data sets. These are ideal for testing the techniques we currently use for interpreting geochemical, petrographic and field information because the relative roles played by different processes are known.

Even though the recently developed methods for calculating mineral-melt equilibria are critical to our ability to accurately simulate natural systems, the mathematical constraints that we use to describe how mixing, eruption, assimilation, etc., interact are equally important. The patterns of geochemical data we use to interpret how magma systems work are dependent on how and when each of the processes interact. This is one of the other primary roles of modeling, the testing of the sensitivity of the chemistry of magma systems to various mixes of processes.

Future development in this field is dependent on two factors. First, the improvement and expansion of the experimental data base used to calibrate our mineral-melt constraints. Second, and equally important, an increase in the interaction between model builders and model users. Without detailed information on the characteristics of natural systems, accurate modeling is impossible.

ACKNOWLEDGMENTS

This work was supported by NSF grant EAR-87-20683. I thank Kelly Russell and Jim Nicholls for asking me to contribute to this short course and my colleagues at OSU for keeping me steered toward the real world.

REFERENCES

- Allegre, C.J., Treuil, M., Minster, J.F., Minster, B. and Albarede, F., 1977, Systematic use of trace elements in igneous processes. Part I: Fractional crystallization processes in volcanic suites. *Contrib. Mineral. Petrol.* 60, 57-75.
- Beeson, M.H., 1976, Petrology, mineralogy, and geochemistry of the East Molokai volcanic series, Hawaii. U.S. Geol. Surv. Prof. Paper 961, 53 p.
- Berman, R.G. and Brown, T.H., 1984, A thermodynamic model for multicomponent melts, with application to the system $\text{CaO-Al}_2\text{O}_3\text{-SiO}_2$. *Geochim. Cosmochim. Acta* 48, 661-678.
- Berman, R.G. and Brown, T.H., 1987, Development of models for multi-component melts: analysis of synthetic systems. In: *Thermodynamic modeling of geological materials: Minerals, fluids and melts. Reviews in Mineralogy* 17, 405-442.
- Bryan, W.B., Finger, L.W. and Chayes, F., 1969, Estimating proportions in petrographic mixing equations by least squares approximation. *Science* 163, 926-927.
- Casadevall, T.J. and Dzurisen, D., 1987, Stratigraphy and petrology of the Uwekahuna Bluff section, Kilauea caldera. In: Decker, R.W., Wright, T.L. and Stauffer, P.H., eds., *Volcanism in Hawaii*. U.S. Geol. Surv. Prof. Paper 1350, 351-376.
- Clague, D.A., Frey, F.A., Thompson, G., and Rindge, S., 1981, Minor and trace element geochemistry of volcanic rocks dredged from the Galapagos Spreading Center: Role of crystal fractionation and mantle heterogeneity. *J. Geophys. Res.* 86, 9469-9482.
- Davidson, P.M. and Lindsley, D.H., 1985, Thermodynamic analysis of quadrilateral pyroxenes. Part II. Model calibration from experiments and applications to geothermometry. *Contrib. Mineral. Petrol.* 91, 390-404.
- Defant, M.J. and Nielsen, R.L., 1989, Interpretation of open system petrogenetic processes: Phase equilibria constraints on magma evolution. *Geochim. Cosmochim. Acta*, in press.
- DePaolo, D.J., 1981, Trace element and isotopic effects of combined wallrock assimilation and fractional crystallization. *Earth Planet. Sci. Lett.* 53, 189-202.
- Drake, M.J., 1976, Plagioclase-melt equilibria. *Geochim. Cosmochim. Acta*, 40, 457-466.
- Ernst, R.E., Fowler, A.D. and Pearce, T.H., 1988, Modelling of igneous fractionation and other processes using Pearce diagrams. *Contrib. Mineral. Petrol.* 100, 12-18.

- Furman, T., Frey, F.A., Jakobsson, S.P., Park, Kye-Hun, 1990, Petrogenesis of mildly alkaline lavas from Vestmannaeyjar, Iceland: The Eldfell (1973) and Surtsey (1963-1967) eruptions. *Contrib. Mineral. Petrol.*, submitted.
- Gallahan, W.E. and Nielsen, R.L., 1989, Experimental determination of the Partitioning of Sc, Y and REE between high Ca pyroxene and natural mafic liquids. *EOS Trans. Am. Geophys. Union* 43, 1402.
- Ghiorsso, M.S. and Carmichael, I.S.E., 1985, Chemical mass transfer in magmatic processes II: Application in equilibrium crystallization, fractionation and assimilation. *Contrib. Mineral. Petrol.* 91: 691-722.
- Gill, J.B., 1981, *Orogenic Andesites and Plate Tectonics*. Springer-Verlag, New York, 390 p.
- Grove, T.L. and Baker M.B., 1984, Phase equilibrium controls on the tholeiitic versus calc-alkaline differentiation trends. *J. Geophys. Res.* 89, 3253-3274.
- Harrison, T.M. and Watson, E.B., 1984, The behavior of apatite during crustal anatexis: Equilibrium and kinetic considerations. *Geochim. Cosmochim. Acta* 48, 1467-1477.
- Helz, R.T., 1987a, Diverse olivine types in lava of the 1959 eruption of Kilauea Volcano and their bearing on eruption dynamics, in *Volcanism in Hawaii*. U.S. Geol. Surv. Prof. Paper 1350, 691-722.
- Helz, R.T., 1987b, Differentiation behavior of Kilauea Iki lava lake, Kilauea Volcano, Hawaii. An overview of past and current work. In: *Magmatic Processes: Physicochemical Principles*, B.O. Mysen, ed., 241-258.
- Helz, R.T. and Thornbur, C.R., 1987, Geothermometry of Kilauea Iki lava lake, Hawaii. *Bull. Volc.* 49, 651-668.
- Irving, A.J., 1978, A review of experimental studies of crystal/liquid trace element partitioning. *Geochim. Cosmochim. Acta* 42, 743-770.
- Juster, T.C., Grove, T.L. and Perfit, M.R., 1989, Experimental constraints on the generation of FeTi basalts, andesites, and rhyodacites at the Galapagos Spreading Center, 85°W and 95°W. *J. Geophys. Res.* 94, B7, 9251-9274.
- Langmuir, C.H., 1980, A Major and Trace Element Approach to Basalts. Ph.D. dissertation, State Univ. of New York at Stony Brook, 331 p.
- Langmuir, C.H., 1989, Geochemical consequence of in situ crystallization. *Nature* 340, 199-205.
- Luhr, J.F., Allen, J.F., Carmichael, I.S.E., Nelson, S.A., and Hasenaka, T., 1988, Primitive calc-alkaline and alkaline rock types from the western Mexican Volcanic Belt. *J. Geophys. Res.* 94, B4, 4415-4530.
- Masuda, A., 1965, Geochemical constraints for rubidium and strontium in basic rocks. *Nature* 205, 555-558.
- McBirney, A.R. and Noyes, R.M., 1979, Crystallization and layering of the Skaergaard intrusion. *J. Petrol.* 20, 487-554.
- McCarthy, T.S. and Hasty, R.A., 1976, Trace element distribution patterns and their relationship to the crystallization of granitic melts. *Geochim. Cosmochim. Acta* 40, 1351-1358.
- Nathan, H.D. and Van Kirk, K., 1978, A model of magmatic crystallization. *J. Petrol.* 19, 66-94.
- Nekvasil, H., 1986, A theoretical thermodynamic investigation of the system Ab-Or-An-Qz(H₂O) and implications for melt speciation. Ph.D. dissertation, Pennsylvania State Univ., University Park, PA, 267 p.
- Nielsen, R.L., 1985, EQUIL.FOR: a program for the modeling of low-pressure differentiation processes in natural mafic magma bodies. *Comp. Geosci.* 11, 531-546.
- Nielsen, R.L., 1988a, A model for the simulation of combined major and trace element liquid lines of descent. *Geochim. Cosmochim. Acta* 52, 27-38.
- Nielsen, R.L., 1988b, TRACE.FOR: A program for the calculation of combined major and trace element liquid lines of descent for natural magmatic systems. *Comp. Geosci.* 14, 15-35.
- Nielsen, R.L., 1989, Phase equilibria constraints on AFC generated liquid lines of descent: Trace element and Sr and Nd isotopes. *J. Geophys. Res.* 94, 787-794.
- Nielsen, R.L., Davidson, P.M. and Grove, T.L., 1988, Pyroxene-melt equilibria: An updated model. *Contrib. Mineral. Petrol.* 100, 790-811.
- Nielsen, R.L. and Dungan, M.A., 1983, Low pressure mineral-melt equilibria in natural anhydrous mafic systems. *Contrib. Mineral. Petrol.* 84, 310-326.
- O'Hara, M.J., and Mathews, R.E., 1981, Geochemical evolution in an advancing, periodically replenished, periodically tapped, continuously fractionating magma chamber. *J. Geol. Soc. London* 138, 237-277.
- Pearce, T.H., 1968, A contribution to the theory of variation diagrams. *Contrib. Mineral. Petrol.* 19, 142-157.
- Reagan, M.K. and Gill, J.B., 1974, Co-existing calc-alkaline and high-niobium basalts from Turrialba Volcano, Costa Rica: Implications for residual titanates in arc magma sources. *J. Geophys. Res.* 94, 4619-4633.
- Roeder, P.L., 1974, Activity of iron and olivine solubility in basaltic liquids. *Earth Planet. Sci. Lett.* 23, 397-410.
- Russell, J.K. and Nicholls, J., 1988, Analysis of petrologic hypotheses with Pearce element ratios. *Contrib. Mineral. Petrol.* 100, 223- 245.

- Stanley, C.R. and Russell, J.K., 1988, PEARCE.PLOT: a Turbo-Pascal program for the analysis of rock compositions with Pearce element ratio diagrams. *Comp. Geosci.* 14, 233-259.
- Stormer, J.C. and Nicholls, J., 1978, XLFRAC: a program for the interactive testing of magmatic differentiation models. *Comp. Geosci.* 4, 143-159.
- Villemant, B., Joron, J.L., Jaffrezic, H., Treuil, M., Maury, R. and Brousse, R., 1980, Cristallisation fractionnée d'un magma basaltique alcalin: la série de la Chaîne de Puyes: II. *Geochimie. Bull. Minéral.* 103, 267-286.
- Wolff, E.W., Garcia, M.O., Jackson, D.B., Koyanagi, R.Y., Neal, C.A., and Okamura, A.T., 1987, The PuuOo eruption of Kilauea Volcano, episodes 1-20, January 3, 1983, to June 8, 1984. *U.S. Geol. Surv. Prof. Paper* 1350, 471-508.
- Wright, T.L. and Doherty, P.C., 1970, A linear programming and least squares computer method for solving petrologic mixing problems. *Geol. Soc. Am. Bull.* 81, 1995-2008.
- Wyers, G.P. and Barton, M., 1987, Geochemistry of a transitional ne-trachybasalt-Q-trachyte lava series from Patmos (Dodecanesos), Greece: further evidence for fractionation, mixing and assimilation. *Contrib. Mineral. Petrol.* 97, 279-291.

THE MATHEMATICS OF FLUID FLOW AND A SIMPLE APPLICATION TO PROBLEMS OF MAGMA TRANSPORT

INTRODUCTION

Among the least understood processes which contribute to the formation of igneous rocks are the mechanisms by which magmas move within and on the surface of the earth. Understanding these phenomena requires learning the physics of deformable materials. The purpose of this chapter is to introduce and review the equations describing fluid flow, to provide a qualitative understanding of their implications for magma behavior and to solve a single, simple application. This application, although somewhat unrealistic, displays the techniques and problems of modeling magma transport.

The problems of magma transport can be placed into categories by the geologic settings where transport takes place:

1. Formation of pockets of melt in the source region and collection into a body whose behavior is dominated by the physical properties of the melt phase.
2. Movement as a discrete body. There are at least two mechanisms for this regime:
 - A. Diapiric movement where the surrounding rocks can deform by flowing.
 - B. Movement along cracks where the surrounding rocks deform by breaking.
3. Movement on the surface of a planet where there is a free surface to the flow.

Between each setting there are transition stages. These transition stages may be where processes with significant effects on the rock texture and composition occur. These stages are among the more poorly understood ones. In addition, within each setting there can be changes in the properties of magma flow. Details of some of the possible changes and their causes are discussed in other chapters. The example in this chapter deals with movement along cracks.

MATHEMATICAL OPERATORS

This section is a review of the mathematical operators and concepts used to express the equations describing fluid flow. The notation for expressing the equations of fluid flow would be very complex if only partial derivatives were used. It turns out, however, that there is a pattern of partial derivatives that is repeated in many if not all the equations. These patterns have been collected and called operators. Use of operators renders the equations neater and more concise although at first glance they appear more mysterious. The two important ones are:

$$\nabla^2 = \partial^2 / \partial X^2 + \partial^2 / \partial Y^2 + \partial^2 / \partial Z^2 \quad (1)$$

and:

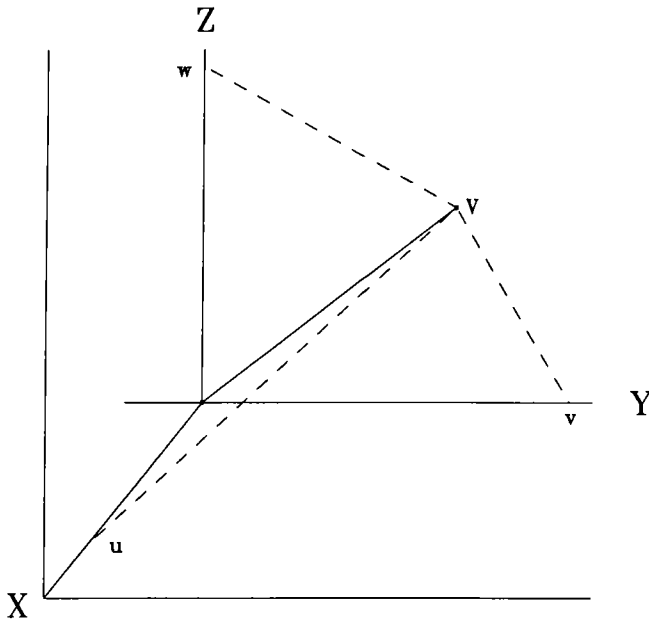


Figure 1. Schematic illustration of the coordinate system discussed in the text. \mathbf{V} is the velocity vector, u , v , and w are the components of the velocity vector along the coordinate axes.

$$D/Dt = \partial/\partial t + u \partial/\partial X + v \partial/\partial Y + w \partial/\partial Z \quad (2)$$

In these operators X , Y , and Z are the coordinates of a position in a flow field, t is the time and u , v , w are the components of the velocity vector at the point (X, Y, Z) and at time t . The components, $[uvw]$, of the velocity vector are respectively parallel to the X , Y , and Z axes of the coordinate system. A convenient coordinate system is shown on Figure 1. The coordinate system is such that X is positive toward the reader, Y is positive towards the right and Z increases upward.

These operators, ∇^2 and D/Dt , must have a function on which to operate. This function can depend on position and time and can be either a scalar like temperature or a vector like velocity. To illustrate, suppose a current of magma is flowing upward and that the flow field is uniform in all horizontal directions. This means that the flow field looks the same all the time everywhere on a horizontal plane. However, in the direction of flow, the flow changes in velocity and temperature. Suppose the temperature increases downward and is given by:

$$T = -AZ^2 \quad (3)$$

where A is a constant. If the fluid is flowing upwards at a constant rate, say S km/sec, then the velocity vector will be given by:

$$\mathbf{V} = 0\mathbf{i} + 0\mathbf{j} + S\mathbf{k} \quad (4)$$

where \mathbf{i} , \mathbf{j} , and \mathbf{k} are unit vectors along the X, Y, and Z axes of the coordinate system. In this example the components of \mathbf{V} are:

$$\begin{aligned} u &= 0 \\ v &= 0 \\ w &= S \end{aligned} \quad (5)$$

Applying the operators [Eqns. (1) and (2)] to T gives:

$$\nabla^2 T = 0 + 0 - 2A \quad (6)$$

$$DT/Dt = 0 + 0 + 0 + S(-2AZ) \quad (7)$$

$$DT/Dt = -2ASZ$$

The properties of the del operator (∇), its physical significance and methods for using it are clearly described by Schey (1973).

DIFFERENTIAL EQUATIONS OF FLUID MECHANICS

The differential equations of fluid mechanics are expressed with these operators and are based on familiar physical laws: Conservation of matter, conservation of momentum, and conservation of energy. In this chapter fluids with constant density (ρ) and viscosity (η) will be discussed. In other chapters, these restrictions will be relaxed to provide more realistic models. With these variables constant, however, the equations can be written as follows:

The equation of continuity

The equation of continuity is an expression of the law of conservation of matter and for fluids of constant density is written:

$$\partial u / \partial X + \partial v / \partial Y + \partial w / \partial Z = 0 \quad (8)$$

If we treat ∇ as a vector operator:

$$\nabla = \partial / \partial X \mathbf{i} + \partial / \partial Y \mathbf{j} + \partial / \partial Z \mathbf{k} \quad (9)$$

then the equation of continuity can be written:

$$\nabla \cdot \mathbf{V} = 0 \quad (10)$$

where \cdot indicates vector multiplication according to the rules for the dot product [see, for example, Hoffmann, 1966].

The general form for the continuity equation when density is not constant is:

$$\partial \rho / \partial t + \nabla \cdot (\rho \mathbf{V}) = 0 \quad (11)$$

On expansion of the term under the del operator one gets:

$$\partial \rho / \partial t + \mathbf{V} \cdot \nabla \rho + \rho \nabla \cdot \mathbf{V} = 0 \quad (12)$$

Each of the terms under the del operators can be further expanded and, in the case of the first del term on the left hand side, the dot product can be written as a sum of products of the two vectors. The final result will contain six terms with derivatives with respect to the spatial variables and one with respect to time.

The Navier-Stokes equations

The Navier-Stokes equations are a set of equations expressing conservation of momentum. There are three equations in the set, one for each component of the velocity vector:

$$\rho \, Du/Dt = - \partial P / \partial X + \eta \, \nabla^2 u \quad (13)$$

$$\rho \, Dv/Dt = - \partial P / \partial Y + \eta \, \nabla^2 v \quad (14)$$

$$\rho \, Dw/Dt = - \rho g - \partial P / \partial Z + \eta \, \nabla^2 w \quad (15)$$

where P is the pressure and g is the acceleration of gravity acting in the negative Z direction, downwards.

Notice that in the presence of a gravitational field, the sign and location of the ρg term depends on the coordinate system employed.

Conservation of energy

There are several ways to write this equation. One of the most handy is an equation in temperature and heat flow:

$$\rho c_p \, DT/Dt - DP/Dt = K \, \nabla^2 T + \Phi \quad (16)$$

where c_p is the heat capacity at constant pressure, K is the thermal conductivity and Φ is an energy dissipation function that measures the loss of energy due to frictional processes in the flow. Viscosity causes kinetic energy to be converted to heat. This function is given by:

$$\begin{aligned} \Phi = \eta \{ & 2[(\partial u / \partial X)^2 + (\partial v / \partial Y)^2 + (\partial w / \partial Z)^2] + \\ & (\partial u / \partial Y + \partial v / \partial X)^2 + (\partial v / \partial Z + \partial w / \partial Y)^2 + (\partial w / \partial X + \partial u / \partial Z)^2 \} \end{aligned} \quad (17)$$

The energy equation is, perhaps, the most complicated of the lot. If there are other sources of heat or heat sinks in the system then additional terms are required. Such sources or sinks could be crystallization or assimilation of solids, vesiculation or absorption of volatiles.

Equations (10)-(16) are the basic equations of fluid mechanics. The variables or unknown values in the equations are the velocity components: u , v , and w ; the temperature, T ; and the pressure, P ; a total of five. Since there are five equations, it is possible, in principal, to determine these variables as functions of time (t) and position (X, Y, Z). However, the catch is in the words "in principal". In practice, seldom can this be done without placing additional constraints on the physical properties of the system.

UNIDIRECTIONAL FLOWS

The equations of flow are much more tractable if all the velocity components but one are zero. To account for the effect of a gravitational field, w will be selected as the nonzero one. With this condition, the equation of continuity becomes:

$$\partial w / \partial z = 0 \quad (18)$$

We originally wrote these equations for conditions of constant density and viscosity. If these properties are not constant then Equation (18) is more complicated.

The Navier-Stokes equations become one instead of three when two velocity components are zero:

$$\rho Dw/Dt = -\rho g - \partial P / \partial Z + \eta \nabla^2 w \quad (19)$$

Expanding the ∇^2 term gives:

$$\rho Dw/Dt = -\rho g - \partial P / \partial Z + \eta [\partial^2 w / \partial X^2 + \partial^2 w / \partial Y^2 + \partial^2 w / \partial Z^2] \quad (19)$$

If we take into account the continuity equation, Equation (18), this last equation can be made even simpler:

$$\rho \partial w / \partial t = -\rho g - \partial P / \partial Z + \eta [\partial^2 w / \partial X^2 + \partial^2 w / \partial Y^2] \quad (19)$$

The energy equation for unidirectional flow, taking into account Equation (18) is:

$$\rho C_p (\partial T / \partial t + w \partial T / \partial Z) - \partial P / \partial t - w \partial P / \partial Z = K \nabla^2 T + \eta [(\partial w / \partial X)^2 + (\partial w / \partial Y)^2] \quad (20)$$

These last two equations describe unidirectional flow of a fluid at constant density and viscosity. They show the reduction in complexity of the math that is possible when such simplifications can be made. Although not discussed here, these simplifications are justified only if the geometry and physics of the real situation are such that the real flow approximates these conditions.

Application to a simple problem

The problem is the flow of magma in a dike. The coordinate system is shown on Figure 2. If we assume the dike is very long then, perhaps, the velocity will change little along strike of the dike. If such is the case, then all derivatives with respect to Y can be set to zero and the equations simplify to:

$$\rho \partial w / \partial t = -\rho g - \partial P / \partial Z + \eta \partial^2 w / \partial X^2 \quad (21)$$

and:

$$\begin{aligned} \rho C_p (\partial T / \partial t + w \partial T / \partial Z) - \partial P / \partial t - w \partial P / \partial Z = \\ K (\partial^2 T / \partial X^2 + \partial^2 T / \partial Z^2) + \eta (\partial w / \partial X)^2 \end{aligned} \quad (22)$$

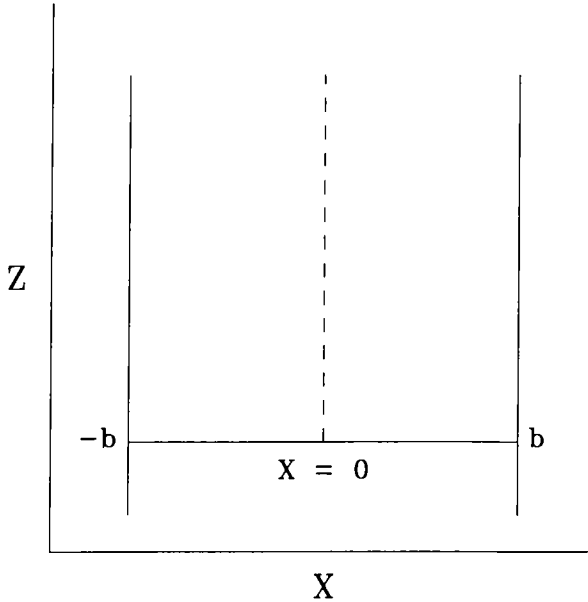


Figure 2. Coordinate system for flow through a dike. X is positive to the right, Z is positive upward and Y is normal to the plane of the figure. The dike is $2b$ m wide.

Equations (21) and (22) are the ones we have to solve as a model for flow through a dike. We simplify even further and look at the steady state situation for which we can set all time derivatives to zero.

Steady state problems are always easier to solve than transient problems because time is no longer a variable. Justification for reducing a problem to a steady state one depends on the physics and observational data for the situation (see Chapter 8, "Flow in a Conduit").

Setting the derivatives with respect to t equal to zero in Equations (21) and (22) gives:

$$\rho g + \frac{\partial P}{\partial Z} = \eta \frac{\partial^2 w}{\partial X^2} \quad (23)$$

and:

$$\rho c_p w \frac{\partial T}{\partial Z} - w \frac{\partial P}{\partial Z} = K \left(\frac{\partial^2 T}{\partial X^2} + \frac{\partial^2 T}{\partial Z^2} \right) + \eta \left(\frac{\partial w}{\partial X} \right)^2 \quad (24)$$

as the two equations describing the flow.

Remembering that the continuity equation requires that the derivative of w with respect to Z be zero, we can apply $\partial/\partial Z$ to Equation (23) and change the order of differentiation to get:

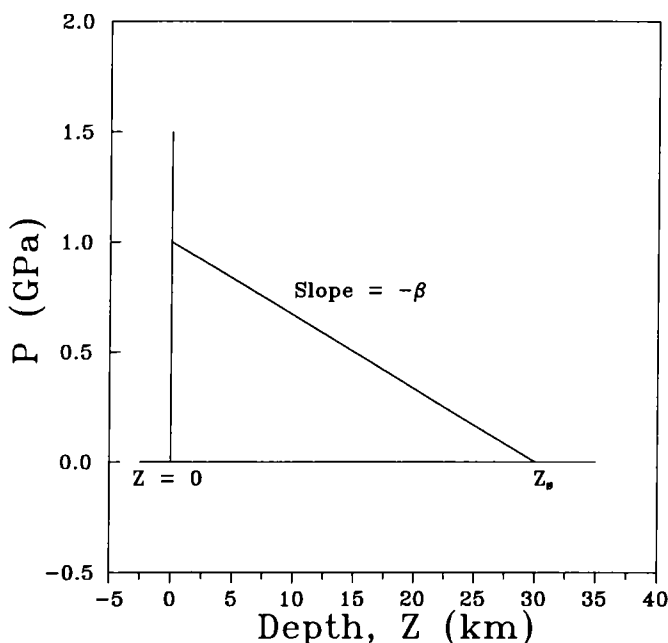


Figure 3. Schematic plot of pressure vs depth (Z) for steady state, unidirectional flow in a dike. Z_s is the value of Z at the surface of the earth. The origin is within the earth, Z_s km below the surface.

$$\partial(\rho g)/\partial Z + \partial^2 P/\partial Z^2 = \eta (\partial^2/\partial X^2) \partial w/\partial z = 0 \quad (25)$$

However, our problem postulates a constant density and we take the acceleration of gravity (g) as constant. Hence any derivative involving ρ and g will be zero and we are left with:

$$\partial^2 P/\partial Z^2 = 0 \quad (26)$$

If the second derivative of a function is zero, the first derivative must be a constant which we will call $-\beta$. If the first derivative is a constant, then the function itself must be linear in the independent variable, in this case, Z . Because Z is chosen as positive upward, a plot of P versus depth will have a negative slope equal to $-\beta$ [see Fig. 3]. Because P is zero at the earth's surface where $Z = Z_s$, the equation describing P as a function of Z can be written:

$$P = \beta(Z_s - Z) \quad (27)$$

Taking the second derivative of Equation (27) and substituting into Equation (23) gives the result:

$$(\rho g - \beta)/\eta = \partial^2 w/\partial X^2 \quad (28)$$

Two integrations of Equation (29) give:

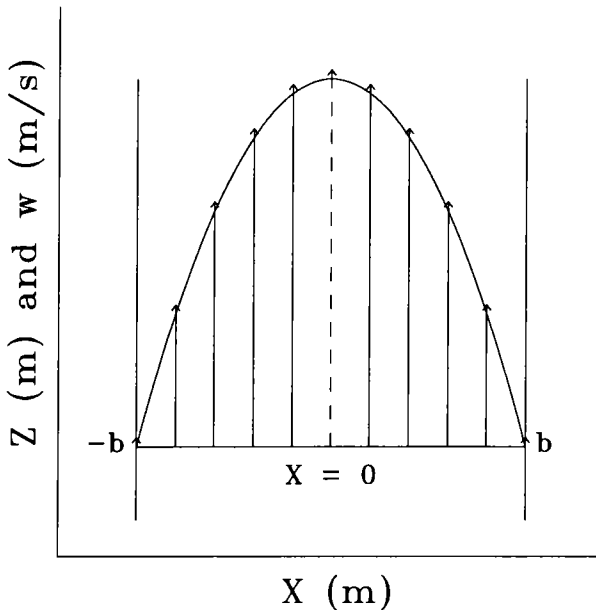


Figure 4. Velocity distribution in a dike $2b$ m wide [see Eqn. (30)]. The only nonzero velocity component is w .

$$w = [(\rho g - \beta)/(2\eta)]X^2 + C_1X + C_2 \quad (29)$$

where C_1 and C_2 are constants of integration.

Notice that a linear pressure gradient is a consequence of the simplifications we have made to the flow problem; it pops out of the math. This is another characteristic of fluid flow problems; simplifications can often introduce properties of the flow that are not immediately obvious. Consequently, the final formulation of a flow problem needs scrutinizing for such effects.

The constants of integration in Equation (29) can be evaluated by using one of the most common boundary conditions in fluid mechanics: The fluid adheres to a solid interface and consequently the velocity of the fluid relative to the solid is zero at the interface. Hence, at $X = \pm b$, w must equal zero. Away from the dike walls, w increases to a maximum at the dike centre ($X = 0$). Substitution of these boundary conditions into Equation (29) gives us the velocity distribution across the dike:

$$w = (\beta - \rho g)(b^2 - X^2)/(2\eta) \quad (30)$$

This result is a famous equation that describes laminar flow between solid walls and is named after its discoverer, Poiseuille flow. The velocity distribution is quadratic. The distribution of velocity vectors across the dike is shown on Figure 4. One important point to note is the location of maximum velocity at the centre of the dike where $X = 0$. Setting $X = 0$ in Equation (30) produces an expression for the maximum velocity:

$$w_m = (\beta - \rho g)b^2/(2\eta) \quad (31)$$

The next step is to solve Equation (24), the energy equation. To do this, we first substitute Equation (30) and its derivatives into Equation (24):

$$-(\rho g - \beta)(b^2 - X^2)(\rho c_p \partial T/\partial Z + \beta)/(2\eta) = K(\partial^2 T/\partial X^2 + \partial^2 T/\partial Z^2) + (\rho g - \beta)^2 X^2/\eta \quad (32)$$

Before we can get a solution to this last equation we have to know something about the boundary conditions, that is, what is the temperature or its gradient at the edge of the dike and does the temperature change in the direction of flow. Because of the symmetry of the problem, it is reasonable, but not required, that the boundary conditions be the same on both sides of the dike. It is in the specification of the boundary conditions that we, as geologists, have a contribution to make. What do we know about rocks that can help a mathematician solve an equation and make sure the solution is relevant? If the conditions and rock types are similar along both sides of the dike in the Z-direction then we might suggest that the rate of transfer of heat across the boundary is a constant independent of Z. Another suggestion might be that the temperature is constant on the boundaries. These two possibilities illustrate the kinds of boundary conditions that one can impose on heat flow problems. One can specify the heat flow itself or temperature, sometimes both.

In this problem, we need only the heat flow boundary conditions at the edges of the dike. We assume the heat loss to the country rocks across the boundary is constant. Then:

$$(\partial T/\partial X) \mathbf{i} = -Q/K \mathbf{i} \text{ at } X = b \quad (33)$$

and

$$(\partial T/\partial X) \mathbf{i} = Q/K \mathbf{i} \text{ at } X = -b \quad (34)$$

where Q is a positive constant and K is the thermal conductivity. The unit vectors are present in these equations because heat flow is a vector quantity and is transported down the temperature gradient from high to low temperatures.

Because Equation (32) contains both X and Z as independent variables we also need some idea of how T varies with Z in addition to the boundary conditions on X. There is no obvious boundary condition to place on the temperature distribution along Z. We could require that heat is transported parallel to Z only by the moving fluid or we could assume a conduction term as well. About all we can do is try several models and see if they make sense. The most simple idea is to expect that the temperature varies very little with Z, that is heat is carried mostly by the moving melt. So, we will postulate that the vertical temperature gradient is a constant:

$$\partial T/\partial Z = \alpha \quad (35)$$

which, in turn, requires that:

$$\partial^2 T/\partial Z^2 = 0 \quad (36)$$

Substituting all these boundary conditions into Equation (32) gives a result:

$$2\eta K \partial^2 T / \partial X^2 = (\beta - \rho g) \{ (\alpha \rho C_p + \beta) b^2 - [\alpha \rho C_p + \beta + 2(\beta - \rho g)] X^2 \} \quad (37)$$

which can be integrated twice:

$$T = -(\beta - \rho g) \{ [\alpha \rho C_p + \beta + 2(\beta - \rho g)] X^4 / (24\eta K) - (\alpha \rho C_p + \beta) b^2 X^2 / (4\eta K) \} \\ + C_1(Z) X + C_2(Z) \quad (38)$$

$C_1(Z)$ and $C_2(Z)$ play the role of constants of integration in ordinary differential equations. However, Equation (37) is a partial differential equation even though no partial derivative with respect to Z is present. Actually, it is still there, we just said it is constant [see Eqn. (35)]. Consequently, these "constants" can be functions of Z and Equation (38) will still satisfy Equation (37).

The boundary conditions at the sides of the dike [Eqns. (33) and (34)] can only be satisfied if $C_1(Z)$ is zero. To see this, take the derivative of Equation (38) with respect to X and substitute $\pm b$ for X in the result:

$$(\rho g - \beta) [(\alpha \rho C_p + \beta - 2)b^3 / (6\eta K) - (\alpha \rho C_p + \beta) b^3 / (2\eta K)] + C_1(Z) = -Q/K \quad (39)$$

$$-(\rho g - \beta) [(\alpha \rho C_p + \beta - 2)b^3 / (6\eta K) + (\alpha \rho C_p + \beta) b^3 / (2\eta K)] + C_1(Z) = Q/K \quad (40)$$

Add the two equations and get:

$$2 C_1 = 0 \quad (41)$$

Hence, $C_1 = 0$. $C_2(Z)$ is evaluated by setting $X = 0$ in Equation (38) with the result that $C_2(Z)$ is equal to the temperature at the centre of the dike, T_m . Notice that T_m is a function of Z . Its gradient is α , Equation (35).

The results of this discussion of the velocity and temperature distribution are:

$$w = (\beta - \rho g)(b^2 - X^2) / (2\eta) \quad (42)$$

and:

$$T_m - T = (\beta - \rho g) \{ (\alpha \rho C_p + \beta + 2(\beta - \rho g)) X^4 / 6 - (\alpha \rho C_p + \beta) b^2 X^2 \} / (4\eta K) \quad (43)$$

The maximum velocity and temperature differences between centre and edge of the dike are:

$$w_m / b^2 = (\beta - \rho g) / (2\eta) \quad (44)$$

and:

$$(T_b - T_m) / b^4 = (\beta - \rho g) [5(\alpha \rho C_p + \beta) + 2(\beta - \rho g)] / (24\eta K) \quad (45)$$

We can also find an expression for the heat flow from the dike at $X = \pm b$:

$$Q / b^3 \mathbf{i} = (\beta - \rho g)(\alpha \rho C_p + \rho g) / (3\eta) \mathbf{i} \quad (46)$$

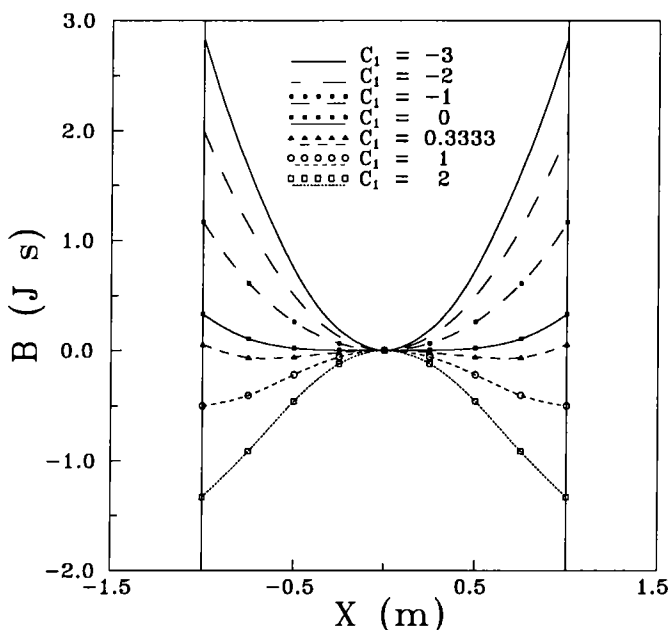


Figure 5. Plot of the scaled temperature, $B = [4\eta K(T_m - T)]/(\beta - \rho g)$, across a one m wide dike. The temperature distributions are shown for various values of $C_1 = (\alpha \rho C_p + \beta)$. $C_2 = (\beta - \rho g)$, is equal to 1.

Equations (42)-(46) describe the temperature and velocity distributions across the dike, provide an estimate of the maximum changes in velocity and temperature across the dike, and a way to calculate the heat loss from the dike.

Interpretation

If we want to apply these equations to a particular dike, we can measure its width (b) and its composition. From the composition we can calculate the density, viscosity and heat capacity of the magma (see chapter by Lange and Carmichael, this volume). As a result, we have these last three equations [Eqns. (44), (45) and (46)] with which we can calculate w_m , T_m , and Q . However, we cannot do this until we sort out the pressure gradient in the country rocks (β) and the temperature gradient in the dike (α).

The quantity $(\beta - \rho g)$ is positive, otherwise the magma would not flow up the dike in a positive Z direction [see Eqn. (42)]. Consequently, if we form the variable $[4\eta K(T_m - T)]/(\beta - \rho g)$ and call it B , then Equation (43) becomes:

$$B = X^2 \{ [\alpha \rho C_p + \beta + 2(\beta - \rho g)]X^2/6 - (\alpha \rho C_p + \beta)b^2 \} \quad (47)$$

The sign of the right hand side of Equation (47) determines the sign of $(T_m - T)$. If the right hand side of Equation (47) is positive then $(T_m - T)$ is positive and the temperature at the centre of the dike is hotter than the temperature at position X in the dike. The sign of the right hand side of Equation (47) depends on the nature of the quantity $(\alpha \rho C_p + \beta)$.

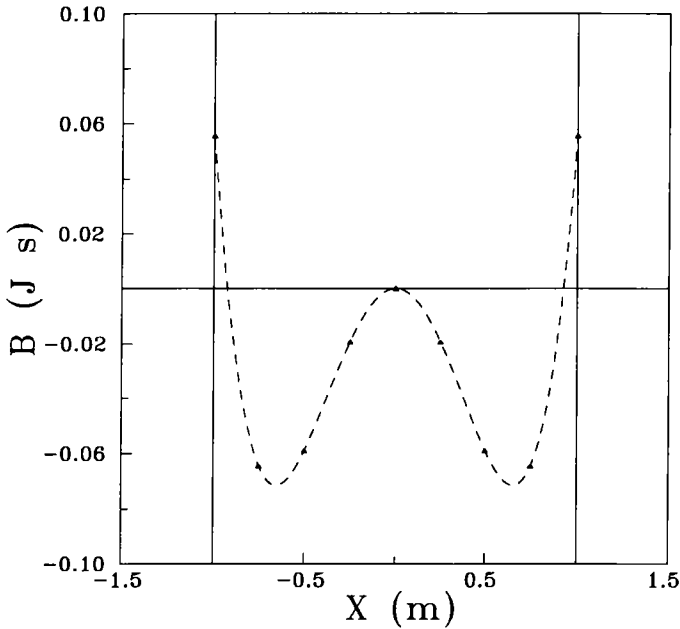


Figure 6. Plot of the scaled temperature, $B = [4\eta K(T_m - T)]/(\beta - \rho g)$, across a one m wide dike for a value of $(\alpha \rho C_p + \beta) = 0.3333$, $(\beta - \rho g) = 1$.

If the vertical temperature gradient, α , can be positive or negative and of sufficient magnitude then $(\alpha \rho C_p + \beta)$ can be either positive, negative or zero.

Several possible temperature distributions are shown on Figure 5. Notice that the temperature difference between the centre of the dike and the point X in the dike can be either positive or negative. There are even values of $(\alpha \rho C_p + \beta)$ for which the temperature difference across the dike can change sign [see the curve labelled $C_1 = 0.3333$, Figure 5].

The roots of Equation (47) occur at $X = 0$ (a double root) and at:

$$X = \pm |b| \sqrt{6} / \sqrt{\{[(\alpha \rho C_p + \beta) + 2(\beta - \rho g)]/(\alpha \rho C_p + \beta)\}} \quad (48)$$

If the coefficient of $|b|$ in Equation (48) is less than one, then two roots of Equation (47) occur within $X = \pm b$ (i.e., within the dike). From this, one can determine that if $[(\alpha \rho C_p + \beta) + 2(\beta - \rho g)]$ is greater than 6, then the roots within $\pm b$ cause the temperature difference to change sign across the dike. An expanded plot of the curve labelled $(\alpha \rho C_p + \beta) = 0.3333$ is shown on Figure 6.

If $[(\alpha \rho C_p + \beta) + 2(\beta - \rho g)]/(\alpha \rho C_p + \beta)$ is negative then the two roots of Equation (47) not at the origin are imaginary and the curve for the temperature distribution is concave upwards and there is no change in sign for the distribution of the temperature difference across the dike. In order for Equation (47) to have imaginary roots, the vertical

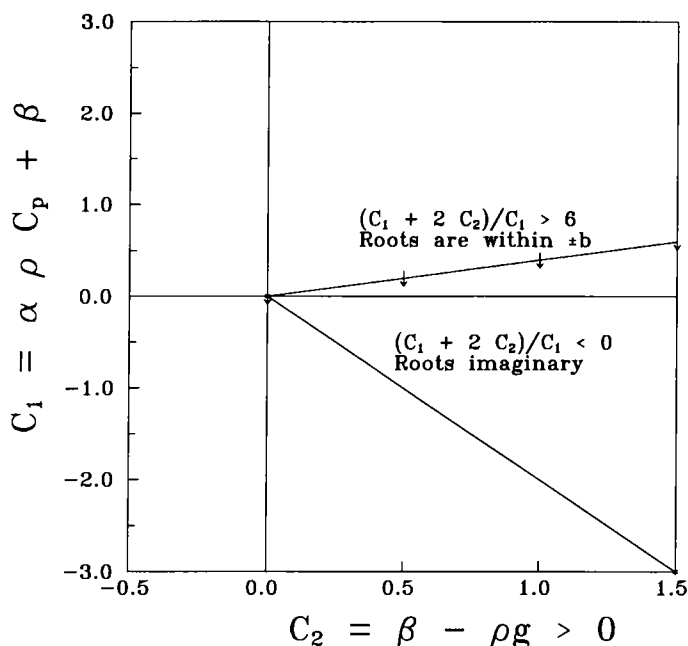


Figure 7. Plot of $C_1 = \alpha \rho C_p + \beta$ vs $\beta - \rho g$. The nature of the roots to Equation (47) depend on these values. C_2 must be positive for upward flow in the dike. The region of C_1 - C_2 values where the roots are within $\pm b$ lies below the curve with down-pointing arrows.

temperature gradient (α) must be negative. The values of $(\alpha \rho C_p + \beta)$ and $(\beta - \rho g)$ that lead to imaginary roots are shown on Figure 7.

There are several possibilities that can be suggested for the vertical temperature gradient, based on thermodynamic variables. If the magma comes up the dike adiabatically at constant entropy, then the pressure-temperature gradient will be given by:

$$(\partial T / \partial P)_S = T (\partial v / \partial T)_P / C_p \quad (49)$$

where v is now the volume, not a velocity component and T is in Kelvin. If the magma rises at constant enthalpy, then:

$$(\partial T / \partial P)_H = [T (\partial v / \partial T)_P - v] / C_p \quad (50)$$

whereas, if the magma rises at its liquidus temperature and pressure, then:

$$(\partial T / \partial P)_G = v / s \quad (51)$$

where s is the entropy and G is the Gibbs energy.

By using the chain rule from differential calculus, these pressure temperature gradients can be converted to temperature depth gradients. The gradients defined by Equations (49) and (51) are positive for silicate melts whereas the gradient defined by Equation (50) is negative. Equation (49) defines a reversible adiabatic gradient, Equation

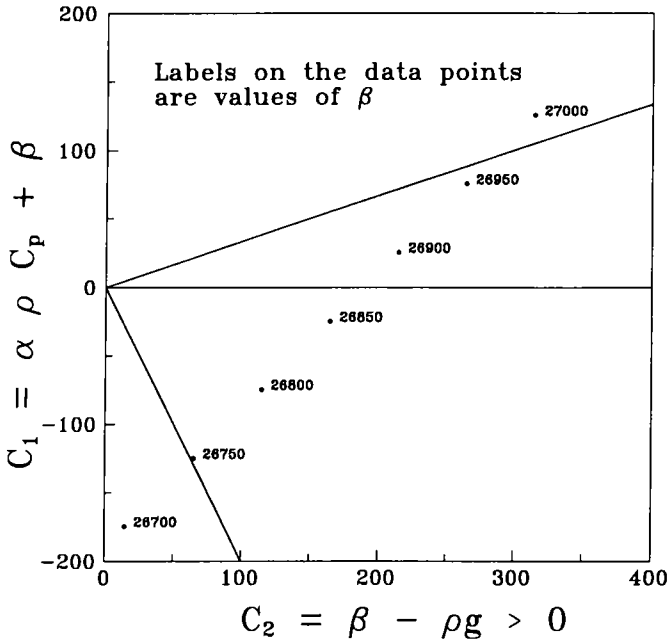


Figure 8. Plot of $C_1 = \alpha\rho C_p + \beta$ vs $C_2 = \beta - \rho g$ for a dry basaltic melt. Labels on the plotted points are the external pressure gradients, β .

(50) is the gradient for an irreversible adiabatic change and Equation (51) is the gradient expected if the melt was at its liquidus temperature and remained so along the vertical extent of the dike. Consequently, it would not be unreasonable to expect almost any sign for the vertical temperature gradient. In addition, the calculated temperature profiles are very sensitive to the pressure and vertical temperature gradients; small changes in these gradients can result in significant changes in the temperature profile. Any type of temperature distribution across a dike is possible given a reasonable vertical temperature gradient and likely external pressure gradients. These are shown on Figure 8 for a dry basaltic melt. The physical properties, ρ , η , and C_p , were derived from data and algorithms in Ghiorso (1985); Ghiorso et al. (1983); Lange and Carmichael (1987); Murase and McBirney (1973); and Shaw (1972).

The external pressure gradient, β , is not simply the change in pressure with depth due to the weight of the overlying rocks:

$$\beta \neq \rho_c g \quad (52)$$

where ρ_c is the density of the country rocks next to the dike. The stress on a horizontal plane beneath the earth's surface is however, equal to the weight of the overlying rocks:

$$\sigma_h = -\rho_c g Z \quad (53)$$

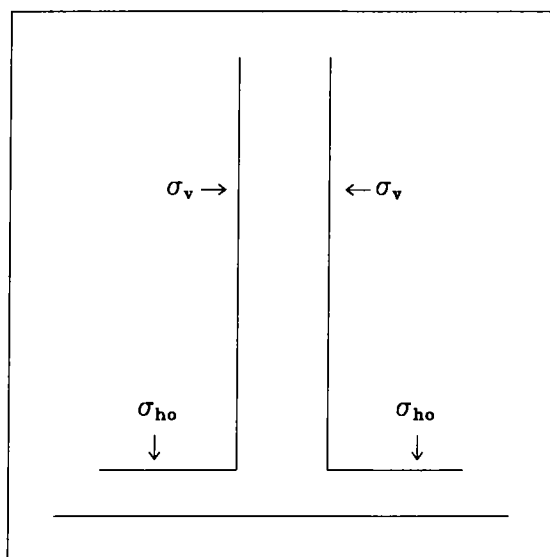


Figure 9. Schematic vertical section through a dike connected to a magma chamber at depth Z_o . The stresses σ_v and σ_{ho} are on vertical and horizontal surfaces, respectively.

The stress on a vertical surface is not equal to that on a horizontal surface; this is true even in non-tectonic regions. At shallow depths in non-tectonic regions, the stress on vertical surfaces is given by:

$$\sigma_v = \sigma_h \nu / (1 - \nu) \quad (54)$$

where ν is Poisson's ratio; a material (physical) property of a substance that is related to its elasticity. Poisson's ratio is a constant of proportionality between stress and strain in uniaxial compression.

Derivation and discussion of Equations (52) and (53) and the reasoning leading to them are found in texts on structural geology (Means, 1976, p. 111-115 and p. 245-253). For our purposes it is important to know that ν is less than 0.5 for real substances and, as a consequence, the stress on a vertical surface is less than on a horizontal one in non-tectonic regions.

The question we have to answer is: How is the stress in the country rock transmitted to the magma in the dike? A sketch of a possibility is shown on Figure 9. In Figure 9 we imagine a dike connected at depth with a magma chamber subjected to the stress on a horizontal surface, σ_h . The magma is forced up through the dike which is held open against the stress on a vertical surface, σ_v . If no other stresses are acting within the magma chamber, then the pressure on the magma at rest will be σ_{ho} , the stress on a horizontal surface at a depth Z_o . The intensity of the pressure in the dike will be less than σ_{ho} because of the stress required to hold the dike open against σ_v and to counteract the weight per unit area of the magma itself ($-\rho gZ$). We can omit this latter quantity from

further consideration because it has been taken into account by the ρg term in Equation (30). The pressure on the magma in the dike is thus given by:

$$P = \sigma_{ho} - \sigma_v = -\rho_c g[Z_o + Zv(1 - v)] \quad (55)$$

and the pressure gradient corresponding to Equation (55) is

$$-\partial P/\partial Z = \beta = \rho_c g v(1 - v)$$

Typically, values of Poisson's ratio for rocks are approximately 0.27. Gabbros have densities near 3000 whereas granites have densities near 2700. If a dike intrudes either of these rock types then β will be in the range 9800-1100, a value smaller than the ρg term for a dry basaltic melt. Consequently, a dike cannot form in these rocks in non-tectonic regions unless the density of the magma is less than in a dry basaltic melt. One obvious way for the density to decrease is by vesiculation. This problem is discussed in Chapter 8 (Jaupart and Tait, 1990).

We can determine the critical value for Poisson's ratio in order to have dikes form. If w is to be nonzero, then $(\beta - \rho g)$ must be greater than zero. w will be exactly zero if $\beta = \rho g$. The critical value of Poisson's ratio that must be exceeded for dike intrusion can be calculated from:

$$\rho/\rho_c = v_c(1 - v_c) \quad (56)$$

The result is :

$$v > v_c \approx 0.45 - 0.48 \quad (57)$$

for dikes to form.

Conclusions

1. Horizontally directed stresses in non-tectonic regions appear to be insufficient for squeezing dry basaltic magmas to the surface. Because basaltic dikes are present in the crust, the discussion in this chapter is at best incomplete or inadequate. Lower magma densities, transient rather than steady state conditions, or tectonic stresses (in the broadest sense) would need investigation before one is satisfied with a model of dike formation.
2. The temperature distribution across a given dike cannot be predicted from a knowledge of its physical properties. This type of phenomenon, sensitive dependence of process on small variations in physical parameters, is at the heart of new studies of physical processes collectively called *chaos* (see Gleick, 1987, for a thorough historical summary).
3. The shape of the temperature distribution across a dike might be determinable from observations of features that depend on the temperature distribution. Such features might include variations in contact metamorphic effects, variations in chilled margin widths and contacts, and variations in the distributions of crystals across

the dike. To implement and interpret these observations they would have to be made along a vertical section through a dike.

4. In order to model magma transport, the properties of the melt, the properties of the included phases, and the external constraints from the country rocks have to be considered.

REFERENCES CITED

- Ghiorso, M.S. (1985) Chemical mass transfer in magmatic processes. I. Thermodynamic relations and numerical algorithms. *Contrib. Mineral. Petrol.*, 90, 107-120.
- Ghiorso, M.S., Carmichael, I.S.E., Rivers, M.L., and Sack, R.O. (1983) The Gibbs free energy of mixing of natural silicate liquids; an expanded regular solution approximation for the calculation of magmatic intensive variables. *Contrib. Mineral. Petrol.*, 84, 107-145.
- Gleick, J. (1987) *Chaos, Making a New Science*. Viking Penguin Inc., New York, 354 pp.
- Hoffmann, B. (1966) *About Vectors*. Dover Publications, Inc., New York, 134 pp.
- Jaupart, C., and Tait, S. (1990) Dynamics of eruptive phenomena. In: J. Nicholls, and J.K. Russell, Eds., *Modern Methods of Igneous Petrology - Understanding Magmatic Processes*, *Rev. Mineral.* 24, this volume.
- Lange, R.A., and Carmichael, I.S.E. (1987) Densities of $\text{Na}_2\text{O-K}_2\text{O-CaO-MgO-FeO-Fe}_2\text{O}_3\text{-Al}_2\text{O}_3\text{-TiO}_2\text{-SiO}_2$ liquids: New measurements and derived partial molar properties. *Geochim. Cosmochim. Acta*, 51, 2931-2946.
- Means, W.D. (1976) *Stress and Strain, Basic Concepts of Continuum Mechanics for Geologists*. Springer-Verlag New York, Inc., New York, 339 pp.
- Murase, T., and McBirney, A.R. (1973) Properties of some common igneous rocks and their melts at high temperatures. *Geol. Soc. Am. Bull.*, 84, 3563-3592.
- Schey, H.M. (1973) *Div, Grad, Curl and All That*. W.W. Norton & Company, Inc., New York, 163 pp.
- Shaw, H.R. (1972) Viscosities of magmatic silicate liquids: An empirical method of prediction. *Am. J. Sci.*, 272, 870-893.

PHYSICAL PROCESSES IN THE EVOLUTION OF MAGMAS

FOREWORD

The most striking feature of the igneous rock suite is its compositional diversity and the explanation of this fact is the main goal of igneous petrology. The production, from a relatively homogeneous mantle source, of a large range of compositions which go to make up the crust, renders igneous processes of major interest to the earth sciences. Furthermore, magma migration and eruption involve a fascinating range of phenomena making them a rewarding object of study.

In this chapter we discuss several aspects of natural convection in fluids and the application of these ideas to the dynamics of magma chambers. The introduction of such concepts into igneous petrology is comparatively recent and represents a considerable shift of emphasis. Previous approaches to the study of igneous differentiation were dominated by experimental petrology in which small scale experiments are used to establish chemical equilibrium relationships between silicate minerals and liquids. The phase diagrams so established have been used in a general way to interpret igneous differentiation sequences as deduced from cumulate rocks and erupted lavas. The only commonly invoked dynamical idea was that of gravitational settling of crystals from less dense magmatic liquid. The generation at depth and ascent of magma to the Earth's surface always involves exchange of heat with the surroundings which induces gradients of temperature, composition and crystal content in the magma. The density gradients which result from these spatial variations in magma properties are acted on by the gravity field and can be shown often to lead to the development of convective instabilities. The resultant dynamical phenomena can be the controlling factor in differentiation processes.

The equations which describe convection are mathematically complex, and a number of people have adopted a numerical approach to solving them, particularly since rapid computers have become available (e.g., see Spera et al., 1986 or Hansen and Yuen, 1987). In this chapter, however, we do not attempt to construct a full model of complex natural systems, but show how to reason with fluid dynamical concepts. We describe the principles involved in the derivation of important equations and give some numerical examples to illustrate orders of magnitude. Our hope is that this chapter will enable the interested student to broach the literature on magmatic processes in which a certain knowledge of fluid dynamics is assumed, and assist the necessary interaction between petrology and fluid dynamics.

INTRODUCTION

Physical properties of magmas

Natural convection is caused by the action of gravity on density gradients, due typically to spatial variations in fluid composition and temperature, but also to factors such as differences in concentration of particles or bubbles. We will generally employ an equation of state for the fluid of the form:

$$\rho = \rho_0 [1 - \alpha(T - T_0) + \beta(C - C_0)] \quad (1)$$

where ρ is the density of the fluid at temperature T and composition C and ρ_0 a reference density at T_0 and C_0 . The coefficient of thermal expansion α and β the compositional analogue of α are both defined to be positive. This equation is for a simple binary system in

which composition can be described in terms of the amount of one of the components. In general, for a multicomponent system such as a natural magma more terms are required.

An important general point is that local variations of fluid density are intrinsic to convection and hence that a convecting body of fluid is not homogeneous. In the example of high Rayleigh Number thermal convection discussed below, the system exhibits boundary layers close to the margins of the container in which steep gradients of fluid temperature (and hence density) exist. Although the interior of the body of fluid may be considered as well-mixed on a gross scale, it is characterised by the existence of fluctuations about mean values of temperature and density. These fluctuations are associated with the physical object of a field of hotter (rising) and colder (descending) plumes, and it is these which effect the convective heat transport in the system.

As magma cools and fractional crystallization takes place in a crustal chamber, gradients in both melt composition and temperature develop which provide the buoyancy force to drive convection. Models have been developed which permit quite accurate calculation of the trends of evolution of the densities of silicate melts during the course of igneous differentiation (e.g., Bottinga and Weill, 1970; Bottinga et al., 1982). The density of a melt with N chemical components is given by:

$$\rho = \frac{\sum_{i=1}^N x_i M_i}{\sum_{i=1}^N x_i V_i} \quad (2)$$

where x_i , M_i and V_i are respectively the mole fraction, molecular mass and partial molar volume of the i^{th} component.

An immediate consequence of (2) is that fractional crystallization (i.e., in which the growing crystals differ in composition from the melt) induces changes in residual melt composition and hence density. Fractional crystallization can be thought of as "splitting" the starting melt into two parts: components preferentially incorporated into the crystals and those preferentially rejected into the residual melt. A useful idea is that of the density in the liquid state (ρ_c) of the chemical components which are removed from the melt by fractional crystallization of a given mineral phase. We can see that if ρ_c is greater than the initial liquid density, fractional crystallization implies a reduction in residual liquid density and vice versa. Consider a mineral consisting of P chemical components with mole fractions r in the mineral formula. We can write:

$$\rho_c = \frac{\sum_{j=1}^P r_j M_j}{\sum_{j=1}^P r_j V_j} \quad \text{where by definition} \quad \sum_{j=1}^P r_j = 1 \quad (3)$$

Sparks and Huppert (1984) called ρ_c fractionation density. For example the fractionation density of pure forsterite (Mg_2SiO_4) is given by:

$$\rho_c (\text{forsterite}) = \frac{\frac{1}{3} M_{\text{SiO}_2} + \frac{2}{3} M_{\text{MgO}}}{\frac{1}{3} V_{\text{SiO}_2} + \frac{2}{3} V_{\text{MgO}}} \quad (4)$$

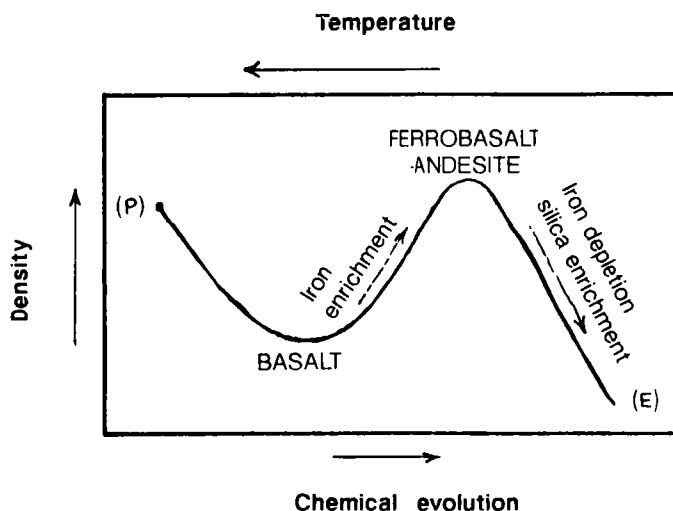


Figure 1. Schematic variations of residual liquid density which can result from the chemical and thermal evolution of a magma by fractional crystallization of a primitive basalt (P) to evolved compositions (E). The minimum and maximum of density may occur despite the monotonic decrease of temperature because as different minerals fractionate, various oxides become depleted or enriched. The density trend is for a magma without dissolved volatile components. The presence of such components tends to reduce magma density and may change the positions of or even remove maxima or minima.

Calculation of the evolution of magma density on a liquid line of descent due to fractional crystallization of any assemblage is possible by simple linear combination of similar formulae for other minerals. Figure 1 gives a schematic diagram of evolution of magma density during differentiation.

The shear viscosity μ is the main parameter which determines the rate of deformation of a region of fluid. Because of the large range of compositions and liquidus temperatures of naturally occurring magmas, their viscosities span an enormous range. Magma viscosity thus plays a primary role in controlling the time scale of evolution of magmatic systems. As a general rule, the more viscous the system, the slower the rate of evolution.

Evidence from fossil magma chambers.

Fossil magma chambers preserved in the geological record as intrusions (e.g., Skaergaard, Stillwater, Bushveld, etc.) indicate the dimensions and geometries of large reservoirs of magma in the continental crust. Horizontal dimensions range from tens to hundreds of kilometers and the vertical scale from several up to a maximum of approximately 10 km (Fig. 2a). Smaller examples are sills, which can have very large horizontal extent and vertical thicknesses ranging from a few tens of meters to a kilometer. Such tabloid geometry is not, however, ubiquitous. Magma is sometimes intruded into very long narrow fractures with steeply dipping sides, as epitomised by the Great "Dyke", an intrusion ~500 km long and ~10 km wide at the current level of exposure (Worst, 1958). Gravity data indicate inwardly dipping sides (Fig. 2b), so that its thickness tapers downwards (Podmore, 1970). Information about magma chambers in the oceanic crust is somewhat less direct. The presence of a magma chamber 4-6 km wide has been inferred from seismic reflection studies of the East Pacific Rise (Detrick et al., 1987), and at Kilauea Volcano, Hawaii the presence of large bodies of magma beneath the summit region and rift zones with a typical horizontal dimension on the order of 10 km and a vertical extent of a few kilometers has been deduced (Ryan et al., 1981; Ho Liu et al., 1990).

The sketch in Figure 2c illustrates a key observation concerning the spatial distribution of rocks in solidified intrusions and provides a clue as to how differentiation takes place. In general the crystallised sequence in contact with the floor of intrusions is substantially thicker than the roof sequence (Wager and Brown, 1968; Shirley, 1987), though both sets of rocks show the same overall sequence of differentiation. Cooling may be expected to be stronger at the roof of an intrusion, and the challenge is to explain why most crystals accumulate on the floor. For some time this was thought to reflect gravitational settling of crystals grown in the body of the magma but this interpretation has recently been challenged as fluid dynamical concepts have been applied to magmatic systems. The problem has as yet not been completely solved but we will discuss several aspects and approaches during the course of this chapter.

Chemical aspects

In addition to an understanding of transport phenomena, an essential idea is that of the phase diagram. Phase diagrams for natural magmas are complex owing to the large number of chemical components present. The crystallization interval tends to be large and in general several chemically different minerals can be simultaneously in equilibrium with a single magma composition. In this chapter we will not discuss many details of chemistry, and in our description of crystallization and compositional convection we shall refer to the simple case of a binary alloy. This is adequate, however, for illustrating many of the basic physical principles involved in the crystallization of multicomponent liquids despite the additional chemical details which may be encountered in a particular case.

It is observed that the degree of chemical differentiation in a given intrusion depends both on its bulk composition and its size. For example both the Palisades Sill (thickness ~350 m.) and the Skaergaard Intrusion (thickness ~3.5 km.) have roughly similar (basaltic) bulk compositions. However, the Skaergaard shows more pronounced chemical differentiation. Felsic intrusions are much less differentiated than mafic intrusions with respect to major elements suggesting the interpretation that the higher the magma viscosity, the less efficient are differentiation processes. However, it is necessary to weigh the evidence carefully in a given case as some felsic rocks can show strong differentiation in their trace element compositions, despite having a rather uniform major element composition. As we will discuss later, this may be an apparent difference due not to the operation of different processes but to the structure of the phase diagrams for igneous rocks. These indicate that while the major element compositions of fractionating assemblage and melt can differ substantially for mafic systems, they can be very similar for felsic systems. In other words the latter are close to the invariant point at which (neglecting the presence of minor components) major element differentiation by fractional crystallization no longer takes place.

An important aspect of the chemical relationships of igneous rocks is that the composition of residual liquid produced by fractional crystallization depends on the amount of crystallization and the difference in composition between the fractionating assemblage and the melt. When the latter is small, very large amounts of crystallization are necessary to produce appreciable differentiation. As a general rule for igneous rocks the production of say rhyolitic melt from a basaltic starting composition requires roughly 90 wt % crystallisation and hence we see that any given volume of felsic melt produced by this mechanism implies the presence of a much greater volume of mafic melt. Another means of producing felsic melt is by fusion of pre-existing felsic crustal rocks, and in this case the limiting factor is not a chemical balance, but a thermal balance between involving the heat content of the mafic melt and the heat required to do the melting. Although all aspects of this problem have not yet been fully considered, it seems clear that given the normal temperatures to be expected in the continental crust, the generation of felsic melt by this mechanism also requires large amounts of mafic melt to provide the necessary heat source (e.g., Huppert and Sparks, 1988).

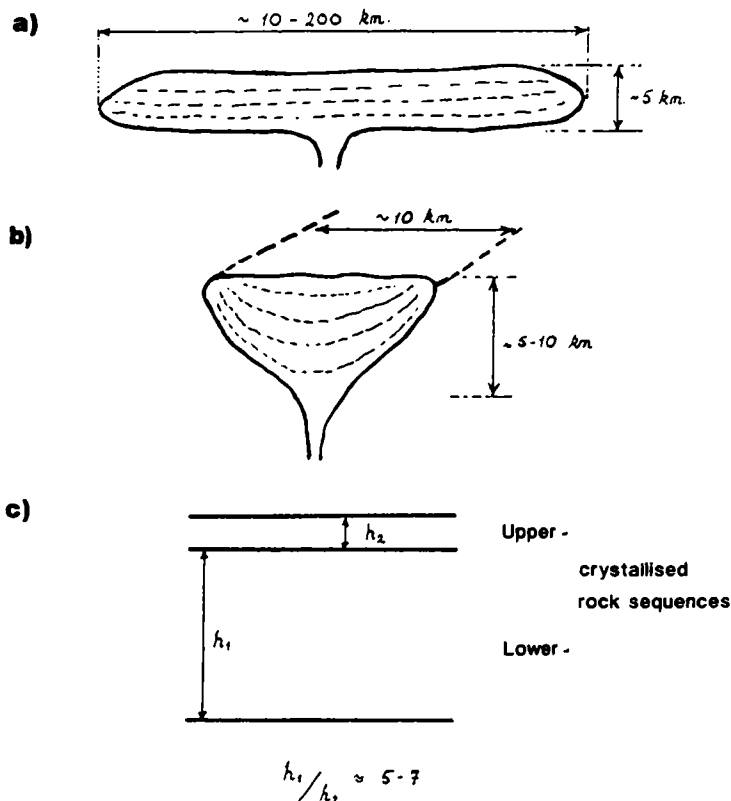


Figure 2. Geometries of layered intrusions within the continental crust. (a) High aspect ratio bodies such as sills and some large mafic intrusions, e.g., Bushveld, Stillwater. (b) Dyke-like bodies. The diagram shows a cross-section, the intrusion being highly elongated in the direction perpendicular to the section. Lateral contacts dip steeply inwards, e.g., Great "Dyke," Jimberlana.

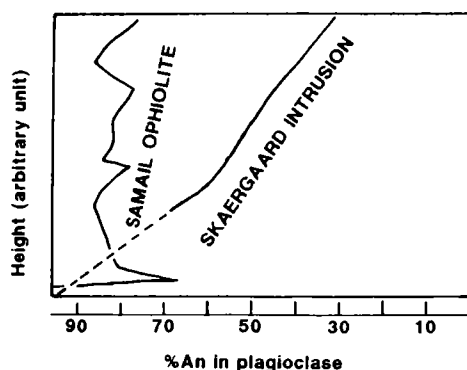


Figure 3. Geochemical differentiation trends from layered igneous rocks, contrasting the continuous evolution shown by the Skaergaard trend with the rather monotonous compositions shown by cumulate rocks from the Samail ophiolite. The Skaergaard trend is believed to result from closed system fractional crystallization whereas the ophiolite trend from a regularly replenished system. After Pallister and Hopson (1981)

Finally (except for a brief summary), we shall restrict our discussion to the evolution of closed systems. It seems clear that magma chamber replenishment is common and in some cases may be an essential feature. To illustrate briefly the importance of replenishment for the geochemical budget of a magmatic system, Figure 3 gives a comparison of cumulus plagioclase compositions from the Skaergaard Intrusion and from the Samail ophiolite (from Pallister and Hopson, 1981). The former shows pronounced evolution of plagioclase composition whereas the latter shows little change. However, many fundamental aspects of the physics can be incorporated in a discussion of closed systems, and the analysis of replenishment phenomena often involves the application in modified form of the same basic ideas. Furthermore it seems reasonable to elucidate which phenomena can be associated with the simpler case of a closed system before considering replenishment, which is really a case of exchange of mass between two interacting systems, a source and a receiving chamber.

THERMAL CONVECTION

In this section we will illustrate some of the basic principles of thermal convection in the context of a hot magma emplaced abruptly into cold country rocks such that the contacts of the intrusion are horizontal. The large temperature contrast results in the development of steep thermal gradients at the contacts, which obviously can lead to thermal convection and eventually crystallization.

An important consideration, regarding where crystallization is likely to begin in a thick layer of magma, is that the liquidus temperature is a function of pressure. A typical figure established experimentally for mafic melts is that the liquidus temperature increases by approximately 10°C per kilobar. Hence for large bodies of mafic melt typically a few kilometers in vertical dimension the liquidus temperature might be as much as 10-25°C higher at the base than at the roof. In the initial stages, we might therefore expect crystallization to develop more rapidly at the floor than at the roof. Before solidification begins at the upper contact, a large temperature difference (ΔT) is available to drive convection. Once solidification has started, the available ΔT is reduced, and the analysis becomes more involved. In this section we try to build up a picture of what the convection and the associated solidification will look like.

Temperature of contact between magma and country rock

Immediately after intrusion, steep thermal gradients develop rapidly by conduction in the magma and the country rocks adjacent to the contacts. Convection always takes a finite time to develop and until instability occurs heat transfer is by conduction. If, for the moment, we consider only this initial conductive stage and assume equal thermal diffusivities for the magma and the country rocks, the temperature of the contact (T_c) is given by :

$$T_c = \frac{T_m + T_r}{2} \quad (5)$$

where T_m and T_r are the initial temperatures of the magma and the country rocks (Carslaw and Jaeger, 1959, p. 55). Figure 4 shows a simple numerical example in which T_c is calculated for mafic magma at 1250°C as a function of the temperature of the crust into which the magma is intruded. As a rule of thumb, we may expect the initial formation of a chilled margin to occur if T_c is found to be below the glass transition temperature (about 700°C for the example of mafic magma given). To understand the subsequent development and preservation of such a chilled margin calls for a more detailed analysis of the heat balance at the upper contact which we discuss below.

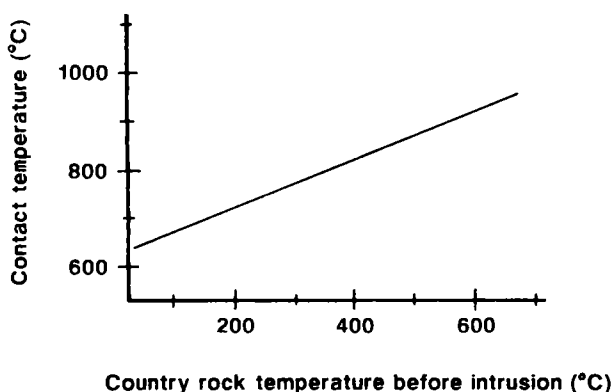


Figure 4. Approximate calculation of the temperature of the contact between cold country rocks and hot magma in the conductive stage before the onset of convection in the magma. For simplicity, we have assumed equal thermal transport properties for magma and country rocks.

Structure of the thermal boundary layers

The early stages of cooling are characterised by the development of cold thermal boundary layers adjacent to the contacts. Neglecting crystallization and assuming a constant contact temperature, the thickness of the boundary layer (δ) as a function of time (t) is obtained by solving the heat conduction equation under transient conditions. Thus, with reference to the sketch of the upper boundary layer in Figure 5a, we must solve :

$$\frac{\partial T}{\partial t} = \kappa \frac{\partial^2 T}{\partial z^2} \quad (6)$$

to obtain T as a function of vertical coordinate (z) and time (t). κ is the thermal diffusivity of the magma. For the boundary layer thickness one obtains:

$$\delta = \sqrt{\pi \kappa t} \quad (7)$$

When the contact is horizontal, formally a mathematical solution always exists in which the fluid velocity is zero everywhere, heat transport is purely by conduction and the solution of Equation (6) for $T(z,t)$ is complete. However, in practice small perturbations and motions are always present and these are found to develop into convective instabilities of the thermal boundary layer when a dimensionless parameter, the Rayleigh Number (Ra_δ) is greater than a certain critical value Ra_c . We write that instability occurs when

$$Ra_\delta = \frac{g \alpha \Delta T \rho \delta^3}{\kappa \mu} = Ra_c \quad (8)$$

where g is the acceleration of gravity, α is the coefficient of thermal expansion and ΔT the temperature difference across the boundary layer. This can be shown using the theoretical techniques of linear stability analysis and demonstrated by experiment. Figure 5b shows photographs from a laboratory experiment illustrating instability and the development of a field of plumes at the upper boundary of a layer of fluid cooled suddenly (from Jaupart and Brandeis, 1986). The plumes are generated from local instabilities and are much smaller than the dimensions of the fluid layer. This is the typical form taken by convection when the driving buoyancy forces are large relative to the dissipative forces in the system. When

buoyancy and dissipative forces are more nearly balanced convection takes a cellular form in which fluid motions are organised on a horizontal spatial scale comparable with the layer depth. In the present course we will discuss only the former, turbulent form of convection which is likely to be most relevant to magma chambers.

In simple physical terms Ra_δ is the ratio of the destabilising buoyancy force per unit volume acting on the fluid in the boundary layer and the viscous force per unit volume. We can understand this using the following simple scaling argument. Consider a sphere of fluid of radius δ which is falling or rising relative to its environment at a velocity v by virtue of a difference in temperature and which exchanges heat by diffusion. The buoyancy force is proportional to $\rho \cdot g \cdot \alpha \cdot \Delta T \cdot \delta^3$. A dimensional argument suggests that the viscous force is proportional to $\delta \cdot v \cdot \mu$. The length scale in the problem is δ and the time scale δ^2/κ , implying that the viscous force is proportional to $\delta \cdot \delta \cdot (\kappa/\delta^2) \cdot \mu$. The ratio of these two forces has the form of the Rayleigh Number given in (8).

Substituting from (7) into (8) we obtain an estimate of the time scale (τ_i) for the development of convective instability based on the Rayleigh Number criterion:

$$\tau_i \approx A \left\{ \frac{\kappa}{g \alpha \rho} \right\}^{2/3} \frac{1}{\kappa} \left\{ \frac{\mu}{\Delta T} \right\}^{2/3} \quad (9)$$

where A is a numerical constant. Note especially the role of viscosity in this expression. We see that the more viscous the fluid, the longer is the time scale of instability, a most important fact because of the very large range of viscosities exhibited by magmas. We also see that, all else being equal, the greater is ΔT the smaller is τ_i . Other parameters do not vary much from case to case. To indicate the order of magnitude to be expected for τ_i for magmatic conditions, we take numerical values of $7 \times 10^{-7} \text{ m}^2 \text{ s}^{-1}$ for κ , $5 \times 10^{-5} / ^\circ\text{C}$ for α , $10 \text{ m} \cdot \text{s}^{-2}$ for g , $2700 \text{ kg} \cdot \text{m}^{-3}$ for ρ (mafic magma) and $2300 \text{ kg} \cdot \text{m}^{-3}$ for ρ (felsic magma). Taking a value of ΔT of 50°C , and a range of magma viscosity of $1 \text{ Pa} \cdot \text{s}$ to $10^7 \text{ Pa} \cdot \text{s}$ we obtain values of τ_i from approximately 10^2 s to 10^7 s , i.e., from on the order of minutes to years.

The lower boundary layer of a horizontal intrusion is dynamically stable with regard to its temperature structure. In the framework of a purely thermal model, one would predict an unstable upper boundary layer and convecting interior, underlain by a stagnant conductive lower boundary layer. Such a model has been considered by Jaupart and Brandeis (1986) whose theory predicts the evolution of temperature in the convecting region and the thickness of the stagnant lower layer. Later, we consider the contribution of chemical composition to melt density and show that this introduces the possibility of convective instability of the lower boundary layer. If circumstances are such that compositionally-induced instability should occur, then the purely thermal model will only be valid until this time, and it is important to know the time scale for compositional instability and compare this with the rate of development of thermal structure.

Structure of the convecting interior

Within the body of the fluid away from the conductive boundary layers, heat transport takes place by convection. A convenient way to consider the thermal structure of the convecting interior, is to decompose the temperature field into a horizontal average (\bar{T}) plus fluctuations (θ). The horizontally-averaged temperature is a function only of the vertical coordinate z . The heat budget for a slice of fluid between z and $z + dz$ (see Fig. 6) may then be written:

$$S \, dz \, \rho \, c_p \, \frac{\partial \bar{T}}{\partial t} = S \, \Phi(z_0) - S \, \Phi(z_0 + dz) + Q \, S \, dz \quad (10)$$

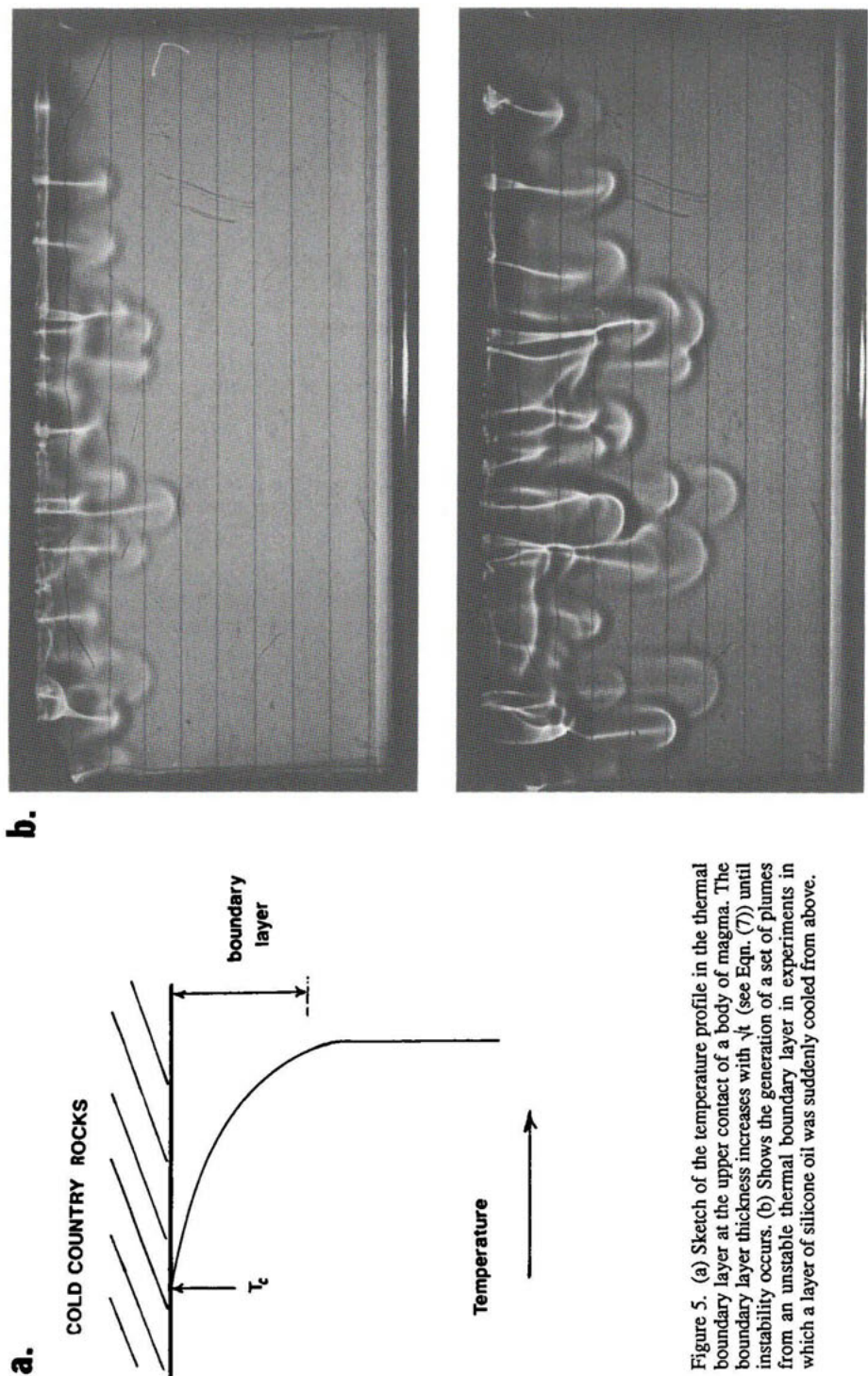


Figure 5. (a) Sketch of the temperature profile in the thermal boundary layer at the upper contact of a body of magma. The boundary layer thickness increases with \sqrt{t} (see Eqn. (7)) until instability occurs. (b) Shows the generation of a set of plumes from an unstable thermal boundary layer in experiments in which a layer of silicone oil was suddenly cooled from above.

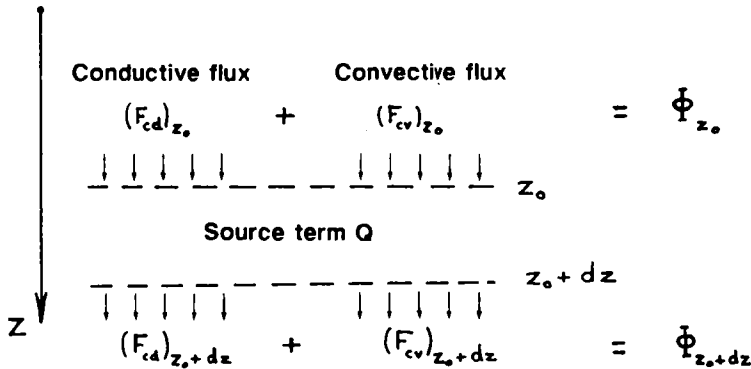


Figure 6. Sketch to illustrate the heat budget of a horizontal slice of fluid leading to the derivation of the differential equation to describe the evolution of temperature in a convecting fluid.

where S is the surface area perpendicular to the z axis c_p is the specific heat capacity and Q represents a source term, such as the release of latent heat from small, growing suspended crystals.

$$\Phi = F_{cd} + F_{cv} \quad (11)$$

represents the sum of the conductive (F_{cd}) and convective (F_{cv}) heat fluxes through a horizontal plane in the fluid. In the limit of infinitesimal dz , Equation (10) becomes the partial differential equation:

$$\rho c_p \frac{\partial \bar{T}}{\partial t} = \frac{\partial \Phi}{\partial z} + Q \quad (12)$$

The conductive heat flux is as usual assumed to be proportional to the local temperature gradient:

$$F_{cd} = -k \frac{\partial \bar{T}}{\partial z} \quad (13)$$

where k is thermal conductivity of the fluid. Substituting from Equations (11) and (13) into (12) we obtain the partial differential equation for temperature valid everywhere in the layer:

$$\rho c_p \frac{\partial \bar{T}}{\partial t} + \frac{\partial F_{cv}}{\partial z} = k \frac{\partial^2 \bar{T}}{\partial z^2} + Q \quad (14)$$

showing the three contributions to the time rate of change of temperature of a fluid element – these are the vertical gradients of the convective and conductive fluxes and the source term (Q).

To understand the convective flux we can envisage the interior of the fluid as consisting of a field of descending plumes slightly colder than the average temperature at any given level and ascending plumes associated with positive temperature fluctuations with respect to the mean. We can see intuitively that the average vertical velocity w is zero everywhere in the fluid. This is a consequence of mass conservation. Picture a fixed horizontal plane in the fluid. As such a surface has no vertical extent, matter cannot accumulate and hence the mass being transported upwards across the plane must exactly balance that being transported downwards. It is equally easy to deduce this formally. A standard approximation in convection theory (Boussinesq approximation) is the assumption that variations of density are neglected except in their contribution to the buoyancy force. The mass conservation equation in this approximation is:

$$\frac{\partial u}{\partial x} + \frac{\partial v}{\partial y} + \frac{\partial w}{\partial z} = 0 \quad (15)$$

where u, v and w are the components of fluid velocity in the x, y , and z directions. Taking the horizontal average of this equation and noting that $\partial u/\partial x$ and $\partial v/\partial y$ cannot make a net contribution to the horizontal average implies

$$\frac{\partial \bar{w}}{\partial z} = 0 \quad \text{which implies} \quad \bar{w} = 0 \quad (16)$$

because we know that $w = 0$ at the horizontal boundaries of the system. Thus, referring to the sketch in Figure 7a, we can write the convective transport of heat as:

$$F_{cv} = f \rho c_p w_1 \theta_1 + (1-f) \rho c_p w_2 \theta_2 \quad (17)$$

where f is the fraction of the horizontal surface area occupied by downgoing plumes with vertical velocity w_1 and temperature fluctuation θ_1 . Subscript 2 refers to upgoing plumes. Negative temperature fluctuations are associated with w positive, and vice versa and hence both contributions in Equation (17) are negative, indicating that convection cools the fluid by transporting heat upwards. The essential physical point to grasp is that the convective transport is effected by correlated fluctuations of velocity and temperature with respect to the mean values.

We now consider a simple case in which the source term $Q = 0$ and motions are sufficiently vigorous that the layer of fluid has a uniform horizontally-averaged temperature outside the boundary layers. The vertical gradient of T is zero, so there is no vertical conduction of heat, and it follows immediately from (14) that in the well-mixed interior where, say, $T = T_m$,

$$\frac{\partial F_{cv}}{\partial z} = -\rho c_p \frac{\partial T_m}{\partial t} \quad (18)$$

We know that $d/dt(T_m)$ is negative because the layer is being cooled. F_{cv} is transporting heat upwards and hence is negative with respect to the z axis. Equation (18) shows us that $\partial/\partial z(F_{cv})$ is positive. The physical interpretation of (18) is sketched in Figure 7b. The absolute magnitude of the convective flux decreases with depth to reach zero at the lower boundary layer where there is negligible motion. The decrease is linear with z which comes from integration of (18) with respect to z . To understand this, note that the ΔT between plumes and environment is a maximum just after they leave the upper boundary layer. As they descend, they exchange heat with the environment, and hence the magnitudes of θ and w decrease, leading to the vertical gradient in F_{cv} .

Thermal flux balance at the roof

We now reconsider the upper contact of an intrusion and explicitly include the formation of a solid layer. Hence latent heat enters the thermal balance. We consider the simple case of a planar solid/liquid interface, i.e., such that the solid has a porosity of zero. In a small time dt the interface advances by an amount da (Fig.8). The heat balance at the interface is thus:

$$F_{(-)} S dt - F_{(+)} S dt + \rho S L da = 0 \quad (19)$$

where L is the latent heat. On the $-ve$ side of the interface the heat flux is conductive and on the $+ve$ side the heat flux is conducted through the boundary layer into the convecting fluid. In symbols:

$$F_{(-)} = -k \frac{\partial T}{\partial z}, \quad F_{(+)} = -F_{cv} \quad (20)$$

In the limit of infinitesimal dt , Equation (19) becomes the differential equation for the interface position as a function of time:

$$\rho L \frac{da}{dt} = -F_{cv} + k \left[\frac{\partial T}{\partial z} \right]_{z=a} \quad (21)$$

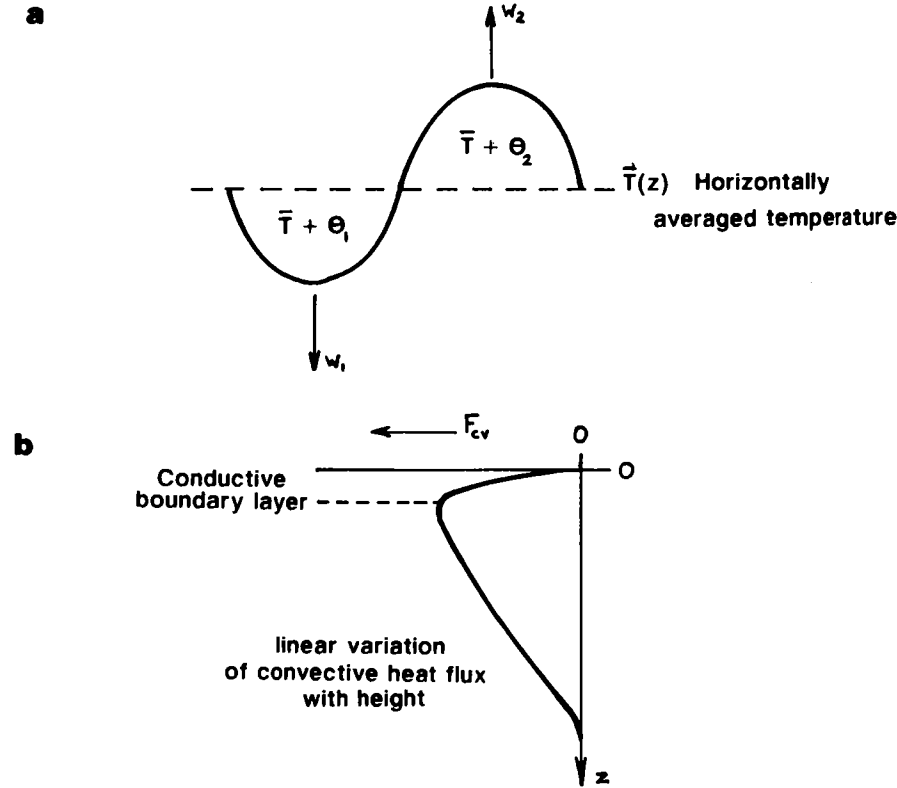


Figure 7. (a) Sketch to illustrate the idea of the temperature structure within the interior of a vigorously convecting fluid. Downward moving (velocity w_1) and upward moving plumes (velocity w_2) are associated with +ve and -ve temperature fluctuations θ_1 and θ_2 with respect to the horizontally-averaged value \bar{T} which is a function only of z . (b) Schematic plot of the convective heat flux in the fluid layer as a function of z obtained by integration of Equation (18).

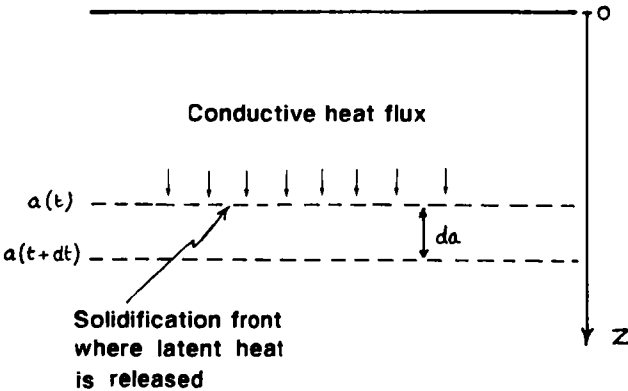


Figure 8. Illustrating with reference to Equation (21) the interface condition for temperature at a planar solidification front. Heat is being conducted out of the fluid across the solid layer and latent heat is being released at a rate proportional to the velocity of advance of the interface.

Initially the conductive flux is very large because of the steep temperature gradients and the solid layer grows rapidly. With time the temperature gradient across the solid diminishes and the rate of solid growth decreases. For a deep layer of magma it is conceivable that the convective heat flux from the interior remains sufficiently high that it eventually becomes comparable to the conductive flux across the solid layer whose growth will then become very slow. The possibility that the convective flux eventually even exceeds the conductive flux causing meltback of the chill has been analysed by Huppert and Sparks (1989). The quantitative conclusions to be drawn from such an analysis depend on various assumptions such as the precise form of the expression for the convective heat flux, however the main point to understand is the essential thermal balance which governs the advance of the interface. Regardless of the precise quantitative details, the important point is that the convective flux slows the advance of the interface and this is likely to be at least partly responsible for the observation that roof sequences of cumulates in intrusions are generally much thinner than floor sequences.

Further complexities of upper boundary layer structure

In magmas, a number of factors complicate the structure of the thermal upper boundary layer, and these must be considered in order to understand better the nature of the instabilities which may develop. Magma viscosity increases strongly with decreasing temperature, both because of changes in melt structure and the presence of crystals in regions where the temperature is below the liquidus. Thus, the steep thermal gradient implies a steep gradient of magma viscosity. This has the effect of stabilising the uppermost, more viscous part of the boundary layer, and the thickness of the boundary layer from which instabilities develop is reduced. The spatial distribution of crystals in the boundary layer is a most important issue. We have considered the simple case of an entirely solid layer forming above a convecting fluid. It is more likely, however, that a partially-solidified zone develops with a gradient of solid fraction between the entirely liquid and entirely solid regions. Depending on the structure of the phase diagram and kinetic effects this zone may have a range of possible thicknesses, crystal growth may be dendritic or take the form of small grains dispersed within the liquid, and some of the melt may become undercooled. All these factors affect what thickness of the boundary layer is unstable, the size of the temperature difference across the unstable part of the boundary layer and hence the heat flux from the convecting layer, and whether or not crystals and/or undercooled melt participate in convective flow. At the present time these issues are not fully resolved but a number of aspects have been considered by several authors (Brandeis and Jaupart, 1986; Kerr et al., 1989, 1990a,b,c; Brandeis and Marsh, 1989; Marsh, 1989).

FREEZING OF A BINARY ALLOY AND COMPOSITIONAL CONVECTION

In this section we will consider some of the phenomena which arise during the solidification of a binary alloy, that is in which two chemical components are present. The density of the fluid is a function of its composition and temperature (Eqn. 1) and the residual liquid released by fractional crystallization can be either more or less dense than the starting liquid. We will refer to the schematic phase diagram shown in Figure 9. Which of the two possible solids crystallises depends on whether the liquid composition is greater or less than the eutectic composition C_E . We will use the conventions that the solid composition is either 0 or C_S (Fig. 9), and that the residual liquid is less dense if C_S crystallises and more dense if the solid has zero composition. A number of different arrangements can be envisaged, depending on the composition of the system and how it is cooled, which can give rise either to dynamically stable or unstable situations.

Solidification and constitutional supercooling

We consider first the structure of a crystallization boundary layer under dynamically stable conditions, for example when the system is cooled from below and the residual

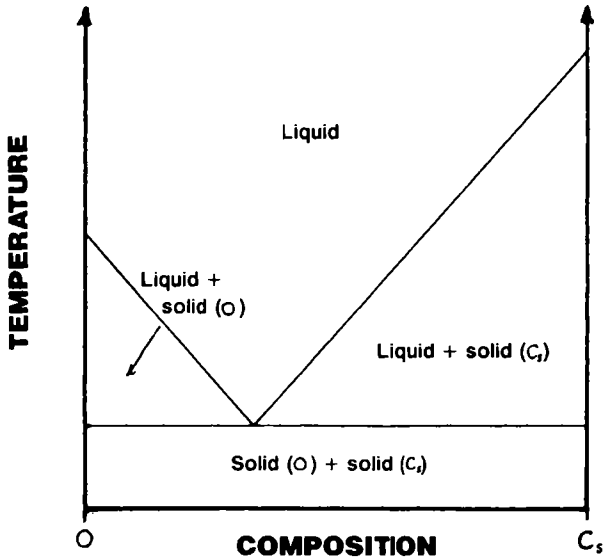


Figure 9. Simple phase diagram for a binary alloy. Two solid compositions are possible, and the liquidus are straight lines.

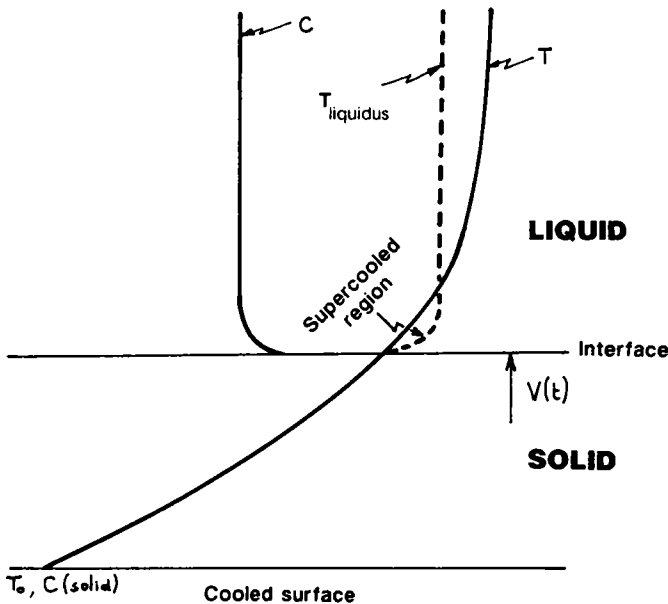


Figure 10. Illustrating the diffusive profiles of temperature and composition developed during solidification of a binary alloy with a planar solid/liquid interface. Note that the thermal boundary layer is considerably thicker than the compositional boundary layer. A gradient in the local value of the liquidus temperature is also induced on the same scale as the compositional boundary layer. The phenomenon of constitutional supercooling is shown: the hatched area is such that the liquidus temperature is locally greater than the actual temperature.

liquid released by crystallization is dense. In this case the composition and temperature fields evolve by diffusion. The solidification front can either be flat or very commonly it develops such that a mixed phase of solid and liquid forms referred to as a mush. The case of a flat interface is illustrated in Figure 10 in which the diffusive profiles of composition and temperature developed ahead of the interface are sketched. We note that the compositional boundary layer is much thinner than the thermal boundary layer because of the general fact that the thermal diffusivity in the liquid (κ_l) is much greater than the compositional diffusivity (D). This situation is described mathematically by diffusion equations: for thermal diffusion in the liquid and solid, and for compositional diffusion in the liquid. The composition of the solid below the interface $h(t)$ is constant. We also have two interface conditions which express the thermal and chemical budgets at the interface:

$$L \frac{dh}{dt} = k_s \left[\frac{\partial T}{\partial z} \right]_{h-} - k_l \left[\frac{\partial T}{\partial z} \right]_{h+}, \quad C_h \frac{dh}{dt} + D \left[\frac{\partial C}{\partial z} \right]_{h+} = 0 \quad (22)$$

where L is the latent heat of crystallization, and C_h is the composition of the liquid just at the interface, and k_s and k_l are the thermal conductivities of the solid and liquid. The rate at which latent heat is released at the moving boundary equals the difference between the thermal fluxes below and above the interface and the chemical diffusive flux is just sufficient to transport away excess solute released at the interface because the solid and liquid differ in composition.

Figure 10 also illustrates the idea of constitutional supercooling, which can lead to instability of the planar solidification front and formation of a so-called "mush." This is a region in which solid and liquid co-exist as an intimate mixture with a highly convoluted local geometry. A criterion for the onset of mush formation can be derived as follows. Consider the case of a planar solidification front advancing into the liquid. We see from (22) that the faster the interface advances, the steeper must be the gradient of composition in the liquid. The gradient of liquid composition implies a gradient of local liquidus temperature. The dashed curve shows the liquidus temperature. At a sufficiently fast rate of advance, this leads to the situation in which the local liquidus temperature in the boundary layer is greater than the actual temperature and hence the liquid is supercooled (Fig. 10). This is often taken to be the condition for the onset of mush formation (Rutter and Chalmers, 1953), and in symbols is written:

$$\left[\frac{\partial T}{\partial z} \right]_{h+} < -\Gamma \left[\frac{\partial C}{\partial z} \right]_{h+} \quad (23)$$

where Γ is the slope of the liquidus curve in Figure 9. Another criterion based on analysis of the linear stability to morphological perturbations of an interface advancing at constant velocity was developed by Mullins and Sekerka (1964), although it does not amount in practice to a very different prediction.

Structure of a "mushy" crystallization boundary layer

In many examples of solidification processes a planar interface is unstable and a mush develops. Depending on the thermal and compositional gradients present, we can envisage cases which are dynamically stable and those which are dynamically unstable. We now consider the case of solidification from below in which the residual liquid released by crystallization is less dense than the starting liquid and convective instability occurs. We know, however, that the boundary layer must first develop, and hence instability occurs at some finite time before which transport is by diffusion. We first consider the diffusive regime, then a criterion for dynamic instability and finally we discuss the form and effects of fully developed convection.

A common approach (e.g., Hills et al., 1983; Fowler, 1985; Huppert and Worster, 1985) is to neglect the locally complex morphological details of the mush and treat it as a

random mixture of solid and liquid, homogeneous at a scale sufficiently large compared to local irregularities. This is like treating the mush as a third phase occupying a transition region between a layer of entirely solid material from an entirely liquid layer (Fig. 11). The macroscopic transport properties of the mush such as thermal diffusivity are calculated as weighted averages of the properties of the liquid and the solid. The problem then becomes one of calculating which regions of space are occupied by solid, by liquid, and by mush.

A simple but informative case is that in which transport of solute is neglected. The positions (as functions of time) of the two interfaces separating liquid from mush and mush from solid are essentially determined by the thermal budget of the system. The local composition (solid plus liquid) is constant and always equal to the initial liquid composition. The local solid fraction is a function only of temperature. Putting these ideas in mathematical terms, in the solid $\{z < a(t)\}$ and liquid $\{z > b(t)\}$ we have standard diffusion equations but within the mush $\{a(t) < z < b(t)\}$ we have additional terms due to crystallization. Thus:

$$\rho c_p \frac{\partial T}{\partial t} = k_s \frac{\partial^2 T}{\partial z^2} \quad \text{in the solid} \quad (24)$$

$$\rho c_p \frac{\partial T}{\partial t} = k_l \frac{\partial^2 T}{\partial z^2}, \quad \text{in the liquid} \quad (25)$$

$$(\rho c_p)_m \frac{\partial T}{\partial t} = k_m \frac{\partial^2 T}{\partial z^2} + \rho_s L \frac{\partial \Phi}{\partial t} \quad \text{in the mush} \quad (26)$$

where $\Phi(z,t)$ is the solid fraction in the mush and the subscript m refers to average properties for the mush. We also require boundary conditions and the two conditions for heat fluxes at the two moving interfaces similar in type to (21). One more condition is required. The simplest is to insist on zero solid fraction at the mush/liquid interface (Hills et al., 1983). We assume local thermodynamic equilibrium everywhere in the mush and, for simplicity use the following equation for a (linear) liquidus (Fig. 9):

$$(T - T_s) = \Gamma (C - C_s) \quad (27)$$

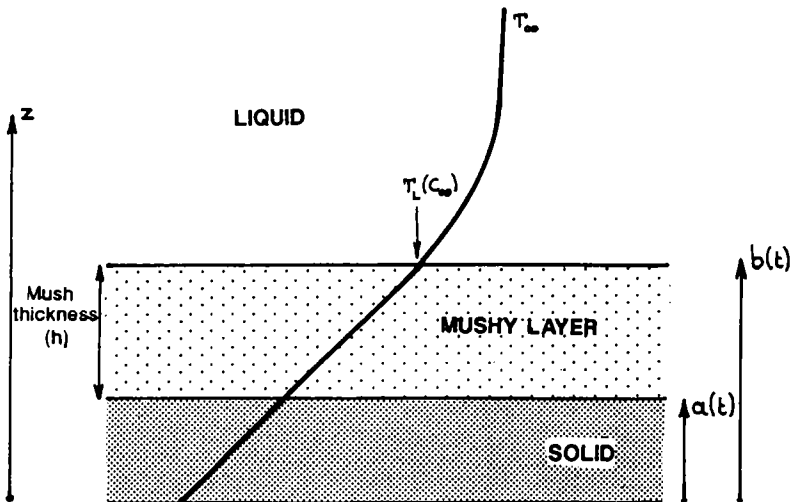


Figure 11. Solidification of a binary alloy in which a mushy layer forms. The cooled boundary is below the eutectic temperature. The mush/solid boundary is at the eutectic temperature T_E . Neglecting compositional diffusion, the mush/liquid interface is at the liquidus temperature of the far field composition $T_L(C_0)$.

Within the mush, the equation relating solid fraction to liquid composition and hence temperature is:

$$(1-\Phi) \frac{\partial C}{\partial t} = (C - C_s) \frac{\partial \Phi}{\partial t} \quad \text{in the mush} \quad (28)$$

In Equations (25) and (28) we have neglected compositional diffusion. In reality this is not true, but a more complete analysis (Worster, 1986) shows that under most circumstances the main results such as the mush thickness are insensitive to compositional diffusion which can, to a good approximation, be entirely neglected. Equation (28) is thus a straightforward mass-balance equation saying that the local composition of the liquid reflects only the amount of fractional crystallization which has taken place. In other words, the temperature gradient due to cooling induces gradients in local liquid composition and porosity by virtue of the assumption of local thermodynamic equilibrium. Equation (26) is a diffusion equation with the source term due to release of latent heat. The source term retards cooling with respect to the case in which no such term is present. In short, although the form of these equations is altered by the presence of the mush and the mathematical analysis is a bit more involved their fundamental character as diffusion equations remains.

The simplest boundary conditions are those of a cold temperature imposed suddenly at the base of a semi-infinite layer of fluid and subsequently held constant. As might be expected, a solution may be found typical of diffusive systems in which the positions of the interfaces are proportional to the square-root of time:

$$a(t) = \lambda_a \sqrt{t} \quad , \quad b(t) = \lambda_b \sqrt{t} \quad (29)$$

The positions of these interfaces are essentially controlled by the thermal budget. λ_b is greater than λ_a , and in the absence of other effects, the mushy layer gets thicker with time.

Figure 12 gives an example numerical solution of diffusion equations for a mush for an aqueous solution of ammonium chloride showing the vertical gradients of temperature, composition and porosity. The major influences on the profile of porosity are the difference between the composition of the crystallising solid and that of the initial liquid ($C_s - C$) and the steepness of the liquidus gradient in the phase diagram (Γ). All else being equal, the greater is ($C_s - C$), the less solid is present at a given height and the larger is Γ , the weaker are the spatial gradients of the dependant variables in the mush.

When freezing is ultimately complete, the composition of the final solid will be uniform everywhere. Such a model might be applied to the solidification of a small body of magma such as a thin dyke emplaced into cold country rocks. Although during freezing, very strong temperature gradients are present, complete solidification is so rapid that no time is available for significant transport phenomena to take place. Gradients in grain size may result reflecting crystal nucleation and growth effects, but the composition of such a dyke is typically uniform.

According to Equation (1), however, we see that before solidification is complete, the gradients in liquid composition and temperature imply gradients in fluid density and this may lead to convection if the density gradients are unstable and sufficient time is available for instability to occur. Convective mass transfer provides a mechanism for the segregation of compatible components entering the crystals and incompatible components in the residual liquid and hence for the production of spatial variations of composition in the final solid.

Onset of compositional convection

The temperature field makes a stabilising contribution to the overall density gradient and the compositional field a destabilising contribution. Figure 13 is a sketch of the approximate form of the overall density gradient which might result, within and above the mush. The diagram is not drawn to scale, and we have for completeness included the

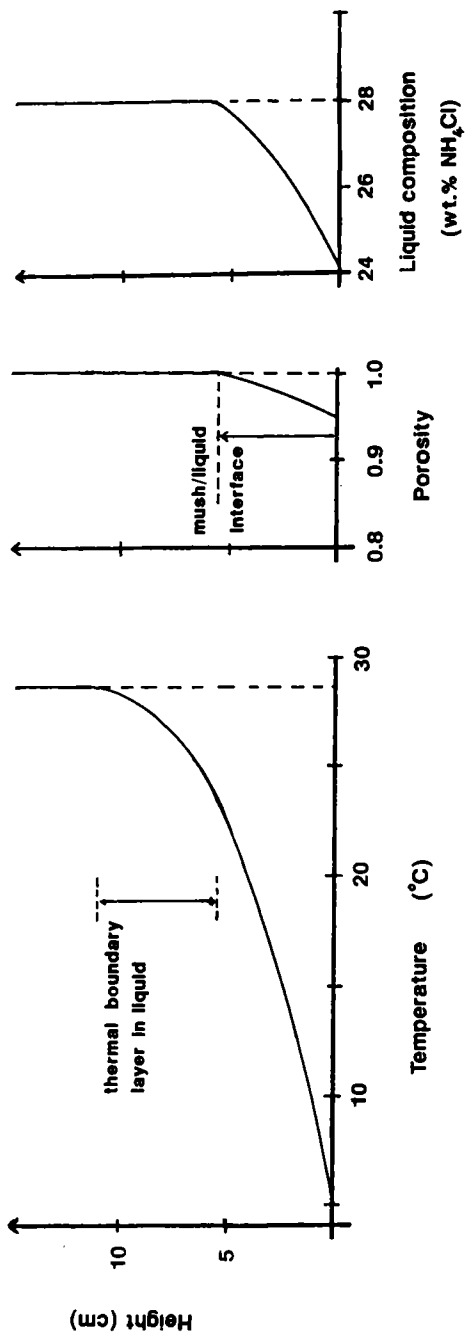


Figure 12 (above). Numerical calculations for the aqueous ammonium chloride system solidifying under diffusive conditions. Profiles are shown of temperature, liquid composition and porosity within the mush. Note the rather high value of porosity which is obtained for this substance. See discussion in text.

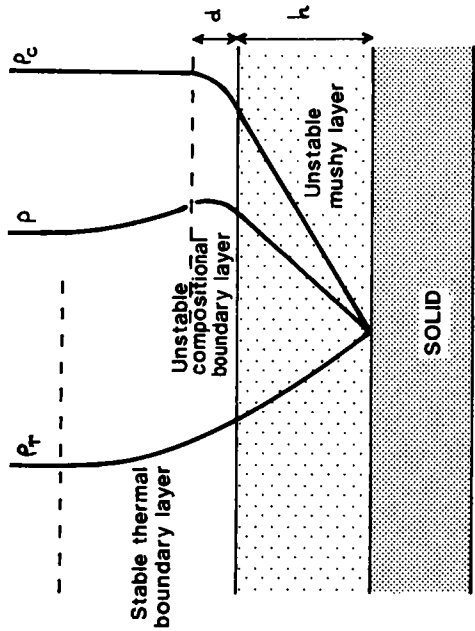


Figure 13 (right). The thermal (ρ_T) and compositional (ρ_c) contributions to the overall density gradient within the liquid. Two parts of the boundary layer are potentially independently unstable – the liquid just above the mush (thickness d) and the liquid within the mush (thickness h).

presence of a compositional boundary layer above the mush, although in practice it is likely to be very thin. Both the mush and the compositional boundary layer above thicken proportional to the square root of time, and initial convective instability may in principle either be restricted to the boundary layer above or involve the fluid within the mush. The instability of a boundary layer ahead of a flat solidification front has been analysed by Coriell et al. (1980) and Hurlle et al. (1983). The critical Rayleigh number for a boundary layer at a mush/liquid interface is somewhat different although the basic analysis is similar (Tait and Jaupart, 1989). The expression for the critical Rayleigh number:

$$Ra_c = \frac{g \Delta \rho_c d^3}{D \mu} \quad (30)$$

where $\Delta \rho_c$ is the compositional density difference across the boundary layer, D is the chemical diffusivity and μ the viscosity. The boundary layer thickness d increases until the critical Rayleigh number is reached. This is exactly similar to the stability argument given for thermal convection. A similar criterion may be devised for instability of the interstitial liquid by treating the mush as a porous medium with some characteristic value of permeability (Π). Thus:

$$Ra_m = \frac{\Pi g h \Delta \rho}{\kappa \mu} \quad (31)$$

where ν is the kinematic viscosity of the fluid and h is the thickness of the mush. This is more awkward than the case of a simple fluid boundary layer because permeability is a function of porosity and pore structure which may vary considerably from case to case. The details of exactly which part of the crystallising boundary layer initially goes unstable is probably of secondary importance as far as the application to magmatic systems is concerned. We can be reasonably sure that instability will eventually occur and that, as convection evolves, fluid from progressively deeper in the mush is likely to participate in the flow.

An important point is that there are two time scales associated with compositional convection, one characteristic of crystal growth and one characteristic of convective instability. Because the compositional boundary layer itself develops by diffusion during crystal growth, it is not possible for the latter to be much shorter than the former. Approximate equality of these time scales corresponds to the case of aqueous solutions for example in which convection is typically seen almost as soon as crystal growth begins. The other possibility, in which crystal growth is more rapid than the development of convective instability may well arise in the case of magmatic crystallization because of the high viscosities of magmas. Specifying a stability criterion enables calculation of a time scale for instability as illustrated by Equation (9). Tait and Jaupart (1989) demonstrated this regime experimentally and made an illustrative calculation to translate the result into a value for a thickness of crystallised rock which could form in this time. For mafic systems they obtained values of the order of tens to a hundred metres. The quantitative details are less important than the general point that a transition of physical regime such as the onset of compositional convection is likely to be recorded in some way in the crystallised rock sequence which forms.

Convective transport of solute

The convective transport of solute by a set of plumes generated at a horizontal crystallization boundary layer can be thought of as broadly analogous to the transport of heat during high Rayleigh number thermal convection, described earlier. The transport of chemical components is essentially due to correlated fluctuations of velocity and composition associated with the plumes, however, the compositional problem is not as simple as the purely thermal case. During solutal convection produced by crystallization the system is being cooled and hence there are inevitably both chemical and thermal gradients in the system. These gradients are developed over different length scales within the fluid

because the thermal diffusivity is much larger than the chemical diffusivity and this complicates the analysis.

Instability of the compositional boundary layer thus leads to a set of thin compositional plumes rising through a thick thermal boundary layer. A number of different regimes can be envisaged according to the way in which the plumes interact with the thermal boundary layer. For example mixing by the plumes might in principle be sufficiently vigorous to produce a constant vertical profile of temperature outside the compositional boundary layer. At the other extreme the plumes could be so thin and sluggish that horizontal diffusion of heat is able to more or less smooth out the thermal fluctuations associated with the plumes. The importance of this is that these two extreme cases represent very different thermal fluxes due to the compositional convection. Laboratory experiments are required to elucidate these points further.

Vertical walls

An important case to consider is that in which the buoyancy to drive convection is generated at a vertical wall rather than a horizontal boundary. This is somewhat different in that there is no convectively stable configuration. Convection will always result and the main task is to calculate the rate at which the flow develops and moves. The boundary layers which develop adjacent to vertical walls have a compound structure if both thermal and compositional buoyancy are being generated because in many cases these will act in opposite senses. Thus compositional buoyancy will tend to generate upflow, whereas the thermal buoyancy might tend to generate downflow. In many situations vertical gradients of composition and temperature develop which in the context of igneous rocks may correspond for example to a magma chamber stratified from hotter more primitive compositions to colder more evolved compositions. A crucial point is that the vertical profile of density (and hence of composition and temperature) which develops depends on the fluid dynamic regime of the plume or boundary layer.

Consider first the simpler case of heating a body of fluid at a vertical sidewall. The following remarks can equally well be applied to cooling from the side, the only difference being that stratification builds up in the opposite sense (i.e., from bottom to top rather than from top to bottom). The production of buoyant fluid causes convection, however, vigorous motions are restricted to a region narrow with respect to the overall size of the container (Figs. 14a,b). This is balanced by a much slower return flow which takes place over the remaining surface area of the container. Upon reaching the top of the container, the buoyant fluid spreads out laterally in a horizontal flow over the whole surface area. Over times much longer than the residence time of a parcel of fluid in the zone of vigorous motion, a stable vertical density stratification is developed in the body of the fluid (Figs. 14a,b).

In the turbulent regime, the characteristic density gradient is steep behind the first descending front and decreases upwards in the container (Fig. 14b). This is a consequence of the increase in turbulent entrainment and hence efficiency of mixing in the direction of the flow, because the stronger the mixing, the harder it is for stratification to become established. Figure 14a shows schematically the results of experiments on laminar thermal convection caused by sidewall heating (Worster and Leitch, 1985). In this case the boundary layer thickens by molecular diffusion rather than turbulent entrainment. The resulting density gradient is found to increase in steepness in the direction of flow. To explain these results, these authors suggested that instead of all fluid in the boundary layer proceeding to the top of the container, as in the turbulent case, fluid flows out of the boundary layer into the growing stratified region in the interior upon reaching its buoyancy level. The most buoyant fluid is close to the wall where viscous drag is the greatest (assuming no horizontal gradients in fluid viscosity) and the mass flux in the boundary layer increases away from the wall. The stark contrast between the vertical density gradients produced by turbulent and laminar convection illustrates the importance of

understanding the fluid dynamic regime. We see that although in both cases the physical process is essentially the same the results are quite different.

The same basic principles apply when the buoyant liquid is produced by fractional crystallization, although additional effects occur because of the compound nature of the boundary layer: a thin compositional layer within a thicker thermal layer (Nilson, 1985). Laboratory experiments suggest, however, that the same basic forms of density profile (Figs. 14a,b) result (Leitch, 1987; Thompson and Szekely, 1988). Chemical gradients in magma chambers which have been deduced from eruption deposits vary from case to case (Hildreth, 1981). However, we can see that this need not necessarily imply different processes of formation. In felsic chambers where the fractionating mineral assemblage does not differ greatly from the melt in its major element composition and the magma viscosity is sufficiently high to produce laminar flow, strong gradients of incompatible trace elements near the roof might be expected. This is illustrated for the Laacher See system by Tait et al. (1989), but may also explain similar gradients in other systems such as the Bishop Tuff chamber (Michael, 1983). In less evolved magmas, where different major and trace elements may have a wide range of distribution coefficients, and where the boundary layer may be laminar or turbulent, a variety of other profiles might result.

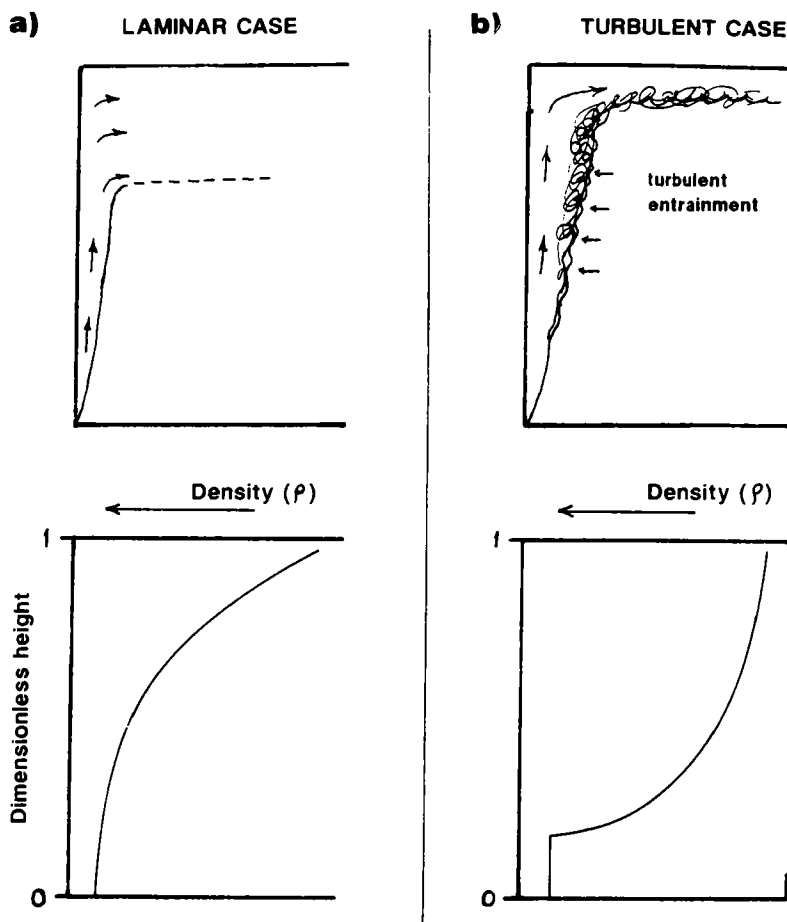


Figure 14. Flow patterns and vertical density gradients resulting from laminar (a) and turbulent (b) convection at a vertical sidewall.

Conclusion

The main points to grasp from the preceding sections are that when a liquid with two or more chemical components is cooled at its boundaries, the thermal gradients which result generate crystallization boundary layers in which there are gradients in both the chemical composition of the residual liquid and the solid fraction. The system becomes inhomogeneous. When, in addition, convective motions occur, material from within the boundary layer can be mixed into the main body of liquid distant from the boundaries which therefore undergoes thermal and chemical evolution. Important consequences for magma chambers is that the magma in the interior of a reservoir may show chemical differentiation without necessarily having directly 'seen' crystallization, and that such chambers are likely often to be chemically and thermally zoned.

SUMMARY OF OTHER PHENOMENA

Having discussed a number of basic principles of crystallization and the transport processes of diffusion and convection, we now summarise a number of phenomena and situations in which these principles can be applied to situations believed to be of geological relevance. It is left to the interested reader to obtain details from the references.

Crystal settling

The study of the interactions between a convective flow and particles distributed within the fluid when the fluid and particle densities differ is a problem of obvious relevance to the investigation of magma chambers, but it is not yet well developed from a fluid- dynamical point of view.

The simplest case of motion of a particle in a body of fluid is that of settling of a spherical object in a stagnant fluid under gravity. When the velocity of settling is sufficiently low that the flow of the fluid around the sphere is laminar the terminal settling velocity (v_t) obeys Stokes law:

$$v_t = \frac{d^2}{18} \frac{g \Delta \rho}{\mu} \quad (32)$$

where $\Delta \rho$ is the density difference between the fluid and the liquid, d is the diameter of the particle and μ is the shear viscosity of the fluid. A similar equation was deduced earlier from dimensional arguments to obtain an intuitive understanding of the Rayleigh number. This expression is valid when the Reynolds number (Re) is small:

$$Re = \frac{v_t d \rho}{\mu} \quad (33)$$

which means that the settling particle has negligible inertia and the motion is determined by a balance between viscous and buoyancy forces. Note that the settling velocity is most sensitive to particle diameter. This has an important implication for magmatic systems because here the crystals start with zero diameter and grow as cooling proceeds. When they are still very small, settling should be negligible and the crystals simply carried along passively by the magma flow. As they become larger, settling can play an increasingly important role.

When particles are in a body of convecting fluid, the upward fluid motions provide a means to keep them in suspension. The profile of particle concentration is determined by the ratio between the Stokes velocity (v_t) and the average vertical convective velocity (w). When $v_t/w \ll 1$, the particle concentration is approximately constant with height in the interior of the fluid. On the other hand when $v_t/w \gg 1$ the particle concentration falls off

very rapidly with height. A number of authors have applied this type of theory and estimated that in the main body of a turbulently convecting magma chamber, w is likely to be much larger than v_t so that the particle concentration may be expected to be approximately constant (e.g., Bartlett, 1969). Some theoretical results are also available for lower Rayleigh number convection in which the flow has an organised, cellular form (Marsh and Maxey, 1985). However, as pointed out by Martin and Nokes (1990) even in a vigorously convecting fluid at the rigid boundaries, fluid velocities drop to zero and there should always be a thin boundary layer in which settling can take place. These authors carried out experiments with a dispersion of a low concentration of particles (<1%) in a thermally convecting fluid. They indeed found that at any given moment the interior of the convecting fluid was well-mixed by convection and the particle concentration was constant, however, with time this concentration steadily decreased as particles settled out in the lower boundary layer.

Koyaguchi et al. (1990) carried out another interesting set of experiments in which they tried higher initial particle concentrations (30%) in a fluid with an applied temperature difference (ΔT) sufficiently high to cause vigorous thermal convection in the absence of particles. They observed an intriguing cyclic behavior. Initially the concentration of particles was sufficiently high that convection was suppressed and an interface separating particle-laden fluid below and particle-free fluid above was observed to descend in the tank. This interface descended at a velocity proportional to the Stokes settling velocity defined by Equation (32) and sedimentation of particles from the lower layer onto the floor of the tank occurred. When the particle-laden lower layer had become sufficiently thin and hence had a large ΔT across it, it became unstable, rapidly overturned and mixed particles back into the fluid throughout the tank. Because sedimentation had occurred, the new uniform concentration of particles was less than the original value. If after remixing, the particle concentration was still sufficient to suppress thermal convection the behavior was repeated. If, after remixing, the particle concentration was sufficiently low that convection could take place the same behavior as reported by Martin and Nokes (1990) was seen.

These experimental papers illustrate some of the novel interactions which may occur between particles and a convecting fluid. Considerable care must be taken, however, when applying these results to magmatic systems. There are at least two major simplifying conditions in the experiments: first that the initial distribution of particles is uniform and second that at the beginning of the experiments the particles already have their final sizes. Either or both of these assumptions could be substantially in error for reasons which we will now illustrate briefly in the next section which discusses some aspects of crystal nucleation and growth.

The kinetics of crystal nucleation and growth

Nucleation and growth of crystals from silicate liquids can be sluggish and it is not straightforward to calculate the spatial and temporal distributions of crystals which result from cooling. Brandeis et al. (1984) present numerical calculations of rates of crystallization, distributions of crystals and grain sizes and a scaling analysis of the system of equations is given in Brandeis and Jaupart (1987). Their analysis is for a one-component melt in the absence of convection. Calculations have also been made for a two-component melt with a simple phase diagram which give broadly similar results (Spohn et al., 1988).

The essence of the analysis is to couple the heat conduction equation including release of latent heat – see Equation (26) – with expressions for the rates of nucleation and growth of crystals as a function of undercooling, the difference between the actual temperature at some position in the melt and the liquidus temperature. A finite undercooling is always required to nucleate crystals, whereas the growth rate is finite at all subliquidus temperatures. The rate of advance of the crystallization front, and the nucleation density and rate of growth of crystals experienced in any given part of the crystallization boundary layer depend in general on the applied temperature gradients and the requirement that the latent

heat released by crystallization must be conducted away. We will just make a few general points here and readers interested in details should refer to the references.

An intrusion is cooled from the roof, floor and walls, and steep thermal gradients exist adjacent to these cooling surfaces. In consequence, the crystal distribution is likely to be far from homogeneous. The results of the above analysis show the propagation of a crystallization boundary layer, over which the solid fraction varies from 1 to 0, from the margin into the magma. The cooling surfaces are also where thermal and compositional buoyancy are generated. Thus, it is possible that crystals may be entrained into convective instabilities and carried away from the margins into the main body of magma. Indeed the presence of dispersed crystals also affects the bulk density of the magma and will influence the production of convective instabilities. A detailed analysis is required to predict the thermal structure of the boundary layer and the distribution of solids, etc., and hence evaluate this possibility. The analysis also indicates that crystal growth is sluggish, for example millimetre-sized crystals such as are often found as phenocrysts in lavas or as cumulus crystals in intrusions might typically take on the order of a year to grow. This is a long time compared to the time scale of convective motions which can be expected, at least in relatively fluid magmas, and indicates that a crystal of such a size may potentially contain a significant record of evolution of the system in such features as compositional zoning.

Another novel possibility can be understood by comparing the characteristic time for convective instability – see Equation (9) – and the characteristic time for crystal nucleation and growth. If the time for the development of convective instability is much shorter than that for the production of crystals, as may be the case in low viscosity magmas, undercooled melt can participate in thermal convection. The numerical results indicate that this may indeed be important in mafic magmas whereas in much more viscous melts the crystallization timescale is likely to be shorter than the convective timescale and hence convection should not involve undercooled magma (Brandeis and Jaupart, 1986). The participation of under-cooled melt in convection during cooling of an aqueous solution from above has more recently been documented experimentally by Kerr et al. (1989).

Magma chamber replenishment

The idea that magma chambers are episodically replenished by new magma from a deeper source is widely accepted and based on a range of evidence from volcanic and plutonic rocks. This has prompted a number of experimental fluid dynamic investigations which demonstrate that a variety of different phenomena may occur depending mainly on the relationships between the densities of the incoming and resident liquids but also on such factors as input rate and magma viscosity. References describing some of these fluid dynamic studies are Huppert and Turner (1981), Huppert et al. (1982), Campbell and Turner (1986), Huppert et al. (1986).

The main types of different behavior which can be imagined are cases in which the new magma is denser than the resident magma, those in which the new magma is less dense, those in which inertia of the incoming melt is negligible and those in which it is not. We illustrate some possible cases in Figures 15a,b,c. If the incoming magma is denser, it can be expected to pond at the base of the chamber. The amount of initial mixing which may take place between the two magmas depends on whether the incoming melt has substantial or negligible inertia.

Consider first the case in which the new magma is less dense than the resident magma. The characteristics of the resulting buoyant plume depend on the input rate, the density difference between the two magmas and the magma viscosities which can be combined into a Reynolds number (Re). At high Re ($>10^3$) plumes are turbulent and at low Re (<1) they are laminar. At intermediate Re a variety of instabilities are observed. Baines and Turner (1969) determined the form of the density gradient resulting from a turbulent plume (this was illustrated in Fig. 14b), and Worster and Huppert (1983) gave a

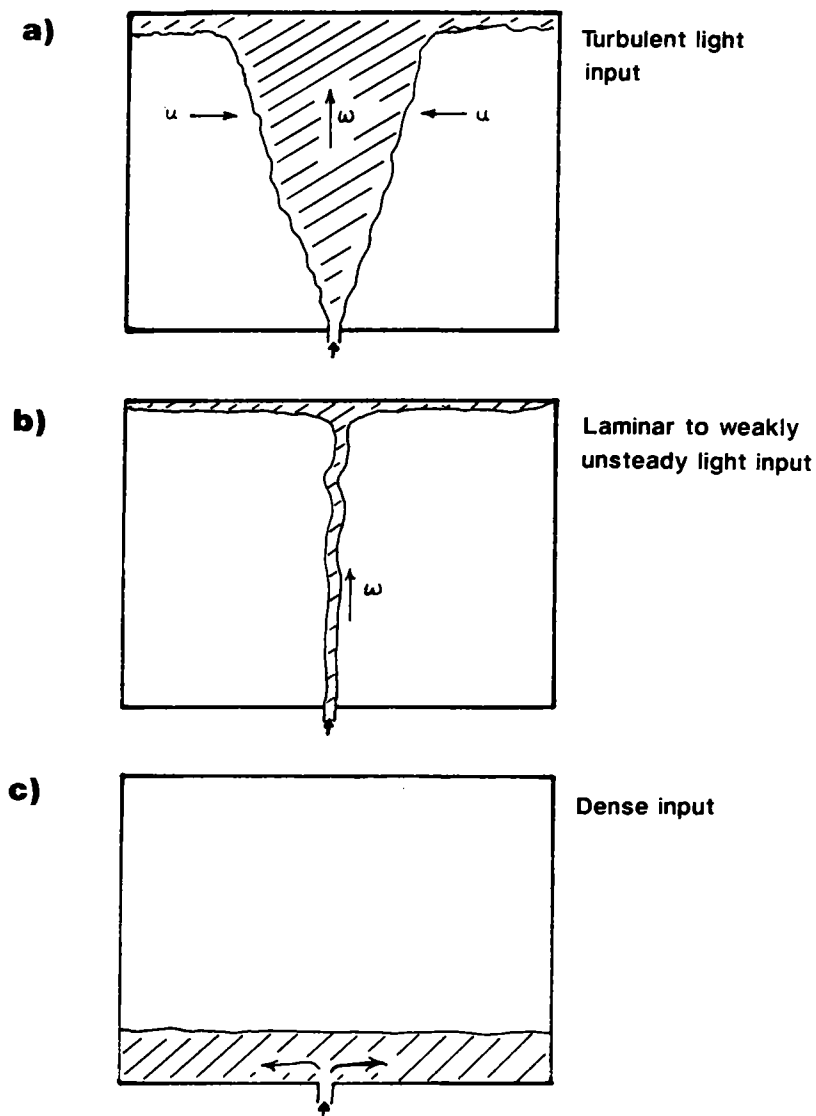


Figure 15. Sketches to illustrate some of the possible fluid dynamic behavior resulting from magma chamber replenishment. See text for discussion.

method to calculate the time evolution of the stratification. We will not give details of the analysis of plumes here but just summarize the main features of turbulent plumes. A snapshot of a turbulent plume shows the boundary with the environment to be highly irregular, however time-averaged profiles at a given value of height are smoothly varying in the horizontal coordinate and generally Gaussian in form. Figure 16 illustrates such a time-averaged profile of vertical velocity. A standard approximation in theory of such plumes is to assume a so-called "top hat" profile (Fig. 16), which amounts to assuming constant properties within the plume at a given height. Second is the entrainment assumption which says that material from the environment is incorporated into the plume at a horizontal velocity (u) which is directly proportional to the average vertical velocity. Thus at all heights:

$$u = \alpha w \quad (34)$$

where α (called the entrainment constant) is determined by experiment. The turbulent plume thus has a conical shape and involves quite efficient mechanical mixing with the environment. Vertical stratification resulting from a turbulent plume would be expected to resemble that sketched in Figure 14b.

A laminar to weakly unstable buoyant plume is sketched in Figure 15b. Mixing with the environment is much less efficient than the previous case. The new melt rises passively to the top of the chamber and very little mixing takes place. The resulting vertical zonation of

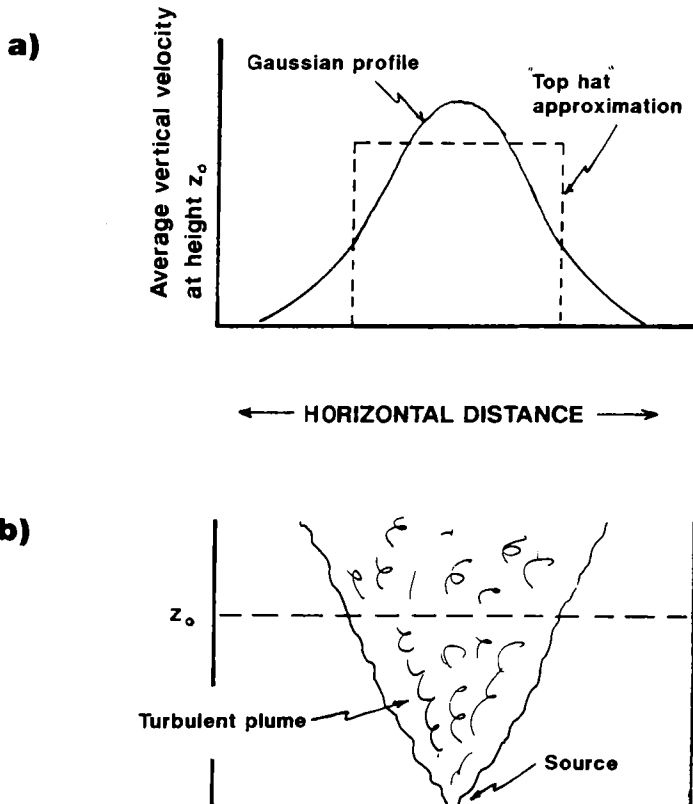


Figure 16. Illustrates the Gaussian time-averaged profiles of vertical velocity observed in a turbulent plume and the typical "top hat" approximation made in turbulent plume theory.

the chamber would essentially be two discrete layers with the new magma overlying the old and therefore be quite unlike the continuous zonation produced by the turbulent plume.

Another case which has been examined experimentally is that in which the new liquid entering the chamber is more dense than the resident magma. In this case, the new magma will have a tendency to pond at the base of the chamber (Fig. 15c). The new magma is likely to be hotter than the resident magma and therefore its excess density results from its different chemical composition. Heat can be exchanged rapidly between the two layers by thermal convection, causing cooling and crystallization in the lower layer. If fractional crystallization in the lower layer reduces the density of the residual liquid a condition may eventually be reached at which the interface between the two layers becomes unstable they mix together. This was the case in the experimental system used by Huppert and Turner (1981) and proposed as a model for mafic magma chambers by Huppert and Sparks (1981). In subsequent papers (see list at beginning of this section) the effects of input rate, viscosity difference between the layers, and initial stratification of the upper layer have been examined. Campbell and Turner (1986) considered a replenishment event in which the new magma was denser but had substantial inertia. Hence a turbulent jet was formed which mixed vigorously as it rose but whose initial kinetic energy eventually became exhausted causing the jet to collapse and flow out sideways along the floor.

REFERENCES

- Baines, W.D. and Turner, J.S. (1969) Turbulent buoyant convection from a source in a confined region. *J. Fluid Mech.* 37, 51-80.
- Bartlett, R.W. (1969) Magma convection, temperature distribution and differentiation. *Am. J. Sci.* 267, 1067-1082.
- Bottinga, Y. and Weill, D.F. (1970) Densities of liquid silicate systems calculated from partial molar volumes of oxide components. *Am. J. Sci.* 269, 169-182.
- Bottinga, Y., Weill, D.F. and Richet, P. (1982) Density calculations for silicate liquids. Revised method for aluminosilicate compositions. *Geochim. Cosmochim. Acta* 46, 909-919.
- Brandeis, G. and Jaupart, C. (1987) The kinetics of nucleation and crystal growth and scaling laws for magmatic crystallization. *Contrib. Mineral. Petrol.* 96, 24-34.
- Brandeis, G. and Jaupart, C. (1986) On the interaction between convection and crystallization in cooling magma chambers. *Earth Planet. Sci. Lett.* 77, 141-156.
- Brandeis, G. and Marsh, B.D. (1989) The convective liquidus in a solidifying magma chamber: a fluid dynamic investigation. *Nature* 339, 613-616.
- Campbell, I.H. and Turner, J.S. (1986) The influence of viscosity on fountains in magma chambers. *J. Petrol.* 27, 1-30.
- Carslaw, H.S. and Jaeger, J.C. (1959) *Conduction of Heat in Solids*. Oxford University Press, London, 510 pp.
- Coriell, S.R., Cordes, M.R., Bottinger, W.J. and Sekerka, R.F. (1980) Convective and interfacial instabilities during unidirectional solidification of a binary alloy. *J. Crystal Growth* 49, 13-28.
- Detrick, R.S., Buhl, P., Vera, E., Orcutt, J., Madsen, J. and Brocher, T. (1987) Multi-channel seismic imaging of a crustal magma chamber along the East Pacific Rise. *Nature* 326, 35-41.
- Fowler, A.C. (1985) The formation of freckles in binary alloys. *IMA J. of Appl. Math.* 35, 159-174.
- Hansen, U. and Yuen, D.A. (1987) Evolutionary structures in double-diffusive convection in magma chambers. *Geophys. Res. Lett.* 14, 1099-1102.
- Hildreth, W. (1981) Gradients in silicic magma chambers: implications for lithospheric magmatism. *J. Geophys. Res.* 86, 10153-10192.
- Hills, R.N., Loper, D.E. and Roberts, P.H. (1983) A thermodynamically consistent model of a slushy zone. *Q. J. Mech. Appl. Math.* 36, 505-539.
- Ho-Liu, P., Johnson, C., Montagner, J-P., Kanamori H. and Clayton, R.W. (1990) Three-dimensional attenuation structure of Kilauea East Rift Zone, Hawaii. *Bull. Volc.* (in press).
- Huppert, H.E. and Sparks, R.S.J. (1980) The fluid dynamics of a basaltic magma chamber replenished by an influx of hot, dense, ultrabasic magma. *Contrib. Mineral. Petrol.* 75, 279-289.
- Huppert, H.E. and Turner, J.S. (1981) A laboratory model of a replenished magma chamber. *Earth Planet. Sci. Lett.* 54, 144-152.
- Huppert, H.E., Turner, J.S. and Sparks, R.S.J. (1983) Replenished magma chambers: effects of compositional zonation and input rates. *Earth Planet. Sci. Lett.* 57, 345-357.

- Huppert, H.E., Sparks, R.S.J., Whitehead, J.A. and Hallworth, M.A. (1986) Replenishment of magma chambers by light inputs. *J. Geophys. Res.* 91, 6113-6122.
- Huppert, H.E. and Sparks, R.S.J. (1989) Chilled margins in igneous rocks. *Earth Planet. Sci. Lett.* 92, 397-405.
- Huppert, H.E. and Sparks, R.S.J. (1988) The generation of granitic magmas by intrusion of basaltic magma into continental crust. *J. Petrol.* 29, 599-624.
- Huppert, H.E. and Worster, M.G. (1985) Dynamic solidification of a binary alloy. *Nature* 314, 703-707.
- Hurle, D.T. J., Jakeman E. and Wheeler, A.A. (1983) Hydrodynamic stability of the melt during solidification of a binary alloy. *Phys. Fluids* 26, 624-626.
- Jaupart, C. and Brandeis, G. (1986) The stagnant bottom layer of convecting magma chambers. *Earth Planet. Sci. Lett.* 80, 183-199.
- Kerr, R.C. Woods, A.W., Worster, M.G. and Huppert, H.E. (1989) Disequilibrium and macrosegregation during solidification of a binary melt. *Nature* 340, 357-362.
- Kerr, R.C. Woods, A.W., Worster, M.G. and Huppert, H.E. (1990a) Solidification of an alloy cooled from above. Part I: equilibrium growth. *J. Fluid Mech.* (in press).
- Kerr, R.C. Woods, A.W., Worster, M.G. and Huppert, H.E. (1990b) Solidification of an alloy cooled from above. Part II: non-equilibrium interfacial kinetics. *J. Fluid Mech.* (in press).
- Kerr, R.C. Woods, A.W., Worster, M.G. and Huppert, H.E. (1990c) Solidification of an alloy cooled from above. Part III: compositional stratification within the solid. *J. Fluid Mech.* (in press).
- Koyaguchi, T. Hallworth, M.A., Huppert, H.E. and Sparks, R.S.J. (1990) Sedimentation of particles from a convecting fluid. *Nature* 343, 447-450.
- Leitch, A.M. (1987) Various aqueous solutions crystallising from the side. In: *Structure and Dynamics of Partially Solidified Systems*, D.E. Loper, ed., NATO ASI Series E, vol. 125.
- Marsh, B.D. (1989) On convective style and vigour in sheet-like magma chambers. *J. Petrol.* 30, 479-530.
- Marsh, B.D. and Maxey, M.R. (1985) On the distribution and separation of crystals in convecting magma. *J. Volc. and Geotherm. Res.* 24, 95-150.
- Martin, D. and Nokes, R. (1990) Crystal settling in a vigorously convecting magma chamber. *Nature* 332, 534-536.
- Michael, P.J. (1983) Chemical differentiation of the Bishop Tuff and other high-silica magmas through crystallization processes. *Geology* 11, 31-34.
- Mullins, W.W. and Sekerka, R.F. (1964) Stability of a planar interface during solidification of a dilute binary alloy. *J. Appl. Phys.* 35, 444-451.
- Nilson, R.H. (1985) Countercurrent convection in a double-diffusive boundary layer. *J. Fluid Mech.* 160, 181-210.
- Pallister, J.S. and Hopson, C.A. (1981) Samail ophiolite plutonic suite: Field relations, phase variation, cryptic variation and layering and a model of a spreading ridge magma chamber. *J. Geophys. Res.* 86, 2593-2644.
- Podmore, F. (1970) The shape of the Great Dyke as revealed by gravity surveying. *Spec. Publ. Geol. Soc. South Africa* 1, 610-620.
- Rutter, J.W. and Chalmers, B. (1953) Prismatic substructure. *Can. J. Phys.* 31, 15-39.
- Ryan, M.P., Koyanagi, R.Y. and Fiske R.S. (1981) Modelling the three-dimensional structure of macroscopic magma transport systems: applications to Kilauea Volcano, Hawaii. *J. Geophys. Res.* 86, 7111-7129.
- Shirley, D.N. (1987) Differentiation and compaction in the Palisades Sill, New Jersey. *J. Petrol.* 28, 835-865.
- Sparks, R.S.J. and Huppert, H.E. (1984) Density changes during the fractional crystallization of basaltic magmas: implications for the evolution of layered intrusions. *Contrib. Mineral. Petrol.* 85, 300-309.
- Spera, F.J., Yuen, D.A., Clark, S. and Hong, H.J. (1986) Double-diffusive convection: magma chambers: simple or multiple layers. *Geophys. Res. Lett.* 13, 153-156.
- Spohn, T., Hort, M. and Fischer, H. (1988) Numerical simulation of the crystallization of multi-component melts in thin dykes or sills 1. The liquidus phase. *J. Geophys. Res.* 93, 4880-4894.
- Tait, S.R. and Jaupart, C. (1989) Compositional convection in viscous melts. *Nature* 338, 571-574.
- Tait, S.R., Jaupart, C. and Vergnolle S. (1989) Pressure, gas content and eruption periodicity of a shallow, crystallising magma chamber. *Earth Planet. Sci. Lett.* 92, 107-123.
- Wager, L.R. and Brown G.M. (1967) *Layered Igneous Rocks*. Oliver and Boyd, London, 588 pp.
- Worst, B.G. (1958) The differentiation and structure of the Great Dyke of Southern Rhodesia. *Trans. Geol. Soc. South Africa* 61, 283-354.
- Worster, M.G. and Huppert, H.E. (1983) Time-dependent density profiles in a filling box. *J. Fluid Mech.* 132, 457-466.
- Worster, M.G. (1986) Solidification of an alloy from a cooled boundary. *J. Fluid Mech.* 167, 481-501.
- Worster, M.G. and Leitch, A.M. (1985) Laminar free convection in confined regions. *J. Fluid Mech.* 156, 301-319.

MAGMA MIXING PROCESSES: INSIGHTS AND CONSTRAINTS FROM THERMODYNAMIC CALCULATIONS

INTRODUCTION

Magma mixing is an important differentiation process contributing to the overall petrological diversity within and between cogenetic igneous rock suites (e.g., Turner and Verhoogen, 1951; Philpotts, 1990). Furthermore, the physical and chemical mixing of compositionally disparate magmas holds fundamental interest because it offers insight into both the fluid dynamic and the physico-chemical behaviour of magmatic systems. Although it is an important magmatic process operating in a variety of tectono-magmatic environments, the physical and chemical principles of magma mixing are incompletely characterized. To a large extent, this reflects the magnitude of the intellectual challenge presented by magma mixing: Full comprehension of magma mixing requires study of both the fluid dynamic and chemical behaviour of open magmatic systems.

The process involves mechanical mixing of distinct crystal-liquid mixtures (magmas), and thus is governed by rheological (e.g., Sparks and Marshall, 1986; Campbell and Turner, 1986) and fluid dynamical considerations (e.g., Blake, 1981; Blake and Ivey, 1986a, b; Huppert et al. 1982; 1986; Oldenburg et al. 1989; Turner and Campbell, 1986). Conversely, from a physical chemical perspective, magma mixing involves an open chemical system which is perturbed from chemical equilibrium by each mixing episode. Generally, the new chemical equilibrium state is attained through complex chemical reactions involving crystallization (O'Hara and Mathews, 1981; Nielsen, 1988), vesiculation (Huppert and Sparks, 1980; Rice, 1981), solid phase resorption and even eruption (e.g., Sparks et al. 1977; Gerlach and Grove, 1982). The dependencies between thermodynamic intensive variables, such as temperature and pressure, and the physical properties of the magma, such as viscosity and density, ensure that the physical and chemical evolution of such magmatic systems are inseparable (e.g., Sparks and Marshall, 1986).

The references cited above allude to the fairly comprehensive and rigorous analysis of the physics of magma mixing processes already in the scientific literature. With few exceptions (e.g., O'Hara, 1980; O'Hara and Mathews, 1981; Nielsen, 1988; Nixon, 1988b), there is less known about the specific chemical paths resulting from mixing of disparate magmas. In this chapter I address the chemical aspects of magma mixing processes with thermodynamic calculation. Unless otherwise stated, the calculations made throughout this chapter utilize the thermodynamic data for silicate melts and solids derived by Ghiorso et al. (1983) and Ghiorso (1985).

There are, in my mind, two main attributes to a thermodynamic examination of magma mixing processes. Firstly, it provides a rationale for testing magma mixing hypotheses with chemical and mineralogical data. Hypotheses which are physically and chemically unreasonable will be inconsistent with the data and will be rejected. Secondly, where magma mixing has demonstrably played a role, thermodynamic calculations elucidate the physical and chemical characteristics of the process (e.g., heat budget, resorption or crystallization rates). Ideally, this exercise provides a means of quantifying how magmatic systems respond during mixing events.

HISTORY OF TREATMENT

Magma mixing depends on the recognition of at least two chemically and/or mineralogically distinct magmas. We can envisage two distinct types of magma mixing based on the genetic relations between the original or *resident* magma and the later *invasive* magma. In the first scenario, successive pulses of magma derived from a common source intersect in time and space. The magma pulses could be related to a single, large magma batch or could represent individual but chemically identical mantle-derived magmas (Nicholls and Russell, 1990b). Although this process creates an open system, it remains an internal differentiation process (Nicholls and Russell, 1990a) because the mixing occurs between parts of the same chemical system, or between chemically identical systems. This theoretical construct may approximate oceanic island or mid-ocean ridge magmatism where there is voluminous and continuous magma generation of more or less uniform composition over a restricted region. In such an environment there is every opportunity for extensive magma recharge or replenishment (O'Hara and Mathews, 1981; Nielsen, 1988; Nielsen, 1990). Recognition of mixing depends upon the resident and invasive magmas being characterized by different degrees of differentiation. If the end-member magmas are mineralogically and chemically identical, in addition to being derived from a common source, there is no means by which to discern the process.

The second magma mixing scenario is an external differentiation process involving unrelated and presumably chemically distinct magmas. Mixing of end-member magmas derived from different sources, ensures that the resident and invasive magmas will be chemically and mineralogically distinct except through chance. Such magmas are related only in space and time and mixing events are easily recognized unless complete equilibration of the resident magma occurs after mixing (*resultant magma*). This model is more characteristic of magma mixing in calc-alkaline systems.

The extent to which magmas mix depends upon the physical properties of the

end-member and intermediate magmas (e.g., Sparks and Marshall, 1986; Philpotts, 1990). Examples in the literature demonstrate that a full range of mixing phenomena exist, from commingled magmas which have not blended to hybrid magmas in which the melt phase has blended entirely (e.g., Sparks and Marshall, 1986; Oldenburg et al., 1989). Indeed, the best evidence for physical and chemical mixing of magmas comes from igneous rocks where incomplete mixing has left unambiguous macroscopic heterogeneities. Hand sample and petrographic features consistent with incomplete mixing of magmas include: compositional banding or streaking (Furman and Spera, 1985; Stasiuk and Russell, 1990), isolated magma inclusions (Bacon, 1986; Michael, 1989), incompatible mineral assemblages (Nixon, 1988a, 1988b) and xenoliths. In particular, rocks of unusual composition in which large numbers of crystalline phases seem to be associated in a state of disequilibrium strongly suggest incomplete physical and chemical mixing of different magmas. These textures clearly indicate the nature of the process because the magma did not attain chemical equilibrium after the mixing event. Whereas the evidence for the occurrence of mixing is clear, the thermodynamic conditions attending the process are not. In these situations, thermodynamic modelling constrains the physical and chemical character of the process.

Petrographic data commonly provide excellent incontrovertible evidence of magma mixing processes. However, chemical criteria, such as compositional variations in major or trace elements, are also used (e.g., Wright and Doherty, 1970; Wright, 1973; Garcia et al., 1989). In resident magmas, where the melt phases have completely blended, more subtle chemically-based criteria commonly provide indications of magma mixing processes. These include: (i) recognition of residual glass compositions thought to be cogenetic but with compositions inconsistent with fractional crystallization (e.g., Dungan and Rhodes, 1978), (ii) coexistence of incompatible minerals and mineral compositions within the same rock (e.g., Nixon, 1988a, Helz, 1987), (iii) reverse chemical zonations in phenocrysts (e.g., Helz, 1987), or (iv) phenocryst minerals exhibiting complex growth histories (e.g., Nixon and Pearce, 1987; Pearce et al., 1987). Unfortunately, magma mixing paths developed from chemical data alone are rarely unique and the feasibility of magma mixing hypotheses needs to be tested with thermodynamic calculations (Russell, 1990) or experimental studies (Grove et al., 1982).

TESTABILITY OF THE MAGMA MIXING HYPOTHESIS

As advanced by Popper (1959), an essential element of scientific hypotheses is that they be testable. This requires that the hypothesis be sufficiently detailed or specific to generate logical and predictable consequences which can be evaluated

against observation and theory (e.g., Greenwood, 1989). Where magma mixing is advanced as a process to explain the chemical diversity of rocks, the hypothesis must be framed in a manner that makes it testable, like any other scientific idea.

Thermodynamic modelling of differentiation processes is one means of expressing hypotheses in a form that can be stringently evaluated. For example, hypotheses involving perfect fractional crystallization can be represented by liquid lines of descent computed from thermodynamic data (e.g., Nicholls et al., 1986; Nicholls, 1990a, Nielsen, 1988, 1990; Russell and Nicholls, 1985; Ghiorso and Carmichael, 1985). Fractional crystallization hypotheses are testable because, where the parent magma composition is specified, the process is univariant and has predictable consequences. *The thermodynamic calculations simply illustrate some of these consequences so that they can be tested against observation.* Subsequent comparisons between the calculated parameters (melt and mineral compositions derived from the model) and the observed data (measured rock, glass and mineral compositions) are tests of the differentiation hypothesis. Inconsistencies between calculation and observation require rejection and modification of the stated hypothesis.

Hypotheses involving magma mixing are more difficult to put in a testable form for two reasons. Firstly, whereas fractional crystallization is univariant, open system processes have more degrees of freedom. Secondly, we require information about the nature of the end-member magmas in order to precisely characterize the magma mixing process. Thus, in situations where mixing is complete between phenocryst-poor magmas, it is virtually impossible to create meaningful hypotheses.

If the magma mixing hypothesis is to be tested by any scientific means, the hypothesis must include statements specifying:

- (i) the initial compositions of the resident and invasive magmas,
- (ii) the modal mineralogy of the magmas prior to mixing, and
- (iii) the proportions of resident and invasive magmas.

These statements reduce the degrees of freedom attending the chemical process and make the magma mixing hypothesis testable because it conforms to material conservation restrictions. Clearly, additional statements placing further restrictions on the process could be added to the hypothesis: these statements would increase the testability of the hypothesis (Popper, 1959).

To include a thermodynamically computed path within the magma mixing hypothesis requires additional statements because we must be even more definite about the process. In short, it requires that the mixing hypothesis conform to the laws governing the conservation of energy. This parallels perfect fractional

crystallization hypotheses which automatically include conservation of energy constraints in the form of distribution coefficients. Fractional crystallization is a definite process and, by definition, it has many implicit restrictions. For example, the chemical system considered during perfect fractional crystallization is defined to be the melt phase of a magma. This chemical system can exchange internal energy with the environment but is chemically closed except to the constituents removed through crystallization. Fractional crystallization is governed by chemical equilibrium principles with the proviso that changes in melt composition are exactly equal to the compositions of the fractionated solid assemblage (Nicholls, 1990a):

$$dn_{\text{MgO,melt}} = - dn_{\text{MgO,solid}} \quad (1)$$

Equations of this type (Equation 1), combined with a thermodynamic description of chemical equilibrium (e.g., Nicholls et al., 1986; Nicholls, 1990a), ensure that fractional crystallization is univariant. At constant pressure it is a unique process depending only on the starting melt composition.

Thermodynamic calculations can model the consequences of the magma mixing process, including: prediction of the stable phase assemblage; coexisting phase compositions; and phase proportions, thus increasing the scientific credibility of magma mixing hypotheses. The sole condition is that the requisite thermodynamic restrictions are explicitly developed for the magma mixing process. For example, we must define a chemical system (that part of the Universe we have chosen to study); a non-trivial exercise because of the open nature of the process. In the following discussion, the system is open to material transfers across the physical boundaries, including: influxes of the invasive magma and outfluxes of fractionated phases. Furthermore, the mixing process is assumed to occur at constant confining pressure, although this need not be so. Other restrictions on the thermodynamic system (e.g., isolated, adiabatic, isenthalpic, etc.; Nicholls, 1990a, b) will govern to a large extent the results of the magma mixing process.

ELEMENTARY PRINCIPLES OF MAGMA MIXING

This section develops several basic concepts pertinent to the physical-chemical behaviour of mixed magmas. The calculational concepts are illustrated with examples based on data from the literature, including: (i) mixing of basalt and dacite, and (ii) mixing of two basalts. The basalt and dacite mixing scenario uses volcanic rock compositions from Iztaccihuatl Volcano, Mexico (Table 1) described and interpreted by Nixon (1988a,b). Nixon (1988b) argued that much of

Table 1. Anhydrous chemical compositions of basalt and dacite melts used in examples. Data are taken from Nixon (1988a,b). Hydrous compositions were created by adding 0.5 and 1.0 wt. % H₂O to the basalt and dacite analyses, respectively. Equivalent mole fractions of "Ghiorso" melt components are reported as New X.

| Sample: | | Basalt: IZ-839 | | Dacite: C-1 | | |
|--------------------------------|-------|----------------|---------|-------------|--------|---------|
| Oxide | Wt. % | Mol. % | New X | Wt. % | Mol. % | New X |
| SiO ₂ | 52.53 | 54.32 | 0.39345 | 63.01 | 67.85 | 0.57390 |
| TiO ₂ | 0.77 | 0.60 | 0.00688 | 0.73 | 0.59 | 0.00621 |
| Al ₂ O ₃ | 14.98 | 9.13 | 0.15743 | 16.59 | 10.53 | 0.16594 |
| Fe ₂ O ₃ | 0.00 | 0.00 | 0.00000 | 0.59 | 0.24 | 0.00377 |
| FeO | 7.03 | 6.08 | 0.06990 | 4.07 | 3.67 | 0.03852 |
| MnO | 0.13 | 0.11 | 0.00131 | 0.08 | 0.07 | 0.00077 |
| MgO | 9.92 | 15.28 | 0.17579 | 3.39 | 5.44 | 0.05718 |
| CaO | 8.89 | 9.84 | 0.11324 | 4.99 | 5.76 | 0.06050 |
| Na ₂ O | 3.33 | 3.33 | 0.05757 | 4.31 | 4.50 | 0.07092 |
| K ₂ O | 1.66 | 1.09 | 0.01888 | 1.85 | 1.27 | 0.02003 |
| P ₂ O ₅ | 0.44 | 0.19 | 0.00554 | 0.19 | 0.09 | 0.00228 |
| Total | 99.68 | | | 99.80 | | |

Table 2. Anhydrous chemical compositions of Kilauea Iki basalts used as an example. Data are taken from Murata and Richter (1966) and represent analyses of glass separates (SG-05) and rocks (SW-02). Equivalent mole fractions of "Ghiorso" melt components are reported as New X.

| Sample: | | Glass: SG-05 | | Basalt: SW-02 | | |
|--------------------------------|-------|--------------|---------|---------------|--------|---------|
| Oxide | Wt. % | Mol. % | New X | Wt. % | Mol. % | New X |
| SiO ₂ | 49.08 | 50.66 | 0.35331 | 50.07 | 52.64 | 0.38354 |
| TiO ₂ | 2.48 | 1.93 | 0.02272 | 2.75 | 2.17 | 0.02508 |
| Al ₂ O ₃ | 12.48 | 7.59 | 0.13442 | 13.70 | 8.49 | 0.14685 |
| Fe ₂ O ₃ | 1.59 | 0.62 | 0.01093 | 1.39 | 0.55 | 0.00951 |
| FeO | 10.05 | 8.68 | 0.10241 | 10.00 | 8.79 | 0.10141 |
| MnO | 0.18 | 0.16 | 0.00186 | 0.17 | 0.15 | 0.00175 |
| MgO | 10.20 | 15.69 | 0.18525 | 7.23 | 11.33 | 0.13068 |
| CaO | 11.05 | 12.22 | 0.14426 | 11.55 | 13.01 | 0.15006 |
| Na ₂ O | 2.04 | 2.04 | 0.03615 | 2.30 | 2.34 | 0.04056 |
| K ₂ O | 0.48 | 0.32 | 0.00560 | 0.60 | 0.40 | 0.00696 |
| P ₂ O ₅ | 0.24 | 0.11 | 0.00309 | 0.28 | 0.13 | 0.00359 |
| Total | 99.87 | | | 100.04 | | |

the chemical and petrographic variation within the andesites and dacites of Iztaccihuatl Volcano could be explained by periodic replenishment of dacite magma reservoirs by basaltic magma accompanied by dynamic fractional crystallization. The second scenario uses examples involving mixing of basaltic magmas from the 1959 eruption of Kilauea Iki, Hawaii. The chemical data (Table 2) representing the end-member magma compositions are from Murata and Richter (1966) and include a high MgO-content glass separate and a lava flow composition with lower MgO content. Several authors have argued that the chemical diversity of the 1959 Kilauea

Iki suite results from magma mixing (e.g., Wright, 1973; Helz, 1987), although Russell and Stanley (1990) suggest that crystal sorting is sufficient to explain the chemical diversity.

We first examine some basic consequences of magma mixing under isobaric conditions. This model departs from magma mixing processes in a number of ways:

- (i) the range of composition (0-100 mole % A or B end-member) is greater than expected in magma mixing because magma mixing involves a resident magma being diluted by another magma.
- (ii) the calculations do not examine the effects of crystallization on melt composition, and
- (iii) the computed phase relations ignore the consequences of path (e.g., which end-member is the resident magma).

These computations do, however, outline a number of considerations which must be addressed in any realistic model.

Melt mixing

The first calculations consider the mixing of two magmas which are fortuitously near their respective liquidus. Whereas this may be rare in nature, mixing of magmatic melt phases attends all magma mixing processes. Initially, each magma (melt, in this case) is distinct in composition and temperature. The question is: How is the equilibrium thermodynamic state of the resident magma modified by the influx of the invasive magma under isobaric conditions?

The temperature attained by the mixed magma depends upon the initial conditions and thermodynamic properties of the end-member magmas as well as the thermodynamic boundary conditions on the mixing process. The resultant temperature is not necessarily unique. A simple approach is to assume that the melts resulting from the addition of the invasive magma B at temperature T_B to the resident magma A at temperature T_A in a fixed proportion (X_A , X_B) will attain a final temperature dictated solely by the proportional mixing of the end-member magma temperatures:

$$T_r = T_A + [T_B - T_A] X_B \quad . \quad (2)$$

Figure 1 shows the resultant temperature which, if nothing else, serves to contrast subsequent models. However, this calculated temperature entirely ignores the physical chemical properties of the melts, notably the heat capacity. In reality, the

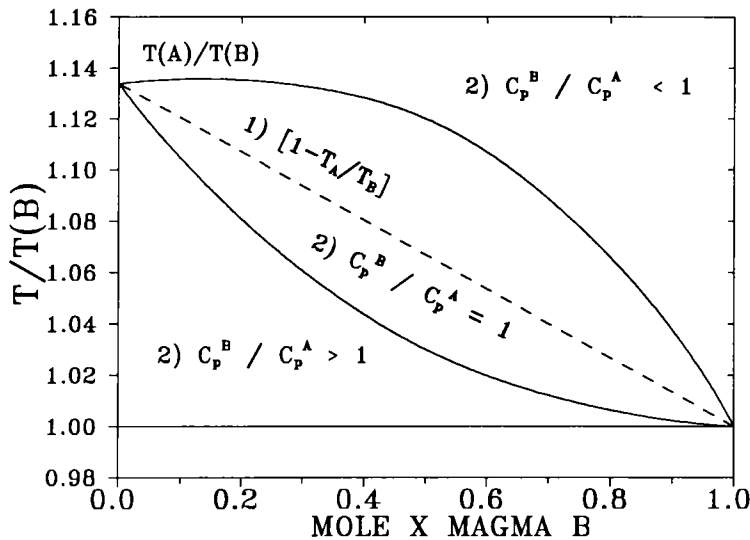


Figure 1. Schematic representation of ambient melt temperature $[T / T_B]$ resulting from mixing of A and B end-member melts. Dashed line represents linear interpolation and the case where the melts have identical heat capacities. Solid lines illustrate the effects of non-equal heat capacities for commingled melts or melts which mix ideally.

Table 3. Sign conventions associated with variations in isobaric heat contents due to magmatic processes including: mixing of melts, crystallization, or vesiculation etc. The convention is based on the concept that ΔH is a measure of the heat absorbed by the system being studied.

| Sign of ΔH | Description | Implication |
|--------------------|-------------|--|
| Negative | Exothermic | The process produces heat which must be (i) transferred out of the magma, (ii) balanced by an energy equivalent endothermic process, or (iii) converted into a temperature rise. |
| 0 | Isenthalpic | The process achieves a complete heat balance. |
| Positive | Endothermic | The process requires heat from an external source in order to proceed or the magma is cooled. |

ambient temperature reached by magmas during mixing reflects temperatures, compositions, and heat capacities of the end-member magmas as well as the heat of mixing of the melts. The linear model portrayed in Figure 1 is acceptable only if the two end-member magmas mix ideally and have identical heat capacities.

The following calculation is appropriate for magmas that have mingled and reached thermal equilibrium but have not mixed (Sparks and Marshall, 1986; Philpotts, 1990). The change in molar heat content for each of the contributory magmas (A and B) is:

$$\Delta h^i = \int_{T_0}^{T_r} c_p^i dT ; \quad i = A, B \quad . \quad (3)$$

Thus, the net enthalpy change attending the mingling and thermal equilibration of magmas A and B is:

$$\Delta H = X_A C_p^A [T_r - T_A] + X_B C_p^B [T_r - T_B] \quad . \quad (4)$$

If we assume that the magmas mix adiabatically then:

$$dq = 0 \quad , \quad (5)$$

$$dS = 0 \quad , \quad (6)$$

and at constant pressure the adiabatic process is equal to the isenthalpic path:

$$dH = 0 \quad . \quad (7)$$

This requires that the change in total heat content be converted to a change in temperature (Table 3) and under the adiabatic constraint the resultant temperature is given by:

$$T_r = \frac{X_B c_p^B T_B + X_A c_p^A T_A}{X_A c_p^A + X_B c_p^B} \quad . \quad (8)$$

The assumptions in this calculation are that the melts are mingled but not mixed, the heat capacities of the melts are independent of temperature, the process is adiabatic and operates at constant pressure. Note that if the end-member magmas have the same heat capacity ($c_p^A = c_p^B$) then Equation 8 reduces to Equation 2. Figure 1 schematically portrays the distribution of temperatures resulting from the mingling of magmas A and B. In fact, the temperatures resulting from thermal equilibration of mingled magmas are identical to the temperatures that would arise from completely mixed melts, if the melts mix ideally and there is no excess heat capacity:

$$c_p^r = X_A c_p^A + X_B c_p^B \quad . \quad (9)$$

Experimental measurements of silicate melt heat capacities indicate little to no excess heat capacity (e.g., Carmichael et al., 1977; Stebbins et al., 1984). Differences in the ambient temperature arising from excess heat capacity are schematically represented in Figure 2 for the case where the heat capacity of the mixture is less than the linear extrapolated value.

In actual fact, there is strong evidence that silicate melts mix non-ideally. In particular, Ghiorso (Ghiorso et al., 1983; Ghiorso 1985) has argued that the majority of the non-ideal behaviour in silicate melts can be modelled in terms of an excess enthalpy function. This implies that for common melt compositions there may be an excess heat of mixing and this term will contribute to changes in magmatic temperature due to adiabatic mixing processes. The molar enthalpy of non-ideal melts at the temperature of interest is given by:

$$h = h^O + \int_{T_o}^{T_r} c_p dT + h^{\text{Excess}} \quad (10)$$

Thus the total heat content contributed to the magma reservoir by the two end-member magmas is calculated from:

$$H = X_A [h^A + h^{\text{A,Excess}}] + X_B [h^B + h^{\text{B,Excess}}] \quad (11)$$

Figure 3 compares the isobaric enthalpy of the chemical systems arising from mixing of basalt and dacite magmas. The curves correspond to (i) the linear interpolation of end-member enthalpies, (ii) the ideal mixing or commingling of melts with different heat capacities, and (iii) mixing of end-member magmas with different heat capacities and non-ideal chemical behaviour. At thermal equilibrium the total heat content of the reservoir is:

$$H_r = h_r + h_r^{\text{Excess}} \quad (12)$$

The change in heat content attending the mixing of the end-member melts is therefore:

$$\Delta H = h_r + h_r^{\text{Excess}} - X_A [h^A + h^{\text{A,Excess}}] - X_B [h^B + h^{\text{B,Excess}}] \quad (13)$$

and is represented by the differences between the enthalpy curves portrayed on Figure 3. Furthermore, the resultant temperature arising from adiabatic mixing of these non-ideal melts can be computed from:

$$T_r = \frac{X_A c_p^A T_A + X_B c_p^B T_B}{c_p^r} + \frac{-\Delta H^{\text{Mix}}}{c_p^r} \quad (14)$$

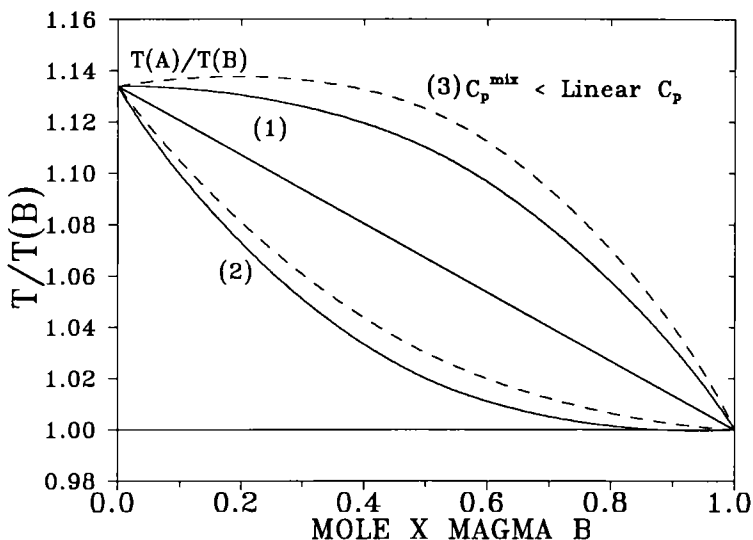


Figure 2. Temperatures resulting from adiabatic mixing of melts A and B: (i) linear model resulting from equal heat capacities, (ii) commingling or ideal mixing with non-equal heat capacities, (iii) schematic effects of excess heat capacity.

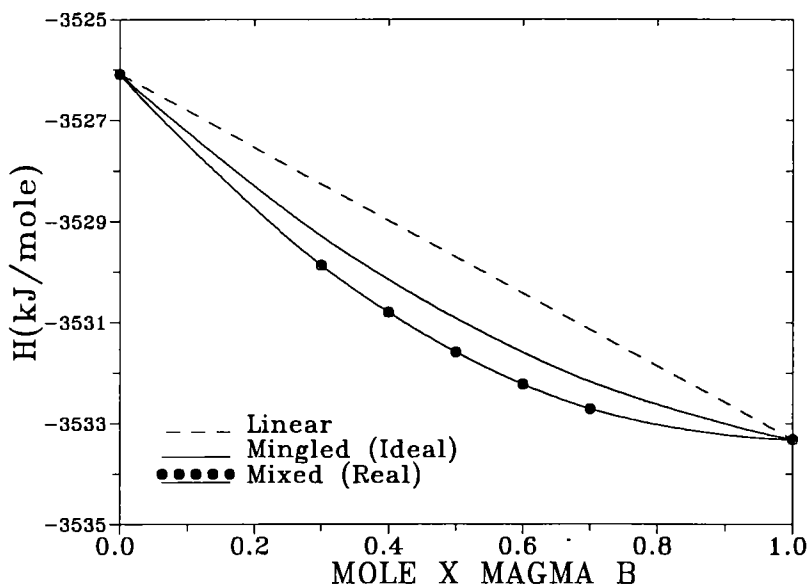


Figure 3. Computed enthalpy of melt mixtures of anhydrous basalt and dacite ($P = 0.1$ GPa) using thermodynamic data of Ghiorsio et al. (1983). Adiabatic processes at constant pressure require $\Delta H = 0$, thus differences between the dashed and solid lines translate into shifts in temperature. For this example the process is slightly exothermic.

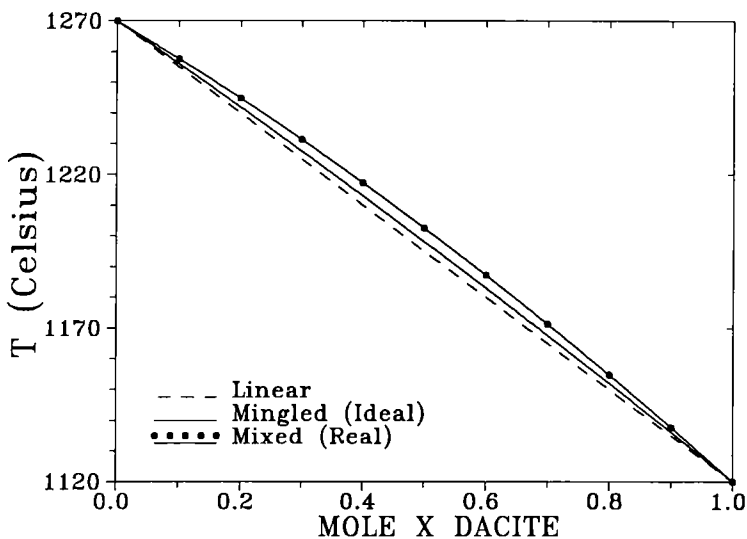


Figure 4. Temperatures resulting from adiabatic mixing of anhydrous basalt and dacite under the assumption: (i) that the magmas are commingled or mix ideally; or (ii) that they mix non-ideally (e.g., Ghiorso et al., 1983).

where ΔH^{Mix} is the temperature-independent excess enthalpy of mixing the two end-member magmas:

$$\Delta H^{\text{Mix}} = h_r^{\text{Excess}} - X_A h_A^{\text{Excess}} - X_B h_B^{\text{Excess}} \quad , \quad (15)$$

and c_p^r is the heat capacity of the resultant melt mixture. In this particular example (Fig. 3), the process is slightly exothermic (Table 3) and corresponds to a small increase in the melt temperature (Fig. 4). The magnitude and sign of ΔH in Equation 13 depends upon the nature of the end-member magmas being mixed. For example, Figure 5 illustrates the change in heat content at constant P resulting from mixing basalt and dacite melts with different water contents. The anhydrous example (Figs. 3 and 4) is slightly exothermic, whereas if the melts contain even small amounts of dissolved water, the same process is endothermic at this pressure (Nicholls and Stout, 1982; Russell 1987). Figure 6 illustrates the corresponding change in temperature resulting from the endothermic mixing of the hydrous melts.

Solid phase saturation

The phases and their compositions which initially saturate a melt depend on confining pressure and melt composition (cf. Nicholls, 1990a). Consequently, the

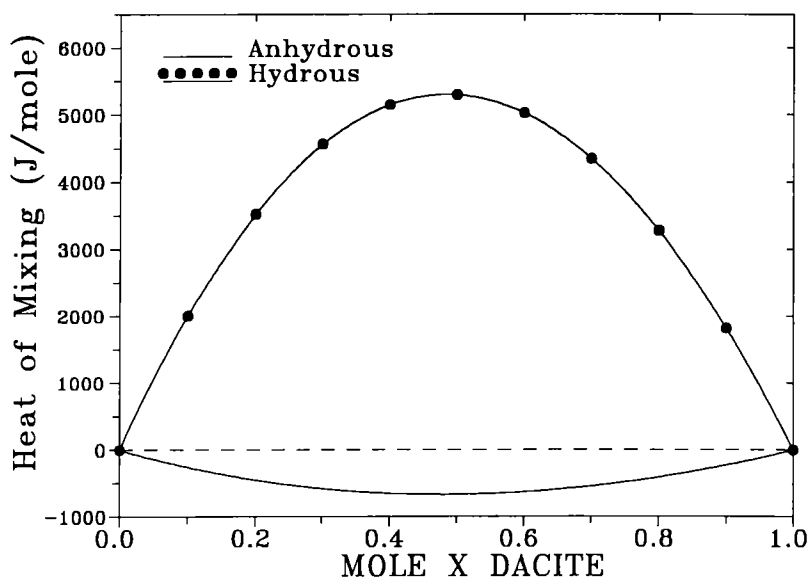


Figure 5. Computed ΔH of mixing of basalt and dacite melts at constant pressure (0.1 GPa) using the regular solution model for silicate melts of Ghiorso et al. (1983). Calculations are made for anhydrous [exothermic] and hydrous [endothermic] conditions (Table 3).

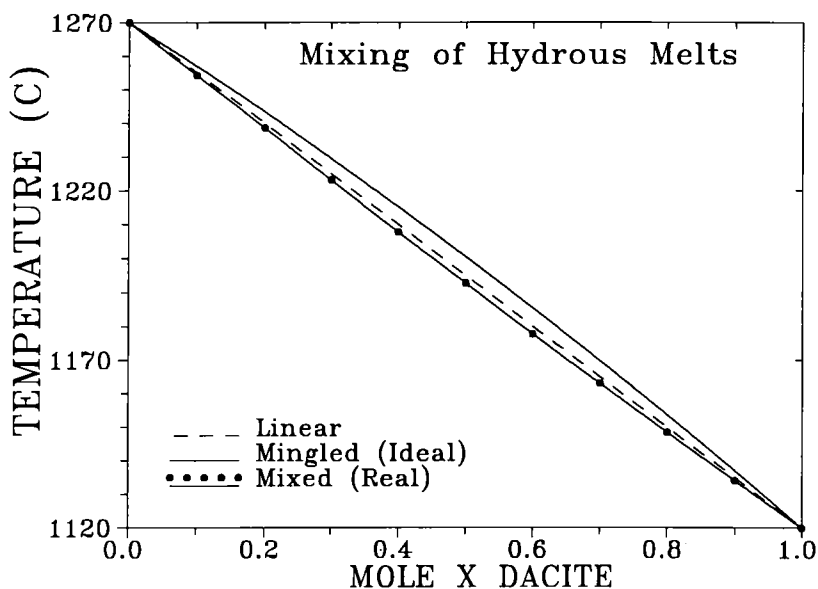


Figure 6. Ambient melt temperatures resulting from adiabatic mixing of hydrous basalt and dacite illustrating effects of endothermic process.

liquidus phase relations of the resident magma will change in response to the invasive melt. Figures 7 and 8 illustrate the apparent liquidus relations for the basalt-dacite example at 0.1 GPa (Table 1) as calculated from the thermodynamic data of Ghiorso et al. (1983). Figure 7 maps the liquidus phase and temperature as a function of magma composition expressed as molar proportion of dacite. The diagram illustrates that dilution of the resident basaltic magma causes the liquidus temperature to decrease and the liquidus phase to change from olivine to Ca-poor pyroxene. All saturation surfaces plotting below the olivine-orthopyroxene liquidus curves are metastable saturation surfaces. They are calculated for a unique melt composition and are pertinent only to that melt composition. Crystallization must occur, changing the melt chemistry and thus the coordinates of the saturation surfaces themselves, before the magmatic system can reach the lower temperature saturation surfaces. Consequently, the actual phase assemblage which would saturate the magma below the liquidus depends on the differentiation path taken (Russell, 1987). Figure 8 summarizes compositions of the saturating phases as a function of system composition.

The liquidus surface for basalt-dacite melt mixtures is compared to the temperatures derived by mixing the two end-member melts (on Fig. 9). The solid line shows the ambient mixed melt temperature resulting from the mixing of basaltic (1270°C) and dacitic (1120°C) melts under adiabatic conditions. Also plotted is the liquidus curve computed for the full range of melt compositions with symbols denoting the identity of the liquidus phase. In this example, the resultant melts have ambient temperatures after mixing either equal to the liquidus temperature (basalt end-member), superliquidus (some basalt-dacite mixtures), or subliquidus, requiring crystallization (dacite end-member).

Oxidation potential and H₂O solubility

Small masses of volatiles, because of their small formula weights, have large effects on magmatic processes. Oxygen fugacity, for example, plays a major role in controlling the ferric:ferrous iron contents of melts (Sack et al., 1980; Kilinc et al., 1983; Kress and Carmichael, 1988) and thus can significantly affect the identities and compositions of crystallizing phases. Depending on the nature of the magmatic process, it has been argued that oxygen fugacity can be intrinsic or extrinsic to magmas and that magmatic systems are open or closed to oxygen infiltration (e.g., Ghiorso and Carmichael, 1985; Carmichael and Ghiorso, 1986; Juster et al., 1989).

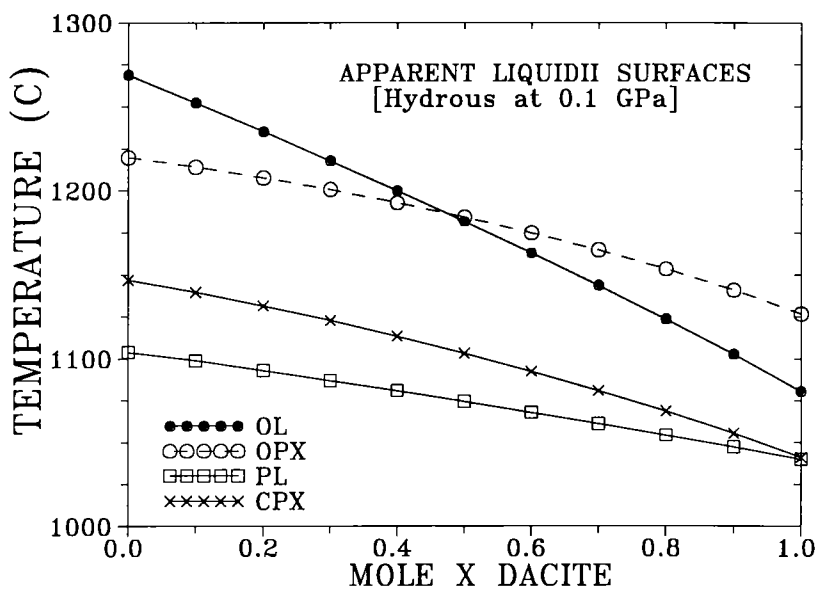


Figure 7. Computed apparent liquidii for melt compositions derived by mixing of basalt and dacite using the thermodynamic data of Ghiorso et al. (1983).

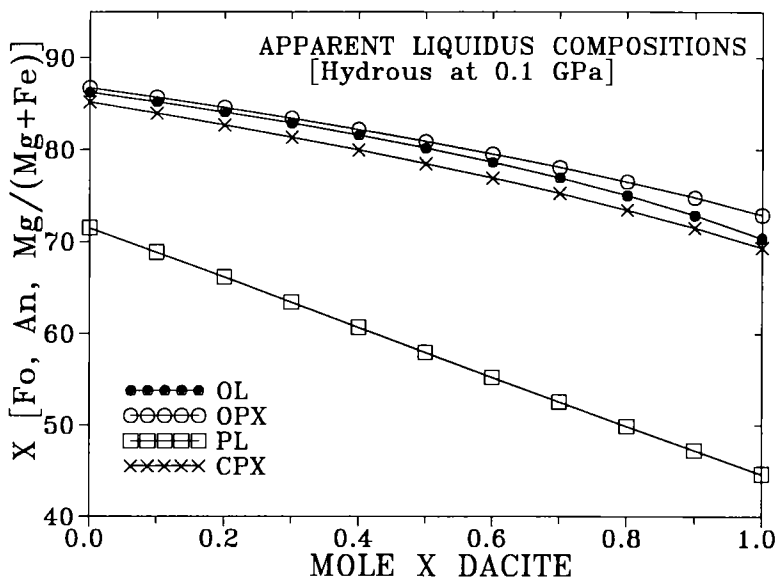


Figure 8. Computed phase compositions on apparent saturation surfaces (see Fig. 7).

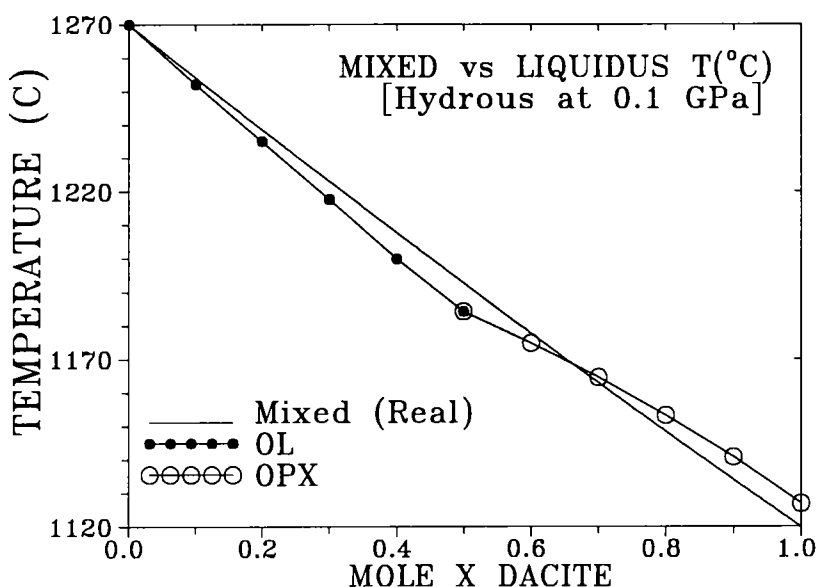


Figure 9. Comparison of ambient mixed melt temperature to liquidus temperature of hydrous melts. Melts toward the basaltic end-member composition are superliquidus and would saturate with olivine whereas melts towards the dacite end-member are saturated with Ca-poor pyroxene.

In modelling magma mixing processes, the resultant oxygen fugacity can be treated as intrinsic and set by the mixed melt composition (e.g., Kress and Carmichael, 1988). Conversely, it may be an extrinsic property reflecting an externally imposed oxygen fugacity or it may depend upon conditions in the end-member magmas prior to mixing. In general, some decision must be made about whether oxygen fugacity or melt composition is the dependent variable and how the variable is governed.

On Figures 10 and 11 are some of the consequences of different assumptions. The FeO contents of melts derived from mixing two basaltic liquids (Table 2) are shown on Figure 10 by the dashed line. These are the compositions which would result from simple linear mixing of the two end-members which are assumed to be equilibrated at oxygen fugacities buffered by QFM (SG-05) and NNO (SW-02). Such a model implies that the oxygen fugacity in the resultant mixture is controlled by the melt composition (Sack et al., 1980; Kilinc et al., 1983; Kress and Carmichael, 1988). The solid line illustrates an alternative: The oxygen fugacity is fixed by QFM, which is consistent with the end-member magma represented by SG-05, and the compositions of the mixed melts respond. In this particular example, olivine saturates the full range of melt compositions and its composition reflects the

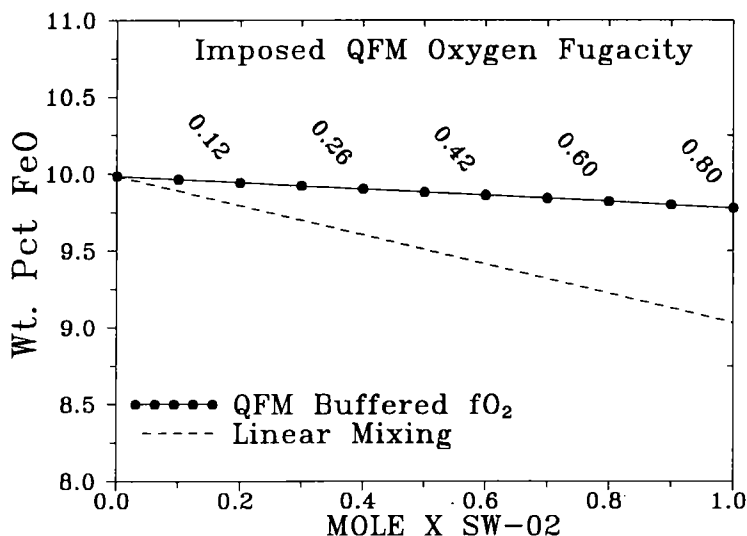


Figure 10. FeO content in melt mixtures derived from two basalt compositions SG-05 and SW-02. Dashed line marks wt. % FeO from linear mixing of end-member compositions. Solid line illustrates effects of QFM oxygen buffer on FeO content of the mixtures. Labels on the solid curve report the attendant shift in liquidus olivine composition (Δ mole % Fo).

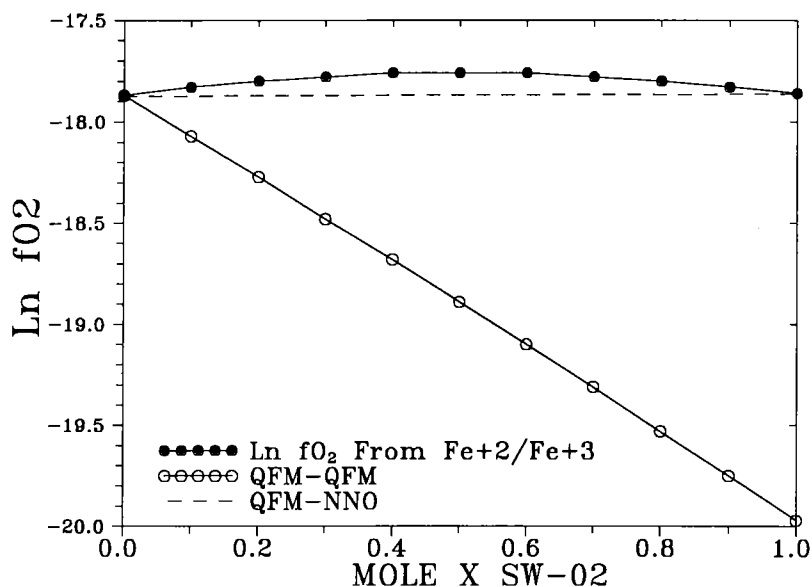


Figure 11. Oxygen fugacity computed from melt compositions derived through mixing of SG-05 at QFM and SW-02 at NNO. Oxygen fugacities arising from linear mixing of the end-member fugacities (dashed line) imply an open system with respect to oxygen. Solid line and filled circles (system closed to oxygen) show computed fugacities predicted from the FeO:Fe₂O₃ ratios of the melts (linear mixing of the compositions). QFM buffered melts define the solid line with the open circles.

externally imposed oxygen fugacity (see labels on Fig. 10).

Conversely, the melt compositions attained by mixing the two end-members may determine the oxygen fugacity. Figure 11 considers the same end-member systems illustrated on Figure 10. The dashed line is a linear extrapolation of the oxygen fugacities computed for SG-05 at QFM and SW-02 at NNO. The solid line with filled dots marks the oxygen fugacity that would be expected to equilibrate with the magma given the resultant magma's temperature and ferric:ferrous content (Kilinc et al., 1983). The oxygen fugacities consistent with the QFM buffer at ambient magma temperatures are shown as open circles for reference.

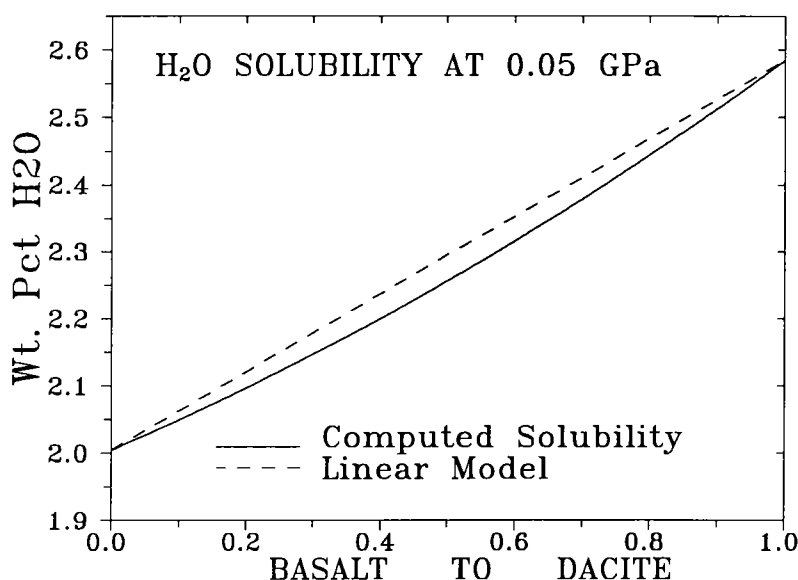


Figure 12. Comparison of H₂O solubility in Basalt - Dacite mixtures to H₂O contents predicted by linear extrapolation of saturated end-member melt compositions. This geometry suggests that vesiculation would occur as a result of mixing these end-member melts.

H₂O is another volatile constituent affecting both the physical and chemical dynamics of magma systems (Jaupart and Tait, 1990). The introduction of H₂O into magmatic systems changes phase relations significantly and thus affects the chemical differentiation of magmas. Of particular interest to magma mixing processes is the geometry of the H₂O saturation surface as a function of the mixed melt composition. Figure 12 illustrates the magmatic H₂O-content expected from the mixing of two, initially H₂O-saturated magmas (dashed line). This is compared to the computed H₂O saturation surface for the mixed melts. The calculation of the saturation surface using the thermodynamic data of Nicholls (1980) and Ghiorso et al. (1983) is

described by Russell (1987). The calculations, depicted by Figure 12, are uncertain because of the uncertainty attached to the thermodynamic properties of H_2O dissolved in silicate melt (Nicholls, 1980; Spera, 1984; Ghiorso et al., 1985, Russell, 1987). For this example, the mixing process would produce a series of H_2O over-saturated melts causing vesiculation and perhaps eruption (e.g., Huppert and Sparks, 1980; Rice, 1981; Gerlach and Grove, 1982; Jaupart and Tait, 1990). Vesiculation processes are also important to calculations involving magmatic heat budgets. Vesiculation can be highly endothermic (Nicholls and Stout, 1982) and consequently provides a heat sink to support crystallization (Russell, 1987). At present there are large uncertainties in the data needed to model the H_2O solubility of silicate melts, however, as the geometry of the H_2O saturation surfaces become better defined as a function of melt composition, temperature and pressure the effects represented in Figure 12 can be examined rigorously.

MODELLING THE MAGMA MIXING PROCESS

The chemical system has been simplified as a combination of two end-member magmas mixed in fixed proportions and isolated prior to equilibration. The fact that the system is isolated after mixing and prior to equilibration means that the chemical path followed by the mixed magmas is constrained by an absence of heat and mass transfer. Chemical models designed to follow real paths must recognize the pre-existence of solid assemblages in both magmas, provide the opportunity for reaction between the solid phase assemblage and the various melts and accommodate the potential for crystallization in the resultant reservoir (e.g., O'Hara, 1980; Nielsen, 1990; Nixon, 1988b). In addition to handling solid and melt phase relations, the calculations should be able to follow specific thermodynamic paths (e.g., Ghiorso and Kelemen, 1987; Nicholls, 1990a; Kelemen, 1990). By studying the consequences of different thermodynamic paths, a more definite picture of the physical chemical behaviour of the magma mixing process may emerge (e.g., Nicholls, 1990a). For example, the thermodynamic calculations could provide estimates of the total flux of heat across the magmatic boundaries during the magma mixing process, thereby constraining physical models for storage or transport (Russell, 1987).

Magmatic paths: fractional mixing vs. equilibrium mixing

To treat the solid phase assemblage requires prediction of: (i) the saturation point of the solid phases as a function of temperature, pressure and melt

composition, (ii) the extent of crystallization for a given magmatic path, (iii) instabilities of pre-existing phases, (iv) the energetics attending the resorption of unstable solids and crystallization of the stable phases, and (v) the extent and nature of solid phase fractionation.

Table 4 distinguishes different magma mixing paths on the basis of the solid phase behaviour. There are eight distinct paths depending on the treatment of the solid assemblage found in the resident, invasive and resultant magmas before and after mixing. The solid assemblages in the resident and invasive magmas can be fractionated (**F**) prior to the mixing event and thus are not available to react in the new magmatic system. Conversely, the solid assemblages can participate in solid-melt reaction processes (**R**) in the new magma. Similarly, the resultant magma can either fractionate the solids that crystallize during the mixing process or allow the assemblage to react with subsequent influxes. The fractionated phase assemblage represents the phases available for accumulation. Not all of the paths listed in Table 4 are equally likely. For example, the third case is characterized by fractionation of the invasive magma's solid assemblage and reaction of the resident magmas solids. We would expect this magma mixing path, whereby the invasive solid assemblage is preserved from reaction while the resident solids react, to be rare in nature. Cases 1 and 8 mark important limits to the magma mixing process. The first case is characterized by complete fractionation of the solid assemblages and represents the *perfect fractional mixing* path. In contrast, the eighth case represents *perfect equilibrium mixing* where all solid phases react with the system to produce a new resultant phase assemblage and residual melt. Presumably, the liquid lines of descent produced by these eight different paths would be distinct.

Table 4. Characterization of magma mixing processes by behaviour of solid assemblages in Resident, Invasive and Resultant magmas. **F** denotes that solids fractionate perfectly during the mixing process and **R** indicates the solids react fully during the mixing process and contribute to the resultant equilibrium state. Case 1 corresponds to ideal perfect fractional mixing and case 8 corresponds to perfect equilibrium mixing.

| Paths: | 1 | 2 | 3 | 4 | 5 | 6 | 7 | 8 |
|------------|---|---|---|---|---|---|---|---|
| Resident: | F | F | R | R | F | F | R | R |
| Invasive: | F | R | F | R | F | R | F | R |
| Resultant: | F | F | F | F | R | R | R | R |

Thermodynamic paths of magma mixing

Thermodynamic theory provides a means to calculate the equilibrium state of a magma resulting from chemical mixing of two magmas of known composition if several additional statements about the initial systems and mixing process are made.

The confining pressure acting on the resident, invasive and resultant magmas is assumed equal and constant. The two end-member magmas have unique and constant temperatures. Prior to mixing, the resident and invasive magmas are assumed to be at chemical equilibrium and to comprise a phase assemblage indicative of their respective equilibrium magmatic conditions.

The thermodynamic calculations are devised to monitor the effects of magma mixing by computing the equilibrium state of the resident magma after it is perturbed by the invasive magma. A theoretical rationale for the computation of multicomponent chemical equilibria in closed petrologic systems is provided by Duhem's Theorem (e.g., Carmichael et al., 1974; Nicholls, 1977; Russell and Nicholls, 1985; Nicholls, 1990a) which states that as long as the bulk composition of the magmatic system is known, the equilibrium state of the system is completely determined by fixing two independent variables (Duhem, 1898; Prigogine and Defay, 1954; Nicholls, 1990a). Duhem's Theorem applies conventionally to closed chemical systems, however, it is easily applied to open system processes if the flux of material is known because the bulk composition is calculated at each point. There remain two independent variables that must be specified at any point in the process.

The bulk composition of the system resulting from mixing is known at each stage because the compositions of the resident and invasive magma are known and the material proportions combined are specified according to the chosen mixing path (Table 4). Perfect fractional mixing, for example, is modelled by adding very small but known quantities of the invasive magma's melt phase to the resident reservoir (see Nielsen, 1990).

Thermodynamic restrictions imposed on chemical systems, such as holding one of the fundamental thermodynamic variables (S , V , T) constant (e.g., Waldbaum, 1971; Nicholls and Stout, 1982; Ghiorso and Kelemen, 1987; Russell, 1987; Nicholls, 1990a), provide another control on the magma mixing process and with P supply the two independent variables required by Duhem's Theorem. Defining one other variable in addition to P defines the chemical equilibrium state of the resultant magma, including: (i) the physical chemical state of each phase, and (ii) the extensive quantities of each phase. The choice of thermodynamic properties as independent variables defines the path the process follows and affects differentiation. To the best of our ability, the properties chosen as independent variables should be tied to concrete knowledge about the system or represent legitimate assumptions that can be made about the system. For example, the value of one of the three remaining fundamental thermodynamic variables (S , V , or T) could be specified or assumed fixed and would correspond to isobaric paths under adiabatic, isochoric, or isothermal conditions (Ghiorso and Kelemen, 1987).

COMPUTATIONAL ALGORITHM

Figure 13 outlines the sequence of calculations for modelling the mixing of two end-member magmas. To begin, the equilibrium phase assemblages, compositions, and proportions of the two initial magmas are computed at predetermined pressure and temperatures. Additionally, the bulk thermodynamic properties for these equilibrium configurations are calculated. Magma mixing is simulated by adding finite amounts of the invasive magma to the resident system and computing a new equilibrium position for the resultant system. First, however, the behaviour of the solid phase assemblage must be specified by choosing one of the eight paths in Table 4 so that the compositional effects of the invasive magma can be computed. For example, the composition of the incremental change applied to the resident magma depends on whether the model path specifies the invasive system to comprise the melt phase alone or the complete melt + solid assemblage. To model some mixing paths (e.g., fractional mixing processes) it is critical that the magnitude of the incremental amount of invasive magma added to the resident system be trivial compared to the size of the resident magma. Knowing the magnitude and size of the invasive magma increment added to the resident system allows computation of the bulk composition and bulk thermodynamic properties of the resultant system prior to the system attaining chemical equilibrium. Before computing the new equilibrium position of the system, one additional extensive or intensive property of the resultant magma is specified (e.g., temperature, total volume, total entropy). Finally, the equilibrium state of the resultant magma is computed, including: the equilibrium phase assemblage, the compositions of the melt and solid phases, and the proportions of each phase (and temperature, if it was not chosen as a fixed property). After a decision is made about whether the solid phases are fractionated or remain as part of the resident magma, the resultant magma is updated to become the new resident magma. Repeating this procedure models the cumulative effects of the mixing process.

Temperature as the independent variable

The equilibrium states of the end-member magmas are computed prior to modelling the mixing process at a constant and predetermined temperature. In this case, pressure and temperature are the two independent variables, and the equilibrium state of the magma is calculated by simultaneous solution of equations describing the material balance relations and thermodynamic equilibrium between the solid and melt phases (Russell and Nicholls, 1985). For an N component system with P solid phases, there are N material balance equations of the form:

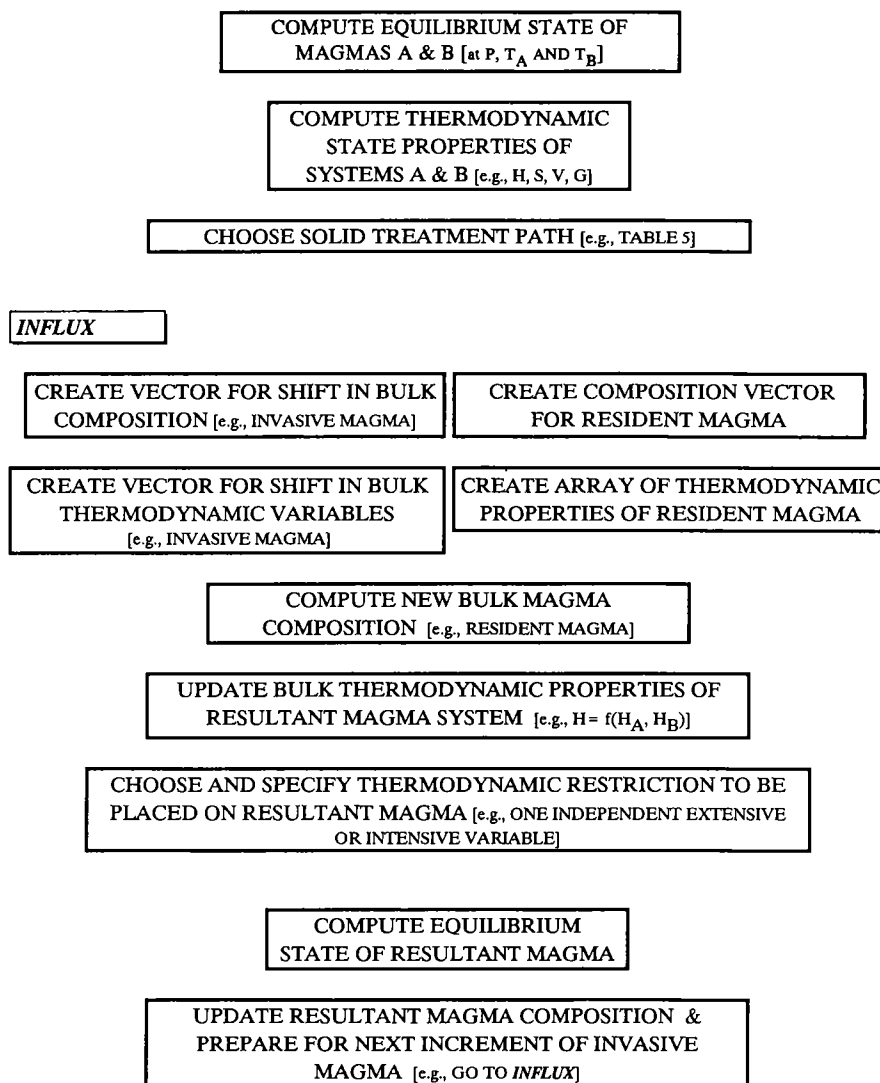


Figure 13: Calculation sequence used to simulate magma mixing processes and the thermodynamic consequences.

$$Y_i + \sum_{j=1}^P \left[\sum_{k=1}^Q r(i, k) m_j x_{jk} \right] - Z_i = 0 \quad , \quad (16)$$

where Z_i and Y_i represent the number of moles of the i^{th} component in the system and melt phase respectively, $r(i, k)$ is the stoichiometric coefficient relating the i^{th} melt component to the k^{th} solid component, m_j is the number of moles of each solid solution with Q components and x_{jk} is the mole fraction of the k^{th} component in the j^{th} solid. The equations representing chemical equilibrium between the solid phase assemblage and the residual melt vary in number depending on the number of phases (P) which saturate the melt and the number of components represented by the solid solution (Q). In general, there are $Q \cdot P$ equations of the form:

$$a_{j,k} - \exp[\Delta G_k^0 / RT] \left[\sum_{i=1}^N [Y_i \gamma_i]^{r(i,k)} \right] = 0 \quad , \quad (17)$$

where $a_{j,k}$ is the activity of the k^{th} component in the j^{th} phase, ΔG_k^0 is the standard state ΔG for the k^{th} equilibria, and γ_i is the activity coefficient for the i^{th} component of the melt phase derived from the regular solution model formulated by Ghiorso et al. (1983).

These equations suffice to solve for chemical equilibrium in a magmatic system of known bulk composition at the temperature and pressure of interest. They are initially solved to supply the starting equilibrium configurations of the two end-member magmas. The thermodynamic equations are non-linear in T , P and solid composition which limits the procedures for solving the set of equations. The Newton-Raphson method is an efficient means of finding solutions to these equations and is easy to implement. Computer programs in C are supplied by Press et al. (1988, p. 286).

Temperature as a dependent variable

Equations 16 and 17 are sufficient when temperature is used as the second independent thermodynamic variable, and are useful in modelling conventional differentiation processes, such as isobaric fractional crystallization, because

temperature can be a defined property at each increment (e.g., Russell and Nicholls, 1985; Nicholls et al., 1986). In magma mixing processes, however, temperature is not an independent thermodynamic variable because mixing of magmas entails a transfer of energy as well as matter. Fixing T fixes the energy transfer along the mixing path. It is difficult to envisage the physical cause of such a path. For example, under isobaric conditions an isothermal assumption would imply a constant and minimum Gibbs free energy at equilibrium.

If we cannot use temperature with pressure as the two independent variables called for by Duhem's Theorem, how can we calculate the equilibrium position of mixed magmas between increments of the invasive magma? If temperature is a dependent variable, we can choose another property of the resultant system, such as V or S , placing major thermodynamic restrictions on the chemical equilibria attending the mixing process. The equilibrium state of the resultant magma after each incremental addition of the invasive magma is solved with Equations 16 and 17 and an equation constraining the thermodynamic variable. For example, the isenthalpic restriction can be imposed with

$$h_l(T_r, P) \cdot Y + \sum_{j=1}^P [m_j h_j(T_r, P)] - [H_B(T_B, P) \cdot X_B + H_A(T_A, P) \cdot X_A] = 0 \quad (18)$$

(e.g., VanZeggeren and Storey, 1970). Variables h_l and h_j are the molar enthalpies of the melt and equilibrium solid phases, respectively, at the new equilibrium temperature. Y is the total moles of the melt phase, and m_j is the moles of the j^{th} solid phase. The last bracketed term on the left hand side of the equation is constant and equal to the total initial enthalpy of the system.

Adiabatic and non-adiabatic paths

I started with, and am continuing to use, the adiabatic restriction. I have chosen this restriction because it makes some sort of geological sense. Picture a magma reservoir just after an influx of the invasive magma. The new chemical system begins to re-equilibrate, meaning that: (i) the reactive part of the solid assemblage changes to become stable with respect to the new residual melt phase, (ii) there are no chemical potential gradients in the resultant reservoir, and (iii) within the system all phases have the same temperature. The process of going from resident magma plus increment of invasive magma to equilibrated new resident magma involves a change in internal energy unless the state of the reservoir stays exactly the same. A portion of the change in internal energy involves heat (q). The

adiabatic restriction simply states that $dq = 0$ and requires that $ds = 0$. Additionally, I have assumed that the mixing process occurs at constant pressure. Therefore, this adiabatic path is also an isenthalpic path (Table 3), meaning that the final equilibrium state of the magma will have a total enthalpy and total entropy identical to the initial values. This requires a zero balance between endothermic and exothermic chemical processes or a change in temperature. The adiabatic restriction is an important thermodynamic path because it corresponds to a zero heat flow boundary condition in physical modelling (e.g., Nicholls, 1990b).

This is a valid assumption if the equilibration process operates fast enough to preclude significant heat transfer to a magma's surroundings. There are, in fact, indications that chemical processes attendant on mixing occur before significant heat is exchanged with the surroundings. Indeed, a number of authors have suggested that eruption commonly occurs shortly after mixing events, suggesting that the adiabatic assumption is a fair one. Ultimately, this assumption can be evaluated by comparing the model results against the geologic evidence.

There are definite repercussions to removing the restriction $dq = 0$ and allowing heat to escape the reservoir. If an adiabatic magma mixing path is not chosen, then another thermodynamic restriction is required. One solution would be to specify a fixed value for dq from a knowledge of the physics of cooling magma bodies (e.g., Jaupart and Tait, 1990, Nicholls, 1990b). This would require knowledge about the efficiency of heat transfer from the magma to the country rock, which in turn requires knowledge about the actual heat transfer process. Alternatively, another fundamental thermodynamic property of the system, such as the volume, could be specified. The validity of restricting another variable can only be judged by whether or not the assumption is geologically meaningful.

MODEL SIMULATIONS

Below, I have modelled the isenthalpic magma mixing path for the Kilauea Iki data found in Table 2. Different paths result depending on which rock compositions are chosen as the resident and invasive magmas. Consequently, I have modelled perfect equilibrium mixing (path 8, Table 4) of SW-2 into SG-5 and vice versa. Both magmas are assumed to begin at temperatures slightly below their liquidii and are olivine saturated (Table 5). The equilibrium state of the resident magma is calculated over a range of compositions resulting from the addition of 0.5 moles of the invasive magma to an initial 100 moles of the resident magma. At the end of these simulations, the resultant reservoirs contain 125 moles of magma in a new equilibrium configuration.

Table 5. Equilibrium conditions of magmas SG-05 and SW-02 prior to mixing at 0.01 GPa on a 100 mole basis. S.I. is the saturation index of solid phases in the residual melt.

| Parameter | SG-05 | SW-02 |
|-------------------------|-----------|-----------|
| T(K) | 1537 | 1455 |
| X (Forsterite) | 0.852 | 0.797 |
| Moles Olivine | 0.9809 | 0.7081 |
| ln fO ₂ | -18.167 | -20.763 |
| Bulk Enthalpy (kJ/mole) | -3485.873 | -3513.616 |
| S.I. (Plagioclase) | 0.5482 | 0.9327 |
| S.I. (Clinopyroxene) | 0.5637 | 0.8270 |

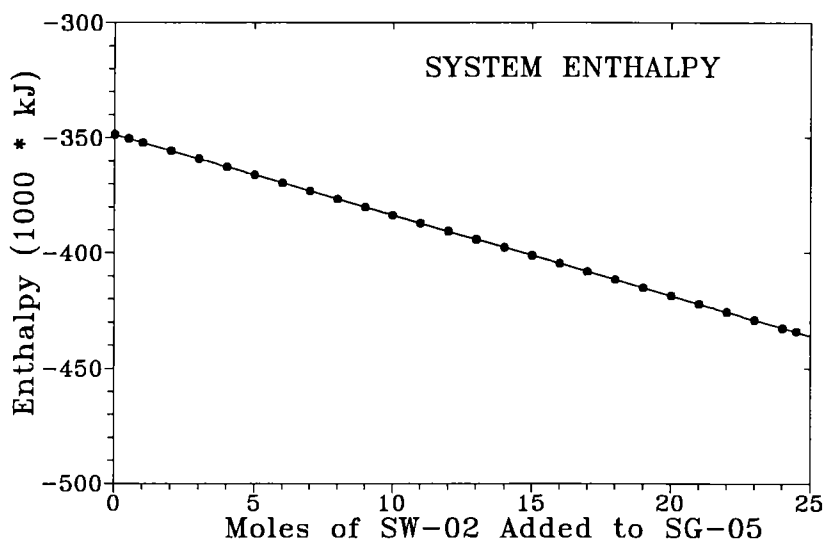


Figure 14. Bulk enthalpy of resident magma resulting from the addition of 0.5 mole increments of cool magma (SW-02) to an initial 100 moles of a hotter (SG-05) reservoir.

The first simulation models the effects of adding the hotter magma, SG-5 to the cooler, SW-2. Figures 14 through 17 summarize the equilibrium position of the resultant magmas as a function of the number of moles of invasive magma added. Figure 14 illustrates the total enthalpy of the system which is fixed by the states of the end-member magmas. Temperature is one of the dependent variables computed along the isenthalpic path and decreases as the extent of mixing increases (Fig. 15). Unfortunately, this parameter is not easily checked against field observations or laboratory measurements. Figure 16 summarizes two parameters, equilibrium olivine compositions and abundances, that can be compared against observation. The mixing causes only slight variations in olivine composition, even when the invasive magma makes up 20% of the reservoir. The total number of moles of

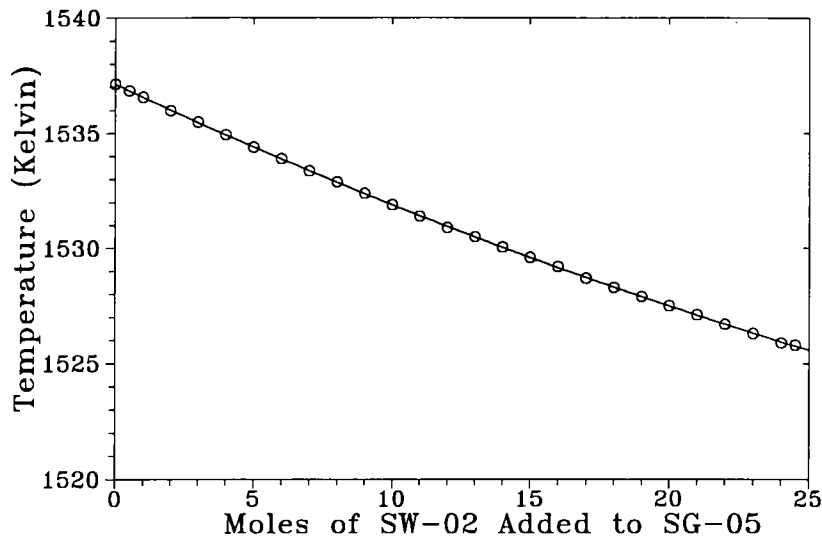


Figure 15. Equilibrium temperature for isenthalpic mixing of SG-05 and SW-02 (see Fig. 14).

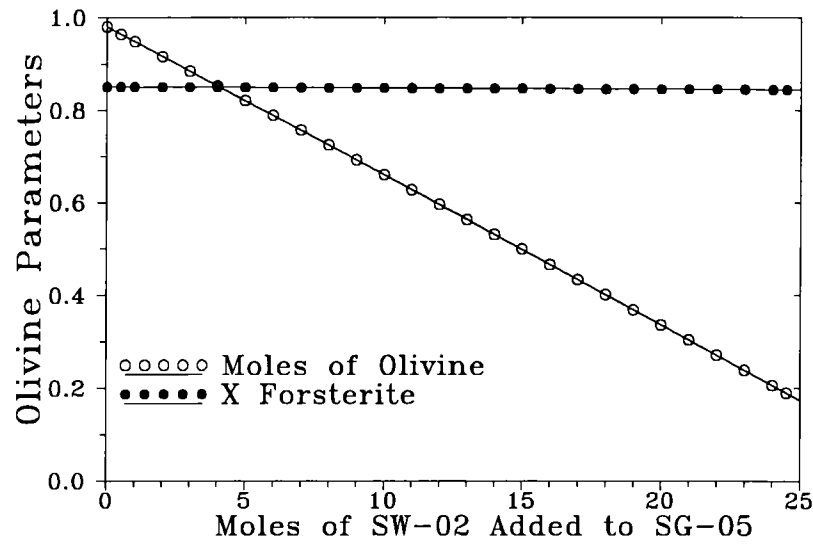


Figure 16. Calculated moles of olivine and olivine composition in the resident magma at equilibrium as a function of isenthalpic mixing.

olivine at each new equilibrium position decreases down the isenthalpic mixing path. In fact, Figure 16 implies that as mixing continues, the resultant magma will reach its liquidus. The composition of the melt phase is also a parameter that can be compared against data (e.g., glass compositions). Figure 17 illustrates the variation in the composition of the residual melt after mixing and shows its deviation from the bulk composition of the system. The difference between melt and system composition at each equilibrium position is a reflection of the amount of olivine

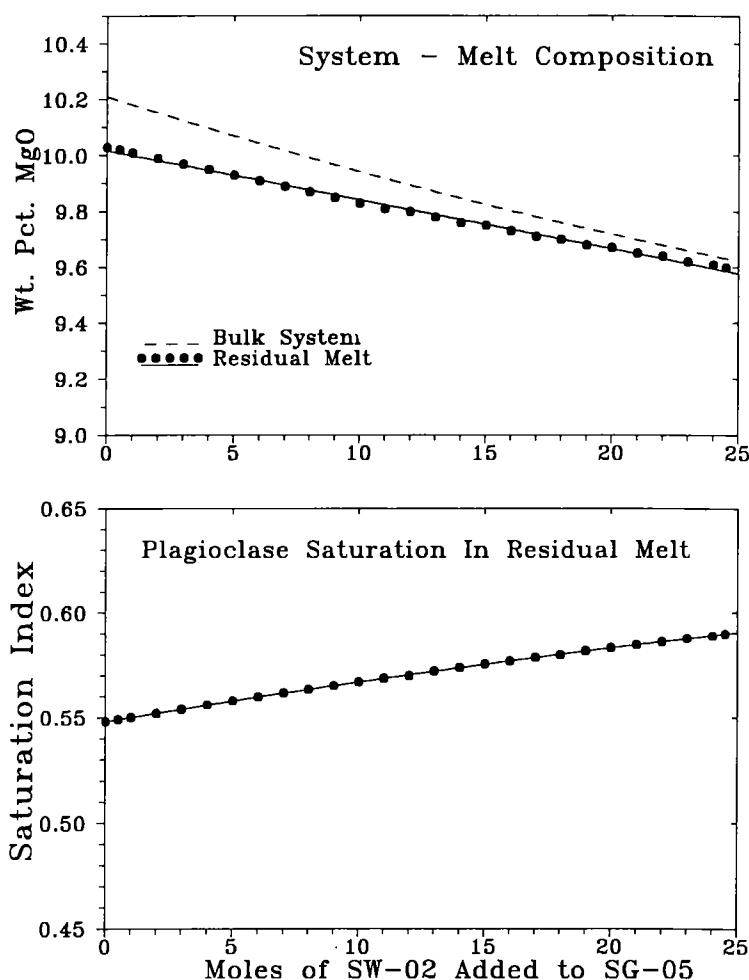


Figure 17. Upper figure compares bulk system and equilibrium residual melt compositions down the mixing path. Lower figure shows plagioclase saturation index (S.I.) for residual melts plotted as a function of mixing SW-02 into SG-05. The increase in S.I. with mixing is the result of lower ambient magma temperatures and changing melt composition.

crystallized: hence, the compositional gap narrows as the extent of mixing increases.

The lower portion of Figure 17 illustrates the calculated saturation index of plagioclase in the residual melt. The saturation index rises in response to decreasing temperature and changing melt composition. Plagioclase will be closer to saturation with mixing and thus will crystallize sooner with any subsequent crystallization.

The consequences of reversing the roles of invasive and resident magmas during mixing are illustrated in parallel figures (Figs. 18-20). Figure 18 illustrates the resultant temperature arising from the isenthalpic mixing of 0.5 mole increments of SG-5 into 100 moles of SW-2. The equilibrium temperature is contrasted with the lower temperatures corresponding to linear interpolation of the end-member magmas. Figure 19 shows equilibrium olivine composition and amount (moles) with successive influxes of the higher temperature invasive magma. Olivine composition varies little over the modelled magma mixing path, however, the amount of olivine decreases dramatically. In fact, at any point beyond the addition of 15 moles of SG-5, the resultant magma is at or above the liquidus and olivine has dissolved.

The residual melt chemistry plotted on Figure 20 is compared to the system composition; where the resultant magma reaches liquidus conditions, the compositions are the same. This effect of the isenthalpic mixing path can be shown explicitly by comparing the computed equilibrium temperature against the corresponding liquidus temperatures for each of the new bulk magma compositions (Fig. 21). Figure 22 illustrates the relation between temperature and system's molar enthalpy resulting from the mixing process. The solid line marks the rise in molar enthalpy and temperature expected from the mechanical mixing of the two end-member magmas. Each data point corresponds to a fixed number of moles of SG-5 added to SW-2 (see labels, Fig. 22). The dashed curve traces the corresponding relation between the resultant temperature and molar enthalpy for the mixed magmas after reaching equilibrium along the isenthalpic mixing path. Note that corresponding points on the two curves share the same molar enthalpy (independent variable) and that the equilibrium temperature is always higher than the linear interpolated temperature over this range of mixing. The horizontal dashed line marks the condition where increasing contributions of SG-5 to SW-2 forces the resultant magma to its liquidus.

A consequence of mixing these end-member magmas, in the equilibrium states summarized in Table 5 and under isenthalpic conditions, is that the resultant magmas eventually reach their liquidi. The rise in temperature is a consequence of the imposed heat balance expressed as an absence of heat loss from the magmatic system. The heat sources and sinks which are expected to balance include: (i) heats

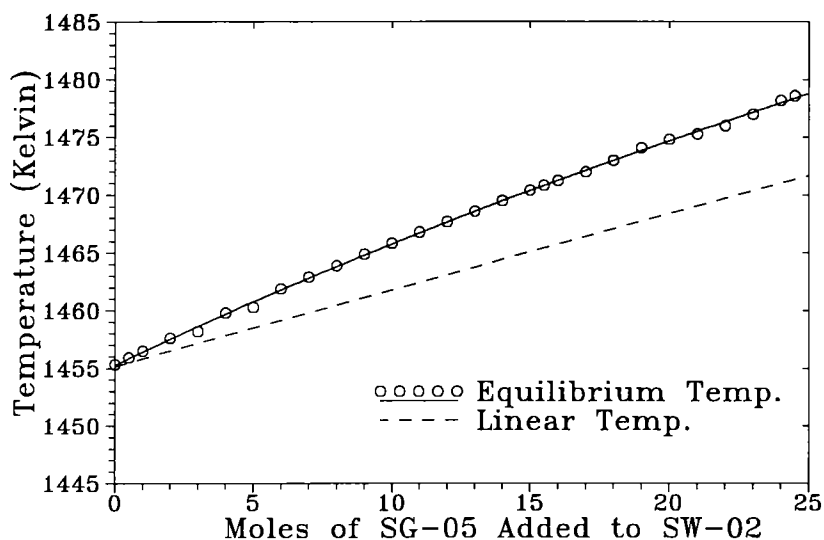


Figure 18. Comparison between equilibrium temperature of resident magma (SW-02) during isenthalpic mixing with invasive magma (SG-05) and linear temperature between end-member magmas.

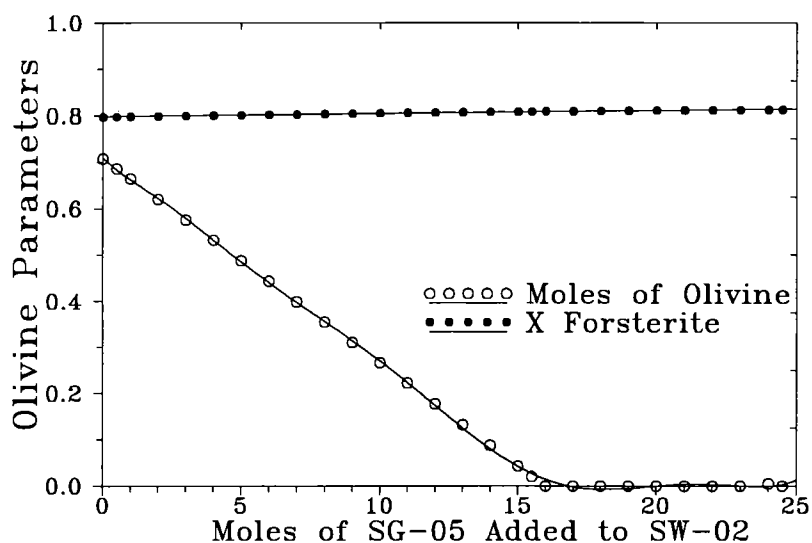


Figure 19. Moles of olivine and composition of olivine as a function of isenthalpic mixing (see Fig. 18).

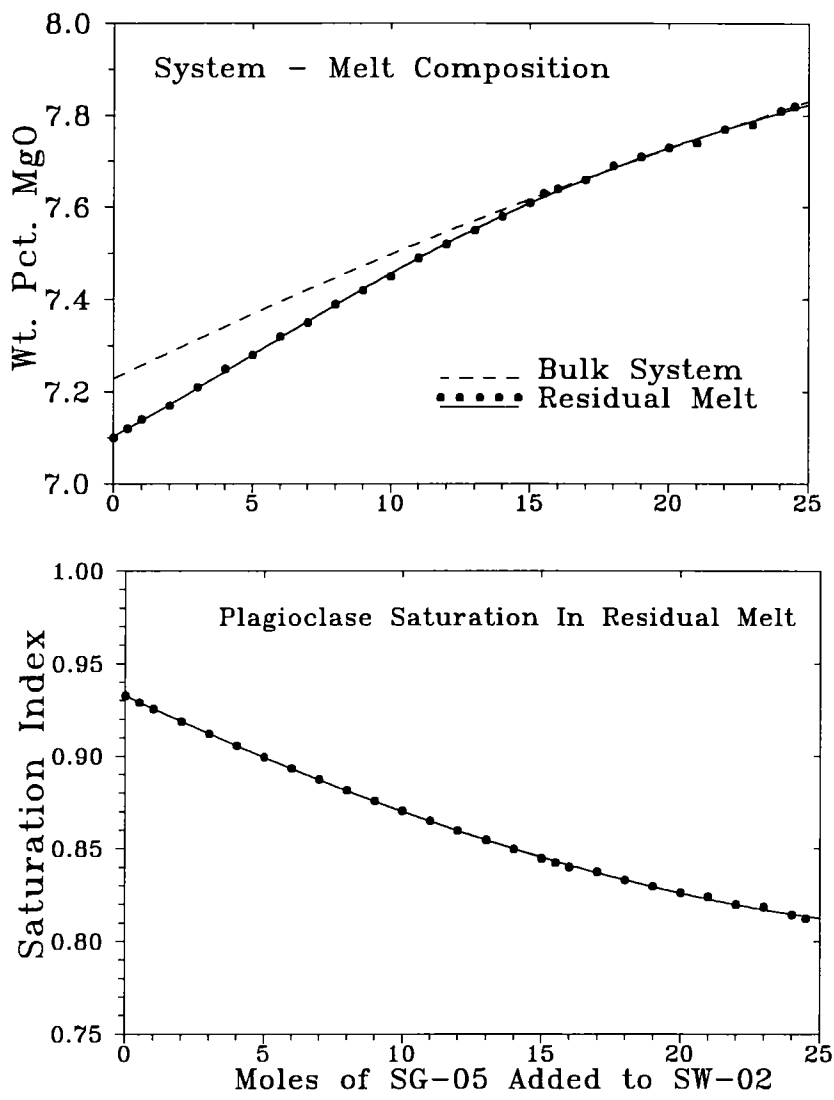


Figure 20. Upper diagram compares bulk system composition to residual melt compositions derived through mixing of SW-02 with SG-05. Lower diagram tracks the saturation potential of plagioclase in the residual melt.

due to mixing of the silicate melts, (ii) heats due to fusion of the disequilibrium solid phase assemblages, and (iii) heats of crystallization for the new equilibrium solid assemblage. As heat transfer to the surroundings is precluded, the heat balance is accomodated by changes in magmatic temperature.

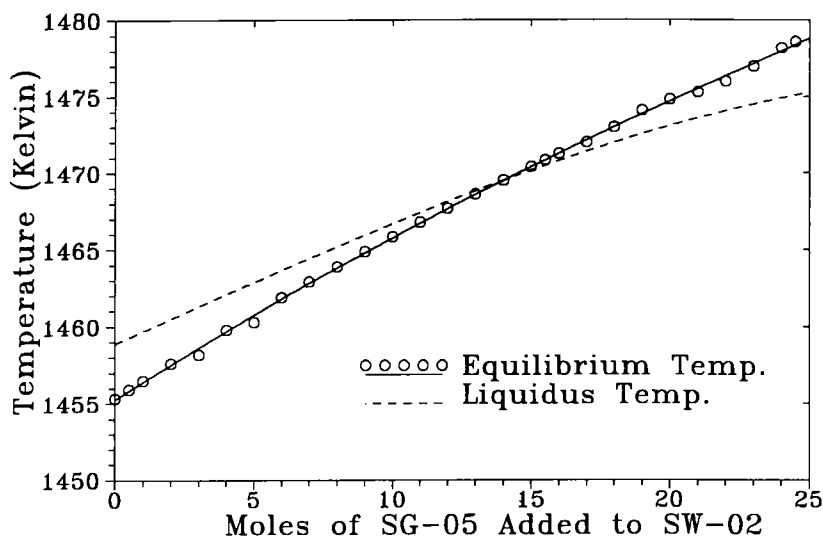


Figure 21. Equilibrium magma temperature after isenthalpic mixing versus corresponding liquidus temperatures.

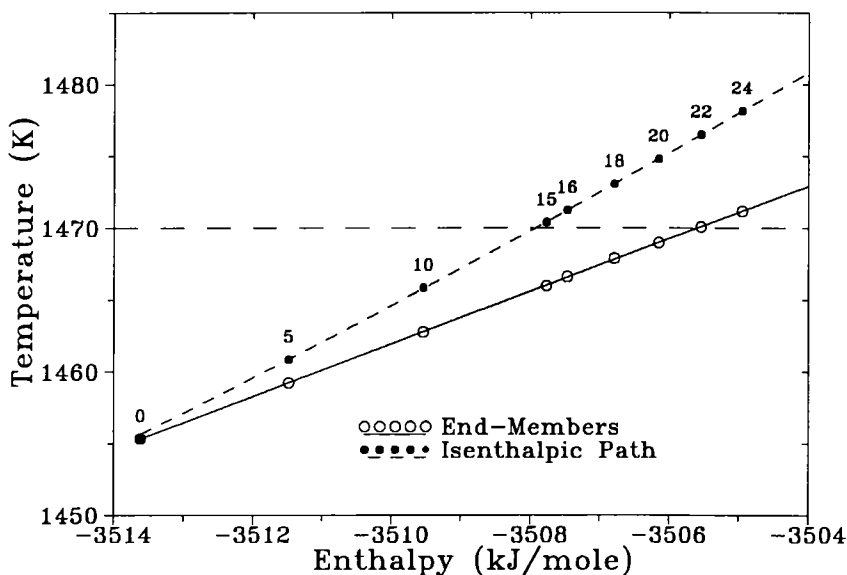


Figure 22. T(K) - H path during isenthalpic mixing of SW-02 (resident magma) and SG-05 (invasive magma). The resulting equilibrium temperature (solid symbols) are shown for various mole amounts of SG-05 added to 100 moles of SW-02. The horizontal line marks the point at which the resulting magma is superliquidus.

CONCLUSIONS

Thermodynamic calculations have the potential to provide new insight into old problems. They guide us to ideas about igneous process that are consistent with phase equilibria and are physically and chemically feasible. In conclusion, there are several points which relate to the modelling of magma mixing processes which bear restatement:

- (1) The important parameters governing differentiation by magma mixing contrast the parameters controlling conventional differentiation such as fractional crystallization. Whereas heat loss and decreasing temperature are the major variables driving conventional differentiation, magma mixing is driven by influxes of magma of different compositions and thermodynamic states. The fact that temperature can rarely be used as an independent variable in modelling magma mixing requires that other geologically sensible thermodynamic restrictions be found.
- (2) Thermodynamic modelling can refine our understanding of this important magmatic process because:
 - (i) The calculations quantify the consequences of magma mixing. The computed parameters are easily compared against actual data and are a measure by which the magma mixing hypotheses can be judged; and
 - (ii) Where the hypothesis is viable, modelling constrains the physical chemical behaviour of the system and gives us estimates of its effects on the surroundings (e.g., heat transfer rates etc.).
- (3) Whereas the thermodynamic simulation of magma mixing increases our current understanding, future studies must also include the physics of the process (e.g., Oldenburg et al., 1989), ensuring that our conceptions are physically reasonable as well as thermodynamically sound.

There is, however, one final consideration which concerns modelling of magmatic processes: The strength and utility of a model resides in its ability to be tested against nature. Models producing only parameters that cannot be compared against observation and measurement are of little scientific use. Thermodynamic modelling of igneous processes is scientifically effective because it provides a plethora of parameters for testing against data.

ACKNOWLEDGMENTS

Research for this manuscript was funded by a Natural Science and Engineering Council operating grant (A0820). I am indebted to Umakanth Thirugnanam for his contribution to the computer programs used to make the calculations presented above and for exposing me to better programming habits. Additionally, I have benefitted from informal discussions with Jim Nicholls and Tom Brown, although any faults in logic or theory remain mine. Constructive reviews by P.J. Michael, J. Nicholls, and C.R. Stanley improved the clarity of the arguments.

REFERENCES

- Bacon, C.R. (1986) Magmatic inclusions in silicic and intermediate volcanic rocks. *J. Volcanol. Geotherm. Res.*, 18, 57-115.
- Basaltic Volcanism Study Project (1981) *Basaltic Volcanism on the Terrestrial Planets*. Pergamon Press, Inc., New York, 1286 p.
- Blake, S. (1981) Eruptions from zoned magma chambers. *J. Geol. Soc. London*, 138, 281-287.
- Blake, S. and Ivey, G.N. (1986a) Magma mixing and the dynamics of withdrawal from stratified reservoirs. *J. Volcanol. Geotherm. Res.*, 237, 153-178.
- Blake, S. and Ivey, G.N. (1986b) Density and viscosity gradients in zoned magma chambers, and their influence on withdrawal dynamics. *J. Volcanol. Geotherm. Res.*, 30, 201-230.
- Campbell, I.H. and Turner, J.S. (1986) The influence of viscosity on fountains in magma chambers. *J. Petrol.*, 27, 1-30.
- Carmichael, I.S.E. and Ghiorso, M.L. (1986) Oxidation-reduction relations in basic magma: a case for homogeneous equilibria. *Earth Planet. Sci. Lett.*, 78, 200-210.
- Carmichael, I.S.E., Nicholls, J., Spera, F.J., Wood, B.J., and Nelson, S.A. (1977) High temperature properties of silicate liquids: applications to the equilibration and ascent of basic magma. *Phil. Trans. Royal Soc. London A*, 286, 373-431.
- Carmichael, I.S.E., Turner, F.J., and Verhoogen, J. (1974) *Igneous Petrology*. McGraw Hill Book Co., 739 p.
- Duhem, P. (1898) On the general problem of chemical statics. *J. Phys. Chem.*, 2, 1-41 and 91-115.
- Dungan, M.A. and Rhodes, J.M. (1978) Residual glasses and melt inclusions in basalts from DSDP Legs 45 and 46: evidence for magma mixing. *Contrib. Mineral. Petrol.*, 67, 417-431.
- Furman, T. and Spera, F.J. (1985) Commingling of acid and basic magma and implications for the origin of I-type xenoliths, I Field and petrochemical relations of an unusual dike complex at Eagle Lake, Sequoia National Park, California, USA. *J. Volcanol. Geotherm. Res.*, 24, 301-318.
- Garcia, M.O., Ho, R.A., Rhodes, J.M., and Wolfe, E.W. (1989) Petrologic constraints on rift-zone processes: Results from episode 1 of the Puu OO eruption of Kilauea Volcano, Hawaii. *Bull. Volcanol.*, 52, 81-96.
- Gerlach, D.C. and Grove, T.L. (1982) Petrology of Medicine Lake Highland volcanics: Characterization of End-members of magma mixing. *Contrib. Mineral. Petrol.*, 80, 147-159.
- Ghiorso, M.S., (1985) Chemical mass transfer in magmatic processes. I. Thermodynamic relations

- and numerical algorithms. *Contrib. Mineral. Petrol.*, 90, 107-120.
- Ghiorso, M.S. and Carmichael, I.S.E. (1985) Chemical mass transfer in magmatic processes II: Application in equilibrium crystallization, fractionation and assimilation. *Contrib. Mineral. Petrol.*, 91, 691-722.
- Ghiorso, M.S. and Kelemen, P.B. (1987) Evaluating reaction stoichiometry in magmatic systems evolving under generalized thermodynamic constraints: Examples comparing isothermal and isenthalpic assimilation. In: *Magmatic Processes: Physicochemical Principles*, The Geochemical Society, Special Publ. 1, 319-336.
- Ghiorso, M.S., Carmichael, I.S.E., Rivers, M.L., Sack, R.O. (1983) The Gibbs free energy of mixing of natural silicate liquids; An expanded regular solution approximation for the calculation of magmatic intensive variables. *Contrib. Mineral. Petrol.*, 84, 107-145.
- Greenwood, H.J. (1989) On models and modeling. *Can. Mineral.* 27, 1-14.
- Grove, T.L., Gerlach, D.C. and Sande, T.W. (1982) Origin of calc-alkaline series lavas at Medicine Lake volcano by fractionation, assimilation and mixing. *Contrib. Mineral. Petrol.*, 80, 160-182.
- Helz, R.T. (1987) Diverse olivine types in lava of the 1959 eruption of Kilauea Volcano and their bearing on eruption dynamics. in *Volcanism in Hawaii*, U.S. Geol. Surv. Prof. Paper, 1350, 691-722.
- Huppert, H.E. and Sparks, R.S.J. (1980) The fluid dynamics of a basaltic magma chamber replenished by influx of hot, dense ultrabasic magma. *Contrib. Mineral. Petrol.*, 75, 279-289.
- Huppert, H.E., Sparks, R.S.J. and Turner, J.S. (1982) Effects of volatiles on mixing in calc-alkaline magma systems. *Nature*, 297, 554-557.
- Huppert, H.E., Sparks, R.S.J., Whitehead, J.A. and Hallworth, M.A. (1986) The replenishment of magma chambers by light inputs. *J. Geophys. Res.*, 91, 6113-6122.
- Jaupart, C. and Tait, S. (1990) Dynamics of eruptive phenomena. In: *Modern Igneous Petrology - Understanding Magmatic Processes* (J. Nicholls and J.K. Russell, eds.), *Reviews in Mineralogy*, 24, this volume.
- Juster, T.C., Grove, T.L., and Perfit, M.R. (1989) Experimental constraints on the generation of Fe-Ti basalts, andesites, and rhyodacites at the Galapagos spreading center, 85°W and 95°W. *J. Geophys. Res.*, 94, 92512-9274.
- Kelemen, P.B. (1990) Reaction between ultramafic rock and fractionating basaltic magma I. Phase relations, the origin of calc-alkaline magma series, and the formation of discordant dunite. *J. Petrol.*, 31, 51-98.
- Kilinc, A., Carmichael, I.S.E., Rivers, M.L., and Sack, R.O. (1983) The ferric-ferrous ratio of natural silicate liquids equilibrated in air. *Contrib. Mineral. Petrol.*, 83, 136-140.
- Kress, V.C. and Carmichael, I.S.E. (1988) Stoichiometry of the iron oxidation reaction in silicate melts. *Amer. Mineral.*, 73, 1267-1274.
- Michael, P.J. (1989) Intrusion of basaltic magma into a crystallizing granitic magma chamber: Cordillera del Paine in the southernmost Andes, Chile. in *Continental Magmatism*, I.A.V.C.E.I. General Assembly, New Mexico Bureau Mines Mineral. Res., Bull. 131, 189.
- Murata, K.J. and Richter, D.H. (1966) Chemistry of the lavas of the 1959-60 eruption of Kilauea Volcano, Hawaii, U.S. Geol. Surv., Prof. Paper 537A, pp.26.
- Nicholls, J. (1977) The calculation of mineral compositions and modes of olivine-two pyroxene-spinel assemblages: problems and possibilities. *Contrib. Mineral. Petrol.*, 60, 119-142.
- Nicholls, J. (1980) A simple thermodynamic model for estimating the solubility of H₂O in magmas. *Contrib. Mineral. Petrol.*, 74, 211-220.
- Nicholls, J. (1990a) Principles of thermodynamic modeling of igneous processes. In: *Modern Igneous Petrology - Understanding Magmatic Processes* (J. Nicholls and J.K. Russell, eds.), *Reviews in Mineralogy*, 24, this volume.
- Nicholls, J. (1990b) The mathematics of fluid flow and a simple application to problems of magma transport. In: *Modern Igneous Petrology - Understanding Magmatic Processes* (J. Nicholls and J.K. Russell, eds.), *Reviews in Mineralogy*, 24, this volume.

- Nicholls, J. and Russell, J.K. (1990a) Pearce element ratios - An overview, example, and bibliography. In: *Pearce Element Ratios: Theory and Application to Geochemical Data Analysis* (J.K. Russell and C.R. Stanley, eds.), Geol. Assoc. Can., Short Course 8, 11-21.
- Nicholls, J. and Russell, J.K. (1990b) Recognition of cogenetic igneous rocks: application to magma batches in Kilauea, 1954-1971. *Contrib. Mineral. Petrol.*, in press Oct. 1990.
- Nicholls, J., Russell, J.K., and Stout, M.Z. (1986) Testing magmatic hypotheses with thermodynamic modelling. In: *Short Course in Silicate Melts* (C.M. Scarfe, ed), Mineral. Assoc. Can., 210-235.
- Nicholls, J. and Stout, M.Z. (1982) Heat effects of assimilation, crystallization, and vesiculation in magmas. *Contrib. Mineral. Petrol.* 81, 328-339.
- Nielsen, R.L. (1988) A model for the simulation of combined major and trace element liquid lines of descent. *Geochim. Cosmochim. Acta* 52, 27-38.
- Nielsen, R.L. (1990) Simulation of igneous differentiation processes. In: *Modern Igneous Petrology - Understanding Magmatic Processes* (J. Nicholls and J.K. Russell, eds.), *Reviews in Mineralogy*, 24, this volume.
- Nixon, G.T. (1988a) Petrology of the younger andesites and dacites of Iztaccihautl Volcano, Mexico: I. Disequilibrium phenocryst assemblages as indicators of magma chamber processes. *J. Petrol.* 29, 213-264.
- Nixon, G.T. (1988b) Petrology of the younger andesites and dacites of Iztaccihautl Volcano, Mexico: II. Chemical stratigraphy, magma mixing, and the composition of basaltic magma influx. *J. Petrol.* 29, 265-303.
- Nixon, G.T. and Pearce, T.H. (1987) Laser-interferometry study of oscillatory zoning in plagioclase: The record of magma mixing and phenocryst recycling in calc-alkaline magma chambers, Iztaccihautl volcano, Mexico. *Amer. Mineral.*, 72, 1144-1162.
- O'Hara, M.J. (1980) Nonlinear nature of the unavoidable long-lived isotopic, trace and major element contamination of a developing magma chamber. *Phil Trans. Royal Soc. London A*, 297, 215-227.
- O'Hara, M.J. and Mathews, R.E. (1981) Geochemical evolution of in an advancing, periodically replenished, periodically tapped, continuously fractionating magma chamber. *J. Geol. Soc. London*, 138, 237-277.
- Oldenburg, C.M., Spera, F.J., Yuen, D.A., and Sewell, G. (1989) Dynamic mixing in magma bodies: Theory, simulations, and implications. *J. Geophys. Res.*, 94, 9215-9236.
- Pearce, T.H., Griffin, M.P., and Kolisnik, A.M. (1987) Magmatic crystal stratigraphy and constraints on magma chamber dynamics: Laser interference results on individual phenocrysts. *J. Geophys. Res.*, 92, 13,745-13,752.
- Philpotts, A.R. (1990) *Principles of Igneous and Metamorphic Petrology*. Prentice Hall, New Jersey, 498 p.
- Popper, K.R. (1959) *The Logic of Scientific Discovery*. Hutchison and Co., London, 480 p.
- Press, W.H., Flannery, B.P., Teukolsky, S.A., and Vetterling, W.T. (1988) *Numerical Recipes in C - The Art of Scientific Computing*. Cambridge University Press, Cambridge, 735 p.
- Prigogine I. and Defay, R. (1954) *Chemical Thermodynamics*. Longmans, Green and Co., London, 543 p.
- Rice, A. (1981) Convective fractionation: a mechanism to provide cryptic zoning (macro-segregation), layering, crescumulats, banded tuffs and explosive volcanism in igneous provinces. *J. Geophys. Res.*, 86, 405-417.
- Russell, J.K. (1987) Crystallization and vesiculation of the 1984 eruption of Mauna Loa. *J. Geophys. Res.*, 92, 13731-13743.
- Russell, J.K. (1990) Formulating and testing the magma mixing hypothesis. *Geol. Assoc. Can. - Mineral. Assoc. Can. Annual Meeting, Progr. Abstr.*, Vancouver, B.C., A115.
- Russell, J.K. and Nicholls, J. (1985) Application of Duhem's Theorem to the estimation of extensive and intensive properties of basaltic magmas. *Can. Mineral.*, 23, 479-488.

- Russell, J.K. and Stanley, C.R. (1990) Origins of the 1954-1960 lavas, Kilauea Volcano, Hawaii: Major element constraints on shallow reservoir magmatic processes. *J. Geoph. Res.*, 95, 5021-5047.
- Sack, R.O., Carmichael, I.S.E., Rivers, M., and Ghiorso, M.S. (1980) Ferric-Ferrous equilibria in natural silicate liquids at 1 bar. *Contrib. Mineral. Petrol.*, 75, 369-376.
- Sparks, R.S.J. and Marshall, L.A. (1986) Thermal and mechanical constraints on mixing between mafic and silicic magmas. *J. Volcanol. Geotherm. Res.* 29, 99-124.
- Sparks, R.S.J., Sigurdsson, H., and Wilson, L. (1977) Magma mixing: A mechanism for triggering acid explosive eruptions. *Nature*, 267, 315-318.
- Spera, F.J., (1984) Carbon dioxide in petrogenesis III: role of volatiles in the ascent of alkaline magma with special reference to xenolith-bearing mafic lavas. *Contrib. Mineral. Petrol.*, 88, 217-232.
- Stasiuk, M.V. and Russell, J.K. (1990) The Bridge River Assemblage in the Meager Mountain volcanic complex, southwestern British Columbia. In: *Current Research, Part E, Geol. Surv. Can., Paper 90-1e*, 227-233.
- Stebbins, J.F., Carmichael, I.S.E., Moret, L.K. (1984) Heat capacities and entropies of silicate liquids and glasses. *Contrib. Mineral. Petrol.*, 86, 131-148.
- Tait, S. and Jaupart, C. (1990) Physical processes in the evolution of magma chambers. In: *Modern Igneous Petrology - Understanding Magmatic Processes* (J. Nicholls and J.K. Russell, eds.), *Reviews in Mineralogy*, 24, this volume.
- Turner J.S. and Campbell, I.H. (1986) Convection and mixing in magma chambers. *Earth Sci. Rev.*, 23, 255-352.
- Turner, F.J. and Verhoogen, J. (1951) *Igneous and Metamorphic Petrology*. McGraw Hill, New York, 602 p.
- Van Zeggeren, F. and Storey, S.H. (1970) *The Computation of Chemical Equilibria*. The Cambridge University Press, London, 176 p.
- Waldbaum, D.R. (1971) Temperature changes associated with adiabatic decompression in geological processes. *Nature*, 232, 545-547.
- Wright, T.L. and Doherty, P.C. (1970) A linear programming and least squares computer method for solving petrologic mixing problems. *Geol. Soc. Amer. Bull.*, 81, 1995-2008.
- Wright, T.L. (1973) Magma mixing as illustrated by the 1959 eruption, Kilauea Volcano, Hawaii. *Geol. Soc. Amer. Bull.*, 84, 849-858.

THE EFFECT OF OXYGEN FUGACITY ON THE REDOX STATE OF NATURAL LIQUIDS AND THEIR CRYSTALLIZING PHASES

INTRODUCTION

In Volume 17 of *Reviews in Mineralogy*, entitled *Thermodynamic Modelling of Geological Materials*, we described theoretical and numerical methods (Ghiorso et al., 1983, Ghiorso, 1985, Ghiorso and Kelemen, 1987, Ghiorso, 1987) for the evaluation of reversible and irreversible chemical reactions in magmatic systems undergoing crystallization, assimilation and/or magma mixing. Numerous petrological applications of these methods were discussed and evaluated against data from the both the field and from experiments (Ghiorso and Carmichael, 1985, 1987). What emerges from this summary is the realization that thermodynamic modelling of low-pressure igneous processes in alkali-poor mafic magmas (and their compositional derivatives) is broadly successful at reproducing our observations and quantifying our petrologic intuition. It is now possible to pose realistic geologic constraints on the evolution of a magmatic system and calculate the crystallization history of the body in response to the imposed conditions. Thus, the testing of igneous hypotheses has been liberated from the parochial restrictions imposed by simple phase diagrams. More importantly, experimentally inaccessible conditions such as isochoric (fixed volume) crystallization or isenthalpic (fixed heat content) assimilation can be investigated numerically, with the assurance that the results are internally consistent (in a thermodynamic sense) with experimentally determined major element partitioning data. In a practical sense, thermodynamic models for magmatic systems have served as tools to interpolate and extrapolate these data. It follows that their success in application depends upon two factors: (1) the appropriateness of the formulation with regard to *both* the liquid and the solid phases, and (2) the quality and scope of the experimental database available to calibrate model parameters.

It is crucial to understand that the deficiencies which arise in application of currently available thermodynamic models to igneous systems are not intrinsic to the thermodynamic approach. Our inability to calculate the solid-liquid phase relations of hydrous minerals such as biotites and amphiboles for example, is due to a paucity of experimental data and an inadequate understanding of the activity-composition relations of the solid phase. Efforts to improve thermodynamic modelling of igneous processes must focus on rectifying these deficiencies. To this end considerable progress has been made in establishing internally consistent thermodynamic formulations for end-member solid phases (Berman, 1988) and in the development of comprehensive models for activity-composition relations of their solid solutions (e.g., Elkins and Grove, 1990, Fuhrman and Lindsley, 1988, Ghiorso, 1990, Sack and Carmichael, 1984, Sack and Ghiorso, 1989, 1991a,b). Recalibration of the liquid solution properties from the experimental liquid-solid phase relations (e.g., Ghiorso et al., 1983, Ghiorso, 1987), utilizing these new formulations for the thermodynamic properties of the solid phases, results in substantial improvement of calculated liquid-solid phase relations but highlights the need for additional experimental work.

One of the most interesting experimental issues yet to be addressed concerns controls on the oxidation state of the magma in response to crystallization under closed or open system conditions. Thermodynamic modelling of the variation in oxidation state during crystallization (Carmichael and Ghiorso, 1986, Ghiorso and Carmichael, 1985) has

served to reveal our ignorance of the subject, but a quantitative analysis of the process is lacking. We model the crystallization of magmatic liquids by forcing them to follow the log f_{O_2} - T relations of known oxygen fugacity buffers, largely because we think that that is approximately the way nature behaves. How the magma manifests this capacity for "self-buffering" remains a mystery, except that it must depend on phases which contain substantial quantities of ferric and ferrous iron, acting in combination. In this chapter we will focus on this issue by examining the oxidation-reduction relations of transition metal ions in igneous systems. We will survey the redox equilibria that controls both the composition and occurrence of the ferromagnesian minerals in magmas, particularly the silicates. The redox state of iron in any phase is a response to the prevailing oxygen fugacity, but only for the liquid has the experimental calibration connecting these variables been made. We examine firstly how the ferric-ferrous ratio in natural liquids can be calibrated experimentally so that values of oxygen fugacity may be obtained. For some ferromagnesian minerals the amount of ferric iron may perhaps be ignored in calculations of the liquid line of descent, but for other minerals such as amphibole, biotite and augite, there may be substantial concentrations of both ferric and ferrous iron. As a change in the ferric/ferrous ratio has a concomitant affect on the FeO/MgO ratio in the liquid, the composition and species of early crystallizing minerals may also be affected by a change in oxygen fugacity. Lastly we suggest experiments involving liquid-hydrous mineral equilibria, for with knowledge of the intensive variables, the composition of the phases, and the concentration and speciation of water, will lead to improved calibration of the thermodynamic properties of the liquid state.

REDOX STATE AND OXYGEN FUGACITY IN NATURAL SILICATE LIQUIDS

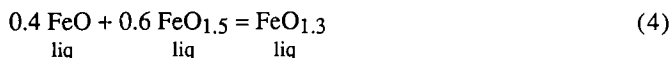
In a multicomponent silicate liquid the ratio of ferric to ferrous iron is a function of temperature, pressure, composition and oxygen fugacity. The relationship between these variables has been calibrated experimentally (at 1 bar) for a wide range of liquid compositions, equilibrated from air down to almost the iron-wüstite buffer (I-W), over a range of temperatures (Sack et al 1980; Kilinc et al 1983; Kress and Carmichael, 1988, 1991). Accordingly, if the concentration of FeO and Fe_2O_3 in a glassy lava is known, then the oxygen fugacity in equilibrium with this redox state can be derived. The relationship is given by the empirical equation:

$$\ln [X_{Fe_2O_3}/X_{FeO}] = a \ln f_{O_2} + b/T + c + \sum X_i d_i \quad (1)$$

where a , b , c and d_i are constants found by regression of over 220 experimental data. The most recent estimate of the parameter a in Equation 1 is 0.196 (Kress and Carmichael, 1991) which is at odds with interpretation of the Fe redox equilibria in the melt in terms of either of the following equivalent reactions:



This can be seen from isothermal plots of $\ln [(X_{FeO_{1.5}})/(X_{FeO})]$ against $\ln f_{O_2}$, which should have a slope of 0.25. However experiments on liquids ranging from andesite through basalt to nephelinite, have a slope closer to 0.2 (Kress and Carmichael, 1988), and confirm Fudali's (1965) initial discovery. The reason for this has been suggested to lie in the partial association of FeO and $FeO_{1.5}$ species in the liquid to form $FeO_{1.3}$ species (Kress and Carmichael, 1988). The distribution coefficient K_D of the homogeneous reaction:



was found to be 0.4 in both natural liquids and liquids in the system CaO-FeO-FeO_{1.5}-SiO₂ (Kress and Carmichael, 1991).

It can be shown by applying Equation 1 that a natural silicate liquid, equilibrated at temperatures above the liquidus with an external oxygen buffer, such as Ni-NiO (NNO), has an approximately constant Fe³⁺/Fe²⁺ ratio (Carmichael and Ghiorso, 1986). This has been verified experimentally by Kress and Carmichael (1988). The constant redox ratio reflects the surprising coincidence of the enthalpy of the liquid redox reaction to the solid redox reaction. This in turn allows the oxygen fugacity for any basic lava to be calculated at any temperature and compared to any convenient experimental oxygen buffer at the same temperature. The difference between the two values, the *relative* oxygen fugacity, will be essentially independent of temperature.

The relative oxygen fugacity data for glassy lavas are reported here with respect to NNO (Huebner and Sato, 1970) and thus ΔNNO is defined to be log₁₀ fO₂(sample) – log₁₀ fO₂(NNO) at the same temperature, which is arbitrarily calculated at 1200°C. Values of ΔNNO for a variety of basic, partially glassy lavas from the continental margin of western Mexico are plotted in Figure 1. The historic eruptions all show a common trend of the lavas becoming both more siliceous and more oxidized as the eruptions proceed, with hornblende entering as a phenocryst phase in the later (oxidized) lavas of Volcan Jorullo and Volcan Colima (Hasenaka and Carmichael, 1987). A compilation of ΔNNO data for basic lavas is presented in Figure 2; those for the oceanic (MORB) basalts are taken from Christie et al., (1986), whereas those for the tholeiitic lavas of Kilauea, Hawaii are taken from Carmichael and Ghiorso (1986). The lavas from western Mexico fall into two groups; the basalts, basaltic-andesites and andesites of the Michoacan-Guanajuato volcanic field (Fig. 1); and the lamprophyric and related lavas of Mascota and Colima. This second group is one comprised principally of minette lavas, a lava type free of feldspar phenocrysts (Luhr et al., 1989; Carmichael et al., 1991) which fall in a field of their own (Fig. 2) near the oxygen buffer hematite-magnetite (H-M). If the entire compositional range of *basic* lavas from MORB to minette is considered, then oxygen fugacity may vary over seven or eight orders of magnitude. Thus, the oxygen fugacity exhibits larger variation than any other variable in petrology.

The range of oxygen fugacity in *silicic* magmas is most conveniently obtained from the composition of their coexisting Fe-Ti oxide microphenocrysts. The experimental calibration of the spinel series (essentially Fe₂TiO₄-Fe₃O₄) with the rhombohedral series (essentially FeTiO₃-Fe₂O₃) as a function of temperature and oxygen fugacity was first made by Buddington and Lindsley (1964). The most recent reformulation of this calibration is given by Ghiorso and Sack (1991). In contrast to basic magmas, the range of oxygen fugacities of quartz-bearing silicic magmas, is (surprisingly!) smaller. The peralkaline rhyolitic lava type, pantellerite, is almost as reduced as the most reduced MORB (Fig. 3), but even the most oxidized ashflows never approach the oxygen fugacities defined by H-M (Carmichael, 1991).

Based on the combination of data from coexisting Fe-Ti oxides and the redox state of glassy lavas, the range of temperature and oxygen fugacity of magmas, either on or close to the surface (low pressure), is portrayed in Figures 4, 5 and 6. We now inquire into the stability of metals and their oxides within this zone of T-log fO₂.

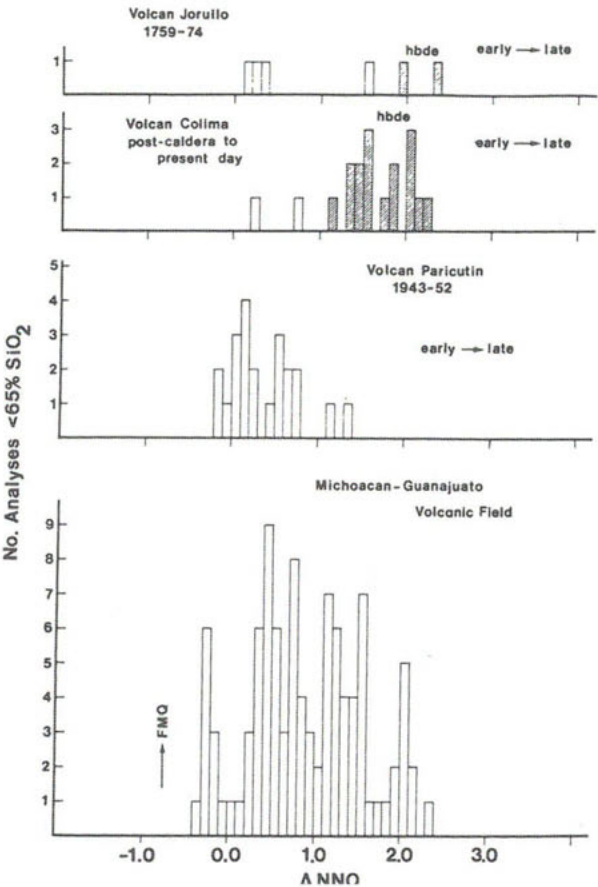


Figure 1. Values of the relative oxygen fugacity (ΔNNO) of the basaltic and andesitic glassy lavas of the western Mexican volcanic belt. Data from Hasenaka and Carmichael (1987).

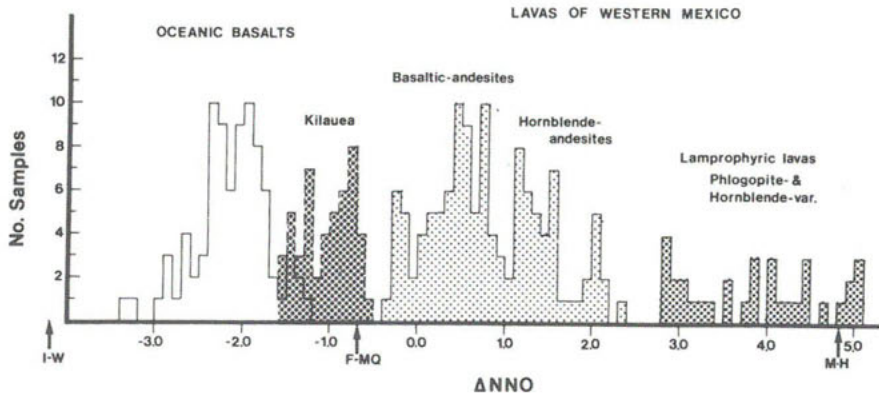


Figure 2. Values of the relative oxygen fugacity (ΔNNO) of glassy basic magmas. Sources of data are cited in text.

SILICIC ASHFLOWS AND LAVAS

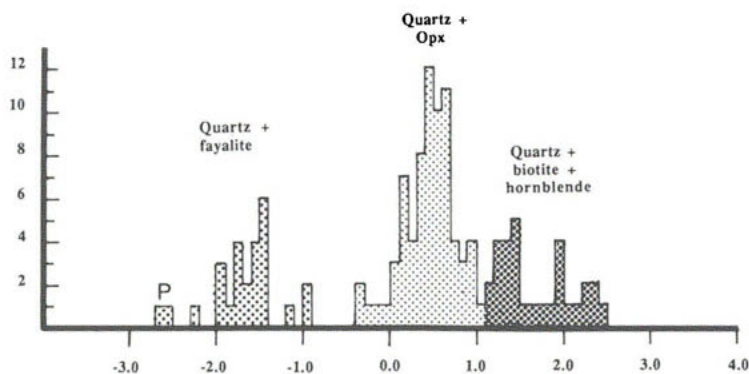


Figure 3. Values of the relative oxygen fugacity (ΔNNO) of silicic magmas. The two lowest values of ΔNNO are for two glassy pantellerites. Data from Ghiorso and Sack (1991).

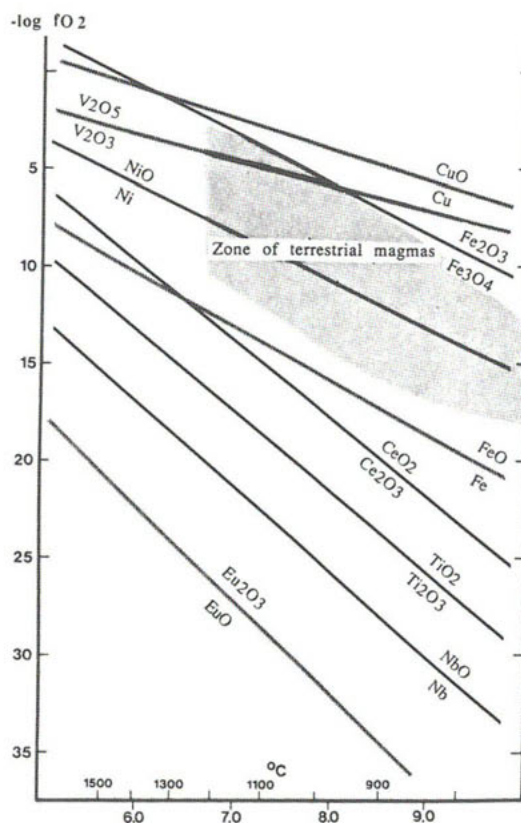


Figure 4. Plot of $\log fO_2$ against inverse temperature (K) for labelled oxidation reactions at 1 bar for pure solids. The zone of terrestrial magmas is from Carmichael (1991).

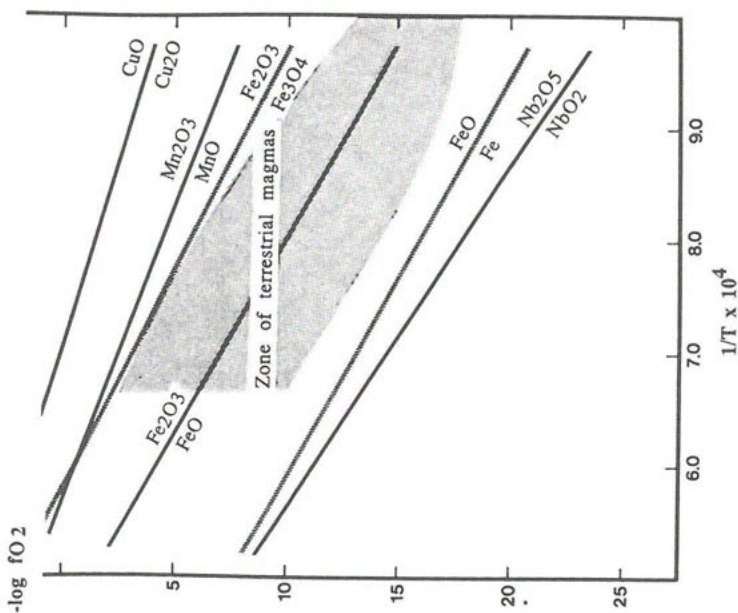
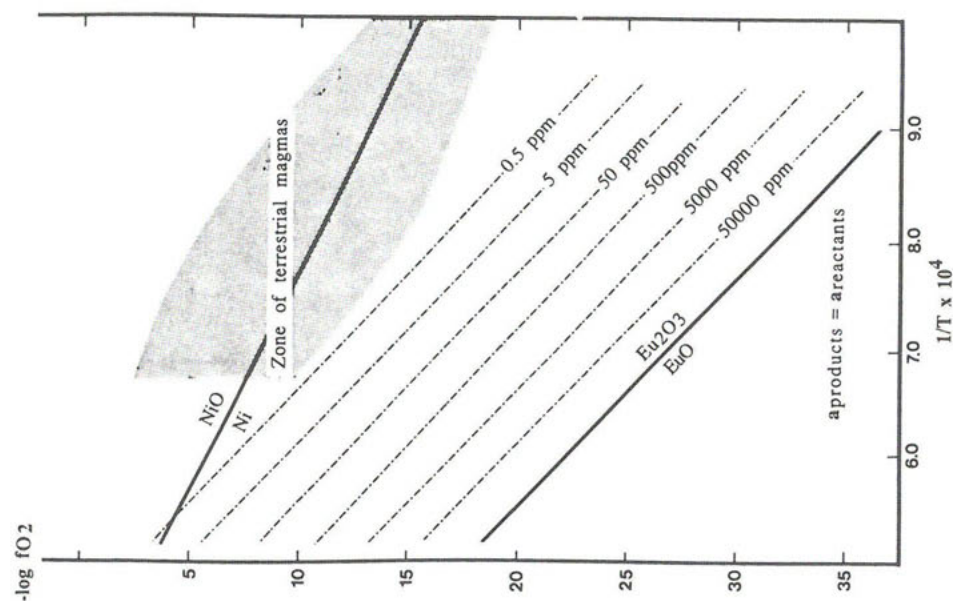
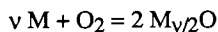


Figure 5 (above). Plot of $\log f_{O_2}$ against inverse temperature (K) for labelled oxidation reactions at 1 bar for pure solids. The zone of terrestrial magmas is from Carmichael (1991).

Figure 6 (right). Plot of $\log f_{O_2}$ versus inverse temperature for $\text{EuO-Eu}_2\text{O}_3$ as pure solids (solid line) and for reduced and equal activities of both products and reactants (dashed lines, labelled). The zone of terrestrial magmas and Ni-NiO are from Figure 7.

METALS OF VARIABLE VALENCE AND OXYGEN FUGACITY

Expressing a general oxidation-reduction reaction involving the metal, M as:



the oxygen fugacity is given by:

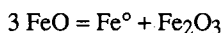
$$\log f_{\text{O}_2} = \Delta G^\circ / 2.303 \text{ RT}$$

in equilibrium with pure solids¹. In Table 1 we present the regression constants for $\log f_{\text{O}_2}$ and values of ΔV° for the solids at 298; the data were taken from Robie et al. (1978) (but also see O'Neill, 1987, 1988). There is a broad increase in entropy with the number of moles of solid, but there are some surprising contrasts. Although FeO was assumed to be stoichiometric, the entropy of the oxidation reaction (based on 1 mole of O_2) is much lower than for the corresponding reactions of Ni, Cu and Nb (Table 1). The smallest entropy change is associated with the largest volume change (Table 1, F, V_2O_5) and the largest entropy change with a rather small volume change (Table 1, C, CoO). Otherwise with few exceptions the magnitude of ΔS° parallels that of the volume change of the solids. The reaction of 4 Mn_3O_4 to 6 Mn_2O_3 has a smaller ΔS° than all but three of the reactions, and a trivial volume change, presumably because of the open structure of Mn_2O_3 . The other reaction with only a small value of ΔS° involves the oxidation of EuO to Eu_2O_3 , which occurs at extremely low oxygen fugacities (Fig. 4).

In Figures 4 and 5 we have plotted $\log f_{\text{O}_2}$ against the inverse of the absolute temperature, and the zone occupied by magmas is highlighted. Based on these standard state solid reactions one would expect to find Cu, both Ni and NiO, V_2O_3 , MnO, Nb_2O_5 , CeO_2 , TiO_2 , and Eu_2O_3 as the stable redox states within the T- $\log f_{\text{O}_2}$ range of magmas.

The position of the equilibrium redox boundary of a simple solid-state reaction (Figs. 4 and 5) will be modified by dilution of both reactant and product phases. If the stoichiometric coefficients of the reactants are greater than those of the products (Table 1, B), then reducing equally the activities of reactants and products shifts the equilibrium to higher and higher oxygen fugacities. A good example of this is EuO which at the ppm level of concentration (Fig. 6) can be measured in iron-free silicate glasses at oxygen fugacities ten or fifteen orders of magnitude higher (Morris et al., 1974) than those of the reaction in the standard state, though it must be remembered that the T- f_{O_2} path of the liquid standard state reaction may be unrelated to that of the solid.

As the concentrations of FeO and Fe_2O_3 far outweigh those of any other metal of variable valence in natural (terrestrial) liquids, coupled reactions involving ferric and ferrous iron may further depress the concentrations of the reduced components. At very low oxygen fugacities, such as those at or below I-W, a disproportionation reaction of FeO occurs in silicate liquids. This is represented by



and is exemplified in the incongruent melting of Fe_2SiO_4 to metallic iron (Fe°) plus a liquid with Fe_2O_3 (Muan, 1955). Accordingly the reactions considered in Table 2 are for

¹We adopt standard state definitions corresponding to unit activity of the pure solid at any temperature and pressure and unit fugacity of the hypothetical ideal gas at any temperature and 1 bar.

Table 1. $\log f_{O_2} = \Delta G^\circ/2.303 RT$ for oxidation reactions in the standard state of pure solids.

| | $\log_{10} f_{O_2}$ | ΔH kJ/mol | ΔS J/mol/K | $\Delta V_{\text{solids}} (298)$ cm ³ |
|--|---------------------|----------------------|-----------------------|---|
| A. $2R + O_2 = 2RO$ | | | | |
| $2Fe + O_2 = 2FeO$ | 6.310 - 27775.2/T | 531.7 | -120.8 | 8.20 |
| $2Ni + O_2 = 2NiO$ | 8.877 - 24461.6/T | 468.3 | -169.9 | 8.76 |
| $2Cu + O_2 = 2CuO$ | 8.683 - 15747.3/T | 301.5 | -166.2 | 10.21 |
| $2Nb + O_2 = 2NbO$ | 8.947 - 43264.2/T | 828.3 | -171.3 | 8.28 |
| B. $4RO + O_2 = 2R_2O_3$ | | | | |
| $4FeO + O_2 = 2Fe_2O_3$ | 13.116 - 28773.5/T | 550.9 | -251.1 | 12.55 |
| $4MnO + O_2 = 2Mn_2O_3$ | 11.009 - 19160.3/T | 386.8 | -210.8 | 9.86 |
| $4EuO + O_2 = 2Eu_2O_3$ | 5.676 - 46756.0/T | 895.1 | -108.7 | 6.14 |
| C. $6RO + O_2 = 2R_3O_4$ | | | | |
| $6FeO + O_2 = 2Fe_3O_4$ | 12.288 - 30351.0/T | 581.1 | -235.2 | 17.05 |
| $6MnO + O_2 = 2Mn_3O_4$ | 12.138 - 23119.6/T | 442.6 | -232.4 | 14.57 |
| $6CoO + O_2 = 2Co_3O_4$ | 18.601 - 19582.2/T | 374.9 | -356.1 | 9.70 |
| D. $2R_2O_3 + O_2 = 4RO_2$ | | | | |
| $2Ti_2O_3 + O_2 = 4TiO_2$ | 11.241 - 41048.1/T | 785.9 | -215.2 | 12.42 |
| $2Ce_2O_3 + O_2 = 4CeO_2$ | 14.308 - 40266.5/T | 770.9 | -232.9 | -0.09 |
| $2V_2O_3 + O_2 = 2V_2O_4$ | 9.579 - 20425.9/T | 391.0 | -183.4 | |
| E. $4R_3O_4 + O_2 = 6R_2O_3$ | | | | |
| $4Fe_3O_4 + O_2 = 6Fe_2O_3$ | 14.755 - 25594.2/T | 490.0 | -282.5 | 3.55 |
| $4Mn_3O_4 + O_2 = 6Mn_2O_3$ | 7.639 - 9975.0/T | 191.0 | -146.2 | 0.42 |
| F. $R_2O_3 + O_2 = R_2O_5$ | | | | |
| $V_2O_3 + O_2 = V_2O_5$ | 4.862 - 13494.7/T | 258.4 | -93.1 | 24.09 |

All data taken from Robie et al (1978) and were fitted over the range 1000-1800 K wherever possible.

Table 2. Standard free energy changes of exchange reactions with Fe_2O_3 (Table 1)

| | |
|-------------------------------------|--|
| $Ni^\circ + Fe_2O_3 = NiO + 2FeO$ | $\Delta G^\circ/2.303RT = -2.120 + 2156/T$ |
| $Cu^\circ + Fe_2O_3 = CuO + 2FeO$ | $\Delta G^\circ/2.303RT = -2.216 + 6513/T$ |
| $2EuO + Fe_2O_3 = Eu_2O_3 + 2FeO$ | $\Delta G^\circ/2.303RT = -3.720 - 8991/T$ |
| $Ce_2O_3 + Fe_2O_3 = CeO_2 + 2FeO$ | $\Delta G^\circ/2.303RT = 0.596 - 5746/T$ |
| $Ti_2O_3 + Fe_2O_3 = 2TiO_2 + 2FeO$ | $\Delta G^\circ/2.303RT = -0.938 - 6156/T$ |

Table 3. Oxidation ratios and concentrations of iron and europium in the glasses of Colima andesites at 1000°C

| Sample | COL 9G | 6G | 17G | 15G | 2G | 7G | 11G |
|-------------------|--------|-------|-------|-------|-------|-------|-------|
| $\log f_{O_2}$ | -8.81 | -8.71 | -8.68 | -7.95 | -9.11 | -8.17 | -9.45 |
| Eu^{2+}/Eu^{3+} | 0.35 | 0.33 | 0.33 | 0.26 | 0.41 | 0.25 | 0.48 |
| Eu^{2+} ppm | 0.28 | 0.28 | 0.29 | 0.25 | 0.30 | 0.20 | 0.45 |
| Eu^{3+} ppm | 0.79 | 0.85 | 0.87 | 0.98 | 0.74 | 0.80 | 0.93 |
| Fe^{2+}/Fe^{3+} | 2.14 | 2.02 | 1.98 | 1.39 | 2.59 | 1.56 | 2.81 |

Data taken from Luhr and Carmichael (1980)

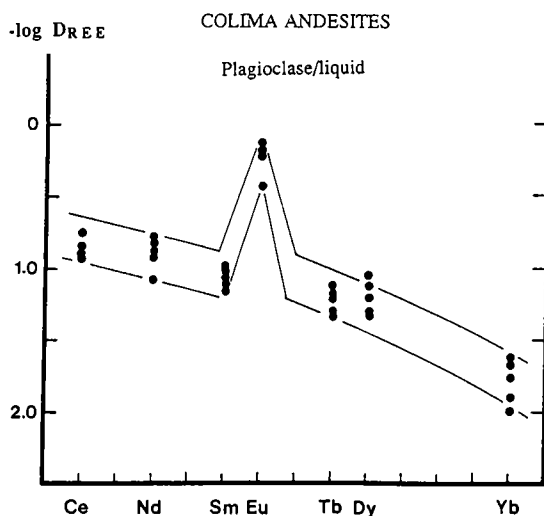


Figure 7. Plot of $\log D$, the distribution coefficient of various rare earths between plagioclase phenocrysts and their residual glassy groundmass for Colima andesites. Data from Luhr and Carmichael (1980).

conditions where Fe° is unstable.

By adding and subtracting the appropriate equations in Table 1, the standard state free energy changes of the exchange reactions are easily derived and are given in Table 2. It is clear that only Cu° is stable with respect to Fe_2O_3 , although Ni° and Fe_2O_3 are stable below 1017 K; otherwise all the reactions run to the right in the range 1000-1800 K.

The activity of EuO in natural liquids with reasonable amounts of ferric and ferrous iron might be extremely low ($\sim 10^{-8}$), and it may be doubted whether this reduced component is available to be preferentially incorporated into plagioclase, and become the source of the well-known Eu anomaly. However Drake and Weill (1975) were able to show that in quasi-natural liquids, doped with Eu up to half the amount of Fe, the distribution of Eu between plagioclase and liquid became increasingly enhanced relative to the other rare earths (all in the trivalent state except perhaps Ce), as the oxygen fugacity was decreased. Drake (1975) proposed that the distribution of Eu between plagioclase and liquid could be used as an indicator of oxygen fugacity, and gave a regression equation (op.cit., Eqn. 8) relating oxygen fugacity to a modelled $\text{Eu}^{2+}/\text{Eu}^{3+}$ ratio in basaltic or andesitic liquids. In Figure 7 we have plotted the distribution coefficient of the REE between plagioclase phenocrysts and glass for a series of young andesitic lavas from Colima (Luhr and Carmichael, 1980). The marked peak in Eu is the europium anomaly, and Drake's experiments indicated that this becomes progressively smaller with increasing oxygen fugacity; indeed the magnitude of the anomaly in these andesites given their oxidized nature is surprising. Using the ferric-ferrous contents of the residual glasses (Luhr and Carmichael, 1980) to calculate (Kilinc et al., 1983) the oxygen fugacity at the typical quench temperature (1000°C), we derive the $\text{Eu}^{2+}/\text{Eu}^{3+}$ ratios (Table 3) in the quenched liquids using Drake's equation.

In accord with the standard state exchange reactions (Table 2), there is a much

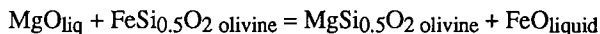
higher proportion of Eu in the trivalent state than there is of iron. Even so the Eu^{2+} concentration seems improbably high (Fig. 6) judging by the higher temperature experiments of Morris et al. (1974) on liquids of simpler composition. These, however, were not made over a wide enough temperature range to extrapolate to 1000°C with confidence.

Although the solid-solid reactions would suggest that Ce^{4+} rather than Ce^{3+} would be stable in natural liquids (Table 2), Schreiber et al. (1980) have shown that in a few simple silicate liquids with small amounts of Ce and Fe (~0.4 to 1.0 wt %), at high oxygen fugacities, the reaction listed in Table 2 goes to the left, and that Ce^{3+} and Fe^{3+} are stable. Unfortunately no experimental data are given in their paper, but nevertheless it would appear that, contrary to the implications of the solid standard state data in Table 2, Ce^{4+} may not exist in magmas.

Clearly, the predictions based on the free-energy changes for pure solids may not be a very good indication of the relative stability of redox metals in the low concentrations of silicate liquids. Certainly, changing from a solid to a liquid standard state may displace the position of redox equilibria to better agree with measurements on silicate liquids. However, the paucity of thermodynamic data on the pertinent liquids (often unstable) does not allow this to be illustrated.

THE EFFECT OF REDOX STATE ON OLIVINE-LIQUID EQUILIBRIUM

The distribution of FeO and MgO between olivine and liquid has been investigated many times since the pioneering study of Roeder and Emslie (1970). The reaction can be represented by



for which the distribution coefficient is

$$K_D = \{\text{FeSi}_{0.5}\text{O}_2/\text{MgSi}_{0.5}\text{O}_2\}^{\text{olivine}} * \{\text{MgO}/\text{FeO}\}^{\text{liquid}}$$

At low oxygen fugacities, near I-W, almost all the iron in the liquid is FeO, but in air, a substantial amount of Fe_2O_3 occurs in the liquid (Table 4; Kilinc et al., 1983). Olivine is always assumed to contain only ferrous iron. An examination of 296 experimental determinations for basaltic and similar lavas, taken mainly from a literature survey, and added to by Snyder and Carmichael (1991), show that K_D is given by the empirical expression:

$$\ln K_D = -1.361 + 1095.3/T - 5.106 (X_{\text{Na}_2\text{O}} + X_{\text{K}_2\text{O}}) - 3.242 (X_{\text{CaO}}) , \quad (5)$$

and the calculated vs observed values for K_D are shown in Figure 8. The liquids cover the range 41.9 to 66.6% SiO_2 ; olivine $\text{Fo}_{98}\text{-Fo}_{52}$; $T = 1337\text{-}1673$ K; $\log f_{\text{O}_2} -0.68$ to -14.1 .

The independence of K_D on oxygen fugacity is illustrated in the data of Table 4. Although oxygen fugacity was varied over a large range, inducing a concomitant change in the Fo content of olivine, there is no change in K_D . The great petrological utility of the Fe-Mg exchange relationship between olivine and liquid is that it can be used to assess whether or not a set of olivine phenocrysts belong to a lava, or if they do, what the concentration of FeO should be, and hence the ferric/ferrous ratio, or lastly, in the case of silicic liquids, what the concentration of MgO should be. Three aspects of utilizing the variation of K_D will be illustrated.

Table 4. Ugandite lava equilibrated at QFM (A) and in air (B)

| | liquid A | liquid B | olivine A | olivine B |
|--------------------------------|----------|----------|-----------|-----------|
| SiO ₂ | 42.14 | 42.63 | 40.08 | 41.78 |
| TiO ₂ | 5.77 | 5.51 | - | - |
| Al ₂ O ₃ | 9.40 | 8.79 | - | - |
| Fe ₂ O ₃ | 2.66 | 11.73 | - | - |
| FeO | 10.00 | 1.31 | 14.51 | 1.95 |
| MnO | 0.18 | 0.12 | 0.25 | 0.16 |
| MgO | 7.92 | 9.75 | 45.02 | 55.66 |
| CaO | 13.81 | 13.29 | 0.99 | 0.51 |
| Na ₂ O | 2.51 | 2.18 | - | - |
| K ₂ O | 4.16 | 2.32 | - | - |
| P ₂ O ₅ | 0.64 | 0.18 | - | - |
| Total | 99.19 | 97.81 | 100.85 | 100.06 |
| T, °C | 1234 | 1201 | | |
| K _D | 0.26 | 0.26 | | |
| Fo (mol %) | - | - | 83.4 | 97.3 |
| Fa | | | 15.1 | 1.9 |

Olivine increases by 14 mol% Fo as the oxygen fugacity is increased from Fayalite-Magnetite-Quartz (FMQ) to air. The amount of Fe₂O₃ in the liquids is derived from the regression equation given by Kilinc et al. (1983).

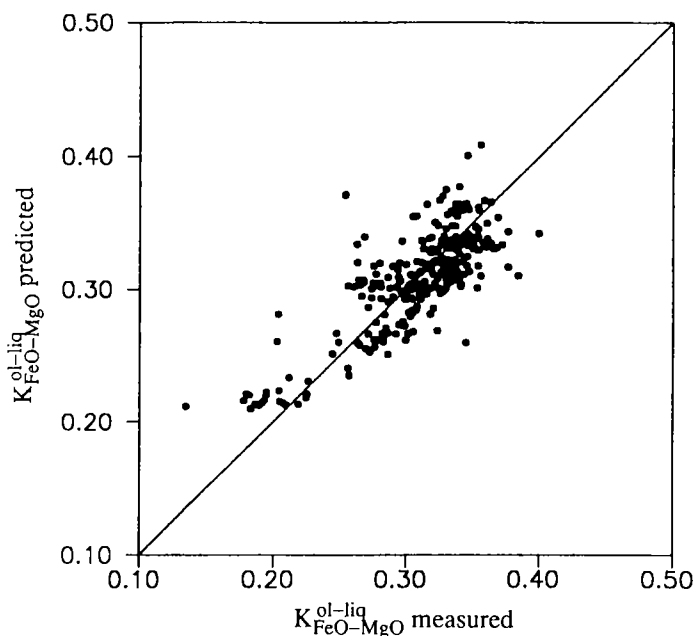


Figure.8. Plot of K_D for olivine liquid equilibria (see text) showing the satisfactory correspondence of the fit Equation (5) with the measured values. The error of a single measurement is about ± 0.04 , so that the scatter is not significantly greater than that arising from individual measurements.

Analyses of residual glasses and coexisting ferromagnesian phases are given in Table 5. A trachybasalt (256; Smith and Carmichael, 1969) contains a glassy groundmass with crystals of olivine and iron-titanium oxides which are smaller than the associated phenocrysts; these we take to be in equilibrium at low pressures. The microprobe was used to analyze the residual glass so that only total iron as $\text{FeO}_{\text{total}}$ is known. From the composition of the iron-titanium oxides, an equilibration temperature and oxygen fugacity are derived from the Ghiorso and Sack (1991) algorithm. These are also given in Table 5. Using a value for $K_D = 0.34$, obtained from the regression Equation (5) above, the amount of FeO in the liquid is calculated to be 5.6 wt %, and thus Fe_2O_3 is 1.0%. As the composition of the liquid and its FeO and Fe_2O_3 contents are now known, by using the Kilinc et al. (1983) relationship, the oxygen fugacity can be calculated at the Fe-Ti oxide quench temperature (904°C). This value (-13.16) is within 0.33 of that derived from the Fe-Ti oxide oxygen sensor.

Silicic liquids provide another example. Here the concentration of MgO is typically very low, and the composition of the bulk rock is often taken as a proxy for that of the liquid (residual glass) in equilibrium with the phenocrysts. The wet chemical analyses of two peralkaline residual glasses (5748G and 3112G; Carmichael, 1962) and their ferromagnesian silicate phenocrysts (olivine and augite in the former and augite and coesynite in the latter) are given in Table 5. Assuming that all the iron in the fayalitic olivine is FeO, we have selected to calculate the amount of MgO in the residual glass, as it contains a substantial amount of FeO (5.9 wt %); the derived value, assuming $K_D = \sim 1$ (Ghiorso et al., 1983), is $\sim 0.30\%$, in disagreement with the analyzed value of 0.13%. This discrepancy could arise from K_D taking a lower value (~ 0.4) in peralkaline silicic liquids, which lie well outside the range of experimental calibration.

Obsidians may have substantial amounts of water, acquired possibly long after eruption, and there is a parallel uncertainty about the iron redox state, and whether that reflects the quenched liquid, or whether it has been modified by eruption, by cooling or by subsequent hydration. The analyses of two metaluminous residual glasses (151G and EC20G) and their coexisting ferromagnesian phenocrysts are given in Table 5. Using the composition of the Fe-Ti oxide phenocrysts, the temperatures and oxygen fugacities of their equilibration are obtained from the Ghiorso and Sack (1991) algorithm. From the oxygen fugacities, values of Fe_2O_3 and FeO for each residual glass are calculated using the Kilinc et al. (1983) relationship; these differ from the amounts found analytically by 0.2 and 0.4 % Fe_2O_3 respectively, not far from the analytical errors. If a value of K_D of ~ 1 is taken, then the amount of MgO in the olivine-residual glass pair (151G) is calculated as 0.14%, rather than 0.09% (Table 5). The reality of the matter is that unless special care is taken in the analysis of the residual glass, these two values do not differ analytically.

Two additional generalizations are evident from these silicic liquid data. Firstly in those with fayalitic olivine, the olivine contains about 100 times more MgO than the liquid so that even 1% of fayalite phenocrysts will contribute as much MgO to the bulk rock as the residual glass. Secondly the olivine contains between 10 and 40 times the amount of FeO as the liquid (Table 5; cf 5748G and 151G). The conclusion seems clear that the composition of a silicic lava, even with only a few percent of phenocrysts, especially fayalite, will not be a reliable proxy for the composition of the liquid, and particularly its FeO/MgO ratio. The residual glass of rhyolites should be separated, purified and analyzed, as should the olivine phenocrysts. Glassy silicic lavas, containing Fe-Ti oxides, offer the only means to establish the extension of the experimentally determined values of K_D to silica rich compositions.

Table 5. Analyses of ferromagnesian phenocrysts and residual glasses. Data taken from Carmichael (1962) and Smith and Carmichael (1969).

| Method of analysis | 256G probe | olivine probe | ilmen. probe | spinel probe | 5748G wet | olivine wet | augite wet | ilmen. probe | 3112G wet | augite wet | cossyr. wet | ilmen. probe | spinel probe |
|------------------------------------|------------|---------------|--------------|--------------|-----------|-------------|------------|--------------|-----------|------------|-------------|--------------|--------------|
| SiO ₂ | 59.50 | | 0.15 | 0.15 | 69.90 | 30.56 | 48.58 | 0.05 | 70.10 | 48.69 | 41.02 | 0.04 | 0.06 |
| TiO ₂ | 1.10 | | 50.20 | 24.40 | 0.54 | 0.72 | 0.71 | 50.10 | 0.41 | 0.86 | 8.92 | 50.60 | 27.20 |
| Al ₂ O ₃ | 17.40 | | 0.16 | 2.01 | 8.80 | 0.09 | 2.06 | nd | 7.60 | 2.04 | 0.94 | | 0.41 |
| Fe ₂ O ₃ | | | 4.90 | 19.40 | 2.10 | 0.10 | 5.69 | 4.70 | 2.90 | 5.60 | 1.31 | 4.00 | 16.20 |
| FeO | 6.50 | 26.20 | 42.70 | 50.80 | 5.90 | 60.81 | 20.15 | 42.70 | 5.60 | 21.96 | 38.84 | 43.10 | 54.40 |
| MnO | 0.06 | 0.46 | 0.69 | 0.70 | 0.30 | 3.43 | 1.31 | 1.96 | 0.34 | 1.25 | 1.16 | 2.17 | 1.71 |
| MgO | 2.50 | 34.40 | 1.29 | 1.54 | 0.13 | 3.47 | 2.67 | 0.21 | 0.04 | 0.89 | 0.07 | 0.09 | 0.25 |
| CaO | 1.60 | 0.45 | 0.23 | 0.18 | 0.52 | 1.13 | 16.93 | 0.04 | 0.53 | 16.36 | 0.45 | 0.04 | |
| Na ₂ O | 6.90 | | | | 6.50 | | 2.32 | | 7.10 | 2.86 | 7.36 | | |
| K ₂ O | 5.50 | | | | 4.70 | | 0.09 | | 4.60 | 0.09 | 0.06 | | |
| P ₂ O ₅ | 0.40 | | | | 0.04 | | | | 0.05 | | | | |
| FeO calc (K _D) | 5.60 | | | | | | | | | | | | |
| MgO calc (K _D) | | | | | 0.34 | | | | | | | | |
| Fe ³⁺ /Fe ²⁺ | | | 0.10 | 0.34 | 0.32 | | 0.25 | 0.10 | 0.47 | 0.23 | 0.03 | 0.08 | 0.27 |
| Temp°C | | | | 904 | | | | | | | | | 848.00 |
| log fO ₂ | -13.16 | | | -13.49 | | | | | | | | | -15.50 |
| ΔNNO | -1.39 | | | -1.72 | | | | | | | | | -2.68 |
| Redox xtal/liq | | | | | | | 0.78 | 0.31 | | 0.49 | 0.06 | 0.17 | 0.57 |

Table 5 (continued). Analyses of ferromagnesian phenocrysts and residual glasses.
Data taken from Carmichael (1960, 1967).

| Method of analysis | 151G | | olivine | | augite | | ilmen. | | spinel | | EC20G | | augite | | opx | | ilmen. | | spinel | |
|------------------------------------|-------|--|---------|--|--------|--|--------|--|--------|--|-------|--|--------|--|-------|--|--------|--|--------|--|
| | wet | | wet | | wet | | probe | | probe | | wet | | wet | | wet | | probe | | probe | |
| SiO ₂ | 72.30 | | 30.62 | | 48.76 | | 0.05 | | 0.13 | | 69.40 | | 51.72 | | 51.88 | | 45.60 | | 0.08 | |
| TiO ₂ | 0.22 | | 0.59 | | 0.47 | | 49.80 | | 21.50 | | 0.59 | | 0.62 | | 0.57 | | 13.50 | | | |
| Al ₂ O ₃ | 12.10 | | 0.33 | | 0.99 | | 0.04 | | 1.15 | | 14.30 | | 1.05 | | 1.46 | | 0.13 | | 1.42 | |
| Fe ₂ O ₃ | 0.20* | | 2.98 | | 3.36 | | 5.70 | | 26.30 | | 0.6† | | 2.40 | | 2.55 | | 16.00 | | 41.70 | |
| FeO | 1.6* | | 58.21 | | 19.42 | | 42.60 | | 49.90 | | 1.7† | | 7.56 | | 16.80 | | 33.80 | | 39.20 | |
| MnO | 0.05 | | 1.24 | | 0.73 | | 0.98 | | 0.88 | | 0.11 | | 1.27 | | 1.88 | | 1.25 | | 1.16 | |
| MgO | 0.09 | | 5.34 | | 5.93 | | 0.62 | | 0.32 | | 0.41 | | 15.12 | | 22.37 | | 3.31 | | 2.12 | |
| CaO | 1.00 | | 0.49 | | 19.47 | | 0.06 | | 0.03 | | 0.92 | | 19.84 | | 2.19 | | 0.03 | | 0.02 | |
| Na ₂ O | 4.90 | | | | 0.66 | | | | | | 4.70 | | 0.32 | | 0.23 | | | | | |
| K ₂ O | 3.50 | | | | 0.11 | | | | | | 5.90 | | 0.06 | | 0.08 | | | | | |
| P ₂ O ₅ | 0.04 | | | | | | | | | | 0.10 | | | | | | | | | |
| FeO calc (K _D) | | | | | | | | | | | | | | | | | | | | |
| MgO calc (K _D) | 0.14 | | | | | | | | | | | | | | | | | | | |
| Fe ³⁺ /Fe ²⁺ | 0.26 | | | | 0.16 | | 0.12 | | 0.47 | | 0.32 | | 0.28 | | 0.14 | | 0.43 | | 0.96 | |
| T, °C | | | | | | | | | 834.00 | | | | | | | | | | 953.00 | |
| log fO ₂ | | | | | | | | | -14.86 | | | | | | | | | | -10.44 | |
| ΔNNO | | | | | | | | | -1.76 | | | | | | | | | | 0.49 | |
| Redox xtal/liq | | | | | 0.62 | | 0.46 | | 1.81 | | | | 0.88 | | 0.44 | | 1.34 | | 3.00 | |

* Not the amount in analysis of glass which is 0.4% Fe₂O₃ and 1.4% FeO
† Not the amount analysed in the glass which is 1.3% Fe₂O₃ and 1.0% FeO

Although it is always assumed that olivine contains only FeO, it can be demonstrated that this cannot be strictly correct. We reason that for a stable phase, such as a silicate liquid, $\partial\mu_{\text{Fe}_2\text{O}_3}/\partial n_{\text{Fe}_2\text{O}_3}$ is positive; thus from the change in concentration of Fe_2O_3 in the liquid with increasing oxygen fugacity (Table 4) it can be deduced that the olivine in air will have a higher activity of Fe_2O_3 . Unfortunately, as the oxygen fugacity increases, the concentration of iron in the olivine decreases, so that although a higher proportion of it will be Fe_2O_3 , it may be too small to measure by conventional wet chemical techniques. Many wet chemical analyses of olivines are given by Deer et al. (1982) who seem uncertain about whether the small amounts of ferric iron in olivine are primary rather than a response to secondary oxidation.

THE EFFECT OF REDOX STATE ON PYROXENE-LIQUID EQUILIBRIA

The literature reveals few examples of complete analyses (with ferric and ferrous determinations) of pyroxenes and their associated liquids. To illustrate the ways in which such data may be used, we return to Table 5 and the analyses of silicic glasses and their augite and orthopyroxene phenocrysts. What we are anxious to establish is whether the $\text{Fe}^{3+}/\text{Fe}^{2+}$ of the liquid is greater or less than the same ratio in the ferromagnesian phenocrysts; put another way, will the continued precipitation or fractionation of those phases increase or decrease the iron redox state of the liquid? We have calculated the relationship

$$(\text{Fe}^{3+}/\text{Fe}^{2+})_{\text{phase}}/(\text{Fe}^{3+}/\text{Fe}^{2+})_{\text{liquid}}$$

and the values are given in Table 5. The reader should understand that the above ratio does not correspond to a thermodynamic quantity, that is one cannot yet write a balanced chemical reaction between liquid and two pyroxene end-members that involves the simple exchange of Fe^{2+} for Fe^{3+} in the solid phase. Replacement of ferric for ferrous iron in the pyroxenes is usually accompanied by coupled substitution of a trivalent for a quadrivalent (e.g., Al^{3+} for Si^{4+}) ion, or a monovalent for a divalent (e.g., Na^+ for Ca^{2+}) ion.

At the oxygen fugacities of these silicic glasses (Table 5), we note that all augites have smaller $\text{Fe}^{3+}/\text{Fe}^{2+}$ ratios than their liquids, and that the single example (EC20) of orthopyroxene has an even smaller ratio. For the Fe-Ti oxide phases, only the spinel phase has a higher redox state than the liquid. However in the peralkaline residual liquids (5748G and 3112G), the high concentration of Fe_2O_3 is *not* a reflection of a high oxygen fugacity, but rather of the high concentration of Na_2O . Thus in contrast to metaluminous silicic liquids, even the spinel phase has a lower value of $\text{Fe}^{3+}/\text{Fe}^{2+}$ than the surrounding peralkaline liquid (Table 5).

At higher oxygen fugacities, $\Delta\text{NNO} = +2$ to $+4$, augitic pyroxenes with substantial amounts of Fe_2O_3 may occur and there are two mineral end-members that contain essential amounts of ferric iron; acmite $\text{NaFeSi}_2\text{O}_6$ and esseneite CaFeAlSiO_6 (Cosca and Peacor, 1987). In highly sodic rhyolitic liquids such as pantellerites, the phenocrysts of augite coexisting with fayalite are sodic hedenbergite, rather than acmite (Table 5). This suggests that acmite itself, or compositions close to it, are only stable above FMQ or NNO (Nicholls and Carmichael, 1969). Another indication of the incompatibility of acmite and fayalitic olivine may be found in the shonkinites of the Shonkin Sag laccolith where the most sodic pyroxenes no longer coexist with olivine (Nash and Wilkinson, 1970).

Esseneite pyroxene was first found in pyrometamorphic sediments from Wyoming (Cosca and Peacor, 1987; Cosca et al., 1989). At another location in Wyoming, a similar

pyroxene has been found with hematite, magnetite and pseudobrookite (all solid solutions) in pyrometamorphic buchite (Foit et al., 1987). Less aluminous compositions have been encountered in experiments on a mafic leucite equilibrated in air by the first author (Table 6, A). In the experimental synthesis of this Ca-rich pyroxene, it was found that the iron redox ratio was higher in the pyroxene than it was in the liquid; accordingly continued precipitation of such a phase would reduce the ferric-ferrous ratio of the liquid. Other examples of pyroxenes with substantial amounts of the esseneite component occur in varieties of alkali gabbros which contain pseudobrookite. The prevailing oxygen fugacity in these assemblages was probably far higher than in most basaltic magmas (Carmichael and Nicholls, 1967), and close to H-M. In redox terms these alkali gabbros may be seen as the plutonic equivalents of the highly oxidized minettes shown in Figure 2.

Table 6. Analyses of ferric-rich pyroxenes and residual liquid.

| | A | B | C | D | E |
|------------------------------------|-------|-------|-------|--------|-------|
| SiO ₂ | 36.00 | 44.89 | 41.89 | 50.34 | 29.51 |
| TiO ₂ | 2.87 | 3.18 | 3.42 | 1.91 | 0.99 |
| Al ₂ O ₃ | 11.73 | 15.56 | 8.81 | 3.09 | 17.95 |
| Fe ₂ O ₃ | 17.77 | 8.95 | 10.31 | 7.77 | 23.89 |
| FeO | 0.26 | 0.72 | 0.79 | 0.32 | 0.69 |
| MnO | 0.23 | 0.48 | 0.12 | 0.30 | 0.11 |
| MgO | 7.67 | 4.18 | 11.63 | 13.83 | 2.68 |
| CaO | 22.38 | 14.55 | 21.55 | 20.32 | 23.40 |
| Na ₂ O | 0.47 | 3.71 | 1.11 | 2.55 | 0.14 |
| K ₂ O | | 2.04 | 0.01 | 0.05 | |
| P ₂ O ₅ | | 0.93 | 0.15 | | |
| Total | 99.38 | 99.19 | 99.64 | 100.48 | 99.36 |
| Fe ³⁺ /Fe ²⁺ | 61.5 | 11.2 | 11.7 | 21.8 | 31.2 |

Pyroxene A was synthesised in air by crystallizing a mafic leucite at 1179°C and B is the residual liquid; C is from alkali gabbro of Papapaholaha, Kauai, Hawaii (White, 1966); D is from a shonkinite from Katzenbuechel, Odenwald, Germany (Yoder and Tilley, 1962) and E is the average analysis of esseneite (Cosca and Peacor, 1987).

Table 7. Analyses of hydrous phenocrysts and host glassy lava.

| | CAM 73 | hbde | olivine | ilmen. | spinel | K-3 | hbde | MAS 3A | Phlog |
|------------------------------------|--------|-------|---------|--------|--------|--------|-------|--------|-------|
| Method of analysis | wet | wet | probe | probe | probe | wet | wet | wet | wet |
| SiO ₂ | 75.04 | 42.27 | 30.20 | 0.02 | 0.11 | 46.67 | 39.31 | 49.86 | 39.81 |
| TiO ₂ | 0.07 | 1.81 | | 49.80 | 15.10 | 2.00 | 4.14 | 1.82 | 2.62 |
| Al ₂ O ₃ | 12.29 | 9.02 | | 0.04 | 0.86 | 18.28 | 15.37 | 12.87 | 13.38 |
| Fe ₂ O ₃ | 0.33* | 8.71 | | 5.60 | 38.10 | 2.99 | 4.71 | 4.45 | 3.21 |
| FeO | 0.71* | 20.86 | 63.00 | 42.50 | 43.80 | 6.56 | 4.66 | 2.91 | 1.14 |
| MnO | 0.05 | 0.85 | 3.65 | 1.71 | 0.96 | 0.20 | 0.10 | 0.14 | 0.03 |
| MgO | 0.04† | 3.64 | 2.63 | 0.31 | 0.13 | 5.02 | 13.89 | 8.63 | 23.10 |
| CaO | 0.58 | 9.16 | 0.14 | 0.02 | 0.01 | 9.59 | 12.54 | 7.44 | 0.00 |
| Na ₂ O | 4.03 | 2.21 | | | | 4.92 | 2.36 | 2.70 | 0.32 |
| K ₂ O | 4.66 | 0.89 | | | | 2.38 | 1.36 | 5.70 | 10.51 |
| P ₂ O ₅ | 0.01 | | | | | 0.38 | 0.04 | 1.46 | 0.00 |
| H ₂ O | | | | | | | 1.34 | | 3.60 |
| FeO calc | 0.91 | | | | | | | | |
| MgO calc (K _D) | 0.01 | | | | | | | | |
| Fe ³⁺ /Fe ²⁺ | 0.11 | 0.38 | | 0.12 | 0.78 | 0.41 | 0.91 | 1.38 | 2.52 |
| T, °C | | | | | | 712.00 | | | |
| log fO ₂ | | | | | | -17.48 | | | |
| Redox xtal/liq | | 3.45 | | 1.10 | 7.10 | | | | |

* Amount of FeO and Fe₂O₃ found in lava, not residual glass

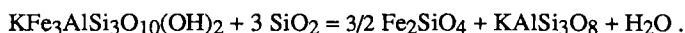
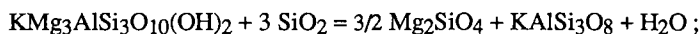
† Amount of MgO found in lava, not residual glass

Thus it appears that a Ca-rich pyroxene can contain substantial amounts of ferric iron in its structure which most likely enters in the form of the component CaFeAlSiO_6 . In those magma types that precipitate augite at high oxygen fugacities, such as minette, shonkinite, mafic leucite and limburgite, the residual liquids may have their iron redox ratios decreased as crystallization proceeds, for augite, in the broadest sense, can contain a higher ferric/ferrous ratio than the liquid. Otherwise augites may be assumed to have ferric/ferrous ratios lower than their liquids in the normal range of oxygen fugacities for basaltic compositions. It is an experimental project of magnitude to calibrate in T-log f_{O_2} -composition space, the variation of the iron redox state of augite over the whole range that it can coexist with liquid.

But there is another effect of oxygen fugacity on the stability of pyroxene that has been revealed by the work of Grove and Juster (1989). At oxygen fugacities defined by FMQ the Ca-poor clinopyroxene, pigeonite, is the near-liquidus phase of basalts and andesites. However if the oxygen fugacity is increased to $\Delta\text{NNO} + 2$ this induces a larger concentration of Fe_2O_3 in the liquid so that the MgO/FeO ratio increases. This promotes the stability of orthopyroxene, the most typical Ca-poor pyroxene of the basic lavas of the continental margin, and destabilizes pigeonite.

HYDROUS MINERALS AND THEIR RELATIONSHIPS TO LIQUIDS

Experimental determination of the compositions of hydrous minerals coexisting with liquid, at and below water saturation, are essential for calibration of the thermodynamic properties of dissolved H_2O in the melt, and the effect of water on the melt activities of the anhydrous components. A good example is the equilibrium of phlogopitic mica, olivine and liquid, represented by the following reactions:



If SiO_2 , KAlSi_3O_8 , and H_2O are taken to represent components dissolved in the liquid, and Mg_2SiO_4 and Fe_2SiO_4 are components in the coexisting olivine, then we have a solid assemblage typical of minettes. As the mica contains iron, it will respond to the prevailing oxygen fugacity, as Wones and Eugster (1965) have shown, but the ferric-ferrous ratio has yet to be calibrated as a function of temperature, bulk composition and oxygen fugacity. If activity-composition relations in the micas were known, then experiments defining a minette liquidus, saturated with phlogopitic mica \pm olivine, over a range of oxygen fugacities and confining pressures, would allow calibration of the thermodynamic properties of the liquid phase.

In minettes the phenocrysts of phlogopite may occur together with olivine, augite and/or spinel. Although most examples of this lava type are not fresh, those that are contain substantial amounts of glass, but analyses of this do not exist. However it is evident from the analyses of phlogopite phenocrysts and the glassy lava that contains them (Table 7), that the redox state of phlogopite is greater than that of the lava; thus it is plausible to believe that continued precipitation of phlogopite would reduce the relative oxygen fugacity (ΔNNO) of the residual liquid.

Activity-composition relations of the amphiboles, particularly of hornblendes, are far from being defined. Cumingtonite is found together with phenocrysts of hornblende, orthopyroxene, quartz and Fe-Ti oxides in several New Zealand rhyolites (Ewart et al.,

1971; Wood and Carmichael, 1973; Ewart et al., 1975), and these assemblages offer another route to extending melt solution models to hydrous compositions, provided that solution theory for the cummingtonites can be developed. The reaction representing the natural assemblage is



and the compositions of the solid phases may be used to provide calibration points for the fugacity of water at the conditions represented by the equilibration of the Fe-Ti oxides. This example illustrates the necessity of having well characterized natural assemblages in addition to experimental liquid-solid equilibria, as such viscous liquids equilibrate with difficulty. This is exemplified by the absence of cummingtonite in the run products of a natural silicic liquid equilibrated within its P-T stability field (Naney, 1983).

But amphibole phenocrysts present problems other than those of documenting their activity-composition relations. In a preceding section on the iron redox state of basic magmas, a curious relationship has been found for the basalts and basaltic-andesites of western Mexico. These become more oxidised as the individual eruptions proceed, and in the more oxidised lavas, phenocrysts of hornblende occur (Hasenaka and Carmichael, 1987). This requires that significant amounts of Fe_2O_3 will occur in the phenocrysts, although to the first writer's chagrin the carefully separated and purified hornblende phases were only analysed for trace metals (Luhr and Carmichael, 1980).

Magmas more basic than andesites may have hornblende phenocrysts, and it is a characteristic phase in many trachyandesites and tephrites. As the groundmass of these lava types does not often quench to glass, the composition of the liquid in equilibrium with hornblende is difficult to establish. In Table 7, the analyses of a tephrite lava (K-3) and its hornblende phenocrysts are tabulated, and the hornblende has a higher redox ratio than the bulk lava. In quartz-bearing silicic lavas, the same relationship is found, and the example given in Table 7 (CAM 73) is of the unusual phenocryst assemblage of fayalitic olivine and hornblende, together with iron-titanium oxides (Carmichael, 1967). As only the bulk composition of the lava has been determined (Table 7), the values of Fe_2O_3 and FeO consistent with the oxygen fugacity derived from the iron-titanium oxide equilibration has been calculated using the Kilinc et al. (1983) algorithm. These are $\text{Fe}_2\text{O}_3 = 0.11\%$ and $\text{FeO} = 0.91\%$ in contrast to 0.33% and 0.71% respectively found in the bulk lava (Table 7). Using an olivine-liquid $K_D = 1$, the amount of MgO calculated to be in equilibrium with the olivine is 0.03% , in comparison to 0.04% in the lava. Thus the hornblende phenocrysts of this silicic lava are more oxidized than the residual liquid (Table 7), and the relationships found or deduced in other lava types also prevail in silicic liquids. Perhaps the only counter example may be in those peralkaline liquids which precipitate an amphibole (Nicholls and Carmichael, 1969), where the high concentration of Fe_2O_3 in the liquid is a response to the high Na_2O content, rather than to a high oxygen fugacity.

IRON-TITANIUM OXIDES AND SULFIDES AND THE REDOX STATE OF THE LIQUID

In the crystallization of MORB magmas the ferromagnesian silicates are accompanied by a spinel phase, plagioclase, and more importantly by an iron-sulfide liquid (Mathez, 1976). The latter can contain substantial amounts of oxygen (Naldrett, 1969; Doyle and Naldrett, 1987), and thus the sulfide phase may behave as an oxygen reservoir (Carmichael and Ghiorso, 1986). If the precipitation of the ferromagnesian phases in a liquid tends to change the iron redox ratio, then addition or withdrawal of oxygen from the

sulfide phase could moderate this affect. Consequently, the relative oxygen fugacity (ΔNNO) of the liquid may remain constant and the value it takes will be determined by the oxygen fugacity of the silicate liquid equilibrating with that of the sulfide phase.

From the foregoing discussions it appears that early crystalizing phases such as augite can have a redox state that is either larger or smaller than the liquid, depending upon the oxygen fugacity. So it is with the Fe-Ti oxides. Generally, a rhombohedral oxide has a lower redox state than the liquid with which is in equilibrium (Table 4). For spinel, the redox ratio depends on composition, so that precipitation of such a phase may increase or decrease the amount of ferric iron in the liquid.

There is an important exception to this general conclusion. Firstly in peralkaline silicic liquids the high concentration of Fe_2O_3 is not a consequence of a high oxygen fugacity, but rather of a high concentration of Na_2O . The evidence of these liquids is that the fractionation of any silicate or oxide increases the redox state of the residual liquid. Whether or not the Fe_2O_3/FeO ratio of the pyroxene ever matches, or exceeds that of a peralkaline liquid is unknown.

CONCLUSIONS

For magmas cooling under conditions such that their oxygen contents are held fixed, or are subject to only minor loss or gain, there are several generalizations that are evident. If the early crystalizing phase has a lower redox state than that of the liquid, for example an olivine phenocryst in a tholeiitic liquid in an oceanic environment, then as temperature decreases, the progressive increase of ferric iron and sulphur in the liquid will induce the formation of a spinel phase, and an immiscible sulfide liquid. The latter Fe-S-O liquid may contain more O than S at FMQ (Doyle and Naldrett, 1987), providing an adequate reservoir for the oxygen needed to sustain a tholeiitic liquid line of descent on the FMQ buffer (Ghiorso and Carmichael, 1985). In combination, the continued formation of olivine, spinel and sulfide liquid, will regulate the iron redox state of the the residual liquid, so that it may resemble a buffered path. Addition or subtraction of oxygen to the system (liquid plus solids) at constant temperature will initially change the proportions of the solids. But should the oxygen *fugacity* change, then the iron redox ratio in the crystalline phases (and the liquid) will also change.

In those highly oxidized natural liquids whose iron redox ratio is greater than that of the precipitating spinel and rhombohedral oxide assemblage, then ultimately a representative of the pseudobrookite series will form, and thereafter the liquid line of descent involving a progressive increase in Fe_2O_3 may cease. The assemblage of a rhombohedral ($FeTiO_3$ - Fe_2O_3) solid solution and a pseudobrookite solid solution will have the effect of constraining the iron redox ratio in the liquid, and at constant temperature will act as a buffer to small changes in the oxygen content of the system. Again if the oxygen *fugacity* changes, at constant temperature, then the solid phases must either change in composition by changing their individual redox ratios, or one will disappear.

Thus one problem of modelling a general liquid line of descent essentially hinges on the relationship between oxygen fugacity and the iron redox ratio of the phases that enter above the solidus. For natural silicate liquids this relationship is well known, but it has yet to be established for any ferromagnesian silicate solid solution series. Today the modelled crystallization path has to constrain the composition of the ferromagnesian minerals to their idealized composition, and for tholeiitic magmas this seems reasonably successful. For more alkaline-rich magmas, such as olivine-basalt or more silica-poor varieties, augite can

show a large range in composition but experimental calibration of this is sadly lacking. Of additional concern is the fact that in these magmas a sulfide phase can even occur in combination with a sulphate-bearing solid phase (Luhr et al., 1984). The "bottom line" is that a vast experimental effort is required to establish the connection between composition, iron redox state, temperature and oxygen fugacity for the ferromagnesian minerals, particularly augite, biotite, the igneous amphiboles, in equilibrium with liquids.

A PETROLOGICAL CONCERN

Today we can calculate with increasing sophistication and precision the crystallization paths of natural silicate liquids, under a variety of stipulated conditions, as this Short Course has been created to illustrate. But by a curious paradox that may be more American than global, the precision that a secure thermodynamic model provides is offset by a generally decreasing accuracy in the analysis of the very lavas that we wish to model. The common belief of geologists that a lava with 63.07% SiO₂ has exactly that (a major oxide concentration known to one or two hundred parts per million!) should have been shattered for all time by the poor agreement on the U.S. Geological Survey standard rocks W-1 and G-1, first analyzed by wet chemical methods in the 1950s (Fairbairn et al., 1951; Fairbairn, 1953). Today the sight of a chemical laboratory with volumetric flasks, burettes and Pt crucibles being ignited is, like the steam engine, long gone, and yet the less precise instrumental techniques that have replaced that arcane craft are dependent on well analyzed standards to be most effective. Nevertheless SiO₂, among others, is still reported to four significant figures, an implied sensitivity wholly illusory. Generally both the microprobe analysis of minerals, and the X-ray fluorescence analysis of rocks, require secure and well characterized standards, and work best if the standards are of natural materials fairly close in composition to the unknowns. Neither technique offers the precision or sensitivity of wet chemistry at its best (e.g., SiO₂; 2 sigma = $\pm 0.16\%$ of amount present). Nor can either technique be used to determine the amounts of ferric and ferrous iron that are found in most igneous rocks.

The analytical fashion of today has all but eliminated the determination of ferric and ferrous iron in the analysis of rocks, although a *calculated* value may be reported for FeO and Fe₂O₃. Even if all the paraphernalia of wet analytical techniques are resurrected, and the apprehension of dealing with HF is overcome, how that effort can be utilized may be very uninspiring. Nevertheless we attempted to demonstrate in this chapter that without knowledge of the redox state of liquid and crystal alike, any modelling of a liquid line of descent can be severely handicapped. As the most convenient and rapid method for the determination of the iron redox state is by wet chemistry, we hope to have rekindled an interest in the craft of analysis (even partial!) of igneous rocks by wet chemistry.

REFERENCES

- Berman, R. G. (1988) Internally-consistent thermodynamic data for minerals in the system Na₂O-K₂O-CaO-MgO-FeO-Fe₂O₃-Al₂O₃-SiO₂-TiO₂-H₂O-CO₂. J. Petrol. 29, 445-552.
- Buddington, A.F., and Lindsley, D.H. (1964) Iron-titanium oxide minerals and synthetic equivalents. J. Petrol. 5, 310-357.
- Carmichael, I.S.E. (1960) The pyroxenes and olivines from some Tertiary acid glasses. J. Petrol. 1, 309-336.
- Carmichael, I.S.E. (1962) Pantelleritic liquids and their phenocrysts. Mineral. Mag. 33, 86-113.
- Carmichael, I.S.E. (1967) The iron-titanium oxides of salic volcanic rocks and their associated ferromagnesian silicates. Contrib. Mineral. Petrol. 14, 36-64.
- Carmichael, I.S.E. (1991) The redox states of basic and silicic magmas: a reflection of their source regions? Contrib. Mineral. Petrol. (in press)
- Carmichael, I.S.E., Nicholls, J. (1967) Iron-titanium oxides and oxygen fugacities in volcanic rocks. J. Geophys. Res. 72, 4665-4687.

- Carmichael, I.S.E., Ghiorso, M.S. (1986) Oxidation-reduction relations in basic magma: a case for homogeneous equilibria. *Earth Planet. Sci.*, 78, 200-210.
- Carmichael, I.S.E., Lange, R.A., Luhr, J.F. (1991) The minettes and associated lavas of the Mascota region, western Mexico. (in preparation).
- Christie, D. M., Carmichael, I. S. E., Langmuir, C. H. (1986) Oxidation states of mid-ocean ridge basalt glasses. *Earth Planet. Sci. Letts.* 79, 397-411.
- Cosca, M.A., Peacor, D.R. (1987) Chemistry and structure of esseneite, CaFeAlSiO_6 , a new pyroxene produced by pyrometamorphism. *Am. Mineral.* 72, 148-156.
- Cosca, M.A., Essene, E.J., Geissman, J.W., Simmons, W.B., Coates, D.A., (1989) Pyrometamorphic rocks associated with naturally burned coal beds, Powder River basin, Wyoming. *Am. Mineral.* 74, 85-100.
- Doyle, C.D., Naldrett, A.J. (1987) The oxygen content of "sulphide" magma and its effect on the partitioning of nickel between coexisting olivine and molten ores. *Econ. Geol.* 82, 208-211.
- Drake, M.J. (1975) The oxidation state of europium as an indicator of oxygen fugacity. *Geochim. Cosmochim. Acta* 39, 55-64.
- Drake, M.J., Weill, D.F. (1975) Partition of Sr, Ba, Ca, Y, Eu^{2+} , Eu^{3+} and other REE between plagioclase feldspar and magmatic liquid: an experimental study. *Geochim. Cosmochim. Acta* 39, 689-712.
- Deer, W.A., Howie, R.A., Zussman, J. (1982) *Rock-forming Minerals*, Vol. 1A: Orthosilicates, John Wiley, 919 pp.
- Elkins, L. T., Grove, T. L. (1990) Ternary feldspar experiments and thermodynamic models. *Am. Mineral.* 75, 544-559.
- Ewart, A. (1971) Notes on the chemistry of ferromagnesian phenocrysts from selected volcanic rocks, central volcanic region. *New Zealand J. Geol. Geophys.* 14, 323-340.
- Ewart, A., Hildreth, W., Carmichael, I.S.E. (1975) Quaternary acid magma in New Zealand. *Contrib. Mineral. Petrol.* 51, 1-27.
- Fairbairn, H.W., Schleet, W.G., Stevens, R.E., Dennen, W.H., Ahrens, L.H. Chayes, F., (1951) A cooperative investigation of precision and accuracy in chemical, spectrochemical and modal analysis of silicate rocks. *U.S. Geol. Surv. Bull.* 980.
- Fairbairn, H.W. (1953) Precision and accuracy of chemical analysis of silicate rocks. *Geochim. Cosmochim. Acta* 4, 143-156.
- Foit, F.F., Hooper, R.L., Rosenberg, P.E. (1987) An unusual pyroxene, melilite, and iron oxide assemblages in a coal-fire buchite from Buffalo, Wyoming. *Am. Mineral.* 72, 137-147.
- Fudali, R.F. (1965) Oxygen fugacities of basaltic and andesitic magmas. *Geochim. Cosmochim. Acta* 29, 1063-1075.
- Fuhrman, M. L., Lindsley, D. H. (1988) Ternary feldspar modeling and thermometry. *Am. Mineral.* 73, 201-215.
- Ghiorso M.S. (1985) Chemical mass transfer in magmatic processes. I. Thermodynamic relations and numerical algorithms. *Contrib. Mineral. Petrol.* 90, 107-120.
- Ghiorso MS (1987) Modeling magmatic systems: thermodynamic relations. In: *Thermodynamic Modeling of Geological Materials: Minerals, Fluids and Melts*, I.S.E.Carmichael and H.P.Eugster, eds. *Reviews in Mineralogy* 17, 443-465.
- Ghiorso, M.S. (1990) Thermodynamic properties of hematite-ilmenite-geikielite solid solutions. *Contrib. Mineral. Petrol.* 104, 645-667.
- Ghiorso M.S., Carmichael I.S.E. (1985) Chemical mass transfer in magmatic processes. II. Applications in equilibrium crystallization, fractionation and assimilation. *Contrib. Mineral. Petrol.* 90, 121-141.
- Ghiorso, M.S., Carmichael, I.S.E. (1987) Modeling magmatic systems: petrologic applications. In: *Thermodynamic Modeling of Geological Materials: Minerals, Fluids and Melts*, I.S.E.Carmichael and H.P.Eugster, eds. *Reviews in Mineralogy* 17, 467-499.
- Ghiorso, M.S., Carmichael, I.S.E., Rivers, M.L., Sack, R.O. (1983) The Gibbs free energy of mixing of natural silicate liquids; an expanded regular solution approximation for the calculation of magmatic intensive variables. *Contrib. Mineral. Petrol.* 84, 107-145.
- Ghiorso M.S., Kelemen P.B. (1987) Evaluating reaction stoichiometry in magmatic systems evolving under generalized thermodynamic constraints: Examples comparing isothermal and isenthalpic assimilation. In: *Magmatic Processes: Physicochemical Principles*, B.O. Mysen, ed. *Geochem. Soc., Special Pub.* 1, 319-336.
- Ghiorso, M.S., Sack, R.O. (1991) Fe-Ti oxide geothermometry: thermodynamic formulation and the estimation of intensive variables in silicic magmas. *Contrib. Mineral. Petrol.* (in press).
- Grove, T.L., Juster, T.C. (1989) Experimental investigations of low-Ca pyroxene stability and olivine-pyroxene-liquid equilibria at 1 atm in natural basaltic and andesitic liquids. *Contrib. Mineral. Petrol.* 103, 287-305.
- Hasenaka, T., Carmichael, I.S.E. (1987) The cinder cones of Michoacan-Guanajuato, Central Mexico: Petrology and Chemistry. *J. Petrol.* 28, 241-269.
- Huebner, J.S., Sato, M. (1970) The oxygen fugacity-temperature relationships of manganese oxide and nickel oxide buffers. *Am. Mineral.* 55, 934-952.
- Kilinc, A., Carmichael, I.S.E., Rivers, M.L., Sack, R.O. (1983) The ferric-ferrous ratio of natural silicate liquids equilibrated in air. *Contrib. Mineral. Petrol.* 83, 136-140.
- Kress, V.C., Carmichael, I.S.E. (1988) Stoichiometry of the iron oxidation reaction in silicate melts. *Am.*

- Mineral. 73, 1267-1274.
- Kress, V.C., Carmichael, I.S.E. (1991) The iron redox state in silicate liquids: the effect of pressure, temperature, oxygen fugacity and composition, with application to the genesis of basic magma. *Contrib. Mineral. Petrol.* (in press)
- Luhr, J.F., Carmichael, I.S.E., (1980) The Colima volcanic complex, Mexico. *Contrib. Mineral. Petrol.* 71, 343-372.
- Luhr, J.F., Carmichael, I.S.E., Varekamp, J.C. (1984) The 1982 eruption of El Chichon volcano, Chiapas, Mexico: Mineralogy and petrology of the pumices. *J. Volcanol. Geotherm. Res.* 23, 68-108.
- Luhr, J.F., Allan, J.F., Carmichael, I.S.E., Nelson, S.A., Hasenaka, T. (1989) Primitive calc-alkaline and alkaline rock types from the western Mexican volcanic belt. *J. Geophys. Res.* 94, 4515-4530.
- Mathez, E.A. (1976) Sulfur solubility and magmatic sulphides in submarine basalt glass. *J. Geophys. Res.* 81, 4269-4276.
- Morris, R.V., Haskin, L.A., Biggar, G.M., O'Hara, M.J., (1974) Measurement of the effects of temperature and partial pressure of oxygen on the oxidation states of europium in silicate glasses. *Geochim. Cosmochim. Acta* 38, 1447-1459.
- Muan, A. (1955) Phase equilibria in the system FeO-Fe₂O₃-SiO₂. *J. Metals* 203, 965-976.
- Naldrett, A.J. (1969) A portion of the system Fe-S-O between 900 and 1080°C and its application to sulphide ore magmas. *J. Petrol.* 10, 171-201.
- Naney, M.T. (1983) Phase equilibria of rock-forming silicates in granitic systems. *Am. J. Sci.* 283, 993-1033.
- Nash, W.P., Wilkinson, J.F.G. (1970) Shonkin Sag laccolith, Montana: Pt I, Mafic minerals and estimates of temperature, pressure, oxygen fugacity and silica activity. *Contrib. Mineral. Petrol.* 25, 241-269.
- Nicholls, J., Carmichael, I.S.E. (1969) Peralkaline acid liquids: a petrological study. *Contrib. Mineral. Petrol.* 20, 268-294.
- O'Neill, H.St.C. (1987) Quartz-fayalite-iron and quartz-fayalite-magnetite equilibria and the free-energy of formation of fayalite (Fe₂SiO₄) and magnetite (Fe₃O₄). *Am. Mineral.* 72, 67-75.
- O'Neill, H.St.C. (1988) Systems Fe-O and Cu-O: Thermodynamic data for the equilibria Fe-"FeO", Fe-Fe₃O₄, "FeO"-Fe₃O₄, Fe₃O₄-Fe₂O₃, Cu-Cu₂O, and Cu₂O-CuO from emf measurements. *Am. Mineral.* 73, 470-486.
- Robie, R.A., Hemingway, B.S., Fisher, J.R. (1978) Thermodynamic properties of minerals and related substances at 298.15K and 1 bar (10⁵ Pascals) pressure and at higher temperatures. *U.S. Geol. Surv. Bull.* 1452.
- Roeder, P.L., Emslie, R.F. (1970) Olivine-liquid equilibria. *Contrib. Mineral. Petrol.* 29, 275-289.
- Sack, R.O., Carmichael, I.S.E. (1984) Fe²⁺ ↔ Mg²⁺ and TiAl₂ ↔ MgSi₂ exchange reactions between clinopyroxenes and silicate melts. *Contrib. Mineral. Petrol.* 85, 103-115.
- Sack, R.O., Carmichael, I.S.E., Rivers, M.L., Ghiorso, M.S. (1980) Ferric-ferrous equilibria in natural silicate liquids at 1 bar. *Contrib. Mineral. Petrol.* 75, 369-376.
- Sack R.O., Ghiorso M.S. (1989) Importance of considerations of mixing properties in establishing an internally consistent database: Thermochemistry of minerals in the system Mg₂SiO₄-Fe₂SiO₄-SiO₂. *Contrib. Mineral. Petrol.* 102, 41-68.
- Sack, R.O., Ghiorso, M.S. (1991a) An internally consistent model for the thermodynamic properties of Fe-Mg-titanomagnetite-aluminate spinels. *Contrib. Mineral. Petrol.* (in press).
- Sack, R.O., Ghiorso, M.S. (1991b) Chromian spinels as petrogenetic indicators: thermodynamics and petrological applications. *Am. Mineral.* (in press).
- Schreiber, H.D., Lauer, H.V., Thanyasiri, T. (1980) The redox state of cerium in basaltic magmas: an experimental study of iron-cerium interactions in silicate melts. *Geochim. Cosmochim. Acta* 44, 1599-1612.
- Smith, A.L., Carmichael, I.S.E. (1969) Quaternary trachybasalts from southeastern California. *Am. Mineral.* 54, 909-923.
- Snyder, D., Carmichael, I.S.E. (1991) Olivine-liquid equilibria in natural basic liquids. *Geochim. Cosmochim. Acta* (submitted).
- White, R.W. (1966) Ultramafic inclusions in basaltic rocks from Hawaii. *Contrib. Mineral. Petrol.* 12, 245-314.
- Wones, D.R., Eugster, H.P. (1965) Stability of biotite: Experiment, theory, and application. *Am. Mineral.* 50, 1228-1272.
- Wood, B.J., Carmichael, I.S.E. (1973) P_{total} , and $P_{\text{H}_2\text{O}}$ and the occurrence of cumingtonite in volcanic rocks. *Contrib. Mineral. Petrol.* 40, 149-158.
- Yoder, H.S., Tilley, C.E. (1962) Origin of basalt magmas: an experimental study of natural and synthetic rock systems. *J. Petrol.* 3, 342-532.

DYNAMICS OF ERUPTIVE PHENOMENA

FOREWORD

The scope of this chapter is limited to the dynamics of lava and gas rising in a volcanic conduit. No mention will be made of the behaviour of eruption columns in the atmosphere, which would deserve a chapter on their own. Some basic knowledge of the main principles of fluid dynamics is assumed. The text contains no complex mathematical derivation and, save for a few simple points, details all the steps required to arrive at a given solution. The aim of this chapter is to highlight a few key physical principles using simple problems of relevance to volcanic eruptions. True eruptions are of course more complex than the examples given and involve various interactions between the variables.

INTRODUCTION

The scientist interested in unravelling melting and crystallization processes in the Earth has two basic sources of information. On the one hand, ancient plutonic complexes brought to the surface by erosion provide the record of crystal cumulate piles which grew out of magma. On the other hand, erupted lavas provide direct samples of crystallizing magmas. The exact correspondence between the two records is a matter of debate. One problem is that a volcanic eruption is not a random and discrete sampling process. It occurs under specific circumstances in the development of the magmatic system, should cause mixing and may be restricted to a small part of the total magma volume stored at depth. Thus, it provides biased evidence of the chemical and thermal evolution which takes place in igneous systems. In other words, the dynamics of the eruption process determines when and how magma is sampled.

BASIC PRINCIPLES AND OBSERVATIONS

Dimensions of volcanic systems

Schematically, a volcanic system is made up of at least three parts: a deep source of magma, a shallow chamber and a volcanic conduit (Fig. 1). Detailed studies of Kilauea volcano (Hawaii) reveal a complex plumbing system with different storage regions

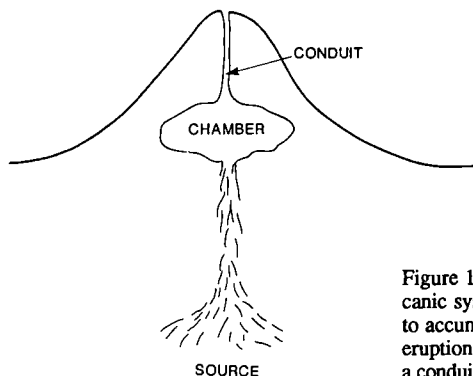


Figure 1. Illustration of the different parts of a volcanic system. Magma is generated at depth and rises to accumulate in a shallow magma chamber. During eruption, magma flows towards the Earth's surface in a conduit.

connected to several eruptive vents (Ryan, 1988; Koyanagi et al., 1988). The aseismic zone beneath the summit caldera has a volume of approximately 10^{10} m^3 (Koyanagi et al., 1976), and probably marks the location of a shallow magma chamber. A similar estimate of $3 \times 10^{10} \text{ m}^3$ has been made at Krafla volcano in Iceland (Einarsson, 1978). In Cascade Range volcanoes, seismic surveys lead to volumes of a few times 10^{10} m^3 (Evans and Zucca, 1988; Stauber et al., 1988), again in the same order of magnitude. It is useful to compare these values with the volume of magma which is expelled in a single eruption: between 10^7 and 10^8 m^3 at Kilauea (Swanson, 1972) and $3 \times 10^8 \text{ m}^3$ at Mount St. Helens in 1980 (Carey and Sigurdsson, 1985). These represent a small fraction ($\leq 1\%$) of the chamber volume. In rare catastrophic events, the erupted volumes are much larger, for example about 10^{10} m^3 in the 1800 YBP Taupo eruption in New Zealand (Walker, 1980) and $2 \times 10^{10} \text{ m}^3$ at Katmai volcano in 1912 (Fierstein and Hildreth, 1986). It is likely that these events represent the emptying of a large part of the magma chamber.

The dimensions of volcanic conduits are known in a few cases. They are approximately cylindrical with radii of about 7 m at the Kilauea summit (Richter et al., 1970), 12 m at Mount St. Helens (Swanson and Holcomb, 1987) and 16 m in the Inyo volcanic system (Eichelberger et al., 1986). Evidence from drill-holes in the latter case, and from deformation studies during eruption at Mount St. Helens in 1980 (Chadwick et al., 1988), suggest that the conduits have the same dimensions at least down to a depth of several hundred meters. No information is available for conduits at greater depths. Eruptions also occur through long fissures which may exceed one kilometer in length and be as wide as a few meters (Swanson et al., 1976). Such eruptions soon focus to a central vent with an approximately cylindrical aperture of similar dimensions to those quoted above.

The depth to the shallowest zone of magma storage is 2-3 km both at Kilauea (Koyanagi et al., 1976) and in Cascade Range volcanoes (Evans and Zucca, 1988). Magma chambers may thus be located within the volcanic edifice itself.

Velocity and mass flux of eruptions

The vertical velocity at the vent is of the order of 200-300 m/s in Plinian events (Wilson et al., 1980). In Hawaiian fire fountains, ballistic considerations lead to estimates of 100-200 m/s (Wilson and Head, 1981). During Strombolian activity, direct photographic measurements lead to values of about 60 m/s (Chouet et al., 1974). During effusive activity, eruption velocities are much smaller. In basaltic volcanoes, average values range from 10^{-2} m/s (at Mauna-Ulu, Swanson, 1973) to 3×10^{-3} m/s (at Etna, Tanguy, 1973). In silicic volcanoes, effusive activity results in dome formation, such that velocity continuously decreases as the dome builds up. Initial velocity values are about 3×10^{-4} m/s for basaltic andesite at La Soufrière de Saint Vincent (Huppert et al., 1982) and 3×10^{-5} m/s for dacite at Mount St. Helens (Christiansen and Peterson, 1981).

Two important facts emerge from these data. During effusive activity, flow velocities reflect directly the composition of lava: they are highest for basalt, intermediate for basaltic andesite and lowest for dacite. On the contrary, in explosive eruptions, flow velocities do not depend markedly on lava type.

As will be shown later, the most important variable is the mass flux of an eruption. At Hawaii, the mass flux has typical values of 10^5 – 10^6 kg/s during fire fountaining and 10^4 kg/s during effusive activity (Vergnolle and Jaupart, 1986). At Mount St. Helens, the mass flux was about 10^7 kg/s during Plinian phases (Carey and Sigurdsson, 1985) and less than 10^3 kg/s during dome growth (Swanson et al., 1987).

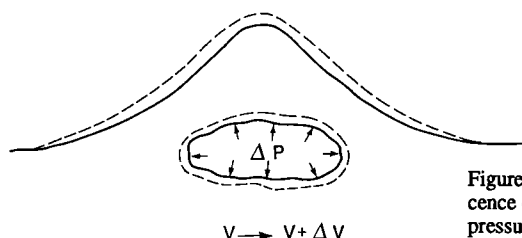


Figure 2. Volcanic eruptions are preceded by tumescence of the volcanic edifice, indicating that an overpressure develops in the magma chamber. Eruption occurs when the tensile stresses generated at the margins by the chamber expansion exceed the strength of country rock.

Eruption triggering

Volcanic eruptions are usually preceded by tumescence of the volcanic edifice and diffuse seismicity in the vicinity of the magma chamber (Fig. 2). These indicate that the chamber undergoes both a volume and pressure increase. Eruption occurs when the pressure rises sufficiently to fracture the surrounding rocks. Two mechanisms can be responsible for such phenomena (Blake, 1981; Blake, 1984; Tait et al., 1989). One is replenishment from a deep source of magma. The other is fractional crystallization. Volatile species are incompatible and hence crystallization leads to an increase of their concentration in the residual melt. The solubility limit must eventually be reached, such that gas exsolution occurs, implying an overall density decrease and hence chamber expansion. The important points are (1) that eruption products do not come directly from the deep source of magma and have evolved chemically in storage at depth, (2) that the chamber is overpressured when eruption starts.

A quantitative model of eruption triggering requires an analysis of how the chamber deforms. The field evidence shows that such deformations are reversible, and hence are essentially in the elastic regime. Consider first the simplest case of a spherical chamber where pressure rises by an amount ΔP (Fig. 2). A standard solution of elasticity theory (see for example McTigue, 1988) shows that the fractional volume change is:

$$\frac{\Delta V}{V} = \frac{3}{4 \mu_c} \Delta P \quad , \quad (1)$$

where μ_c is the rigidity of the surrounding geological formations. This overpressure acts to develop tensile stresses τ at the chamber margins, equal to:

$$\tau = \frac{1}{2} \Delta P \quad . \quad (2)$$

Thus, eruption starts when the rocks fail in tension. Denoting the tensile strength by σ_T , the criterion for failure is:

$$\tau = \sigma_T \quad , \quad (3)$$

which corresponds to a critical overpressure ΔP_c such that:

$$\Delta P_c = 2 \sigma_T \quad . \quad (4)$$

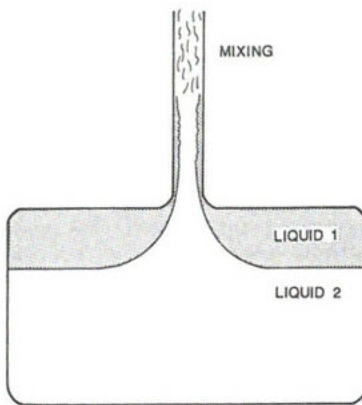


Figure 3. Schematic diagram showing how a stratified chamber empties into a conduit. In the case shown, the chamber is made of two liquids layers which mix as they are drawn into the eruption conduit.

Laboratory determinations of the tensile strength of common rock types are typically about 9 MPa for basalt, 14 MPa for granite and 4 MPa for sedimentary rocks (Touloukian et al., 1981). These values are for selected pristine samples of small size. However, a volcanic edifice is penetratively fractured as a result of eruptive and tectonic events, so the laboratory values must be treated as upper bounds. Thus, a maximum estimate for overpressures at the start of an eruption is 30 MPa (300 bars). Direct estimates of the chamber overpressure in the range from 1 to 10 MPa have been made using the characteristics of dyke formation and propagation (Einarsson and Brandsdottir, 1978; Rubin and Pollard, 1989). A typical value for the rigidity of rocks is 10^{10} Pa (Touloukian et al., 1981). Using Equation (1), these numerical estimates imply that, upon eruption, the fractional volume increase of the chamber is between values of 10^{-4} and 10^{-3} .

A more realistic treatment of the problem requires the true chamber geometry. For example, in the case of a cylindrical chamber, the tensile stress at the margins is equal to the applied overpressure, i.e., $\tau = \Delta P$ (compare with the spherical case above). Another difficulty lies in the need to know the elastic properties of a large edifice with a long history of deformation and failure. It is clear, however, that small pressure and volume changes are sufficient to generate eruptions. In other words, large pressure and volume changes cannot be sustained in a closed magma reservoir lying at shallow depth below the Earth's surface. This is an important consideration in the thermodynamic modelling of crystallization processes.

Effect of eruptions on the magma chamber

An eruption induces flow in the magma chamber which perturbs the resident liquid. Several studies have considered how outflow affects liquid reservoirs which are stratified either continuously (Spera et al., 1986) or in discrete layers (Koyaguchi, 1985; Blake and Ivey, 1986; Freundt and Tait, 1986; Lister, 1989). We will not review all these studies, but an obvious conclusion emerges: the stronger the flow, the larger the perturbation to the chamber (Fig. 3). An important variable is the thickness of resident liquid affected by outflow, called the drawdown depth, which is mainly determined by the strength of the gradients in liquid density and viscosity in the chamber and the mass flux of the eruption. For large drawdown, melts from a large depth range are erupted simultaneously and get mixed in the conduit.

In assessing how an eruption samples the chamber, a critical parameter is velocity into the conduit. This velocity differs from the eruption velocity at the earth's surface because of the behaviour of volatiles. Eruptions are in steady-state conditions, which means that their characteristics stay constant over times long compared to that which is taken to rise from chamber to vent. Therefore, the mass flux stays constant and, in particular, has the same value at the conduit entry and at the surface vent. At height z in the conduit, let W denote the average vertical velocity, S the conduit cross-section, α the volume fraction of gas and ρ_l the liquid density. The mass flux of lava can therefore be written:

$$G_l = \rho_l (1-\alpha) W S \quad . \quad (5)$$

The lava density does not vary significantly as a function of temperature, pressure and dissolved gas concentration. Thus, denoting by indices 1 and 2 the values of the variables at the bottom and top of the conduit, we obtain:

$$W_2 = W_1 \frac{S_1}{S_2} \frac{1-\alpha_1}{1-\alpha_2} \quad . \quad (6)$$

Thus, variations of the conduit dimensions and gas volume fraction act to change velocity. There are no observational constraints on ratio S_1/S_2 . A magma parcel rising in the conduit experiences a large pressure decrease which results in exsolution of dissolved volatile species and gas expansion: thus the gas volume fraction is much larger at the vent than at depth. For example, Hawaiian fire fountains are such that $\alpha_2 \sim 99\%$ (Vergnolle and Jaupart, 1990). In contrast, there is little gas in the magma chamber itself and hence at the conduit entry: maximum estimates for α_1 are 1% (Tait et al., 1989). This difference of gas content is responsible for a 100-fold increase of velocity between the conduit bottom and top.

The large velocity values observed at the vent result in large part from what happens in the conduit. The useful variable is therefore not velocity but mass flux, which is conserved.

THE PROPERTIES OF VOLCANIC LIQUIDS

An eruption involves a mixture of magma, crystals and gas which rises in a conduit towards the Earth's surface. To understand the dynamics of the phenomenon, one must define the state of the mixture and its physical properties. An important factor is whether the mixture is fragmented or not. One is dealing with a gaseous jet carrying suspended lava clots in the former case and with an essentially liquid phase in the latter.

Physical properties of lava

The mixture which rises in the conduit is in general not a pure liquid, but partially crystallized magma carrying suspended gas bubbles. It is the properties of this mixture which matter here. The density of silicate melts is discussed in other parts of this book.

The viscosity of silicate melts. There is now an extensive body of data as well as a set of semi-empirical relationships which allow the calculation of the viscosity of a silicate melt as a function of the molar fractions of its oxide components (Urbain et al., 1983; Ryan and Blevins, 1987). For our present purposes, the two most important factors are the silica content and the amount of dissolved water. For water-saturated aphyric magmas, viscosity values range from 1 Pas, for MgO-rich mafic lavas (picrites), to more than 10^7 Pas for rhyolites. The effect of water is large and, roughly speaking, amounts to a decrease by one order of magnitude for every two percent dissolved water (per mass). The amount of dis-

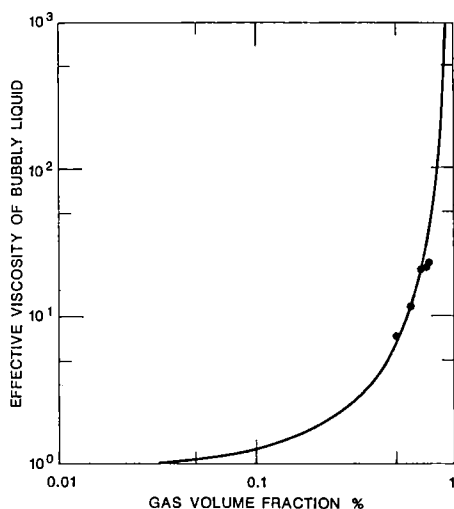


Figure 4. Viscosity increase due to the presence of bubbles in a liquid (from Eqn. 8). The plot shows the ratio of the viscosity of the bubbly liquid to that of the pure liquid as a function of the gas volume fraction. Dots represent data by Sibree (1934).

solved water decreases with decreasing confining pressure (see below) and hence the melt viscosity increases as exsolution takes place during ascent towards the Earth's surface.

The viscosity of bubbly liquids. The rheological properties of bubbly liquids, called "foams", have been studied extensively because of important industrial applications (Kraynick, 1988). In the presence of bubbles and during flow in a conduit, shear is applied to small thicknesses of liquid between neighbouring bubbles. This leads to an increase to the "effective" viscosity for the mixture.

At small gas volume fractions, drop deformation gives rise to an elastic-like response but does not affect the shear stress-strain rate relationship which remains linear, as in a Newtonian fluid, with viscosity given by (Schowalter, 1978, p. 271-275):

$$\mu_m = \mu_l (1 + n \alpha) , \quad (7)$$

where n is a coefficient. For gas bubbles, n is usually taken to be 1 for bubbles of negligible viscosity (Taylor, 1932). However, dynamic interfacial phenomena contribute complex effects and, in general, n is greater than 1 (Kraynick, 1988, p. 330). The limiting case is when bubbles behave as rigid spheres and corresponds to $n = 5/2$.

At large gas volume fractions, bubbles are strongly deformed and separated by very thin liquid films. This leads to shear-thinning behavior such that viscosity decreases with increasing shear rate. The effective viscosity exceeds that of the liquid by a large amount (Schwartz and Princen, 1987). Further, such foams exhibit a yield stress, below which there is no flow, and the phenomenon of "slip at the wall", where the liquid film which wets the conduit lubricates the flow (Princen, 1985; Kraynick, 1988).

For intermediate gas volume fractions, available data indicates that the shear stress-shear strain relationship is also linear (Sibree, 1934). A reasonable fit to the data can be obtained with a critical law of the form:

$$\frac{\mu_m}{\mu_l} = \left\{ \frac{1}{1 - \alpha/\alpha_c} \right\}^n , \quad (8a)$$

where α_c is the critical volume fraction above which the foam breaks down, and n a critical exponent. There are foams with a values in excess of 0.98 and a good approximation is therefore $\alpha_c \approx 1$. As α goes to zero, Equation (8a) has the limiting form:

$$\frac{\mu_m}{\mu_l} = 1 + n \alpha, \quad (8b)$$

which can be compared to the expression for dilute foams (7). Figure 4 shows the data of Sibree (1934) and the predictions of Equation (8a) with $n = 5/2$. Note the very large viscosity increase for volume fractions in excess of 70%.

The viscosity of suspensions. The presence of crystals also acts to increase the mixture viscosity. There is an extensive body of experimental data and several empirical relationships are also available in the form of critical laws:

$$\frac{\mu_m}{\mu_l} = \left\{ \frac{1}{1 - \Phi/\Phi_c} \right\}^n, \quad (9)$$

where Φ is the volume fraction of crystals and Φ_c the volume fraction above which the mixture behaves as a solid. Recent determinations are $\Phi_c = 0.65$ and $n = 1.625$ (Jeffrey and Acrivos, 1976).

The temperature dependence of viscosity. Viscosity varies strongly as a function of temperature. This is an important factor when the rising magma loses large amounts of heat to the country rock. This depends on the preexisting thermal structure of the volcanic edifice which remains largely unconstrained. In practice, the dominant effect is to either reduce the size of the conduit as magma freezes against the cold walls or widen it as magma melts the country rock (Bruce and Huppert, 1989).

The solubility of gas species in silicate melts

The major volatile species which are found dissolved in common magmas are H_2O and CO_2 . At low concentration, solubility follows Henry's law, depending only on pressure and temperature. Detailed thermodynamical models are available, but, for our present purposes, it is sufficient to express solubility as a function of pressure only. The following expressions have been determined, with $x(P)$ denoting solubility in mass fraction and P pressure in Pascals (Burnham, 1979; Stolper and Holloway, 1988):

$$CO_2 \text{ in basalt} \quad x(P) = 4.4 \times 10^{-12} P \quad (10a)$$

$$H_2O \text{ in basalt} \quad x(P) = 6.8 \times 10^{-8} P^{0.7} \quad (10b)$$

$$H_2O \text{ in rhyolite} \quad x(P) = 4.1 \times 10^{-6} P^{0.5} \quad (10c)$$

For example, basalt and rhyolite may contain as much as 2.7 wt % and 4.1 wt % water respectively at 1 kbar.

The density of magmatic gases

The equations of state for the major gas species involved in volcanic eruptions, H_2O and CO_2 , are now well known. At pressures less than a few hundred bars, it is sufficient to treat them as ideal gases. However, for deeper systems where pressures exceed 1 kbar, the equation of state is more involved, requiring many empirically-adjusted constants.

Satisfactory results are obtained with an equation of the so-called "Redlich-Kwong" form (Bottinga and Richet, 1981):

$$P = \frac{R T}{(V-b)} - \frac{a}{[V(V+b)T^{1/2}]} \quad , \quad (11)$$

where R is the ideal gas constant and a and b are in fact functions of volume (Bottinga and Richet, 1981). Throughout the following, for the sake of simplicity, we shall use the ideal gas approximation.

The fragmentation process

As lava rises in the conduit, pressure decreases and hence volatile species can no longer be kept in solution. This leads to a large volume increase and to large values of the gas volume fraction. Let us consider a mass M of lava which is just saturated at pressure P_i and erupted at a lower pressure P_e . We make two assumptions. (1) The gas phase does not escape, which corresponds to the "homogeneous flow assumption" (see below). (2) The exsolution reaction keeps pace with the decompression of the magma, i.e., we assume thermodynamic equilibrium between the melt and gas phases. We also make use of the fact that the mass of gas represents a small fraction of the total mass, and hence can be neglected in comparison with the mass of melt.

The mass of gas at pressure P_e is given by equations of state:

$$M_g = M \{ x(P_i) - x(P_e) \} \quad . \quad (12a)$$

This gas occupies a volume V_g such that:

$$\rho_g V_g = M_g = \rho_l V_l \{ x(P_i) - x(P_e) \} \quad . \quad (12b)$$

where ρ_g is the gas density at pressure P_e . Thus, the gas volume fraction is calculated to be:

$$\alpha = \frac{1}{1 + \frac{\rho_g}{[x(P_i) - x(P_e)] \rho_l}} \quad . \quad (13)$$

Consider, for example, that the material is erupted at atmospheric pressure and that the vapor phase is pure water. In rhyolite, concentrations are commonly several weight percent: very large gas volume fractions ensue (Fig. 5). Similar estimates are obtained for water in basalt. Only for the much less soluble CO_2 do values of the gas volume fraction drop below 90%.

The gas phase occurs as gas bubbles. Consider first that the bubbles all have the same dimensions. The maximum gas volume fraction for touching undeformed spheres is obtained for rhomboidal dodecahedron packing geometry as 74% (Princen et al., 1980).

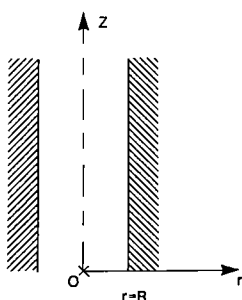
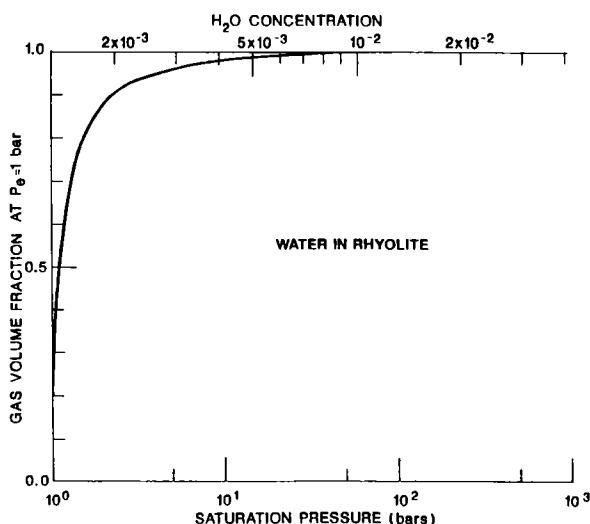


Figure 5 (above). Gas volume fraction at a pressure of one atmosphere for rhyolitic magma as a function of water concentration (expressed in weight fraction) or saturation pressure.

Figure 6 (left). Coordinate system used to derive the equations for flow in a vertical cylindrical conduit.

For larger values, the bubbles are deformed by their neighbours and a flat film of liquid exists between each adjacent pair. Gas volume fractions in excess of 95% can be achieved (Princen et al., 1980). A striking volcanic example is provided by "reticulite", a pumice erupted during high fire fountains in Hawaiian volcanoes with 98% gas volume fraction. It is clear that close packing cannot allow any high value of the gas volume fraction, and that a rearrangement must occur when values as high as those predicted by Equation (14) are reached: this is achieved by fragmentation, where bubbles burst and coalesce into a gas jet carrying fragments of their walls. Fragmentation is a poorly understood phenomenon involving the rupture of liquid films, which is enhanced by shear acting to stretch them. It is common practice to assume that it occurs when the gas volume fraction reaches the close packing threshold of 74%, on the grounds that the average pumice porosity is close to that value (Houghton and Wilson, 1989). However, there are clearly volcanic ejecta with higher gas volume fraction. Indeed, assuming close packing conditions with undeformed spherical bubbles, the total gas volume fraction may be higher than 74% because the liquid regions between bubbles may themselves contain smaller vesicles. It is clear that studies of the fragmentation process are needed.

Conclusion

The important result of this section is that the rheological properties of volcanic lavas and the solubility of major volatile species are non-linear functions of the governing parameters. This goes a long way to explaining the complex phenomenology of volcanic

systems. During ascent towards the surface, decompression induces major changes in the physical properties of the rising mixture. Viscosity increases both because of the presence of gas bubbles and because the concentration of dissolved volatiles decreases. On the other hand, density decreases because of the presence of the gas phase. Complex flow phenomena may arise because the amount of gas bubbles and the crystal content may not be constant across the width of the volcanic conduit. A major change of flow properties occurs upon fragmentation, when the ascending mixture behaves as a gas jet laden with particles.

FLOW EQUATIONS

Basic principles and equations

For flow in volcanic conditions, it is sufficient to consider purely vertical motion through a vertical conduit in steady-state. The vertical coordinate is positive upwards (Fig. 6). As a first approximation, it is assumed that gas and liquid move with the same velocity w , which corresponds to the "homogeneous" flow model. In principle, three different equations are necessary to describe the flow conditions in the volcanic conduit: one for mass conservation, another for energy and finally, one for the momentum balance.

The mass conservation equation has already been discussed above (Eqn. 5). Note that it was written for the liquid phase only and in integral form. The full steady-state differential form would be

$$\frac{\partial}{\partial x}(\rho u) + \frac{\partial}{\partial y}(\rho v) + \frac{\partial}{\partial z}(\rho w) = 0, \quad (14a)$$

where u and v are the horizontal velocity components and ρ is the mixture density, i.e.,

$$\rho = \rho_l (1-\alpha) + \rho_g \alpha \quad (14b)$$

where α is the gas volume fraction. In the case of a conduit of variable cross-section, the flow streamlines follow the conduit edges and hence the horizontal velocity components u and v are not zero. The surface integral of (14a) over a horizontal plane at height z yields:

$$\frac{d}{dz} \left(\int_S \rho w \, ds \right) = 0, \quad (15a)$$

where S is the conduit cross-section at height z . Equation (15a) is just a statement that the mass flux G is conserved in the conduit:

$$G = \int_S \rho w \, ds = \text{constant}. \quad (15b)$$

The energy equation requires the specification of two effects. The rising mixture loses heat to the surrounding country rocks, at a rate which depends on the poorly known initial thermal structure of the volcanic system and on the time elapsed since the beginning of eruption. This may lead to chilling of the melt against the conduit walls, implying a reduction of the conduit open to flow. With time, the rising magma continues to lose heat to the conduit walls and hence to heat it up, which may lead to melt back the chilled margin and eventually the country rocks as well (Bruce and Huppert, 1989). A second thermal effect is due to the work of pressure forces during decompression as magma rises towards the surface. This is an important consideration for the gas phase only because the compressibility of magma is small and can be considered negligible in this context. In adiabatic conditions, the temperature of the gas phase would decrease by large amounts, however,

assuming thermal equilibrium between magma and gas, it can be shown that temperature does not vary significantly because the mass fraction of gas is small (Buresti and Casarosa, 1989). It is therefore sufficient to consider isothermal conditions for the actively flowing magma.

The final equation is that for the conservation of momentum. Its vertical component is expressed as follows:

$$\rho w \frac{\partial w}{\partial z} = - \frac{\partial P}{\partial z} + \nabla^2 w - \rho g, \quad (16)$$

where $\nabla^2 w$ is the Laplacian of the velocity. This equation shows four terms, from left to right: acceleration (inertial term), pressure gradient, viscous effects and weight. The driving term is the pressure gradient which acts against the other three. The horizontal components of the momentum equation reduce to:

$$0 = \frac{\partial P}{\partial x} = \frac{\partial P}{\partial y}. \quad (17a)$$

We shall focus on cylindrical conduits with radial coordinate r , and hence:

$$0 = \frac{\partial P}{\partial r}. \quad (17b)$$

Thus, pressure depends on z only.

There are two classes of flow with different dynamics. Taking a velocity scale W , and scaling all spatial coordinates with R , the conduit radius, one can estimate the magnitude of the inertial and viscous terms. Their ratio is called the Reynolds number and is defined as follows:

$$Re = \frac{2 \rho W R}{\mu} = \frac{2}{\pi} \frac{Q}{R \mu} \quad (18)$$

where Q is the mass flux scale:

$$Q = \pi \rho W R^2. \quad (19)$$

When Re is smaller than about 2000, viscous forces dominate the momentum balance and inertial effects can be neglected: flow is in the laminar regime. When Re exceeds this critical value, inertial forces dominate and flow is in the turbulent regime. Using the values given in the first section for these variables, we find that all types of effusive activity are in the laminar regime. During explosive activity, the Reynolds number is also below critical as long as lava is not fragmented. Upon fragmentation, flow essentially involves a gas phase with very small viscosity, and the Reynolds number becomes supercritical. The important conclusion is that fragmentation is an important process not only because it determines the state of the volcanic mixture but also because it leads to a change of flow dynamics.

The mass flux of an eruption

Consider a cylindrical conduit of radius R and assume that fragmentation does not occur. This is valid for effusive activity and for the unfragmented part of explosive columns. The velocity field depends only on r and z , the radial and vertical coordinates (Fig. 6). The vertical momentum Equation (16) reduces to:

$$0 = -\frac{\partial P}{\partial z} + \mu \left\{ \frac{1}{r} \frac{\partial}{\partial r} \left(r \frac{\partial w}{\partial r} \right) + \frac{\partial^2 w}{\partial z^2} \right\} - \rho g . \quad (20)$$

Because the conduit radius is much smaller than the total conduit height, vertical derivatives of velocity can be neglected compared to radial ones. Thus, Equation (20) is simplified further to:

$$\frac{1}{r} \frac{\partial}{\partial r} \left(r \frac{\partial w}{\partial r} \right) = \frac{1}{\mu} \left\{ \frac{dP}{dz} + \rho g \right\} . \quad (21)$$

This equation can be integrated with respect to r using the following boundary conditions:

$$w = 0 \text{ at } r = R \text{ (no slip at a rigid wall) ,} \quad (22a)$$

$$\frac{\partial w}{\partial r} = 0 \text{ at } r = 0 \text{ (radial symmetry) .} \quad (22b)$$

This leads to:

$$w = \frac{1}{4\mu} \left\{ \frac{dP}{dz} + \rho g \right\} \{ r^2 - R^2 \} . \quad (23)$$

From this, the mass flux can be found by integration across the conduit:

$$G = \int_0^R \rho w \, 2\pi r dr , \quad (24a)$$

$$G = -\frac{\rho \pi R^4}{8\mu} \left\{ \frac{dP}{dz} + \rho g \right\} . \quad (24b)$$

The mass flux is proportional to R^4 and hence is extremely sensitive to the conduit size. This is all the more important as it is likely that the conduit gets enlarged by the erupting mixture through erosion (Carey and Sigurdsson, 1989) or melting (Bruce and Huppert, 1989). Note that, because of our choice of coordinate system, the pressure gradient is negative, and that the higher the mixture density, the smaller the mass flux.

Equation (24b) can be rewritten differently. The average velocity W is such that:

$$G = \pi \rho W R^2 . \quad (25)$$

Substituting this definition into Equation (24b) and rearranging, we find:

$$0 = -\frac{dP}{dz} + \frac{8\mu W}{R^2} - \rho g \quad (26)$$

which is simply the horizontal average of the momentum equation.

Constant conduit radius. To complete the solution, one must specify the conduit radius, the initial pressure and the density and viscosity of the mixture. As noted above, the density decreases together with pressure because of gas exsolution and expansion. For the moment, we neglect this effect and focus on the essential driving terms: we take ρ and μ to be constant. The mass flux G is constant, and hence Equation (24b) can be integrated from $z = 0$ (conduit bottom) to $z = H$ (conduit top):

$$\int_0^H G \, dz = G H = -\frac{\rho \pi R^4}{8 \mu} \{ [P(H)-P(0)] + \rho g H \} . \quad (27)$$

$P(0)$ can be identified with the pressure at the top of the magma chamber:

$$P(0) = P_a + \rho_r g H + \Delta P , \quad (28)$$

where P_a denotes the atmospheric pressure, negligible in this problem, $\rho_r g H$ the lithostatic pressure at depth H in country rocks of density ρ_r , and ΔP the chamber overpressure. Substituting for this expression into (27), one finds:

$$G = \frac{\rho \pi R^4}{8 \mu H} \{ \Delta P + (\rho_r - \rho) g H + [P_a - P(H)] \} . \quad (29)$$

This shows that an eruption is driven by two effects: the chamber overpressure and the density contrast between lava and country rock.

The mass flux depends on the overpressure ΔP and the exit pressure $P(H)$ (Fig. 7). Two cases obtain.

(1) Either the lava viscosity is very low or fragmentation has occurred. In this case, the exit pressure in steady-state conditions must be close to the atmospheric value. Thus:

$$P(H) \approx P_a . \quad (30a)$$

In this case, the eruption slows down as the chamber overpressure decreases. Figures 8 and 9 show some results which illustrate the influence of viscosity and conduit radius on mass flux. It can be seen that, for a realistic choice of parameters, the values are consistent with the observed ones given in the first section.

(2) During effusion of viscous lava, a dome or a spine of height e forms (Fig. 7), leading to an exit pressure given by:

$$P(H) = P_a + \rho g e . \quad (30b)$$

In this case, the eruption slows down because of two factors: one is that the chamber overpressure decreases and the other is that the exit pressure increases with e , i.e., as the lava dome builds up. A systematic relationship between eruption rate and dome height has been documented in the 1979 eruption of La Soufrière de Saint Vincent (Huppert et al., 1982) and during the period 1981-1983 at Mount St. Helens (Swanson et al., 1987). Eventually, the eruption stops when the following condition is satisfied:

$$e = \frac{\Delta P + (\rho_r - \rho) g H}{\rho g} . \quad (31)$$

Thus, the eruption may stop when the chamber is still overpressured, which is evidently an unstable situation. During the recent eruption of Mount St. Helens, several episodes of dome growth were interrupted by explosive events (Christiansen and Peterson, 1981). The full solution requires the knowledge of e as a function of time, i.e., one must treat the conduit flow coupled to the spreading of lava away from the vent. This is outside the scope of this chapter, and the interested reader should refer to Huppert et al. (1982).

Variable conduit radius. All else being equal, variations of conduit radius imply changes of velocity, as shown by the mass conservation equation. They also imply that

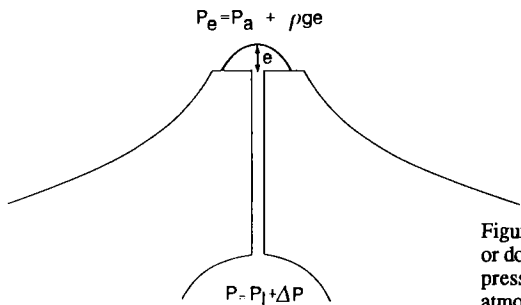


Figure 7. Sketch of the effect of a lava flow or dome above an eruptive vent: the effective pressure at the vent is not equal to one atmosphere but depends on the thickness of lava.

Figure 8. Mass flux in a conduit of 10 m radius and 3 km height as a function of chamber overpressure. Curves are drawn for various viscosities and densities. In these calculations, it is assumed that there is no density contrast between lava and country rock.

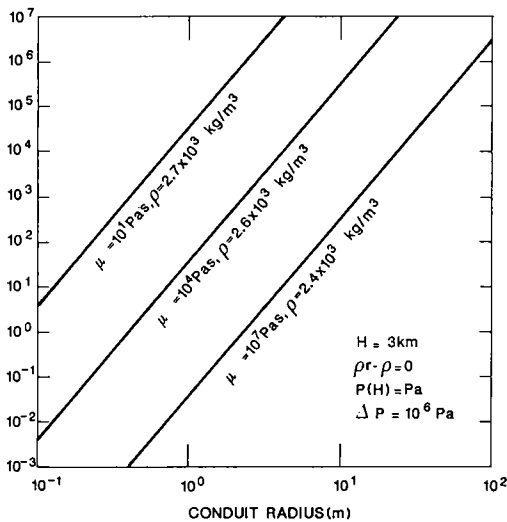
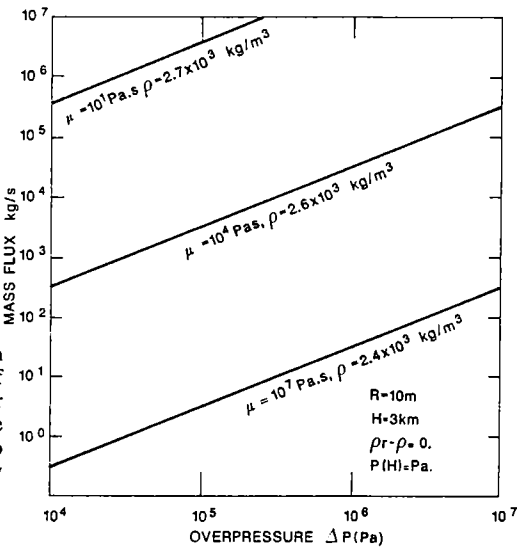


Figure 9. Mass flux as a function of conduit radius.

velocity cannot be purely vertical as the flow lines must be parallel to the conduit edges. However, unless size variations are very sharp, the implied dynamic effects are negligible compared to shear due to horizontal velocity gradients. Therefore, Equation (24b) still holds. It is more practical to write it in the following form:

$$\frac{dP}{dz} = -\rho g - G \frac{8\mu}{\pi \rho R^4} . \quad (32a)$$

Assuming again that the mixture properties do not vary, this can be integrated from $z = 0$ to $z = H$:

$$P(H) - P(0) = -\rho g H - \frac{8\mu G}{\pi \rho} \int_0^H \frac{dz}{R^4} . \quad (32b)$$

The solution therefore requires the specification of R as a function of z , which is difficult in practice.

It is important to realize that the pressure gradient in Equation (32a) is the dynamic pressure gradient during flow inside the conduit. Depending on the circumstances, this may be smaller or larger than the lithostatic pressure gradient which prevails in the surrounding immobile country rocks. Thus, there may be a pressure difference between the interior and the exterior of the conduit, which is supported by the rigidity of country rock. Wilson et al. (1980) developed an argument whereby an eruption always tends towards the lithostatic pressure gradient: they reasoned that any excess pressure would promote erosion of the conduit walls and enlargement of the conduit, and, conversely, that any pressure deficit would lead to narrowing. This constraint yields an equation for the conduit radius. Substituting the lithostatic pressure gradient ($-\rho_r g$) into Equation (32a) and rearranging, we obtain:

$$R^4 = G \frac{8\mu}{\pi \rho (\rho_r - \rho) g} . \quad (33)$$

If the assumption of constant mixture density and viscosity is valid, this equation implies that the conduit radius is constant. In the more realistic case of variable mixture properties, treated in the next section, this equation leads to variations of the conduit radius.

Conclusion. The mass flux of an eruption depends on the flow regime (laminar or turbulent), on the pressure conditions both in the magma chamber and at the vent, and on the density contrast between the rising lava and country rocks. In unfragmented conditions and in conduits of similar size, mass flux and eruption velocity are inversely proportional to lava viscosity. This accounts for the measured values given at the beginning of this chapter. Variations of eruption rate occur as the thickness of the lava at the vent changes..

COMPRESSIBLE FLOW

Laminar regime and variable properties

We have seen that both the lava viscosity and density vary as pressure decreases. Hence, the preceding demonstration is only approximate. The gas volume fraction depends on pressure, implying that both viscosity and density vary with height in the conduit. From (17b), pressure does not depend on r , the radial coordinate, and hence Equations (25) and (26) still hold. However, direct integration is no longer feasible owing to the non-linear equations for viscosity and density.

The momentum equation is kept in the form (32), with now ρ , μ and possibly R varying as a function of depth. One must specify the following functions:

$$\rho(\alpha) \quad (34a)$$

$$\mu(\alpha, x) \quad (34b)$$

$$R(z) \quad (34c)$$

The first of these is given by Equations (14) and (16) and requires the Equation of state of the gas phase. For the second, one must include the effects of bubbles as well as that of the concentration of dissolved volatiles. The solution requires the use of a computer, using a numerical procedure outlined in Figure 10. The most important point is that one must proceed by trial and error. One chooses a mass flux G and an initial pressure $P(0)$, then solve for the exit pressure $P(H)$. The solution is such that the exit pressure corresponds to the value specified either by (30a) or (30b), depending on the topography of the lava flow above the vent.

Choking conditions

When fragmentation occurs, flow becomes turbulent and the radial velocity profile changes in the conduit (Fig. 11). The flow has a complex structure with many small-scale eddies which keep the mixture stirred. One can define an average vertical velocity over several eddies: this is constant in the middle of the conduit and drops to zero in thin boundary layers at the walls. Another modification is that the inertial terms can no longer be neglected in the momentum balance.

The vertical velocity w can therefore be taken as independent of r to a good approximation and is equal to the horizontal average. It is convenient to write the governing equations in average form. Let us consider first a conduit of constant cross-section S . Mass conservation dictates that the mass flux per unit area G^* is constant:

$$G^* = \rho w = \text{constant} . \quad (35)$$

The momentum balance can be taken for a control volume $V = Sdz$ between heights (z) and $(z+dz)$ (Fig. 12). In steady-state, one writes that the vertical momentum in that volume stays constant:

$$\frac{d}{dt} (\rho w V) = 0 . \quad (36)$$

Several effects contribute to the momentum balance: the momentum fluxes through the horizontal surfaces at (z) and $(z + dz)$, pressure, shear at the vertical conduit walls and finally the weight of the mixture. Equation (36) imposes that their net effect is null, which is written as:

$$0 = S \{ \rho w_z^2 - \rho w_{z+dz}^2 \} + S \{ P(z) - P(z + dz) \} - Ldz \tau - \rho g V , \quad (37)$$

where τ is the wall shear stress and L is the perimeter of the conduit at height z ($2\pi R$ for a circle of radius R). Dividing by $V = Sdz$, letting dz tend to zero and rearranging, we find:

$$\frac{d}{dz} (\rho w^2) = - \frac{dP}{dz} - \frac{L}{S} \tau - \rho g . \quad (38a)$$

We now introduce the mass conservation constraint, which yields:

PROGRAM TO CALCULATE ERUPTION CONDITIONS

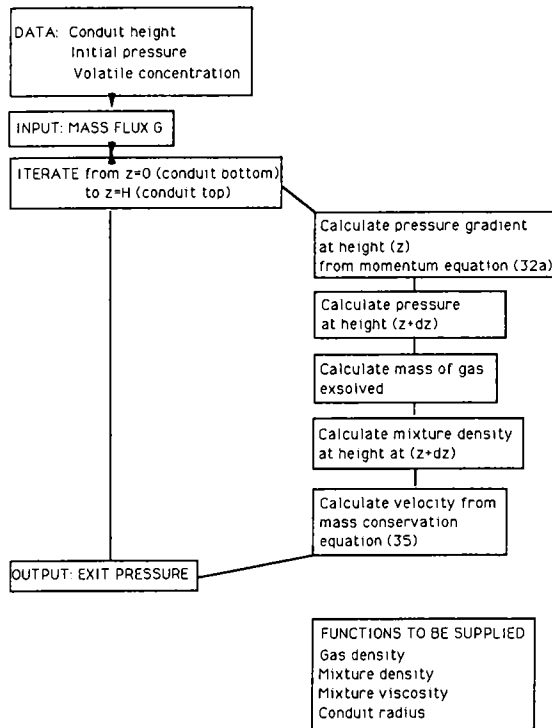


Figure 10. Outline for numerical code providing solution to the variable property compressible flow model. The basic principle is that the mass flux is not known a priori and must be found such that the exit pressure has the required value.

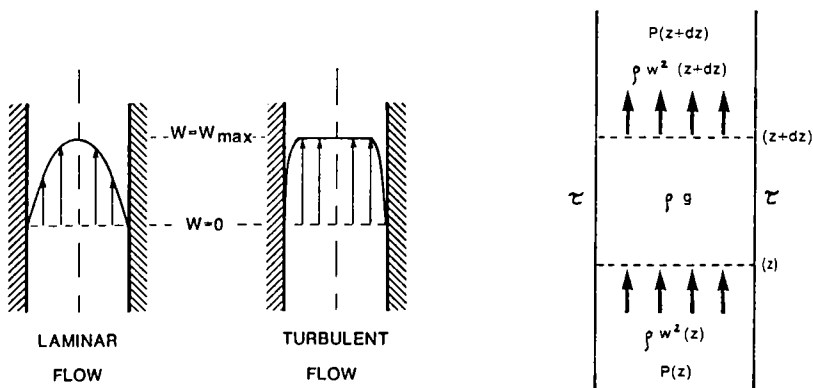


Figure 11 (left). Horizontal profile of velocity in a conduit, emphasizing the difference between laminar and turbulent regimes. In the latter case, the true flow field is much more complex than shown, with eddies maintaining the liquid well-mixed.

Figure 12 (right). Control volume to write the conservation of vertical momentum. Several effects act to change the momentum: the difference in the momentum fluxes through the surfaces at (z) and $(z + dz)$, stresses at the walls, pressure and weight.

$$G^* \frac{dw}{dz} = - \frac{dP}{dz} - \frac{L}{S} \tau - \rho g. \quad (38b)$$

As shown by the mass conservation equation, a change of density implies one of velocity. This density change depends only on pressure, and hence the derivative of velocity depends on that of pressure. From (35), one obtains:

$$\frac{dw}{dz} = \frac{d}{dz} \left\{ \frac{G^*}{\rho} \right\} = -G^* \frac{1}{\rho^2} \frac{d\rho}{dz} = -G^* \frac{1}{\rho^2} \frac{d\rho}{dP} \frac{dP}{dz}. \quad (39)$$

Substituting this result into Equation (38b) and rearranging:

$$\frac{dP}{dz} \left\{ 1 - \frac{G^{*2}}{\rho^2} \frac{d\rho}{dP} \right\} = - \frac{L}{S} \tau - \rho g. \quad (40a)$$

In the case of a cylindrical conduit of radius R, this is:

$$\frac{dP}{dz} \left\{ 1 - \frac{G^{*2}}{\rho^2} \frac{d\rho}{dP} \right\} = - \frac{2}{R} \tau - \rho g. \quad (40b)$$

The LHS of this equation becomes singular when the following condition is met:

$$\frac{G^{*2}}{\rho^2} \frac{d\rho}{dP} = 1, \quad (41a)$$

or, using (35):

$$w = \left\{ \frac{d\rho}{dP} \right\}^{-1/2}. \quad (41b)$$

This defines the maximum velocity in a conduit of constant cross-section called the "choking" velocity. In order to evaluate the derivative of density with respect to pressure, we consider again a mass M of liquid saturated at pressure P_i . At a lower pressure P, the mass of gas exsolved is:

$$M_g = \{ x(P_i) - x(P) \} M \quad (42)$$

The mass of liquid M_l is therefore equal to $(M - M_g)$. The total volume V is the sum of the liquid and gaseous parts:

$$\begin{aligned} V &= V_l + V_g = \frac{M_l}{\rho_l} + \frac{M_g}{\rho_g} \\ &= M \left\{ \frac{1 - [x(P_i) - x(P)]}{\rho_l} + \frac{x(P_i) - x(P)}{\rho_g} \right\}. \end{aligned} \quad (43)$$

Thus, the density of the mixture is:

$$\frac{1}{\rho} = \frac{V}{M} = \left\{ \frac{1 - [x(P_i) - x(P)]}{\rho_l} + \frac{x(P_i) - x(P)}{\rho_g} \right\}. \quad (44)$$

Differentiating with respect to pressure, we get:

$$\frac{d}{dP} \left(\frac{1}{\rho} \right) = - \frac{1}{\rho^2} \frac{d\rho}{dP} = (x(P_i) - x(P)) \frac{d}{dP} \left(\frac{1}{\rho_g} \right) - \left(\frac{1}{\rho_g} - \frac{1}{\rho_l} \right) \frac{dx}{dP}. \quad (45)$$

This shows explicitly that two factors act to change the mixture density: gas expansion and exsolution. The thermodynamic path must be specified to calculate the derivative of gas density with respect to pressure. As argued above, it is usually sufficient to consider isothermal conditions.

Chouet et al. (1974), Kieffer (1976) and Wilson et al. (1980) give numerical values for various gas and gas/liquid mixtures. For typical volcanic conditions, and various plausible H_2O and CO_2 contents, the choking velocity takes values between 300 and 500 m/s. These values define the maximum velocity in a conduit of constant cross-section, and hence also imply a maximum permissible mass flux. It is possible to exceed these velocities in conduits of variable cross-section with nozzle shapes (Shapiro, 1953, p. 89-90; Wilson et al., 1980). In practice, however, it is difficult to achieve much higher velocities and, indeed, there is little evidence that volcanoes do so. We found in the first section that measured velocity values during explosive eruptions of several types of volcanoes are close to the above estimates of the choking velocity. The important fact is that, by definition, the maximum velocity in a conduit does not depend on lava viscosity.

Conduit flow in explosive eruption regimes

To obtain more details on the evolution of variables in the conduit, one must integrate the momentum Equation (38b). After fragmentation, flow is in the turbulent regime such that the shear stress at the conduit walls is equal to:

$$\tau = C_f \rho w^2, \quad (46)$$

where C_f is a non-dimensional friction coefficient. In rough conduits, which is certainly the case of volcanoes, it depends on wall roughness according to an empirical law of the form:

$$C_f = a (h/2R)^b, \quad (47a)$$

where h is the roughness height. Coefficients a and b depend on the type of roughness and must be determined from direct flow measurements (Davies, 1972, p. 34). An upper bound may be obtained by taking $h = 2R$ and the coefficients of Huitt (1956), which leads to:

$$C_f \approx 0.055. \quad (47b)$$

This leads to high values of the shear stress. For example, considering an explosive eruption with a total mass flux of 10^7 kg/s in a conduit with 15 m radius, and taking a velocity of 300 m/s, one finds a wall shear stress of 2.3×10^5 Pa (2.3 bars). The importance of this is best seen by calculating the implied pressure drop. From Equation (40b), and again for a radius of 15 m, the friction pressure drop is 3.1×10^4 Pa/m (0.3 bars per meter of conduit). In comparison, the lithostatic pressure "drop" is about 2.5×10^4 Pa/m.

Generalized momentum balance

Wall roughness acts to enhance turbulence and thus tends to lower the critical Reynolds number. Thus, some volcanic eruptions with high mass flux and low viscosity lava may be in turbulent conditions before fragmentation. In theory, one must use the laminar equations up to the critical Reynolds number and then change to the turbulent formulation. However, as long as the Reynolds number is not too large, the laminar equations provide estimates which are good enough considering the other simplifying assumptions which have been made. Alternatively, one may also use the full momentum Equation (16) including inertial terms together with a generalized friction coefficient which reduces to

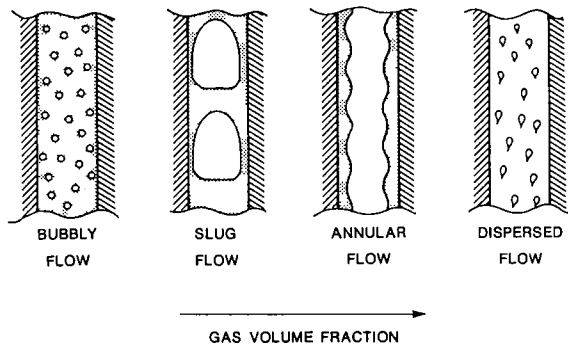


Figure 13. The four major regimes of separated liquid/gas flow. The gas volume fraction increases from left to right.

both cases in the limits of small and high Reynolds numbers. A good choice for a cylindrical conduit is the following:

$$C_f^* = \frac{16}{Re} + C_f \quad (48)$$

This allows a generalized momentum equation. Upon fragmentation, the Reynolds number must be taken as effectively infinite. It is clear that there is some degree of uncertainty in the friction law and hence the model predictions must be regarded as approximate.

Conclusion. In fragmented eruption conditions which are a characteristic feature of explosive volcanic activity, the mass flux is determined by compressible effects and does not depend on the viscosity of the melt. In conduits of constant cross-section, there is a maximum permissible velocity called the "choking" velocity.

OTHER EFFECTS ON FLOW CONDITIONS

Separated flow

The gas phase is lighter than the liquid and hence moves with respect to it. In general, therefore, one should solve for the gas and liquid phase separately. There are essentially four regimes of two-phase flow, defined by the geometrical relationships between gas and liquid (Fig. 13) and depending essentially on the volume fraction of gas. The bubbly regime is characterized by a suspension of discrete bubbles in a continuous liquid phase. At larger volume fraction, gas is carried in the form of slugs which are almost as wide as the conduit, leading to an intermittent regime. At still higher volume fraction, gas flows in a continuous stream. If the gas flux is not too large, this results in annular flow, with a central gas jet and liquid films against the conduit walls. At very high gas flux, such liquid films are not stable and are disrupted by the gas jet: this is the dispersed regime where a mixture of gas and liquid droplets rises turbulently in the conduit. These regimes have volcanic counterparts. Effusive activity is such that vesicular lava flows out of the volcanic vent, and hence corresponds to bubbly flow in the conduit. Strombolian activity is characterized by series of discrete explosions which are due to the bursting of large gas slugs: it is in the slug regime. Finally, in explosive forms of volcanic activity, a jet carrying lava clots and pumice fragments erupts at high velocity: This is in the dispersed regime.

In the volcanic case, the gas volume fraction is always small at depth. Thus, the various separated flow regimes develop out of bubbly flow, and hence imply transitions of regime. Such transitions require that the gas bubbles collect and coalesce, which can occur in two ways. At high gas volume fraction such that bubbles are in contact with each other, coalescence is achieved upon fragmentation and flow switches directly from the bubbly to the dispersed regime. At lower gas volume fraction, coalescence occurs as bubbles rise through liquid and collide against each other. This may proceed in the conduit during ascent if the bubbles rise through the liquid with large enough velocities. A more likely location is the magma chamber itself, where the liquid velocity is small. We shall see that there is evidence that it is the latter which prevails in true volcanic systems.

In conditions of separated flow, the momentum balance must be written for each phase separately, including a specification of how they interact with each other. Each one of the separated regimes corresponds to a specific kind of interaction. The flow equations follow from the same basic principles and are outside the scope of the present course. The interested reader should refer to books by Wallis (1969), Butterworth and Hewitt (1977), and to Vergnolle and Jaupart (1986) for volcanological applications. In practice, these equations do not lead to significant differences with the "homogeneous" model if the relative velocity of the two phases is small compared to the average velocity of the mixture.

In silicic volcanoes, the large viscosity of magma does not allow the gas bubbles to have significant velocity with respect to the liquid phase. Thus, separated flow effects are negligible and the homogeneous approximation used previously is strictly valid. The only flow transition is that of fragmentation.

In basaltic volcanoes, several lines of evidence indicate that flow is separated. Slug flow, which is the feature of Strombolian activity, cannot be achieved by a fragmentation-type process, i.e., when bubbles are in close packing: it requires bubble motion through the liquid. Several lines of evidence suggest that flow is already separated in the magma chamber. Gas composition studies at Kilauea volcano (Hawaii) show that magma is saturated with CO_2 in the magma chamber (Gerlach and Graeber, 1985). Direct measurements of the gas and lava mass fluxes during Strombolian explosions and Hawaiian fire fountains show indeed that gas accumulation takes place at depth prior to flow in the conduit (Chouet et al., 1974; Vergnolle and Jaupart, 1990). In these conditions, the mass conservation equation must be split in two parts: one for each phase. For liquid, this is expressed as before:

$$G_l = \rho_l (1-\alpha) w_l, \quad (49)$$

where w_l now denotes the velocity of the liquid phase. For gas, two components are involved: gas dissolved in the rising lava with mass fraction x and gas in a separated stream. The total mass flux of gas is therefore:

$$G_g = \rho_g \alpha w_g + x \rho_l (1-\alpha) w_l, \quad (50)$$

where w_g is the velocity of the gas phase, which is larger than that of liquid. This implies that the gas budget of an eruption must be made independently of the lava budget. In other words, the mass of gas which is erupted is not equal to that which was dissolved in the liquid erupted simultaneously.

The physics of bubble growth

We have so far assumed equilibrium conditions with two consequences: at pressure P , the mass of gas dissolved in magma and the density of the exsolved gas phase are calculated using the solubility law and the equation of state at that pressure.

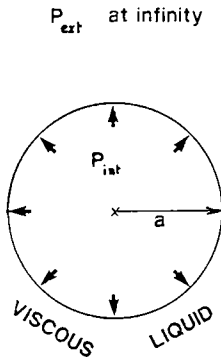


Figure 14. Diagram illustrating how a bubble expands in a viscous fluid. The expansion induces flow in the liquid and the pressure inside the bubble does not adjust to the far-field value instantaneously.

Bubble nucleation. Bubble nucleation requires supersaturation, i.e., the volatile concentration exceeds the solubility limit by a finite amount. Theory for this process in silicate melts is not well-developed (Toramaru, 1989; Bottinga and Javoy, 1990).

Bubble expansion. As pressure decreases, gas inside bubbles expands and hence bubbles grow larger. This volume increase is achieved by deforming the fluid outside the bubble, which can be very viscous. Such deformation is effected by a pressure difference between the bubble and the liquid. To elucidate the basic principles of this phenomenon, consider the following simple problem (Fig. 14).

An isolated spherical bubble with internal pressure P_{int} and radius a , in a fluid of viscosity μ at pressure P_{ext} . The origin of coordinate system is at the bubble center. In spherical symmetry, the only component of the velocity field is the radial one u , which depends only on r , the radial coordinate. The Navier-Stokes equations reduce to:

$$\text{Continuity: } 0 = \frac{\partial}{\partial r}(r^2 u) . \quad (51a)$$

$$\text{Momentum: } 0 = -\frac{\partial P}{\partial r} + \mu \left\{ \frac{1}{r^2} \frac{\partial}{\partial r} (r^2 \frac{\partial u}{\partial r}) - \frac{2}{r^2} u \right\} . \quad (51b)$$

The boundary conditions are as follows. Continuity dictates that the liquid follows the motion of the bubble interface at $r = a$:

$$u_{r=a} = \frac{da}{dt} . \quad (52a)$$

Continuity of normal stress at the bubble wall is written as:

$$P_{int} = P_{r=a} + \tau_{rr} \big|_{r=a} + \frac{2\sigma}{a} , \quad (52b)$$

where σ is the coefficient of surface tension. τ_{rr} is the normal viscous stress equal to:

$$\tau_{rr} \big|_{r=a} = 2\mu \frac{\partial u}{\partial r} \big|_{r=a} . \quad (52c)$$

Finally, the far-field pressure is given by P_{ext} , which is supposed to be a known function of time:

$$\lim_{r \rightarrow \infty} P = P_{\text{ext}} \quad (52d)$$

Using (52a) and the continuity Equation (51a), the velocity field is:

$$u = \frac{a^2}{r^2} \frac{da}{dt} \quad (53)$$

Substituting into the momentum balance yields:

$$0 = \frac{\partial P}{\partial r} \quad (54)$$

Thus, the pressure field is uniform in the liquid, which is true for all spherically symmetric motion. Substituting the velocity expression (53) into the normal stress equation, we obtain:

$$P_{\text{int}} = P_{\text{ext}} + \frac{2\sigma}{a} + 4\mu \frac{1}{a} \frac{da}{dt} \quad (55)$$

This expression shows that the internal pressure exceeds that in the liquid due to two effects. One is the effect of surface tension. In basaltic melts, the coefficient of surface tension takes values of 0.3-0.4 kg/s² depending on pressure (Khitarov et al., 1979; Walker and Mullins, 1981). Thus, for bubbles with radii larger than 0.01 mm, the surface tension effect amounts to less than 1 bar and can be considered negligible. The other effect is that of the normal stress due to the motion of the liquid phase. For viscous silicic magma, this viscous term can exceed 10 bars, depending on the rate of pressure variation (given by the rate of ascent).

Chemical diffusion. Consider that, at initial concentration of dissolved volatiles x_i at pressure P_i , gas bubbles are nucleated and start to grow. Assume further for simplicity that there is only one nucleation event, such that all bubbles appear at the same time and that their number remains constant thereafter. Consider finally for clarity that surface tension and viscous retardation effects are negligible. Subsequent pressure release causes expansion of the bubbles and diffusion of the volatile species into them. Local thermodynamic equilibrium at the bubble/melt interface requires that the concentration of dissolved volatiles at the interface is equal to the solubility at the interior gas pressure, i.e., P_{int} . Ignoring diffusion for the moment, as the magma rises, pressure decreases and the interface concentration decreases. In the magma far from the bubble, the volatile concentration has its original value x_i , which thus becomes larger than that at the interface. This sets up a concentration gradient in the liquid which drives chemical diffusion into the bubble. The mass flux of volatiles into the bubble is expressed as:

$$j = -D \frac{\partial x}{\partial r} \bigg|_{r=a} \quad (56)$$

where D is the diffusion coefficient.

Conclusion. The equilibrium assumptions made in the flow models lead to overestimates of the mass and volume of the gas phase in eruptions. A complete solution requires elaborate calculations and, unfortunately, stringent assumptions on the nucleation process.

GENERAL CONCLUSION

Flow models account for the basic observations that eruption velocities depend on lava composition in the effusive regime and are weakly sensitive to the lava composition in

explosive regimes. These models are useful to show which variables are important; however, they rely on simplifying assumptions which preclude detailed comparisons with true eruptions.

The mass flux and regime of volcanic eruptions depend on the viscosity and volatile content of magma and on pressure in the chamber feeding them. In turn, the eruption mass flux determines how the chamber is sampled. At high mass flux, an eruption induces strong flow in the chamber and hence magma mixing. Indeed, pumice samples from explosive eruptions contain mixed populations of crystals which did not grow from the same melts (Tait, 1988; Pyle et al., 1988). Therefore, the composition of erupted magma must be studied with due consideration of the way in which it has been transported to the surface. For example, chemical differences between a pyroclastic flow and a lava dome from the same eruption may be due solely to changes in the way the magma chamber was sampled. Another important effect to bear in mind in basaltic volcanoes is that the gas phase may behave independently from the liquid phase.

REFERENCES

- Blake, S. (1981) Volcanism and the dynamics of open magma chambers, *Nature* 289, 783–785.
- Blake, S. (1984) Volatile oversaturation during the evolution of silicic magma chambers as an eruption trigger, *J. Geophys. Res.* 89, 8237–8244.
- Blake, S. and Ivey, G.N. (1986) Magma mixing and the dynamics of withdrawal from stratified reservoirs, *J. Volcanol. Geotherm. Res.* 27, 153–178.
- Bottinga Y. and Richet, P. High pressure and temperature equation of state and calculation of the thermodynamic properties of gaseous carbon dioxide, *Am. J. Sci.* 281, 615–660.
- Bottinga, Y. and Javoy, M. (1990) Mid-ocean ridge basalt degassing: bubble nucleation, *J. Geophys. Res.* 95, 5125–5131.
- Bruce, P.M. and Huppert, H.E. (1989) Thermal control of basaltic fissure eruptions, *Nature* 342, 665–667.
- Buresti, G. and Casarosa, C. (1989) One-dimensional adiabatic flow of equilibrium gas-particle mixtures in long vertical ducts with friction, *J. Fluid Mech.* 203, 251–272.
- Burnham, C.W. (1979) The importance of volatile constituents, in *The Evolution of Igneous Rocks*, ed. by H.S. Yoder, pp. 439–482, Princeton University Press, Princeton, N.J..
- Butterworth, D. and Hewitt, G.F. (1977) *Two-Phase Flow and Heat Transfer*, Oxford Univ. Press, London, 514 pp.
- Carey, S.N. and Sigurdsson, H. (1985) The May 18 eruption of Mount St. Helens 2. Modelling of dynamics of the Plinian phase, *J. Geophys. Res.* 90, 2948–2958.
- Carey, S.N. and Sigurdsson, H. (1989) The intensity of Plinian eruptions, *Bull. Volcanol.* 51, 28–40.
- Chadwick, W.W., Archuleta, R.J. and Swanson, D.A. (1988) The mechanics of ground deformation precursory to dome-building extrusions at Mount St. Helens 1981–1982, *J. Geophys. Res.* 93, 4351–4366.
- Chouet, B., Hamisevicz, N. and McGetchin, T.R. (1974) Photoballistics of volcanic jet activity at Stromboli, Italy, *J. Geophys. Res.* 79, 4961–4975.
- Christiansen, R.L. and Peterson, D.W. (1981) Chronology of the 1980 eruptive activity, in: *The 1980 eruptions of Mount St. Helens*, Washington, U.S. Geol. Surv. Prof. Paper 1250, 17–30.
- Davies, J.T. (1972) *Turbulence Phenomena*, Academic, New York, 412 pp.
- Eichelberger, J.C., Carrigan, C.R., Westrich, H.R. and Price, R.H. (1986) Non-explosive silicic volcanism, *Nature* 323, 598–602.
- Einarsson, P. (1978) S-wave shadows in the Krfala caldera in NE Iceland - evidence for a magma chamber in the crust, *Bull. Volcanol.* 41, 1–9.
- Einarsson, P. and Brandsdottir, B. (1980) Seismological evidence for lateral magma intrusion during the July 1978 deflation of the Krfal volcano in NE Iceland, *J. Geophys.* 47, 160–165.
- Evans, J.R. and Zucca, J.J. (1988) Active high-resolution seismic tomography of compressional wave velocity and attenuation structure at Medicine Lake volcano, Northern California Cascade Range, *J. Geophys. Res.* 93, 15016–15036.
- Fierstein, J. and Hildreth, W. (1986) Ejecta dispersal and dynamics of the 1912 eruptions at Novarupta, Katmai National Park, Alaska, *EOS Trans. Am. Geophys. Union* 67, 1246.
- Freundt, A. and Tait, S.R. (1986) The entrainment of high-viscosity magma into low-viscosity magma in eruption conduits, *Bull. Volcanol.* 48, 325–339.
- Gerlach, T.M. and Graeber, E. (1985) Volatile budget of Kilauea volcano, *Nature* 313, 273–277.

- Houghton, B.F. and Wilson, C.J.N. (1989) A vesicularity index for pyroclastic deposits, *Bull. Volcanol.* 51, 451-462.
- Huitt, J.L. (1956) Fluid flow in simulated fractures, *Am. Inst. Chem. Eng. J.* 2, 259-264.
- Huppert, H.E., Shepherd, J.B., Sigurdsson, H. and Sparks, R.S.J. (1982) On lava dome growth, with application to the 1979 lava extrusion of the Soufrière of Saint Vincent, *J. Volcanol. Geotherm. Res.* 14, 199-222.
- Jaupart, C. and Vergnolle, S. (1988) Laboratory models of Hawaiian and Strombolian eruptions, *Nature* 331, 58-60.
- Jaupart, C. and Vergnolle, S. (1989) The generation and collapse of a foam layer at the roof of a basaltic magma chamber, *J. Fluid Mech.* 203, 347-380.
- Jeffreys, D.J. and Acrivos, A. (1976) The rheological properties of suspensions of rigid particles, *Am. Inst. Chem. Eng. J.* 22, 417-432.
- Khitrov, N.I., Lebedev, Y.B., Dorfman, A.M. and Bagdasarov, N.S. (1979) Effects of temperature, pressure and volatiles on the surface tension of molten basalt, *Geochem. Int.* 16, 78-86.
- Koyaguchi, T. (1985) Magma-mixing in a conduit, *J. Volcanol. Geotherm. Res.* 25, 365-369.
- Koyanagi, R.Y., Unger, J.T., Endo, E.T. and Okamura, A.T. (1976) Shallow earthquakes associated with inflation episodes at the summit of Kilauea volcano, Hawaii, *Bull. Volcanol.* 39, 621-631.
- Koyanagi, R.Y., Tanigawa, W.R. and Nakata, J. (1989) Seismicity associated with the eruption, in: *The Puu Oo eruption of Kilauea volcano, Hawaii: Episodes 1 through 20, January 3, 1983 through June 1984*, ed. by E.W. Wolfe, U.S. Geol. Surv. Prof. Paper 1463, 183-236.
- Kraynick, A.M. (1988) Foam flows, *Ann. Rev. Fluid Mech.* 20, 325-357.
- Lister, J.R. (1989) Selective withdrawal from a viscous two-layer system, *J. Fluid Mech.* 198, 231-254.
- McTigue, D. (1987) Elastic stress and deformation near a finite spherical magma body: resolution of the point source paradox, *J. Geophys. Res.* 92, 12931-12940.
- Princen, H.M. (1979) Highly concentrated emulsions, 1, *J. Colloid Interface Sci.* 71, 55-66.
- Princen, H.M. (1985) Rheology of foams and highly concentrated emulsions. II. Experimental study of the yield stress and wall effects for concentrated oil-in-water emulsions. *J. Colloid Interface Sci.* 105, 150-171.
- Pyle, D.M., Ivanovich, M. and Sparks, R.S.J. (1988) Magma-cumulate mixing identified by U-Th disequilibrium dating, *Nature* 331, 157-159.
- Richter, D.H., Eaton, J.P., Murata, K.J., Ault, W.U. and Krivoy, H.L. (1970) Chronological narrative of the 1959-1960 eruption of Kilauea volcano, Hawaii, U.S. Geol. Surv. Prof. Paper 537E, 73 pp.
- Rubin, A.M. and Pollard, D.D. (1987) Origins of blade-like dikes in volcanic rift zones, U.S. Geol. Surv. Prof. Paper 1350, 1449-1470.
- Ryan, M.P. (1988) The mechanics and three-dimensional internal structure of active magma systems: Kilauea volcano, Hawaii, *J. Geophys. Res.* 93, 4213-4248.
- Ryan, M.P. and Blevins, J.Y.K. (1987) The viscosity of synthetic and natural silicate melts and glasses at high temperatures and 1 bar (105 Pascals) pressure and at higher pressures. U.S. Geol. Surv. Bull. 1764, 563 pp.
- Schowalter, W.R. (1978) *Mechanics of non-Newtonian fluids*, Pergamon, 300 pp.
- Schwartz, L.W. and Princen, H.M. (1987) A theory of extensional viscosity for flowing foams and concentrated emulsions, *J. Colloid Interface Sci.* 75, 246-270.
- Shapiro, A.H. (1953) *The dynamics and thermodynamics of compressible fluid flow*, Wiley, New York, 647 pp.
- Sibree, J.O. (1934) The viscosity of froth, *Trans. Faraday Soc.* 30, 325-331.
- Sparks, R.S.J. (1978) The dynamics of bubble formation and growth in magmas: a review and analysis, *J. Volcanol. Geotherm. Res.* 3, 1-37.
- Spera, F.J., Yuen, D.A., Greer, J.C. and Sewell, G. (1986) Dynamics of magma withdrawal from stratified magma chambers, *Geology* 14, 723-726.
- Stauber, D.A., Green, S.M. and Iyer, H.M. (1988) Three-dimensional P velocity structure of the crust below Newberry volcano, Oregon, *J. Geophys. Res.* 93, 10095-10107.
- Stolper, E. and Holloway, J.R. (1988) Experimental determination of the solubility of carbon dioxide in molten basalt at low pressure, *Earth Planet. Sci. Lett.* 87, 397-408.
- Swanson, D.A. (1972) Magma supply rate at Kilauea volcano 1952-1971, *Science* 175, 169-170.
- Swanson, D.A. (1973) Pahoehoe flows from the 1969-1971 Mauna-Ulu eruption, Kilauea volcano, Hawaii, *Geol. Soc. Am. Bull.* 84, 615-626.
- Swanson, D.A., Duffield, W.A., Jackson, D.B. and Peterson, D.W. (1979) Chronological narrative of the 1969-1971 Mauna-Ulu eruption of Kilauea volcano, Hawaii, U.S. Geol. Surv. Prof. Paper 891, 59 pp.
- Swanson, D.A., Dzurisin, D., Holcomb, R.T., Iwatsubo, E.Y., Chadwick, W.W., Casadevall, T.J., Ewert, J.W. and Heliker, C.C. (1987) Growth of the lava dome at Mount St. Helens, Washington (USA) 1981-1983. *Geol. Soc. Am. Spec. Paper* 212, 1-16.

- Tait, S.R., Samples from the crystallizing boundary layer of a zoned magma chamber, *Contrib. Mineral. Petrol.* 100, 470-483.
- Tait, S.R., Jaupart, C. and Vergnolle, S. (1989) Pressure, gas content and eruption periodicity of a shallow crystallizing magma chamber, *Earth Planet. Sci. Lett.* 92, 107-123.
- Tanguy, J.C. (1980) L'Etna: Etude pétrologique et paléomagnétique, Implications volcanologiques, Unpub. doctoral thesis, University Paris 6, 618 pp.
- Taylor, G.I. (1932) The viscosity of a fluid containing small drops of another fluid, *Proc. Roy. Soc. Lond. A* 138, 41-48.
- Toramaru, A. (1989) Vesiculation process and bubble size distribution in ascending magmas with constant velocities, *J. Geophys. Res.* 94, 17523-17542.
- Touloukian, Y.S., Judd, W.R. and Roy, R.F. (1981) *Physical Properties of Rocks and Minerals. Data series on material properties, Vol.1-2*, McGraw-Hill, New York.
- Urbain, G., Bottinga, Y. and Richet, P. (1982) Viscosity of liquid silica, silicates and aluminosilicates, *Geochim. Cosmochim. Acta* 46, 1061-1072.
- Vergnolle, S. and Jaupart, C. (1986) Separated two-phase flow and basaltic eruptions, *J. Geophys. Res.* 91, 12841-12860.
- Vergnolle, S. and Jaupart, C. (1990) Dynamics of degassing at Kilauea volcano, Hawaii, *J. Geophys. Res.* 95, 2793-2809.
- Walker, G.P.L. (1980) The Taupo pumice: products of the most powerful known (ultraplinian) eruption? *J. Volcanol. Geotherm. Res.* 8, 69-94.
- Walker, D. and Mullins, O. (1981) Surface tension of natural silicate melts from 1200°C-1500°C and implications for the melt structure, *Contrib. Mineral. Petrol.* 76, 455-462.
- Wallis, G.B. (1969) *One-Dimensional Two-Phase Flow*, McGraw-Hill, New York, 408 pp.
- Wilson, L., Sparks, R.S.J. and Walker, G.P.L. (1980) Explosive volcanic eruptions, IV, The control of magma properties and conduit geometry on eruption column behaviour, *Geophys. J. Roy. Astr. Soc.* 63, 117-148.
- Wilson, L. and Head, J.W. (1981) Ascent and eruption of basaltic magma on the Earth and Moon, *J. Geophys. Res.* 86, 2971-3001.

MELT FRACTION DIAGRAMS: THE LINK BETWEEN CHEMICAL AND TRANSPORT MODELS

INTRODUCTION

The direct application of transport models to the long standing issues in petrology has often been a frustrating exercise. Rarely can one confidently identify detailed physical processes that drive petrologic diversity. Part of the difficulty originates in the construction of physical and chemical models; they often appear as fundamentally different enterprises. Chemical petrology has traditionally sought to characterize equilibrium states and to advance the formalisms of physical chemistry, the independent variables being taken from the usual thermodynamic ensemble: T, P, etc. Physical petrology differs in that the independent variables are space and time, and the effort is directed at identifying the structures and fluxes that follow from nonequilibrium states. It seems timely then to consider elements that are common to both chemical and physical descriptions of petrologic processes. A unification of this kind is guaranteed to succeed eventually as Nature does not seem to suffer the distinction.

The situation is particularly acute in the current generation of petrogenetic models. A quick review of the abstracts from the IAVCEI meeting on Continental Magmatism held in Santa Fe in 1989, reveals that petrologic diversity was attributed to magma mixing, crystal fractionation and partial melting in roughly equal proportions. Application of isotopic data has permitted estimation of the relative contributions of crustal and mantle "components" (Ruiz et al., 1988). When taken together in petrogenetic modeling, these processes are usually iterated until some degree of internal consistency is achieved. While all these assertions may well be true and data are available for a large number and variety of igneous suites, the issues regarding the time and length scales with which geochemical variations occur are not well constrained (Marsh, 1989a; Miller et al., 1988). The few studies where the temporal evolution is well constrained, e.g., Reagan et al. (1987) reveal markedly different time scales as a function of composition. Although many of the fluid models purported to mimic magma chambers have yielded a substantial literature on the behavior of pure fluids and salt solutions, less effort has been directed to the notion of geological constraints vis-à-vis geologic observables or the generation of testable hypothesis. This is testimony to the long absence of a detailed treatment of the most important element in magmatic systems: solidification.

Magmas are unlike other geophysical fluids, such as the oceans and atmospheres, in that their physicochemical history is dominated by phase changes. It is apparent from both laboratory and numerical experiments that many of the traditional formalisms of fluid dynamics can not be taken off the shelf and applied to magmatic systems, despite their convenience and the affection with which they are held (one notable exception being eruption processes and products). The self organization in crystallizing, viscous fluids is not a simple extension of that predicted by theory and experiment in constant property, single component fluids. The physical meaning of dimensionless numbers appearing in the governing equations for solidifying fluids must be interpreted and applied cautiously, a point well made by Bennon and Incropera (1987b) and Oldenburg and Spera (1990). Crystallization partitions the magma body into a region at the margins of solid and adjacent crystal-liquid "mush", and a fluid or "slurry" interior where crystallization occurs in an expanse of melt. The general physicochemical theory has been elucidated in the works of

Hills, Roberts and Loper (1978; 1983; 1988a,b,c; 1987), has been discussed in the geological context by Marsh (1988b; 1989b) and Morse (1988) and has been the subject of state-of-the-art numerical models originating in the engineering community (Beckermann and Viskanta, 1988a; Bennon and Incropera, 1987b; Thompson and Szekeley, 1989).

Our point of departure is to consider the generic magma system shown in Figure 1. A body of magma is cooling from the margin inwards and some time after intrusion we expect the system to partition itself into three regions: a region of solid which includes the country rock, an adjacent region of crystals and liquid (mush) where the melt fraction ranges from 0% to the that fraction at which the framework can no longer be self supporting, and a region of fluid magma (slurry). Depending on the phase diagram, initial geotherm, lithology of the country rock and thermophysical and transport properties, the regions of solid, mush and melt will distribute themselves according to the extant heat transfer processes. The primary question with respect to the schematic shown in Figure 1 is: what determines the partitioning of the crystallization processes between the mushy region and those in the interior? Both are potentially important in petrogenetic processes

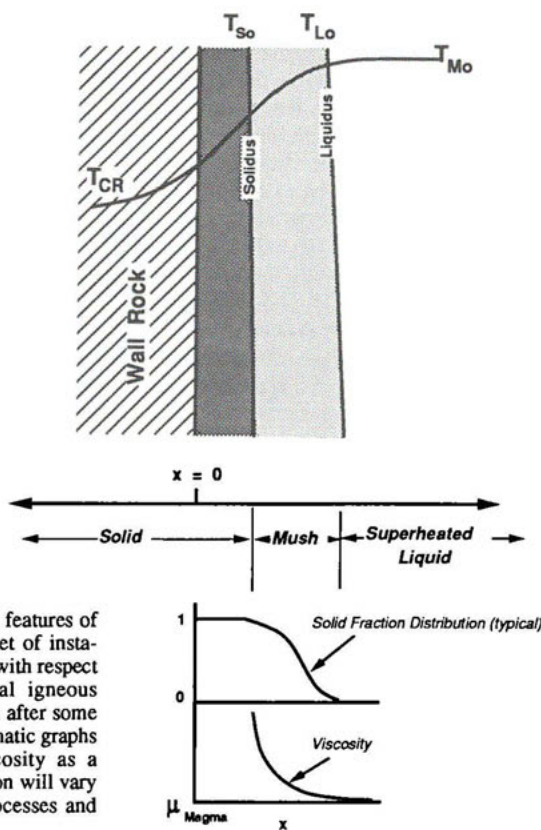


Figure 1. Coordinate system and general features of solidification problem. Prior to the onset of instability, the direction of growth is arbitrary with respect to gravity. The origin is the original igneous contact. The schematic shows the system after some time has passed; also shown are two schematic graphs of solid fraction distribution and viscosity as a function of distance. the actual distribution will vary depending on available heat transfer processes and thermo-physical properties.

(e.g., Langmuir, 1989; McBirney et al., 1985; Morse, 1988). In the mushy region crystal-liquid separation will depend on porous media flow, in the slurry crystal settling may occur. There is no question that substantial crystallization can occur in a distributed fashion in magma chambers as evidenced by numerous lava and ash flows with 10% to 50 % crystals. Much of the crystallization can also occur at the margins as documented at the Hawaiian lava lakes. Thus, when invoking crystal liquid separation, whether by solutal convection, crystal settling of some kind, magma mixing or partial melting, one needs to know the spatial and temporal distribution of mush and slurry (Marsh, 1988a). As discussed below, this also directly influences the rheology and hence the segregation mechanisms. Identifying the physical and chemical parameters that govern the partitioning of magmatic systems is one of the most geologically relevant challenges facing magma physics.

It is not difficult to appreciate that a treatment of transport phenomena should begin with as complete a solidification model as can be assembled. In this contribution we will consider one of the central components that links the thermodynamic treatments of magmatism with the attendant physical processes. This component is the melt fraction distribution, usually reported as a function of temperature: $f_m(T)$.

MELT FRACTION DISTRIBUTIONS

A general energy conservation expression

The extremely detailed structure of a crystal-liquid mush precludes direct, quantitative description. An alternative macroscopic approach is to invoke mixture theory which describes, in an formally average sense, the local state of the system. Mixture theory has provided a very serviceable description of flow in porous media and has recently been adapted to the study of crystallization (Beckermann and Viskanta, 1988a,b; Bennon and Incropera, 1987a,b; Oldenburg and Spera, 1990). A portion of the discussion below follows directly from these works and the interested student of transport is directed there for a thorough discussion of the continuum treatment of mixture theory. The fundamental components of mixture theory are equations for the conservation of mass, energy, linear momentum and chemical species. These usually form a formidable array of coupled, nonlinear partial differential equations which precludes direct interpretation in terms of a single dimensionless number or length scale. We will focus on only one of the conservation expressions: the conservation of energy, for it is here that the influence of the physical chemistry on the transport is most readily apparent.

The expression for conservation of energy is typically cast directly in terms of temperature, however there are advantages in considering the more primitive thermodynamically dependent variable enthalpy. The advantages follow from the fact that the temperature can be written as a continuous function of enthalpy and hence the most formidable nonlinearities attendant with phase change problems can be recast in terms of the relationship between the enthalpy, h , and temperature (Cao et al., 1989; Hunter and Kuntler, 1989). In practice this means that enthalpy can be written as a continuous variable and in numerical models, cpu intensive front tracking techniques can be avoided. Notable treatments of the enthalpy method to solve solidification problems are those of Baxter (1962), Shamsundar and Sparrow (1975), and Voller (1985).

Consider a general expression for the conservation of energy in an incompressible fluid where there is no viscous dissipation or heat sources such as radioactivity decay. Local thermal equilibrium is assumed, the temperature of adjacent liquid and solid phases is

assumed to be the same. In a fixed volume the conservation of specific enthalpy for an assemblage of n phases is

$$\frac{\partial}{\partial t} \left(\sum_{i=1}^n g_i \rho_i h_i \right) + \nabla \cdot \left(\vec{u} \sum_{i=1}^n g_i \rho_i h_i \right) = \nabla \cdot \left(\sum_{i=1}^n g_i k_i \nabla T \right), \quad (1)$$

where t is time, g_i is the volume fraction of phase i , ρ_i the density, h_i the specific enthalpy, k_i the conductivity, T the temperature, u the velocity, n the total number of phases, and the vector operators have their usual meaning. We will initially only consider systems where all the crystallization occurs at the boundaries and the porous crystal framework is infinitely rigid, hence the mush zone is delimited by the solidus and liquidus isotherms. Assuming constant heat capacity and that the difference between the enthalpy content in coexisting liquid and solid phases in the volume is equal to the latent heat, (1) can be written as:

$$\rho c^* \frac{\partial \theta}{\partial \tau} + \vec{U} \cdot \nabla \theta = \nabla \cdot (k^* \nabla \theta) + \frac{L}{\rho_l c_l (T_L - T_S)} \sum_{j=1}^{n-1} (\rho_l c_l - \rho_{sj} c_{sj}) \frac{dg_{sj}}{d\tau}, \quad (2)$$

where the subscript s indicates a solid phase, l the liquid phase and where

$$\rho c^* = \frac{g_l \rho_l c_l + \sum_{j=1}^{n-1} g_{sj} \rho_{sj} c_{sj}}{\rho_l c_l}, \quad k^* = \frac{g_l k_l + \sum_{j=1}^{n-1} g_{sj} k_{sj}}{k_l}, \quad (3)$$

and

$$\tau = \frac{t \kappa_l}{L}, \quad \vec{U} = \frac{\vec{u} \kappa_l}{L}, \quad \theta = \frac{T - T_S}{T_L - T_S}, \quad (4)$$

where κ_l is the liquid molecular thermal diffusivity, L the length scale in the direction of solidification, T_L the liquidus temperature, T_S the solidus temperature and where we invoke the saturation condition:

$$g_l + \sum_{j=1}^{n-1} g_{sj} = 1. \quad (5)$$

Note that temperature differences are normalized to the difference between the solidus and liquidus temperatures. This could be relaxed as Equation (2) can be written as a general equation for the entire expanse of solid-crystals-melt (Beckermann and Viskanta, 1988b; Bennon and Incropera, 1987a), however we wish to focus on the enthalpy changes associated specifically with phase change. When written in conjunction with ancillary equations for conservation of energy in solid and liquid only regions, Equation (2) is entirely consistent with mixture theory.

Equation (2) is difficult to apply in practice as it requires that the specific heats and latent heats be known for every phase as well as the instantaneous volume fraction of each phase as required by the latent heat term, the last one on the right hand side of (2). The large number of phases and complex exchange equilibria make it difficult to construct thermodynamically consistent forward models of phase volume fractions and system properties as a function of the intensive variables, notable exceptions being the models of

Ghiorso (1985) and Nekvasil (1988). In the absence of a complete thermodynamic formulation, phase equilibria experiments provide the only means by which to reliably obtain phase volume fractions. Unfortunately, this data is rarely reported and often only as volume percent melt and hence detailed knowledge of the volume changes in solid phases is usually unavailable. One expedient is to consider the system as an effective binary. This requires only that the volume melt fraction as a function of temperature be known. Thermophysical properties such as specific heat capacity and latent heat for the solid phases will need to be chosen to represent effective average values. While not entirely satisfying, such devices permit us to combine the numerical methods and laboratory data at hand.

If we chose to represent the system as an effective binary, Equation (2) will be written as:

$$\rho c^* \frac{\partial \theta}{\partial \tau} + \vec{U} \cdot \nabla \theta = \nabla \cdot (k^* \nabla \theta) - \frac{d\theta}{d\tau} \sum_{k=0}^i \frac{\theta^{k-1}}{Ste_k}, \quad (7)$$

where the Stefan number, Ste_k , is defined as:

$$Ste_k = \frac{c_s(T_L - T_S)}{\Delta h_{l-s} k a_k}, \quad (8)$$

and the volume melt fraction has been written as a general polynomial in dimensionless temperature:

$$g_l = f_m(\theta) = \sum_{k=0}^i a_k \theta^k. \quad (9)$$

The Stefan number(s), (8), are actually a sequence of dimensionless coefficients providing a measure of the sensible heat to the latent heat content in the crystal-liquid region. They are the dimensionless group that establishes the proper similitude for comparison of numerical and experimental results against real systems. The Stefan number(s) given in (8) also include the influence of the slope of the solid fraction distribution curve. For a system with a linear (constant slope) melt fraction distribution, i equal to one, a single Stefan number is obtained; the additional terms in the sequence account for the higher order derivative terms associated with a nonlinear distribution; the form given in (8) explicitly accounts for the nonlinearity of the melt fraction distribution. The nonlinearity due to the latent heat term of (7) appears explicitly for i greater than one.

In metallurgical and engineering applications the melt fraction distribution is often assumed to be linear and the lever rule is used to describe the melt variation with temperature. Examples and discussions of the expressions for the melt fraction distribution have been given by Clyne and Kurtz (1981) and Hills and Roberts (1988a) and are based on a modified form of the Scheil equation. The melt fraction distribution for geological materials need not be linear, see Figure 2, and the utility of writing the melt fraction, $f_m(T)$, as a general nonlinear function is immediately apparent. The coefficients in (9), a_k , are obtained by curve fitting experimental data. An additional and important consideration is that the melt fraction during melting may not be a simple reversal of the solidification curves as the crystals may be zoned and present a changing compositional face as melting proceeds (Hills and Roberts, 1988b; Roberts and Loper, 1987). In addition, volatile constituents may exist metastably in the form of structurally bound water in the inosilicates and phyllosilicates and upon melting yield large jumps in melt percentage over small

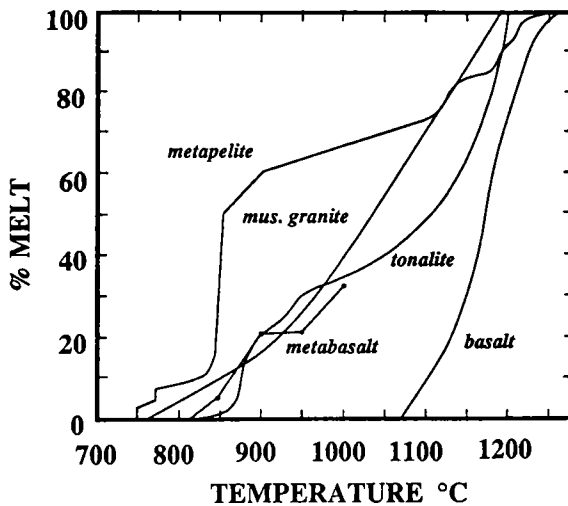


Figure 2. Melt fraction as a function of temperature for five rock types: basalt (Marsh, 1981), muscovite granite (Wyllie, 1977), tonalite (Rutter and Wyllie, 1988), metapelite (Vielzeuf and Holloway, 1988) and metabasalt (Beard and Lofgren, 1989). Patiño Douce and Johnston (1990) give a metapelite melting curve that is approximately linear between 800 to 1000°C.

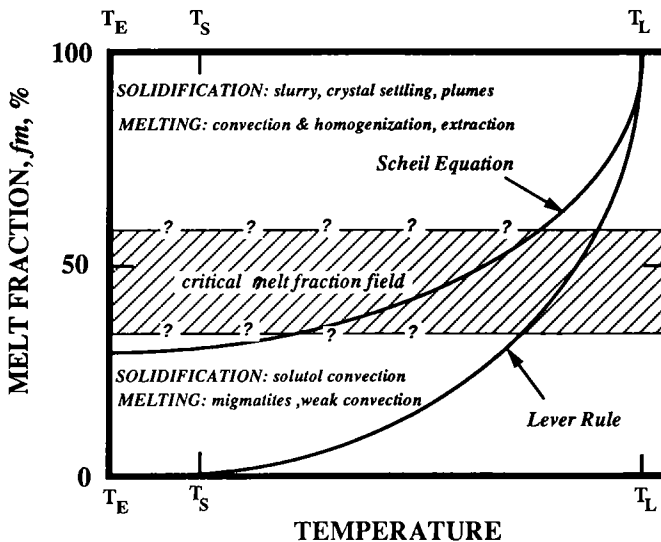


Figure 3. Schematic melt fraction as a function of temperature. Scheil equation and lever rule provide an envelope for natural systems as a function of crystal-liquid equilibrium. As shown, the critical melt fraction field is not truly a function of temperature and is drawn to represent the range of experimentally determined values.

temperature intervals as seen in Figure 2. A heterogeneous spectrum of crystal sizes will also influence the rate at which melting proceeds (Sheckler and Dinger, 1990). Finally, caution must be exercised when using the $f_m(T)$ obtained from experimental data, such as that in Figure 2, in transport models. These curves are constructed by interpolating between data points that represent discrete experiments where it is implicitly assumed that the kinetics of passing from one experimentally determined value of the solid fraction to the next along the $f_m(T)$ curve are negligible. One useful assumption is the fast-melting approximation of (Hills et al., 1983), which simply assumes that changes in temperature, no matter how small, yield an immediate and concomitant change in the local percent solid. Note that this does not imply that chemical equilibrium is maintained, e.g. diffusion in the solids may be neglected. This assumption seems to be applicable in the solidification portion of the coupled solidification/melting problem as nucleation is heterogeneous and under-coolings are demonstrably small (Cashman and Marsh, 1988). A discussion of the kinetics of reaction in the context of a general theory for the physiochemical evolution of a multicomponent system can be found in (Ghiorso, 1987; Hills and Roberts, 1988a).

Generic elements of melt fraction curves

In addition to playing a central role in the heat transfer, the melt fraction distribution largely determines the rheological partitioning and subsequent chemical evolution of the body. This partitioning will in turn delimit portions the phase diagram in which certain segregation processes may dominate, say crystal settling as opposed to solutal convection. The permeability and yield strength of the mush, and temperature and compositional differences of the mush and slurry, will also depend on the degree of chemical equilibrium between crystals and melt.

To appreciate some of the generic aspects of melt fraction distributions, consider Figure 3. Schematic melt fraction curves are shown and have been drawn as smooth curves for illustrative purposes. The abscissa is temperature with T_L being the liquidus, T_S the solidus and T_E the eutectic temperature. For a multicomponent system with solid solution the melt fraction distribution will depend on the degree of equilibrium maintained, or similarly whether crystals are removed. If equilibrium can be maintained, the lever rule provides the expression for melt fraction where it has been written for a binary with solid solution as (Bennon and Incropera, 1987a; Clyne and Kurtz, 1981):

$$f_m(T) = 1 - \frac{1}{1-k} \left(\frac{T_L - T}{T_F - T} \right) \quad (10)$$

where T_L is the liquidus temperature for a given composition, T_F the fusion temperature of the pure end member component and k is the partition coefficient (not to be confused with the use of k as the thermal conductivity in the preceding section). The partition coefficient is the ratio of the slope of the liquidus to solidus curves; if the liquidus and solidus lines are straight then k is a constant. In general it also will be a function of temperature. For perfect fractionation, the Scheil equation can be invoked to describe the melt fraction:

$$f_m(T) = \left(\frac{T_F - T}{T_F - T_L} \right)^{1/(k-1)}, \quad (11)$$

The nonequilibrium melt fraction will extend across a greater temperature range than the equilibrium case as the composition is constantly changing. This has been aptly

demonstrated by comparing the percent crystallization curves for equilibrium and nonequilibrium crystallization of olivine tholeiite as given by Figs. 13 and 5 of Ghiorso (1985). The crystallization interval for the equilibrium case is about 150 °C, for the nonequilibrium case about 400 °C. The lever rule and Scheil equation provide an envelope for natural systems, the actual position depending on the components, the ability of diffusion in the solid to sustain equilibrium, and the rate of heat removal.

Spanning this envelope in Figure 3 is a field labeled critical melt fraction. The intent is not to portray this field explicitly as a function of temperature but rather just to identify that portion of the diagram consistent with existing experiments. This field delimits the region of mush from the slurry. Recall that the mush was defined to be the region of crystals and liquid where the melt fraction was low enough to yield an effectively rigid framework of crystals. The slurry is that portion where crystals exist in an expanse of melt. This rheological subdivision of the chamber can then be mapped directly onto the phase diagram, or melt fraction distribution curve in the absence of a phase diagram. The self partitioning of a multi-phase system was explored in the axiomatic works work of Brandeis and Marsh (1989; 1990) who introduced the concept of the convective liquidus. The convective liquidus is defined as the isotherm associated with the transition from a mush to a slurry. Thus, when identifying a temperature difference to scale thermal convection in the slurry, the temperature difference will be that between the intrusion temperature and the convective liquidus. One implication of this work is that the temperature differences available to drive convection in multicomponent systems are dynamic quantities and do not necessarily follow from initial temperature differences and geometry (again see discussions by Bennon and Incropera (1987b) and Oldenburg and Spera (1990)). A related concept originating in the metallurgical literature is the concept of the contiguity limit. Contiguity is a measure of solid-to-solid grain contact in partially molten systems (German, 1985; Miller et al., 1988; Ryerson et al., 1988) and the contiguity limit is the volume melt fraction at which a "rigid" aggregation of crystals takes on a suspension like behavior. In the geophysical literature this transition is called the critical melt fraction (Arzi, 1978; van der Molen and Paterson, 1979; Wickham, 1987).

Identifying the convective liquidus in real systems is difficult; there is little unequivocal geological data to indicate what melt fraction corresponds to the convective liquidus. In the experiments of Brandeis and Marsh, as in the Hawaiian lava lakes, the convective liquidus was approximately the intrusive temperature. Lava flows have a upper limit of crystallinity of ~50% (Marsh, 1981); granitic rock undergoing melting by the flow of basalt in the feeder dikes of the Columbia River basalt begins to disaggregate at about ~50% melt (W. Taubeneck, oral comm., also see Kitchen (1989)). Experiments by Jurewicz and Watson (1985; Miller et al., 1988) also suggest a critical melt fraction of ~50%. At "high" strain rates, 10^{-5}s^{-1} , van der Molen and Paterson (1979) propose that the critical melt fraction is 30-35%. Experiments on partially molten granitic aggregates by Dell'Angelo and Tullis (1988) display a variety of deformation mechanisms from cataclasis to melt enhanced deformation as a function of melt fraction in the range of 0-15%. From the available examples, it is clear that the constitutive relations of a partial melt will depend on the strain rate, physical chemistry and grain size, making it difficult to generalize the rheology of partial melts.

Viscosity in magmatic liquids is primarily a function of temperature, crystal content and composition (McBirney and Murase, 1984; Ryerson et al., 1988; 1988; Spera et al., 1982). The viscosity of rhyolites can change up to seven orders of magnitude over approximately 700 °C, the viscosity of tholeiitic basalt by two orders of magnitude over 400 °C. It is important to note that in the physical modeling of the flow of interdendritic

liquid the appropriate viscosity expression will be that of a crystal free fluid, although still temperature and compositionally dependent, and formulations such as those given by Shaw (1969; 1972) and Bottinga and Weill (1972) can be used. For convection in the slurry where intratelluric crystals will be present, the viscosity expressions of Ryerson et al. (1988) and Spera et al. (1988) should be employed. Strongly temperature dependent viscosity influences convection by partitioning the flow field into a region of cold, viscous boundary layers where the strain rates are an order of magnitude (typically more) less than that of the free fluid, thus creating an effectively smaller container where the temperature differences available to drive convection are those between the interior and the temperature where the viscosity increases by about an order of magnitude. Although the variable viscosity reorganizes the flow field, the parameterization of the heat transfer can be done with the usual dimensionless groups where an effective viscosity is used in place of the true viscosity (Chu and Hickox, 1990). Variable viscosity strongly inhibits the efficiency of solutal convection as a means of melt segregation. This is simply and dramatically shown in the work of Tait and Jaupart (1989) and Chen and Thangram (1982). Tait and Jaupart point out that there are two time scales to be considered in extrapolating laboratory experiments to real systems, one for crystal growth and one for the convective instability. The net result is that solidification proceeds on essentially conductive time scales. Although some local compositional convection did occur in the experiments, it is not clear that this will occur in geological systems where the fluid density changes are not monotonic and viscosities relatively high. The net result is that fluid experiments with low and constant viscosity salt solutions may show a degree of self organization that is not consistent with real magmas.

The specification of the permeability in the magmatic mush is difficult; bear in mind that permeability K , like thermal and species diffusivity, is a tensor quantity and is described by nine coefficients. The permeability is an important property when estimating the efficiency of intercrystalline flow driven by the buoyancy changes associated with crystallization. One expression for steady fluid velocity in a porous media is given by Darcy's Law (Lowell, 1985):

$$\vec{u} = -\frac{K}{\mu}[\nabla P + \rho \vec{g}], \quad (12)$$

where u is the fluid velocity, K the permeability, μ dynamic viscosity, ρ density and g the acceleration of gravity. Note that one important parameter group is the ratio of the permeability to the dynamic viscosity. They vary in a sympathetic manner with regard to the efficiency of porous flow: when the permeability is low the viscosity will be high. The net effect being an inhibition of flow. Conversely, when the permeability is high the viscosity will be lower.

Permeability expressions are usually constructed as a function of porosity by invoking a simple geometrical model, such as a ball and stick or parallel plates, for the porous framework (Bear, 1972). It is commonly assumed that the permeability is locally homogeneous and isotropic: all the off diagonal terms are zero and the on diagonal terms have the same magnitude and so are functionally scalar quantities. One expression for permeability commonly employed is the Kozeny-Carman equation (Bennon and Incropera, 1987b):

$$K = K_o \left[\frac{f_m^3}{(1-f_m)^2} \right], \quad (13)$$

where the constant K_o is a function of the detailed structure of the crystal interfaces. Beckermann and Viskanta (1988b) use an expression similar to (12):

$$K = \frac{d_m^2 f_m^3}{175(1 - f_m)^2}, \quad (14)$$

where d_m is the mean diameter of the crystals. An alternative form based on a microscopic flow between parallel plates is (Lowell, 1985):

$$K = \frac{d_m^2 f_m^2}{72\pi}, \quad (15)$$

Permeability expressions (13-15) are thought to be most appropriate for moderate melt fractions, f_m less than about 50%. In practice, determining the permeability is largely an empirical exercise.

It is not clear how to extrapolate from the existing body of laboratory work on melt distribution (Daines and Richter, 1988; Jurewicz and Watson, 1985; Waff and Bulau, 1982) to high melt fractions and to establish an expression for permeability as a function of temperature and hence percent melt. Although the laboratory experiments provide an expression for the melt fraction as a function of temperature, it is less clear how an interconnected network forms. The experiments of Daines and Richter (1988) show a remarkable degree of interconnectivity: almost all melt pockets were connected at melt fraction as low as 2% in a powered mixture of olivine and basalt powder. Thus, perhaps it is a safe assumption that the porosity can be used directly in the permeability expressions given above.

The melt fraction partitions the phase diagram by virtue of rheological constraints and by controlling the efficiency of solutal convection. One feature of Figure 3 is that the temperature differences available to drive thermal convection and efficient crystal liquid segregation will be, at most, the difference between the intrusion temperature and the temperature corresponding to the intersection of the melt fraction curve and the critical melt fraction field. The efficiency of fractionation driven by the density changes attendant with crystallization in the mush will depend critically on the ratio of the permeability to the dynamic viscosity.

GEOLOGICAL IMPLICATIONS

The MASH hypothesis and a baseline physical state

One interesting new paradigm for convergent margin magmatism is the MASH, melting-assimilation-storage-homogenization hypothesis of Hildreth and Moorbath (1988) that was developed to explain arc magmatism in the Andes. This carefully documented work suggests that much of the base-level chemical signature of arc magmas is generated in the deep crust by repeated interaction, i.e. underplating and penetrative intrusion of mantle basalts with deep crust. A variety of compositions can be generated by melting rocks with cratonic affinities, or perhaps more importantly, by remelting previous underplated material with subsequent homogenization. This process ultimately yields a "steady-state" region at or above the basalt solidus with a concomitant reduction in the ductility contrast. These highly ductile interactions have been documented in the field (DeBari et al., 1987). Thus,

the usual viscosity barriers that inhibit differentiation (Marsh, 1988a) are removed and a wide variety of physicochemical interactions are possible. A similar hypothesis has been developed in island arcs to explain the origin of andesite (Takahashi, 1986).

There are two corollaries that follow from the MASH hypothesis: first, there is a base-level physical state that could provide a conceptual framework for the physical history as the base-level chemical signature does for the chemical history. Secondly, that magmatism is explicitly a crustal scale phenomena and the notion and quantification of path dependence should be addressed. The good news is that this clears the air for paradigms whose content may involve as much structural and metamorphic as igneous petrology. The bad news is it requires field and lab work on a scale difficult to manage and fund in a geological environment where no one is sure what is signal and what is noise. The length scales over which heterogeneity are manifested are highly variable depending on the quantity being measured, e.g. isotopes, major elements, etc., as discussed by (Hill et al., 1985; Miller et al., 1988). In the hunt for generic elements in a magmatic system, establishing a possible parent magma or isotopic provenance is only one of a number of elements that will ultimately comprise a sufficient "explanation".

The baseline physical state will be determined by the competing processes of penetrative intrusion of basaltic magmas, partial melting, ascent and segregation. The melting of lower to mid crustal rocks to generate petrologic diversity has been invoked: in Mexico, Mahood and Halliday (1988) find that the stable and unstable isotopic data are consistent with an origin of the rhyolites from melting of lower crustal rocks; in the central Cascades, Smith and Leeman (1987) suggest that mantle derived magmas induced melting at crustal levels to generate dacitic magmas. Experimental work by Beard and Lofgren (1989) indicates an origin for tonalites by melting of metamorphosed mafic rocks. Experiments by Conrad et al. (1988) show that the silicic magmas of the Taupo Volcanic zone could have originated by partial melting of a metaluminous source. The major and trace element and isotopic character of some plutonic rocks is also consistent with an origin by partial melting of mafic to intermediate deep crust, and subsequent mixing with partial melts of more cratonic affinities (Chappell and Stephens, 1988; Fleck and Criss, 1985; Gromet and Silver, 1987; Hawkesworth et al., 1982; Hill et al., 1988; Hill et al., 1986; Saleeby et al., 1987; Whitney, 1988).

The large volumes and extended duration of silicic magmatism in extensional regions appears to require a continuous source of more primitive and hotter magma to generate and sustain long lived magmatic centers, e.g. Halliday et al. (1989). This has been discussed in some length by Barton (1989), Hildreth (1981) and Whitney (1988) and proposed more recently in Nevada and Utah by Gans et al. (1989), Best et al. (1989) and Warren et al. (1989). One particularly interesting example is the relationship between the Timber Mountain Tuff and the Black Mountain plutonic complex which may provide an exceptional opportunity to explore the relationship between mafic plutonism and silicic ignimbrites (Vogel and Cambray, 1990). Glazner and Ussler (1988) argue that these underplated basalts can be geophysically imaged and are responsible for midcrustal increases in the P wave velocity. It has also been proposed that this underplating and penetrative intrusion of basaltic magma at upper crustal magma chambers is probably the source of enclaves in plutonic rocks and mingled textures in volcanic rocks (Bacon, 1986; Grove et al., 1988), and has also been proposed to be the cause of eruptions (Eichelberger, 1980; Warren et al., 1989).

The generic element in all the studies given above is the transport of heat and mass by mafic magmas, and the role of crustal melting; including young mafic crust that is

isotopically indistinguishable from mantle, see discussion in Davidson et al. (1987). This does not preclude closed system crystal fractionation as an important process. The distinction between crystal fractionation and partial melting may well be irrelevant, or at least geochemically indistinguishable, in a region that is maintained at or near the basalt solidus and subject to re-intrusion. This could yield a magmatic complex subject to some of the kind of melting and extraction phenomena described by Naslund (1986), Beard (1990) and Fountain et al. (1989).

The extent of partial melting and subsequent convective homogenization will depend on a variety of factors: the initial temperature contrast between the basalt and the surroundings, the melt fraction distribution, and the thermophysical properties of the materials (Bergantz, 1989b; Fountain et al., 1989). The melt fraction is critical as it determines both the efficiency of porous media convection and compaction in moving the melt away from the body. For a single episode of underplating, the maximum melt fraction at the contact is plotted as a function of initial temperature in Figure 4; the calculations are discussed in Bergantz (1989b). The contiguity limit was taken to be ~50% and is shown as a dashed horizontal line. The important point is that the host lithology exerts a strong influence on the subsequent transport by virtue of the melt fraction distribution. In these calculations it was assumed that the two phase region was infinitely rigid and hence no compaction could occur. Fountain et al. (1989) incorporate a compaction model with underplating and demonstrate that the coupled two phase flow can yield significant amounts of magma that will collect into a chamber. The upward progress of this seems limited to less than about the half width of the mafic intrusion.

Both the models of Bergantz (1989b) and Fountain et al. (1989) assumed that the heat transfer can be adequately characterized by conduction. Huppert and Sparks (1988) have explored the interaction between basalt and crust with laboratory experiments that demonstrate the variety of fluid instabilities that can occur during underplating with vigorous convection. These models find their greatest application in systems with substantial amounts of superheat as their "basalt" was superheated and had a lower melting temperature than the countryrock. Experiments done by Bergantz (1989a), in which the relationship of melting ranges between the model "basalt" and "countryrock" was maintained and the "basalt" was intruded at the liquidus did not demonstrate vigorous convection. These differing results indicate that geological systems can have diverse responses to underplating depending on the degree of superheat, supercooling, melt fraction distribution and viscosity relations.

If the magma is superheated, the convective liquidus is very near the solidus or the system is open, such as flow in a dike, the progress of solidification will undergo some interesting time dependent behavior. This has been explored by in a number of papers in the engineering literature, e.g. Cheung and Epstein (1984) and subsequently in the geological case by Huppert and Sparks (1989). These formalisms have been extended by Bergantz (1990) for systems with a temperature dependent solid fraction distribution. Initial cooling at the margins upon intrusion or dike flow will yield a region of mush whose thickness will reach a maximum and then retreat in the face of a continued thermal flux supplied by convection. If the enthalpy content of the chamber is infinite then the early formed region of mush and solid will retreat, ultimately yielding a contact that has the same temperature of the flowing melt, providing the thermal conductivities are the same. If the enthalpy content is finite, an oscillation can occur: solidification and mush growth at early times, followed by retreat of the mush as convection proceeds and the mush may not retreat all the way back to the contact as the vigor of convection itself is decreasing. As convection dies the mush thickness grows again. This is shown in Figure 5 (see Bergantz

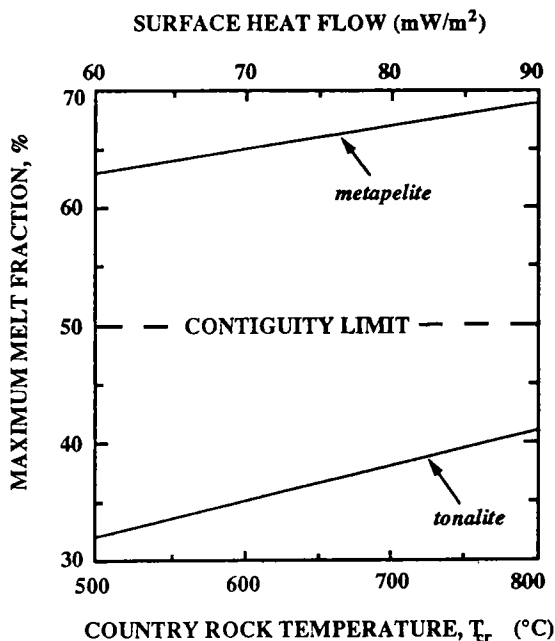


Figure 4. Maximum melt fraction as a function of the ambient temperature in the country rock. This maximum will occur near the contact and is not the average melt fraction of the partially molten region. Typical surface heat flow is plotted along the upper axis, basalt temperature at time of underplating is 1250°C.

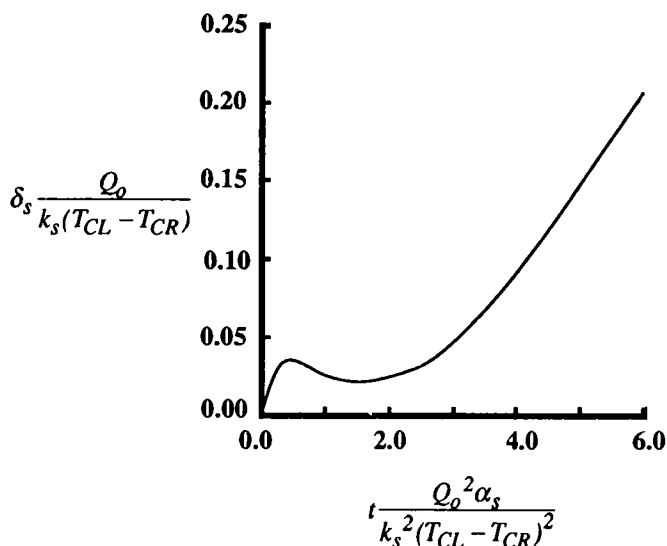


Figure 5. Dimensionless position of solidus isotherm relative to contact as a function of dimensionless time for a closed, convecting multicomponent system where melting is also occurring at the margins (Bergantz, 1990). Parameters: Q_o is convective heat flux at time equal zero, α the thermal diffusivity, k conductivity, T_{CL} convective liquidus temperature, T_{CR} country rock temperature in the far field, t time, d position of the solidus.

(1990) for details of the calculations) which is a plot of the dimensionless thickness of the solid as a function of dimensionless time, note the oscillation per the discussion above.

The geological implications of these types of coupled solidification/melting behavior are that some degree of fractionation can be attained by virtue of ascent and that repeated intrusion can yield spatial variations in melt fraction distribution in a manner that is difficult to generalize. This segregation may be important in the internal chemical organization of magma moving upward in the crust where material that crystallizes early on may or may not be remelted to yield cryptic spatial heterogeneities. This is also important in terms of understanding the heat transfer systematics attendant with plutonism where it is commonly assumed that efficient internal convection must occur as a means of reducing the ductility contrast between magma and country rock e.g. Mahon et al.(1988). As shown above, the heat transfer at the margins will depend on the solidification process which will inhibit efficient heat transfer to the surroundings. Thus, the isotherm that defines the region where yielding will occur will migrate into the intrusion and the magma body will then be intruding itself and telescoping upward into the crust leaving refractory phases and forming concentrically zoned suites. The net effect of this rheological partitioning is to induce a vertical stretching of magma bodies in the mid crust, below the brittle-ductile transition. Understanding this processes by examining the plutonic record is difficult as the strain field as given by rock fabrics can have contributions from a variety of processes (Paterson et al., 1989).

The thermal and mechanical perturbations that are ultimately manifested as volcanoes and plutons represent crustal scale processes (Chappell and Stephens, 1988; Hollister et al., 1989; Miller et al., 1988). Intermediate to evolved plutons in the mid-to-deep crust are testimony to the fact that petrogenetic processes need not all occur at 1kb (Marsh, 1989a) or require rapid cooling with vigorous convection. The demonstrably open system character of magmatism in every tectonic setting, and the striking diversity of chemical types in some volcanic fields, suggests that magmas are gregarious and that magma chambers are essentially thermal windows in the crust which act as manifolds (Hill et al., 1985). Magmatic systems assemble themselves from the bottom up, perhaps yielding a crustal scale thermal regime as pictured by Marsh (1984) and shown schematically in Figure 6, where the perturbation isotherms which delimit the region of mobilization open outward and downward.

Quantitative treatments of the crustal thermal regime during intrusion can be found in Marsh (1982), Singer et al. (1988), Mahon et al. (1988) and Mareschal and Bergantz (1990). One useful way to demonstrate the way in the initial geotherm, volume and periodicity of intrusion, and influence of the thermal regime at the lower boundary is to write the heat equation as a Green's function formulation where it is assumed that the heat transfer can be written as a linear equation (no temperature dependence in thermophysical properties or source term):

$$T(x, z, t) = \iint G(\bar{r}, t | \bar{r}', \tau) \Big|_{\tau=0} F(\bar{r}') dz' dx' + \frac{\alpha}{k} \iiint G(\bar{r}, t | \bar{r}', \tau) Ag(\bar{r}') dz' dx' d\tau - \frac{\alpha}{k} \iint \frac{\partial G}{\partial z} \Big|_{z=H} T_H(x', \tau) dx' d\tau \quad (16)$$

where α is the thermal diffusivity, k conductivity, r a general spatial variable, $F(r)$ the initial geotherm, T_H the temperature at the bottom of the crust or region of underplating, $g(r, t)$ the thermal source term distribution for the sensible and latent associated with

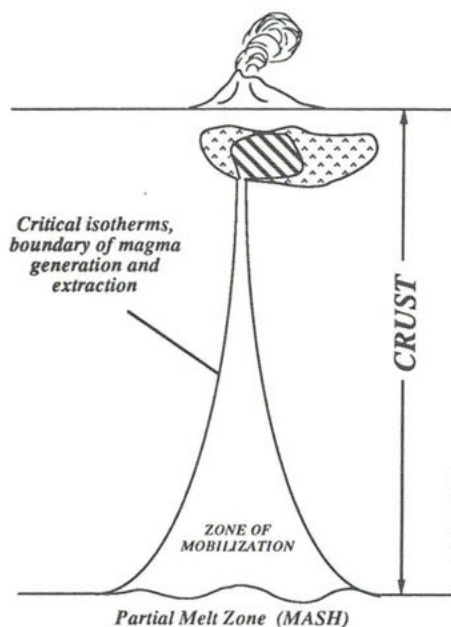


Figure 6. Schematic of crustal scale perturbation thermal field after Marsh (1984). Magmas that ultimately form shallow complexes can have contributions from a number of crustal levels.

intrusion and $G(r,t;r,\tau)$ the Green's function. The actual form of the Green's function will depend on the coordinate system, but should be understood to be the response of a homogeneous system with homogeneous boundary conditions to a impulse source. It is apparent from (16) that the temperature field in the crust can be written as the convolution of the Green's function with the initial geotherm, lower boundary temperature and thermal source term. The influence of crustal rheology and of melt fraction, as a function of lithology, will appear in the explicit form given for the source term, $g(r,t)$. It is this term which will determine the general morphology of the perturbation isotherms shown in Figure 6. In detail, the perturbation isotherms will not be smooth, that will depend on the form of $g(r,t)$ (Bergantz, in prep.) and on the intrusion to extrusion ratio, a quantity difficult to estimate. However, it is useful to inquire whether the MASH paradigm can be extended to a crustal scale by virtue of a thermal parameterization.

The melt fraction distribution plays a key role in quantifying magmatic processes at all scales. It provides a means of understanding how the magma chambers are partitioned in terms of the progress of solidification, rheology, and eligibility to undergo mixing and extraction. A wide variety of fluid structures have been proposed for magmas and there is no question they play a role in driving petrologic diversity. Experimental work to provide volume melt and solid phase fraction diagrams are urgently needed to further refine the detailed structures and their relevance to magmatic processes.

REFERENCES

- Arzi, A. A. (1978) Critical phenomena in the rheology of partially melted rocks. *Tectonophysics* 44, 173-184.
- Bacon, C. R. (1986) Magmatic inclusions in silicic and intermediate volcanic rocks. *J. Geophys. Res.* 1986, 6091-6112.
- Barton, M. D. and Hanson, R. B. (1989) Magmatism and the development of low-pressure metamorphic belts: Implications from the western United States and thermal modeling. *Geol. Soc. Am. Bull.* 101, 1051-1065.
- Baxter, D. C. (1962) The fusion time of slabs and cylinders. *J. Heat Trans.* 84, 317-326.
- Bear, J., 1972, Dynamics of Fluids in Porous Media, New York, American Elsevier, 770 pp.
- Beard, J. S. (1990) Partial melting of metabasites in the contact aureoles of gabbroic plutons in the Smartville Complex, Sierra Nevada, California. *Abbrev.* 303-314.
- Beard, J. S. and Lofgren, G. E. (1989) Effects of water on the composition of partial melts of greenstone and amphibolite. *Science* 244, 195-197.
- Beckermann, C. and Viskanta, R. (1988a) Double-diffusive convection during dendritic solidification of a binary mixture. *Physico-chemical Hydrodynamics* 10, 195-213.
- Beckermann, C. and Viskanta, R. (1988b) Natural convection solid/liquid phase change in porous media. *Int. J. Heat Mass Trans.* 31, 35-46.
- Bennon, W. D. and Incropera, F. P. (1987a) A continuum model for momentum, heat and species transport in binary solid-liquid phase change systems I. Model formulation. *Int. J. Heat Mass Trans.* 30, 2161-2170.
- Bennon, W. D. and Incropera, F. P. (1987b) A continuum model for momentum, heat and species transport in binary solid-liquid phase change systems II. Application to solidification in a rectangular cavity. *Int. J. Heat Mass Trans.* 30, 2171-2187.
- Bergantz, G. W. (1989a) Thermal and dynamical state of the crust following underplating: Implications for melt generation and petrologic diversity. *EOS, Trans. Am. Geophys. Union* 70, 1320.
- Bergantz, G. W. (1989b) Underplating and partial melting: Implications for melt generation and extraction. *Science* 245, 1093-1095.
- Bergantz, G. W. (1990) Conjugate solidification and melting in multicomponent open and closed systems. *Int. J. Heat Mass Trans.*, in review.
- Best, M. G., Christiansen, E. H. and Blank, R. H. J. (1989) Oligocene caldera complex and calc-alkaline tuffs and lavas of the Indian Peak volcanic field, Nevada and Utah. *Geol. Soc. Am. Bull.* 101, 1076-1090.
- Bottinga, Y. and Weill, D. F. (1972) The viscosity of magmatic silicate liquids: A model for calculation. *Am. J. Sci.* 272, 438-475.
- Brandeis, G. and Marsh, B. D. (1989) The convective liquidus in a solidifying magma chamber: a fluid dynamic investigation. *Nature* 339, 613-616.
- Brandeis, G. and Marsh, B. D. (1990) Transient magmatic convection prolonged by solidification. *Geophys. Res. Lett.* 17, 1125-1128.
- Cao, Y., Faghri, A. and Chang, W.-S. (1989) A numerical analysis of Stefan problems for generalized multi-dimensional phase-change structures using the enthalpy transforming model. *Int. J. Heat Mass Trans.* 32, 1289-1297.
- Cashman, K. V. and Marsh, B. D. (1988) Crystal size distribution (CSD) in rocks and the kinetics and dynamics of crystallization. *Contrib. Mineral. Petrol.* 99, 292-305.
- Chappell, B. W. and Stephens, W. E. (1988) Origin of intracrustal (I-type) granite magmas. *Trans. Roy. Soc. Edinburgh* 79, 71-86.
- Chen, C. F. and Thangham, S., (1982), Effects of viscosity variation and cooling rates on crystallization and subsequent double-diffusive convection. In: 7th Int. Heat Transfer Conference, pp. 363-368.
- Cheung, F. B. and Epstein, M., (1984), Solidification and melting in fluid flow, in *Advances in Transport Processes*, A. S. Majumdar and R. A. Mashelkar, eds., Wiley Eastern Ltd., New Delhi, pp. 35-117.
- Chu, T. Y. and Hickox, C. E. (1990) Thermal convection with large viscosity variation in an enclosure with localized heating. *J. Heat Trans.* 112, 388-395.
- Clyne, T. W. and Kurtz, W. (1981) Solute redistribution during solidification with rapid solid state diffusion. *Met. Trans. A* 12, 965-971.
- Conrad, W. K., Nicholls, I. A. and Wall, V. J. (1988) Water-saturated and undersaturated melting of metaluminous and peraluminous crustal compositions at 10 kb: Evidence for the origin of silicic magmas in the Taupo Volcanic Zone, New Zealand, and other occurrences. *J. Petrol.* 29, 765-803.
- Daines, M. J. and Richter, F. M. (1988) An experimental method for directly determining the interconnectivity of melt in a partially molten system. *Geophys. Res. Letters* 15, 1459-1462.

- Davidson, J. P., Dungan, M. P., Ferguson, K. M. and Colucci, M. T. (1987) Crust-magma interactions and the evolution of arc magmas: the San Pedro-Pellado volcanic complex, southern Chilean Andes *Geology* 15, 443-446.
- DeBari, S., Mahlburg Kay, S. and R.W., K. (1987) Ultramafic xenoliths from Adagdak volcano, Adak, Aleutian Islands, Alaska: Deformed igneous cumulates from the moho of an island arc. *J. Geol.* 95, 329-341.
- Dell'Angelo, L. N. and Tullis, J. (1988) Experimental deformation of partially melted granitic aggregates. *J. Metamorphic Geol.* 6, 495-515.
- Eichelberger, J. C. (1980) Vesiculation of mafic magma during replenishment of silicic magma reservoirs. *Nature* 288, 446-450.
- Fleck, R. J. and Criss, R. E. (1985) Strontium and oxygen isotopic variations in Mesozoic and Tertiary plutons of central Idaho. *Contrib. Mineral. Petrol.* 90, 291-308.
- Fountain, J. C., Hodge, D. S. and Shaw, R. P. (1989) Melt segregation in anatectic granites: a thermo-mechanical model. *J. Volc. Geothermal Res.* 39, 279-296.
- Gans, P. B., Mahood, G. A. and Schermer, E., 1989, Synextensional Magmatism in the Basin and Range Province, *Geol. Soc. Am. Special Paper* 233, 53 pp.
- German, R. M. (1985) The contiguity of liquid phase sintered microstructures. *Met. Trans.* 16, 1247-1252.
- Ghiorso, M. S. (1985) Chemical mass transfer in magmatic systems I. Thermodynamic relations and numerical algorithms. *Contrib. Mineral. Petrol.* 90, 107-120.
- Ghiorso, M. S. (1987) Chemical mass transfer in magmatic processes III. Crystal growth, chemical diffusion and thermal diffusion in multicomponent silicate melts. *Contrib. Mineral. Petrol.* 96, 291-313.
- Ghiorso, M. S. and Carmichael, I. S. E. (1985) Chemical mass transfer in magmatic processes II. Applications in equilibrium crystallization, fractionation and assimilation. *Contrib. Mineral. Petrol.* 90, 121-141.
- Glazner, A. F. and Ussler, W. (1988) Trapping of magma at midcrustal density discontinuities. *Geophys. Res. Lett.* 15, 673-675.
- Gromet, L. P. and Silver, L. T. (1987) REE variations across the Peninsular Ranges Batholith: Implications for batholithic petrogenesis and crustal growth in magmatic arcs. *J. Petrol.* 28, 75-125.
- Grove, T. L., Kinzler, R. J., Baker, M. B., Donnelly-Nolan, J. M. and Leshner, C. E. (1988) Assimilation of granite by basaltic magma at Burnt Lava flow, Medicine Lake volcano, northern California: Decoupling of heat and mass transfer. *Contrib. Mineral. Petrol.* 99, 320-343.
- Halliday, A. N., Mahood, G. A., Holden, P., Metz, J. M., Dempster, T. J. and Davidson, J. P. (1989) Evidence for long residence times of rhyolitic magma in the Long Valley magmatic system: the isotope record in precaldra lavas of Glass Mountain. *Earth Planetary Sci. Lett.* 94, 274-290.
- Hawkesworth, C. J., Hammil, M., Gledhill, A. R., van Calsteren, P. and Rogers, G. (1982) Isotope and trace element evidence for late-stage intra-crustal melting in the High Andes. *Earth Planetary Sci. Letters* 58, 240-254.
- Hildreth, W. (1981) Gradients in silicic magma chambers: implications for lithospheric magmatism. *J. Geophys. Res.* 86, 10,153-10,192.
- Hildreth, W. and Moorbath, S. (1988) Crustal contributions to arc magmatism in the Andes of Central Chile. *Contrib. Mineral. Petrol.* 98, 455-489.
- Hill, M., O'Neil, J. R., Noyes, H., Frey, F. and Wones, D. R. (1988) Sr, Nd and O isotope variations in compositionally zoned and unzoned plutons in the central Sierra Nevada batholith. *Am. J. Sci.* 288-A, 213-241.
- Hill, R. I., Silver, L. T., Chappell, B. W. and Taylor, H. P. (1985) Solidification and recharge of SiO₂-rich plutonic magma chambers. *Nature* 313, 643-646.
- Hill, R. I., Silver, L. T. and Taylor, H. P. J. (1986) Coupled Sr-O isotope variations as an indicator of source heterogeneity for the Northern Peninsular Ranges batholith. *Contrib. Mineral. Petrol.* 92, 351-361.
- Hills, R. N., Loper, D. E. and Roberts, P. H. (1983) A thermodynamically consistent model of a mushy zone. *Q. J. Appl. Math.* 36, 505-538.
- Hills, R. N. and Roberts, P. H. (1988a) A generalized Scheil-Phann equation for a dynamical theory of a mushy zone. *Int. J. Non-Linear Mechanics* 23, 327-339.
- Hills, R. N. and Roberts, P. H. (1988b) On the formulation of diffusive mixture theories for two-phase regions. *J. Engineering Mathematics* 22, 93-106.
- Hills, R. N. and Roberts, P. H. (1988c) On the use of Fick's law in regions of mixed phase. *Int. Comm. Heat Mass Trans.* 15, 113-119.
- Hollister, L. S., Hyndman, D. W. and Saleeby, J. B. (1989) A composite crustal section through mid- to late-Cretaceous collisional magmatic arcs in western North America. *Geol. Soc. Am. Abstr. Programs* 21, 94.

- Hunter, L. W. and Kuntler, J. R. (1989) The enthalpy method for heat conduction problems with moving boundaries. *J. Heat Trans.* 111, 239-242.
- Huppert, H. E. and Sparks, R. S. J. (1988) The generation of granitic magmas by intrusion of basalt into continental crust. *J. Petrol.* 29, 599-624.
- Huppert, H. E. and Sparks, R. S. J. (1989) Chilled margins in igneous rocks. *Earth Planetary Sci. Letters* 92, 397-405.
- Jurewicz, S. R. and Watson, E. B. (1985) The distribution of partial melt in a granitic system: the application of liquid phase sintering theory. *Geochim. Cosmochim. Acta.* 49, 1104-1121.
- Kitchen, D. E. (1989) The disequilibrium partial melting and assimilation of Caledonian granite by Tertiary basalt at Barnesmore, Co. Donegal. *Geol. Mag.* 126, 397-405.
- Langmuir, C. H. (1989) Geochemical consequences of in situ crystallization. *Nature* 340, 199-205.
- Loper, D. E. and Roberts, P. H. (1978) On the motion of an iron-alloy core containing a slurry. I. General theory. *Geophys. & Astrophys. Fluid Dynam.* 9, 298-321.
- Loper, D. E. and Roberts, P. H., (1987), A Boussinesq model of a slurry, *in* Structure and Dynamics of Partially Solidified Systems, D. E. Loper ed., Martinus Nijhoff, Dordrecht, The Netherlands, pp. 291-323
- Lowell, R. P. (1985) Double-diffusive convection in partially molten silicate systems: its role during magma production and in magma chambers. *J. Volc. Geothermal Res.* 26, 1-24.
- Mahon, K. I., Harrison, T. M. and Drew, D. A. (1988) Ascent of a granitoid diapir in a temperature varying medium. *J. Geophys. Res.* 93, 1174-1188.
- Mahood, G. A. and Halliday, A. N. (1988) Generation of high-silica rhyolite: a Nd, Sr, and O isotopic study of Sierra La Primavera, Mexican neovolcanic belt. *Contrib. Mineral. Petrol.* 100, 183-191.
- Mareschal, J.-C. and Bergantz, G. B. (1990) Constraints on thermal models of the Basin and Range province. *Tectonophysics* 174, 137-146.
- Marsh, B. D. (1981) On the crystallinity, probability of occurrence, and rheology of lava and magma. *Contrib. Mineral. Petrol.* 78, 85-98.
- Marsh, B. D. (1982) On the mechanics of igneous diapirism, stoping and zone melting. *Am. J. Sci.* 282, 808-855.
- Marsh, B. D., (1984), Mechanics and energetics of magma formation and ascent, *in* Studies in Geophysics, Explosive Volcanism: Inception, Evolution and Hazards, F. R. Boyd, ed., National Academy Press, Washington, DC, pp. 67-83.
- Marsh, B. D. (1988a) Causes of magmatic diversity. *Nature* 333, 397.
- Marsh, B. D. (1988b) Crystal capture and retention in convecting magma. *Geol. Soc. Am. Bull.* 100, 1720-1737.
- Marsh, B. D. (1989a) Magma chambers. *Ann. Rev. Earth Planet. Sciences* 439-474.
- Marsh, B. D. (1989b) On convective style and vigor in sheet-like magma bodies. *J. Petrol.* 30, 479-530.
- McBirney, A. R., Baker, B. H. and Nilson, R. H. (1985) Liquid Fractionation. Part I: Basic principles and experimental simulations. *J. Volc. Geothermal Res.* 24, 1-24.
- McBirney, A. R. and Murase, T. (1984) Rheological properties of magmas. *Ann. Rev. Earth Planet. Sci.* 12, 337-357.
- Miller, C. F., Watson, E. B. and Harrison, T. M. (1988) Perspectives on the source, segregation and transport of granitoid magmas. *Trans. Royal Soc. Edinburgh* 79, 135-156.
- Morse, S. A. (1988) Motion of crystals, solute, and heat in layered intrusions. *Canadian Mineral.* 26, 209-224.
- Naslund, H. R. (1986) Disequilibrium partial melting and rheomorphic layer formation in the contact aureole of the Basistoppen sill, East Greenland. *Contrib. Mineral. Petrol.* 93, 359-367.
- Nekvasil, H. (1988) The calculation of equilibrium crystallization paths of compositionally simple hydrous felsic melts. *Am. Mineral.* 73, 956-965.
- Oldenburg, C. M. and Spera, F. J. (1990) Simulation of phase change and convection in magma bodies. *Int. J. Heat Mass Trans.*, in press.
- Patiño Douce, A. and Johnston, A.D. (1990) Phase equilibria and melt productivity in the pelitic system: implications for the origin of peraluminous granitoids and aluminous granulites. *Contrib. Mineral. Petrol.*, in review.
- Paterson, S. R., Vernon, R. H. and Tobisch, O. T. (1989) A review of the criteria for the identification of magmatic and tectonic foliations in granitoids. *J. Struct. Geol.* 11, 349-363.
- Reagan, M. K., Gill, J. B., Malavassi, E. and Garcia, M. O. (1987) Changes in magma composition at Arenal volcano, Costa Rica, 1968-1985: Real time monitoring of open system differentiation. *Bull. Volc.* 49, 415-434.
- Roberts, P. H. and Loper, D. E., (1987), Dynamical processes in slurries, *in* Structure and Dynamics of Partially Solidified Systems, D. E. Loper ed., Martinus Nijhoff, Dordrecht, The Netherlands, pp. 229-290

- Ruiz, J., Patchett, P. J. and Arculus, R. J. (1988) Nd-Sr isotope composition of lower crustal xenoliths-Evidence for the origin of mid-tertiary felsic volcanics in Mexico. *Contrib. Mineral. Petrol.* 99, 36-43.
- Rutter, M.J., Wyllie, P.J. (1988) Melting of vapor-absent tonalite at 10 kbar to simulate dehydration melting in the deep crust. *Nature* 331, 159-160.
- Ryerson, F. J., Weed, H. C. and Piwinski, A. J. (1988) Rheology of subliquidus magmas 1. Picritic compositions. *J. Geophys. Res.* 93, 3421-3436.
- Saleeby, J. B., Sams, D. B. and Kistler, R. W. (1987) U/Pb zircon, strontium, and oxygen isotopic and geochronological study of the southernmost Sierra Nevada batholith, California. *J. Geophys. Res.* 92, 10,443-10466.
- Shamsundar, N. and Sparrow, E. M. (1975) Analysis of multidimensional conduction phase change via the enthalpy model. *J. Heat Trans.* 97, 333-340.
- Shaw, H. R. (1969) The rheology of basalt in the melting range. *J. Petrol.* 10, 1969.
- Shaw, H. R. (1972) Viscosities of magmatic liquids: an empirical method of prediction. *Am. J. Sci.* 272, 870-893.
- Sheckler, C. A. and Dinger, D. R. (1990) Effect of particle size distribution on the melting of soda-lime-silica glass. *J. Am. Ceram. Soc.* 73, 24-30.
- Singer, B. S., Myers, J. D., Linneman, S. R. and Angevine, C. L. (1988) The thermal history of ascending magma diapirs and the thermal and physical evolution of magmatic conduits. *J. Volc. Geothermal Res.* 93.
- Smith, D. R. and Leeman, W. P. (1987) Petrogenesis of Mount St. Helens dacitic magmas. *J. Geophys. Res.* 92, 10,313-10,334.
- Spera, F. J., Borgia, A., Strimple, J. and Feigenson, M. (1988) Rheology of melts and magmatic suspensions 1. Design and calibration of concentric cylinder viscometer with application to rhyolitic magma. *J. Geophys. Res.* 93, 10,273-10,294.
- Spera, F. J., Yuen, D. A. and Kirschvink, S. J. (1982) Thermal boundary layer convection in silicic magma chambers: Effects of temperature-dependent rheology and implications for thermogravitational chemical fractionation. *J. Geophys. Res.* 87, 8755-8767.
- Tait, S. and Jaupart, C. (1989) Compositional convection in viscous melts. *Nature* 338, 571-574.
- Takahashi, E. (1986) Genesis of calc-alkali andesite magma in a hydrous mantle-crust boundary: petrology of lherzolite xenoliths from the Ichinomegata crater, Oga peninsula, Northeast Japan, Part II. *J. Volc. Geothermal Res.* 29, 355-395.
- Thompson, M. E. and Szekeley, J. (1989) Density stratification due to counterbuoyant flow along a vertical crystallization front. *Int. J. Heat Mass Trans.* 32, 1021-1035.
- van der Molen, I. and Paterson, M. S. (1979) Experimental deformation of partially-melted granite. *Contrib. Mineral. Petrol.* 70, 299-318.
- Vielzeuf, D. and Holloway, J.R. (1988) Experimental determination of the fluid-absent melting relations in the pelitic system. *Contrib. Mineral. Petrol.* 98, 257-276.
- Vogel, T. A. and Cambray, F. W. (1990) The tectonic relationship between large ash-flow eruptions and mid-crustal intrusions: Timber Mountain Tuff, Nevada and Black Mountain Plutonic Complex, Death Valley, California. *EOS, Trans. Am. Geophys. Union. Abstr. Fall Meeting*, submitted
- Voller, V. R. (1985) A heat balance integral method for estimating practical solidification parameters. *IMA J. Applied Math.* 35, 223-232.
- Waff, H. S. and Bulau, J. R. (1982) Experimental studies of near-equilibrium textures in partially molten silicates at high pressures. *Adv. Earth Planet. Sci.* 12, 229-236.
- Warren, R. G., Byers, F. M. J., Broxton, D. E., Freeman, S. H. and Hagan, R. C. (1989) Phenocryst abundances and glass and phenocryst compositions as indicators of magmatic environments of large-volume ash flow sheets in southwestern Nevada. *J. Geophys. Res.* 94, 5987-6020.
- Whitney, J. A. (1988) The origin of granite: The role and source of water in the evolution of granitic magmas. *Geol. Soc. Am. Bull.* 100, 1886-1897.
- Wickham, S. M. (1987) The segregation and emplacement of granitic magmas. *J. Geol. Soc. London* 144, 281-297.
- Wyllie, P.J. (1977) Crustal anatexis: An experimental review. *Tectonophysics* 43, 41-71.

TEXTURAL CONSTRAINTS ON THE KINETICS OF CRYSTALLIZATION OF IGNEOUS ROCKS

INTRODUCTION

In the past 10 years, studies of magmatic processes have evolved from the study of simple fluids to become integrated investigations of the interaction between chemical and physical parameters of magmas: the time- and length-scales of melting and crystallization provide a dynamic feedback between the thermal and chemical evolution of the solid + liquid system. Thus the accurate description of the crystallization behavior of geologic systems is required in order to merge thermodynamic models of melt evolution on cooling (i.e. chemical evolution of the system) with physical models of melt storage and differentiation. Theoretical models of crystallization in multicomponent silicate systems, however, are complicated not only by the difficulty in predicting nucleation and growth kinetics of such systems at a single point in time, but also by our incomplete understanding of the evolution of crystallizing systems through episodes of magmatic transport and cooling.

Quantitative analysis of rock textures provides an important link between the simplified systems of theory and experiment, and the complexities of natural processes. Textures can provide information on both the *rates* of solidification processes (crystallization) and on the *pathways* through which those processes occurred. Crystal *shape* can be quantified by Fourier analysis (e.g. Erlich et al., 1972) or fractal analysis (e.g. Fowler et al., 1989) and is controlled by cooling rate (e.g. Lofgren, 1980). The *spatial arrangement* of crystals in a rock will be controlled by the order of crystallization (e.g. Hawkes, 1967) and the relative rates of crystal settling (e.g. Marsh, 1988a). The *size distribution* of crystals is the direct result of the effective undercooling at which a magma crystallized (e.g. Marsh, 1988b; Cashman and Marsh, 1988), and will in turn control rock strength (Skolnick et al., 1988), magma viscosity (e.g. Marsh, 1981) and reactivity (total crystal surface area). Finally, textural analysis has been used to analyze the deformation (e.g. Daniel et al., 1987) and subsolidus recrystallization (e.g. Boudreau, 1987) histories of igneous rocks.

The primary goal of this chapter is to integrate kinetic information obtained from quantitative textural studies of igneous rocks with currently available theoretical, experimental and numerical studies of crystallization kinetics in igneous rocks. Natural systems provide time-controlled experiments on scales inaccessible in the laboratory, and with complexities unapproachable by computer experiments; thus *in situ* crystallization experiments provide information on the crystallization of geologic systems unavailable by other means. I start with a review of theoretical and experimental constraints on nucleation and growth in simple systems in order to provide an overview of both the power and limitations of classical theory for predictions of crystallization kinetics in complex systems. I then review recent numerical models linking the crystallization history of a magmatic system with its thermal evolution (e.g. Brandeis et al., 1984; Brandeis and Jaupart, 1987; Spohn et al., 1988). While these numerical experiments yield important insights into the time-evolution of crystallization as a function of cooling, they are limited in their direct application to most magmatic systems due to our inadequate understanding of the kinetics of

crystallization in complex systems. Finally, I present a compilation of quantitative textural data on natural systems, interpreted in the framework of crystal size distribution (CSD) theory (e.g. Randolph and Larson, 1971; Marsh, 1988b; Cashman and Marsh, 1988).

NUCLEATION

Nucleation may be described as the initial formation of the smallest particle of a new phase during a phase transformation. Nucleation is classified as homogeneous (arising from random thermal fluctuations) or heterogeneous (nucleating on a pre-existing substrate). Classical theory predicts the steady state homogeneous nucleation rate of a phase transformation in a one-component system (e.g. the condensation of water from steam); rigorous extensions of classical theory to multi-component systems, however, do not exist at this time. Excellent reviews of classical theory are given by Dowty (1980), Kirkpatrick (1981), and James (1982); I will only briefly review the forms of the nucleation equations here; in addition I will briefly discuss experimental results (primarily in glass ceramic materials) reported since 1981.

Theory

Homogeneous nucleation. The kinetics of nucleation in a phase transformation depend on the thermodynamic driving force available for the reaction. In geologic systems that driving force is a supersaturation due either to a temperature change (usually referred to as undercooling, ΔT) or to a change in concentration of one or more components (supersaturation, Δc). In the formulations presented below it is assumed that the driving force for crystallization is undercooling, although the equations take exactly the same form for a driving force of supersaturation.

The steady state nucleation rate (I) is the product of the attachment frequency (kinetic barrier) and the concentration of critical nuclei (thermodynamic barrier):

$$I = vN_v \exp \left\{ - \frac{(\Delta G_a + \Delta G^*)}{RT} \right\} \quad (1)$$

with $v = kT/h$ the frequency with which an atom attempts to overcome the energy barrier (k is the Boltzmann constant and h is Planck's constant), N_v the number of atoms per unit volume of the reactant phase, ΔG_a the activation energy involved in attaching an atom to the nucleus, and ΔG^* the thermodynamic driving force for the transformation; the pre-exponential term is usually treated as a constant over the temperature range of interest. For a spherical cluster, the free energy needed to create a cluster of critical size (ΔG^*) is

$$\Delta G^* = \frac{16\pi}{3} \frac{\sigma^3}{\Delta G_v^2} \quad (2)$$

where σ represents the interfacial energy between the nucleus and surrounding medium and ΔG_v is the free energy change per unit volume ($\Delta G/V_m$; V_m is the molar volume of the crystal phase); ΔG can be calculated if the thermodynamic properties of the transformation are known. The complete expression for ΔG in a single component system is

$$\Delta G(T) = -\Delta H_f \frac{(T_m - T)}{T_m} - \int_T^{T_m} \Delta C_p(T) dT + T \int_T^{T_m} \frac{\Delta C_p(T)}{T} dT \quad (3)$$

with ΔH_f the enthalpy of fusion and $\Delta C_p(T)$ the change in heat capacity associated with the phase transformation (fusion) over the relevant temperature range; T_m is the melting temperature. Simplified expressions for ΔG are often used, however, especially when thermodynamic data are incomplete. Over small temperature ranges ΔC_p can be considered constant and

$$\Delta G = -\Delta H_f \frac{(T_m - T)}{T_m} - \Delta C_p \left\{ (T_m - T) - T \ln \left(\frac{T_m}{T} \right) \right\} \quad (4)$$

At very small undercoolings ΔC_p is often ignored, and

$$\Delta G \approx -\Delta H_f \frac{\Delta T}{T_m} \quad (5)$$

It is important to remember that these simplified expressions are close to valid only for small deviations in temperature, and even (3) is valid only for a one-component system at a constant pressure; in a multicomponent system terms must be added for partial molar enthalpy and entropy of mixing, while nucleation due to a change in pressure must involve the $\int \Delta V_T(P) dP$ contribution to $\Delta G(T, P)$ (see Lange and Carmichael, this volume).

Equation (1) results in a nucleation rate that first increases then decreases with increasing undercooling, a shape commonly attributed to competing effects of the thermodynamic driving force and the kinetic barrier to nucleation. Assuming that thermodynamic data are available for the system of interest, the main problem in quantitatively relating theory to experiment lies in evaluating σ and ΔG_a . The simplest method of determining these parameters from experimental data is to divide the nucleation curve into two separate parts: $I = A \exp(-\Delta G_a/RT)$ for $T < T_{\text{Imax}}$ and $I = A \exp(-\Delta G^*/RT)$ for $T > T_{\text{Imax}}$, where T_{Imax} is the temperature at which the nucleation rate is maximized and A is the preexponential term. While slopes and intercepts of Arrhenius plots can easily be used to estimate σ , ΔG_a and A in this way, Rowlands and James (1979) demonstrate that the assumption on which this approach is based (that $\Delta G^* \gg \Delta G_a$ for $T > T_{\text{Imax}}$ and $\Delta G_a \gg \Delta G^*$ for $T < T_{\text{Imax}}$) is probably incorrect, and suggest that the humped shape of the nucleation curve can be generated simply by the $T\Delta T^2$ term in the denominator of the exponential expression for the chemical driving force: as ΔT becomes very large, T becomes very small and the nucleation rate decreases. The effect of the kinetic term is to raise T_{Imax} and to decrease the overall rates, but ΔG^* is non-negligible in the area of rapid nucleation change where $T < T_{\text{Imax}}$.

Alternatively, ΔG_a may be expressed in terms of an effective diffusion coefficient

$$D = D_o \exp(-\Delta G_a/RT) \quad (6)$$

where the pre-exponential term $D_o = \alpha_o^2 v$; α_o^2 is the interatomic "jump distance" ($\sim 3 \times 10^{-8}$ cm for the distance between two silicons joined by a bridging oxygen in a silicate melt;

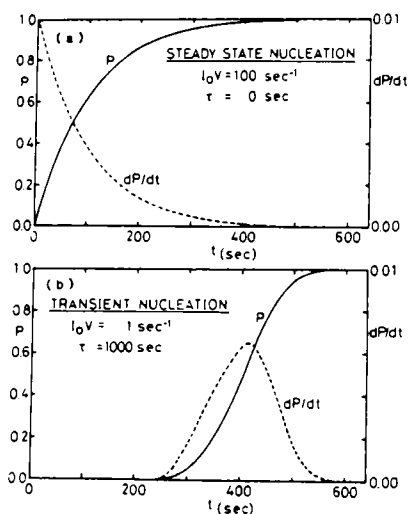


Figure 1. Examples of calculated nucleation probability, P , as a function of time, t ; dashed lines indicate dP/dt . (a) Steady-state nucleation. (b) Transient nucleation. From Tsuchiyama (1983).

McKeown et al., 1985), and v is again kT/h . Diffusion is commonly related to the liquid viscosity (η) by the Stokes-Einstein approximation, which equates the temperature-dependence of v with that of the bulk viscosity such that

$$D = kT/3\pi\alpha_0\eta \quad (7)$$

and the expression for nucleation rate becomes

$$I = \frac{A_c T}{\eta} \exp(-\Delta G^*/RT) = \frac{K_1}{\eta} \exp\left(-k_2 \frac{\sigma^3}{T(\Delta G_v)^2}\right) \quad (8)$$

where $A_c = N_v k/3\pi\alpha_0^2$. Thus if the liquid viscosity and the thermochemical data are known, measured nucleation rates can be plotted as $\ln(\eta I)$ vs. $1/(\Delta G_v)^2 T$ and should theoretically yield a straight line whose slope is a function of σ and intercept is A_c . However, the above relationship between viscosity and the kinetic barrier to nucleation assumes that the fundamental microscopic process (i.e., atomic displacement or bond breaking) is the same for nucleation and viscous flow. While this seems intuitively reasonable, the applicability of this assumption in complex network-forming liquids has never been established (Weinberg and Zanotto, 1989).

The nucleation rates expressed by Equations (1) and (8) are steady state nucleation rates (e.g., $dN(t)/dt = 0$). However, the supersaturation condition alone is necessary but not sufficient for nucleation of a new phase - a metastable zone exists where the spontaneous creation of crystallites of a new phase (homogeneous nucleation) is unlikely although the deposition of material on a pre-existing surface (growth) is probable; in this region a finite amount of time is required for nucleation to achieve a steady rate. An approximate solution for the transient (time-dependent) nucleation rate I' (valid for small time t) is

$$I' = I \exp\left(-\frac{\tau_t}{t}\right) \quad (9)$$

where τ_f is the time constant for transient behavior. For $t > 5\tau_f$, the number of crystals present in a crystallizing volume ($N(t)$) approaches an asymptotic limit of

$$N(t) = I \left(t - \pi^2 \frac{\tau_f}{6} \right) \quad (10)$$

(Kashchiev, 1969; Volterra and Cooper, 1985). A comparison of nucleation probabilities (P) in steady state and transient models is shown in Figure 1. Nucleation probabilities decrease with time in the steady state model as a result of a steadily decreasing melt volume; the nucleation probability in the transient model has a maximum, the position of which is a function of τ_f . $\ln(\tau_f)$ is linearly related to $1/T$ (James, 1985), and should yield a means of determining the kinetic barrier ΔG_a that is independent of measured viscosities (Volterra and Cooper, 1985), although the time- and temperature-dependence of the transient time constant are certainly related to melt viscosity. In an analysis of experimental data in glass-forming systems, however, Weinberg and Zanotto (1989) find the predicted linear relationships only for $T > T_{\text{max}}$; they conclude that the temperature dependence in homogeneous nucleation of glasses is not yet understood.

Kirkpatrick (1983) uses experimental data to formulate a qualitative model for nucleation in silicate melts based on the above relationship between ΔG_a and τ_f . He predicts higher nucleation rates both for less polymerized melts (e.g. a viscosity effect) and for less polymerized crystals, and supports his model by the commonly observed metastable nucleation of olivine in rapidly cooled experiments (e.g. Walker et al., 1976; Grove, 1978). The ease with which a crystal nucleates will be a function of the entropy of fusion, which in turn reflects the change in structural order between the mineral and melt. The observed ease of nucleation for minerals with large ΔS_f resulting from a large structural change between melt and crystal (e.g. olivine) relative to those with small ΔS_f and correspondingly small structural change between mineral and melt structure (e.g. plagioclase) appears counter-intuitive, but occurs because a large structural change between the crystal and melt will create a relatively large driving force for a given undercooling (Carmichael et al., 1974). Thus polymerization of both the melt and the crystallizing mineral assemblage *will* control the order of crystallization and qualitatively this model is consistent with observations; however, we still lack the means to quantitatively predict nucleation behavior.

Heterogeneous nucleation. While the theory above is developed for homogeneous nucleation, heterogeneous nucleation, where nucleation occurs on a pre-existing substrate, is probably dominant in geologic systems (e.g. Berkebile and Dowty, 1982; Lofgren, 1983). Heterogeneous nucleation is modeled by reducing the kinetic barrier:

$$I_{\text{HET}} = N_s \nu \exp \left\{ - \frac{(\Delta G_{\text{HET}}^* + \Delta G_a)}{RT} \right\} \quad (11)$$

where $\Delta G_{\text{HET}}^* = \Delta G^* f(\theta)$, and N_s is the number of formula units of liquid in contact with the substrate per unit area. For a spherical cap of material precipitated on a flat substrate, $f(\theta) = (2 + \cos \theta)(1 - \cos \theta)^2/4$, where $\cos \theta = (\sigma_{ms} - \sigma_{cs})/(\sigma_{cm})$; subscripts represent the interfacial energy of the melt (m), substrate (s) and crystal (c). The increase in nucleation rate due to heterogeneous nucleation is thus a function of the contact angle between crystal,

melt and substrate and of the total surface area of the catalyzing substrate (in turn dependent on particle size, number density and state of dispersion). Impurities producing heterogeneous nucleation may be as small as a single molecule (Meyer, 1986); if the number of impurities is small relative to the precipitation rate, saturation effects may occur (Weinberg et al., 1984; Zanotto and Weinberg, 1988).

Experimental constraints

The entire formulation presented above was developed for phase transformations in one-component systems; there is no formal theory available for consideration of phase transformations in multi-component systems, although some very qualitative predictions can be made (e.g. Smith et al., 1987). Most of the available experimental work on silicates has involved precipitation in congruent glass-forming systems, where nucleation appears to be homogeneous (i.e., is observed to nucleate internally), and the processes of nucleation can be isolated. Experiments are usually isothermal, although they may involve a second heating step to a temperature of high growth rates in order to grow nucleated crystals to an observable size. Number densities are then plotted as a function of time to determine nucleation rates. Matching these rates with those predicted by classical theory has proved difficult, however, especially in the lithium disilicate system (e.g. Neilson and Weinberg, 1979; Rowlands and James, 1979a,b; James, 1985; Zanotto and James, 1985; Weinberg and Zanotto, 1989). While estimated values of σ are reasonable, modeling the observed nucleation data requires a temperature-dependence of σ of the form $\sigma = \sigma_0 \cdot bT$ (Rowlands and James, 1979b; James, 1985). In addition, the assumed shape of the critical nucleus greatly affects the average value of σ ; by modeling lithium disilicate nuclei as platelets instead of spheres James (1985) further improved the agreement between predicted and observed rates. The pre-exponential term has yet to be modeled successfully for the lithium disilicate data, however, with predicted values many orders of magnitude from experimental results (Weinberg and Zanotto, 1989).

While a predictive model for nucleation rates remains elusive, certain generalizations can be made relating the relative positions of the temperature at which nucleation rate is maximized (T_{Imax}) and the melting temperature T_m to the ratio of the difference in the specific heat between the crystal and liquid divided by the entropy of fusion ($\Delta C_p/\Delta S_f$; Weinberg, 1986) and to a parameter proportional to the reduced activation energy for viscous flow. This relationship is explored in the adiabatic (isenthalpic) theory of Meyer (1986), who models nucleation based on ordinary statistical (temperature) fluctuations rather than isothermal heterophase fluctuations. An approximation from this model (the asymptotic limit for the case of large molecules) yields an estimate of T_{Imax}/T_m of:

$$\frac{T_{\text{Imax}}}{T_m} \approx 0.6 \frac{\Delta S_f}{c_p} \left\{ \exp \left(\frac{\Delta S_f}{c_p} \right) - 1 \right\}^{-1} \quad (12)$$

with c_p the average value for the heat capacity between the solid and liquid at the transition temperature. This formulation was tested for predictions of nucleation in homogeneous glasses by Zanotto (1987) and found to work well in systems for which sufficient data were available (Table 1; included in this table is an estimated T_{Imax} for anorthite and albite, calculated using the thermodynamic data of Stebbins et al., 1982; 1984 and Berman and Brown, 1985). Prediction of the location of T_{Imax} is important for several reasons. In

Table 1. Calculated and experimental values of T_{imax}/T_L . T_{1d}/T_L calculated from the adiabatic equation of Meyer (1986); all data presented here is from Zanotto (1987) with the exception of albite and anorthite, where data is from Stebbins et al. (1982; 1984) and Berman and Brown (1985).

| COMPOSITION | T_L (K) | $\Delta S/C_p$ | Adiabatic T_{1d}/T_L | Experimental T_{imax}/T_L | T_g/T_L |
|---|-----------|----------------|---------------------------|---------------------------------------|-----------|
| $\text{Na}_2\text{O} \cdot \text{SiO}_2$ | 1362 | 0.19 | 0.59 | 0.54 | 0.54 |
| $\text{Li}_2\text{O} \cdot 2\text{SiO}_2$ | 1307 | 0.18 | 0.58 | 0.55 | 0.55 |
| $\text{Na}_2\text{O} \cdot 2\text{CaO} \cdot 3\text{SiO}_2$ | 1564 | 0.14 | 0.58 | 0.55 | 0.55 |
| $\text{CaO} \cdot \text{SiO}_2$ | 1817 | 0.23 | 0.57 | 0.58 | 0.57 |
| $\text{BaO} \cdot 2\text{SiO}_2$ | 1693 | 0.09 | 0.60 | 0.58 | 0.57 |
| SiO_2 | 1996 | 0.06 | 0.64 | | 0.74 |
| $\text{CaO} \cdot \text{Al}_2\text{O}_3 \cdot 2\text{SiO}_2$ | 1830 | 0.18 | 0.55 | | 0.60 |
| $\text{Na}_2 \cdot \text{Al}_2\text{O}_3 \cdot 6\text{SiO}_2$ | 1373 | 0.13 | 0.56 | | 0.77 |

glass-forming systems, for example, the ability of a glass to nucleate homogeneously appears to depend on the relationship between T_{imax} and the glass transition temperature T_g - if $T_{\text{imax}} < T_g$, homogeneous nucleation does not occur (James, 1985; Zanotto, 1987). Note that by this criterion neither anorthite nor albite would be expected to nucleate homogeneously (Table 1). It is important to note, however, that since T_g is a function of cooling rate as well as of composition (e.g. Uhlmann and Yinnon, 1983; Turnbull, 1987), it is possible that conditions favorable for homogeneous nucleation may occur under conditions of slow cooling, while glass formation (i.e., inhibition of nucleation) will be favored by rapid cooling rates. The relative positions of T_{imax} for co-precipitating minerals will also be important in determining rock textures, as has been observed in experiments on basaltic melts (e.g. Lofgren, 1983).

Nucleation studies on multicomponent geologic systems are much more difficult to constrain than those in simple glass-forming systems, as even small amounts of additives may significantly increase nucleation rates (e.g. Kuo and Kirkpatrick, 1982a), and homogeneous nucleation may never occur (Berkebile and Dowty, 1982). Even heterogeneous nucleation appears to be sporadic and unpredictable at $\Delta T < 60^\circ$, probably due both to the statistical nature of the process and to the reliance on the number and distribution of sites for heterogeneous nucleation (Berkebile and Dowty, 1982; Tsuchiyama, 1983). In attempting to replicate experimentally the textures observed in lunar and terrestrial basalts, Lofgren (1983) showed that the entire range of textures produced in basalt by experimental variations in cooling rate could be duplicated by experimental variations in the kind and density of nuclei. Rates of heterogeneous nucleation may also be affected by the nature of the substrate; for example, olivine appears able to nucleate on substrates other than olivine, while plagioclase will only nucleate on itself or another complex tectosilicate (Lofgren, 1983). Convective stirring also increases rates of nucleation (Kouchi et al., 1986), possibly due to a phenomenon the chemical engineers call "secondary nucleation" (e.g. Budz et al., 1984), where crystallites are physically removed from the growing crystal surface to serve as new nucleation sites. Finally, initial homogeneous nucleation of fine precipitates (e.g.

observed precipitation of ferrite spinel due to internal oxidation by cation diffusion in transition metal-bearing aluminosilicate glasses; Cook et al., 1990) may in turn act as heterogeneous nucleation sites. Given the paucity of experimental data on multicomponent systems (due to the inherent difficulty of the experiments) and the observation that magmas are rarely superheated, an assumption of heterogeneous nucleation seems reasonable for crystallization over a broad range of geologic conditions.

CRYSTAL GROWTH

After the energy barrier for the formation of a new crystal has been surmounted (nucleation), the system adjusts to a state of greater stability (growth), thus consideration of crystal growth rates and mechanisms is relevant as soon as the nucleus reaches the critical size. While nucleation experiments require subsequent episodes of crystal growth in order to count the number of nucleation sites (thus making separation of the two processes difficult), crystal growth experiments can be seeded so that growth times are known and models are better constrained. Rate-controlling processes to be considered in crystallization include reaction at the crystal-melt interface, diffusion of components to and from the interface, removal of heat generated at the interface, and bulk flow of the melt. The first two of these four processes are generally considered to be dominant in geologic systems. The nature of the crystal-liquid interface has a decisive influence on the kinetics and morphology of crystallization in one-component systems. While it is difficult to isolate the effects of surface processes, it has been noted that (1) some crystal faces grow faster than others although they dissolve at the same rate (e.g. Kuo and Kirkpatrick, 1985), and (2) some substances retard or inhibit growth but have no effect on dissolution (Baronnet, 1984). This observed lack of reciprocity between growth and dissolution under the same hydrodynamic conditions suggests that the process of attachment to the crystal surface can be rate-controlling under some conditions (e.g. small ΔT). At large ΔT or in multicomponent systems, diffusion of components is thought to dominate the rate process (e.g. Kirkpatrick, 1981). Crystal growth processes are reviewed by Dowty (1980), Kirkpatrick (1981), Uhlmann (1982) and Baronnet (1984), and will only be summarized here.

Theory

Crystallization without a change in composition. The simplest forms of the crystal growth equations are those formulated for one-component phase transformations, which are by definition isothermal and do not require transport of components to the interface. Overall growth rates are a function of thermodynamic driving force (ΔG_c ; in turn a function of undercooling or supersaturation) and an activation energy ΔG^+ which is similar to, but probably not identical to ΔG_n , the kinetic barrier for nucleation. Growth rate (Y) is usually written as a balance between the forward rate of attachment ($= v \exp(-\Delta G^+/RT)$) and the rate of detachment ($= v \exp[-(\Delta G_c + \Delta G^+)/RT]$) multiplied by the thickness of each layer added (α) and the fraction of sites available for attachment (f):

$$Y = f\alpha v \exp(-\Delta G^+/RT) \{1 - \exp(-\Delta G_c/RT)\} \quad (13)$$

Note that the growth rate has the same functional form as the nucleation rate. The thermodynamic driving force close to the liquidus temperature is often approximated by Equation (5), although the same constraints apply to this approximation as described for nucleation. Similarly, it seems reasonable to equate the activation energy ΔG^+ with the breaking of bonds, which in turn is probably a function of melt viscosity, thus the Stokes-Einstein approximation is invoked and the growth rate becomes

$$Y = \frac{Y_R}{\eta} \{1 - \exp(\Delta H_f \Delta T / RTT_m)\} \quad (14)$$

Y_R (the 'reduced growth rate') includes the pre-exponential terms from (13), the constants from the Stokes-Einstein relation and the functional dependence of the growth rate on ΔT . Y_R thus becomes a means of characterizing the temperature dependence of the growth rate and is considered to be a measure of the fraction of available growth sites on the crystal surface. Growth mechanisms are classified based on the ΔT dependence of Y_R : normal (continuous) growth is temperature-independent; screw dislocation growth involves a pre-exponential term that is a linear function of ΔT , and growth controlled by surface nucleation will yield a Y_R vs. ΔT plot relation showing positive curvature. Plots of $Y\eta$ vs ΔT also provide information on growth mechanisms, exhibiting a positive slope for the case of continuous growth, a dependence on ΔT^2 for screw dislocations, and a dependence on $\exp(1/T\Delta T)$ for surface nucleation (see Baronnet, 1984, for a detailed discussion of this topic).

Predictive models of interface behavior emphasize the relationship between crystal habit and molecular attachment energy - the relative growth rate of a face always increases with increasing attachment energy (e.g. Hartman and Bennema, 1980). Jackson (1958) first showed that the nature (ease of creation) of a crystal interface (α_c) could be modeled as a function of the ratio of surface interaction energy to thermal energy:

$$\alpha_c = \frac{\Delta H_f}{RT_m} \zeta = \frac{\Delta S_f}{R} \zeta \quad (15)$$

where the anisotropy factor ζ is the number of nearest neighbor sites in the plane of the surface; ζ is largest for the most closely packed plane. At small ΔS_f ($< 2R$, e.g. metals) there exists no barrier to the movement of the interface, thus defects are not important, the growth rate anisotropy is small, and isotropic non-faceted minerals are formed: $Y\eta \sim \Delta S_f \Delta T$. It has been observed that when $\alpha_c > 2$ the configuration is stable for layer spreading (presumably because ΔH_f is proportional to bond strength); this promotes large growth anisotropy on different crystal faces, as well as an asymmetry in rates of crystallization and melting in the vicinity of the melting point. It is important to note, however, that the application of this approach to silicates is not straightforward; for this reason Sunagawa (1977) stresses the importance of studying surface morphologies of natural crystals to understand growth processes. In a multicomponent system ΔS_f must be replaced by ΔS_n , the total entropy change on crystallization; ΔS_f is commonly large, promoting a layer spreading mechanism and growth with a smooth interface (Baronnet, 1984).

Crystallization in multicomponent systems. Crystal growth in a multicomponent system is fundamentally different from crystal growth in a single-component system. The most critical difference is that the melt composition will change with crystallization, affecting both the nucleation and growth rate functions as well as the effective undercooling at a given temperature. In addition, the Stokes-Einstein approximation for activation energy as a function of viscosity is only reasonably valid for a crystal growing from its own melt; in high-viscosity multicomponent systems, the activation energy for growth is less than the activation energy of viscous flow that determines the induction period $\tau_{i,x}$ for both nucleation and growth (Gutzow et al., 1977; Kalinina et al., 1980). In addition, a mineral has a diminished peak growth rate when it grows from a multicomponent system compared to growth from its own melt.

At large values of ΔT or in the case of multicomponent melts that crystallize with a large change in composition, diffusion-controlled growth, where transport of material to the crystal interface is rate-controlling, must be considered. The basic diffusion equation (assuming constant T , no diffusion in the solid, and no volume change in the system) for one-dimensional crystal growth involves a source term (a function of Y) to account for the crystal acting as a source or sink for diffusing components:

$$\frac{\delta c}{\delta t} = D \frac{\delta^2 c}{\delta x^2} + Y(t) \frac{\delta c}{\delta x} \quad (16)$$

If diffusion through the melt to the growing crystal is slow relative to the rate of advance of the interface, concentration gradients will be established in the liquid and cause a reduction of growth rate with time. For this scenario, $Y = Cr^{1/2}$ (C is a constant) and a steady state is never achieved. This simple solution requires an assumption of interface equilibrium as a boundary condition, however, which removes the driving force for crystallization. Lasaga (1982) derives a general solution for Equation (16), coupling the interface reaction with diffusion by describing Y as an explicit function of the melt composition at the interface for any time t . Thus the solution requires that the growth rate be known as a function of melt composition. Ghiorso (1987) expands the model of Lasaga (1982) to allow for coupled diffusion of melt species and to include a thermodynamic driving force calculated for the multicomponent system. He shows that liquid activity/composition relations will significantly affect the disequilibrium compositions of the precipitated material. For example, since the evolution of a system away from its initial melt composition will depend on both the incorporation of components at the crystal surface and the transport of material to the interface, oscillatory zoned crystals may develop without the necessity of invoking a perturbation in intensive variables.

Experimental constraints

Crystal growth experiments in basalt and basalt analogue systems continue to provide necessary constraints on theoretical models; these experiments are done isothermally with introduced seed crystals so that nucleation need not be considered. Most workers find evidence that crystal growth at small values of ΔT ($< 45^\circ\text{C}$) proceeds under conditions of interface-control; supporting evidence includes not only the prevalence of faceted crystals and suggestions of screw dislocations (Kouchi et al., 1983) but also the commonly-observed linear dependence of growth on time (e.g. Kirkpatrick et al., 1979; Muncill and Lasaga,

1987). A caution against interpolating simplicity of mechanism at the atomistic level from bulk crystallization results, however, lies in *in situ* observations of crystal growth that show different growth mechanisms involved in the growth of a single crystal (e.g. Tsukamoto et al., 1983).

Constant cooling rate experiments have been used successfully for interpreting cooling conditions of basaltic rocks (e.g. Walker et al., 1978; Lofgren et al., 1979; Grove, 1990). Results from these experiments show that the initial temperature qualitatively determines the final texture by controlling the density and form of the pre-existing nuclei (i.e., all nucleation is heterogeneous); for this reason superheated samples show sporadic crystallization behavior dependent on the distribution of remaining seed crystals. Cooling rate is quantitatively correlated with both crystal size (e.g. Fig. 2) and crystal number density (Lofgren et al., 1979). An observed increase in crystal number density with increased rate of cooling is controlled by an increase in the effective ΔT of nucleation. Once an initial group of nuclei are formed, the final crystal size will be determined by mass balance constraints resulting in a decrease in average crystal size with increasing rate of cooling. Cooling rate variations may also induce the precipitation of metastable phases: for example, Kirkpatrick et al. (1983) and Baker and Grove (1985) reproduce the observed metastable appearance of olivine in tholeiites and basaltic andesites.

One of the more useful qualitative observations from crystal growth experiments is the effect of ΔT on the morphology of crystals; these observations provide an index for the undercooling under which crystallization occurred (e.g. Lofgren, 1980). The observed sequence of crystal morphologies becomes less compact with increased undercooling, from the small ΔT faceted crystals ($<40^\circ\text{C}$ for the experiments of Muncill and Lasaga, 1987) characteristic of interface-controlled growth through acicular skeletal crystals ($40^\circ - 60^\circ\text{C}$), dendrites ($60^\circ - 80^\circ\text{C}$) and spherulites ($>80^\circ\text{C}$); Muncill and Lasaga (1988) found that the stability field of the faceted (lath-shaped) crystals increased in a water-saturated system, although the relative sequence of morphologies remained the same. Dendrites form in response to the development of diffusion profiles (either thermal or chemical) in the melt as growth rates vary along irregularities in the crystal-melt interface. Dendrite growth has been modeled by analogy to viscous fingering in fluids (Langer, 1989); although this approach is not yet predictive, it has shown that a dendrite is a sensitive amplifier of weak fluctuations in its immediate environment, and may thus provide details on minor thermal and chemical anomalies in a melt during rapid crystal growth. Dendrites have also been the obvious target of fractal analysis (e.g. Sander, 1986; Nittman and Stanley, 1986). For example, Fowler et al. (1989) model dendritic olivine in Archaen komatiites using a kinetic variant of the stochastic diffusion-limited aggregation (DLA) model to calculate estimated instantaneous growth rates of $3 \times 10^{-7}\text{cm/s}$. While there is an intuitive appeal to relating fractal dimension of a crystal to effective undercooling, a systematic fractal analysis of experimental run products has yet to be done. The transition from dendritic to spherulitic habit is probably controlled to some extent by crossing the glass transition (Fenn, 1977), as revealed by the characteristic spherulite habit of devitrification products in rhyolite glass.

Much of the quantitative experimental work on crystallization in geologic systems is reviewed in Kirkpatrick (1981). Incorporation of this data into a comprehensive crystal growth model was initiated by Lasaga (1982) in his work on the anorthite-albite system. As explained above, to do this, Y must be known as a function of melt composition. By

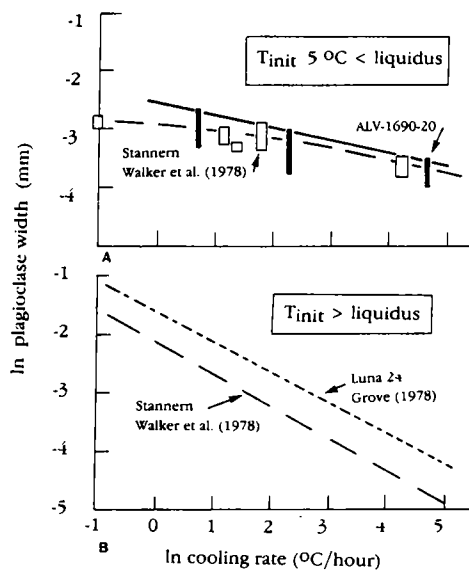


Figure 2. Experimentally determined relationship between plagioclase width and cooling rate for three compositions for which plagioclase is a liquidus or near-liquidus phase. From Grove (1990).

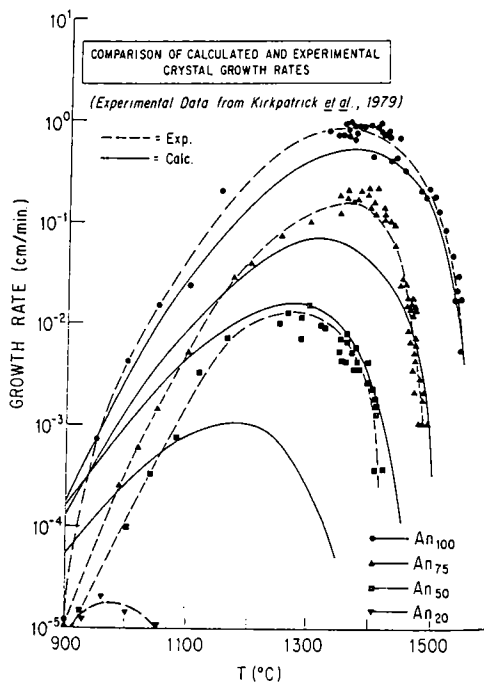


Figure 3. Comparison of calculated growth rates with experimental data at various temperatures and compositions in the plagioclase system. From Lasaga (1982).

assuming that the functional dependence of Y , on ΔT measured for anorthite was the same for the entire plagioclase system, Lasaga was able to parameterize $Y\eta/\Delta T$ as an expansion in ΔT . Additional terms in (14) could then be determined as a function of T and η . This approach results in a good fit to the experimental data of Kirkpatrick et al. (1979) for An_{50} - An_{100} , but fails to match the data for An_{20} (Fig. 3; note the strong compositional dependence of the maximum rate of growth Y_{\max} , the result of compositional dependence of both liquidus temperature T_L and viscosity η). Muncill and Lasaga (1987) extend the experimental data base to determine growth rates for more albitic compositions. They find that the solution presented by Lasaga (1982) predicts the form of the Y vs. ΔT curves fairly well to compositions of An_{30} , but still fails for more albitic compositions. In addition, Muncill and Lasaga (1988) find that adding H_2O to the An-Ab system appears to change the ΔT dependence of the growth curves (Fig. 4a,b); they suggest that their inability to model their results may lie in the inadequacies of the Stokes-Einstein approximation for the kinetic barrier for growth.

One deficiency of these predicted growth models in multicomponent systems has been the poor definition of ΔG_c . The thermodynamic model of Ghiorso (1985) for basaltic melts allows the thermodynamic driving force for growth to be calculated as an explicit function of melt composition. Ghiorso (1987) provides a calculated example of equilibrium (thermodynamically-controlled) plagioclase crystallization from an olivine tholeiite. He calculates the driving force for growth for the plagioclase saturation surface at specific liquid bulk compositions and undercoolings, and uses the functional dependence of the reduced growth rate on ΔT determined by Lasaga (1982). He then solves the generalized growth equation assuming a constant D matrix of $10^{-6} \text{cm}^2/\text{s}$ and viscosities calculated from Shaw (1972). An important result of his calculation is that even at small undercoolings ($\Delta T = 5\text{-}10^\circ\text{C}$), the initial stage of growth where interface control dominates is short, with diffusional processes rapidly becoming rate-controlling.

Prediction of the functional dependence of Y on ΔT is necessary for extensions of the models of Lasaga (1982) and Ghiorso (1987) to more complex systems. Dearnley (1983) suggests a more generalized parameterization of the functional dependence of the growth rate on ΔT as empirically-derived for the corresponding states equation (CSE) for growth rates of small organic molecules (e.g. Magill et al., 1973):

$$\log \left(\frac{Y}{Y_{\max}} \right) = f(\theta) \quad (17)$$

where $\theta = (T_L - T)/(T_L - T_\infty)$. T_∞ is considered to be the kinetically-limiting value of the glass transition temperature at infinite time (i.e., the low- T horizontal tangent to a time-temperature-transformation curve; this is effectively the undercooling at which the crystal growth rate drops to 0). If the CSE equation is valid for silicate systems, the predicted value of $Y/Y_{\max} = 1$ at $\theta = 0.14$ can be used to obtain T_∞ . Alternatively, Equation (17) may be combined with experimental data in the standard growth equation form (e.g. Eqn. 14) to calculate T_∞ . Dearnley (1983) parameterizes growth curves from published data for diopside, plagioclase and basaltic systems to show the applicability of this approach (Fig. 5). Another method of calculating T_∞ may be to use the relationship $T_g \sim T_\infty$ obtained for the diopside-anorthite system by Taniguchi (1990). If this parameterization of T_∞ is used for An_{100} (assuming $T_g = 1100^\circ\text{C}$; Stebbins et al., 1984), $\theta = 0.18$ at $T_{Y_{\max}}$, an agreement

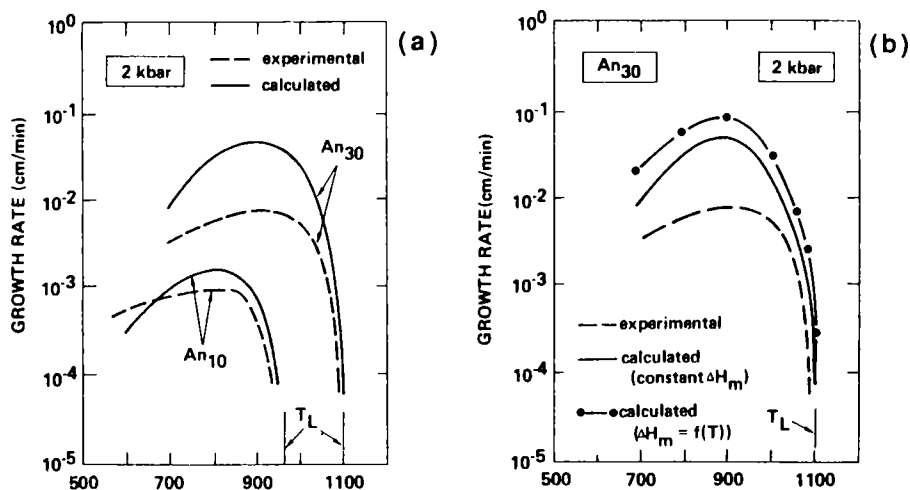


Figure 4. (a) Plot of calculated and experimental growth-rate curves as a function of temperature for 2-kbar H_2O -saturated experiments. (b) Comparison of calculated growth rate curves for a constant ΔH_f and for the condition $\Delta H_f = f(T)$. From Muncill and Lasaga (1988).

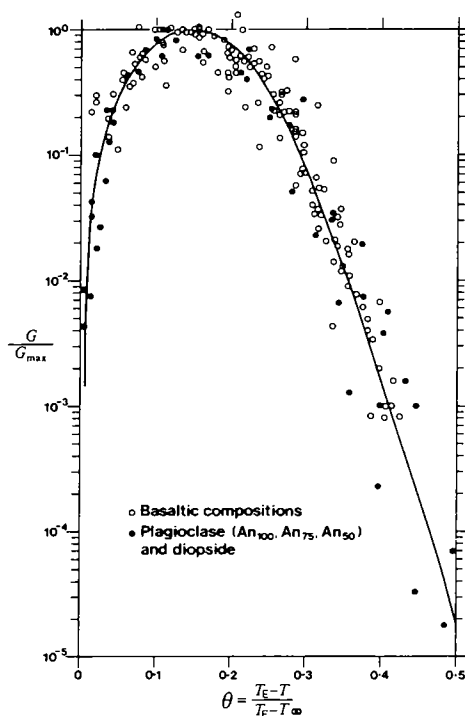


Figure 5. Growth rate (here denoted G) normalized to peak growth rate (G_{max}) plotted as a function of reduced temperature $\theta = (T - T_{\infty}) / (T_L - T_{\infty})$. Points plotted are from published growth rate curves for basaltic compositions, diopside and plagioclase feldspar; solid curve is based on data from small organic molecules (e.g. Magill et al., 1973). From Dearnley (1983).

within the error of the data in Figure 5. While the data to fully test this parameterization are not available, Dearnley's results may provide a useful starting point for models of systems where detailed experimental data do not exist.

Necessary to any crystallization model for multicomponent systems are measurements of both melt and solid diffusion coefficients. Diffusion in silicate melts and glasses is reviewed by Hofmann (1980) and Watson and Baker (1990). For example, new results on chemical interdiffusion in the dacite-rhyolite system by Baker (1990) suggest that the Stokes-Einstein expression is *not* appropriate for relating diffusion to viscosity in these silicic melts; instead he finds that Eyring's equation $D = (kT)/(\alpha_o\eta)$ better predicts his diffusion data for Si in 65-70% SiO₂ melts. Diffusivities of Si and Al are small ($\sim 2\text{-}4 \times 10^{-11}$ cm²/s at 1200°C) and are rate-controlling. Dissolution experiments (where dissolution is defined as a process during which the crystal composition does not respond to the changing melt composition) also provide diffusion rate data; a recent paper by Zhang et al. (1989) comprehensively reviews this topic. They model the non-convective dissolution rate (melt growth rate) using effective binary diffusion coefficients and demonstrate that, unlike growth where a steady state can be achieved through the operation of interface equilibrium (e.g. Lasaga, 1981), non-convective dissolution is time-dependent. Convective dissolution experiments are more common (e.g. Kuo and Kirkpatrick, 1985; Tsuchiyama, 1985a). Convective dissolution is time-independent as rates are controlled by diffusion across a boundary layer (δ): $V_{dis} = bD/\delta$; b describes the concentration gradient (Zhang et al., 1989). While this linear equation is simpler mathematically than the time-dependent diffusion equation, accurate extraction of diffusion rates from experimental data requires that the thickness of the boundary layer be known. Zhang et al. (1989) present an example for the digestion of crustal rocks in a basaltic magma chamber: for $D = 10^{-7} - 10^{-8}$ cm/s, $b = 0.1 - 0.3$, and $\delta = 20$ cm, they calculate dissolution rates of $1.6 \times 10^{-9} - 4.8 \times 10^{-11}$ cm/s.

Finally, compositional zoning in crystals (especially plagioclase) produced under *isothermal* crystallization conditions (e.g. Allegre et al., 1981; Loomis, 1982; Tsuchiyama, 1985b) suggests the intrinsic role of kinetics (and the relationship between interface- and diffusion-controlled growth) in the partitioning of elements between crystal and melt. Interpretation of zoning profiles in natural crystals, especially plagioclase, has long proved a tantalizing quest. Crystal stratigraphy was first attempted by Anderson (1984). He and later workers (e.g. Nixon and Pearce, 1987; Pearce et al., 1987) have concluded that while exact correlation of zoning profiles between neighboring crystals is impossible, major zones of resorption can be identified in most phenocrysts of a sample. Detailed zoning studies in phenocrysts from volcanic rocks show evidence of complex crystallization histories (e.g. Kuo and Kirkpatrick, 1982b; Nixon and Pearce, 1987; Pearce et al., 1987a; Stamatiopoulou-Seymour et al., 1990); plagioclase in particular commonly contains major compositional breaks that have been interpreted as evidence of magma transport and mixing. Pearce (1987) develops a simple model to explain zoning patterns in crystals - he suggests that the size of the local system (the "fictive volume") is the most important control on finer-scale zoning patterns, a conclusion consistent with the control of initial nucleation density on texture evidenced in programmed cooling experiments. Bracketing growth rates can profitably be used in conjunction with this approach to set time limits for different crystallization events (e.g. Pearce et al., 1987b).

COUPLED NUCLEATION AND GROWTH (AVRAMI EQUATION)

Crystallization of a silicate melt involves the combined processes of both nucleation and crystal growth - together these processes define the rate of liquid-to-solid transformation (where the word transformation is used here as a general expression to denote the complete phase change of a one-component system; i.e., the formulation presented below is applicable not only to crystallization of a melt, but also for condensation of a liquid from a gas, vesiculation of a gas from a liquid, etc.) required to properly model the chemical and thermal evolution of magmatic systems. The mathematical description of this transformation was developed by Johnson and Mehl (1939) and Avrami (1939, 1940, 1941), and is known as either the JMA equation or the Avrami equation. Assumptions include (1) a one-component system, (2) an isothermal transformation (a result of the assumption of a single component), and (3) homogeneous nucleation with the nuclei distributed randomly in space (i.e., the embryos for nucleation are not exhausted until the transformation is complete). A complete description of the derivation can be found in Kirkpatrick (1981) and will not be repeated here. The general form of the Avrami equation is

$$\phi = 1 - \exp(-Kt^m) \quad (18)$$

where ϕ is the fraction transformed, K is a function of the crystal shape, nucleation and growth rates, and m describes the time dependence of nucleation and growth. Equation (18) yields sigmoidal curves, with the crystallization time $\tau_K = f(m)K^{-1/m}$. Zanotto and Galhardi (1988) show that $f(m) = 0.584$ when $m = 4$, the case when nucleation and growth rates are constant, and (18) becomes

$$\phi = 1 - \exp(-k_v I Y^3 t^4) \quad (19)$$

with k_v a volumetric shape factor. If nucleation is instantaneous (as appears to be the case for truly heterogeneous nucleation) and is followed by growth, Equation (18) becomes

$$\phi = 1 - \exp(-k_v N_v Y^3 t^3) \quad (20)$$

where N_v is the number of nuclei per unit volume. For the intermediate case with nucleation a decreasing function of time, $3 < m < 4$. The Y^3 term dictates that the exponent in the Avrami equation is very sensitive to the form of the growth rate, and can vary from 1.5 to 4 depending on the combined forms of the nucleation and growth curves. For example, $m = 2.5$ for diffusion-controlled growth with a constant number of particles (Zanotto and Galhardi, 1988). A general expression for transformation under limiting conditions of time-dependent nucleation and growth rates may be written as

$$\phi = 1 - \exp\left\{-k_v \int_0^t I(\tau^+) \left[\int_{\tau^+}^t Y(t^+) dt^+ \right]^3 d\tau^+\right\} \quad (21)$$

where τ^+ is the time of nucleation of a new phase.

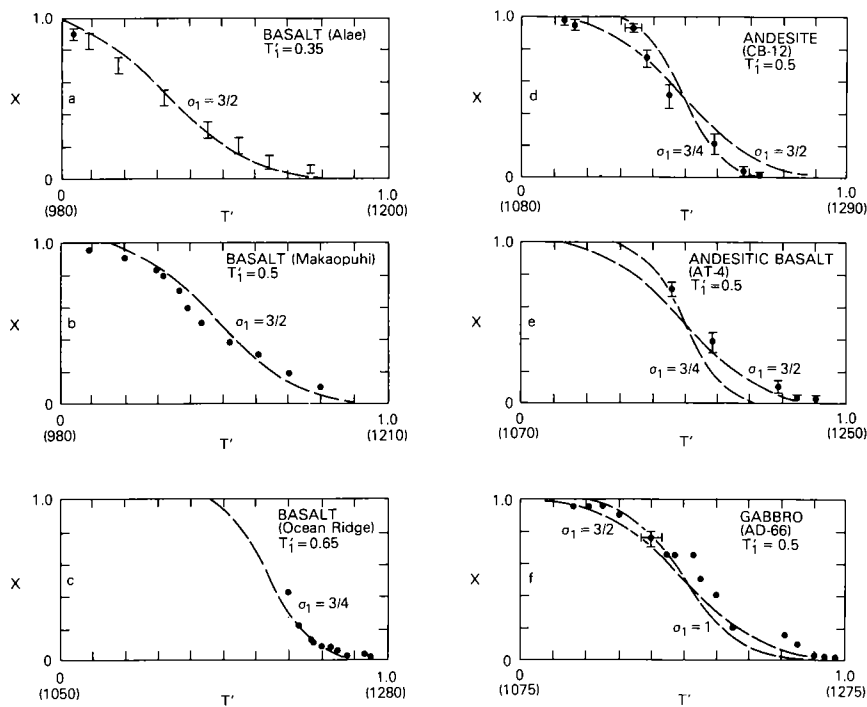


Figure 6. The variation of crystallinity (here denoted X) with temperature (T') as found in (a) tholeiitic basalt of Alae lava lake, (b) tholeiitic basalt of Makaopuhi lava lake, (c) tholeiitic basalt from the FAMOUS area of the mid-Atlantic ridge, (d) Aleutian andesite, (e) Aleutian basaltic andesite, and (f) Aleutian gabbro. From Marsh (1981).

The wide variety of possible exponents in the Avrami equation makes it impossible to determine the nucleation and growth behavior of even a one-component transformation solely from the time-dependence of the transformed volume. Additionally, nucleation and growth mechanisms may change during the course of a transformation: for example, the isothermal transformation of $\text{BaO} \cdot 2\text{SiO}_2$ glass investigated by Zanutto and James (1988) was extremely sensitive to growth rate and changed exponent m (representing a change controlling mechanism) during the transformation from 4 (constant I , interface-controlled growth) at the beginning of the transformation to 2.68 (close to the predicted value for constant number of particles and diffusion-controlled growth) near the end of the transformation.

The functional form of the crystallization history of a multicomponent system over a range of temperatures is unknown, although Kirkpatrick (1976, 1977, 1981) suggests that the transformation should remain sigmoidal in shape - he uses examples of crystallinity vs. depth measured in cores from the Hawaiian lava lakes Alae and Makaopuhi, and converts depth to time through the measured rate of advance of the crust-melt interface. Under most conditions, the variation of crystallinity with time in natural samples is difficult to measure, but the variation of crystallinity with temperature is well known (e.g. Marsh, 1981) - it too is sigmoidal (Fig. 6). In fact, equilibrium crystallization models show that both temperature-time curves and crystallinity-temperature curves are sigmoidal for the conductive cooling and resultant crystallization of an olivine tholeiite (Ghiorso and Carmichael, 1985;

Ghiorso, 1988; Fig. 7a,b). Note that both the observational data presented by Marsh and the calculated curves for equilibrium crystallization of Ghiorso and Carmichael show that most crystallization occurs in a relatively small temperature range (50-75°C) relative to the entire temperature range between the liquidus and solidus. This transformation pattern results in the non-uniform liberation of latent heat over the crystallization interval in time as well as temperature, as shown in Figure 7c (produced by combining the data of Figs. 7a and b). This plot too is generally sigmoidal in form, and represents the limiting case of growth controlled by heat diffusion out of the system. Much more complex transformation curves may be formed, however, when physical processes involved with magmatic cooling are more complex (see the results of a combined convection-conduction model in Ghiorso, 1988).

The linked problem of crystallization and conductive cooling was modeled by Kirkpatrick (1976) and extended by Brandeis et al. (1984), Brandeis and Jaupart (1987) and Spohn et al. (1988), in simple (respectively one- and two-component) melts. While these models lack the thermodynamic complexities of Ghiorso (1987, 1988) and are limited by the paucity of kinetic data for natural melts, they provide a foundation for examining the coupling between kinetics and thermal history of a magma.

Brandeis and Jaupart (1987) model a one-component system with a crystallization history described by the time derivative of Equation (21), given by Kirkpatrick (1976) as

$$\frac{d\phi}{dt} = k_v(1 - \phi(t))Y(t) \int_0^t I(\tau^+) \left(\int_{\tau^+}^t Y(t) dt \right)^2 d\tau^+ \quad (22)$$

Brandeis and Jaupart formulate Y and I as functions of (ΔT) rather than functions of time; this requires knowledge of the undercooling as a function of time, as discussed below. They couple Equation (22) with a one-dimensional conductive cooling model that includes a source term for latent heat. Parameterization of these equations results in time (τ_c) and length (d_s) scales for heat transfer based on conductive heat flow in the country rock:

$$d_s = (\kappa \tau_c)^{1/2} \quad (23a)$$

(κ is thermal diffusivity); a time scale for crystallization (τ_c , derived from Eqn. 19) based on maximum growth (Y_{\max}) and nucleation (I_{\max}) rates

$$\tau_c = (Y_{\max}^3 I_{\max})^{-1/4} \quad (23b)$$

and a size scale (R_c) for nucleation and growth as previously defined by Winkler (1949) and Shaw (1965):

$$R_c = \left(\frac{Y_{\max}}{I_{\max}} \right)^{1/4} \quad (23c)$$

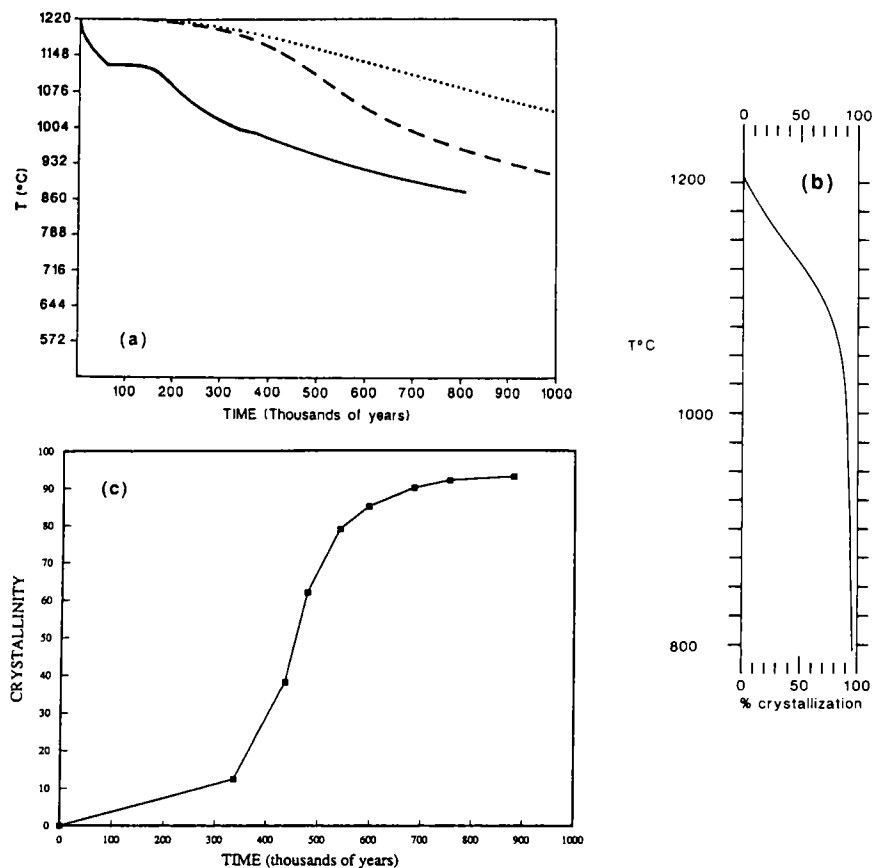


Figure 7. (a) Temperature-time profiles at the center of a cooling olivine tholeiite intrusive body (10^3 km^3). The solid curve corresponds to a convective-conductive model, the dashed curve to a conductive model with variable latent heat of fusion and the dotted curve to a conductive model with an averaged constant latent heat of fusion over the crystallization interval. The magma is intruded at the liquidus temperature (1220°C) and the temperature of the country rock is 500°C . From Ghiorso (1988). (b) Calculated change in crystallinity with temperature for the fractional crystallization of an olivine tholeiite along the QFM buffer at 1 bar. From Ghiorso and Carmichael (1985). (c) Calculated crystallinity vs. time curve using data from (a) and (b), assuming a conductive cooling model with variable latent heat of fusion.

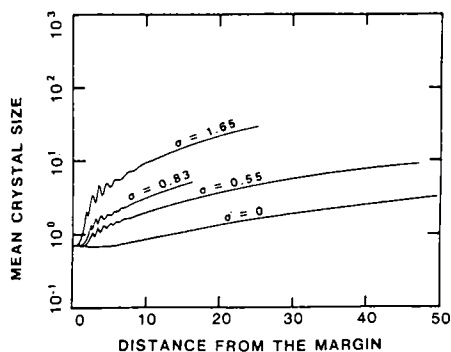


Figure 8. Mean crystal size (radius) versus distance from the margin in dimensionless variables for different values of the Stefan number σ . From Brandeis and Jaupart (1987a).

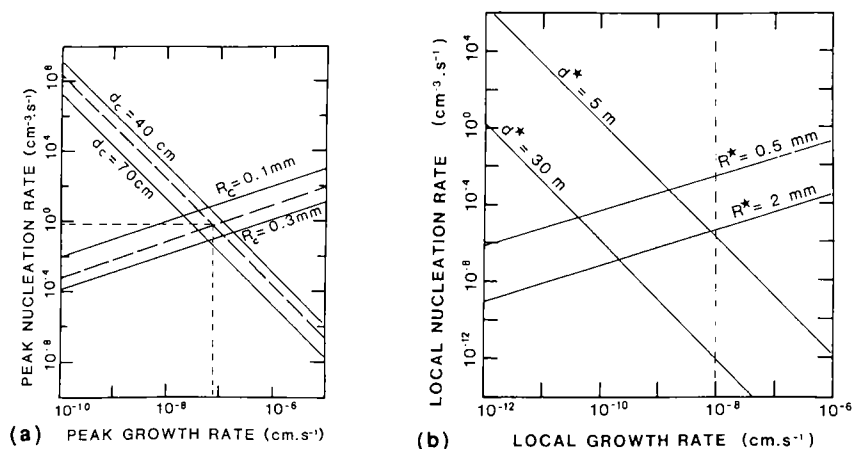


Figure 9. Relationships between the values of nucleation and growth rates (a) in transient conditions prevailing close to the margins and (b) in quasi-equilibrium conditions prevailing in the interior of large magma chambers. The intersections of the curves define the domain of plausible values for the kinetic rates in natural conditions. From Brandeis and Jaupart (1987a).

The parameterization in Equation (23b) involves an implicit assumption of interfacial growth and continuous nucleation ($m = 4$). The dimensionless Stefan number Γ can be defined as $\Delta H_f / C_p \Delta T$; in a one-component system, all the latent heat will be released at a single fusion temperature ($\Gamma = \Delta S_f / C_p$), and will only be modified if the system is quenched instantly to a much lower temperature; if the undercooling of the system is allowed to evolve with time during crystallization, Γ will be time-dependent. The crystallization front moves at a rate proportional to $t^{1/2}$ (as dictated by the Stefan solution) with the scaling parameter $1/\Gamma$. The dependence of average crystal size on distance from an intrusion margin can then be calculated, as shown in Figure 8 for different values of Γ ; oscillations in the calculated size curves arise from temperature (ΔT) oscillations that Brandeis and Jaupart (1984) attribute to cyclic nucleation events with accompanying releases of latent heat. Since these curves are highly dependent on the assumed form of the nucleation function, better constraints on the form of the nucleation function at small undercoolings are needed; a separate parameterization for conditions of growth *without* nucleation might also be appropriate.

Brandeis and Jaupart (1987a) use Figure 8 to infer crystallization kinetics from measurements of mean crystal sizes and rate of increase in size with distance across dikes (e.g. Gray, 1970). They use the scaling presented in Equations (23a,b,c) to develop a relationship between peak growth rate and peak nucleation rate, contoured for different values of d_s and R_c (Fig. 9a), and estimate typical crystal growth and nucleation rates in dikes of, respectively, 10^{-7} cm/s and $1/\text{cm}^3\text{s}$. These rate estimates imply a crystallization time close to a dike margin of $2 \times 10^5 \text{ s}$ (2-3 days). In contrast, crystallization of a large intrusion (small ΔT ; Fig. 9b) must occur close to equilibrium, and rate estimates require knowledge of both the thickness of the crystallization interval (ϵ) and its relationship to the length scale of heat removal: $d_s/\epsilon = \omega$, where d_s is scaled based on heat conduction in the *country rock*. Brandeis and Jaupart estimate $1 < \omega < 10$, but do not explore the variation of ω as a function of the parameters of their model. If ω is known, growth and nucleation rates can be estimated directly from Equations (23a,b,c); for example, when $\omega = 1$, Y_{\max} and I_{\max} can be calculated knowing only R_c and d_s : $Y_{\max} = R_c K / d_s^2$ and $I_{\max} = Y_{\max} / R_c^4$.

Spohn et al. (1988) extend the work of Brandeis and Jaupart (1987) to model crystallization of a binary eutectic system, which allows investigation of the evolution of undercooling in a system where both the melt composition and the liquidus temperature are allowed to vary. In contrast to the one-component model, they predict longer crystallization times (due to the C_p contribution of cooling from the liquidus to the solidus), more complex ϕ vs. time curves, and no temperature oscillations at the crystallization front. While Spohn et al. do not explicitly account for the effect of nucleation delay, they account for heterogeneous nucleation by removing the kinetic barrier to nucleation for a variable fraction of nuclei. The thermodynamic barrier to nucleation is modeled using Equation (2 and 5); growth is assumed to be interface-controlled and to occur at small ΔT (Eqn. 14). Differentiation of Equations (1) and (14) with respect to temperature

$$\frac{(T_L - T_{lmax})^3}{T_L^2(T_L - 3T_l)} = \frac{4k\sigma^3}{\Delta H_f^2 \Delta G_a} \quad (24a)$$

$$\frac{T_{Ymax}}{T_L - T_{Ymax}} = \frac{\Delta G_a}{RT_L} \quad (24b)$$

then allows parameterization of I and Y vs. ΔT curves as a function of T_{lmax}/T_L and T_{Ymax}/T_L under the condition that the kinetic barriers to nucleation and growth (ΔG_a) are identical and can be defined by (24b). Neither the assumption that the activation energies are equivalent nor the values of T_{lmax}/T_L , T_{Ymax}/T_L , I_{max} or Y_{max} are well-constrained for geologic systems, although in Tables 1 and 2 I present a tabulation of available experimental results. In addition, Spohn et al. assume that T_{lmax}/T_L and T_{Ymax}/T_L are constant and independent of concentration, and that I_{max} and Y_{max} are constant for each end member, despite the changing composition of the liquid. Clearly these assumptions represent a major departure from the situation encountered in natural systems where as the liquid changes composition, the precipitating solid does as well, resulting in significant variations in nucleation and growth rate maxima as a function of changing liquid composition (i.e., Tables 1 and 2).

As discussed above, a major question to be addressed through coupled crystallization and cooling models is the relationship of the time- and length-scales of crystallization to those of cooling; this question has implications for most models of magmatic processes. Spohn et al. (1988) introduce a parameterization based on the Avrami number (Av), a ratio of the time scales of crystallization (τ_c ; Eqn. 23b) and heat transfer (τ_h ; Eqn. 23a):

$$Av \equiv (I_{max} Y_{max}^3) \left(\frac{d_s^2}{K} \right)^4 \quad (25)$$

where d_s is the dike half width. The time to crystallize a body of magma (τ_c) is determined by the time required for heat removal from the system

$$\tau_s(\xi) = 0.25 \left(\frac{\xi}{\Lambda(\xi)} \right)^2 \quad (26a)$$

Table 2. Compilation of available growth rate data for multicomponent systems. Crystallizing minerals in the Fenn and Swanson data are abbreviated as AF-alkali feldspar; QZ-quartz; PL-plagioclase.

| COMPOSITION | T_L (K) | $T_{Y_{max}}/T_L$ | $Y_{max}(\text{cm/s})$ |
|-----------------------------------|-----------|-------------------|------------------------|
| Fenn (1977) | | | |
| AF-Ab90 2.7% H_2O | 1218 | 0.84 | 5.0×10^{-6} |
| AF-Ab90 5.4% H_2O | 1113 | 0.86 | 5.2×10^{-6} |
| AF-Ab90 9.0% H_2O | 1048 | 0.93 | 2.5×10^{-6} |
| AF-Ab70 1.7% H_2O | 1243 | 0.87 | 3.2×10^{-6} |
| AF-Ab70 4.3% H_2O | 1113 | 0.88 | 3.2×10^{-6} |
| AF-Ab70 9.5% H_2O | 1038 | 0.93 | 2.4×10^{-6} |
| AF-Ab50 2.8% H_2O | 1228 | 0.82 | 6.3×10^{-6} |
| AF-Ab50 6.2% H_2O | 1080 | 0.90 | 5.7×10^{-6} |
| Swanson (1977) | | | |
| QZ-Gr + 3.5% H_2O | 1143 | 0.87 | 10^{-8} |
| QZ-Gd + 6.5% H_2O | 963 | 0.90 | 10^{-7} |
| QZ-Gd + 12% H_2O | 943 | 0.79 | 10^{-8} |
| AF-Gr + 3.5% H_2O | 1163 | 0.83 | 10^{-7} |
| AF-Gd + 6.5% H_2O | 953 | 0.89 | 10^{-7} |
| AF-Gd + 12% H_2O | 923 | 0.78 | 10^{-8} |
| PL-Gr + 3.5% H_2O | 1233 | 0.88 | 10^{-6} |
| PL-Gd + 6.5% H_2O | 1213 | 0.85 | 10^{-6} |
| PL-Gd + 12% H_2O | 1173 | 0.74 | 10^{-8} |
| Kirkpatrick et al. (1979) | | | |
| AN100 | 1830 | 0.88 | 1.5×10^{-2} |
| AN75 | 1778 | 0.89 | 2.5×10^{-3} |
| AN50 | 1723 | 0.88 | 1.7×10^{-4} |
| Muncill and Lasaga (1987;1988) | | | |
| AN40 | 1698 | 0.89 | 8.3×10^{-5} |
| AN30 | 1663 | 0.90 | 1.5×10^{-5} |
| AN20 | 1610 | 0.90 | 2.5×10^{-6} |
| AN10 | 1524 | 0.94 | 8.3×10^{-7} |
| AN30 (2KB) | 1373 | 0.83 | 1.5×10^{-4} |
| AN10 (2KB) | 1239 | 0.89 | 1.7×10^{-5} |

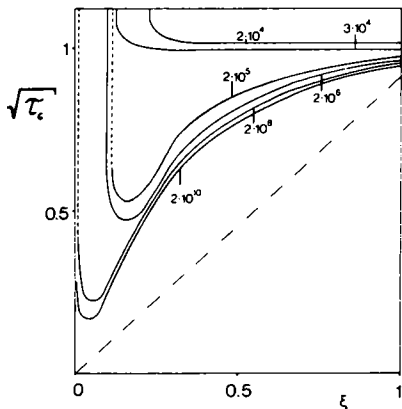


Figure 10. Square-root of crystallization times (solid lines), τ_c as a function of normalized distance ξ for varying values of the Avrami number; the dashed line gives the solution of a purely thermal Stefan problem. From Spohn et al. (1988).

where ξ is the scaled distance from the dike margin and $\Lambda(\xi)$ is a constant that depends on Γ ($\Lambda \sim \Gamma^{1/2}$, Carslaw and Jaeger, 1959; Spohn et al. use a value of Λ between 0.3 and 0.6, which is appropriate for their assumption that Γ is of the order 10^{-1}), and by the time to nucleate and grow crystals

$$\tau_{\kappa} = (\tau_i \tau_{\gamma}^3)^{1/4} \quad (26b)$$

For a dike width on the order of a meter $\tau_{\kappa} \approx 10/(Av^{1/4})$; larger dikes require a different constant. If the country rock temperature is much less than the magma temperature, $\tau_s(\xi = 1) \approx \tau_c(\xi = 1)$ and Equations (26a,b) can then be equated to determine the point at which $\tau_s = \tau_{\kappa} \equiv \xi_0$. This implies that as $\xi_0 \rightarrow 0, Av \rightarrow \infty$, and crystallization time is given by Equation (26a), the limit of the purely thermal Stefan problem. In contrast, a small dike with $Av < 10^4$ will not crystallize even at the dike center, as the crystallization time will exceed the time scale of heat removal. For values of $Av \sim 5 \times 10^4$, $\xi_0 \approx 1$ and τ_c will be independent of distance from the margin except at very small values of ξ (Fig. 10); this in turn implies a constant grain size across much of the dike. Small Avrami numbers will be generated either by small dike size or by small values of I_{\max} and Y_{\max} . Spohn et al. (1988) show that the Avrami number may be estimated from the derived gradient of dimensionless mode crystal size (dimensionless peak grain size, ρ_{ma}) at the dike center in their numerical experiments from the relations

$$\log \rho_{ma} = -0.083 \log Av - 0.6 \quad (27a)$$

and

$$\frac{d \log \rho_{ma}}{d \log \xi} = 0.149 \log Av - 0.2157 \quad (27b)$$

Once Av and ρ_{ma} have been determined, Y_{\max} can be evaluated from the measured peak crystal size at the dike center (R_m)

$$\rho_{ma} \equiv \frac{R_m}{(Y_{\max} d_s^2 / \kappa)} \quad (27c)$$

Maximum nucleation rates can be similarly estimated from changes in scaled number density (ι) of crystals at the dike center using the empirical relations

$$\log \iota(\xi = 1) \approx -0.72 \log Av + 1.682 \quad (28a)$$

$$\frac{d \log \iota(\xi = 1)}{d \log \xi} \approx -0.5411 \log Av + 1.267 \quad (28b)$$

$$\iota(\rho) \equiv \frac{N(R_m)}{(I_{\max} d_s^2 / \kappa)} \quad (28c)$$

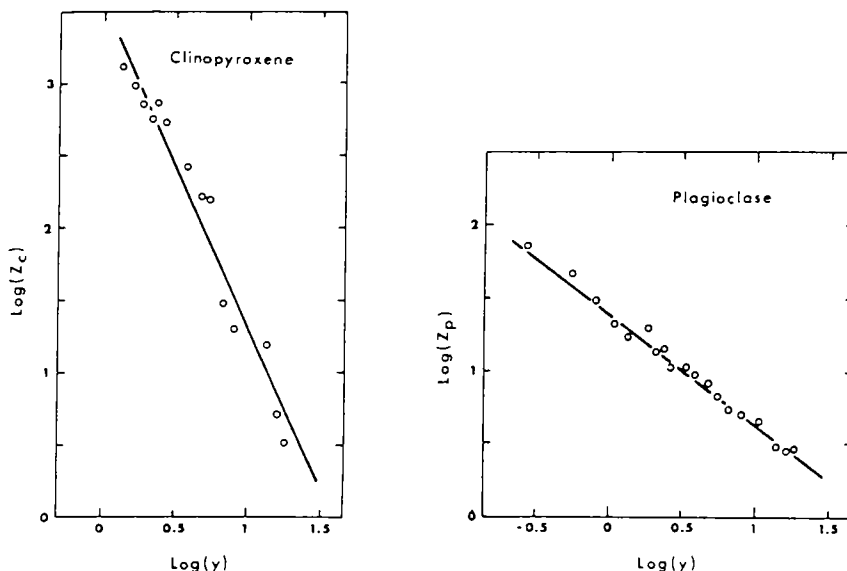


Figure 11. Variation in the relative number of clinopyroxene (here denoted Z_c) and plagioclase (Z_p) crystals per cm^3 across the Kigaviarluk dike (width = 106 m). From Gray (1970).

In an example using average grain sizes measured across two tholeiite dikes, Spohn et al. (1988) calculate Avrami numbers of 2×10^7 and 3×10^6 for dikes of, respectively, 145 and 208 cm width. The inverse correlation between Av and dike width is consistent with the inverse correlation of Av and τ_c : larger dikes would be expected to require a longer time to cool and crystallize. Estimated growth and nucleation rates based on their parameterizations are, respectively, 10^{-6} cm/s and $0.4\text{-}1/\text{cm}^3\text{s}$.

CRYSTALLIZATION IN NATURAL SYSTEMS

As illustrated above, the final texture of an igneous rock should reflect the integrated nucleation and growth history of the constituent minerals over the duration of the crystallization interval (assuming no subsolidus changes in grain size). A fundamental observation about igneous rock textures is that with some notable exceptions, variations in grain size throughout a dike, sill, lava flow sequence or intrusion are small (2-3 orders of magnitude). This observation suggests that the crystallization process and/or rate does not vary tremendously, except under extreme conditions (e.g. chilled margins). As mentioned above, one of the most important questions pertaining to the crystallization of magmatic (multicomponent) systems is the development of the undercooling with time. The relationship between ΔT and T is complex, as undercooling drives the crystallization process, but is itself a function of changing melt composition and mineral species precipitated. In this section, methods of estimating crystallization rates from rock textures will be reviewed; estimated rates may then be used to invert the problem and determine the evolution of ΔT during cooling and crystallization.

Crystallization of dikes

Dikes have long provided an attractive target for linking the textural development of cooling magmas to their thermal evolution, because of the relatively simple thermal histories attributed to dike emplacement (e.g. Winkler, 1949; Gray, 1970, 1978a; Ikeda, 1977). Conversely, rock textures have also been used to constrain cooling histories of basalt flows (e.g. Long and Wood, 1986; DeGraff et al., 1989). Winkler (1949) first used the scaling relationship between average grain size and rates of nucleation and growth presented in Equation (23b) to address the kinetics of dike crystallization. Gray (1970; 1978a) proposed that for flash-injected dikes (instantaneous emplacement) the number density of crystals (N_v) should vary as a function of scaled distance from the margin (ξ) as $N_v \sim \xi^q$ (Fig. 11), where the value of q is controlled by the time history of nucleation; q is thus related to, although not identical to, the Avrami exponent m (Eqn. 18). Exponent q is negative, as would be predicted by observed experimental correlations between number density and cooling rate (e.g. Lofgren et al., 1979), but appears to be unrelated to total dike width (6-240 m) and only broadly related to mineral species (e.g. q for plagioclase is consistently less negative than q for oxides); the data are insufficient to determine the q dependence on crystallization order. Gray (1978a) measured crystal sizes in the same samples but found no consistent variation in the relative size distributions across the dike, or with measured values of q . Problems with Gray's model include the assumption of flash injection for large dikes, and use of a straight conductive cooling model without inclusion of terms for heat evolution and convection prior to and during solidification.

Ikeda (1977) measured grain size distributions for the much smaller Iritono basaltic andesite dikes (<5 m), where the assumption of conductive cooling is better justified. Ikeda also includes a latent heat term in his cooling model; he finds a linear relationship between log (peak grain size; measured) and log (cooling time; calculated, Fig. 12a). Time-averaged growth rates for plagioclase can be calculated from these data (Table 3); these estimates are minimum values since there is no way of determining when nucleation occurred. Estimated plagioclase growth rates of 1.7×10^{-6} to 7×10^{-10} cm/s are a decreasing function of increasing distance from the margin and increasing dike width (Fig. 12b). Both of these observations are consistent with the scaling analysis of Spohn et al. (1988). Measured size variations across the 90 cm dike can be used to estimate $Av = 5 \times 10^4$, $Y_{\max} = 7 \times 10^{-8}$ cm/s, and $I_{\max} = 10^4/\text{cm}^3\text{s}$ using Equations (27a,b,c). The maximum growth rate calculated in this manner is about 3 times higher than the time-averaged growth rate determined from Ikeda's data and cooling model (2.4×10^{-8} cm/s).

Larger dikes present increasing complexities of analysis due to the possibilities of (a) long-term duration of flow, and (b) the possibility of convection during cooling and resultant redistribution of phenocrysts. As an example, crystal size measurements across a 27 m wide diabase dike in Salvador, Brazil (Kneeder, 1989), show complex size relationships across the dike for pre-emplacement oxide phenocrysts, but exhibit a regular increase in size of groundmass (post-emplacement) plagioclase (Fig. 13a; Table 3). Both oxide and plagioclase crystal populations show an abrupt decrease in number density at the dike margin, then a constant number density across the dike interior (Fig. 13b). A comparison of a log (ξ) vs. log (R_m) plot for plagioclase in the 27 m Salvador diabase and 90 cm Iritono basaltic andesite dikes shows that the smaller dike has a steeper slope (greater change in grain size with scaled

Table 3. Textural data and estimated growth rate data for plagioclase in basaltic dikes (from Ikeda, 1977; Kneedler, 1989) and programmed cooling experiments (from Walker et al., 1978; Grove, 1990). R_m is the size at the maximum of the distribution (ρ_{max}); R_3 is the range of measured sizes at half the maximum peak height.

| DIKE WIDTH | R_m (μm) | R_3 (μm) | τ | Y (cm/s) |
|----------------------|-------------------|-------------------|-------------------|-----------------------|
| IRITONO | | | | |
| 5cm | 5 | 3-8 | 3.0×10^2 | 1.7×10^{-6} |
| 30cm | 14 | 9-29 | 1.1×10^4 | 1.3×10^{-7} |
| 30cm | 15 | 9-22 | 1.1×10^4 | 1.4×10^{-7} |
| 60cm | 39 | 22-84 | 4.4×10^4 | 8.9×10^{-8} |
| 90cm, at 4cm | 8 | 3-14 | 2.0×10^3 | 4.0×10^{-7} |
| 90cm, at 10cm | 12 | 5-22 | 8.1×10^3 | 1.5×10^{-7} |
| 90cm, at 20cm | 19 | 10-41 | 4.0×10^4 | 4.8×10^{-8} |
| 90cm, at 35cm | 21 | 9-41 | 8.9×10^4 | 2.4×10^{-8} |
| 1.5m, at 20cm | 38 | 20-69 | 4.0×10^4 | 9.5×10^{-8} |
| 1.5m, at 75cm | 45 | 30-80 | 2.7×10^5 | 1.7×10^{-8} |
| 5m | 70 | 30-290 | 3.0×10^6 | 2.3×10^{-9} |
| 15m | 190 | 50-300 | 2.7×10^7 | 7.0×10^{-10} |
| SALVADOR | | | | |
| 27m, at 0.15m | 25 | 10-60 | 2.1×10^4 | 1.2×10^{-7} |
| 27m, at 3.35m | 90 | 50-150 | 1.0×10^7 | 9.0×10^{-10} |
| 27m, at 1.04m | 125 | 50-200 | 1.0×10^8 | 1.3×10^{-10} |
| Grove (1990) | | | | |
| 110°C/hr | 36 | | 6.5×10^3 | 5.5×10^{-7} |
| 9.5°C/hr | 57 | | 7.6×10^4 | 7.5×10^{-8} |
| 0.2°C/hr | 94 | | 3.6×10^5 | 2.6×10^{-8} |
| Walker et al. (1978) | | | | |
| 100°C/hr | 10 | | 7.2×10^3 | 1.2×10^{-7} |
| 10°C/hr | 33 | | 7.2×10^4 | 4.4×10^{-8} |
| 1°C/hr | 110 | | 7.2×10^5 | 1.5×10^{-8} |

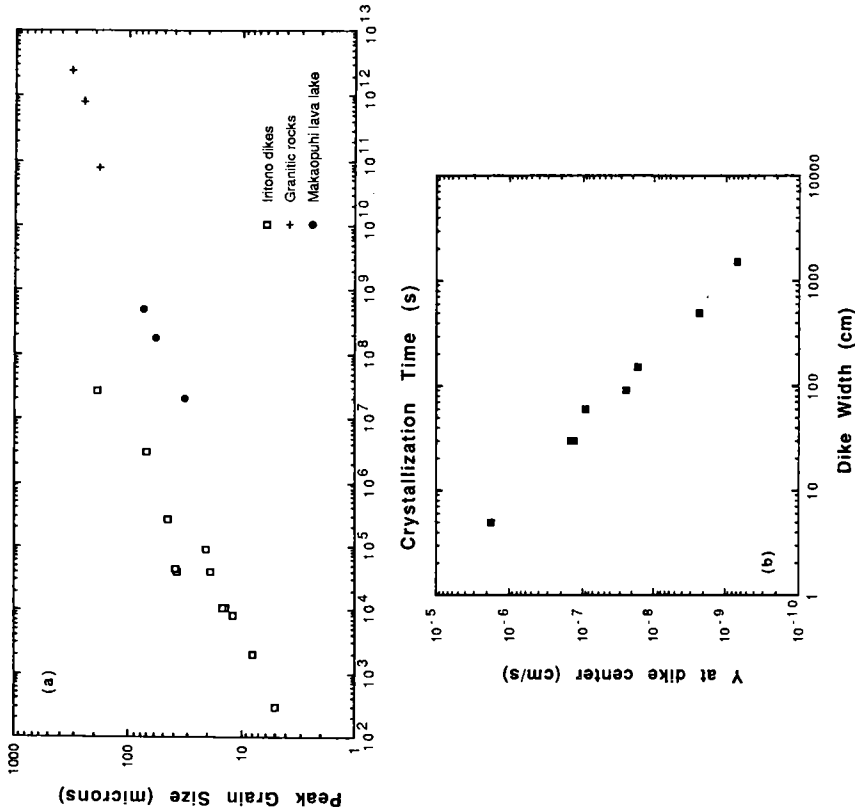


Figure 12. (a) Peak grain sizes (R_m) of plagioclase in microns plotted against their estimated time of crystallization. (b) Growth rate (Y) at the dike center as a function of total dike width. Data from Ikeda (1977).

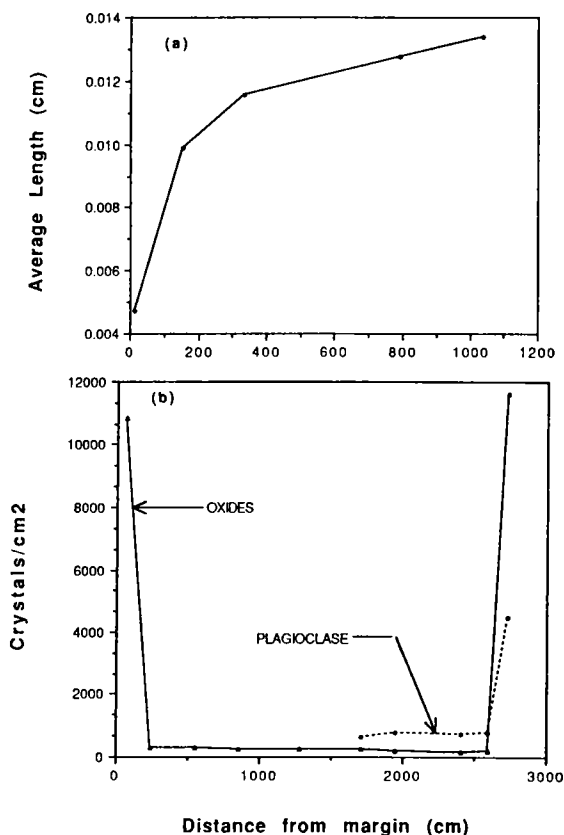


Figure 13. (a) Average plagioclase width (apparent short axis) as a function of distance from the margin in the Salvador diabase dike. (b) Number density of crystals per cm² across Salvador diabase dike. From Kneeder (1989).

distance) and smaller average grain size than the larger dike, as would be expected for the steeper temperature gradients and shorter crystallization time of the smaller dike (Fig. 14). The small slope for groundmass plagioclase crystallizing in the Salvador diabase results in an estimated $Av = 3.3 \times 10^3$, while this value for the Avrami number is smaller than any considered by Spohn et al. (1988) for small dikes, it is consistent with the approximately constant grain size and number density across the dike (constant τ_c ; see Fig. 10). The growth rate at the dike center calculated from the relations of Spohn et al. (1988) is 1.8×10^{-10} cm/s; this is close to the value of 1.3×10^{-10} cm/s obtained from a crystallization time estimate from a conductive cooling model with latent heat (Eqn. 4-143, Turcotte and Schubert, 1982), and is consistent with the trend of decreasing maximum growth rate with increasing dike size shown in Figure 12b.

Crystallization rate data from textural measurements in dikes can be related to cooling rate experiments if the temperature range of the crystallization interval ($T_L - T_S$) is known, with cooling rate inversely proportional to the time a melt has to crystallize. For most basaltic melts, $T_L - T_S$ is 200-250°C, although for a given melt the crystallization interval has been shown to increase for very large cooling rates (>100°C/hr; e.g. Walker et al., 1976, 1978; Grove, 1978). Minimum plagioclase growth rates calculated from programmed

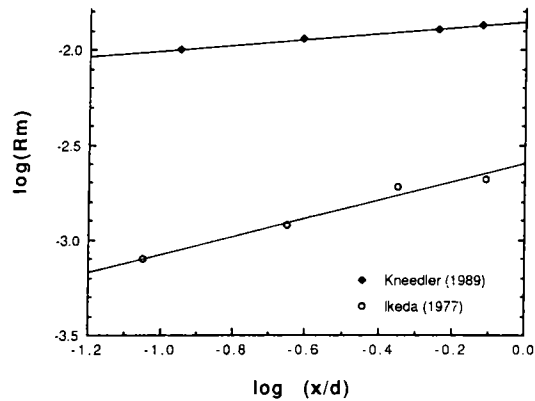


Figure 14. Log peak grain size (R_m) vs. log normalized distance (ξ) for the 90 cm Iritono dike (slope = 0.47; data from Ikeda, 1977) and the 27 m Salvador dike (slope = 0.15; data from Kneeder, 1989).

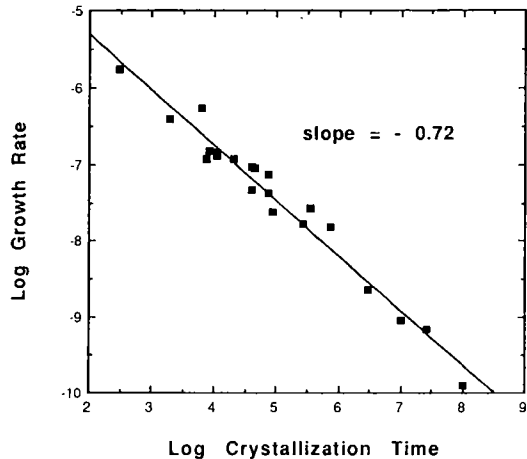


Figure 15. Variation in calculated plagioclase growth rates from basaltic melts with estimated crystallization time. Data from Ikeda (1977), Walker et al. (1978), Kneeder (1989) and Grove (1990).

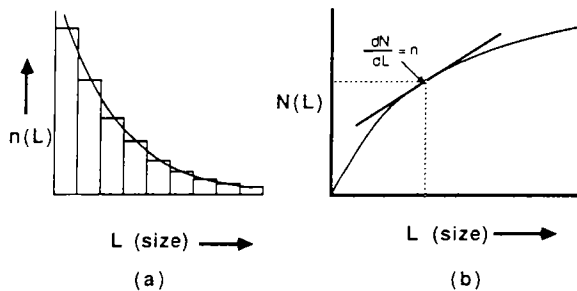


Figure 16. (a) Population density (n) is the number of crystals in any size range divided by the size interval. (b) On a plot of cumulative number of crystals against size (L), population density is the slope of the curve. From Marsh (1988a).

cooling experiments for an assumed crystallization interval of 200°C are also tabulated in Table 3; again these rates represent a minimum because the time delay for nucleation is unknown, although the delay should be small for experiments with initial temperatures below the liquidus. Time-averaged plagioclase growth rates from all the data of Table 3 show a consistent relationship with crystallization time (cooling rate; Fig. 15) that is clearly related to effective undercooling. Although the relationship between undercooling and cooling rate is unknown, an order of magnitude estimate may be made using the empirical relationship between growth rate and undercooling for plagioclase crystallization from a basalt melt from Maaloe et al. (1989; their Eqn. 1): the effective undercooling appears to change from 2°C - 0.2°C as the cooling rate drops from 100 to 1°C/hr. It is interesting to note that the growth rate of dendritic olivine in Archaen komatiites estimated from fractal analysis (3×10^{-7} cm/s; Fowler et al., 1989) is identical to the plagioclase growth rates I've derived from the experiments that have undergone rapid cooling: cooling rates of 100-110°C yield growth rates of $1.2 - 5.5 \times 10^{-7}$ cm/s.

Crystal size distributions

Crystallization rates determined from textural measurements in dikes represent a time average of a crystallization process that may not be linear in time; it is desirable, therefore, to investigate crystallization in samples that have not fully crystallized in order to better understand the crystallization process. Kirkpatrick (1977) used the known cooling history of Kilauea's Makaopuhi lava lake to determine *in situ* crystallization rates in samples of varying crystallinity collected from drill cores. He obtained maximum growth rates of $1.7 - 11 \times 10^{-10}$ cm/s and nucleation rates (corrected for the fraction crystallized) of $6.8 \times 10^{-3} - 2/\text{cm}^3\text{s}$, rates very similar to those estimated above for plagioclase growth in the Salvador diabase dike (small ΔT). He found that both rates *increased* with increasing fraction crystallized, a result he attributed to an increase in effective ΔT with time in accord with the predictions of his kinetic crystallization model (Kirkpatrick, 1976). He defends this result in response to Gray (1978b) by calling on the dominance of interface processes during the course of crystallization (Kirkpatrick, 1978). We thus return to the fundamental question of what controls undercooling in a multicomponent system.

Theory. An empirical approach to the determination of *in situ* bulk crystallization rates in igneous systems was introduced by Marsh (1988b) and Cashman and Marsh (1988): as demonstrated by chemical engineers (e.g. Randolph and Larson, 1971; Jancic and DeJong, 1984; Jancic and Grootsholten, 1984; Youngquist, 1984), measured crystal size frequency distributions (CSDs) for crystals grown from a melt show a negative exponential correlation between frequency and size that may be used to extract average nucleation and growth rates, given constraints on crystallization time. While the mixed suspension, mixed product removal (MSMPR) model of the chemical engineers is not directly analogous to crystallization in a magma chamber, it provides a steady state end member for analysis of crystal growth in an open magmatic system. Crystal size distributions are formulated according to an equation governing the conservation of *numbers* of crystals as they nucleate and grow in a magmatic system. In order to do this, the number density (n) of crystals must be known as a function of crystal size (L). A straight histogram of number of crystals per unit volume ($N(L)$) versus size (Fig. 16a) is unsatisfactory since the shape of the histogram curve is

dependent upon the width of the chosen size class; for that reason the mathematically stable population density ($n(L)$), defined as the slope of the cumulative number density curve at any given size class is used (Fig. 16b):

$$N(L) = \int_0^L n(L) dL \quad (29)$$

From (29) we see that

$$n(L) = \frac{dN(L)}{dL} \quad (30)$$

where $n(L)$ is the number of crystals per unit length (L) per unit volume of magma and thus has units of cm^{-4} . Given a magmatic system with a characteristic residence (crystallization) time $\tau \equiv V/Q$ (where both the system volume V and the system flux rate Q are assumed constant), a number balance may be written based on the amount of crystallization that occurs within the system:

$$\frac{\delta n}{\delta t} + \frac{\delta(Yn)}{\delta L} + \frac{n}{\tau} = 0 \quad (31)$$

A further simplification can be made if the growth rate (Y) is not a function of size L , and (31) becomes

$$\frac{\delta n}{\delta t} + Y \frac{\delta n}{\delta L} + \frac{n}{\tau} = 0 \quad (32)$$

A general solution for (32) is $n = C_o f(L/Y\tau - t/\tau) e^{-t/\tau}$ where $f(L/Y\tau - t/\tau)$ is an arbitrary function and C_o is a constant to be determined by the initial condition. At steady state ($\delta n/\delta t = 0$) Equation (32) reduces to

$$\frac{dn}{dL} + \frac{n}{Y\tau} = 0 \quad (33)$$

which has the analytic solution

$$n = n^o \exp\left(-\frac{L}{Y\tau}\right) \quad (34)$$

where n^o is the population density at size 0 (i.e., the nuclei population density). Thus a plot of $\ln(n)$ vs. L for a system obeying the constraints outlined above will be a straight line with slope $1/Y\tau$ and intercept n^o (Fig. 17), and an average growth rate may be determined directly if the residence time τ is known. Equation (32) may also be solved for conditions of batch (zero flux) crystallization - in this case the melt volume is a function of time. While the negative exponential form of the solution is maintained, the pre-exponential term is time-dependent, and derivation of rate data from measured size distributions is more difficult (for a more complete discussion see Marsh, 1988b).

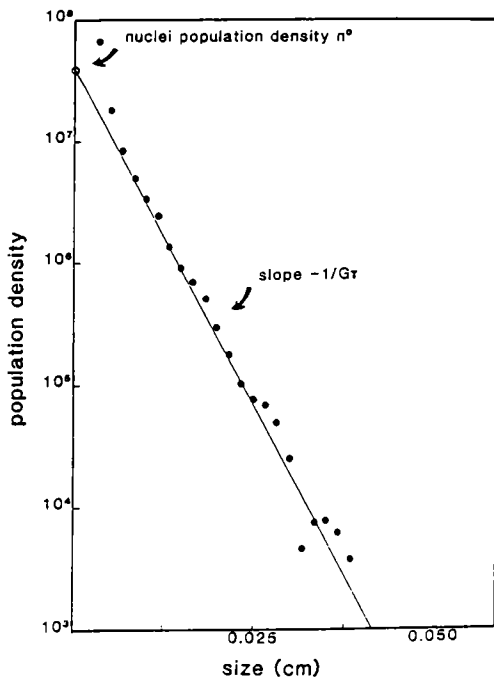


Figure 17. Typical CSD ($\ln(n)$ vs. (L)) plot for plagioclase in Makaopuhi lava lake samples. The slope of the line is $-1/Y\tau$, the y-axis intercept is the nuclei population density n° . From Cashman and Marsh (1988).

Figure 18. Moment number density fractions based on numbers (n_F), length (l_F), area (a_F) and mass (m_F). The dominant size (L_d) associated with each distribution is a simple integer multiple of $Y\tau$, here denoted $G\tau$. From Marsh (1988a).

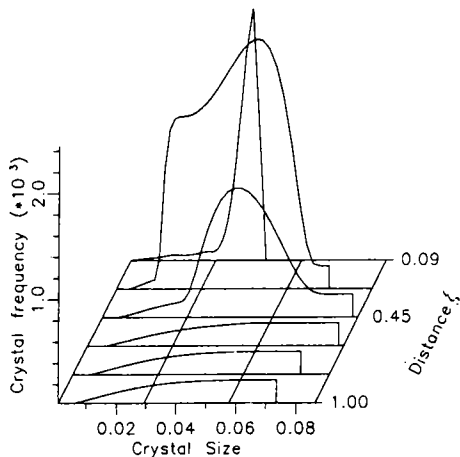
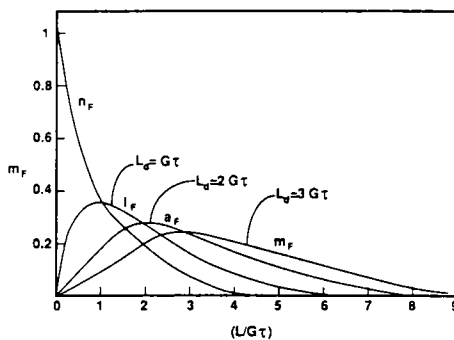


Figure 19. Calculated crystal size frequency distributions for the initially-precipitating phase in an idealized binary eutectic system. heterogeneous nucleation is modeled by omitting the kinetic barrier to nucleation for a fraction of sites (here 0.10). From Spohn et al. (1988).

The nucleation rate may be calculated from parameters determined from the $\ln(n)$ vs. L plot, since

$$I = \frac{dN}{dt} \Big|_{L=0} = \left(\frac{dN}{dL} \right) \Big|_{L=0} \left(\frac{dL}{dt} \right) = n^o Y \quad (35)$$

The interdependence of nucleation and growth rates expresses the classical view of competition between nucleation and growth, with resulting textures controlled by mass balance considerations; substitution into Equation (23c) illustrates the control of the initial nucleation density on final texture, since $R_c = (Y/I)^{1/4} = (1/n^o)^{1/4}$. As shown above, nucleation and growth rates may also be written as a function of undercooling (ΔT):

$$I = k^1 \Delta T^a \quad (36)$$

$$Y = k^2 \Delta T^b \quad (37)$$

where a and b represent the kinetic order of crystal nucleation and growth, respectively, and k^1 and k^2 are constants. Equations (36) and (37) may be combined with (35):

$$n^o = k^3 Y^{i-1} \quad (38)$$

where the kinetic order $i = a/b$ and $k^3 = (k^1/k^2)^{a/b}$; a plot of $\ln n^o$ vs. Y should yield a straight line of slope $i - 1$. When the kinetic order i is equal to 1, the size distribution is not affected by undercooling. When the kinetic order is greater than 1, both n^o and Y increase with undercooling, but Y more slowly than I , with the net result a smaller crystal size at higher ΔT .

Finally, the moments of the population distribution, defined as

$$M_z \equiv \int_0^L L^z n(L) dL \quad (39)$$

represent the total number of crystals (zeroeth moment, $z = 0$; $N_{TOTAL} = n^o Y \tau$), total length of crystals (1st moment), total crystal area (2nd moment) and total crystal mass (3rd moment) when integrated over the entire size range. The number densities of each moment for $z > 0$ show a maximum in the distribution as a function of L (Fig. 18); these maxima define a dominant crystal size (L_d) determined on a length-weighted basis ($L_d = Y \tau$), an area-weighted basis ($L_d = 2Y \tau$), or on a mass-weighted basis ($L_d = 3Y \tau$); in general $L_d = zY \tau$. Alternatively, the median size for the distribution may be obtained; for example, the median size on a length-weighted basis occurs when $M_1(L)/M_1(\infty) = 0.5$; this is equivalent to determining a half-life for radioactive decay.

While the negative exponential form of Equation (34) is mathematically reasonable, it is puzzling with respect to its implication for the evolution of individual crystals. As an illustration, the exponentially decreasing size distributions measured in most volcanic rocks (shown schematically in Fig. 16a) differ significantly from the crystal size distributions calculated by Spohn et al. (1988), the latter being simple inversions of the predicted nucleation versus time curves (e.g. Fig. 19), based on the implicit assumptions that (1) all

crystals grow at the same rate, and (2) all crystals grow. Both of these assumptions have been challenged by chemical engineers. Repeated experiments on precipitation of salts have demonstrated size-dependent growth, where small ($<10\text{ }\mu\text{m}$) crystals grow at significantly *slower* rates than larger crystals (e.g. Fig. 20). Jancic et al. (1984) explain this result as the product of 'growth dispersion' and model it by adding a growth diffusivity term to the population balance equation; the 'dispersion length' can then be defined as the crystal size at which growth dispersion dominates the growth function (defined to be $\sim 10\text{ }\mu\text{m}$ in Fig. 20). A physical explanation for growth dispersion lies in probable differences in the dislocation structure of individual crystals. Both growth dispersion and size-dependent growth result in curved CSD plots, however, and thus cannot explain the steady decrease in crystals of larger sizes. Engineers have also observed apparently stable (i.e., non-growing) populations of small crystals in supersaturated solutions (Larson, pers. comm.). Maaloe et al. (1989) propose a growth probability model that incorporates these observations. They suggest that the statistical (random) element of surface nucleation during crystal growth may result in growth probabilities of (very slightly) less than one. Such probabilistic growth would have the effect of reducing the crystal number population of successively larger size classes.

Isobaric cooling. We tested the applicability of CSDs to magmatic crystallization by analyzing the Makaopuhi lava lake samples used by Kirkpatrick (Cashman and Marsh, 1988). All CSDs measured on plagioclase are linear when plotted as $\ln(n)$ vs. L (e.g. Fig. 17), with slopes that increase with decreasing depth in the lava lake (increasing fraction crystallized; Fig. 21). In contrast to the conclusions of Kirkpatrick (1977), results from CSD analysis suggest that both growth and nucleation rates *decrease* with increasing crystallinity (increasing time), and that these average growth rates of 10^{-10} to 6×10^{-11} cm/s are slightly lower than Kirkpatrick's estimates, which are maximum rates (based on the maximum width measured in each sample). If growth rate is not a constant value for all crystals, then the fastest growing (largest) crystal would be expected to yield a growth rate that diverges from the average rate with time, as observed in the similarity of growth rate estimates from the two methods for the least crystallized sample (.99 compared to 1.7×10^{-10} cm/s at 40% crystallinity) and the increasing divergence with increasing crystallinity (6×10^{-11} compared with 5×10^{-10} cm/s at 80% crystallinity). In both studies, however, (1) plagioclase growth rates are on the order of 10^{-10} cm/s and (2) nucleation rates are between 10^{-1} and 10^{-3} /cm³s, with magnitudes that vary much more with time than growth rates. Comparison with rate data for plagioclase crystallization presented in Maaloe et al. (1989) suggests that these rates indicate crystallization at extremely small values of ΔT (0.01-0.001°C).

The dependence of plagioclase nucleation and growth rates on undercooling has been examined using CSD measurements of phenocryst and groundmass plagioclase in Mount St. Helens dacite (Cashman, 1988; 1990). Phenocryst size distributions for samples erupted from 1980 to 1986 are constant; phenocrysts probably grew prior to eruption at 7-12 km (Rutherford and Devine, 1988), and bracketing times of 30-150 years (the latter being the approximate repose time of the volcano) yield growth rate estimates of 3 to 10×10^{-12} cm/s and nucleation rates of 5 to 21×10^{-6} /cm³s. Growth and nucleation rates of skeletal-to-acicular microlites in the blast dacite (assumed to have grown at high ΔT in response to intrusion of magma into the volcanic edifice in March, 1980) are, respectively, 1 to 3×10^{-11} cm/s and 9 to 16×10^3 /cm³s, while groundmass microphenocrysts in the dome lavas (grown at

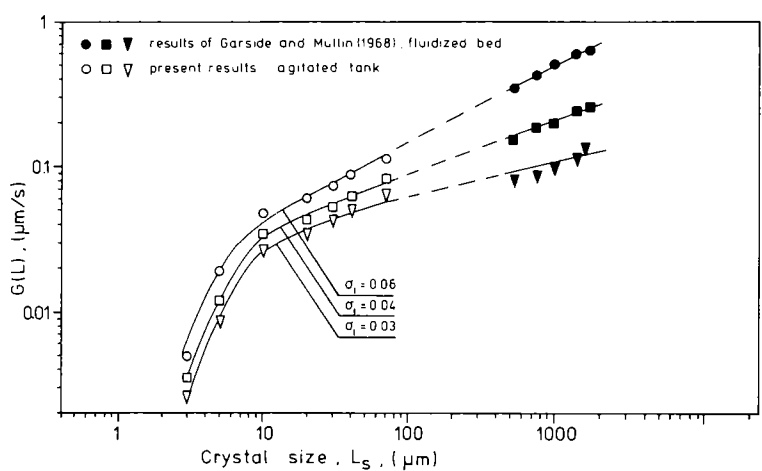


Figure 20. Surface integration kinetics (growth rate denoted $G(L)$) of potash alum crystals at 30°C as a function of crystal size and supersaturation. From Jancic and Grootsholten (1984).

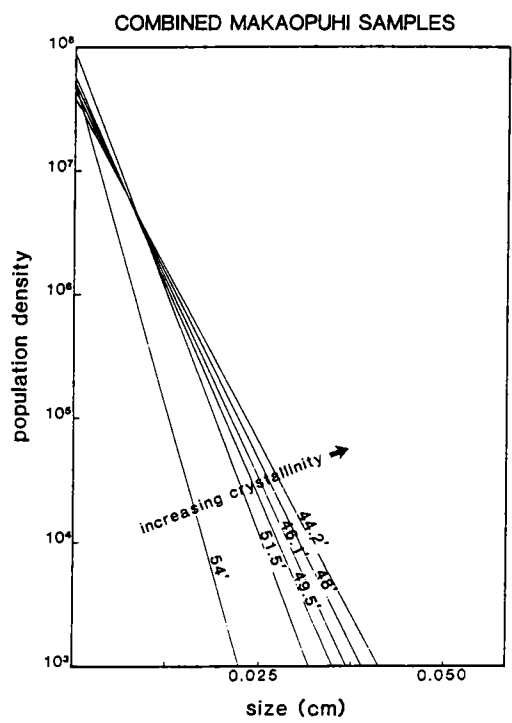


Figure 21. Combined plot of CSDs of plagioclase in Makaopuhi samples drilled from the indicated depths. The slope of the line decreases with increasing crystallization, representing the increase in crystallization time (increasing $Y\tau$). From Cashman and Marsh (1988).

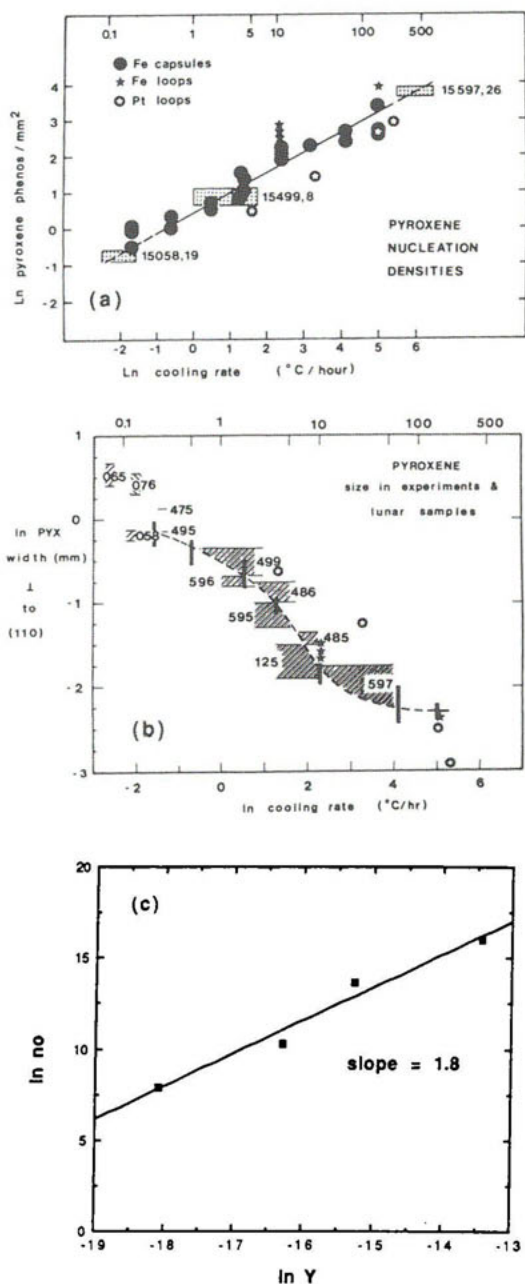


Figure 22. (a) A comparison of pyroxene phenocryst nucleation density in cooling rate experiments performed on quartz-normative lunar basalt 15597. Boxes show nucleation densities of three lunar QN basalts. From Lofgren et al. (1979). (b) Comparison of pyroxene phenocryst size in controlled cooling rate experiments on the 15597 composition. Bars are pyroxene sizes measured in Fe-capsule experiments, hatched boxes are lunar QN basalts, and loop experiments as indicated above. From Lofgren et al. (1979). (c) $\ln (n^{\circ})$ vs. $\ln (Y)$ plotted from the data of (a) and (b). Nucleation rates (I) and growth rates (Y) were calculated assuming a crystallization interval of 200°C . The slope of the line is determined by the dependence of Y and I on undercooling ΔT .

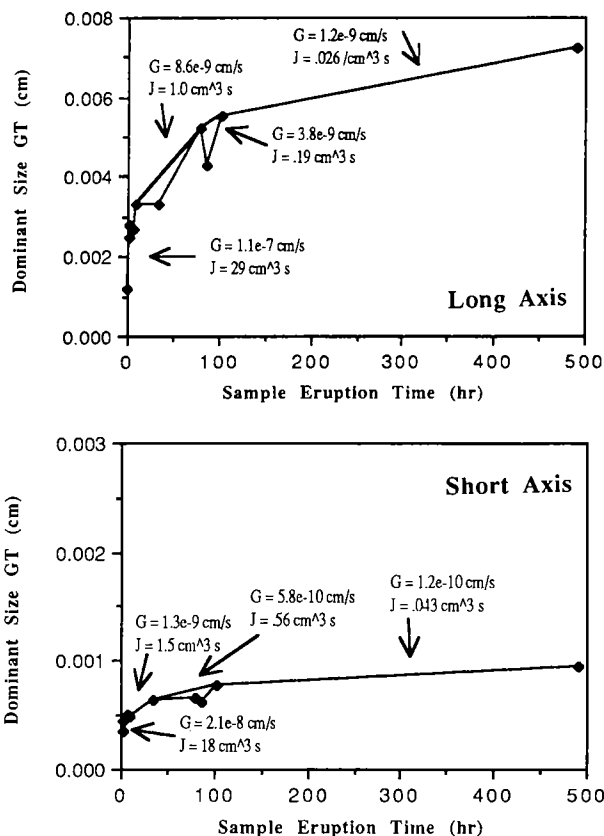


Figure 23. Dominant size (L_D) of apparent long and short axes of plagioclase from the 1984 Mauna Loa eruption. Heavy lines delineate points of approximately constant slope; slopes of these lines were used to determine growth (here denoted G) and nucleation (here denoted J) rates for these time periods. From Bonini (1990).

moderate ΔT at a shallow level) increase in size from 1980 to 1986 at rates of $2\text{--}4 \times 10^{-11}$ cm/s, with effective nucleation rates of $10^2\text{--}10^2/\text{cm}^3\text{s}$. Thus plagioclase growth rates under widely varying conditions of undercooling are relatively constant, while estimated nucleation rates vary by nine orders of magnitude between the rapidly quenched microlites and pre-existing phenocrysts.

Supporting experimental evidence for the relative dependence of nucleation and growth rates on ΔT can be examined using pyroxene crystallization data from the cooling rate experiments of Lofgren et al. (1979). Pyroxene number densities and maximum size measured as a function of cooling rate (Fig. 22a,b) can be converted to nucleation and growth rates as described above. Nucleation rates can in turn be converted to nuclei population densities (n^0) using Equation (35) for use in a $\ln(n^0)$ vs. $\ln(Y)$ plot (Eqn. 38; Fig. 22c); from these data the kinetic order $i = 2.8 = a/b$. If the CSE parameterization of Y presented by Dearnley (1983) is applicable to multicomponent crystallization, then the kinetic order of the growth rate (b, Eqn. 37) is 1, with the constant k^1 a function of Y_{\max} and $T_L - T_\infty$ (cf. Eqn. 17). This in turn requires the kinetic order of nucleation (a) to be 2.8, a result consistent

both with the plagioclase data from Mount St. Helens and with the inverse correlation between crystal number density and cooling rate (ΔT) observed in dikes and programmed cooling experiments.

Isothermal depressurization. While crystallization in dikes and in the Makaopuhi lava lake occurred under conditions of isobaric cooling, syn-eruptive crystallization of volcanic rocks probably occurs more frequently under conditions of isothermal depressurization and degassing (e.g. Sparks and Pinkerton, 1978; Lipman et al., 1985; Swanson et al., 1989). Apparent long and short axis measurements of plagioclase crystals of constant eruption-temperature vent samples from the 1984 Mauna Loa eruption (described in Lipman et al., 1985; Lipman and Banks, 1987) increase in $Y\tau$ with time at a continually decreasing rate (Fig. 23; Bonini, 1990). Plagioclase crystallinity over the same time period increases from 5.5% in the earliest samples to an approximately constant value of 14-16% for the last 400 hours of the eruption - this value corresponds nicely to the equilibrium value of 16.1% plagioclase at 1140°C (the measured eruption temperature) predicted by the thermodynamic model SILMIN (e.g. Ghiorso, 1985), and suggests that the observed decreasing rates of crystallization represent the system's approach to the new equilibrium imposed by the eruption. Growth and nucleation rate estimates for different segments of the eruption are determined from the slopes of the heavy line segments shown in Figure 23. Assuming that crystallization commenced at the initiation of the eruption, both apparent long and short axis growth rates decreased by 2 orders of magnitude during the first 100 hours of the eruption, at which point they appeared to reach steady state values of, respectively, 10^{-9} and 10^{-10} cm/s. Figure 23 illustrates the added information derived from a time sequence of samples - the time-averaged long axis growth rate for the final product (the slope of the line connecting the largest $Y\tau$ value to the origin) is 3.8×10^{-9} cm/s, significantly less than apparent growth rates early in the eruption.

A similar pattern of increasing crystal size with time is observed in groundmass plagioclase from successive samples of the Mount St. Helens dome lavas (Cashman, 1990); by analogy with the isobaric cooling models, decreasing growth rates with time can be interpreted as reflecting the system's approach to equilibrium. The time constant for reaching steady state appears to be on the order of 2-6 months for Mount St. Helens compared to days for Mauna Loa, the difference probably reflecting differences in both melt composition and the initial effective undercooling. Such patterns of the time-dependence of crystal size resemble results of *isothermal* (as compared to programmed cooling) crystallization experiments (e.g. Nabalek et al., 1978). These experiments show that at a given undercooling, crystal size will increase with time at a decreasing rate and then level off at an equilibrium value; nucleation densities also achieve an equilibrium that may require a *decrease* in number from the initial value (see Fig. 2, Nabalek et al., 1978). Changes in growth rate with time are accompanied by changes in crystal morphology (reflecting growth at decreasing ΔT as the melt is held at a fixed T). While the paucity of available data makes generalization of these results difficult, the data suggest that measurements of changing crystallinity and crystal size may help to constrain conditions of near-surface degassing and transport.

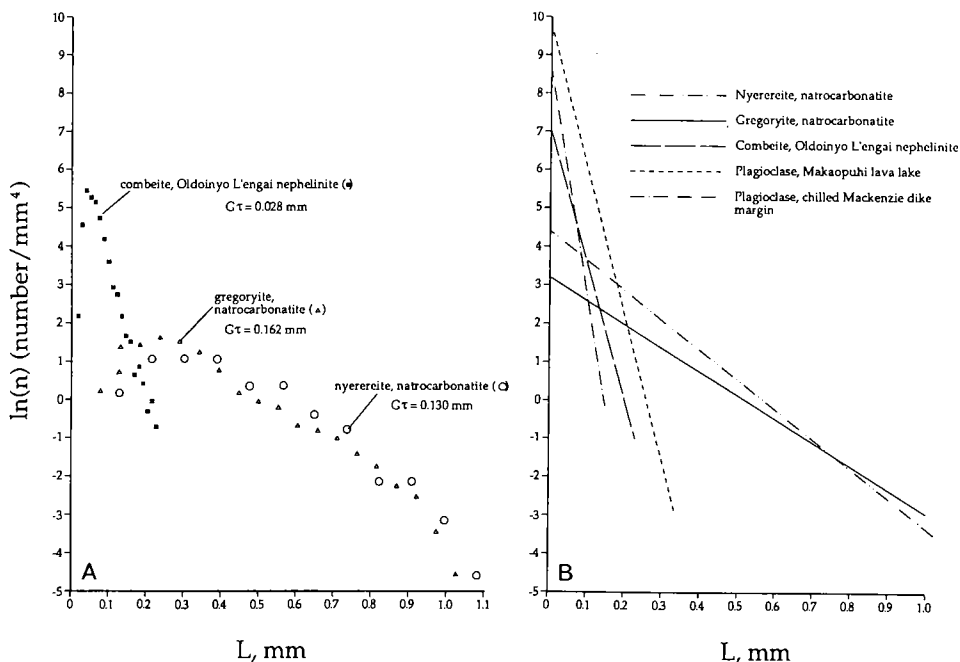


Figure 24. (a) CSD data for gregoryite (triangles) and nyerereite (circles) in natrocarbonatite and combeite (squares) in peralkaline nephelinite. The downward curvature at small L is an artifact of the optical resolution at the scale of the measurement, which is poorer for the carbonate phenocrysts because they are larger. (b) Comparison of CSDs for the above phases plus average plagioclase phenocrysts from Makaopuhi lava lake (Cashman and Marsh, 1988) and a tholeiite dike of the Mackenzie dike swarm. From Peterson (1990).

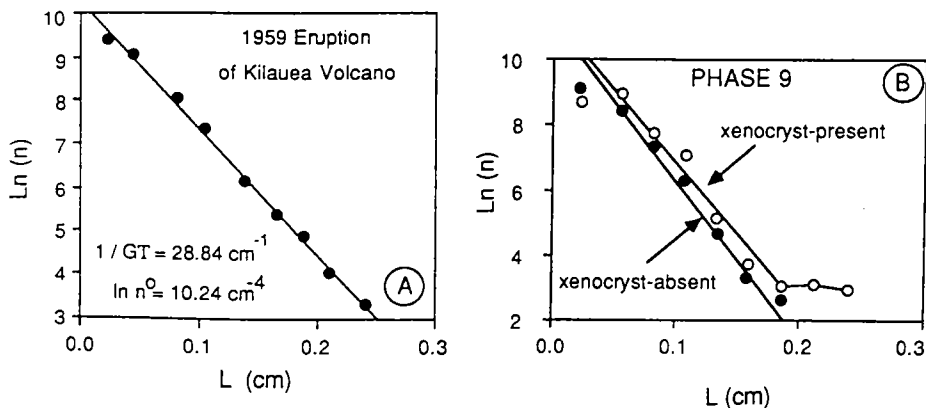


Figure 25. (a) Combined CSD plot for non-xenocrystic olivine in picrites from the 1959 eruption of Kilauea. (b) Comparison between measured xenocryst-present and xenocryst-absent CSDs from a single phase of the 1959 eruption. Note the pronounced flattening of the CSD plot at large crystal sizes in the xenocryst-present results. From Mangan (1990).

Crystallization caused by change in supersaturation. Isothermal, isobaric crystallization due to changes in supersaturation is unusual under most conditions of igneous crystallization; a possible example, however, is the coexisting nephelinite (+ combeite) and natrocarbonatite (+ gregoryite + nyerereite) magmas at Oldoinyo L'engai volcano, Tanzania. Peterson (1990) presents evidence that natrocarbonatite was formed by a discrete episode of liquid immiscibility from extremely peralkaline nephelinites. He measured CSDs of gregoryite and nyerereite (both Na,K,Ca carbonates) in natrocarbonatite and of combeite (Na,Ca silicate) as shown in Figure 24a. If both combeite and gregoryite nucleated in response to the liquid immiscibility event, the carbonate minerals must have grown at a rate 5 times that of combeite (2.5×10^{-10} compared to 5×10^{-11} cm/s for an inferred residence time of 2 years). A possible explanation for this difference is the extremely low viscosity of the carbonatite melt (Peterson, 1990).

Residence times. As mentioned in the introduction to this section, most igneous rocks exhibit a small range in phenocryst size; formulated in terms of the CSD approach, this may be viewed as a constancy of the slope parameter $Y\tau$. Peterson (1990) compiled selected CSDs to address the compositional dependence of growth rates (Fig. 24b) - the *slope* is related to the dominant crystal size (rate of change of number density with increasing size) and the *intercept* is controlled by the total number (modal abundance) of the species. Here silicate minerals in many basic volcanic rocks are shown to have approximately constant values of $Y\tau$ despite variations in mineral and melt compositions. Similarities of estimated crystallization times for Makaopuhi lava lake and Oldoinyo L'engai nephelinite (2-3 years) thus suggest similar mineral growth rates in these systems. An extension of this comparison is attempted through the tabulation of all available CSD data in Table 4. Phenocrysts in lavas with slightly longer estimated storage times (e.g. Kilauea Iki, Mount St. Helens) have $Y\tau$ values 5-10 times greater than the silicate minerals shown in Figure 24b, consistent with approximately constant values of growth rate Y (although as noted above, there does appear to be a slight compositional dependence of Y). In contrast, anorthoclase megacrysts in phonolite lavas from Mt. Erebus, Antarctica represent an extreme in measured size distributions, with widths of individual crystals separated from bombs erupted in 1984 and 1988 yielding $Y\tau = 0.33 - 0.37$ cm, approximately 100 times that of plagioclase in Makaopuhi lava lake (Dupre, 1990). While τ for the anorthoclase is unknown, we do know that the current lava lake has been homogeneous in bulk composition and anorthoclase content since its inception in 1972, suggesting that the crystallization time is significantly longer than 18 years; bracketing growth rates of 10^{-10} to 5×10^{-11} cm/s would suggest effective τ values of 100-200 years.

If the growth rate of minerals in basic silicate melts is approximately constant at 10^{-10} to 5×10^{-11} cm/s (Table 4; interestingly, these rates are consistent with bracketing estimates of *dissolution* rates of Zhang et al., 1989 mentioned earlier), measured crystal size distributions can be used to estimate crystal residence times in magmatic systems, as demonstrated by Mangan (1990). The 1959 Kilauea eruption pumice contained two populations of olivine crystals: xenocrysts transported by a mantle-derived magma and phenocrysts from magma stored at shallow levels in the rift zone. Measured CSDs of olivine phenocrysts are linear, with constant slopes for all eruptive episodes (Fig. 25a) despite the small number of crystals measured per sample (25-150) and the large variation in crystallinity (5.5 - 38.5 modal % olivine). An average $Y\tau$ of .035 cm suggests a residence time of 11-22 years for estimated growth rates of, respectively, 10^{-10} and 5×10^{-11} cm/s; this estimate is within the subsurface

Table 4. Compilation of available CSD data for igneous rocks; nucleation and growth rates are derived for systems where growth time is known or can be estimated. Data from the following sources. a. Cashman and Marsh (1988), b. Mangan (1990), c. Bonini (1990), d. Kneedler (1989), e. Peterson (1990), f. Cashman (1988, 1990), g. Congdon and Marsh (in prep.), and h. Dupre (1990).

| LOCATION | COMPOSITION | MINERAL | $Y\tau$ (cm) | n^a | τ (yr) | Y (cm/s) | I (no./cm ³ s) |
|-------------------------------|-------------|-------------------------|--------------|-----------------------|-------------|---------------------|-----------------------------|
| ^a Makaopuhi | Basalt | Plagioclase | .002 | 3.42×10^5 | .25 | 1×10^{-10} | 3×10^2 |
| | | | .004 | 2.68×10^7 | .98 | 6×10^{-11} | 2×10^3 |
| | | Ilmenite | .002 | 4.49×10^6 | .15 | 5×10^{-10} | 2×10^3 |
| | | | .008 | 4.50×10^5 | .77 | 3×10^{-10} | 2×10^4 |
| ^b Kilauea | Basalt | Olivine | .035 | 2.80×10^4 | 5 | 2×10^{-10} | 6×10^6 |
| | | | | | 35 | 3×10^{-11} | 9×10^7 |
| ^c Mauna Loa | Basalt | Plagioclase | .001 | 1.90×10^9 | .00015 | 2×10^{-7} | 4×10^2 |
| | | | .007 | 1.23×10^7 | .057 | 4×10^{-9} | 5×10^2 |
| ^d Brazil | Diabase | Plagioclase | .002 | 1.08×10^8 | .00067 | 1×10^{-7} | 1×10^1 |
| | | | .006 | 1.98×10^5 | 3 | 6×10^{-11} | 1×10^4 |
| ^e Oldoinyo L'engai | Nephelinite | Combeite | .003 | 1.25×10^7 | 2 | 4×10^{-11} | 5×10^4 |
| | Carbonatite | Gregoryite | .016 | 2.48×10^5 | 2 | 2×10^{-10} | 6×10^5 |
| ^f Mt. St. Helens | Dacite | Plagioclase phenocrysts | .009 | 2.14×10^6 | 30 | 1×10^{-11} | 2×10^5 |
| | | | | | 150 | 3×10^{-12} | 6×10^6 |
| | | groundmass | .0002 | 4.45×10^{10} | .06 | 2×10^{-11} | 1×10^4 |
| | | | .0006 | 8.39×10^9 | .14 | 3×10^{-9} | 1×10^2 |
| | | microlites | .0001 | 1.38×10^{15} | 1.4 | 1×10^{-11} | 1×10^1 |
| ^g Shonkin Sag | Shonkinite | Clinopyroxene | .05 | 3.50×10^3 | | | |
| ^h Mt. Erebus | Phonolite | Anorthoclase | .35 | 1.49×10^1 | | | |

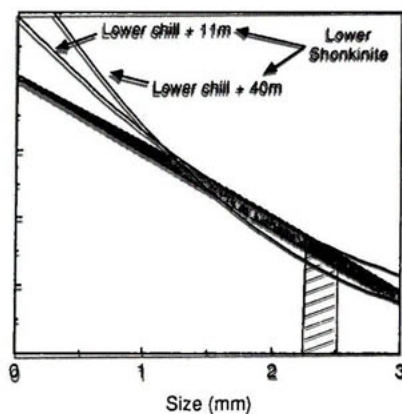


Figure 26. Clinopyroxene CSDs from the Shonkin Sag laccolith; the range of the chilled margin CSDs is stippled; broad hatched region denotes range of $5Y\tau$ values permissible from the chilled margin slopes. From Congdon and Marsh (in prep.).

storage time estimate of 5-35 years provided by compositional systematics of the Kilauean lavas (Wright and Fiske, 1971). Additionally, Mangan (1990) demonstrates that while the inclusion of xenocrysts in the CSDs does not significantly alter the phenocryst slope and intercept, the presence of xenocrysts is recognizable in the flattening of the distribution at large crystal sizes (Fig. 24b). This leads to the question of the utility of CSDs in inferring physical processes undergone by the magma in addition to its chemical and thermal history.

Effect of physical processes. Marsh (1988b) examines the effect of crystal fractionation and accumulation on resultant CSDs. The Stokes settling velocity (V_s) of a crystal in a melt is proportional to L^2 ; the *number-based* settling flux through a volume (Q_n) is then $n(L)V_s = k_s L^2 n(L)$. If the *mass* settling flux is required, this expression must be integrated over the mass-based CSD moment ($\rho k_s L^3 n(L)$), or

$$\int_0^\infty Q_m = k_m \int_0^\infty L^5 n(L) dL \quad (40)$$

Equation (40) is the fifth CSD moment (cf. Eqn. 39; recall that moments of the number conservation equation represent multiplication of the steady state population balance by increasingly higher orders of size L), implying that the crystal size dominating the mass flux during settling is large (the maximum in the distribution is at size $L_D = 5Y\tau$). Thus accumulation of phenocrysts due to crystal settling is predicted to increase the population density at large crystal sizes, creating concave upward CSDs. Integration of Equation (40) over the entire size range (assuming the steady state expression for $n(L)$, cf. Eqn. 32) yields a fractionation potential proportional to $(Y\tau)^6$, thus the relative ability of different minerals to fractionate in a magma is strongly dependent on their relative sizes ($Y\tau$). Marsh (1988a) derives a relationship between crystal settling rate and velocity of advance of the 'crystal capture' front to show that the residence time of a crystal in the suspension zone ahead of the capture zone (t_d) is simply $2/9t$, assuming that the position of the capture front is a large (0.9) fraction of the position of the liquidus isotherm. If t_d is directly equated with τ , then the largest crystal remaining in the suspension zone will increase with time (t) as $L_D = 2/9 Yt$. Since the mass settling flux is dominated by much larger sizes, this will lead to a depletion zone directly below the capture front.

Congdon and Marsh (in prep.) have tested the sensitivity of CSDs to physical processes in a detailed study of the Shonkin Sag laccolith, a classic example of in situ differentiation of an initially crystal-rich magma. Measured clinopyroxene sizes in the crystal-rich chilled margin yield linear CSDs (Fig. 26) with relatively large $Y\tau$ values of 0.05 cm; low n° values suggest that phenocryst nucleation rates were small (10^{-6} to $10^{-8}/\text{cm}^3\text{s}$). Interior samples show an increase in the small crystal population relative to the chilled margin due to post-intrusion crystallization (Fig. 26). Flattening of CSDs at large crystal sizes in the accumulative zone (lower shonkinite) occurs as predicted, and the crystal size at which curve-flattening becomes apparent is close to the $5Y\tau$ values determined from the chilled margin samples. Thus it appears that CSDs *can* be used to identify physical processes. One should caution, however, that non-linear CSDs cannot be interpreted uniquely without additional lines of evidence, since non-linear conditions of crystal growth (e.g. growth dispersion or size-dependent growth) will also give rise to curved CSDs.

Further potential applications of CSDs. An obvious application of CSD analysis lies in the interpretation of vesicle size distributions (VSDs). Vesiculation in response to pressure changes during an eruption involves bubble growth assumed to occur isothermally by volatile diffusion and decompression; theories of vesiculation are reviewed in Sparks (1978) and Toramaru (1989). Measured VSDs in some volatile-rich mid-ocean ridge basalts ("popping rocks") are commonly linear (Sarda and Graham, 1990; Fig. 27). Using inferred ascent times and estimated nucleation depths, Sarda and Graham estimate bubble nucleation and growth rates of approximately $5.5 \times 10^{-3} \text{ cm}^3/\text{s}$ and 10^{-7} cm/s . The relative mobility of bubbles in melt, however, suggests that deviations from the expected linear relationship will arise from processes of bubble migration, coalescence or resorption (e.g. Sahagian, 1985; Sahagian et al., 1989; Walker, 1989), thus complicating the resultant VSDs (e.g. Fig. 27d).

Textural studies of metamorphic crystallization may provide insight into interpretation of plutonic rock textures. Measured CSDs for olivine, pyroxene and magnetite in high-temperature (1000°C) basaltic hornfels from the Isle of Skye are linear, while garnet and magnetite in regionally metamorphosed pelitic schists from south-central Maine have CSDs which are bell-shaped (Cashman and Ferry, 1988; Fig. 28). The bell-shaped form can be interpreted as the result of two processes: (1) initial continuous nucleation and growth of crystals to form linear CSDs, and (2) later loss of small crystals due to Ostwald ripening (annealing of a dispersed phase). Ostwald ripening has also been suggested as a process operative in diagenesis (Morse and Casey, 1988) and hydrothermal alteration of illite (Eberl and Srodon, 1988; Eberl et al., 1990; for a review of Ostwald ripening theory see Baronnet, 1984). It has been suggested that slowly cooled plutonic rocks may also experience subsolidus ripening (e.g. Boudreau, 1987; Hunter, 1987). In fact, the early stages of crystallization from a melt may also involve the loss of very-early-formed small crystals (e.g. Nabalek et al., 1978) as predicted for modeled phase transitions in *finite* systems (Schmelzer and Ulbricht, 1987; Schmelzer and Schweitzer, 1987). If subsolidus textural modification plays a role in the generation of plutonic textures, two results from studies of metamorphic CSDs may contribute to their interpretation: (1) the large crystals in regional metamorphic rocks retain the original size frequency distribution (Fig. 28) and may be used to obtain quantitative information on the original conditions of crystal nucleation and growth, (2) the extent of annealing increases with increasing metamorphic grade, reflecting increasing duration of elevated temperatures - the extent of annealing may thus have potential as a cooling rate indicator.

CONCLUSIONS

In summary, natural systems provide time-controlled experiments on scales unreachable in the laboratory, and with complexities unapproachable by computer experiments. Since temperature (undercooling) cannot be directly scaled with time, *in situ* crystallization experiments provide information unavailable by other means.

The kinetics of crystallization in simple silicate systems have been studied extensively for glass ceramic systems (e.g. Uhlmann, 1982; James, 1982), but predictive models for nucleation behavior, in particular, remain inadequate. Part of the problem in creating models of nucleation lies in the difficulty of experimentally isolating the nucleation process; crystal growth measurements are more accessible experimentally, and for this reason crystal growth

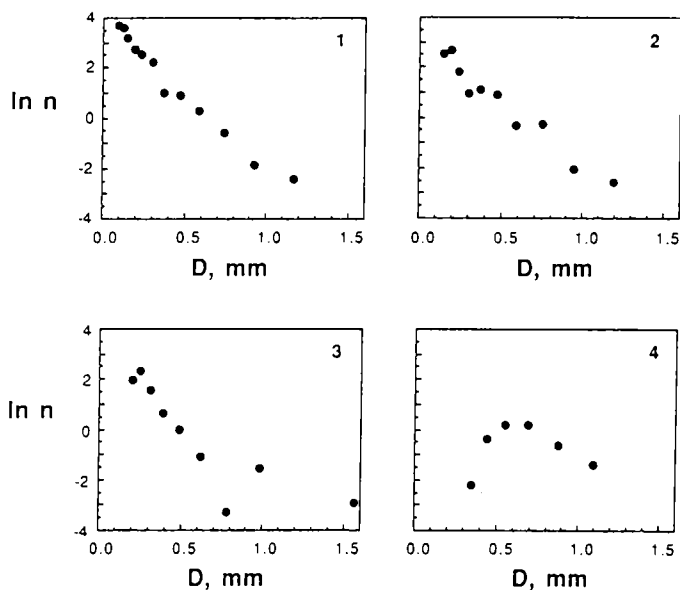


Figure 27. Vesicle size distributions in mid-ocean ridge popping rocks (D is vesicle diameter). Distributions 1, 2 and 3 are linear and suggest continuous nucleation and growth; depletion of small bubbles in 4 may result from bubble coalescence, ripening or significant growth after nucleation is complete. From Sarda and Graham (1990).

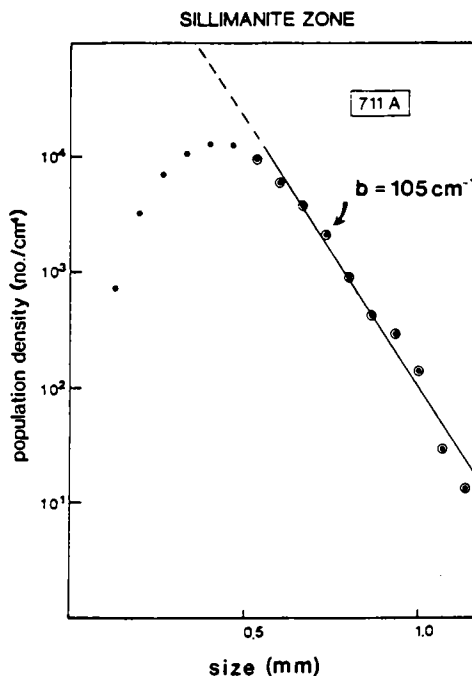


Figure 28. CSD plot of sillimanite zone garnet; note the linear slope preserved in the large crystal sizes. From Cashman and Ferry (1988).

is better understood (e.g. Dowty, 1980; Kirkpatrick, 1981; James, 1982; Baronnet, 1984). However, predictive models of crystal growth (e.g. Lasaga, 1982) require accurate models for the temperature and compositional dependence of both the thermodynamic and kinetic driving forces for crystallization, information that is currently limited. The CSE parameterization of the position of Y_{\max} as a function of T , T_L and T_{∞} suggested by Dearnley (1983) provides a potentially useful model that requires further testing. Similarly, application of the adiabatic nucleation model of Meyer (1986) to simple systems suggests that the position of T_{\max} relative to T_L has an approximately constant value of 0.55 - 0.60 (exceptions are low ΔS_f minerals such as albite and quartz). Additionally, while experimental crystallization rate data is a necessary link between processes in natural melts and numerical models, experimental growth rate data is confined to simple systems and conditions of moderately large undercooling, while growth rate estimates in complex natural systems suggest that under most conditions, undercoolings remain very small.

Quantitative textural studies of dikes suggest a pronounced dependence of growth rate on total crystallization time (e.g. Ikeda, 1977), which is in turn related to effective undercooling, a function of both total dike width and distance from the dike margin. By analogy, minimum crystallization rates may be estimated from programmed cooling experiments if a temperature interval of crystallization is assumed. Growth rates determined in this way show the same relationship between growth rate and total crystallization time seen in the dike studies, reflecting a systematic relationship between growth rate and cooling rate (effective undercooling) for plagioclase in basaltic systems. While the data are not available for other mineral systems, there is no reason to believe that similar patterns would not exist for other silicate minerals (i.e., the similarity in dendritic olivine growth rates estimated by Fowler et al., 1989, using fractal analysis to the growth rates of plagioclase under conditions of rapid cooling estimated from programmed cooling rate experiments).

Analysis of measured crystal size frequencies provides a means of extracting effective (bulk) kinetic information from geologic systems that can help to constrain the dynamic feedback between physical models of magmatic systems and rates of chemical change. The information from measured CSDs to date can be summarised as follows:

(1) Plagioclase growth rates do not appear to be particularly sensitive to either undercooling or melt composition under most natural conditions of crystallization (with the exception being crystallization at very high rates of cooling - large effective undercoolings). Melt composition appears to be of secondary importance except for extremely low melt viscosities (e.g. Peterson, 1990).

(2) Nucleation rates are much more sensitive than growth rates to applied undercoolings; final lava textures are strongly controlled by conditions of nucleation, as illustrated by the interdependence of average size, nucleation rate, growth rate and nuclei population density (eqs. 23c and 35). Not enough data are currently available to be able to evaluate the compositional dependence of nucleation rates.

(3) The limited data available suggest that olivine growth rates are similar to those of plagioclase - rates 10^{-10} - 10^{-11} cm/s encompass most of the measured values. Experimental constraints on rates of plagioclase crystallization at small undercoolings in basaltic melts are almost nonexistent, but parameterization of unpublished data presented by Maaloe et al. (1989) suggests that growth rates of this magnitude require undercoolings of $< 0.001^{\circ}\text{C}$. This in turn implies that most crystallization in magmatic systems occurs under approxi-

mately equilibrium conditions. Given initial *disequilibrium* conditions (due to rapid transport, eruption, phase separation, etc.) the time to reach equilibrium will be a function of melt composition and original effective undercooling; crystal size versus time curves for Mauna Loa basalt and Mount St. Helens dacite suggest that equilibrium rates in these systems are approached in days to months.

(4) The limited range of calculated growth rates allows CSDs to be used to estimate crystal residence times. This provides a tool that could potentially be used for tracking the physical evolution/development of a magma storage system with time, thus providing a link between the textural, thermal and structural evolution of magmatic systems.

(5) While the shapes of crystal size frequency curves are fundamentally related to the crystallization kinetics, they also contribute information on physical processes experienced by the magma (e.g. crystal accumulation or depletion).

(6) Finally, quantitative textural analysis may also be useful in studies of vesiculation (e.g. Sarda and Graham, 1990) and, by analogy with studies of metamorphic textures (e.g. Cashman and Ferry, 1988), in investigations of subsolidus modifications to original size distributions of plutonic rocks.

In summary, recent numerical (e.g. Brandeis and Jaupart, 1987; Spohn et al., 1988) and quantitative textural (e.g. Cashman and Marsh, 1988; Cashman, 1988; 1990) studies of magmatic crystallization present coherent picture of the crystallization process that includes (1) final textures dominated by the initial conditions of nucleation (and the rate of subsequent approach to equilibrium conditions) and (2) overall crystallization rates dominated by the rate of heat removal from the system, as illustrated both by the approximately constant crystal size across large dikes and the constant mean crystal size of 1-4 mm for basic intrusions, as tabulated by Brandeis et al. (1984). This remarkable homogeneity of crystal size must reflect a fundamental constancy of process, as noted by Marsh (1988) and Cashman and Marsh (1988). Growth rates estimated from textural measurements are approximately constant at 10^{-10} to 5×10^{-11} cm/s under most magmatic cooling conditions and are identical to those calculated for the center of large dikes (very slow rates of cooling). This observation suggests not only that most crystallization occurs at very small effective undercoolings, but also that measured CSDs can be used to estimate magmatic (subliquidus, near-surface) residence times (e.g. Mangan, 1990). Alternatively, the consistency of combined growth rate estimates from studies of dike crystallization and programmed cooling rate experiments provide an estimate of overall crystal growth rate under conditions where cooling rate can be determined. Together these observations should provide more realistic constraints on physical models of processes involved with magmatic segregation, transport, storage and eruption than are currently being utilized.

APPENDIX: STEREOLOGY AND IMAGE ANALYSIS

Quantitative analysis of rock textures may be approached by separation of individual particles, serial sectioning of a sample, or, most commonly, through use of thin sections (planar sections). The latter method requires transformation of measurements made in two dimensions to actual three-dimensional properties by the "unfolding" of the distribution, accomplished through the mathematical constructs of stereology. Reviews of this subject may be found in DeHoff and Rhines (1968), Underwood (1970), Groves (1977), Weibel (1979; 1980), Exner (1983), Vander Voort (1984) and Russ (1986); Cashman and Marsh

(1988) discuss stereological problems as they relate to crystal size distributions. Geometrical properties that can be obtained exactly from measurements on planar sections include (1) volume fraction of a phase (e.g. point-counting method of Chayes, 1950), (2) the area of surfaces or interfaces, and (3) the lengths of lines or edges. Determination of particle size distributions, number of particles, averages of particle properties and degree of particle orientation, however, all require geometric assumptions of particle shape and/or distribution. Furthermore, such transformations can only be solved analytically for uniform spheres. In the following discussion I attempt to provide an overview of the problem, a brief examination of the potential use of serial sections and section pairs, and an introduction to automated techniques of textural measurements (image analysis) in addition to commenting on the possible ramifications of the inaccuracy of current transformation methods on measured crystal size distributions.

For the simplest case of a spherical particle, the diameter of that particle d completely defines the probability (d/V) that a random plane will intersect the sphere, where V is the volume in which the sphere is contained. If there are p such spheres contained in the volume, the number intersected by a random plane (N_A) will be pd/V , or

$$N_A = N_v d \quad (A1)$$

where N_v is the number of particles contained in the volume (the unknown). If the spheres are not uniform in size, then d must be replaced by \bar{D} , the average particle diameter, and

$$N_v = \frac{N_A}{\bar{D}} \quad (A2)$$

Thus the fundamental problem in the determination of the number of crystals per unit volume from a planar section is an independent method for determining mean grain size. Gray (1978b) suggests two possible estimates of N_v :

$$N_v \approx \frac{N_A^{1.5}}{\sqrt{V_{mode}}} \quad (A3)$$

where V_{mode} is the modal volume of the phase of interest and thus proportional to the chance of intersection, and

$$N_v \approx \frac{N_A}{\max(010)\text{width}} \quad (A4)$$

with the maximum width another estimator of intersection probability. Serial sections provide a more accurate estimate of average particle size (Cruz-Orive, 1980; DeHoff, 1983), where the number of serial planes hitting a given particle i (m_i) multiplied by the distance between planes (h) can be summed over the number of particles (N):

$$N_v = \frac{N_A}{\sum_{i=1}^N (m_i h / N)} \quad (A5)$$

Another multiple section estimator of mean size involves the use of section pairs (e.g. Sterio, 1984; Bendtsen and Nyergaard, 1989) to evaluate the percentage of particles that appear on two sequential planes. Serial sections have not been extensively used to date for textural measurements of geologic samples due to the labor involved in both sample preparation and analysis; however, the automation of analysis promised by the rapidly advancing sophistication of image processing systems suggests that this approach will be an important line of future research.

For reasons stated above, much of the stereological literature to date has focussed on the evaluation of measurements made on planar sections, and, more specifically, on distributions of spheres. Geometrically it is easy to show (e.g. Krumbein, 1935; Kellerhals et al., 1975) that the probability of intersecting a sphere with a plane of random orientation to produce a small circle of diameter $\leq y$ is h/r , where r is the true radius ($= x/2$, where x is the true diameter), and the element of frequency of intersection is dh/r :

$$h = \left(r^2 - \frac{y^2}{4} \right)^{1/2} = \frac{1}{2} (x^2 - y^2)^{1/2} \quad (A6)$$

and

$$dh = -\frac{1}{2} (x^2 - y^2)^{1/2} y dy \quad (A7)$$

From Equations (A6 and A7) we can write the distribution of circle diameters expected from a large number of such intersections as the integral over dh :

$$G(y) = \left(\frac{1}{x} \right) \int_x^0 \left\{ \frac{-y}{(x^2 - y^2)^{1/2}} \right\} dy = 1 - \left\{ 1 - \left(\frac{y}{x} \right)^2 \right\}^{1/2} \quad (A8)$$

The derivative of the distribution function with respect to apparent diameter y is the probability density of the function:

$$G'(y) = g(y) = \left(\frac{y}{x} \right) (x^2 - y^2)^{1/2} \quad (A9)$$

The probability density function is unusual in that it goes to infinity at $y = x$, but by definition the area under the curve is finite and equal to 1 (Fig. A1a). The mean of a continuous distribution is equal to its first moment; for spheres of uniform size the mean of the distribution is $0.785x$.

A rigorous analysis is more difficult for a collection of spheres of different sizes, since the apparent size distribution is affected not only by the probability that the apparent diameter of any one sphere will be smaller than its true diameter due to the effect of sectioning, but also because there exists a greater chance of intersecting a large sphere than a small one. The relationship between the observed density function $g(y)$ and the true distribution function $F(x)$ was first derived by Wicksell (1925):

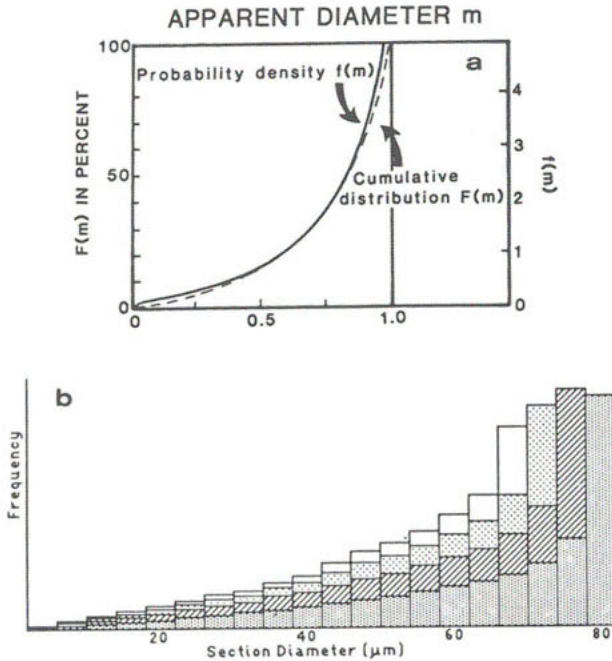


Figure A1. (a) Cumulative distribution function (here $F(m)$) and probability density function (here $f(m) = F'(m)$) for random intersections of a sphere. From Cashman and Marsh (1988). (b) Size histogram of circles measured from intersection on several sphere sizes is the sum of the individual distributions shown by the differently shaded bars. From Russ (1986).

$$g(y) = y \int_0^{\infty} (x^2 - y^2)^{1/2} dF(x) / M_1 \quad (A10)$$

where M_1 is the first moment (the mean) of the true distribution $F(x)$. As for Equation (A1), solutions are difficult to use in any but the simplest of observed distributions because the true mean of the distribution is generally unknown.

The most common method of obtaining solutions to (A10) is to use empirical measurements of $G(y)$ grouped in the form of a histogram. Equation (A10) can then be viewed as a system of linear equations joining the midpoints (a_i) of the histogram bins of width (w_i) and upper limits (b_i) (e.g. Ripley, 1981):

$$w_i g(a_i) = a_i \sum_{j \geq i} \frac{w_j f(a_j)}{M_1 (b_j^2 - a_i^2)^{1/2}} \quad (A11)$$

Since the measured size distribution will reflect the contribution of sections from many size classes (e.g. Fig. A1b), a finite difference method of back substitution (Saltykov, 1967) can be used to calculate the true size distribution, assuming that particles in the largest bin belong only to the largest size class, that those in the second largest bin are a combination of those in the second-largest size class and cut sections of the largest size class, etc. - tables of coefficients for use with this method are presented in most of the stereology reviews presented above. Unfortunately, the Saltykov method is not very accurate, as errors are accu-

mulated in small size classes, and perturbations in the measured distribution is locally amplified in the estimated sphere size frequency (e.g. Anderssen, 1976). Remedies for this instability involve smoothing of the measured distribution $G(y)$ prior to unfolding. Smoothing methods include parameterization based on assumed form of the distribution (e.g. Keiding et al., 1972), replacement of the histogram by the more stable cumulative distribution function (e.g. the product integration method of Anderssen and Jakeman, 1975a,b) and use of a kernel estimator (e.g. Taylor, 1983).

The effects of these stereological problems on measured crystal size distributions are discussed by Cashman and Marsh (1988). They show that (1) the sectioning effect in a population of uniform spheres will generate a CSD plot with a positive rather than a negative slope, as a result of the calculated distribution function shown in Fig. A1a; (2) sectioning of a size distribution of spheres will produce a measured distribution that is the additive function of the sectioning effects (Figure A1b) - the CSD slopes thus produced would be expected show a slight increase in the small crystal classes than exist in the true distribution. This effect will be offset, however, by the smaller probability of intersecting a small crystal than a large crystal. The only true size distribution data available for volcanic rocks are those of Dupre (1990), where anorthoclase crystals were physically separated from vesicular kenyte bombs (Fig. A2). Here size distributions show the same negative exponential distribution seen in thin section in other volcanic systems. While the errors inherent in the stereological problems are difficult to ascertain, a comparison of kinetic data calculated using three different methods of N_A to N_V conversion (Table A1) show a 25% difference in calculated growth rates and less than an order of magnitude difference in calculated nucleation rates; these differences are significantly less than measured variations illustrated throughout the text.

While a full discussion of automated image analysis is well beyond the scope of this appendix, I would like to comment on a few aspects of the process of imaging, and present references for the interested reader. The mathematical foundation for image processing is presented in Serra (1982); Boolean operations involving the interaction of "structuring elements" with the areas of interest ("hit or miss transformations") allow quantitative characterization of image features (see Fabbri, 1984, and Petruk, 1989 for geologic examples). Methods of fractal analysis (e.g. Kennedy, 1985; 1986; Fowler et al., 1989) are available and have started to be incorporated into commercial image analysis systems. Practical aspects of the process of image analysis are thoroughly discussed by Russ (1988). He elaborates on steps of image analysis which include (1) image acquisition (collection, digitization and processing), (2) feature discrimination (including conversion to a binary image), (3) editing of binary image (including a series of morphological operators as detailed in Serra, 1982), (4) measurement to produce data (this may include shape and orientation measurements on individual crystals in addition to size classification) and (5) stereological interpretation to obtain the data of interest. As mentioned above, the capacity to stack serial sections in order to reconstruct a 3-D image has already been developed for new methods of image acquisition (e.g. CATSCAN and MRI); the ability to make measurements on these 3-D reconstructions will soon be available as well.

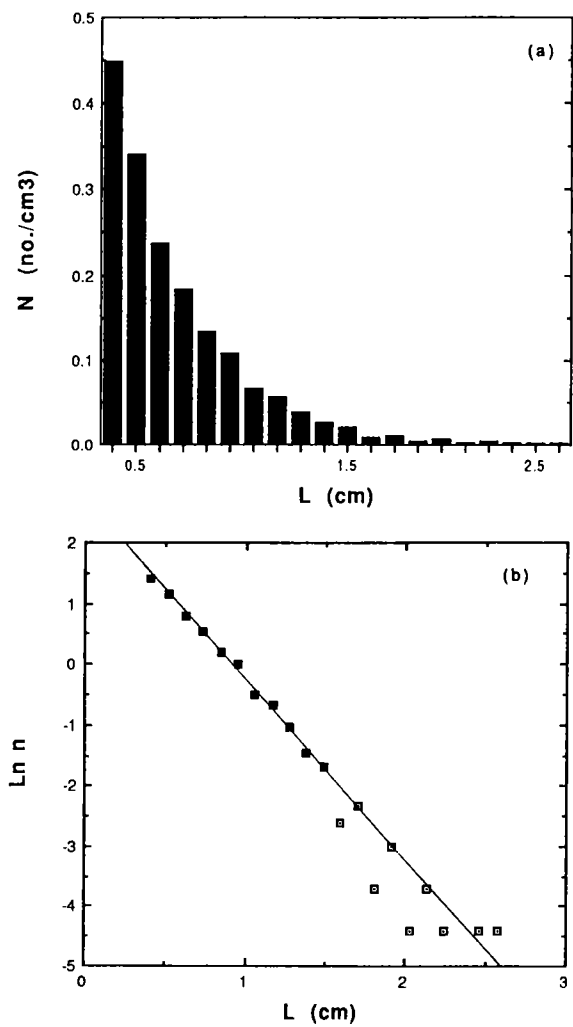


Figure A2. (a) Crystal size histogram and (b) CSD plot of 2000 anorthoclase crystals individually separated from a volcanic bomb from the 1984 eruption of Mt. Erebus (slope yields $Y\tau = 0.34$ cm). Sizes measured are maximum widths of each crystal; open squares in (b) were not used in the slope determination due to the very small number of crystals of widths > 1.5 cm. Data from Dupre (1990).

Table A1. Comparison of N_v estimates for measured crystal sizes from Makaopuhi samples 68-1-21, 20% crystallized. Methods used are 1. $N_v = N_A^{1.5}$ (Kirkpatrick, 1977); 2. $N_v = N_A^{1.5}/\sqrt{V_{mode}}$ (Gray, 1978b); 3. $N_v = N_v/\bar{D}$ (DeHoff and Rhines, 1968) where \bar{D} used is that of each individual size class.

| METHOD | SLOPE $1/Y\tau$ | INTERCEPT n^0 | Y cm/s | I no./cm³s |
|--------|--------------------|--------------------|-----------------------|-------------------|
| 1 | 522 | 9.5×10^7 | 6.1×10^{-11} | 5.8×10^3 |
| 2 | 522 | 2.2×10^8 | 6.1×10^{-11} | 1.3×10^2 |
| 3 | 387 | 2.9×10^8 | 8.2×10^{-11} | 2.4×10^2 |

In conclusion, in the light of the difficulties inherent in trying to reconstruct three-dimensional data from two dimensions, combined with the ease of measurement afforded by automated imaging systems, certain measurement techniques are suggested to minimize these problems. First, measurement of a large number of crystals per sample will minimize fluctuations due to perturbations in sample homogeneity (although Mangan, 1990 found consistent results between samples with very different measured numbers of crystals). Second, measurement of three mutually perpendicular sections will allow for check of preferred orientation (e.g. Cashman, 1988). Third, while area measurements are preferable for crystal shapes that can be approximated as spheres (e.g. olivine; equivalent sphere diameter may then be used as a linear measure of size), minerals that are anisotropic in shape (e.g. plagioclase) pose greater measurement problems. Since apparent crystal width is much less sensitive to orientation than crystal length, width measurements are recommended for stable size distributions (although length measurements help to provide an estimate of maximum growth rates), as has been common in the geologic literature (e.g. Kirkpatrick, 1977; Walker et al., 1978; Lofgren et al., 1979; Grove, 1990). Finally, modern imaging systems will soon be handling three-dimensional reconstructions from serial sections routinely that will render the stereological approximations obsolete.

ACKNOWLEDGEMENTS

This chapter benefitted from reviews by Becky Lange, Jim Nicholls and Alex Navrotsky. I'd like to thank Tony Peterson, Maggie Mangan and Roger Congdon for sharing preliminary versions of their manuscripts with me. Bruce Marsh not only initiated my interest in textural analysis but has also continued to provide insight (it was he who sent me Dearnley's (1983) paper). Caroline Klug helped with the figures, and Becky Lange contributed not only helpful discussions but also much-needed tennis breaks. Financial support for this research was provided by National Science Foundation grants EAR 8803215 and EAR 8916930.

REFERENCES

- Allegre C.J., Provost, A. and Jaupart, C. (1981) Oscillatory zoning: pathological case of crystal growth. *Nature*, 294, 223-228.
- Anderson, A.T. (1984) Probable relations between plagioclase zoning and magma dynamics, Fuego Volcano, Guatemala. *Amer. Mineral.*, 69, 660-676.
- Anderssen, R.S. (1976) Stable procedures for the inversion of Abel's equation. *J. Inst. Math. Applic.*, 17, 329.
- Anderssen, R.S. and Jakeman, A.J. (1975a) Abel type integral equations in stereology. II. Computational methods of solution and the random spheres approximation. *J. Microsc.*, 105, 135-153.
- Anderssen, R.S. and Jakeman, A.J. (1975b) Product integration for functionals of particle size distribution. *Utilitas Mathematica*, 8, 111-126.
- Avrami, M. (1939) Kinetics of phase change I. *J. Chem. Phys.*, 7, 1103-1112.
- Avrami, M., (1940) Kinetics of phase change, II. *J. Chem. Phys.*, 8, 212-224.
- Avrami, M. (1941) Granulation, phase change, and microstructure. *J. Chem. Phys.*, 9, 177-184.
- Baker, D.R. (1990) Chemical interdiffusion of dacite and rhyolite: anhydrous measurements at 1 atm and 10 kbar, application of transition state theory, and diffusion in zoned magma chambers. *Contrib. Mineral. Petrol.*, 104, 407-423.
- Baker, M.B. and Grove, T.L. (1985) Kinetic controls on pyroxene nucleation and metastable liquid lines of descent in a basaltic andesite. *Amer. Mineral.*, 70, 279-287.
- Baronnet, A. (1984) Growth kinetics of the silicates. *Fortschr. Mineral.*, 62, 187-232.
- Bendtsen, T.F. and Nyengaard, J.R. (1989) Unbiased estimation of particle number using sections - an historical perspective with special reference to the stereology of glomeruli. *J. Microsc.* 153, 93-102.
- Berkebile, C.A. and Dowty E. (1982) Nucleation in laboratory charges of basaltic composition. *Amer. Mineral.*, 67, 886-899.
- Berman, R.B. and Brown, T.H. (1988) Heat capacity of minerals in the system Na₂O-K₂O-CaO-MgO-FeO-Fe₂O₃-Al₂O₃-SiO₂-TiO₂-H₂O-CO₂: representation, estimation, and high temperature extrapolation. *Contrib. Mineral. Petrol.*, 89, 168-183.
- Bonini, J.A. (1990) Microphenocryst development during the 1984 Mauna Loa eruption. Unpubl. Jr. Paper, Princeton University.

- Boudreau, A.E. (1987) Pattern formation during crystallization and the formation of fine-scale layering. In: *Origins of Igneous Layering*, I. Parsons, ed., D. Reidel Publ. Co., Dordrecht, The Netherlands, 453-471.
- Brandeis, G. and Jaupart, C. (1987a) Characteristic dimensions and times for dynamic crystallization. In: *Parsons, I., ed., Origins of Igneous Layering*, D. Reidel Publ. Co., 613-639.
- Brandeis, G. and Jaupart, C. (1987b) Crystal sizes in intrusions of different dimensions: Constraints of the cooling regime and the crystallization kinetics. *Geochem. Soc. Spec. Publ.* 1, 307-318.
- Brandeis, G. and Jaupart, C. (1987c) The kinetics of nucleation and crystal growth and scaling laws for magmatic crystallization. *Contrib. Mineral. Petrol.*, 96, 24-34.
- Brandeis, G. and Jaupart, C. (1987d) Towards scaling laws for the interpretation of igneous structures. In *Loper, D.E., ed., Structure and dynamics of partially solidified systems*, Martinus Nijhoff Publ, 327-347.
- Brandeis, G., Jaupart, C. and Allegre, C.J. (1984) Nucleation, crystal growth and the thermal regime of cooling magmas. *J. Geophys. Res.*, 89, 10161-10177.
- Budz, J., Karpinski, P.H. and Naruc, Z. (1984) Influence of hydrodynamic conditions on secondary nucleation rates in a fluidized bed. In: *Advances in Crystallization from Solutions*. Youngquist, G.R., ed., AIChE Symposium Series 80, 89-97.
- Carmichael, I.S.E., Turner, F.J. and Verhoogen, J. (1974) *Igneous Petrology*. McGraw-Hill Book Co., New York, 739pp.
- Carslaw, H.S. and Jaeger, J.C. (1959) *Conduction of Heat in Solids*. Oxford Univ. Press, 510 pp.
- Cashman, K.V. (1988) Crystallization of Mount St. Helens dacite: A quantitative textural approach. *Bull. Volcanol.*, 50, 194-209.
- Cashman, K.V. (1990) Groundmass crystallization of Mount St. Helens dacite, 1980-1986 - A tool for interpreting shallow magmatic processes. *Contrib. Mineral. Petrol.* (in press).
- Cashman, K.V. and Ferry, J.M. (1988) Crystal size distribution (CSD) in rocks and the kinetics and dynamics of crystallization III. Metamorphic crystallization. *Contrib. Mineral. Petrol.*, 99, 401-415.
- Cashman, K.V. and Marsh, B.D. (1988) Crystal size distribution (CSD) in rocks and the kinetics and dynamics of crystallization II. Makaopuhi lava lake. *Contrib. Mineral. Petrol.*, 99, 401-405.
- Chayes, F. (1950) On the bias of grain-size measurements made in thin section. *J. Geol.*, 58, 156-160.
- Congdon R.D. and Marsh, B.D. (in prep.) Crystal size distributions in the Shonkin Sag laccolith and implications for a differentiation model.
- Cook, G.B., Cooper, R.F. and Wu, T. (1990) Chemical diffusion and crystalline nucleation during oxidation of ferrous iron-bearing magnesium aluminosilicate glass. *J. Non-Crystalline Solids*, 120, 207-222.
- Cruz-Orive, L.-M. (1980) On the estimation of particle number. *J. Microsc.*, 120, 15-27.
- Daniel, T., Gapais, D., Labit, C. and LeCorre, C. (1987) An application of textural and morphological image processing to deformation analysis within granitic rocks. *Acta Stereol.*, 6, 1041-1046.
- Dearnley, R. (1983) Basaltic systems and a corresponding states equation for crystal growth rates. *Nature*, 304, 151-152.
- DeGraff, J.M., Long, P.E. and Aydin, A. (1989) Use of joint-growth directions and rock textures to infer thermal regimes during solidification of basaltic lava flows. *J. Volcanol. Geotherm. Res.*, 38, 309-324.
- DeHoff, R.T. (1983) Quantitative serial sectioning analysis: preview. *J. Microsc.*, 131, 259-263.
- DeHoff, R.T. and Rhines, F.N. (1968) *Quantitative Microscopy*. McGraw-Hill Book Co., 422 pp.
- Dowty, E. (1980) Crystal growth and nucleation theory and the numerical simulation of igneous crystallization. In: *Physics of Magmatic Processes*. R.B. Hargraves, ed., Princeton University Press, Princeton, 419-485.
- Dupre, R.M. (1990) The origin of anorthoclase megacrysts from Mount Erebus, Ross Island, Antarctica. Unpubl. B.A. Thesis, Princeton University.
- Eberl, D.D. and Srodon, J. (1988) Ostwald ripening and interparticle-diffraction effects for illite crystals. *Amer. Mineral.*, 73, 1335-1345.
- Eberl, D.D., Srodon, J., Kralik, M., Taylor, B.E. and Peterman, Z.E. (1990) Ostwald ripening of clays and metamorphic minerals. *Science*, 248, 474-477.
- Erlich, R., Vogel, T.A., Weinberg, B., Kamilli, D.C., Byerly, G. and Richter, H. (1972) Textural variation in petrogenetic analysis. *Geol. Soc. Amer. Bull.*, 83, 665-676.
- Exner, H.E. (1983) Surface microscopy. In: *Physical Metallurgy*. Cahn, R.W. and Haasen, P., eds., North-Holland Physics Publ., Amsterdam, pp.621-647.
- Fabbri, A.G. (1984) *Image Processing of Geological Data*. Van Nostrand Reinhold Co., New York, 244 pp.
- Fenn, P.M. (1977) The nucleation and growth of alkali feldspars from hydrous melts. *Can. Mineral.*, 15, 135-161.
- Fowler, A.D., Stanley, H.E. and Daccord, G. (1989) Disequilibrium silicate mineral textures: fractal and non-fractal features. *Nature*, 341, 134-138.
- Ghiorso, M.S. (1985) Chemical mass transfer in magmatic processes I. Thermodynamic relations and numerical algorithms. *Contrib. Mineral. Petrol.*, 90, 107-120.
- Ghiorso, M.S. (1987) Chemical mass transfer in magmatic processes III. Crystal growth, chemical diffusion and thermal diffusion in multicomponent silicate melts. *Contrib. Mineral. Petrol.*, 96, 291-313.
- Ghiorso, M.S. (1988) Temperatures in and around cooling magma bodies. In: *Perchuk, L.L., ed., Advances in Geochemistry*, Springer-Verlag, New York.
- Ghiorso, M.S. and Carmichael, I.S.E. (1985) Chemical mass transfer in magmatic processes II. Applications in equilibrium crystallization, fractionation and assimilation. *Contrib. Mineral. Petrol.*, 90, 121-141.
- Gray, N.H. (1970) Crystal growth and nucleation in two large diabase dikes. *Can. J. Earth Sci.*, 7, 366-375.
- Gray, N.H. (1978a) Crystal growth and nucleation in flash-injected basic dikes. *Can. J. Earth Sci.*, 15, 1904-1923.

- Gray, N.H. (1978b) Nucleation and growth of plagioclase, Makaopuhi lava lakes, Kilauea Volcano, Hawaii: Discussion. *Geol. Soc. Amer. Bull.*, 89, 797-798.
- Grove, T.L. (1978) Cooling histories of Luna 24 very low Ti (VLT) ferrobasalts: An experimental study. *Proc. Lunar Planet. Sci. Conf.*, 9th, 565-584.
- Grove, T.L. (1990) Cooling histories of lavas from Serocki Volcano. *Proc. Ocean Drilling Prog.*, 106/109, 3-8.
- Groves, M.J. (1977) Particle Size Analysis. 3rd Particle Size Analysis Conf., U. of Salford, 492 pp.
- Gutzow, I. (1980) Induced crystallization of glass-forming systems: a case of transient heterogeneous nucleation, Part 1. *Contemp. Phys.*, 21, 121-137.
- Gutzow, I., Zlateva, E., Alyakov, S. and Kovatscheva, T. (1977) The kinetics and mechanism of crystallization in enstatite-type glass-ceramic materials. *J. Mater. Sci.*, 12, 1190-1202.
- Hawkes, D.D. (1967) Order of abundant crystal nucleation in a natural magma. *Geol. Mag.*, 104, 473-486.
- Hofmann, A.W. (1980) Diffusion in natural silicate melts: a critical review. In: *Physics of Magmatic Processes*. Hargraves, R.B., ed., Princeton University Press, Princeton, N.J., 385-417.
- Hunter, R.H. (1987) Textural equilibrium in layered igneous rocks. In: *Origins of Igneous Layering*. I. Parsons, ed., D. Reidel Publ. Co., Dordrecht, 473-503.
- Ikeda, Y. (1977) Grain size of plagioclase of the basaltic andesite dikes, Iritono, central Abukuma plateau. *Can. J. Earth Sci.*, 14, 1860-1866.
- Jackson, K.A. (1958) Interface structure. In: *Growth and Perfection of Crystals*. Doremus, R.H., Roberts, B.W. and Turnbull, D., eds., John Wiley and Sons, New York.
- James, P.F. (1982) Nucleation in glass-forming systems - a review. In: *Nucleation and Crystallization in Glasses*. Simmons, J.R., Uhlmann, D.R. and Beall, G.H., eds., Amer. Ceram. Soc., Columbus, Ohio, 1-48.
- James, P.F. (1985) Kinetics of crystal nucleation in silicate glasses. *J. Non-Crystalline Solids*, 73, 517-540.
- Jancic, S.J. and deJong E.J. (1984) *Industrial Crystallization 84*. Elsevier, Amsterdam, 498 pp.
- Jancic, S.J. and Grootscholten, P.A.M. (1984) *Industrial Crystallization*. Delft University Press, Dordrecht, The Netherlands, 434 pp.
- Jancic, S.J., van Rosmalen, G.M. and Peeters, J.P. (1984) Growth dispersion in nearly monosize crystal populations. In: *Industrial Crystallization 84*. Jancic, S.J. and deJong E.J., ed., Elsevier, Amsterdam, 43-49.
- Johnson, W.A. and Mehl, R.F. (1939) Reaction kinetics in processes of nucleation and growth. *Amer. Inst. Mining Eng., Tech. Publ.* 1089, 1-27.
- Kalinina, A.M., Filipovich, V.N. and Fokin, V.M. (1980) Stationary and non-stationary crystal nucleation rate in a glass of $2\text{Na}_2\text{O} \cdot \text{CaO} \cdot 3\text{SiO}_2$ stoichiometric composition. *J. Non-Crystalline Solids*, 38/39, 723-728.
- Kashchiev, D. (1969) Solution of the non-steady state problem in nucleation kinetics. *Surface Sci.*, 14, 209-220.
- Keiding, N., Jensen, S.T. and Ranek, L. (1972) Maximum likelihood estimation of the size distribution of liver cell nuclei from the observed distribution in a plane section. *Biometrics*, 28, 813-829.
- Kellerhals, R., Shaw, J. and Arora, V.K. (1975) On grain size from thin sections. *J. Geol.*, 83, 79-96.
- Kennedy, S.K. (1985) Microcomputer image acquisition and shape and size analyses with applications in sedimentology. *The Compass*, 62, 205-210.
- Kennedy, S.K. (1986) FRACT - a FORTRAN subroutine to calculate the variable necessary to determine the fractal dimensions of closed forms. *Computers and Geosci.*, 12, 705-712.
- Kirkpatrick, R.J. (1976) Towards a kinetic model for magma crystallization: *J. Geophys. Res.*, 81, 2565-2571.
- Kirkpatrick, R.J. (1977) Nucleation and growth of plagioclase, Makaopuhi and Alae lava lakes, Kilauea Volcano, Hawaii. *Geol. Soc. Amer. Bull.*, 88, 78-84.
- Kirkpatrick, R.J. (1978) Nucleation and growth of plagioclase, Makaopuhi lava lakes, Kilauea Volcano, Hawaii: Reply. *Geol. Soc. Amer. Bull.*, 89, 799-800.
- Kirkpatrick, R.J. (1981) Kinetics of crystallization of igneous rocks. In: *Kinetics of Geochemical Processes*. Lasaga, A.C. and Kirkpatrick, R.J., eds., Reviews in Mineralogy, 8, 321-398.
- Kirkpatrick, R.J. (1983) Theory of nucleation in silicate melts. *Amer. Mineral.*, 68, 66-77.
- Kirkpatrick, R.J., Klein, L., Uhlmann, D.R. and Hays, J.F. (1979) Rates and processes of crystal growth in the system anorthite-albite. *J. Geophys. Res.*, 84, 3671-3676.
- Kirkpatrick, R.J., Reck, B.H., Pelly, I.Z. and Kuo, L.-C. (1983) Programmed cooling experiments in the system $\text{MgO} - \text{SiO}_2$: kinetics of a peritectic reaction. *Amer. Mineral.*, 68, 1095-1101.
- Klein, L.C., Handwerker, C.A., Uhlmann, D.R. (1977) Nucleation kinetics of sodium disilicate. *J. Crystal Growth*, 42, 47-51.
- Kneedler, A.E. (1989) Quantitative petrographic study of two diabase dikes intruded into the Sao Francisco Craton, Brasil. Unpubl. Sr. Thesis, Princeton University.
- Kouchi, A., Tsuchiyama, A. and Sunagawa, I. (1986) Effect of stirring on crystallization kinetics of basalt: texture and element partitioning. *Contrib. Mineral. Petrol.*, 93, 429-438.
- Kouchi, A., Sugawara, Y., Kashima, K. and Sunagawa, I. (1983) Laboratory growth of sector zoned clinopyroxenes in the system $\text{CaMgSi}_2\text{O}_6 - \text{CaTiAl}_2\text{O}_6$. *Contrib. Mineral. Petrol.*, 83, 177-184.
- Krumbein, W.C., Thin-section mechanical analysis of indurated sediments. *J. Geol.*, 43, 482-496.
- Kuo, L.-C. and Kirkpatrick, R.J. (1982a) Small angle X-ray scattering study of pre-nucleation behavior of titanium-free and titanium-bearing diopside glasses. *Amer. Mineral.*, 67, 676-685.

- Kuo, L.-C. and Kirkpatrick, R.J. (1982b) Pre-eruption history of phryic basalts from DSDP Legs 45 and 46: Evidence from morphology and zoning patterns in plagioclase. *Contrib. Mineral. Petrol.*, 79, 13-27.
- Kuo, L.-C. and Kirkpatrick, R.J. (1985) Kinetics of crystal dissolution in the system diopside-forsterite-silica. *Amer. J. Sci.*, 285, 51-90.
- Lange, R.A. and Carmichael, I.S.E. (1990) Thermodynamic properties of silicate liquids with an emphasis on density, thermal expansion and compressibility (this volume).
- Langer, J.S. (1989) Dendrites, viscous fingers, and the theory of pattern formation. *Science*, 243, 1150-1156.
- Lasaga, A.C. (1981) Implication of a concentration dependent growth rate on the boundary layer crystal-melt model. *Earth Planet. Sci. Lett.*, 56, 429-434.
- Lasaga, A.C. (1982) Towards a master equation in crystal growth. *Amer. J. Sci.*, 282, 1264-1288.
- Lipman, P.W. and Banks, N.G. (1987) Aa flow dynamics, Mauna Loa 1984. *U.S. Geol. Surv. Prof. Paper* 1350, 1527-1567.
- Lipman, P.W., Banks, N.G. and Rhodes, J.M. (1985) Degassing-induced crystallization of basalt magma and its effects on lava rheology. *Nature*, 317, 604-607.
- Lofgren, G.E. (1980) Experimental studies on the dynamic crystallization of silicate melts. In: *Physics of Magmatic Processes*. R.B. Hargraves, ed., Princeton University Press, Princeton, N.J., 487-551.
- Lofgren, G.E. (1983) Effect of heterogeneous nucleation on basaltic textures: a dynamic crystallization study. *J. Petrol.*, 24, 229-255.
- Lofgren, G.E., Grove, T.L., Brown, R.W. and Smith, D.P. (1979) Comparison of dynamic crystallization techniques on Apollo 15 quartz normative basalts. *Proc. Lunar Planet. Sci. Conf.* 10th, 423-438.
- Long, P.E. and Wood, B.J. (1986) Structures, textures and cooling histories of Columbia River basalt flows. *Geol. Soc. Amer. Bull.*, 97, 1144-1155.
- Loomis, T.P. (1982) Numerical simulations of crystallization processes of plagioclase in complex melts. *Contrib. Mineral. Petrol.*, 81, 219-229.
- Maaloe, S., Tumyr, O. and James, D. (1989) Population density and zoning of olivine phenocrysts in tholeiites from Kauai, Hawaii. *Contrib. Mineral. Petrol.*, 101, 176-186.
- Magill, J.H., Li, H.M. and Gandica, A. (1973) A corresponding states equation for crystallization kinetics. *J. Crystal Growth*, 19, 361-364.
- Mangan, M.T. (1990) Crystal size distribution systematics and the determination of magma storage times: the 1959 eruption of Kilauea volcano, Hawaii. *J. Volcanol. Geotherm. Res.* (in press).
- Marsh, B.D. (1981) On the crystallinity, probability of occurrence, and rheology of lava and magma. *Contrib. Mineral. Petrol.*, 78, 85-98.
- Marsh, B.D. (1988a) Crystal capture, sorting, and retention in convecting magma. *Geol. Soc. Amer. Bull.*, 100, 1720-1737.
- Marsh, B.D. (1988b) Crystal size distributions (CSD) in rocks and the kinetics and dynamics of crystallization I. Theory. *Contrib. Mineral. Petrol.*, 99, 277-291.
- McKeown, D.A., Waychunas, G.A. and Brown, G.E. (1985) EXAFS study of the coordination environment of aluminum in a series of silica-rich glasses and selected minerals with the $\text{Na}_2\text{O}-\text{Al}_2\text{O}_3-\text{SiO}_2$ system. *J. Non-crystalline Solids*, 74, 349-371.
- Meyer, E. (1986) Adiabatic nucleation. *J. Crystal Growth*, 74, 425-438.
- Morse, J.W. and Casey, W.H. (1988) Ostwald processes and mineral paragenesis in sediments. *Amer. J. Sci.*, 288, 537-560.
- Muncill, G.E. and Lasaga, A.C. (1987) Crystal-growth kinetics of plagioclase in igneous systems: One-atmosphere experiments and application of a simplified growth model. *Amer. Mineral.*, 72, 299-311.
- Muncill, G.E. and Lasaga, A.C. (1988) Crystal-growth kinetics of plagioclase in igneous systems: Isothermal H_2O -saturated experiments and extension of a growth model to complex silicate melts. *Amer. Mineral.*, 73, 982-992.
- Nabalek, P.I., Taylor, L.A. and Lofgren, G.E. (1978) Nucleation and growth of plagioclase and the development of textures in a high-alumina basaltic melt. *Proc. Lunar Planet. Sci. Conf.* 9th, 725-741.
- Neilson, G.F. and Weinberg, M.C. (1979) A test of classical nucleation theory: Crystal nucleation of lithium disilicate glass. *J. Non-Crystalline Solids*, 34, 137-147.
- Nittmann, J. and Stanley, H.E. (1986) Tip splitting without interfacial tension and dendritic growth patterns arising from molecular anisotropy. *Nature*, 321, 663-668.
- Nixon, G.T. and Pearce, T.H. (1987) Laser-interferometry study of oscillatory zoning in plagioclase: The record of magma mixing and phenocryst recycling in calc-alkaline magma chambers, Iztaicuiatl volcano, Mexico. *Amer. Mineral.*, 72, 1144-1162.
- Pearce, T.H. (1987) The theory of zoning patterns in magmatic minerals using olivine as an example. *Contrib. Mineral. Petrol.*, 97, 451-459.
- Pearce, T.H., Griffin, M.P., Kolisnik, A.M. (1987a) Magmatic crystal stratigraphy and constraints on magma chamber dynamics: Laser interference results on individual phenocrysts. *J. Geophys. Res.*, 92, 13745-13752.
- Pearce, T.H., Russell, J.K. and Wolfson, I. (1987b) Laser-interference and Nomarski interference imaging of zoning profiles in plagioclase phenocrysts from the May 18, 1980, eruption of Mount St. Helens, Washington. *Amer. Mineral.*, 72, 1131-1143.
- Peterson T.D. (1990) Petrology and genesis of natrocarbonatite. *Contrib. Mineral. Petrol.*, 105, 143-155.
- Petrunk, W. (1989) Image Analysis in Earth Sciences. *Mineral. Assoc. Canada, Short Course*, 16, 156 pp.
- Randolph, A.D. and Larson, M.A. (1971) *Theory of Particulate Processes*. Academic Press, New York, 251 pp.

- Ripley, B.D. (1981) *Spatial Statistics*. John Wiley and Sons, New York, 252 pp.
- Rowlands, E.G. and James, P.F. (1979a) Analysis of steady state crystal nucleation rates in glasses. Part 1. Methods of analysis and application to lithium disilicate glass. *Phys. Chem. Glass.*, 20, 1-8.
- Rowlands, E.G. and James, P.F. (1979b) Analysis of steady state crystal nucleation rates in glasses. Part 2. Further comparison between theory and experiment for lithium disilicate glass. *Phys. Chem. Glass.*, 20, 9-14.
- Russ, J.C. (1986) *Practical Stereology*. Plenum Press, New York, 185 pp.
- Russ, J.C. (1988) *Computer Assisted Microscopy: The Measurement and Analysis of Images*. North Carolina State University, Raleigh.
- Rutherford, M.J. and Devine, J.D. (1988) The May 18, 1980, eruption of Mount St. Helens 3. Stability and chemistry of amphibole in the magma chamber. *J. Geophys. Res.*, 93, 11949-11959.
- Sahagian, D.L. (1985) Bubble migration and coalescence during solidification of basaltic lava flows. *J. Geol.*, 93, 205-211.
- Sahagian, D.L., Anderson, A.T. and Ward, B. (1989) Bubble coalescence in basalt flows: comparison of a numerical model with natural examples. *Bull. Volcanol.*, 52, 49-56.
- Saltykov, S.A. (1967) The determination of the size distributions of particles in an opaque material from a measurement of the size distribution of their sections. In: *Stereology*. Elias, H., ed., Springer, Berlin, p.163.
- Sander, L.M. (1986) Fractal growth processes. *Nature*, 322, 789-793.
- Sarda, P. and Graham, D. (1990) Mid-ocean ridge popping rocks: implications for degassing at ridge crests. *Earth Planet. Sci. Lett.*, 97, 268-289.
- Schiffman, P. and Lofgren, G.E. (1982) Dynamic crystallization studies on the Grande Ronde pillow basalts, central Washington. *J. Geol.*, 90, 49-78.
- Schmelzer, J. and Schweitzer, F. (1987) Ostwald ripening of bubbles in liquid-gas solutions. *J. Non-Equilib. Thermodyn.*, 12, 255-270.
- Schmelzer, J. and Ulbricht, H. (1987) Thermodynamics of finite systems and the kinetics of first-order phase transitions. *J. Coll. Inter. Sci.*, 117, 325-338.
- Serra, J. (1982) *Image Analysis and Mathematical Morphology*. Academic Press, New York, 610pp.
- Shaw, H.R. (1972) Viscosities of magmatic silicate liquids: An empirical method of prediction. *Amer. J. Sci.*, 272, 870-893.
- Skolnick, M., Brechner, E. and Marineau, P. (1988) Morphological algorithms for analysis of geological phase structure. S.P.I.E. Conf. on Visual Communication and Image Processing, 154-161.
- Smith, G.L., Neilson, G.F. and Weinberg, M.C. (1987) Crystal nucleation in lithium borate glass. *Phys. Chem. Glass.*, 28, 257-261.
- Sparks, R.S.J. (1978) The dynamics of bubble formation and growth in magmas: A review and analysis. *J. Volcanol. Geotherm. Res.*, 3, 1-37.
- Sparks, R.S.J. and Pinkerton, H. (1978) Effects of degassing on rheology of basaltic lava. *Nature*, 276, 385-386.
- Spohn, T., Hort, M. and Fischer, H. (1988) Nucleation simulation of the crystallization of multicomponent melts in thin dikes or sills I. The liquidus phase. *J. Geophys. Res.*, 93, 4880-4894.
- Stamatopoulou-Seymour, K., Vlassopoulos, D., Pearce, T.H. and Rice, C. (1990) The record of magma chamber processes in plagioclase phenocrysts at Thera Volcano, Aegean Volcanic Arc, Greece. *Contrib. Mineral. Petrol.*, 104, 73-84.
- Stebbins, J.F., Carmichael, I.S.E. and Moret, L.K. (1984) Heat capacities and entropies of silicate liquids and glasses. *Contrib. Mineral. Petrol.*, 86, 131-148.
- Stebbins, J.F., Weill, D.F., Carmichael, I.S.E. and Moret, L.K. (1982) High temperature heat contents and heat capacities of liquids and glasses in the system $\text{NaAlSi}_3\text{O}_8$ - $\text{CaAl}_2\text{Si}_2\text{O}_8$. *Contrib. Mineral. Petrol.*, 80, 276-284.
- Sterio, D.C. (1984) The unbiased estimation of number and sizes of arbitrary particles using the disector. *J. Microsc.*, 134, 127-136.
- Sunagawa, I. (1977) Natural crystallization. *J. Crystal Growth*, 42, 214-223.
- Swanson, S.E. (1977) Relation of nucleation and crystal-growth rate to the development of granitic textures. *Amer. Mineral.*, 62, 966-978.
- Swanson, S.E., Naney, M.T., Westrich, H.R. and Eichelberger, J.C. (1989) Crystallization history of Obsidian Dome, Inyo Domes, California. *Bull. Volcanol.*, 51, 161-176.
- Taniguchi, H. (1990) Application of the WLF-equation to the viscous behavior of diopside-anorthite melt. *EOS, Trans. Amer. Geophys. Union*, 71, 951.
- Taylor, C.C. (1983) A new method for unfolding sphere size distributions. *J. Microscopy*, 131, 57-66.
- Toramaru, A. (1989) Vesiculation process and bubble size distribution in ascending magmas with constant velocities. *J. Geophys. Res.*, 94, 17523-17542.
- Tsuchiyama, A. (1983) Crystallization kinetics in the system $\text{CaMgSi}_2\text{O}_6$ - $\text{CaAl}_2\text{Si}_2\text{O}_8$: the delay in nucleation of diopside and anorthite. *Amer. Mineral.*, 70, 687-698.
- Tsuchiyama, A. (1985a) Partial melting kinetics of plagioclase-diopside pairs. *Contrib. Mineral. Petrol.*, 91, 12-23.
- Tsuchiyama, A. (1985b) Dissolution kinetics of plagioclase in the melt of the system diopside-albite-anorthite, and origin of dusty plagioclase in andesites. *Contrib. Mineral. Petrol.*, 89, 1-16.
- Tsuchiyama, A. (1985c) Crystallization kinetics in the system $\text{CaMgSi}_2\text{O}_6$ - $\text{CaAl}_2\text{Si}_2\text{O}_8$: development of zoning and kinetic effects on element partitioning. *Amer. Mineral.*, 70, 474-486.

- Tsukamoto, K., Abe, T. and Sunagawa, I. (1983) In situ observation of crystals growing in high temperature melts or solutions. *J. Crystal Growth*, 63, 215-218.
- Turcotte, D.L. and Schubert, G. (1982) *Geodynamics*. John Wiley and Sons, New York, 450 pp.
- Turnbull, D. (1987) Modes of formation of amorphous solids: An overview. *Diffusion and Defect Data*, 53/54, 9-20.
- Uhlmann, D.R. (1982) Crystal growth in glass-forming systems: a ten year perspective. In: *Nucleation and Crystallization in Glasses*. Simmons, J.R., Uhlmann, D.R., Beall, G.H., eds., Amer. Ceram. Soc., Columbus, Ohio, 80-124.
- Uhlmann, D.R. and Yinnon, H. (1983) The formation of glasses. In: *Glass: Science and Technology*. Uhlmann, D.R. and Kreidl, N.J., eds., Academic Press, New York, 1-47.
- Underwood, E.E. (1970) *Quantitative Stereology*. Addison-Wesley Publ. Co., Reading, Massachusetts, 274 pp.
- Vander Voort, G.F. (1984) *Metallography: Principles and Practice*. McGraw-Hill Book Co., New York, 410-508.
- Volterra, V. and Cooper, A.R. (1985) Numerical calculation of induction times for crystallization of glasses. *J. Non-Crystalline Solids*, 74, 85-95.
- Walker, D., Kirkpatrick, R.J., Longhi, J. and Hays, J.F. (1976) Crystallization history of lunar picritic basalt sample 12002: Phase-equilibria and cooling-rate studies. *Geol. Soc. Amer. Bull.*, 87, 646-656.
- Walker, D., Powell, M.A., Lofgren, G.E. and Hays, J.F. (1978) Dynamic crystallization of a eucrite basalt. *Proc. Lunar Sci. Conf.* 9th, 1369-1391.
- Walker, G.P.L. (1989) Spongy pahoehoe in Hawaii: a study of vesicle-distribution patterns in basalt and their significance. *Geology*, 15, 84-87.
- Watson, E.B. and Baker, D.R. (1990) Chemical diffusion in magmas: an overview of experimental results and geochemical implications. In: *Advances in Physical Geochemistry*. Kushiro, I. and Perchuk, L. (eds.), Springer, Berlin, 6 (in press).
- Weibel, E.R. (1979) *Stereological Methods, v.1: Practical Methods for Biological Morphology*. Academic Press, New York, 415 pp.
- Weibel, E.R. (1980) *Stereological Methods, v.2: Theoretical Foundations*. Academic Press, New York, 340 pp.
- Weinberg, M.C. (1986) On the location of the maximum homogeneous crystal nucleation temperature. *J. Non-Crystalline Solids*, 83, 98-113.
- Weinberg, M.C. and Zanotto, E.D. (1989) Re-examination of the temperature dependence of the classical nucleation rate: Homogeneous crystal nucleation in glass. *J. Non-Cryst. Sol.*, 108, 99-108.
- Weinberg, M.C., Neilson, G.F. and Uhlmann, D.R. (1984) Homogeneous versus heterogeneous crystal nucleation in $\text{Li}_2\text{O} \cdot 2\text{SiO}_2$ glass. *J. Non-Crystalline Solids*, 68, 115-122.
- Wicksell, S.D. (1925) The corpuscle problem I. A mathematical study of a biometric problem. *Biometrika*, 17, 84-99.
- Winkler, H.G.F. (1949) Crystallization of basaltic magma as recorded by variation in crystal size in dikes. *Mineral. Mag.*, 28, 557-574.
- Wright, T.L. and Fiske, R.S. (1971) Origin of the differentiated and hybrid lavas of Kilauea Volcano, Hawaii. *J. Petrol.*, 12, 1-65.
- Youngquist, G.R. (1984) *Advances in Crystallization from Solutions*. AIChE Symposium Series 80, 126 pp.
- Zanotto, E.D. (1987) Isothermal and adiabatic nucleation in glass. *J. Non-Crystalline Solids*, 89, 361-370.
- Zanotto, E.D. and James, P.F. (1985) Experimental tests of the classical nucleation theory for glasses. *J. Non-Crystalline Solids*, 74, 373-394.
- Zanotto, E.D. and Galhardi, A. (1988) Experimental test of the general theory of transformation kinetics: Homogeneous nucleation in a $\text{Na}_2\text{O} \cdot 2\text{CaO} \cdot 3\text{SiO}_2$ glass. *J. Non-crystalline Solids*, 104, 73-80.
- Zanotto, E.D. and James, P.F. (1988) Experimental test of the general theory of transformation kinetics: Homogeneous nucleation in a $\text{BaO} \cdot 2\text{SiO}_2$ glass. *J. Non-crystalline Solids*, 104, 70-72.
- Zanotto, E.D. and Weinberg, M.C. (1988) Saturation effects in homogeneous and heterogeneous crystal nucleation. *J. Non-Crystalline Solids*, 105, 53-62.
- Zhang, Y., Walker, D. and Lesher, C.E. (1989) Diffusive crystal dissolution. *Contrib. Mineral. Petrol.*, 102, 492-513.

